

Advances in Civil Engineering

Ultimate Load-Carrying Capacity of Structures

Lead Guest Editor: Lingkun Chen

Guest Editors: Zhiyong Chen, Peng Liu, and Ying Chen





Ultimate Load-Carrying Capacity of Structures

Advances in Civil Engineering

Ultimate Load-Carrying Capacity of Structures

Lead Guest Editor: Lingkun Chen

Guest Editors: Zhiyong Chen, Peng Liu, and Ying Chen



Copyright © 2023 Hindawi Limited. All rights reserved.

This is a special issue published in "Advances in Civil Engineering." All articles are open access articles distributed under the Creative Commons Attribution License, which permits unrestricted use, distribution, and reproduction in any medium, provided the original work is properly cited.






Chief Editor

Cumaraswamy Vipulanandan, USA
















Associate Editors

Chiara Bedon , Italy
Constantin Chalioris , Greece
Ghassan Chehab , Lebanon
Ottavia Corbi, Italy
Mohamed ElGawady , USA
Husnain Haider , Saudi Arabia
Jian Ji , China
Jiang Jin , China
Shazim A. Memon , Kazakhstan
Hossein Moayedi , Vietnam
Sanjay Nimbalkar, Australia
Giuseppe Oliveto , Italy
Alessandro Palmeri , United Kingdom
Arnaud Perrot , France
Hugo Rodrigues , Portugal
Victor Yepes , Spain
Xianbo Zhao , Australia

Academic Editors

José A.F.O. Correia, Portugal
Glenda Abate, Italy
Khalid Abdel-Rahman , Germany
Ali Mardani Aghabaglou, Turkey
José Aguiar , Portugal
Afaq Ahmad , Pakistan
Muhammad Riaz Ahmad , Hong Kong
Hashim M.N. Al-Madani , Bahrain
Luigi Aldieri , Italy
Angelo Aloisio , Italy
Maria Cruz Alonso, Spain
Filipe Amarante dos Santos , Portugal
Serji N. Amirkhania, USA
Eleftherios K. Anastasiou , Greece
Panagiotis Ch. Anastasopoulos , USA
Mohamed Moafak Arbili , Iraq
Farhad Aslani , Australia
Siva Avudaiappan , Chile
Ozgur BASKAN , Turkey
Adewumi Babafemi, Nigeria
Morteza Bagherpour, Turkey
Qingsheng Bai , Germany
Nicola Baldo , Italy
Daniele Baraldi , Italy

Eva Barreira , Portugal
Emilio Bastidas-Arteaga , France
Rita Bento, Portugal
Rafael Bergillos , Spain
Han-bing Bian , China
Xia Bian , China
Huseyin Bilgin , Albania
Giovanni Biondi , Italy
Hugo C. Biscaia , Portugal
Rahul Biswas , India
Edén Bojórquez , Mexico
Giosuè Boscato , Italy
Melina Bosco , Italy
Jorge Branco , Portugal
Bruno Briseghella , China
Brian M. Broderick, Ireland
Emanuele Brunesi , Italy
Quoc-Bao Bui , Vietnam
Tan-Trung Bui , France
Nicola Buratti, Italy
Gaochuang Cai, France
Gladis Camarini , Brazil
Alberto Campisano , Italy
Qi Cao, China
Qixin Cao, China
Iacopo Carnacina , Italy
Alessio Cascardi, Italy
Paolo Castaldo , Italy
Nicola Cavalagli , Italy
Liborio Cavaleri , Italy
Anush Chandrappa , United Kingdom
Wen-Shao Chang , United Kingdom
Muhammad Tariq Amin Chaudhary, Kuwait
Po-Han Chen , Taiwan
Qian Chen , China
Wei Tong Chen , Taiwan
Qixiu Cheng, Hong Kong
Zhanbo Cheng, United Kingdom
Nicholas Chileshe, Australia
Prinya Chindaprasirt , Thailand
Corrado Chisari , United Kingdom
Se Jin Choi , Republic of Korea
Heap-Yih Chong , Australia
S.H. Chu , USA
Ting-Xiang Chu , China

Zhaofei Chu , China
Wonseok Chung , Republic of Korea
Donato Ciampa , Italy
Gian Paolo Cimellaro, Italy
Francesco Colangelo, Italy
Romulus Costache , Romania
Liviu-Adrian Cotfas , Romania
Antonio Maria D'Altri, Italy
Bruno Dal Lago , Italy
Amos Darko , Hong Kong
Arka Jyoti Das , India
Dario De Domenico , Italy
Gianmarco De Felice , Italy
Stefano De Miranda , Italy
Maria T. De Risi , Italy
Tayfun Dede, Turkey
Sadik O. Degertekin , Turkey
Camelia Delcea , Romania
Cristoforo Demartino, China
Giuseppe Di Filippo , Italy
Luigi Di Sarno, Italy
Fabio Di Trapani , Italy
Aboelkasim Diab , Egypt
Thi My Dung Do, Vietnam
Giulio Dondi , Italy
Jiangfeng Dong , China
Chao Dou , China
Mario D'Aniello , Italy
Jingtao Du , China
Ahmed Elghazouli, United Kingdom
Francesco Fabbrocino , Italy
Flora Faleschini , Italy
Dingqiang Fan, Hong Kong
Xueping Fan, China
Qian Fang , China
Salar Farahmand-Tabar , Iran
Ilenia Farina, Italy
Roberto Fedele, Italy
Guang-Liang Feng , China
Luigi Fenu , Italy
Tiago Ferreira , Portugal
Marco Filippo Ferrotto, Italy
Antonio Formisano , Italy
Guoyang Fu, Australia
Stefano Galassi , Italy

Junfeng Gao , China
Meng Gao , China
Giovanni Garcea , Italy
Enrique García-Macías, Spain
Emilio García-Taengua , United Kingdom
DongDong Ge , USA
Khaled Ghaedi, Malaysia
Khaled Ghaedi , Malaysia
Gian Felice Giaccu, Italy
Agathoklis Giaralis , United Kingdom
Ravindran Gobinath, India
Rodrigo Gonçalves, Portugal
Peilin Gong , China
Belén González-Fonteboa , Spain
Salvatore Grasso , Italy
Fan Gu, USA
Erhan Güneyisi , Turkey
Esra Mete Güneyisi, Turkey
Pingye Guo , China
Ankit Gupta , India
Federico Gusella , Italy
Kemal Hacıfendioglu, Turkey
Jianyong Han , China
Song Han , China
Asad Hanif , Macau
Hadi Hasanzadehshooiili , Canada
Mostafa Fahmi Hassanein, Egypt
Amir Ahmad Hedayat , Iran
Khandaker Hossain , Canada
Zahid Hossain , USA
Chao Hou, China
Biao Hu, China
Jiang Hu , China
Xiaodong Hu, China
Lei Huang , China
Cun Hui , China
Bon-Gang Hwang, Singapore
Jijo James , India
Abbas Fadhil Jasim , Iraq
Ahad Javanmardi , China
Krishnan Prabhakan Jaya, India
Dong-Sheng Jeng , Australia
Han-Yong Jeon, Republic of Korea
Pengjiao Jia, China
Shaohua Jiang , China

MOUSTAFA KASSEM , Malaysia
Mosbeh Kaloop , Egypt
Shankar Karuppanan , Ethiopia
John Kechagias , Greece
Mohammad Khajehzadeh , Iran
Afzal Husain Khan , Saudi Arabia
Mehran Khan , Hong Kong
Manoj Khandelwal, Australia
Jin Kook Kim , Republic of Korea
Woosuk Kim , Republic of Korea
Vaclav Koci , Czech Republic
Loke Kok Foong, Vietnam
Hailing Kong , China
Leonidas Alexandros Kouris , Greece
Kyriakos Kourousis , Ireland
Moacir Kripka , Brazil
Anupam Kumar, The Netherlands
Emma La Malfa Ribolla, Czech Republic
Ali Lakirouhani , Iran
Angus C. C. Lam, China
Thanh Quang Khai Lam , Vietnam
Luciano Lamberti, Italy
Andreas Lampropoulos , United Kingdom
Raffaele Landolfo, Italy
Massimo Latour , Italy
Bang Yeon Lee , Republic of Korea
Eul-Bum Lee , Republic of Korea
Zhen Lei , Canada
Leonardo Leonetti , Italy
Chun-Qing Li , Australia
Dongsheng Li , China
Gen Li, China
Jiale Li , China
Minghui Li, China
Qingchao Li , China
Shuang Yang Li , China
Sunwei Li , Hong Kong
Yajun Li , China
Shun Liang , China
Francesco Liguori , Italy
Jae-Han Lim , Republic of Korea
Jia-Rui Lin , China
Kun Lin , China
Shibin Lin, China

Tzu-Kang Lin , Taiwan
Yu-Cheng Lin , Taiwan
Hexu Liu, USA
Jian Lin Liu , China
Xiaoli Liu , China
Xuemei Liu , Australia
Zaobao Liu , China
Zhuang-Zhuang Liu, China
Diego Lopez-Garcia , Chile
Cristiano Loss , Canada
Lyan-Ywan Lu , Taiwan
Jin Luo , USA
Yanbin Luo , China
Jianjun Ma , China
Junwei Ma , China
Tian-Shou Ma, China
Zhongguo John Ma , USA
Maria Macchiaroli, Italy
Domenico Magisano, Italy
Reza Mahinroosta, Australia
Yann Malecot , France
Prabhat Kumar Mandal , India
John Mander, USA
Iman Mansouri, Iran
André Dias Martins, Portugal
Domagoj Matesan , Croatia
Jose Matos, Portugal
Vasant Matsagar , India
Claudio Mazzotti , Italy
Ahmed Mebarki , France
Gang Mei , China
Kasim Mermerdas, Turkey
Giovanni Minafò , Italy
Masoomah Mirrashid , Iran
Abbas Mohajerani , Australia
Fadzli Mohamed Nazri , Malaysia
Fabrizio Mollaioli , Italy
Rosario Montuori , Italy
H. Naderpour , Iran
Hassan Nasir , Pakistan
Hossein Nassiraei , Iran
Satheeskumar Navaratnam , Australia
Ignacio J. Navarro , Spain
Ashish Kumar Nayak , India
Behzad Nematollahi , Australia

Chayut Ngamkhanong , Thailand
Trung Ngo, Australia
Tengfei Nian, China
Mehdi Nikoo , Canada
Youjun Ning , China
Olugbenga Timo Oladinrin , United Kingdom
Oladimeji Benedict Olalusi, South Africa
Timothy O. Olawumi , Hong Kong
Alejandro Orfila , Spain
Maurizio Orlando , Italy
Siti Aminah Osman, Malaysia
Walid Oueslati , Tunisia
SUVASH PAUL , Bangladesh
John-Paris Pantouvakis , Greece
Fabrizio Paolacci , Italy
Giuseppina Pappalardo , Italy
Fulvio Parisi , Italy
Dimitrios G. Pavlou , Norway
Daniele Pellegrini , Italy
Gatheeshgar Perampalam , United Kingdom
Daniele Perrone , Italy
Giuseppe Piccardo , Italy
Vagelis Plevris , Qatar
Andrea Pranno , Italy
Adolfo Preciado , Mexico
Chongchong Qi , China
Yu Qian, USA
Ying Qin , China
Giuseppe Quaranta , Italy
Krishanu ROY , New Zealand
Vlastimir Radonjanin, Serbia
Carlo Rainieri , Italy
Rahul V. Ralegaonkar, India
Raizal Saifulnaz Muhammad Rashid, Malaysia
Alessandro Rasulo , Italy
Chonghong Ren , China
Qing-Xin Ren, China
Dimitris Rizos , USA
Geoffrey W. Rodgers , New Zealand
Pier Paolo Rossi, Italy
Nicola Ruggieri , Italy
JUNLONG SHANG, Singapore

Nikhil Saboo, India
Anna Saetta, Italy
Juan Sagaseta , United Kingdom
Timo Saksala, Finland
Mostafa Salari, Canada
Ginevra Salerno , Italy
Evangelos J. Sapountzakis , Greece
Vassilis Sarhosis , United Kingdom
Navaratnarajah Sathiparan , Sri Lanka
Fabrizio Scozzese , Italy
Halil Sezen , USA
Payam Shafigh , Malaysia
M. Shahria Alam, Canada
Yi Shan, China
Hussein Sharaf, Iraq
Mostafa Sharifzadeh, Australia
Sanjay Kumar Shukla, Australia
Amir Si Larbi , France
Okan Sirin , Qatar
Piotr Smarzewski , Poland
Francesca Sollecito , Italy
Rui Song , China
Tian-Yi Song, Australia
Flavio Stochino , Italy
Mayank Sukhija , USA
Piti Sukontasukkul , Thailand
Jianping Sun, Singapore
Xiao Sun , China
T. Tafsirojjan , Australia
Fujiao Tang , China
Patrick W.C. Tang , Australia
Zhi Cheng Tang , China
Weerachart Tangchirapat , Thailand
Xiixin Tao, China
Piergiorgio Tataranni , Italy
Elisabete Teixeira , Portugal
Jorge Iván Tobón , Colombia
Jing-Zhong Tong, China
Francesco Trentadue , Italy
Antonello Troncone, Italy
Majbah Uddin , USA
Tariq Umar , United Kingdom
Muahmmad Usman, United Kingdom
Muhammad Usman , Pakistan
Mucteba Uysal , Turkey

Ilaria Venanzi , Italy
Castorina S. Vieira , Portugal
Valeria Vignali , Italy
Claudia Vitone , Italy
Liwei WEN , China
Chunfeng Wan , China
Hua-Ping Wan, China
Roman Wan-Wendner , Austria
Chaohui Wang , China
Hao Wang , USA
Shiming Wang , China
Wayne Yu Wang , United Kingdom
Wen-Da Wang, China
Xing Wang , China
Xiuling Wang , China
Zhenjun Wang , China
Xin-Jiang Wei , China
Tao Wen , China
Weiping Wen , China
Lei Weng , China
Chao Wu , United Kingdom
Jiangyu Wu, China
Wangjie Wu , China
Wenbing Wu , China
Zhixing Xiao, China
Gang Xu, China
Jian Xu , China
Panpan , China
Rongchao Xu , China
HE YONGLIANG, China
Michael Yam, Hong Kong
Hailu Yang , China
Xu-Xu Yang , China
Hui Yao , China
Xinyu Ye , China
Zhoujing Ye, China
Gürol Yildirim , Turkey
Dawei Yin , China
Doo-Yeol Yoo , Republic of Korea
Zhanping You , USA
Afshar A. Yousefi , Iran
Xinbao Yu , USA
Dongdong Yuan , China
Geun Y. Yun , Republic of Korea

Hyun-Do Yun , Republic of Korea
Cemal YİĞİT , Turkey
Paolo Zampieri, Italy
Giulio Zani , Italy
Mariano Angelo Zanini , Italy
Zhixiong Zeng , Hong Kong
Mustafa Zeybek, Turkey
Henglong Zhang , China
Jiupeng Zhang, China
Tingting Zhang , China
Zengping Zhang, China
Zetian Zhang , China
Zhigang Zhang , China
Zhipeng Zhao , Japan
Jun Zhao , China
Annan Zhou , Australia
Jia-wen Zhou , China
Hai-Tao Zhu , China
Peng Zhu , China
QuanJie Zhu , China
Wenjun Zhu , China
Marco Zucca, Italy
Haoran Zuo, Australia
Junqing Zuo , China
Robert Černý , Czech Republic
Süleyman İpek , Turkey


Contents

Corrigendum to “Research on Integrated Design of Modular Steel Structure Container Buildings Based on BIM”

Meng Su, Bauer Yang, and Xiaomin Wang

Corrigendum (4 pages), Article ID 9841763, Volume 2023 (2023)

Path Attenuation and Source Characteristics during the 2019 Sichuan Changning Earthquake Sequence in China

Zhijun Jiang , Lei Zhang , and Qi Zhang 






Research Article (11 pages), Article ID 8141103, Volume 2022 (2022)

Effects of Stiffener Type on Fatigue Resistance of Steel-UHPC Composite Bridge Decks

Xiugui Sun , Jianhua Hu , Yu Li, and Guoping Huang 

Research Article (11 pages), Article ID 6606129, Volume 2022 (2022)

Hysteretic Behavior of H-Shaped Honeycombed Steel Web Composite Columns with Rectangular Concrete-Filled Steel Tube Flanges

Jing Ji, Yubo Lin , Liangqin Jiang , Wen Li, Hongguo Ren , Ruili Wang, Zihao Wang , MaoMao Yang, and Chenyu Yu 


Research Article (24 pages), Article ID 1546263, Volume 2022 (2022)

Research on Integrated Design of Modular Steel Structure Container Buildings Based on BIM

Meng Su , Bauer Yang , and Xiaomin Wang 





Research Article (13 pages), Article ID 4574676, Volume 2022 (2022)

Bearing Behavior of H-Shaped Honeycombed Steel Web Composite Columns with Rectangular Concrete-Filled Steel Tube Flanges under Eccentric Compression Load

Jing Ji, Chenyu Yu, Liangqin Jiang, Jiedong Zhan, Hongguo Ren , Sixue Hao, Shaojie Fan , Li Jiang, Yubo Lin, and Lingjie He


Research Article (21 pages), Article ID 2965131, Volume 2022 (2022)

Experimental and Numerical Investigation on Dynamic Properties and Human-Induced Vibrations of an Asymmetric Steel-Plated Stress-Ribbon Footbridge

Yi Zhang , Wei He , Jiewen Zhang , and Hua Dong 

Research Article (21 pages), Article ID 2028378, Volume 2021 (2021)

Sandy Soil Liquefaction Prediction Based on Clustering-Binary Tree Neural Network Algorithm Model

Yu Wang and Jiachen Wang 







Research Article (6 pages), Article ID 3603853, Volume 2021 (2021)

Influence of Water-Structure and Soil-Structure Interaction on Seismic Performance of Sea-Crossing Continuous Girder Bridge

Jie Guo, Kumpeng Wang , Hongtao Liu, and Nan Zhang 


Research Article (12 pages), Article ID 7215289, Volume 2021 (2021)

“Relief-Retaining” Control Technology of Floor Heave in Mining Roadway with Soft Rock: A Case Study

Ai Chen , Xuebin Li , Xuesheng Liu , Yunliang Tan , Ke Xu , and Honglei Wang 

Research Article (13 pages), Article ID 1455052, Volume 2021 (2021)

Equivalent Resilient Modulus Inversion and Calculation of Different Asphalt Pavement Structures

Mingming Cao , Wanqing Huang, Yiwen Zou, and Zhiyong Wu


Research Article (9 pages), Article ID 2620559, Volume 2021 (2021)

Research on Hysteretic Models for Prestressed and Non-Prestressed Steel Reinforced Concrete Frames

Huihui Luo  and Kun Wang 

Research Article (11 pages), Article ID 9442180, Volume 2021 (2021)

Numerical Analysis for Dynamic Response of In Situ Blasting Expansion of Large Cross-Section Tunnel with Small Net Distance

Min Zhang 



Research Article (7 pages), Article ID 2896782, Volume 2021 (2021)

Girder Longitudinal Movement and Its Factors of Suspension Bridge under Vehicle Load

Guoping Huang , Jianhua Hu , Haibo Liu, and Xiugui Sun



Research Article (14 pages), Article ID 1443996, Volume 2021 (2021)

Experimental and Numerical Study on Ultimate Shear Load Carrying Capacity of Corroded RC Beams

Zhanzhan Tang , Zhixiang He, Zheng Chen, Lingkun Chen , Hanyang Xue, and Hanqing Zhuge


Research Article (12 pages), Article ID 4848483, Volume 2021 (2021)

Analysis on the Influence of Increasing Seismic Fortification Intensity on Seismic Performance of Underground Station

Ying Zeng , Shiguang Xu , and Shiqian Yin


Research Article (7 pages), Article ID 8158607, Volume 2021 (2021)

Stability Analysis of the Shiliushubao Landslide Based on Deformation Characteristics and External Trigger Factors in the Three Gorges Reservoir

Guilin Luo , Guangming Ren, Xiaojun Bao, Xili Yang, and Teng Liu


Research Article (12 pages), Article ID 2714918, Volume 2021 (2021)

Modulus Inversion Layer by Layer of Different Asphalt Pavement Structures

Mingming Cao , Wanqing Huang, Yiwen Zou, and Guomin Liu

Research Article (10 pages), Article ID 1928383, Volume 2021 (2021)


Calculation Model of Shear Capacity of Multiple Composite Core Column Joints Based on Softened Tension-Compression Bar Model

Xu Wentao  and Yang Chengyu

Research Article (11 pages), Article ID 6832188, Volume 2021 (2021)

Contents

Improvement of Automatic Calculation Method of CASE Bearing Capacity

Guosong Liu  and Junlin Wang 

Research Article (8 pages), Article ID 3667193, Volume 2021 (2021)

Corrigendum

Corrigendum to “Research on Integrated Design of Modular Steel Structure Container Buildings Based on BIM”

Meng Su,¹ Bauer Yang,² and Xiaomin Wang³

¹*School of Architectural Science and Engineering, Yangzhou University, Yangzhou 225127, China*

²*Yangzhou Tonglee Reefer Container Co Ltd., Yangzhou 225102, China*

³*Jiangsu Provincial Architectural D&R Institute Co Ltd., Nanjing 210019, China*

Correspondence should be addressed to Meng Su; 834157071@qq.com

Received 19 September 2022; Accepted 19 September 2022; Published 10 February 2023

Copyright © 2023 Meng Su et al. This is an open access article distributed under the Creative Commons Attribution License, which permits unrestricted use, distribution, and reproduction in any medium, provided the original work is properly cited.

In the article titled “Research on Integrated Design of Modular Steel Structure Container Buildings Based on BIM” [1], there was an error in the legends of Figures 7–10.

Specifically, these figure legends were included in the wrong order. The wording of all figure legends and the images in all figures were correct, but the figure legends were applied to the incorrect figure.

The correct figure and legends are as follows.

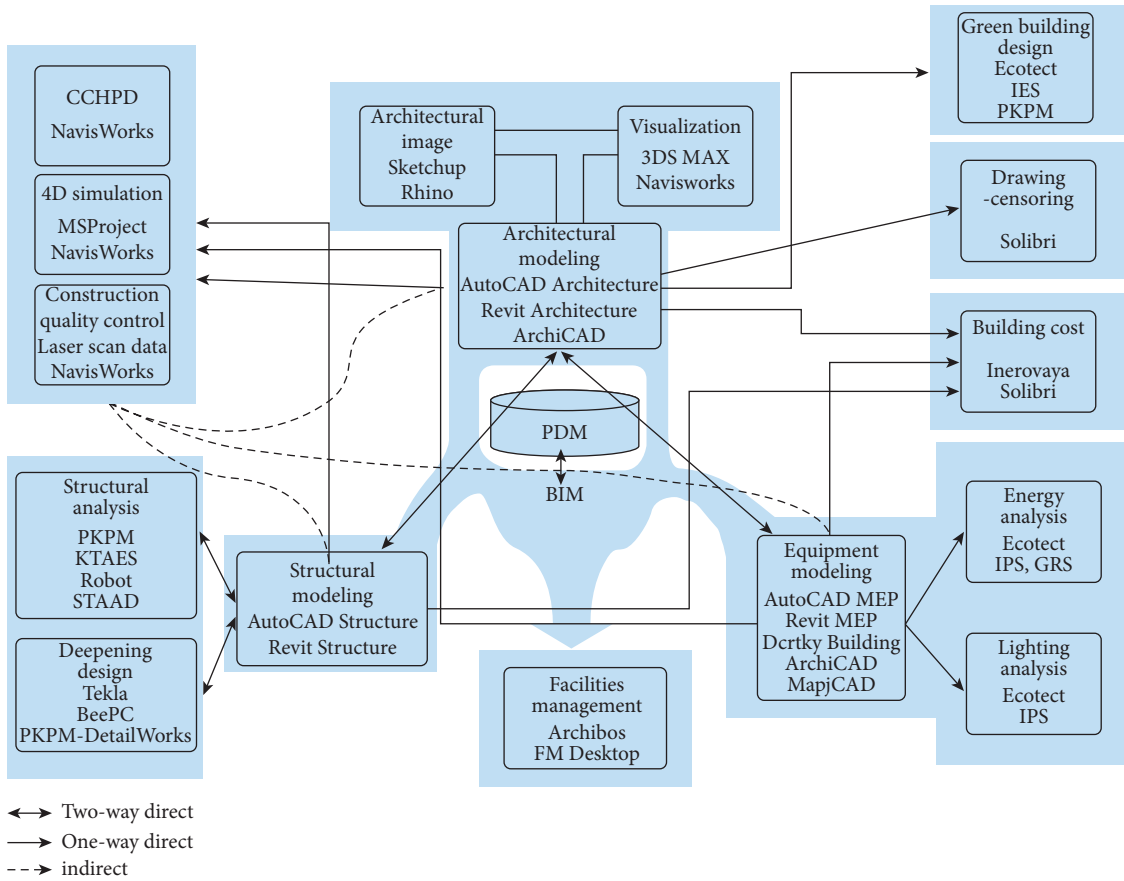


FIGURE 7: Integrated design information and software relationship based on BIM and PDM.

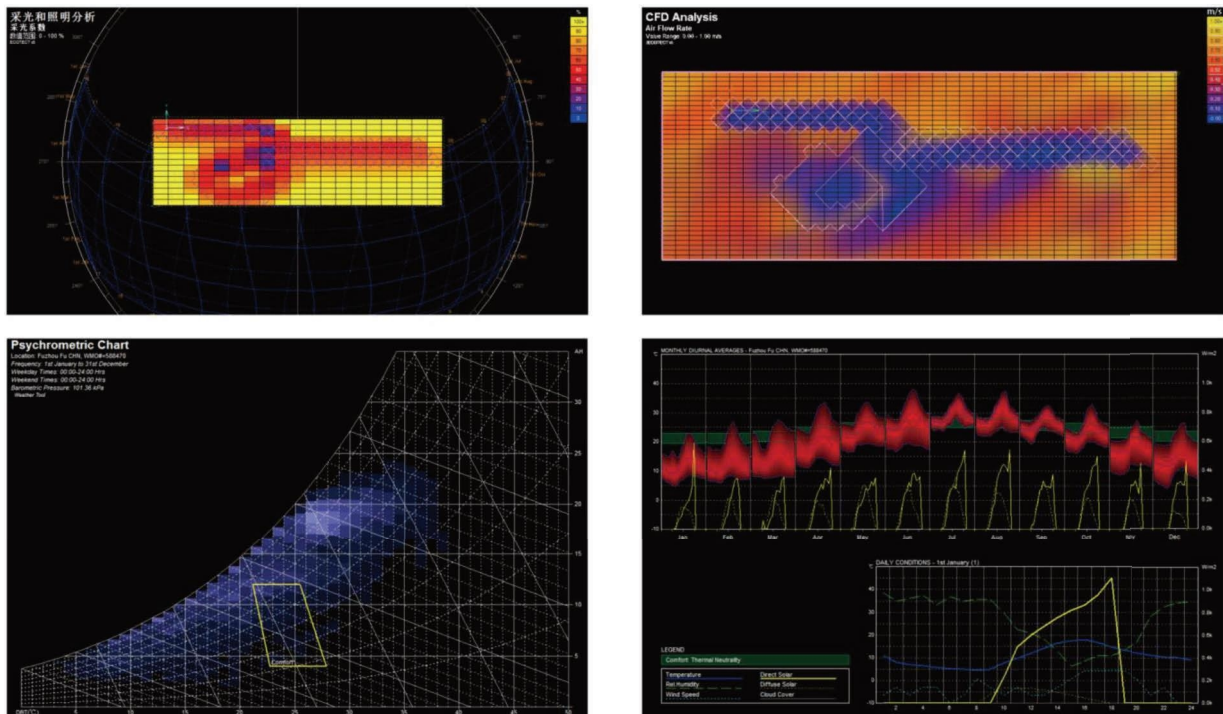


FIGURE 8: Analysis of greening of container buildings (Zhangzhou Shuangyu island hotel).



FIGURE 9: Photo of pilot projects. (a) Container modular fire station under construction. (b) Photo of “Xiangyu” residence in Yangzhou software park. (c) Indoor photo of the container pilot project. (d) Photo of Yangzhou Suburb park maker center.

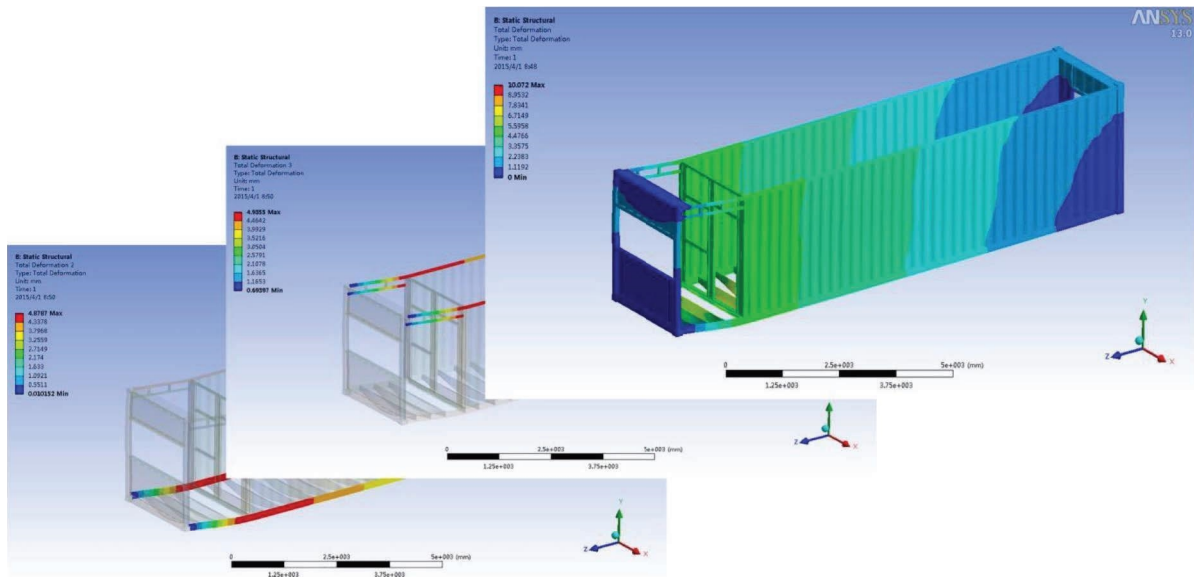


FIGURE 10: Finite element stress analysis on modules of a container building.

References

- [1] M. Su, B. Yang, and X. Wang, "Research on integrated design of modular steel structure container buildings based on BIM," *Advances in Civil Engineering*, vol. 2022, Article ID 4574676, 13 pages, 2022.

Research Article

Path Attenuation and Source Characteristics during the 2019 Sichuan Changning Earthquake Sequence in China

Zhijun Jiang ^{1,2}, Lei Zhang ^{1,2} and Qi Zhang ³

¹Key Laboratory of Earthquake Engineering and Engineering Vibration, Institute of Engineering Mechanics, China Earthquake Administration, Key Laboratory of Earthquake Disaster Mitigation, Ministry of Emergency Management, Harbin 150080, China

²College of Architectural Science and Engineering, Yangzhou University, Yangzhou 225127, China

³School of Civil Engineering and Architecture, China Three Gorges University, Yichang 443002, China

Correspondence should be addressed to Qi Zhang; zhangqi_1988@hotmail.com

Received 12 November 2021; Revised 14 December 2021; Accepted 22 March 2022; Published 26 April 2022

Academic Editor: Qian Chen

Copyright © 2022 Zhijun Jiang et al. This is an open access article distributed under the Creative Commons Attribution License, which permits unrestricted use, distribution, and reproduction in any medium, provided the original work is properly cited.

To give an insight into the path attenuation and source characteristics of the 2019 Sichuan Changning earthquake sequence, 99 strong-motion recordings at 33 stations were studied. The S-wave Fourier amplitude spectra were used to determine the path-attenuation function and key parameters of the seismic source characteristics of this sequence. The results show the following: (1) The geometric spreading effect presents hinged-trilinear characteristics, and the corresponding geometric spreading rates were -0.97 , 0.29 , and -0.73 with the crossover distances 90 km and 183 km. (2) The quality factor Q is correlated with frequency and expressed as $217 \times f^{0.82}$ for the range from 0.1 to 10.0 Hz. (3) The seismic moment was inversely proportional to the cube of the corner frequency, and their product was 2.37×10^{16} N.m/s³. (4) The stress drop varied from 1.18 to 12.44 MPa. Both the attenuation effect and source parameters of this sequence are significantly different from those of the Lushan and the Wenchuan aftershock sequences in the Sichuan region of China.

1. Introduction

At 22:55:43 (UCT+8) on June 17, 2019, an earthquake with magnitude M_s 6.0 struck the town of Shuanghe and its surrounding area in Changning County, Sichuan, China. It is the largest earthquake recorded in the southern margin of Sichuan Basin till now, where seismic activity had been frequented in recent years [1–3]. Then, a series of earthquakes occurred after the mainshock. The Changning Shuanghe anticline was developed in its vicinity, with the axis of the anticline in the northwest (NW)–southeast (SE) direction and the NW section bent to SW. The formation on the north wing of the anticline was steep with a dip angle in the range of 57–60° and an inclination to NE. Some small thrust faults have also developed near the anticline [3]. Hu et al. (2019) determined that the focal mechanism of the Changning main earthquake was a thrust-type earthquake, with a strike-

slip component, and its strike/dip/slip angles were 309°/68°/41°, respectively [1].

Sichuan, a province of China located in an area vulnerable to intensive seismic activity, has been struck by several devastating earthquakes, such as the Wenchuan Mw 7.9 Earthquake in 2008, Lushan Mw 6.6 Earthquake in 2013, Jinggu Mw 6.1 Earthquake in 2014, and Jiuzhaigou Ms 7.0 Earthquake in 2017 [4–8]. These earthquakes endured extensive losses of life and property. In addition, several earthquakes occurred in the southern margin of Sichuan Basin, such as the Xingwen Ms 5.7 earthquake in 2018 and Changning Ms 6.0 earthquake in 2019 [9, 10]. To gain an in-depth understanding of the ground motion characteristics of earthquakes in southern margin of Sichuan Basin, studying the propagation and source features of these earthquakes is necessary.

The path attenuation of ground motion primarily involves geometric spreading and anelastic attenuation.

Because of the thickness of the crust and the energy dissipation characteristics of the crustal medium [11–15], the geometric spreading rate, crossover distance, quality factor Q , and other parameters have enhanced discreteness. For the geometric spreading effect in the Sichuan region, Ren et al. (2013) [7] and Wang et al. (2017) [8] inverted the Wenchuan aftershock sequence and the Jiuzhaigou main shock with a geometric spreading rate of -1 (the coefficient of the geometric spreading term). Since the strong-motion stations used in their studies have a small source distance and the seismic rays propagate primarily along the upper crust, a simple geometric spreading term is also used to obtain satisfactory results. To reflect the influence of the Moho reflection mechanism on the seismic wave propagation path, Zhang (2016) [16] used the hinged-bilinear form to reflect the geometric spreading effect in the Sichuan area, and the near-field and far-field geometric spreading rates were -1 and -0.5, respectively. Wen et al. (2015) used a hinged-trilinear function to reflect the geometric spreading effect of the ground motion of the Lushan aftershock sequence while studying the source characteristics of the Lushan aftershock sequence [17]. Regarding the anelastic attenuation of ground motion, Ren et al. (2013), Zhang (2016), Wang et al. (2017), and Wen et al. (2015) determined the crustal quality factors of the Wenchuan, Jiuzhaigou, and Lushan aftershock regions using the generalized inversion method [7, 8, 16, 17]. Wang et al. (2008) and Zhang et al. (2007) used two-dimensional tomography and a genetic algorithm to retrieve the quality factors of the Sichuan Basin [18, 19].

In terms of the source characteristics, Yu et al. (2012) determined the source stress drop parameters of the Wenchuan aftershock sequence [20]. Wen et al. (2015) and Wang et al. (2017) inverted the Lushan earthquake aftershock sequence and the Jiuzhaigou main earthquake and found that the stress drop of the Jiuzhaigou earthquake was greater than that of the Lushan aftershock sequence [8, 17]. Zhang (2016) determined the seismic stress drop, seismic moment, corner frequency, and other key parameters in Western China (including Sichuan, Yunnan, and Gansu), as well as the relationship between the seismic moment and corner frequency [16]. In addition, Liu et al. (2010) obtained the spatial distribution characteristics of the stress drop parameters in the Sichuan area using 323 recordings of small earthquakes based on the Brune source model [21].

The average stress drop of Wenchuan earthquake sequence obtained by Zhang (2016) is larger than that of Lushan aftershock sequence obtained by Wen et al. (2015), and the average stress drop from Yu et al. (2012) and Wang et al. (2017) are the same, which are between the results of Zhang (2016) and Wen et al. (2015). The possible reason is that the magnitude of aftershock sequence selected by Wen et al. (2015) is small, resulting in a small average stress drop. In addition, the stress release in the Longmenshan fault zone during Wenchuan earthquake also led to the smaller average stress drop of Lushan aftershock sequence. Compared with Yu et al. (2012), Zhang (2016) selected the earthquakes from the border of Sichuan and Yunnan, in which the stress drop was significantly larger [21], resulting in a significantly larger average stress drop. These results showed that the path attenuation and focal characteristic

parameters of earthquakes in the Sichuan region exhibited obvious spatial variability.

The above conclusions were all based primarily on strong-motion data from North Central Sichuan. At present, the studies on the path attenuation and source characteristics of earthquakes in the Southern margin of Sichuan Basin are few. The strong-motion recordings obtained in the Changning earthquake sequence provided a valuable opportunity to study the source characteristics and path-attenuation effect in this area.

In this study, the Fourier spectrum of the Changning earthquake sequence was analyzed. Its seismic source spectrum, geometric spreading effect, and anelastic attenuation mechanism in the frequency domain were observed. The seismic moment, corner frequency, and stress drop of this earthquake sequence were determined based on the Brune seismic source model [22]. These parameters obtained can, in turn, provide a reference to reveal the attenuation law of ground motion parameters of earthquakes in Sichuan.

2. Data and Processing

Abundant strong motion recordings were obtained when the mainshock of Changning earthquake occurred, and the peak ground acceleration recorded by the station 051GXT was the largest. Its east-west, north-south, and vertical components were 573.47 cm/s^2 , 393.77 cm/s^2 , and 381.36 cm/s^2 , respectively. After the main shock, a series of aftershocks occurred and recorded, namely, four earthquakes with M_s 5.0–5.9, six earthquakes with M_s 4.0–4.9, and 52 earthquakes with M_s 3.0–3.9. The most intense aftershock was the earthquake on July 4, 2019, with M_s 5.6.

For this study, to prevent site amplification caused by terrain effect, improve the accuracy of site amplification estimation and the signal-to-noise ratio of strong-motion recordings. Strong-motion recordings were selected by referring to four criteria, which are as follows:

- (1) The magnitude should be larger than M_s 4.0 and R should be less than 300 km because the strong-motion instruments at large distance for small earthquake may not be triggered [23].
- (2) Stations should be located in free fields to prevent the influence of topographic effect on the site amplification.
- (3) All selected events should be recorded by at least two stations. It is because there should be more recordings for each event to ensure that the scattering of the calculated source and path parameters will be at a relatively low level [7].
- (4) The peak ground acceleration of selected recordings should be greater than 1 cm/s^2 because the recordings with low PGA will be contaminated by the noise [7].

Finally, 99 strong-motion recordings at 33 strong-motion stations obtained during nine earthquakes (M_s 4.1–6.0) were selected. The hypocenter locations, focal mechanisms, the style of the faulting of earthquakes [24], and the record numbers are listed in Table 1. Figures 1 and 2 show the

TABLE 1: Parameters of selected earthquakes used in this study.

No.	Date year/month/day/h/min	Depth (km)	Ms	Longitude (°)	Latitude (°)	Style of faulting	Records number
1	2019/06/17/22/55	16	6.0	104.905	28.344	Reverse-oblique	27
2	2019/06/17/23/36	16	5.1	104.805	28.418	Reverse-oblique	18
3	2019/06/18/00/29	10	4.1	104.845	28.340	Strike-slip	3
4	2019/06/18/00/37	10	4.2	104.874	28.386	Reverse	2
5	2019/06/18/05/03	14	4.5	104.857	28.379	Reverse	3
6	2019/06/18/07/34	17	5.3	104.869	28.368	Reverse	15
7	2019/06/22/22/29	10	5.4	104.793	28.424	Reverse	24
8	2019/06/23/08/28	14	4.6	104.833	28.383	Strike-slip	3
9	2019/06/24/09/23	10	4.1	104.800	28.440	Unknown	4

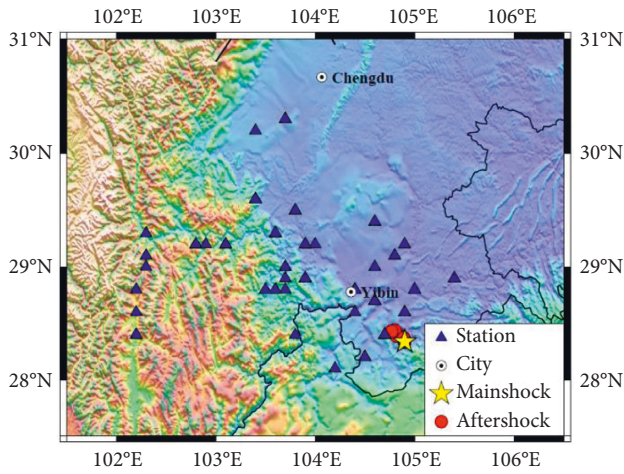
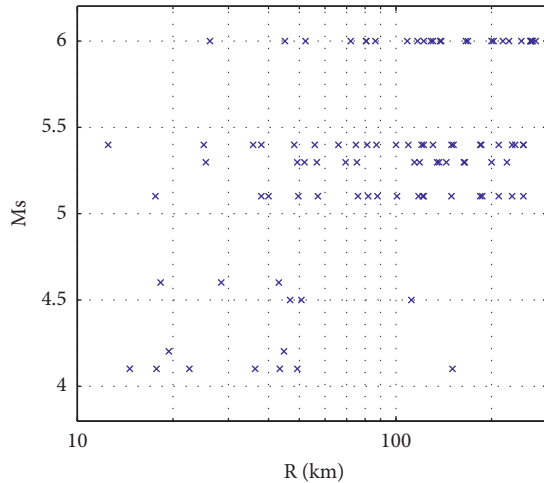


FIGURE 1: Map showing topography overlapped by the epicenters of the Changning earthquakes (yellow star) and aftershocks (red dot) and the locations of the stations used in this study.

FIGURE 2: Magnitude of M_s versus distance for all recordings from nine earthquakes.

distribution of the selected earthquake epicenter and station locations and the distance-dependent magnitude of the recordings used in this study, respectively. The horizontal strong-motion seismograms at the station 051YBT for nine earthquakes are shown in Figure 3.

Baseline correction was performed on all recordings, and Butterworth filtering was conducted with a bandwidth ranging from 0.05 to 30 Hz [25]. The 30 Hz low-pass filtering is performed to remove the high-frequency noise, and the high-pass corner frequency was set as 0.05 Hz according to the shape of the Fourier amplitude spectrum at low frequency. In addition, the frequency band studied in this paper is mainly between 0.1 Hz and 20 Hz to ensure that the signal-to-noise ratio of this frequency band is greater than 3. According to the Husid function [26] and the cumulative root-mean-square function [27], the S-wave of the acceleration recordings for the three components were intercepted. The onset of the S-wave arrival time was identified by Husid plot, which shows the buildup of the energy of an accelerogram with time [26]. The end instant of the S-wave was detected using the cumulative root mean square (RMS) function. Specifically, the end instant of the S-wave is defined as the starting point of the decreasing tendency of the cumulative RMS curve along with the time [27]. Figure 4 shows a demonstration of how the onset and the end of the S-wave recorded at 051YBT in Changning mainshock are automatically identified. To remove the truncated error, a cosine-type tapered window was used. Before the onset and after the end of the S-wave, a time series with a duration corresponding to 10% of the S-wave was added to the S-wave part to run the tapering. The magnitude of the Fourier spectrum was calculated from the fast Fourier transform. Then, the Fourier spectrum was smoothed using the method proposed by Konno [28]. Figure 5 shows the calculated and smoothed Fourier spectrum of the NS component at 051YBT in Changning mainshock after filtering. The smoothed Fourier spectra in the two horizontal orthogonal directions were combined within the frequency domain to represent the Fourier spectrum in the horizontal direction [29].

3. Geometric Spreading Effect

Ground motion can be described as a convolution of the source, path, and site effects in the time domain. Upon the basic assumption of a point-source earthquake, the observed spectrum of an earthquake can be expressed as a linear multiplication of the following three factors [30]:

$$O_{ij}(f, R_{ij}) = S_i(f)P(f, R_{ij})G_j(f), \quad (1)$$

where O_{ij} is the Fourier spectrum of the observed ground motion of Station j in earthquake i (i refers to the number of

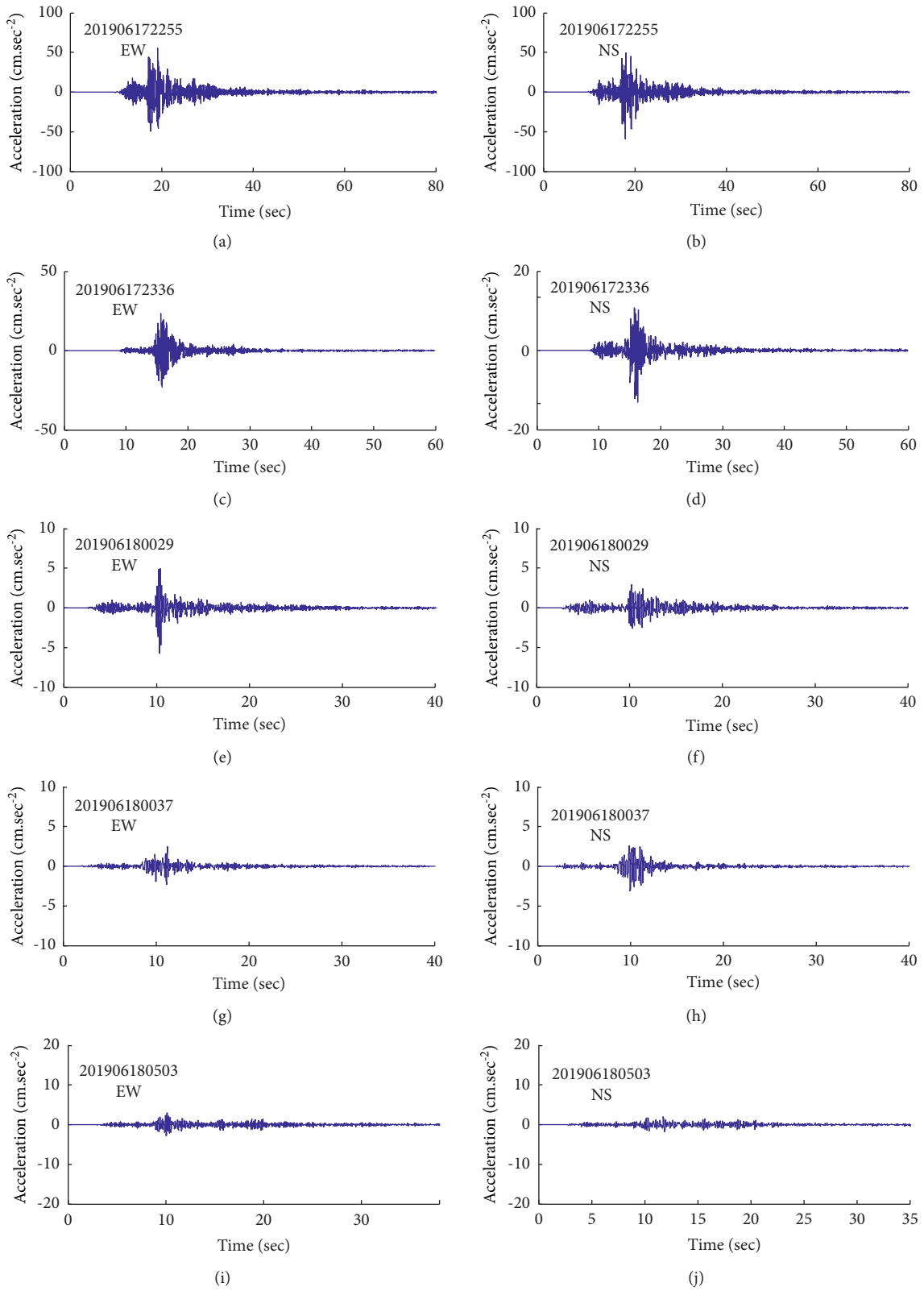


FIGURE 3: Continued.

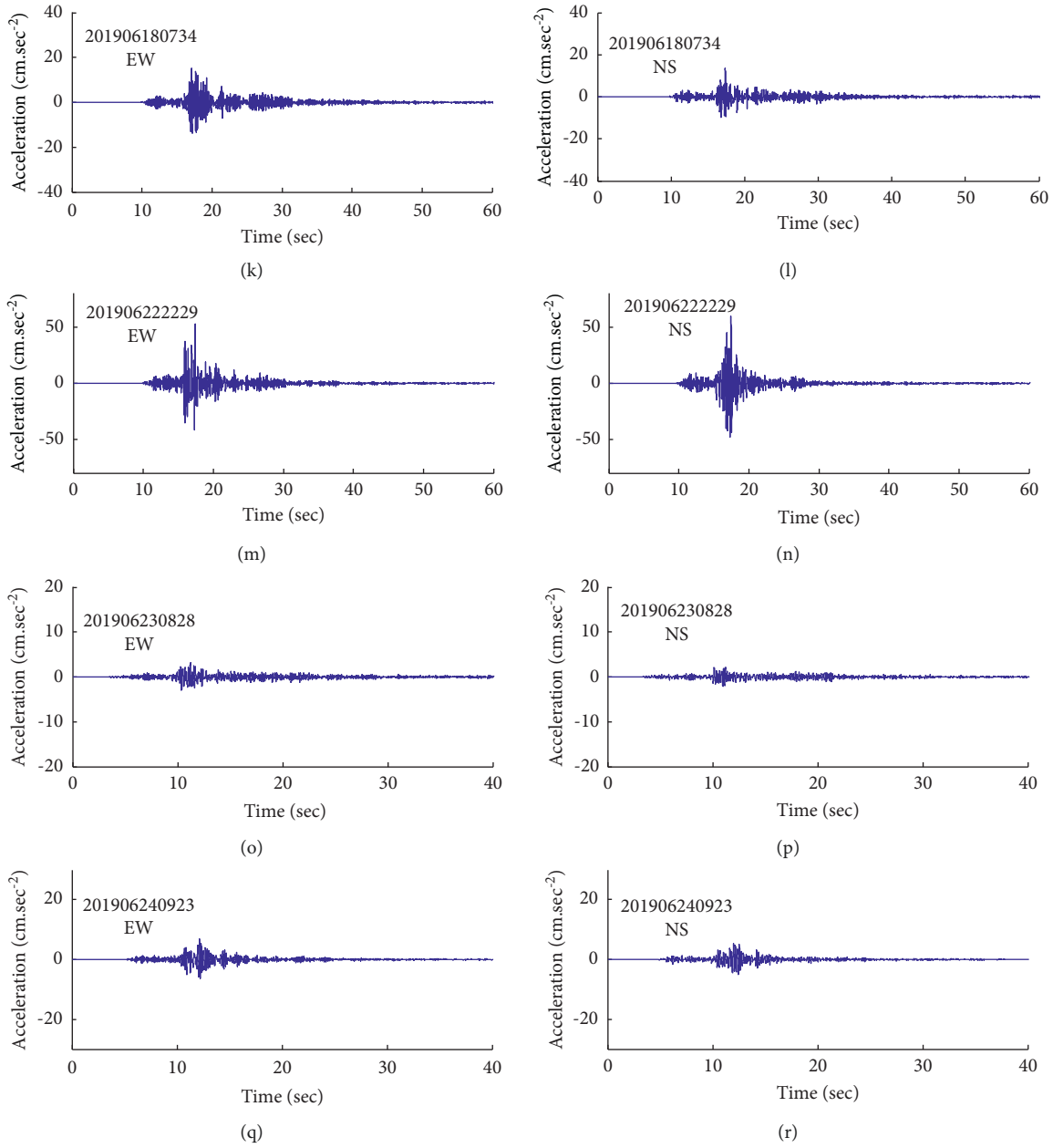


FIGURE 3: The horizontal strong-motion seismograms for nine earthquakes at the station 051YBT.

the earthquake in Table 1, and the unit of Fourier spectrum is $\text{m}\cdot\text{s}^{-1}$, S_i is the source spectrum of earthquake i , P_{ij} is the path-attenuation function that represents the path effect, R_{ij} is the distance between Station j and earthquake i , and it refers to the source distance in this study, and G_j is the site response of Station j . The distance attenuation term P_{ij} in equation (1) consists of the geometric spreading and anelastic attenuation effects, which can be rewritten as

$$P_{ij}(f) = g(R_{ij})\exp(d(f)R_{ij}), \quad (2)$$

where $g(R_{ij})$ is the geometric spreading function, and the rest is the anelastic attenuation effect is as follows:

$$d(f) = -\frac{\pi f}{Q_S(f)}\beta_S, \quad (3)$$

where $Q_S(f)$ is the frequency-dependent S-wave quality factor of the crustal medium, and β_S is the shear-wave velocity of the crust. $\beta_S = 3.6 \text{ km/s}$ in this study [31–33]. Substituting equation (2) in equation (1) and applying the logarithm of both sides of the resulting equation yields the following form:

$$\ln[O_{ij}(f)] - \ln[S_i(f)] - \ln[G_j(f)] = \ln(P_{ij}(f)), \quad (4)$$

$$\ln(P_{ij}(f)) = \ln[g(R_{ij})] + d(f)R_{ij}. \quad (5)$$

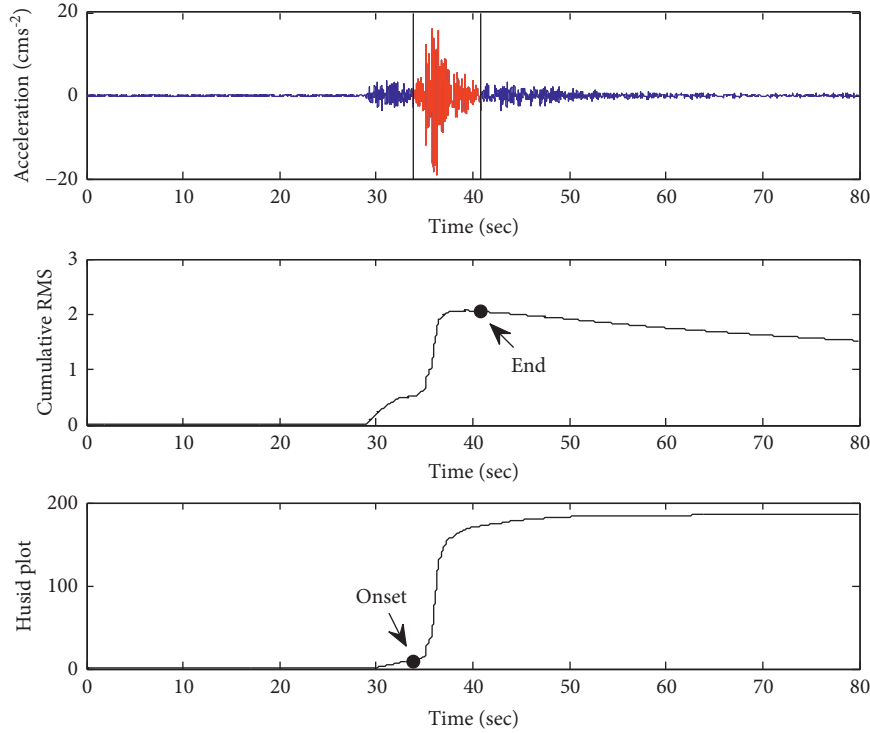


FIGURE 4: The detection of the S-wave of the NS component at 051YBT in Changning mainshock.

The geometric spreading function $g(R_{ij})$ can be expressed in the form of a hinged-trilinear [13], as given in

$$g(R) = \begin{cases} b_1 \ln(R), & R_{ij} \leq R_1 \\ b_1 \ln(R_1) + b_2 \ln\left(\frac{R}{R_1}\right), & R_1 < R_{ij} \leq R_2 \\ b_1 \ln(R_1) + b_2 \ln\left(\frac{R_2}{R_1}\right) + b_3 \ln\left(\frac{R}{R_2}\right), & R_{ij} > R_2 \end{cases} \quad (6)$$

The parameters b_1 , b_2 , b_3 , R_1 , and R_2 are regression coefficients. R_1 and R_2 are the crossover distances at which the geometric spreading rate changes.

To determine the geometric spreading function as shown in equation (6), the source spectrum, site response, and anelastic attenuation term must be eliminated.

The site response term $G_j(f)$ in equation (4) can be rewritten as follows:

$$G_j(f) = A_j(f) \exp(-\pi\kappa_0 f), \quad (7)$$

where $A_j(f)$ is the site amplification provided by the near-surface soil, and κ_0 represents the attenuation effect of the soil layer near the surface on high-frequency ground motions. The velocity of the shear wave at the sites of the strong-motion stations is typically required to determine the site response, $A_j(f)$. Most stations selected in this study lacked the horizontal-to-vertical ratio (H/V) of the Fourier spectrum [34]. Anderson and Hough (1984) [35] suggested a way to

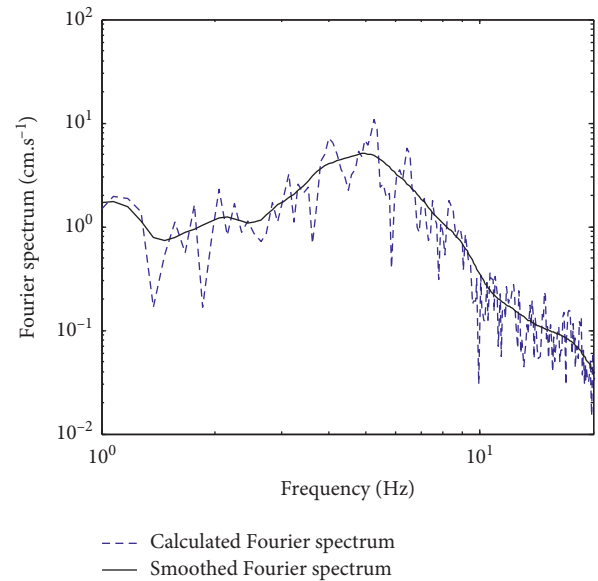


FIGURE 5: The calculated and smoothed Fourier spectrum of the NS component at 051YBT in Changning mainshock after filtering.

describe the shape of the high-frequency part of the Fourier amplitude spectrum with

$$O_{ij}(f) = O_0 \exp(-\pi\kappa f), \quad (8)$$

where O_0 is the ground motion amplitude determined by the seismic source and path term, and κ is the near-surface attenuation coefficient that can control the frequency-dependent attenuation rate of the amplitude. Equation (7) was

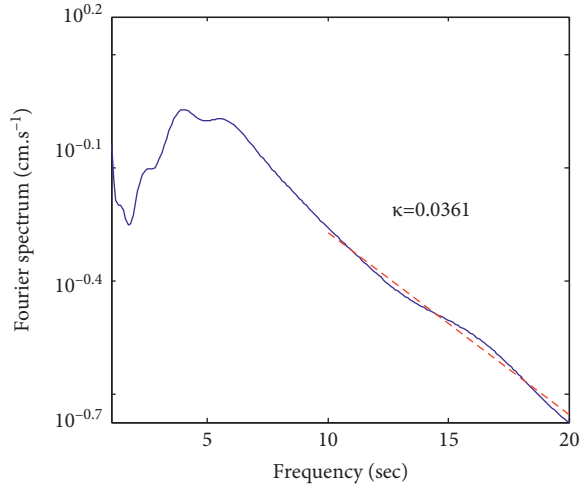


FIGURE 6: Calculation diagram of κ using the vertical component of Fourier spectrum at 051YBT in Changning mainshock.

fitted using the recordings of each station in a single logarithmic coordinate system to obtain the κ -value of each station site. Take the slope of Fourier spectrum in the range of 10Hz-20 Hz as k . Then, $\kappa = k/(-\pi \times \lg e)$ [35]. Figure 6 gives the calculation diagram of κ using the vertical component of the Fourier spectrum at 051YBT in Changning mainshock. The dependency of κ on the source distance R at each station was then fitted based on a first-order relationship to obtain the coefficient κ_0 . Notably, a part of the κ_0 -value has already been accounted for in the H/V ratio. Thus, it should be subtracted from the near-surface attenuation term for the horizontal component [34]. Hence, the site response for the horizontal component can be rewritten as follows:

$$G_j(f) = \frac{H}{V} \exp(-\pi\kappa_{0V}f), \quad (9)$$

where κ_{0V} should be determined via the vertical Fourier spectrum of the ground motion. Figure 7 shows the distance-dependent variation of κ with respect to the vertical component of the recordings as contained in this dataset. By fitting the data points, as shown in Figure 7, κ_{0V} can be determined as 0.0327. The average value of H/V from the same station can then be calculated. Based on κ_{0V} , the site response term $G_j(f)$ can be obtained using equation (8). $G_j(f)$ is then substituted in equation (4) to eliminate the influence of site response and modify the observed ground motion to the corresponding value of the bedrock site.

To determine the source spectrum S_i , the path-attenuation term must be used to modify the Fourier spectrum of the bedrock site to the source position after the effect of the site response is eliminated. Therefore, the path-attenuation term must be determined first. The geometric spreading and anelastic attenuation terms are coupled. Thus, it is difficult to separate them using strong motion data. The geometric attenuation term is generally considered independent of frequency [11, 13, 34, 36], and the effect of anelastic attenuation can be ignored in the near-field ($R < 100$ km) [36]. Consequently, the source spectrum of each earthquake was

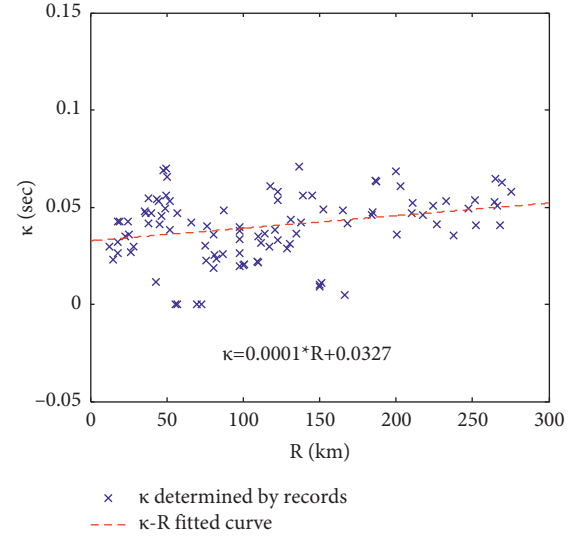


FIGURE 7: Dependency between κ and distance.

initially determined using the observed ground motion with a distance shorter than 100 km. According to the theory of seismic wave propagation, the source spectrum can be derived from the correction of the observed value of the Fourier spectrum at the bedrock site using the geometric spreading effect function (R^{-1}) [34]. Accordingly, the corrected values of the Fourier spectrum from the same earthquake were averaged to obtain the approximate value of the first-order estimate of the source spectrum S_i of this earthquake [36].

The distance attenuation $P_{ij}(f)$ can be obtained by substituting S_i and G_j in equation (4). When the frequency is 0.3 Hz, the dependence of $P_{ij}(f)$ on R is shown in Figure 8. As observed from Figure 8, $P_{ij}(f)$ rapidly decreases as R increases; however, $P_{ij}(f)$ decreases at a decelerated rate as R increases. When R is greater than the threshold, the decrease rate of $P_{ij}(f)$ increases again, clearly indicating the effect of the reflection mechanism of the Moho surface.

To determine the parameters b_1 , b_2 , b_3 , R_1 , and R_2 , the value range of each coefficient was set up, and the optimal solution of the path effect function nearest to the data point trend was identified using the grid search method. The value ranges of b_1 , b_2 , b_3 , R_1 , R_2 , and d for grid search are -0.8~1.3, -0.5~0.5, -0.4~-1, 50~100, 100~200, and -0.01~0, respectively. Based on the grid search method, the mean values of b_1 , b_2 , b_3 , R_1 , and R_2 are -0.97, 0.29, -0.73, 90 km, and 183 km, respectively.

The curve of the obtained path-attenuation term ($f = 0.3$ Hz) is plotted in Figure 8. It can be observed that the data points are evenly distributed on both sides of the fitted curve. Meanwhile, the path-attenuation terms of the Lushan and Wenchuan aftershocks obtained by [7, 17] are also provided. These terms were obtained by substituting the geometric attenuation function and Q-value in [7, 17] in equations (2) and (3). Given that Wen et al. (2015) and Ren et al. (2013) represented the path-attenuation characteristics of the Lushan and the Wenchuan aftershock sequences, respectively, the difference between them and the results in

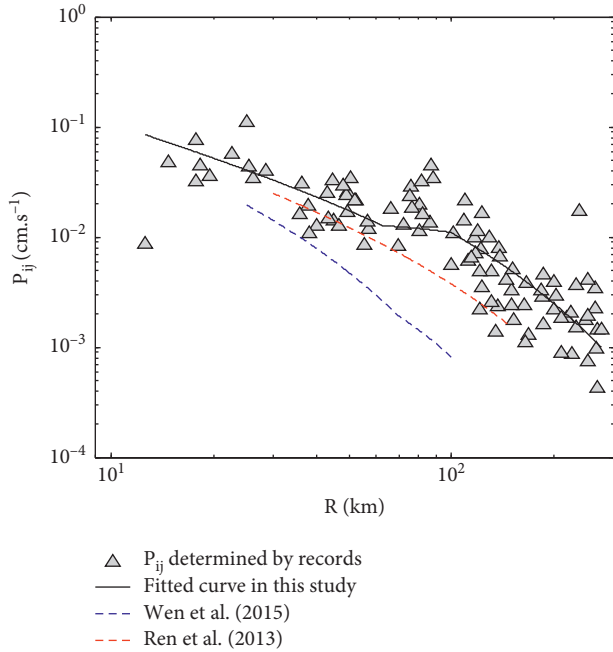


FIGURE 8: Distribution of $P_{ij}(f)$ versus hypocentral distance.

this study showed that the path-attenuation effect of the Changning earthquake sequence was different from those of the Lushan and the Wenchuan aftershock sequences.

4. Quality Factor Q

The coefficient $d(f)$ was determined by the grid search method, and the quality factor $Q(f)$ of the S-wave can be determined using equation (3). The variation trend of the quality factor $Q(f)$ with frequency is shown in Figure 9. The relationship between Q and f was fitted in the form of $Q(f) = Q_0 f^n$ and $Q(f) = 217f^{0.82}$. Meanwhile, other research results in Sichuan are presented. Notably, the Q -value results in this study are larger than those of [7, 17] but close to the results of [18, 19]. It shows that the Q -value in the Changning earthquake area is larger than that in the Lushan and Wenchuan aftershock areas but close to the average level of the Q -value in the Sichuan area.

The Q -value of the quality factor in this study was higher than that of [7, 17]. There are two reasons that can interpret it. (1) Compared with the strong motion recordings selected by [7, 17], the hypocenter distance of this dataset was larger, the seismic rays, which arrived at the far-field station, passed through the deeper crustal medium, and the quality factor Q of the deep-crustal medium was larger. (2) The quality factor of the crustal medium was correlated with the thickness of the crust. It is generally believed that the quality factor is smaller when the crust thickness is larger [34]. The Changning earthquake sequence occurred in the southern margin of the Sichuan Basin and the areas studied by [7, 17] were located in the North Central Sichuan. The crustal thickness in Sichuan increased gradually from south to north [37]. This trend is consistent with the spatial distribution trend of the Q -value obtained by [7, 17].

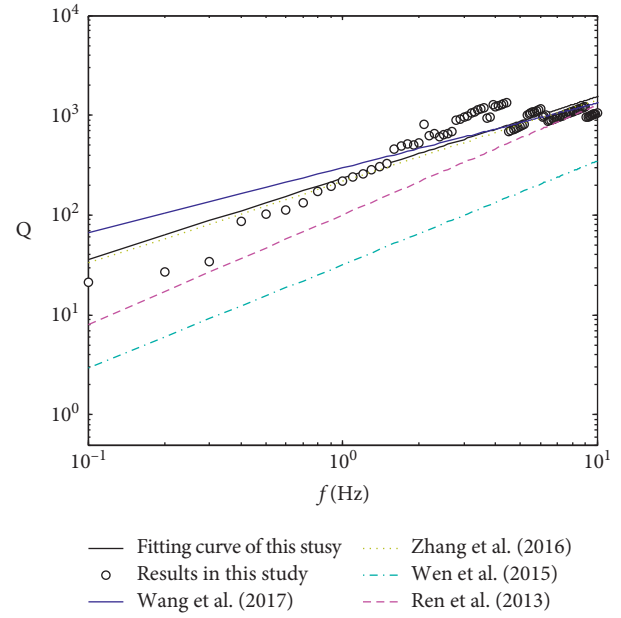


FIGURE 9: Quality factor Q for Changning earthquake region.

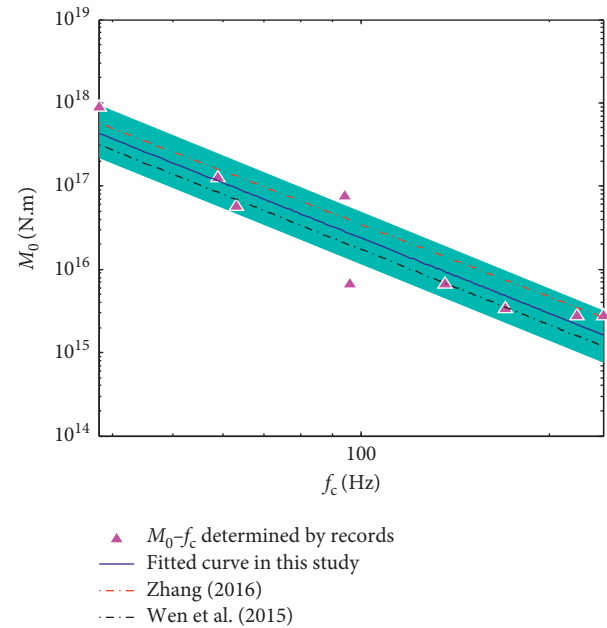


FIGURE 10: Seismic moment M_0 versus the corner frequency f_c .

5. Seismic Source Spectrum

The path-attenuation term $P_{ij}(f)$ (both the geometric and anelastic attenuation terms) was derived from a previous study. If G_j and $P_{ij}(f)$ are known, the source spectrum can be determined more accurately according to equation (4) using the full dataset as the influence of the quality factor Q was considered. The source displacement spectrum $S(f)$ (ratio of $(2\pi)^2$ to the source acceleration spectra) can be expressed as follows:

TABLE 2: Source parameters obtained in this study.

No. of earthquakes	1	2	3	4	5	6	7	8	9
$\Delta\sigma$ (MPa)	9.55	5.17	3.36	3.29	1.18	2.84	12.45	5.95	7.90
f_c (Hz)	0.38	0.59	1.36	1.7	0.96	0.63	0.94	2.22	2.44
$M_0/N.m(\times 10^{17})$	8.81	1.27	0.068	0.034	0.068	0.58	0.76	0.028	0.028

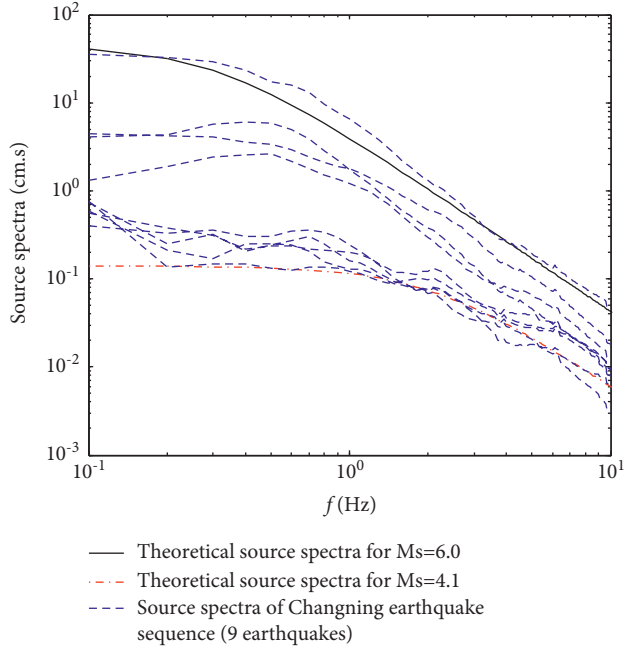


FIGURE 11: Seismic source displacement spectra versus the theory model of the Changning seismic sequence.

$$S(f) = \frac{\mathfrak{R}_{\Theta\Phi}VF}{4\pi\rho\beta_s^3R_0} \frac{M_{0i}}{1 + f/f_{ci}^2}, \quad (10)$$

where $\mathfrak{R}_{\Theta\Phi}$ is the radiation pattern, which is usually equal to $\sqrt{2/5}$ [16]. F reflects the free-surface effect of the shear-wave, with a value set to 2.0. V is the distribution coefficient that considers the S-wave energy along two orthogonal directions whose values are typically set to 0.7. Additionally, ρ is the rock mass density of the seismic source, whose value was set to 2.8 g/cm^3 in this study. β_s is the average shear-wave velocity of the rock in the seismic source area, with an approximate value of 3.6 km/s . R_0 is the reference distance of the seismic source, with a value of 1 km . M_{0i} is the seismic moment of earthquake i , and f_{ci} is the corner frequency of the source spectrum of earthquake i .

Using the seismic source displacement spectrum, the seismic moment M_{0i} and corner frequency f_{ci} of each earthquake can be determined from the least-squares fitting using the interval search algorithm. The search interval of magnitude is $M - 0.5 \sim M + 0.5$, and the search interval of f_c is $0.02 \sim 5 \text{ Hz}$. When the frequency is between 0.1 and 10 Hz , the solution that can minimize the difference between the theoretical source displacement spectrum and the observed result is the optimal solution.

Figure 10 presents the relationship between the determined seismic moment M_0 and corner frequency f_c for the Changning sequence with a 68.3% confidence interval. The relationship between M_0 and the corner frequency f_c shows an obvious inverse relationship, and the relationship between M_0 and f_c is $M_0f_c^3 = 2.37 \times 10^{16} \text{ N}\cdot\text{m/s}^3$. This relationship indicates that the seismic source features of the Changning seismic sequence show self-similarity. The results of Zhang (2016) [16] and Wen et al. (2015) [17] are also presented. The results of [16, 17] differ from those obtained in this study, however, they are included in the 68.3% confidence interval. The comparison results show that the relationship between M_0 and f_c for the Changning earthquake sequence is slightly different from those of the Wenchuan earthquake sequence and the Lushan aftershock sequence.

The stress drop parameter $\Delta\sigma$ can be derived from equation (11) given the values of M_0 and f_c , and the resulting $\Delta\sigma$ and f_c of the Changning earthquake sequence are listed in Table 2. Using equation (11), the mean stress drop value of 4.68 MPa can be determined, which is close to the mean stress drop value of 4.89 MPa for global intraplate earthquakes [38]. Wen et al. (2015) and Yu (2012) obtained the mean stress drop values of 3.14 MPa and 3.8 MPa for the Lushan and Wenchuan aftershock sequences, respectively. These values are lower than those of the Changning earthquake sequence.

$$\Delta\sigma = \frac{7M_0}{16} \left(\frac{2\pi f_c}{2.34\beta_s} \right)^3. \quad (11)$$

Figure 11 presents the displacement spectra of the source of the Changning earthquake sequence with magnitudes derived in this study in the range of $4.1 < M_s < 6.0$. The calculated Brune theoretical displacement spectra for two earthquakes with magnitudes $M_s 4.1$ and $M_s 6.0$, with a $\Delta\sigma$ of 4.68 MPa , are also provided. It can be observed that, even though the stress decrease ($\Delta\sigma$) associated with the Changning earthquake sequence was relatively discrete, the displacement spectra of the seismic sources matched the theoretical model, as well as the theoretical values, thus indicating that the seismic sources of this earthquake sequence conform to the Brune (1970) point-source model.

6. Conclusions

In this study, the path-attenuation effect term and seismic source characteristic parameters of the Changning earthquake sequence were derived based on the analyses of the S-wave Fourier amplitude spectra of strong-motion recordings obtained from 33 strong-motion stations in nine

earthquakes of the 2019 Changning earthquake sequence. The main conclusions were as follows:

- (1) The path-attenuation effect of the Changning earthquake sequence matched the mechanism associated with the Moho effect, and the attenuation trend of the ground motion with the propagation path was significantly different from that of the aftershock sequences of Lushan and Wenchuan.
- (2) The geometric spreading term of the Changning earthquake sequence exhibited hinged-trilinear characteristics, with average geometric spreading rates of -0.97, 0.29, and -0.73 in the three segments and average crossover distances of 90 km and 183 km. The quality factor Q was correlated with frequency, and the relationship between the two was $Q(f) = 217 \times f^{0.82}$ in the frequency band of 0.1–10 Hz. The Q -value was larger than that of the aftershock areas of Lushan and Wenchuan but close to the average Q -value in Sichuan.
- (3) The seismic moment of the Changning earthquake sequence varied from 2.75×10^{15} N·m to 8.75×10^{17} N·m, and the corner frequency varied from 0.38 Hz to 2.36 Hz. The seismic moment was inversely proportional to the cube of the corner frequency, and the product was 2.37×10^{16} N·m/s³. It indicated that the seismic source features of the Changning seismic sequence show self-similarity. The stress drop $\Delta\sigma$ ranged between 1.18 and 12.44 MPa, with an average value of 4.68 MPa. The source characteristics were different from those of the Wenchuan earthquake sequence and the Lushan aftershock sequence.

Data Availability

Data for this study were provided by China Strong Motion Network Centre at Institute of Engineering Mechanics, China Earthquake Administration.

Conflicts of Interest

The authors declare that there are no conflicts of interest regarding the publication of this paper.

Acknowledgments

The authors thank the Scientific Research Fund of the Institute of Engineering Mechanics, China Earthquake Administration (Grant nos. 2018D11 and 2020D13), the Science and Technology Research Project of Education Department of Hubei Province (Grant no. Q20191210), and the Ministry of Housing and Urban-Rural Development of China Research Project (No.2017-K9-010). The authors also thank China Strong Motion Network Centre at Institute of Engineering Mechanics, China Earthquake Administration, for providing the data for this study.

References

- [1] X. H. Hu, S. Z. Sheng, and Y. G. Wan, "Study on focal mechanism and post-seismic tectonic stress field of the Changning," *Progress In Geophysics*, vol. 5, 2020.
- [2] X. Lei, Z. Wang, and J. Su, "The december 2018 ML 5.7 and january 2019 ML 5.3 earthquakes in south Sichuan Basin induced by shale gas hydraulic fracturing," *Seismological Research Letters*, vol. 90, no. 3, pp. 1099–1110, 2019.
- [3] P. Wu, J. R. Su, and C. M. Huang, "Characteristic of shear-wave splitting in the Yibin area, Sichuan province," *Earthquake Research in China*, vol. 33, no. 3, pp. 414–423, 2017.
- [4] J. Hu, W. Zhang, L. Xie, Q. Zhang, and Z. Jiang, "Strong motion characteristics of the M_w 6.6 Lushan earthquake, Sichuan, China - an insight into the spatial difference of a typical thrust fault earthquake," *Earthquake Engineering and Engineering Vibration*, vol. 14, no. 2, pp. 203–216, 2015.
- [5] J. J. Hu, Q. Zhang, Z. J. Jiang, L. L. Xie, and B. F. Zhou, "Characteristics of strong ground motions in the 2014 M_s 6.5 Ludian earthquake, Yunnan, China," *Journal of Seismology*, vol. 20, no. 1, pp. 361–373, 2016.
- [6] Y. Ren, H. Wang, P. Xu et al., "Strong-motion observations of the 2017 M_s 7.0 Jiuzhaigou earthquake: comparison with the 2013 M_s 7.0 Lushan earthquake," *Seismological Research Letters*, vol. 89, no. 4, pp. 1354–1365, 2018.
- [7] Y. Ren, R. Wen, H. Yamanaka, and T. Kashima, "Site effects by generalized inversion technique using strong motion recordings of the 2008 Wenchuan earthquake," *Earthquake Engineering and Engineering Vibration*, vol. 12, no. 2, pp. 165–184, 2013.
- [8] H. W. Wang, Y. F. Ren, and R. Z. Wen, "Source spectra of the 8 August 2017 Jiuzhaigou M_s7.0 earthquake and the quality factor of the epicenter area," *Chinese Journal of Geophysics*, vol. 60, no. 10, pp. 4117–4123, 2017.
- [9] X. Lei, Z. W. Wang, Z. Wang, and J. Su, "Possible link between long-term and short-term water injections and earthquakes in salt mine and shale gas site in Changning, south Sichuan Basin, China," *Earth and Planetary Physics*, vol. 3, no. 6, pp. 510–525, 2019.
- [10] X. Lei, J. Su, and Z. Wang, "Growing seismicity in the Sichuan Basin and its association with industrial activities," *Science China Earth Sciences*, vol. 63, no. 11, pp. 1633–1660, 2020.
- [11] T. I. Allen and G. M. Atkinson, "Comparison of earthquake source spectra and attenuation in eastern North America and southeastern Australia," *Bulletin of the Seismological Society of America*, vol. 97, no. 4, pp. 1350–1354, 2007.
- [12] T. I. Allen, P. R. Cummins, T. Dhu, and J. F. Schneider, "Attenuation of ground-motion spectral amplitudes in southeastern Australia," *Bulletin of the Seismological Society of America*, vol. 97, no. 4, pp. 1279–1292, 2007.
- [13] G. M. Atkinson and R. F. Mereu, "The shape of ground motion attenuation curves in southeastern Canada," *Bulletin of the Seismological Society of America*, vol. 82, no. 5, pp. 2014–2031, 1992.
- [14] A. Zandieh and S. Pezeshk, "Investigation of geometrical spreading and quality factor functions in the new Madrid seismic zone," *Bulletin of the Seismological Society of America*, vol. 100, no. 5A, pp. 2185–2195, 2010.
- [15] A. Zandieh, S. Pezeshk, and K. W. Campbell, "An equivalent point-source stochastic simulation of the NGA-west2 ground-motion prediction equations," *Bulletin of the Seismological Society of America*, vol. 108, no. 2, pp. 815–835, 2018.
- [16] Q. Zhang, "Study on regional differentiation of ground motion attenuation relationship," Doctorate Dissertation,

- Institute of Engineering Mechanics China Earthquake Administration, Harbin, 2016.
- [17] R. Z. Wen, H. W. Wang, and Y. F. Ren, "Estimation of source parameters and quality factor based on generalized inversion method in Lushan earthquake," *Journal of Harbin Institute of Technology*, vol. 47, no. 4, pp. 58–63, 2015.
- [18] S. Y. Wang, S. P. Pei, and Z. H. Xu, "Crustal S-wave Q estimated from ML amplitude I:attenuation in different tectonic regions of China," *Chinese Journal of Geophysics*, vol. 50, no. 6, pp. 1740–1747, 2007.
- [19] Y. J. Zhang, H. Z. Qiao, and W. Z. Cheng, "Attenuation characteristics of the media in Sichuan Basin region," *Journal of Seismological Research*, vol. 30, no. 1, pp. 43–48, 2007.
- [20] T. Yu and X. J. Li, "Inversion of strong motion data for source parameters of Wenchuan aftershocks, attenuation function and average site effect," *Acta Seismologica Sinica (Chinese edition)*, vol. 34, no. 5, pp. 621–632, 2012.
- [21] L. F. Liu, Y. J. Su, and J. Liu, "Study on temporal and spatial features of stress drop for low-to-moderate earthquake in sichuan and yunnan region," *Journal of Seismological Research*, vol. 33, no. 3, pp. 314–319, 2010.
- [22] J. N. Brune, "Tectonic stress and the spectra of seismic shear waves from earthquakes," *Journal of Geophysical Research*, vol. 75, no. 26, pp. 4997–5009, 1970.
- [23] D. M. Boore, J. P. Stewart, E. Seyan, and G. M. Atkinson, "NGA-West2 equations for predicting response spectral accelerations for shallow crustal earthquakes," PEER Report, 2013.
- [24] G. X. Yi, F. Long, and M. J. Liang, "Focal mechanism solutions and seismogenic structure of the 17 June 2019 Ms6.0 Sichuan Changning earthquake sequence," *Chinese Journal of Geophysics*, vol. 62, no. 9, pp. 3432–3447, 2019.
- [25] H. Wang and R. Wen, "Attenuation and basin amplification revealed by the dense ground motions of the 12 July 2020 Ms 5.1 tangshan, China, earthquake," *Seismological Research Letters*, vol. 92, no. 4, pp. 2109–2121, 2021.
- [26] R. Husid, "Gravity effects on the earthquakes response of yielding structures," Ph. D. thesis, California Institute of Technology, Los Angeles, 1967.
- [27] M. W. McCann and H. C. Shah, "Determining strong-motion duration of earthquakes," *Bulletin of the Seismological Society of America*, vol. 69, no. 4, pp. 1253–1265, 1979.
- [28] K. Konno and T. Ohmachi, "Ground-motion characteristics estimated from spectral ratio between horizontal and vertical components of microtremor," *Bulletin of the Seismological Society of America*, vol. 88, no. 1, pp. 228–241, 1998.
- [29] S. Drouet, S. Chevrot, F. Cotton, and A. Souriau, "Simultaneous inversion of source spectra, attenuation parameters, and site responses: application to the data of the French accelerometric Network," *Bulletin of the Seismological Society of America*, vol. 98, no. 1, pp. 198–219, 2008.
- [30] D. M. Boore, "Simulation of ground motion using the stochastic method," *Pure and Applied Geophysics*, vol. 160, no. 3, pp. 635–676, 2003.
- [31] X. W. Bao, X. X. Sun, M. J. Xu et al., "Two crustal low-velocity channels beneath SE Tibet revealed by joint inversion of Rayleigh wave dispersion and receiver functions," *Earth and Planetary Science Letters*, vol. 415, pp. pp16–24, 2015.
- [32] G. Laske, G. Masters, Z. Ma, and M. Pasyanos, "Update on CRUST1.0 - a 1-degree global model of earth's crust," in *Proceedings of the EGU General Assembly Conference*, Vienna, Austria, April, 2013.
- [33] Y. Luo, L. F. Zhao, Z. X. Ge, X. B. Xie, and Z. X. Yao, "Crustal Lg-wave attenuation in Southeast Asia and its implications for regional tectonic evolution," *Geophysical Journal International*, vol. 226, pp. 1873–1884, 2021.
- [34] A. Meghdadi and J. Shoja-Taheri, "Ground-motion attenuation and source spectral shape for earthquakes in eastern Iran," *Bulletin of the Seismological Society of America*, vol. 104, no. 2, pp. 624–633, 2014.
- [35] J. G. Anderson and S. E. Hough, "A model for the shape of the fourier amplitude spectrum of acceleration at high frequencies," *Bulletin of the Seismological Society of America*, vol. 74, pp. 1969–1993, 1984.
- [36] G. M. Atkinson, "Empirical attenuation of ground-motion spectral amplitudes in southeastern Canada and the north-eastern United States," *Bulletin of the Seismological Society of America*, vol. 94, no. 3, pp. 1079–1095, 2004.
- [37] L. Dong, X. Z. Shen, and Y. P. Qian, "Study on velocity and density contrasts across the Moho in the southeastern margin of the Tibetan Plateau," *Chinese Journal of Geophysics*, vol. 63, no. 3, pp. 915–927, 2020.
- [38] B. P. Allmann and P. M. Shearer, "Global variations of stress drop for moderate to large earthquakes," *Journal of Geophysical Research: Solid Earth*, vol. 114, no. B1, 2009.

Research Article

Effects of Stiffener Type on Fatigue Resistance of Steel-UHPC Composite Bridge Decks

Xiugui Sun ¹, **Jianhua Hu** ², **Yu Li**,³ and **Guoping Huang** ⁴

¹Hunan University, Changsha 410082, China

²Hunan Communication and Water Conservancy Group LTD., Changsha 410000, China

³Hunan Provincial Communications Planning, Survey and Design Institute Co., Ltd., Changsha 410000, China

⁴College of Civil Engineering, Hunan City University, Yiyang 413000, China

Correspondence should be addressed to Jianhua Hu; 402950468@qq.com and Guoping Huang; gphuag@hnu.edu.cn

Received 24 October 2021; Accepted 17 January 2022; Published 7 February 2022

Academic Editor: Lingkun Chen

Copyright © 2022 Xiugui Sun et al. This is an open access article distributed under the Creative Commons Attribution License, which permits unrestricted use, distribution, and reproduction in any medium, provided the original work is properly cited.

Recent research showed that ultrahigh-performance concrete (UHPC) and orthotropic steel bridge decks could be integrated to form steel-UHPC composite sections offering superior load-carrying capacity and fatigue resistance. This study investigates the effects of longitudinal stiffener types on the fatigue resistance of steel-UHPC composite sections. Three types of longitudinal stiffeners were compared, including U-ribs, bulb flat ribs, and plate ribs. Finite element analysis and full-scale fatigue tests were performed to investigate the load-carrying capacity and fatigue resistance of the composite bridge decks with different stiffeners. Besides, the proposed steel-UHPC composite bridge decks were compared with conventional orthotropic steel decks. The results show that steel box girders with bulb flat rib composite deck have reasonable fatigue resistance, construction efficiency, and economic benefits. This study is expected to promote the design and evaluation of economic steel-UHPC composite bridge decks to achieve higher mechanical performance and long-term durability.

1. Introduction

Orthotropic steel decks (OSDs) have been widely used in long-span bridges to bear wheel loads. Conventional OSDs are composed of vertical and horizontal stiffeners and a top plate. The longitudinal rib can be categorized in two forms: open rib and closed rib. The two types of longitudinal ribs have different characteristics in mechanical performance, structural characteristics, applicable conditions, and so on. A large number of scholars have done intensive research on the two types of ribs in OSDs. With the same amount of steel used, the open ribs are often associated with lower torsional and flexural rigidity and stability of the OSD and the so-called U-ribs have been widely used in conventional OSDs. However, the open ribs are easier to manufacture and construct than U-ribs that require much time for grooving and rolling. In addition, fillet welding can be adopted to weld open ribs on the steel top plate, avoiding partial penetration welding of the U-rib, which thus ensures the welding quality and better fatigue performance [1].

Engineering practice shows that fatigue and pavement damages are common in OSDs [2–4]. The damages are closely associated with the relatively low stiffness of the OSDs, in particular, the low local stiffness. Under mechanical loading, a high stress range can be generated in conventional OSDs and may significantly reduce the fatigue life of welded joints that are prone to fatigue. To enhance the fatigue resistance, Europe and Japan used composite decks to increase the stiffness and reduce the stress ranges. Compared with conventional OSDs, composite decks utilize a layer of reinforced concrete integrated with the steel deck plate via shear connectors, such as headed shear studs that are welded on the top surface of the steel plate and embedded in the concrete deck.

While the use of composite sections increased the stiffness of the OSDs, the conventional composite decks have limitations. First, the concrete must be thick enough to deliver sufficient load-carrying capacity, and a thick concrete deck can significantly increase the deck weight. Second, the service life of reinforced concrete is limited because

conventional concrete has low crack resistance and is brittle in tension. In real-life applications, there are many factors that can cause concrete cracking, such as thermal effects and shrinkage [5–7]. To address these limitations, ultrahigh-performance concrete has been used to replace the conventional concrete in composite bridge decks [2]. The use of UHPC greatly improved the load-carrying capacity and the long-term durability [8, 9], due to its very high compressive strength, crack resistance, and dense microstructures [10–13]. The steel-UHPC composite deck system has been applied in many projects, such as the Zhuzhou Fengxi Bridge (a self-anchored suspension bridge with a main span of 300 m) and the Yueyang Dongting Lake Bridge in China (a suspension bridge with a main span of 1480 m). However, in the existing studies, U-ribs were used in the steel-UHPC composite OSDs. Engineering practices show that the rigidity of the bridge decks can be greatly enhanced by the use of steel-UHPC composite sections. Therefore, it is hypothesized that the rigidity of the stiffener is no longer the controlling factor of the rigidity of the bridge deck system. It is further postulated that the stiffener can be either open or closed. Currently, there is limited research on the performance and design of composite OSDs with open ribs [14–16].

This study aims to investigate the performance of steel-UHPC composite OSD with open ribs. To this end, this study evaluates the effects of bulb flat ribs on the load-carrying capacity and fatigue resistance of the composite OSD through finite element analysis and experimental testing. To ensure this research is practicable for engineering practices, the Xiangtan Zhaohua Xiangjiang River Bridge in China is taken as the background bridge structure. This study is expected to promote the design and evaluation of composite bridge decks to achieve higher mechanical performance and long-term durability.

2. Description of the Bridge

Figure 1 shows the Xiangtan Zhaohua Xiangjiang River Bridge, which is a single-tower, self-anchored, suspension bridge crossing the Xiangjiang River. It is a signature bridge of Xiangtan City in China, connecting the Zhaoshan District and the Jiuhua District. The layout of its span is 45 m + 168 m + 228 m + 2 × 45 m, as depicted in Figure 2. The design grade is Urban Grade I Main Road, with II(2) navigation grade. The design speed of vehicles on the bridge is 60 km/h, and the width of the main stiffening beam of the bridge is 39.5 m.

In regard to the bridge tower, a double-column structure was adopted, the elevation of the tower column is curved, and the overall shape is like a budding lotus flower. The height of the tower above the cap is 124.8 m, with the tower column set with two beams. With respect to the main cable, the span layout is 163.1 m + 223.1 m. The transverse spacing of the main cable is 33.9 m, and the single main cable is composed of 39 strands of steel cables. The main cable is constructed by prefabricated parallel steel cables one by one, each of which consists of 127 ϕ 5.1 mm galvanized high-strength parallel steel wires. A total of 32 pairs of slings are



FIGURE 1: Depiction of the Xiangtan Zhaohua Xiangjiang River Bridge.

set in the whole bridge, the standard spacing of which is 10.8 m.

The steel stiffening beam is a flat streamline box girder of a single box with three cells, with a total length of 377 m, which is divided into 37 sections. The standard section is 10.8 m in length, and 195T in weight. The thickness of the top plate of the girder is 12 mm, and the top plate of the box girder is stiffened by the bulb flat ribs, which are 12 mm thick and 260 mm high, with a transverse spacing of 450 mm. Headed shear studs (ϕ 13 × 40 mm) were welded in the traffic area of the girder, with a spacing of 225 mm; ϕ 10 ribbed steel mesh is set in the UHPC layer, with a spacing of 37.5 mm, and the 50 mm thick UHPC layer is steam cured at high temperature to form a composite deck system. The steel stiffening beam is shown in Figure 3.

3. Composite Deck with the Open Rib

This study attempts to design a steel-UHPC composite deck with plate ribs and a steel-UHPC composite deck with bulb flat ribs. Figure 4 shows a total of four types of composite OSDs investigated in this study, including (1) conventional composite OSD with a reinforced concrete deck and U-ribs; (2) steel-UHPC composite OSD with U-ribs, designated as UCD-U; (3) steel-UHPC composite OSD with bulb flat ribs, designated as UCD-B; and (4) steel-UHPC composite OSD with plate ribs, designated as UCD-P. The four types of OSDs are compared, in terms of flexural rigidity, steel consumption, and deck weight.

Based on the above four types of composite OSDs, eight different schemes of the composite section are proposed and investigated in this study, as listed in Table 1. Scheme 1 is a conventional OSD without any concrete layer on the steel deck plate. Scheme 1 is used as the control to evaluate the other schemes. Compared with Scheme 1, Scheme 2 has a higher flexural rigidity and a lower steel consumption. Specifically, the flexural rigidity is increased by 22%, and the steel consumption is reduced by 16%, indicating that the use of a thin (50 mm) layer of UHPC can effectively increase the rigidity and also save steel. Schemes 3 to 5 show that adjusting the arrangement spacing of the bulb flat steel ribs can match the composite deck structures with different deck stiffness. Compared with Scheme 1, Schemes 3 to 5 achieve higher stiffness of the composite deck and a lower steel consumption; Schemes 6 to 8 show that adjusting the height and arrangement spacing of the plate ribs can match the

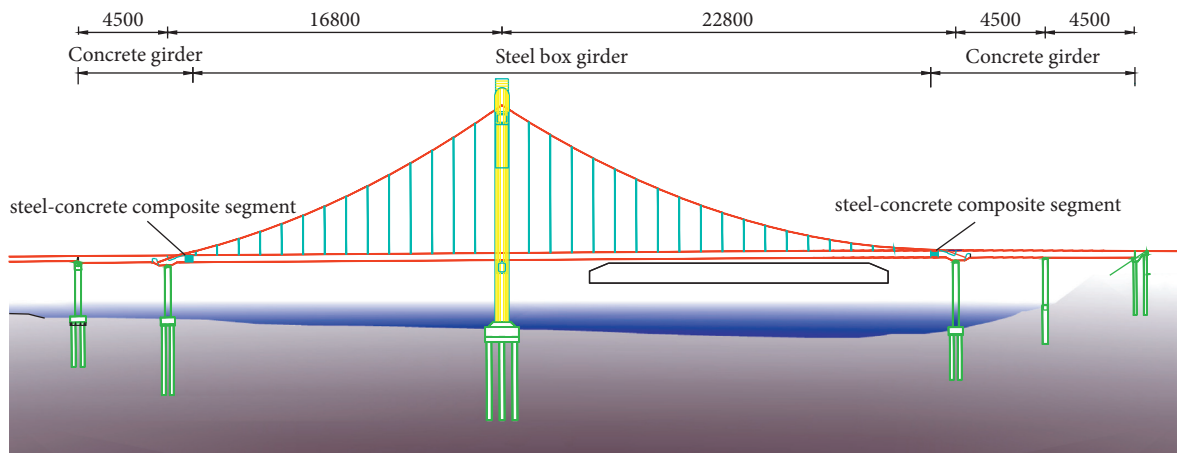


FIGURE 2: General layout of the Xiangtan Zhaohua Xiangjiang River Bridge (unit: cm).

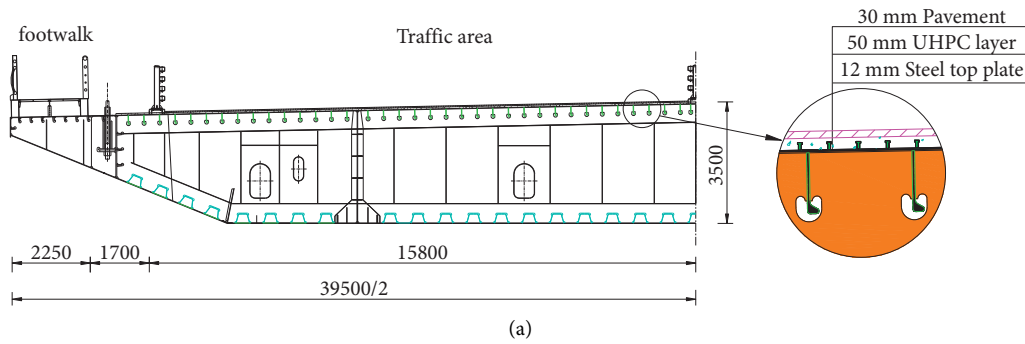


FIGURE 3: Design of steel box girder: (a) cross section of the steel box girder; (b) section diagram of the steel box girder; (c) bulb flat ribs welding; (d) diaphragm-bulb flat rib weld (unit: mm).

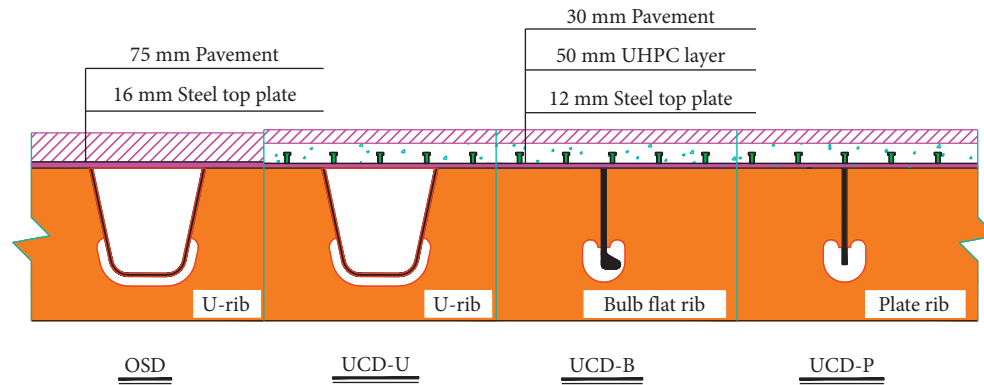


FIGURE 4: Four types of bridge deck schemes.

composite deck structures with different deck stiffness. However, the steel consumption of these three schemes is higher than that of Scheme 2, and the rigidity of the bridge deck structure is generally small, and the weight of the bridge deck structure increases greatly. According to the above comparison, the rigidity of the UCD-B is in the middle of UCD-U and OSD; its steel consumption is consistent with that of the UCD-U; its weight of the bridge deck structure is consistent with UCD-U and OSD. Therefore, the composite bridge deck with bulb flat ribs is a reasonable and feasible bridge deck structure.

According to the comparison of indexes in Schemes 3 to 5, all indexes of the bridge deck in Scheme 4 are relatively balanced, so Scheme 4 is recommended as the design scheme of composite bridge deck with bulb flat ribs. In order to further verify the bearing capacity and fatigue performance of the composite deck with bulb flat ribs, a detailed study is conducted on the load-carrying capacity and fatigue performance of the composite deck, elaborated in the following part.

4. Load-Carrying Capacity

4.1. Finite Element Model. The finite element model of the steel box girder is established by the software ANSYS. In order to simulate the stress of the main girder and reduce the influence of boundary conditions, eight standard segments (21.6 m) of steel box girder are selected to establish a finite element model. In the model, the steel structure is simulated by the element Shell 63, and the UHPC layer by the element Solid 45. The boundary conditions of the FE model were as follows: (1) the steel anchor box should be subject to vertical restraint; (2) some lifting points should be subject to transverse and longitudinal restraint.

The FEA in this study did not account for the material nonlinearity of the UHPC, and the reasons are as follows: on the one hand, experimental investigations revealed that the reinforced UHPC exhibited high cracking strength (i.e., 42.7 MPa) and, on the other hand, their theoretical analyses indicated that the maximum tensile stress of the UHPC layer was only 13.1 MPa under design traffic loads, much less than its cracking strength. Thus, the UHPC layer is assumed to

behave in the linear-elastic range. The elastic modulus and Poisson's ratio of UHPC were 42.6 GPa and 0.2, respectively. The steel material of the box girder is Q345qD, a steel grade for bridges in China that has a yield strength of 345 MPa. The model is shown in Figure 5.

4.2. Loading. The static strength calculation of the box girder considers the effects of constant load and live load of vehicles. According to China code (JTG D60-2004), the vehicle load is 550 kN standard vehicle, and the impact factor is considered as 1.3. The vehicle load dimensions are shown in Figure 6.

Figure 7 shows the arrangement of loading. Under the vehicle load, the stress distribution of the orthotropic plate is local, while the vehicle wheelbase is long. In order to simplify the calculation, only two 140 kN rear axles of the vehicle are considered for loading. The longitudinal arrangement of the vehicle load is as follows: (a) loading middle of sling diaphragm; (b) loading across common diaphragm; and (c) loading across sling diaphragm.

The transverse loading arrangement of the vehicle is as follows: (a) loading above the longitudinal rib; (b) loading between longitudinal ribs; and (c) loading along the web of longitudinal rib, as shown in Figure 8. Considering the combination of three kinds of longitudinal loading and three kinds of transverse loading, a total of nine loading conditions are calculated for the deck system.

5. Results and Discussion

Table 2 summarizes the results of the nine loading conditions. The results include the deck deflection, UHPC principal tensile stress, top plate stress, longitudinal rib stress, and diaphragm stress of the three deck systems. According to the mechanical characteristics of three bridge deck schemes, some observations are summarized as follows: (1) UCD-B and UCD-U have little difference in the deck stiffness, which is larger than that of the OSD. (2) The stress of steel structure in UCD-U and UCD-B is significantly lower than that in OSD. (3) The structural stress level of UCD-B is the same as that of UCD-U, but the stress of some positions is lower than that of UCD-U.

TABLE 1: Comparison of different types of deck structures.

Scheme	Longitudinal rib	Thickness of top plate	Rib spacing	Height of rib	Deck parameters (mm)			Deck bending rigidity (mm^4/m)	Deck index	
					Thickness of UHPC layer	Thickness of pavement	Thickness of UHPC layer		Steel consumption (kg/m^2)	Total mass of deck (kg/m^2)
1	8 mm U-rib	16	600	280	0	75	$2.55E+8$	199.8	383.3	
2	8 mm U-rib	12	600	280	50	30	$3.12E+8$	168.4	389.7	
3	12 mm bulb plat rib	12	500	260	50	30	$2.55E+8$	159.0	380.3	
4	12 mm bulb plat rib	12	450	260	50	30	$2.76E+8$	166.2	387.5	
5	12 mm bulb plat rib	12	400	260	50	30	$3.01E+8$	175.2	396.5	
6	14 mm plate rib	12	300	210	50	30	$1.50E+8$	171.1	392.4	
7	16 mm plate rib	12	350	240	50	30	$2.04E+8$	180.3	401.6	
8	18 mm plate rib	12	400	270	50	30	$2.70E+8$	189.6	410.8	

Note. Scheme 1 is a traditional orthotropic steel deck (OSD). Scheme 2 is UHPC composite deck with U-ribs (UCD-U). Schemes 3 to 5 are UHPC composite decks with bulb flat ribs (UCD-B). Schemes 6 to 8 are UHPC composite decks with plate ribs (UCD-P). The total mass of the deck includes the weight of longitudinal rib, steel top plate, UHPC layer, and pavement.

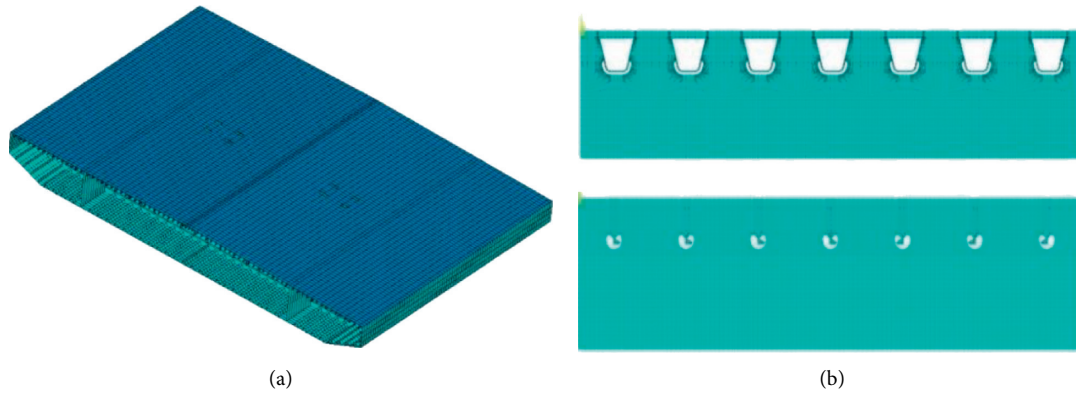


FIGURE 5: Finite element model of the OSD: (a) iso view; (b) cross sections.

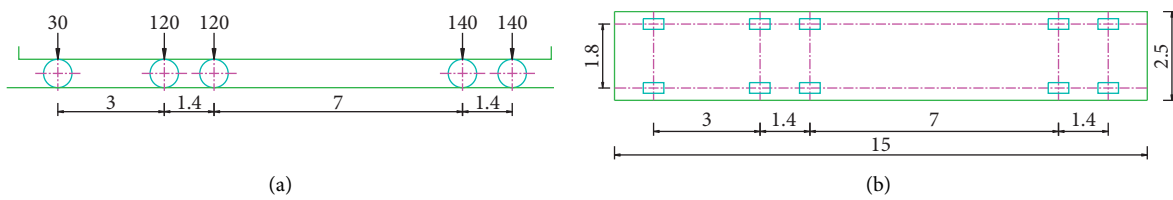


FIGURE 6: Depiction of the vehicle load for the load-carrying capacity: (a) elevation view; (b) top view (unit: meter for length and kN for force).

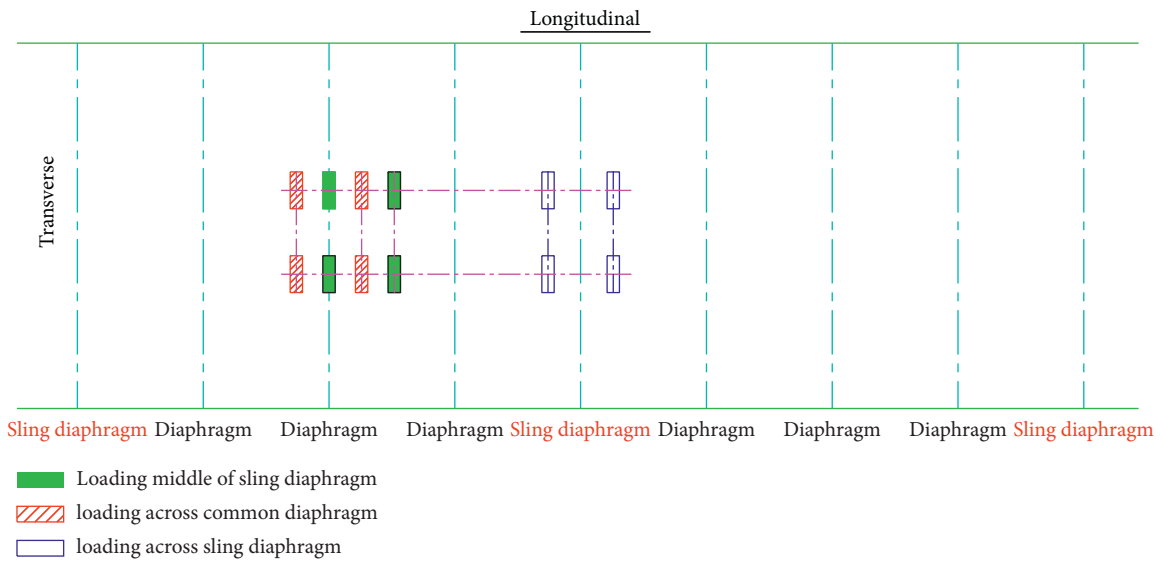


FIGURE 7: Longitudinal loading arrangement.

6. Fatigue Performance

6.1. *Fatigue Load and Details.* In this study, the standard single-vehicle load model of fatigue vehicle in China code (JTG D64-2015) is adopted for applying fatigue loading, as shown in Figure 9. The vehicle has four axles, and the weight of each axle is 120 kN, so the total weight of the vehicle is 480 kN, regardless of the impact factors. In order to facilitate calculation and improve the computational efficiency, only

two rear axles are used for the loading in this study. Besides, the coupling effect of the front and the rear axles is not considered in this study.

Four fatigue details are selected for calculation and comparison, with the location of fatigue details as displayed in Figure 10. The diaphragm at the middle lifting point is taken as the checking diaphragm for the four fatigue details, and subsequent adverse loading is carried out for the fatigue details on the checking diaphragm.

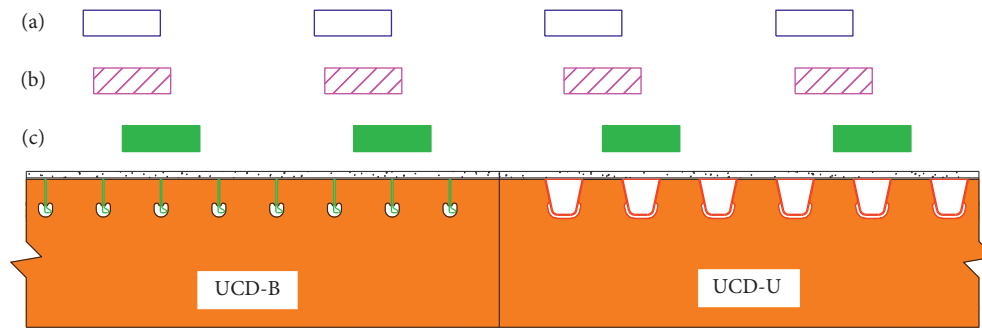


FIGURE 8: Transverse loading arrangement: (a) loading along the web of longitudinal ribs; (b) loading between the longitudinal ribs; (c) loading above the longitudinal ribs.

TABLE 2: Deflection and stress of the bridge deck under dead load and live load.

Scheme	Deflection (mm)	Principal tensile stress of UHPC (MPa)	Principal tensile stress of top plate (MPa)	Stress of diaphragm (MPa)	Stress of longitudinal rib (MPa)
OSD	23.8	—	122.4	225.1	263.7
UCD-U	21.8	13.1	51.1	158.4	154.4
UCD-B (scheme 4)	22.1	12.0	53.8	116.0	154.7

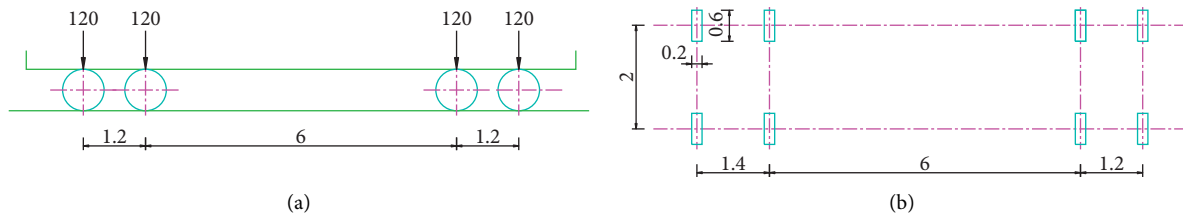


FIGURE 9: Layout of vehicle load for fatigue testing: (a) elevation view; (b) top view (unit: meter for length and kN for force).

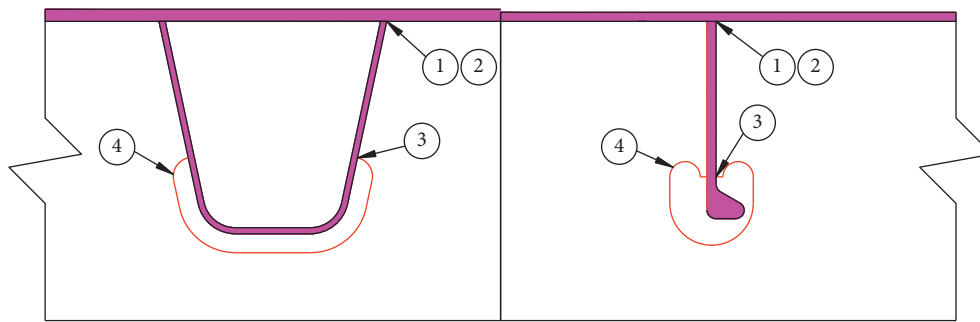


FIGURE 10: Fatigue detail.

6.2. Loading Types

6.2.1. *Transverse Loading.* Eurocode 3 stipulates that the fatigue driving trace is distributed in the area of 0.25 m around the center line of the lane at a certain frequency. To determine the most unfavorable position of the transverse direction of the axle, the wheel load is placed at 0.25 m to the left of the lane center line at first as the starting point and then moved 0.1 m to the right each time. Subsequently, the stress conditions at each loading point are calculated, respectively, with each fatigue detail corresponding to 6 load conditions. According to the calculation results of 6 working

conditions of each fatigue detail, the most unfavorable transverse loading position is determined. The transverse loading is shown in Figure 11.

6.2.2. *Longitudinal Loading.* After determining the most unfavorable transverse loading position, the wheel action is kept unchanged at this position. The front axle of the standard fatigue vehicle driving direction is taken as the starting point at the distance of 3.3 m from the checking calculation diaphragm, with taking every 0.3 m forward movement as a working condition, which gradually loads to

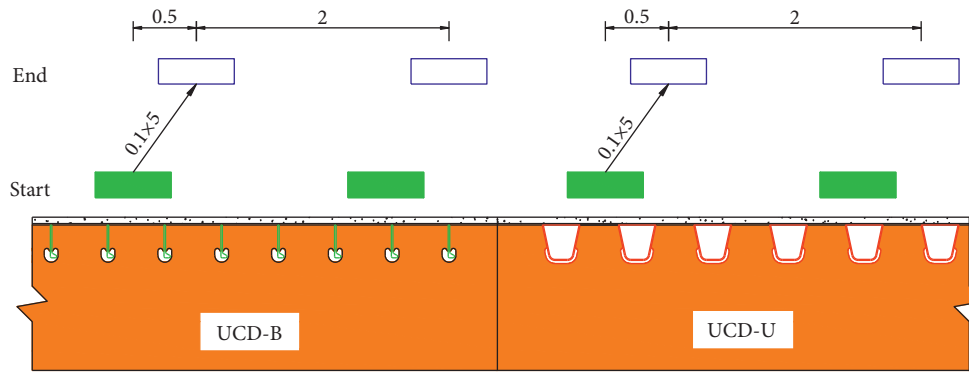


FIGURE 11: Transverse loading (unit: m).

3.3 m of the checking calculation diaphragm at the rear axle distance as the end. Each fatigue detail corresponds to 23 load cases. The longitudinal direction is shown in Figure 12.

6.3. Results and Discussion of Finite Element Analysis. According to the 23 longitudinal loading conditions corresponding to each fatigue detail, the most unfavorable fatigue stress amplitude of each detail is extracted. Specific data are shown in Table 3. The comparison conclusion is as follows:

- (1) The stress amplitude of each fatigue detail in UCD-U and UCD-B is significantly lower than that in OSD, indicating that the UHPC composite deck is effective for avoiding fatigue failure.
- (2) Compared with UCD-U, UCD-B shows a larger drop in fatigue stress and better fatigue performance in each fatigue detail.

7. Fatigue Test

7.1. Specimen, Test Setup, and Instrumentation. Figure 13 shows the specimen for the model tests. The overall dimensions of the specimen are 5500 mm × 3150 mm × 1062 mm (length × width × height), including two diaphragms and seven bulb flat ribs, with the spacing of 450 mm. The bulb flat rib is 260 mm in height and 12 mm in thickness, and the top plate of the deck is 12 mm in thickness. The steel material of these components is Q345qD, a steel grade for bridges in China that has a yield strength of 345 MPa. Shear studs are welded on the steel top plate, with steel mesh being laid, and a 50 mm thick UHPC layer is poured at last, consistent with the prior studies [17–20]. The UCD-B is formed by high-temperature steam curing.

Figure 14(a) shows the test model and the setup. The specimen is supported by two rigid steel beams that are anchored on the strong floor, and it is loaded using a hydraulic actuator (capacity: 500 kN) fixed on a rigid steel frame. According to the finite element analysis results, the stress amplitude of the welding toe between diaphragm and stiffener (see Detail 3 in Figure 10) of the UCD-B is the largest, so the fatigue test focuses on the position. A

steel plate measured as 600 mm × 200 mm is placed between the actuator and the specimen to simulate the uniformly distributed wheel load. A rubber pad is placed between the steel base plate and the steel top plate as the energy-absorbing material. According to the finite element analysis, the maximum tensile stress amplitude at the weld toe of the diaphragm-to-rib welded joint is 67 MPa. This full-scale model test is intended to study the fatigue characteristics of this fatigue detail under the action of 1.3 times of stress amplitude 87 MPa ($1.3 \times 67 \text{ MPa} = 87 \text{ MPa}$). Figure 14(b) shows the deployment of the strain gauges at the weld toe of the diaphragm-to-rib welded joint.

7.2. Results and Discussion of the Fatigue Test. In this test, 2.5 million loads are applied under the action of 1.3 times the fatigue stress amplitude of the real bridge, and the overload fatigue performance of the test model in the long service life under the design stress amplitude is studied. During the test, when the number of load cycles is 0, 0.1 million, 0.5 million, 1.0 million, 1.5 million, 2 million, and 2.5 million, the fatigue loading is paused, and a static load test is performed. The static loading results of detail 3 after each cycle are as follows: 86.8 MPa (0), 89.4 MPa (0.5 million), 91.2 MPa (1 million), 89.7 MPa (1.5 million), 90.8 MPa (2 million), and 92.6 MPa (2.5 million). Through the static load test and model inspection, no fatigue crack or slip is found at the fulcrum. Moreover, the whole composite bridge deck structure is intact.

According to the S–N describing the fatigue performance of the structure, any stress amplitude and the corresponding number of cycles are satisfied: $\sigma_i^m N_i = C$, where m and C are constants related to the material and structural details and σ_i and N_i are equivalent stress amplitude and equivalent cycle times, respectively. If the structural design stress amplitude is σ' , and the number of cycles is N' ; then, according to the Miner linear cumulative damage criterion $\sum (n_i/N_i) = 1$, N_i can be expressed as $N_i = (\sigma'/\sigma_i)^m N'$. According to the code, if $m = 3$, which is conservative, the number of cycles corresponding to the design stress amplitude (67 MPa) is 5.5 million.

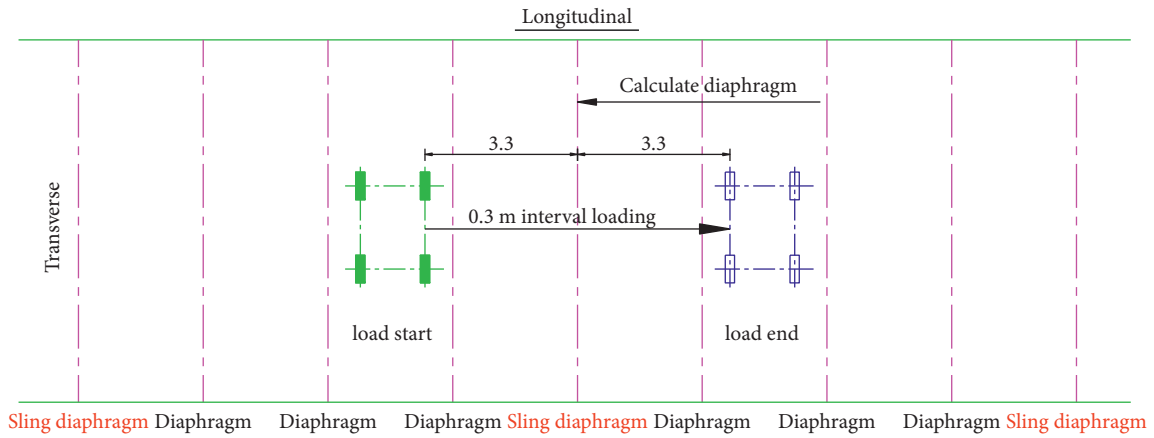


FIGURE 12: Longitudinal loading (unit: m).

TABLE 3: Maximum stress amplitude of each detail (unit: MPa).

Scheme	Stress amplitude				UHPC	
	Detail 1 SX	Detail 2 SY	Detail 3 S1	Detail 4 S1	SX	SY
(1) OSD	95	161	132	96	—	—
(2) UCD-U	28.6	34.4	74	77	1.7	8.1
(2) Decrease compared with (1)	70%	79%	44%	20%	—	—
(3) UCD-B	10.5	21.9	67	55	2.3	8.2
(3) Decrease compared with (1)	89%	86%	49%	43%	—	—

Note. SX is the transverse normal stress of bridge. SY is the longitudinal normal stress of bridge. S1 is the principal stress.

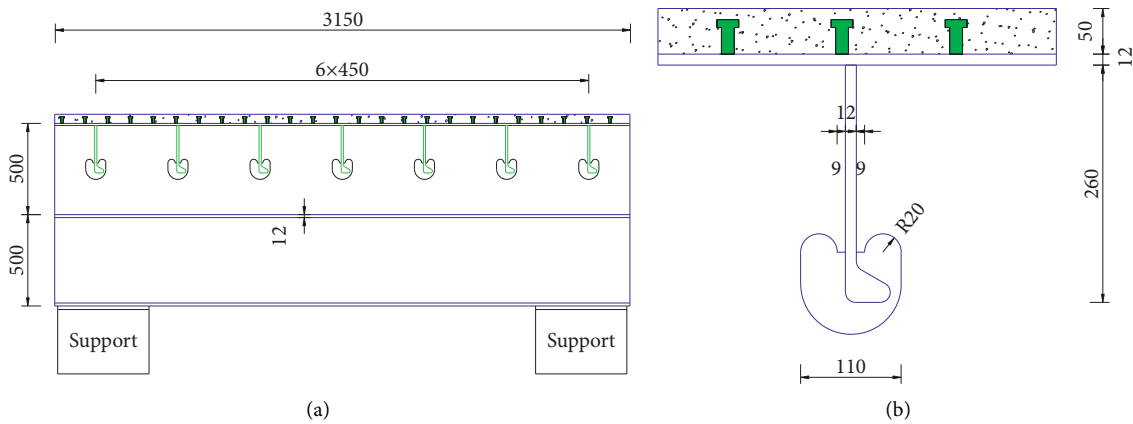


FIGURE 13: Full-scale specimen: (a) elevation view; (b) cross section (unit: mm).

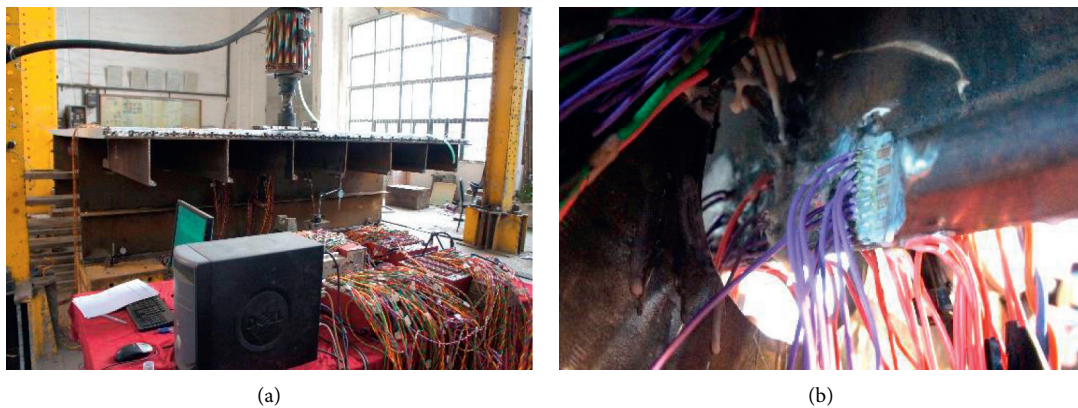


FIGURE 14: Fatigue test: (a) the specimen and test setup; (b) the strain gauges deployed on the tested specimen.

8. Conclusions

In this study, a new composite deck structure with bulb flat steel and UHPC is proposed. The load-carrying capacity and fatigue performance of the composite deck are fully studied by FEA and model tests. Based on the research, the following conclusions are obtained:

- (i) Through the preliminary comparison of four kinds of bridge deck structures, UCD-P has large steel consumption, self-weight, and low deck stiffness, so it is not a suitable stiffener for composite bridge deck; UCD-B shares the basically same steel consumption and deck weight as UCD-U, with slightly smaller deck stiffness, so it is a reasonable stiffener form for the composite bridge deck.
- (ii) The FEA calculation results of three kinds of bridge deck structures reveal that the rigidity of UCD-B is in the middle of UCD-U and OSD, while the stress of UCD-B is the smallest among these three schemes, and the bearing capacity of the deck meets the design requirements.
- (iii) The FEA calculation results of three kinds of bridge deck structures indicate that the fatigue stress amplitude of the composite bridge deck is lower than that of the orthotropic steel bridge deck, and the fatigue stress amplitude of UCD-B is the smallest, so its fatigue performance is the best.
- (iv) The fatigue test is carried out on a UCD-B panel specimen. Under the action of 1.3 times the fatigue stress amplitude of the real bridge, no fatigue crack is observed in the steel structure and UHPC, after experiencing 2.5 million cycles.

Data Availability

The data used to support the findings of this study are available from the author Xiugui Sun (xgsun2013@hnu.edu.cn) upon request.

Conflicts of Interest

The authors declare no conflicts of interest.

Acknowledgments

This research was funded by the Natural Science Foundation of Hunan Province (grant no. 2021JJ50143), Hunan Science and Technology Talent Promotion Project (grant no. 2019TJ-Y08), and the Hunan Education Department Foundation Funded Project of China (grant nos. 21B0713 and 18A401). This study has received the help of Dr. Bao Y in the preparation of papers and data collation.

References

- [1] Federal Highway Administration (Fhwa), *US Department of Transportation. Manual for Design, Construction and Maintenance of Orthotropic Steel Deck Bridges*, Books Express Publishing, Berkshire, UK, pp. 2–23, 2012.
- [2] Q. H. Zhang, Y. Z. Bu, and Q. Li, “Review on fatigue problems of orthotropic steel bridge deck,” *China Journal of Highway and Transport*, vol. 30, no. 3, pp. 14–30, 2017.
- [3] Z. Xiang, Z. Zhu, Y. Huang, and T. Wang, “FEM analysis on fatigue cracking mechanism of diaphragm cutout in orthotropic steel decks,” in *Proceedings of the ASCE/The 4th orthotropic bridge conference proceedings*, pp. 125–136, Tianjin, China, September 2015.
- [4] Z. W. Zhu, Y. Huang, and Z. Xian, “Fatigue performance of floorbeam cutout detail of orthotropic steel bridge on heavy freight transportation highway,” *China Journal of Highway and Transport*, vol. 30, no. 3, pp. 104–112, 2017.
- [5] Y. Bao, W. Meng, Y. Chen, G. Chen, and K. H. Khayat, “Measuring mortar shrinkage and cracking by pulse pre-pump Brillouin optical time domain analysis with a single optical fiber,” *Materials Letters*, vol. 145, pp. 344–346, 2015.
- [6] Y. Bao, M. Valipour, W. Meng, K. H. Khayat, and G. Chen, “Distributed fiber optic sensor-enhanced detection and prediction of shrinkage-induced delamination of ultra-high-performance concrete overlay,” *Smart Materials and Structures*, vol. 26, no. 8, Article ID 085009, 2017.
- [7] Q. Zhang, Y. Liu, Y. Bao, D. Jia, Y. Bu, and Q. Li, “Fatigue performance of orthotropic steel-concrete composite deck with large-size longitudinal U-shaped ribs,” *Engineering Structures*, vol. 150, pp. 864–874, 2017.
- [8] Y. Liu, Q. Zhang, W. Meng, Y. Bao, and Y. Bu, “Transverse fatigue behaviour of steel-UHPC composite deck with large-size U-ribs,” *Engineering Structures*, vol. 180, pp. 388–399, 2019.
- [9] J. Qi, Y. Bao, J. Wang, L. Li, and W. Li, “Flexural behavior of an innovative dovetail UHPC joint in composite bridges under negative bending moment,” *Engineering Structures*, vol. 200, Article ID 109716, 2019.
- [10] W. Meng and K. H. Khayat, “Effect of hybrid fibers on fresh properties, mechanical properties, and autogenous shrinkage of cost-effective UHPC,” *Journal of Materials in Civil Engineering*, vol. 30, Article ID 04018030, 2018.
- [11] W. Meng and K. H. Khayat, “Mechanical properties of ultra-high-performance concrete enhanced with graphite nanoplatelets and carbon nanofibers,” *Composites Part B: Engineering*, vol. 107, pp. 113–122, 2016.
- [12] W. Meng, M. Valipour, and K. H. Khayat, “Optimization and performance of cost-effective ultra-high performance concrete,” *Materials and Structures*, vol. 50, no. 1, p. 29, 2017.
- [13] W. Meng and K. H. Khayat, “Improving flexural performance of ultra-high-performance concrete by rheology control of suspending mortar,” *Composites Part B: Engineering*, vol. 117, pp. 26–34, 2017.
- [14] Z. W. Zhu, Y. Huang, P. X. Wen, W. Chen, Y. G. Shi, and X. D. Shao, “Investigation on fatigue performance of orthogonality bridge deck with steel-UHPC composite system under random traffic flows,” *China Journal of Highway and Transport*, vol. 30, no. 3, pp. 200–209, 2017.
- [15] S. Zhang, X. Shao, J. Cao, J. Cui, J. Hu, and L. Deng, “Fatigue performance of a lightweight composite bridge deck with open ribs,” *Journal of Bridge Engineering*, vol. 21, no. 7, Article ID 04016039, 2016.
- [16] Z. Zhu, T. Yuan, Z. Xiang, Y. Huang, Y. Zhou, and X. D. Shao, “Stress behaviors and fatigue performance of details in orthotropic steel bridges with UHPC-deck plate composite system under in-service traffic flows,” *Journal of Bridge Engineering*, vol. 23, no. 3, pp. 1–21, 2018.
- [17] B. A. Graybeal, *Material Property Characterization of Ultra-high Performance Concrete (No. FHWA-HRT-06-103)*, Federal

Highway Administration, Office of Infrastructure Research and Development, McLean, VA, USA, 2006.

- [18] A. Sriram, B. Petersen, and S. Sritharan, *Design Guide for Precast UHPC Waffle Deck Panel System, Including Connections*; FHWA-HRT-13-032, US Department of Transportation Federal Highway Administration, Washington, DC, USA, 2013.
- [19] B. Graybeal, *Design and Construction of Field-Cast UHPC Connections*, United States Federal Highway Administration, McLean, VA, USA, 2014.
- [20] M. Tohru and E. Brühwiler, "Tensile fatigue behaviour of ultra-high performance fibre reinforced concrete (UHPCFR)," *Materials and Structures*, vol. 47, pp. 475–491, 2014.

Research Article

Hysteretic Behavior of H-Shaped Honeycombed Steel Web Composite Columns with Rectangular Concrete-Filled Steel Tube Flanges

Jing Ji,^{1,2} Yubo Lin ,¹ Liangqin Jiang ,^{1,2} Wen Li,¹ Hongguo Ren ,³ Ruili Wang,⁴ Zihao Wang ,³ MaoMao Yang,¹ and Chenyu Yu ¹

¹College of Civil and Architectural Engineering, Northeast Petroleum University, Heilongjiang Key Laboratory of Disaster Prevention, Mitigation and Protection Engineering, No. 99 Xuefu Road, Longfeng, Daqing 163318, China

²Key Laboratory of Earthquake Engineering and Engineering Vibration, Institute of Engineering Mechanics, China Earthquake Administration, No. 29 Xuefu Road, Nangang, Harbin 150000, China

³Handan Key Laboratory of Building Physical Environment and Regional Building Protection Technology, School of Architecture and Art, Hebei University of Engineering, No. 19 Taiji Road, Handan Economic and Technological Development District, Handan 056038, China

⁴School of Management Engineering and Business, Hebei University of Engineering, No. 199 Guangming South Road, Hanshan, Handan 056038, China

Correspondence should be addressed to Hongguo Ren; renhongguo771126@163.com and Zihao Wang; wangzihao20211031@163.com

Received 7 November 2021; Accepted 27 December 2021; Published 1 February 2022

Academic Editor: Lingkun Chen

Copyright © 2022 Jing Ji et al. This is an open access article distributed under the Creative Commons Attribution License, which permits unrestricted use, distribution, and reproduction in any medium, provided the original work is properly cited.

This study aims to investigate the hysteretic behavior of H-shaped honeycombed steel web composite columns with rectangular concrete-filled steel tube flanges (STHCCs). Taking the shear span ratio (λ_s), axial compression ratio (n), steel ratio of section (α), aspect ratio of section (D/B), yield strength of steel tube (f_{yk}), and compressive strength of concrete (f_{ck}) as the main parameters, we designed 22 full-scale STHCCs. By comparing the load-displacement curves between test and simulation, the rationality of finite element modeling method was verified. The quasi-static analysis of 22 specimens was carried out, and the influence regularity of different variables on the hysteretic behavior, skeleton curves, ductility, energy dissipation, resistance degradation, and stiffness degradation of STHCCs was obtained. The results show that the hysteresis curves of all the specimens show full shuttle shape and strong energy dissipation capacity. λ_s , α , and f_{yk} have great influence on the bearing capacity of skeleton curves. With the increase of α and f_{yk} , the initial stiffness of the specimens gradually increases. The stiffness degradation rate of the specimens gradually slows down, and the energy dissipation coefficient gradually decreases by increasing λ_s , α , and f_{yk} , but energy dissipation capacity is still at a high level. The resistance degradation of specimens increases gradually by increasing λ_s , α , f_{yk} , and D/B . The ductility of specimens gradually increases by increasing n , α , and f_{ck} . The maximum bulging deformation and maximum stress of specimens appear at the column foot. The trilinear skeleton curve model and restoring force model of STHCCs are established by statistical regression.

1. Introduction

STHCCs, short for H-shaped honeycombed steel web composite columns with rectangular concrete-filled steel tube flanges, are a kind of novel composite members formed by

connecting two concrete-filled rectangular steel tube flanges with a honeycombed steel web. The core concrete can effectively prevent and delay the local buckling of the steel tube and the instability failure of the specimens; the steel tube also has certain restraint action on the concrete, which results in

the core concrete under a state of triaxial compression; and the compressive strength and the ability to resist deformation of the core concrete can be significantly improved.

Since the twentieth century, a lot of research has been carried out regarding concrete-filled steel tube (CFST) columns and honeycombed columns at home and abroad. Sakino et al. [1] designed and fabricated 114 short CFST columns with different parameters of the shape of the steel tube, the tensile strength of the steel tube, the diameter-thickness ratio of the steel tube, and the strength of the concrete, and a formula for the ultimate axial bearing capacity was proposed. The mechanical behavior of concrete-filled double-layer circular steel tube columns was studied by Essopjee and Dundu [2]. The tests of 32 specimens subjected to axial compression were conducted, and the bearing capacity formula of concrete-filled double-layer circular steel tube columns was proposed. Anupriya et al. [3] carried out experimental research on honeycomb beams with stiffeners and without stiffeners, analyzed the failure mode of honeycomb beams under concentrated load, and also proposed a method for calculating the compressive strength of honeycomb beams webs after buckling. The nonlinear buckling analysis of 30 STHCCs with different parameters were carried out by Ji et al. [4]. According to the finite element (FE) simulation results, the formula for calculating the stability bearing capacity of STHCCs was derived. In order to investigate the axial compression behavior of short STHCCs with different parameters, an experimental study of 16 short STHCCs was designed and carried out by Ji et al. [5], and the calculation formula of the axial bearing capacity for this type of short column was established. In 2020, Ji et al. [6] investigated the eccentric compression performance of 17 STHCCs by ABAQUS software and derived the calculation formula of eccentric compression bearing capacity for STHCCs. Low-cycle repeated loading tests on CFST beam-column structures were conducted by Varma et al. [7], the FE model of the structure was established, and the reliability of the model was verified, which provided a basis for the calculation of the bearing capacity of CFST structures. Gajalakshmi and Helena [8] took the diameter-thickness ratio of steel tube as a variable to conduct low-cycle repeated loading tests on four circular CFST columns, analyzed the variations of hysteretic curves for CFST columns under different loading levels, and proposed a simplified damage accumulation equation of CFST columns. Low cyclic loading tests on recycled CFST columns and ordinary CFST columns were carried out by Chen et al. [9] and Tang et al. [10]. The

influence of axial compression ratio, steel tube strength, steel tube thickness, and other parameters on the seismic behavior of CFST columns was discussed, and a fitting formula for skeleton curve based on Boltzmann mathematical model was proposed. The seismic capacity of 16 ultralarge high strength concrete-filled circular steel tube (HCFTST) columns under cyclic loading was analyzed by Wang et al. [11], and a strength model to predict the bending moment bearing capacity was proposed. Five specimens of multi-cavity CFST specially shaped columns were designed and fabricated by Yin et al. [12]. Through the combination of quasi-static and numerical simulation, the failure mode, hysteresis characteristic, stiffness degradation, ductility, and energy dissipation capacity of each specimen were obtained, and the effect of various parameters on the mechanism of force was explained. The calculation method of characteristic points' values for skeleton curve for solid-web steel reinforced concrete T-shaped column was proposed by Liu et al. [13], and the restoring force model was established, which provided the basis for elastic-plastic seismic response analysis of this type of structure.

The research on STHCCs is mainly aimed at axial compression and stability, and few studies have been done on the hysteretic behavior of this kind of composite columns. Based on the research results of axial compression test of STHCCs, the quasi-static analysis of 22 STHCCs under low cyclic loading is further carried out by ABAQUS software. The influence of different parameters on the hysteretic behavior, skeleton curve, ductility, energy dissipation capacity, resistance attenuation, and stiffness degradation of STHCCs is investigated. The hysteretic behavior and failure form of STHCCs are obtained, and the restoring force model of such columns is established.

2. Specimen Overview

Taking the shear span ratio (λ_s), axial compression ratio (n), steel ratio of section (α), aspect ratio of section (D/B), yield strength of steel tube (f_{yk}), and compressive strength of concrete (f_{ck}) as the main parameters, we design 22 full-scale STHCCs. The schematic diagram and specific parameters of the specimens are shown in Figure 1 and Table 1. Considering the confinement effect of steel tube on concrete, pitch-height ratio, hole-height ratio, and slenderness ratio, the nominal axial compression ratio (n) [14] of the specimens is calculated as follows:

$$n = \frac{N}{N_u} = \frac{N}{\left[(d/h_w)^{-0.39} + (s/h_w)^{0.717} + \xi^{0.178} + \bar{\lambda}_{oy}^{-0.227} - 1.284 \right] \times \varphi \sum A_{sci} \times f_{sc}}, \quad (1)$$

where $\bar{\lambda}_{oy}$ refers to the conversion slenderness ratio of the columns, f_{sc} refers to the equivalent strength of CFST section, A_{sci} denotes the section area of single-limb CFST, N_u denotes the design value of axial compression bearing

capacity of the columns, φ represents the stability coefficient of CFST axial compression specimens, and s/h_w and d/h_w represent the pitch-height ratio and the hole-height ratio, respectively.

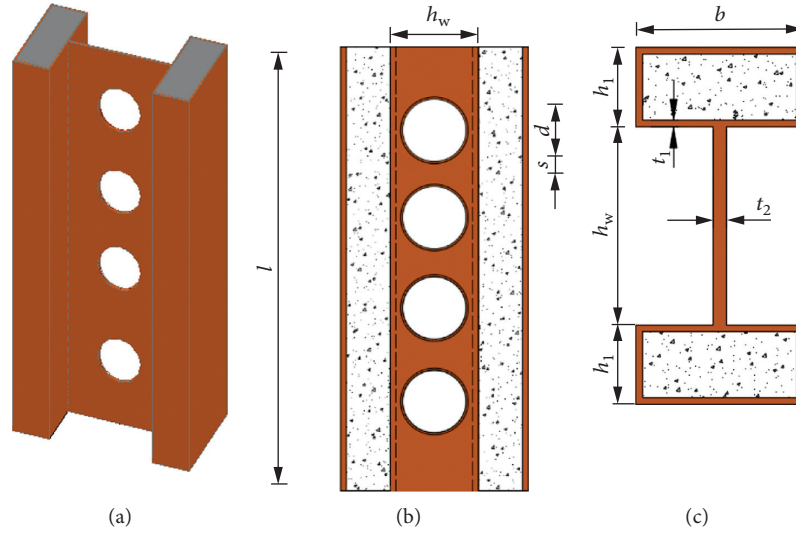


FIGURE 1: The three-dimensional model of STHCCs. (a) Three-dimensional model. (b) Longitudinal section of STHCCs. (c) Cross section of STHCCs.

TABLE 1: Specific parameters of 22 STHCC specimens.

Specimens	$h_1 \times b \times h_w \times t_1 \times t_2$ (mm)	L (mm)	D/B	λ_s	n	α	f_{ck} (MPa)	f_{yfk} (MPa)
STHCC1	$320 \times 500 \times 400 \times 8 \times 10$	2160	2.08	2.08	0.4	0.044	40	235
STHCC2	$320 \times 500 \times 400 \times 8 \times 10$	2550	2.08	2.45	0.4	0.044	40	235
STHCC3	$320 \times 500 \times 400 \times 8 \times 10$	2750	2.08	2.64	0.4	0.044	40	235
STHCC4	$320 \times 500 \times 400 \times 8 \times 10$	3460	2.08	3.33	0.4	0.044	40	235
STHCC5	$320 \times 500 \times 400 \times 8 \times 10$	3460	2.08	3.33	0.1	0.044	40	235
STHCC6	$320 \times 500 \times 400 \times 8 \times 10$	3460	2.08	3.33	0.2	0.044	40	235
STHCC7	$320 \times 500 \times 400 \times 8 \times 10$	3460	2.08	3.33	0.3	0.044	40	235
STHCC8	$320 \times 500 \times 400 \times 8 \times 10$	3460	2.08	3.33	0.4	0.044	30	235
STHCC9	$320 \times 500 \times 400 \times 8 \times 10$	3460	2.08	3.33	0.4	0.044	50	235
STHCC10	$320 \times 500 \times 400 \times 8 \times 10$	3460	2.08	3.33	0.4	0.044	60	235
STHCC11	$320 \times 500 \times 400 \times 4 \times 10$	3460	2.08	3.33	0.4	0.021	40	235
STHCC12	$320 \times 500 \times 400 \times 6 \times 10$	3460	2.08	3.33	0.4	0.032	40	235
STHCC13	$320 \times 500 \times 400 \times 10 \times 10$	3460	2.08	3.33	0.4	0.056	40	235
STHCC14	$320 \times 500 \times 400 \times 8 \times 10$	3460	2.08	3.33	0.4	0.044	40	345
STHCC15	$320 \times 500 \times 400 \times 8 \times 10$	3460	2.08	3.33	0.4	0.044	40	390
STHCC16	$320 \times 500 \times 400 \times 8 \times 10$	3460	2.08	3.33	0.4	0.044	40	420
STHCC17	$320 \times 550 \times 400 \times 8 \times 10$	3460	1.89	3.33	0.4	0.042	40	235
STHCC18	$320 \times 600 \times 400 \times 8 \times 10$	3460	1.73	3.33	0.4	0.041	40	235
STHCC19	$320 \times 650 \times 400 \times 8 \times 10$	3460	1.60	3.33	0.4	0.040	40	235
STHCC20	$280 \times 500 \times 400 \times 8 \times 10$	3460	1.92	3.33	0.4	0.048	40	235
STHCC21	$400 \times 500 \times 400 \times 8 \times 10$	3460	2.40	3.33	0.4	0.031	40	235
STHCC22	$480 \times 500 \times 400 \times 8 \times 10$	3460	2.72	3.33	0.4	0.034	40	235

Note. h_w , h_1 , b , t_1 , and t_2 denote the web width, flange steel tubes height, flange steel tubes width, flange steel tubes thickness, and web thickness, respectively. $\lambda_s = l/(2h_1 + h_w)$, $D/B = (2h_1 + h_w)/b$, $\alpha = A_s/A_c$. A_s and A_c represent the area of flange steel tube and concrete, respectively.

3. Finite Element Model

3.1. Constitutive Model for Materials

3.1.1. Constitutive Model for Steel. According to the metal plasticity theory, the stress-strain curves of steel are generally determined by the tensile test of standard specimens. Here, the ideal bilinear elastoplastic constitutive model (CM) is adopted as CM of steel.

3.1.2. Constitutive Model for Concrete. Mander et al. [15], Teng et al. [16], Han [17], and Pagoulatou et al. [18] have successively given the CM of confined concrete; the CM of unconfined concrete has been given in Code for Design of Concrete Structures (GB50010-2010) by China [19]; and the comparison between them is shown in Figure 2. Through comparative analysis, the CM of confined concrete proposed by Han et al. [17] is adopted as CM of concrete. It is known

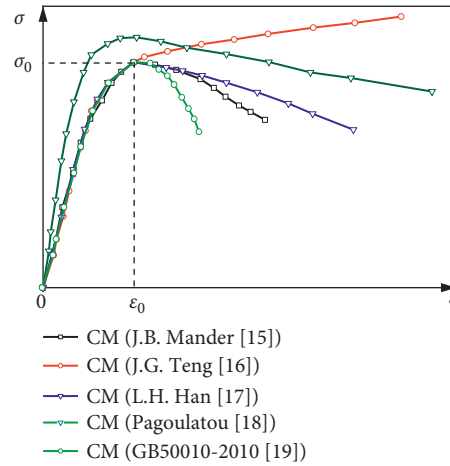


FIGURE 2: Typical constitutive models for concrete.

that concrete is anisotropic material with uneven internal structure and complex mechanical behavior, so the influence of plastic damage on concrete is considered during the FE modeling process.

3.2. Modeling Process and Boundary Conditions. The three-dimensional solid element with eight nodes (C3D8R) was adopted to simulate steel tubes, concrete, and steel webs, and the FE models of STHCCs were established by ABAQUS software [20], as shown in Figure 3. The contact interaction between steel tube and concrete was set as normal contact and bond slip contact in tangential direction, thus shear stress can be transmitted between steel tube and concrete [21]. The friction coefficient (μ) was set as 0.3 [22].

A reference point was set at the center of the upper surface of STHCCs as shown in Figure 3, and the reference point was coupled with the corresponding specimen surfaces, which could ensure that the stress on the specimen surface was uniform in the process of axial compression, and could avoid the bias of the members as well. The displacement in X , Y directions and the rotation in three directions of the reference point were restricted ($U_x = U_y = U_{R_x} = U_{R_y} = U_{R_z} = 0$), while the bottom of STHCCs was completely fixed. In order to ensure the quality of meshing and the accuracy of calculation, 80 mm was taken as the mesh size of FEM, and the mesh shape was mainly hexahedron.

4. Experimental Verification of FE Models

In order to verify the rationality of the above-mentioned modeling method, numerical simulation analysis on 14 specimens selected from [5] was carried out, and the specific parameters of the 14 specimens are listed in Table 2. The load-displacement curves of specimens obtained by simulation analysis are shown in Figure 4. Compared with the existing test curves, the load-displacement curves obtained by numerical simulation were in good agreement with the test results. The simulation results of the axial compression bearing capacity (N_u^S) of the specimens were extracted correspondingly and compared with the existing test results

(N_u^T) subsequently, and the maximum error was 5.58%, as shown in Figure 5. The error was within a reasonable range, which indicated that the modeling method was applicable to such composite columns.

5. Loading Procedure

In the process of quasi-static analysis, the axial load (N) is applied firstly to the top of the columns, then a force-displacement hybrid control program is used for lateral loading, and the loading procedure involved a force control step and a displacement control step as shown in Figure 6. In the force control stage, the increment of lateral load (P) was $\pm 1/3$ times the yielding load (P_y). The loading procedure was changed into the displacement control stage, and the increment of displacement was 0.4 times the peak displacement (Δ_m). Each displacement load step was repeated twice. When the lateral load of the specimens dropped below 85% of the peak load, the specimens were regarded as failure [23].

6. Parameter Analysis

6.1. Hysteresis Curves. The hysteresis curves of 22 STHCCs under low cyclic loading can be obtained by FE analysis as shown in Figure 7. The elasticity, elastic-plastic, plastic, ultimate bearing capacity, energy dissipation capacity, and ductility of the specimens can be reflected from the hysteresis curves [24]. It is indicated in Figure 7 that the hysteretic curves of all the specimens are relatively full, and there is no obvious pinching phenomenon from the early stage to the late stage. α has a great influence on the hysteresis curves of STHCC specimens; with the increase of α , the hysteresis curve gradually becomes fuller, and the ultimate displacement of the specimens gradually increases. After reaching the peak load, the decrease of the bearing capacity of the specimens gradually slows down, and the ductility becomes better.

6.2. Skeleton Curves. The skeleton curves can intuitively reflect the force condition of STHCC specimens during the whole process of quasi-static simulation analysis, and the

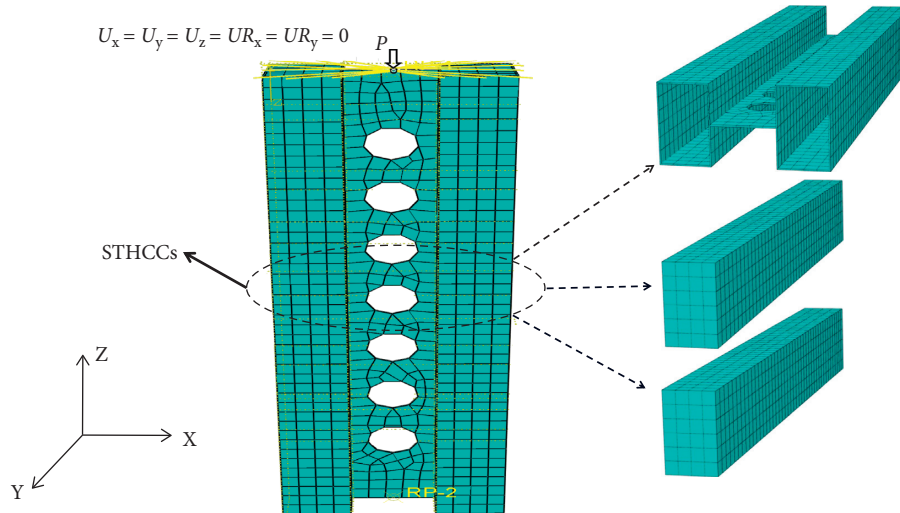


FIGURE 3: The FE model of STHCCs.

TABLE 2: Comparison of simulation and test value subjected to axial compression.

Specimens	$h_1 \times b \times h_w \times t_1 \times t_2$ (mm)	L (mm)	λ	f_{yf} (MPa)	f_{yw} (MPa)	ξ	f_{cu} (MPa)	N_u^T (kN)	N_u^S (kN)	$ N_u^T - N_u^S /N_u^T$ (%)
STHCC1	$50 \times 100 \times 100 \times 1.7 \times 06$	370	12.82	269	321	0.60	49.50	741.21	736.94	0.58
STHCC2	$50 \times 100 \times 100 \times 2.3 \times 06$	370	12.82	282	321	0.88	49.50	864.59	912.83	5.58
STHCC3	$50 \times 100 \times 100 \times 3.8 \times 06$	370	12.82	286	321	1.60	49.50	1182.15	1184.33	1.20
STHCC4	$50 \times 100 \times 100 \times 2.3 \times 06$	370	12.82	282	321	0.82	53.17	1067.75	1037.13	2.87
STHCC5	$50 \times 100 \times 100 \times 2.3 \times 06$	370	12.82	282	321	0.66	65.60	1173.69	1168.35	0.45
STHCC6	$50 \times 100 \times 100 \times 2.3 \times 06$	370	12.82	282	321	0.78	55.69	1086.86	1053.54	3.08
STHCC7	$50 \times 100 \times 100 \times 1.7 \times 08$	370	12.82	269	325	0.60	49.50	763.17	781.58	2.41
STHCC8	$50 \times 100 \times 100 \times 1.7 \times 12$	370	12.82	269	331	0.60	49.50	798.26	786.84	1.43
STHCC9	$50 \times 100 \times 100 \times 2.3 \times 06$	270	9.35	282	321	0.88	49.50	948.52	957.48	0.94
STHCC10	$50 \times 100 \times 100 \times 2.3 \times 06$	470	16.28	282	321	0.88	49.50	841.31	863.90	2.44
STHCC11	$50 \times 100 \times 100 \times 1.7 \times 06$	270	9.35	269	321	0.60	49.50	781.37	761.63	1.53
STHCC12	$50 \times 100 \times 100 \times 1.7 \times 06$	470	16.28	269	321	0.60	49.50	716.92	733.36	2.29
STHCC13	$50 \times 100 \times 100 \times 3.8 \times 06$	270	9.35	286	321	1.60	49.50	1268.30	1273.31	0.40
STHCC14	$50 \times 100 \times 100 \times 3.8 \times 06$	470	16.28	286	321	1.60	49.50	1076.86	1088.53	1.08

Note. f_{yf} , f_{yw} , and f_{cu} denote the measured average value of the yield strength of the steel tube flange, the measured average value of the yield strength of the steel web, and the measured average value of the axial compressive strength of the cube concrete, respectively. λ is the slenderness ratio, $\lambda = 2\sqrt{3}l/b$, ξ represents the confinement effect coefficient of the steel tube, $\xi = A_s f_{yf} / A_c f_{ck}$, and f_{ck} refers to the standard value of f_{ck} of concrete calculated from the measured value.

skeleton curves of 22 STHCCs are shown in Figure 8. It is noteworthy that the skeleton curves can be roughly divide into three stages: elastic deformation stage, elastic-plastic stage, and load decline stage, which are similar to the load-displacement curves of the specimens obtained by axial compression tests. The skeleton curves of the specimens show a linear trend at the initial loading stage; at the same time, the specimens show elastic deformation. With the increase of horizontal load, the skeleton curves change into nonlinear gradually, and elastic-plastic deformation appears for the steel tubes. The plastic damage of concrete continues to accumulate until the load reaches the peak load. After the peak load, the skeleton curves begin to decline. It is demonstrated that the specimens show excellent bearing capacity.

With the increase of λ_s , the initial stiffness of the specimens and the bearing capacity gradually decrease; it can be found that the magnitude of the decline of skeleton curves

slows down gradually, as shown in Figure 8(a). Figures 8(b) and 8(c) show that the influence of n ($n < 0.4$) and f_{ck} ($f_{ck} < 60$ MPa) on the bearing capacity of the specimens is not obvious and that the slope of the curves is similar. Figures 8(d) and 8(e) show that with the increase of α and f_{yfl} , the bearing capacity and deformation capacity increase obviously. Figures 8(f) and 8(g) show that with the increase of D/B , the slope of the descending stage of the skeleton curves decreases gradually.

6.3. Establishment of Skeleton Curve Model and Restoring Force Model

6.3.1. Simplified Skeleton Curve Model. In order to obtain the characteristics of STHCC skeleton curves, the skeleton curves should be normalized firstly [25], as shown in Figure 9.

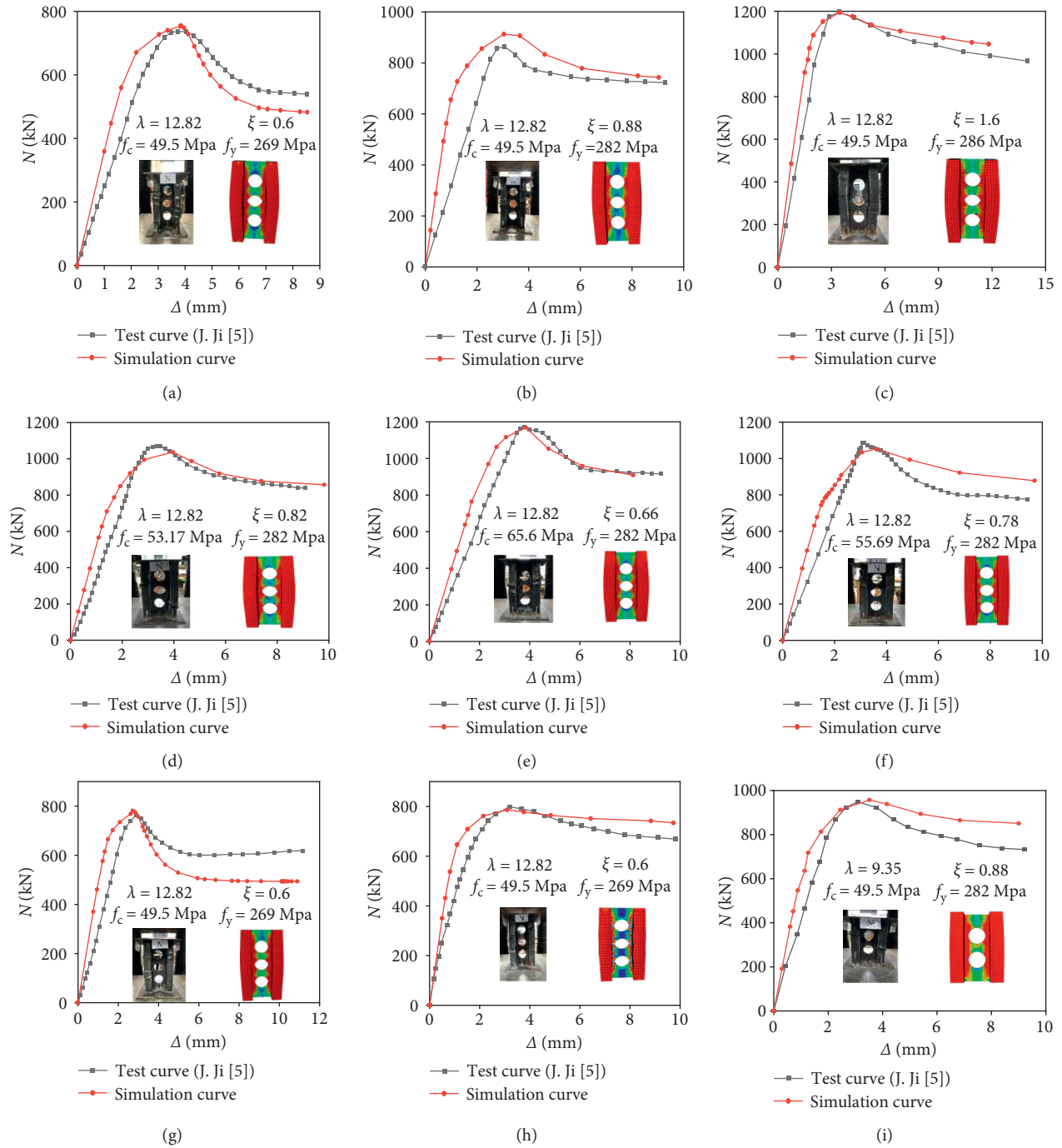


FIGURE 4: Continued.

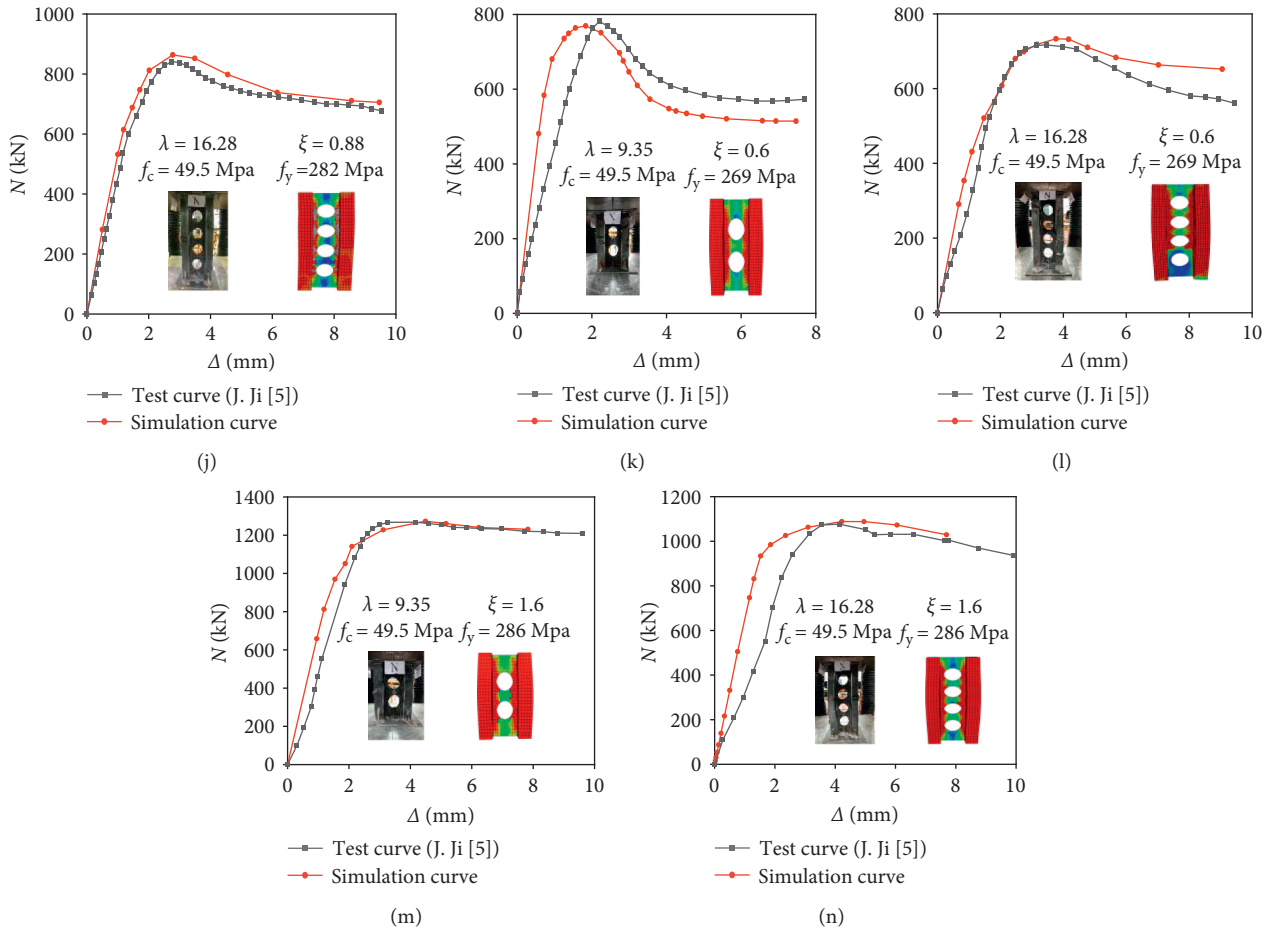


FIGURE 4: Comparisons of load-displacement curves between simulation and test results. (a) STHCC1. (b) STHCC2. (c) STHCC3. (d) STHCC4. (e) STHCC5. (f) STHCC6. (g) STHCC7. (h) STHCC8. (i) STHCC9. (j) STHCC10. (k) STHCC11. (l) STHCC12. (m) STHCC13. (n) STHCC14.

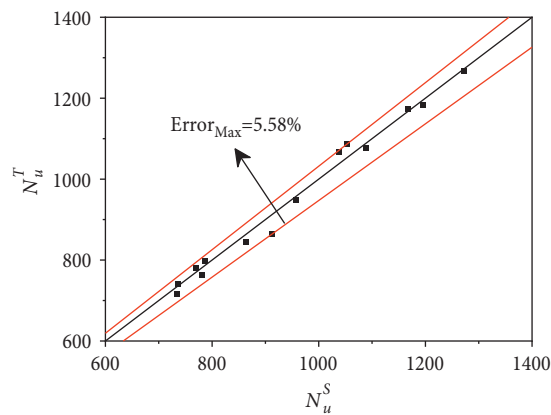


FIGURE 5: Comparison between N_u^T and N_u^S of 14 STHCCs.

It can be found from Figure 9 that the skeleton curves conform to the trilinear law [26, 27], which can be simplified as a calculation model, as shown in Figure 10, and the specific simplified rules are as follows:

- (1) A trilinear model consists of three stages: elastic stage, elastic-plastic stage, and decline stage, where the yield point, peak point, and limit point are considered.

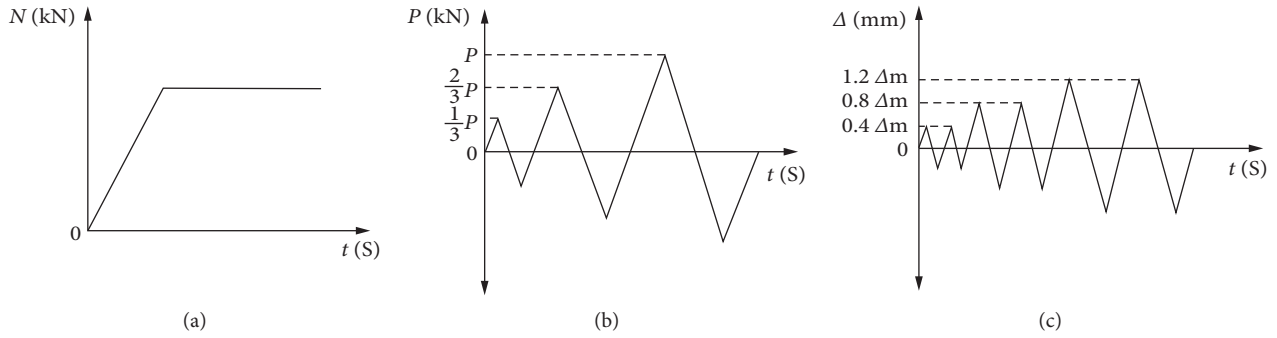


FIGURE 6: Loading procedure. (a) Axial force loading. (b) Single-cycle loading of lateral force. (c) Double-cycle loading of lateral displacement.

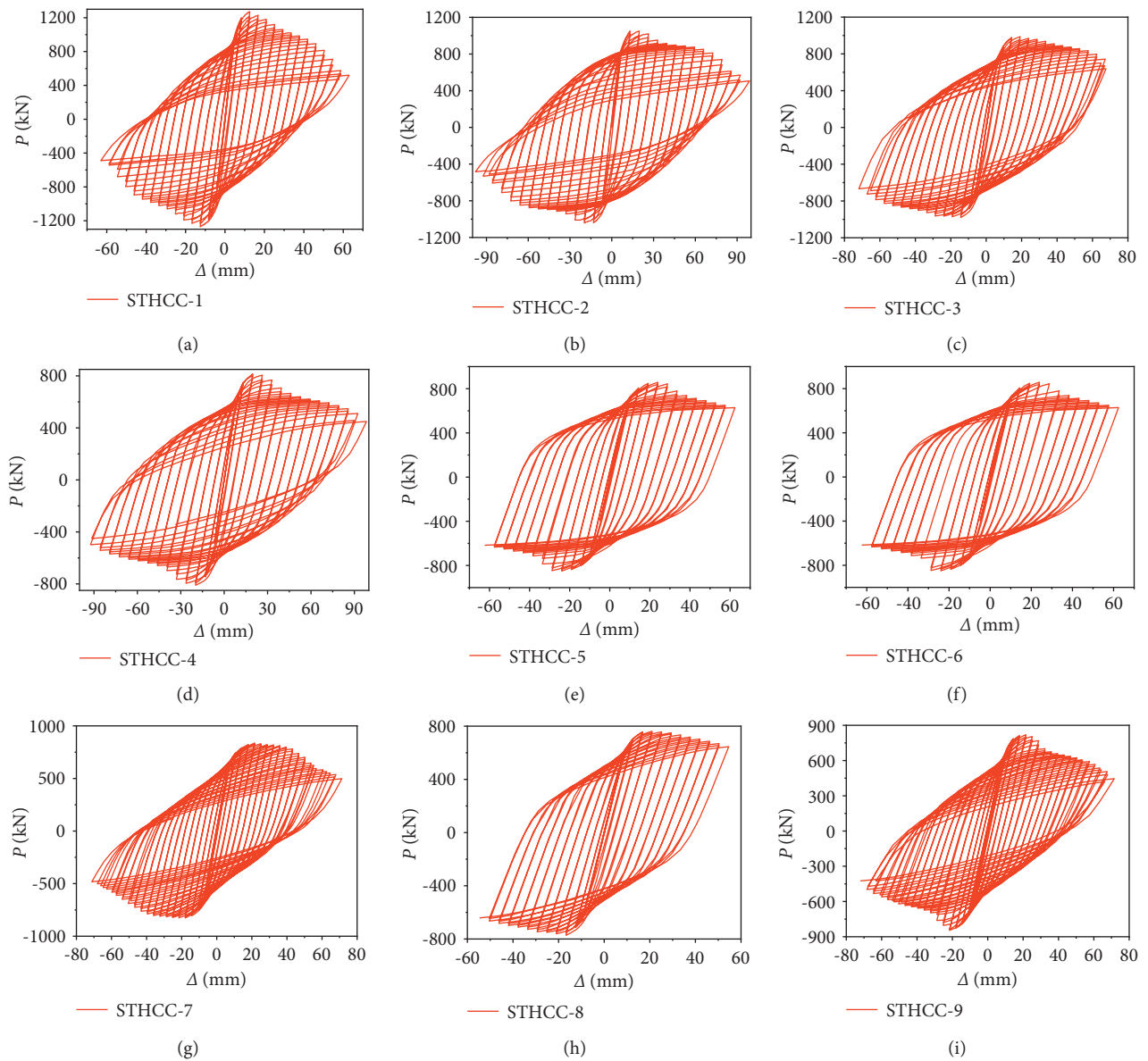
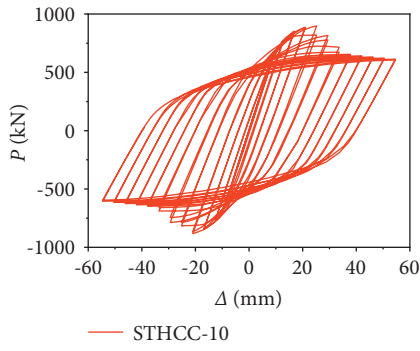
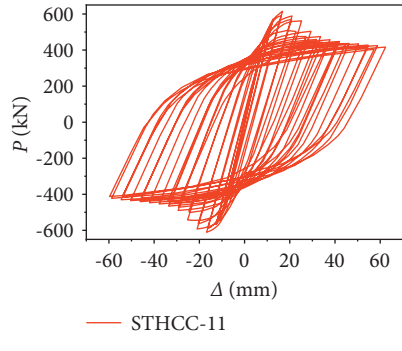


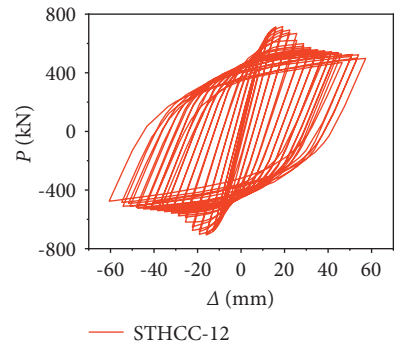
FIGURE 7: Continued.



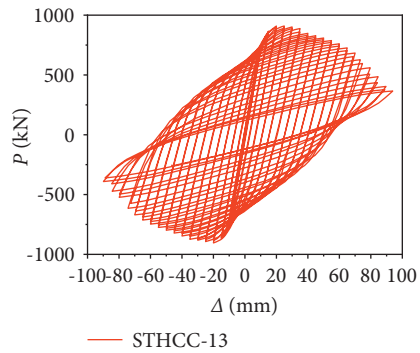
(j)



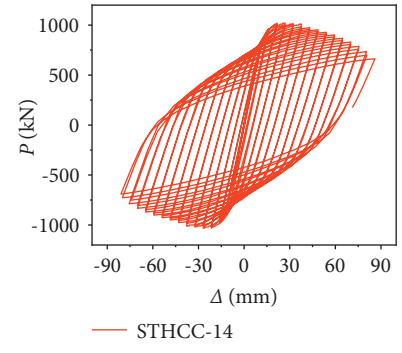
(k)



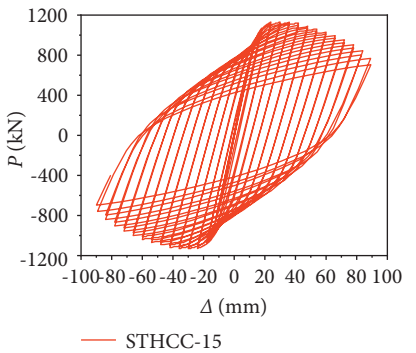
(l)



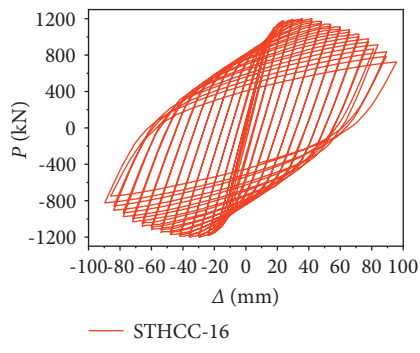
(m)



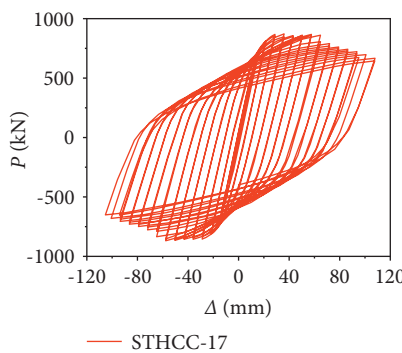
(n)



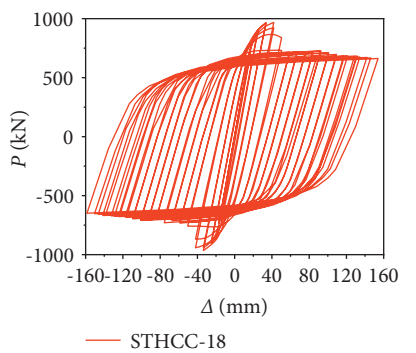
(o)



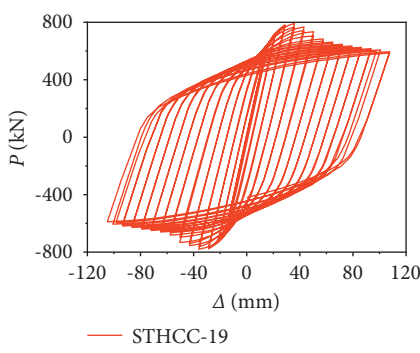
(p)



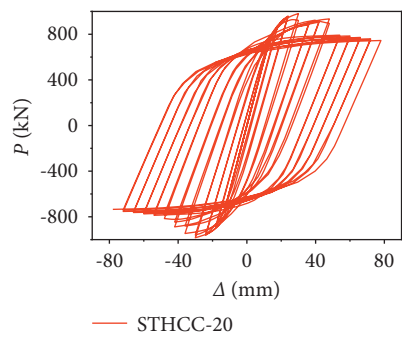
(q)



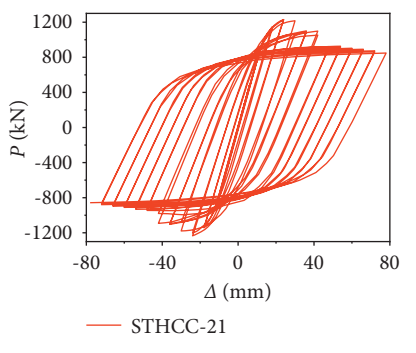
(r)



(s)



(t)



(u)

FIGURE 7: Continued.

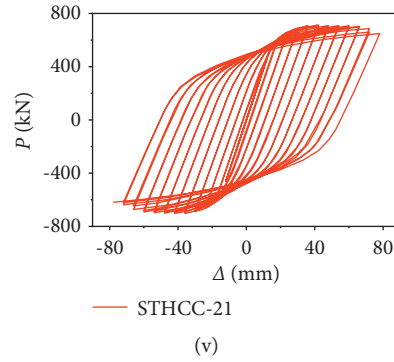


FIGURE 7: Hysteresis curves of 22 STHCCs. (a) STHCC1. (b) STHCC2. (c) STHCC3. (d) STHCC4. (e) STHCC5. (f) STHCC6. (g) STHCC7. (h) STHCC8. (i) STHCC9. (j) STHCC10. (k) STHCC11. (l) STHCC12. (m) STHCC13. (n) STHCC14. (o) STHCC15. (p) STHCC16. (q) STHCC17. (r) STHCC18. (s) STHCC19. (t) STHCC20. (u) STHCC21. (v) STHCC22.

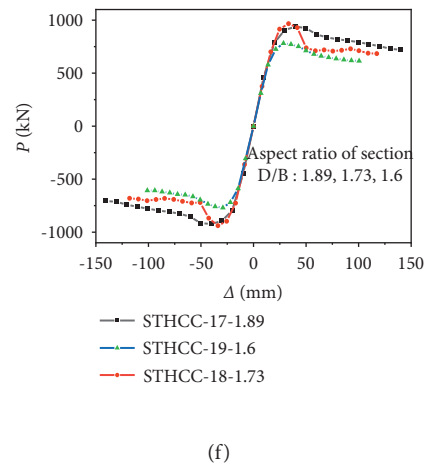
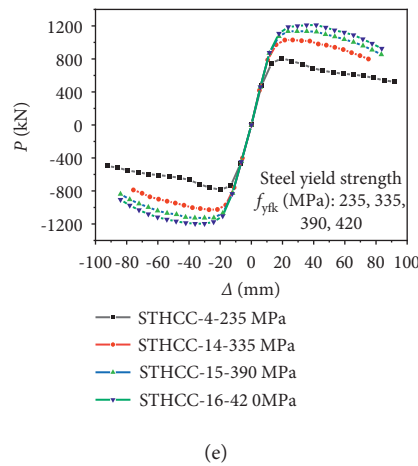
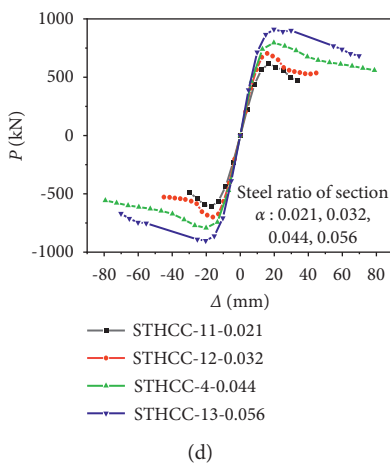
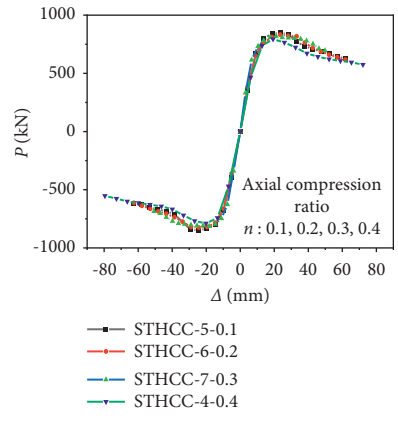
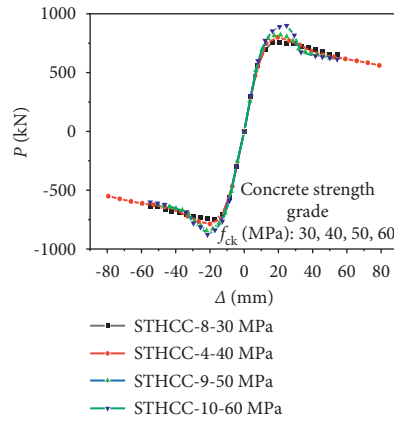
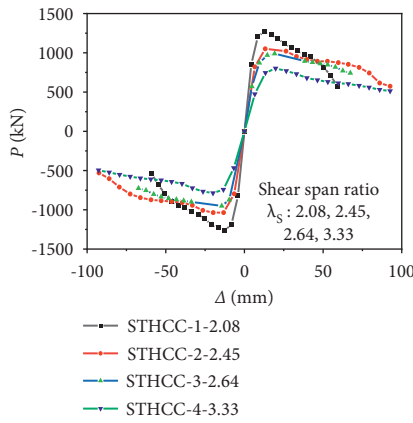


FIGURE 8: Continued.

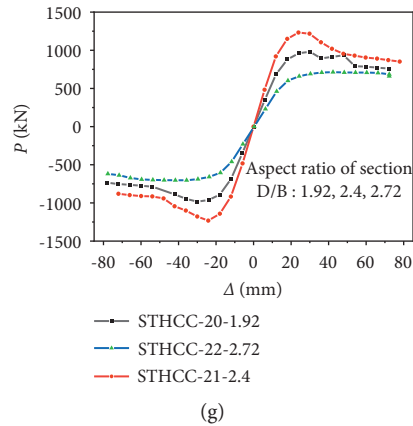


FIGURE 8: Skeleton curves of STHCCs with different parameters. (a) λ_s : 2.08, 2.45, 2.64, 3.33. (b) f_{ck} : 30 MPa, 40 MPa, 50 MPa, 60 MPa. (c) n : 0.1, 0.2, 0.3, 0.4. (d) α : 0.021, 0.032, 0.044, 0.056. (e) f_{yk} : 235 MPa, 335 MPa, 390 MPa, 420 MPa. (f) D/B : 1.89, 1.73, 1.6. (g) D/B : 1.92, 2.4, 2.72.

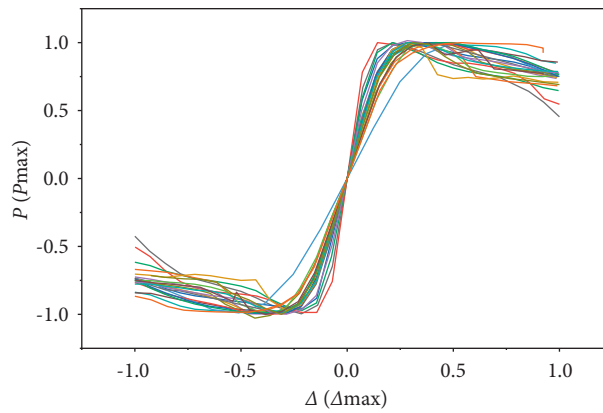


FIGURE 9: Skeleton curves of 22 STHCC specimens.

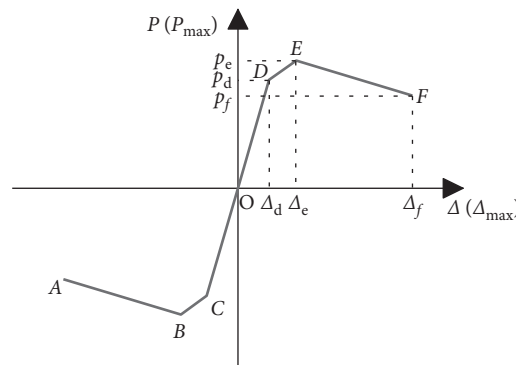


FIGURE 10: Trilinear skeleton curve model for 22 STHCC specimens.

- (2) The values of characteristic points for skeleton curve model are the average positive direction and negative direction values of characteristic points for each specimen.
- (3) It is considered that the specimens are at the elastic stage before yield point; hence, the elastic stiffness is selected as the stiffness. When the load value raises between the yield point and the peak point, the specimen is considered to be at the elastic-plastic

stage. After the peak point, there comes a declining stage, in which the stiffness of the specimens remains at the same value, and the equation of the skeleton curve is shown in Table 3.

6.3.2. Comparisons of Regression Values and Simulation Values of the Skeleton Curves. The comparisons of calculation results and simulation results of the skeleton curves for 22 specimens are illustrated in Figure 11. It can be found

TABLE 3: The equation of the skeleton curve.

Section	Regression equation	Slope
OD	$P/P_{\max}^+ = 4.81 (\Delta/\Delta_{\max}^+)$	4.81
DE	$P/P_{\max}^+ = 0.98 (\Delta/\Delta_{\max}^+) + 0.68$	0.98
EF	$P/P_{\max}^+ = -0.42 (\Delta/\Delta_{\max}^+) + 1.14$	-0.42
OC	$P/P_{\max}^- = 4.73 (\Delta/\Delta_{\max}^-)$	4.73
CB	$P/P_{\max}^- = 1.00 (\Delta/\Delta_{\max}^-) - 0.66$	1.00
BA	$P/P_{\max}^- = -0.41 (\Delta/\Delta_{\max}^-) - 1.12$	-0.41

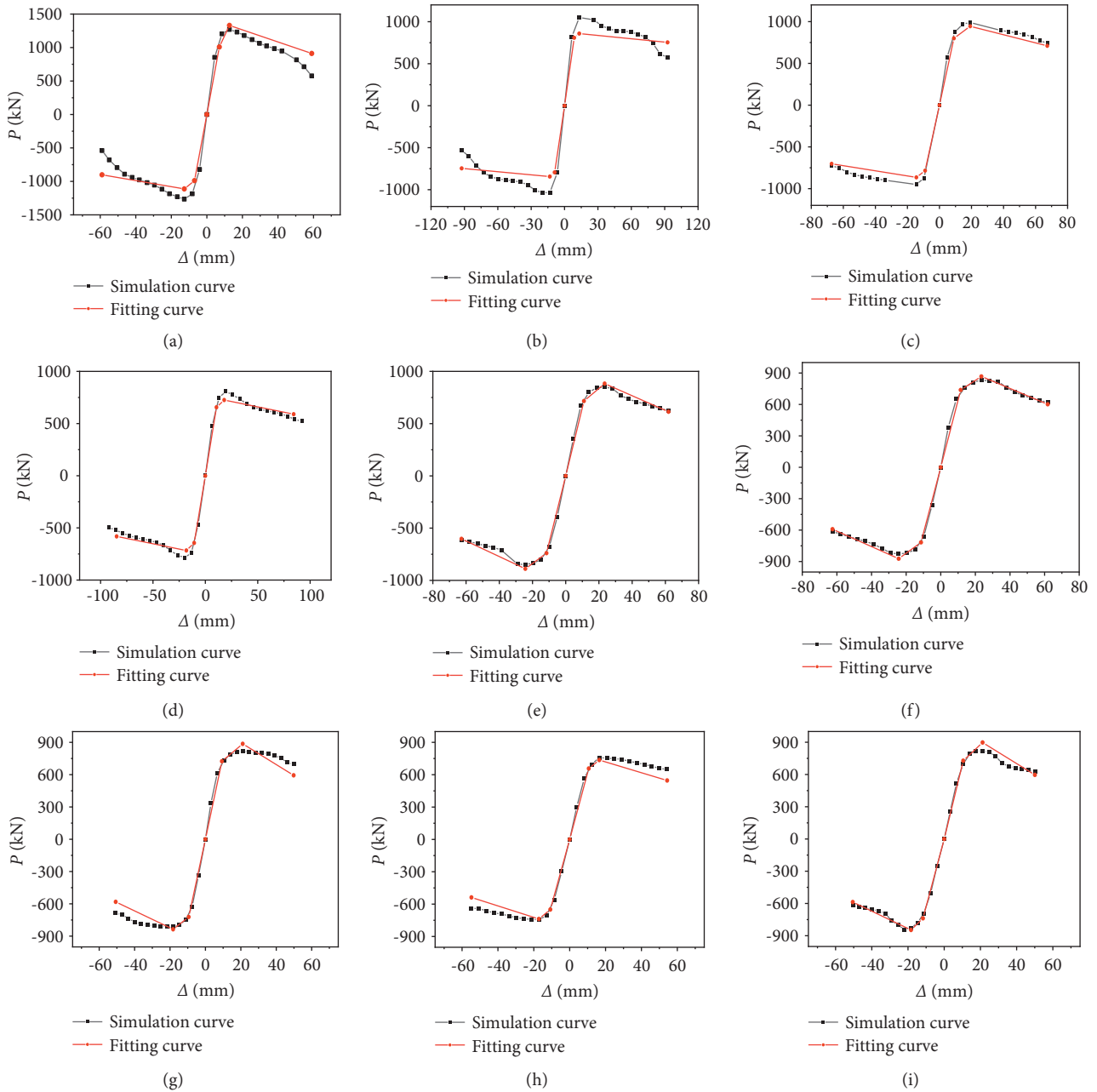


FIGURE 11: Continued.

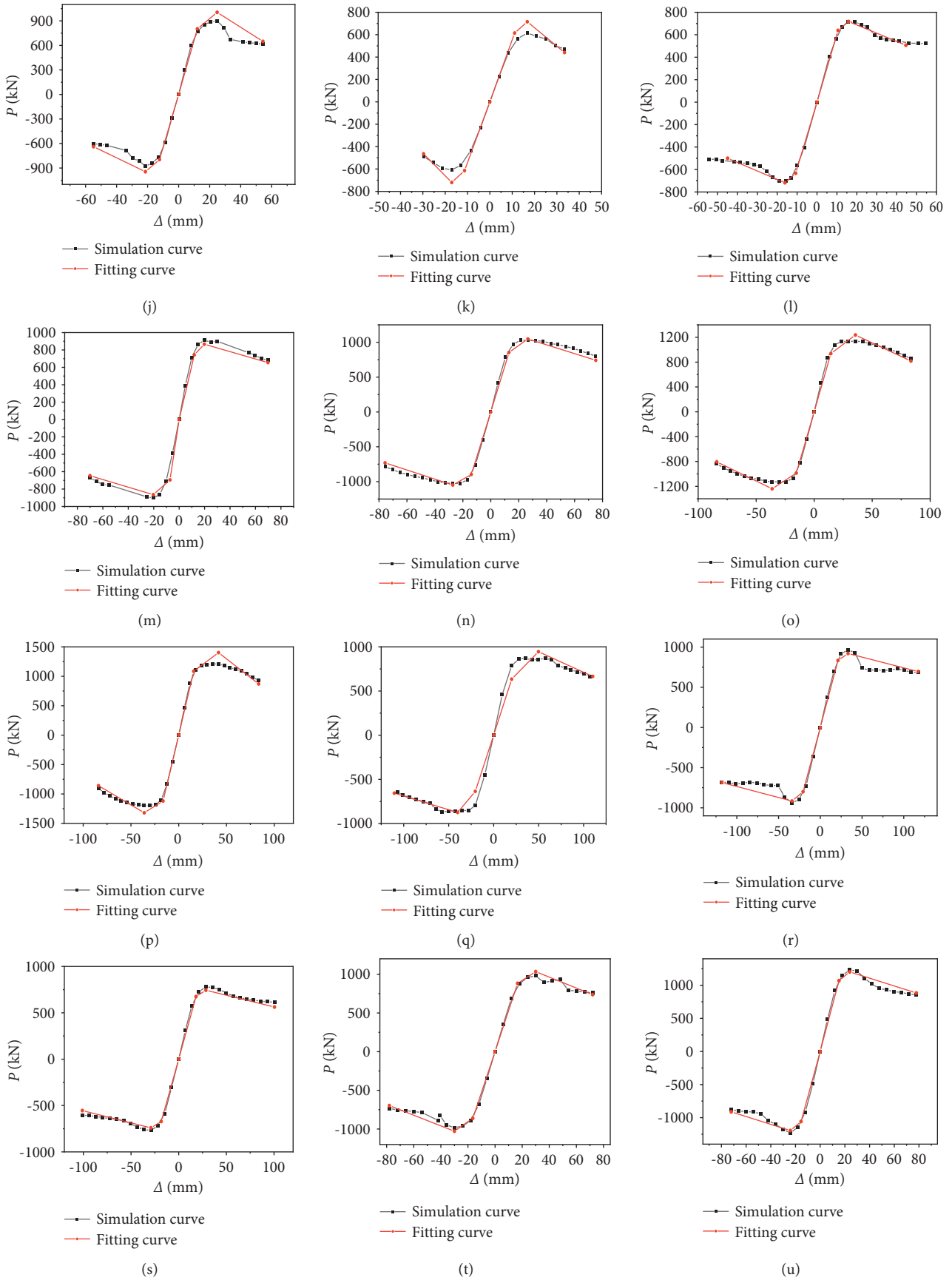


FIGURE 11: Continued.

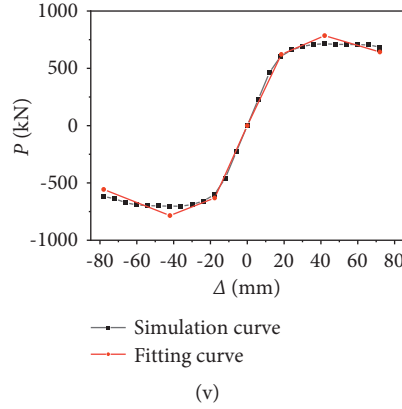


FIGURE 11: Comparisons of skeleton curve model between calculation and simulation. (a) STHCC1. (b) STHCC2. (c) STHCC3. (d) STHCC4. (e) STHCC5. (f) STHCC6. (g) STHCC7. (h) STHCC8. (i) STHCC9. (j) STHCC10. (k) STHCC11. (l) STHCC12. (m) STHCC13. (n) STHCC14. (o) STHCC15. (p) STHCC16. (q) STHCC17. (r) STHCC18. (s) STHCC19. (t) STHCC20. (u) STHCC21. (v) STHCC22.

that the calculation results are in good agreement with the simulation results, which indicates that the skeleton curve model obtained by statistical regression can reflect the load-displacement relationships accurately.

6.4. Stiffness Degradation. The stiffness of the specimens is reflected by the secant stiffness (K_i) [10, 28], which could be expressed by

$$K_i = \frac{|+P_i| + |-P_i|}{|+\Delta_i| + |-\Delta_i|}, \quad (2)$$

where P_i denotes peak horizontal load of the first cycle under the i -th control displacement and Δ_i refers to the corresponding displacement.

The secant stiffness (K_i) versus the horizontal displacement (Δ) relationships of 22 STHCCs are shown in Figure 12. It can be seen from Figure 12 that the stiffness degradation trends of STHCCs are similar. K_i shows a decreasing trend with the increase of Δ , and the curves gradually slow down with the increase of Δ . λ_s , α , D/B , and f_{yk} have a significant impact on the secant stiffness, and with the increase of λ_s , α , and f_{yk} , the stiffness degradation rate of the specimen gradually slows down. With the increase of D/B , the stiffness degradation rate of the specimen improves, and the stiffness degradation phenomenon becomes more significant.

6.4.1. Degradation Law of Stiffness. It is found that the secant stiffness of the specimens decreases constantly during the whole loading and unloading process. In Figure 13, point 1 represents the i -th horizontal load peak point under forward loading, and point 2 represents the i -th horizontal load peak point under reverse loading. The slope of the line from point 1 to point 2 expresses secant stiffness. The relationships between K_i/K_0 and Δ_i/Δ_{max} can be obtained by statistical regression based on the test results, as shown in Figure 14. The regression formula is expressed as follows:

$$K_i/K_0 = 1.221e^{-3.023\Delta_i/\Delta_{max}} + 0.045, \quad (3)$$

where K_i denotes the secant stiffness of the first stage horizontal load peak under the i -th control displacement and Δ_i refers to the i -th control displacement.

6.5. Ductility. Ductility is regarded as a main parameter to measure the deformation performance of the specimens [29], and it can be explained by the ductility coefficient (μ), which can be calculated by the following equation:

$$\mu = \frac{(|\Delta_u^+| + |\Delta_u^-|)}{(|\Delta_y^+| + |\Delta_y^-|)}, \quad (4)$$

where Δ_u^+ , Δ_y^+ refer to positive limit displacement and yield displacement, respectively, and Δ_u^- , Δ_y^- denote negative limit displacement and yield displacement, respectively.

6.5.1. Simulation Results. The ductility coefficients of 22 specimens determined by the above-mentioned calculation method are shown in Table 4. The existing research [25, 30, 31] shows that μ of steel reinforced concrete (SRC) columns ranges from 3.50 to 6.00 when λ_s value is greater than 2. Table 4 shows that the ductility of STHCCs is similar to that of SRC columns, which indicates that the specimens have good deformation behavior.

6.5.2. Shear Span Ratio. The relationships between P_u , μ , and λ_s of the STHCCs are shown in Figure 15. With the increase of λ_s , P_u and μ of the STHCCs decrease gradually. When λ_s changes from 2.08 to 2.45, 2.64, 3.33 in turn, P_u of STHCCs decreases by 17.32%, 5.97%, and 18.92%, respectively, and μ decreases by 9.21%, 1.01%, and 45.83%, respectively.

6.5.3. Axial Compression Ratio. The relationships between P_u , μ , and n of the STHCCs are shown in Figure 16. It can be seen from Figure 16 that when n changes from 0.1 to 0.3, P_u of the STHCCs decreases by 1.92% and 1.81%, respectively, and μ increases by 8.93% and 85.76%, respectively, in which n has a significant effect on the ductility of the STHCCs.

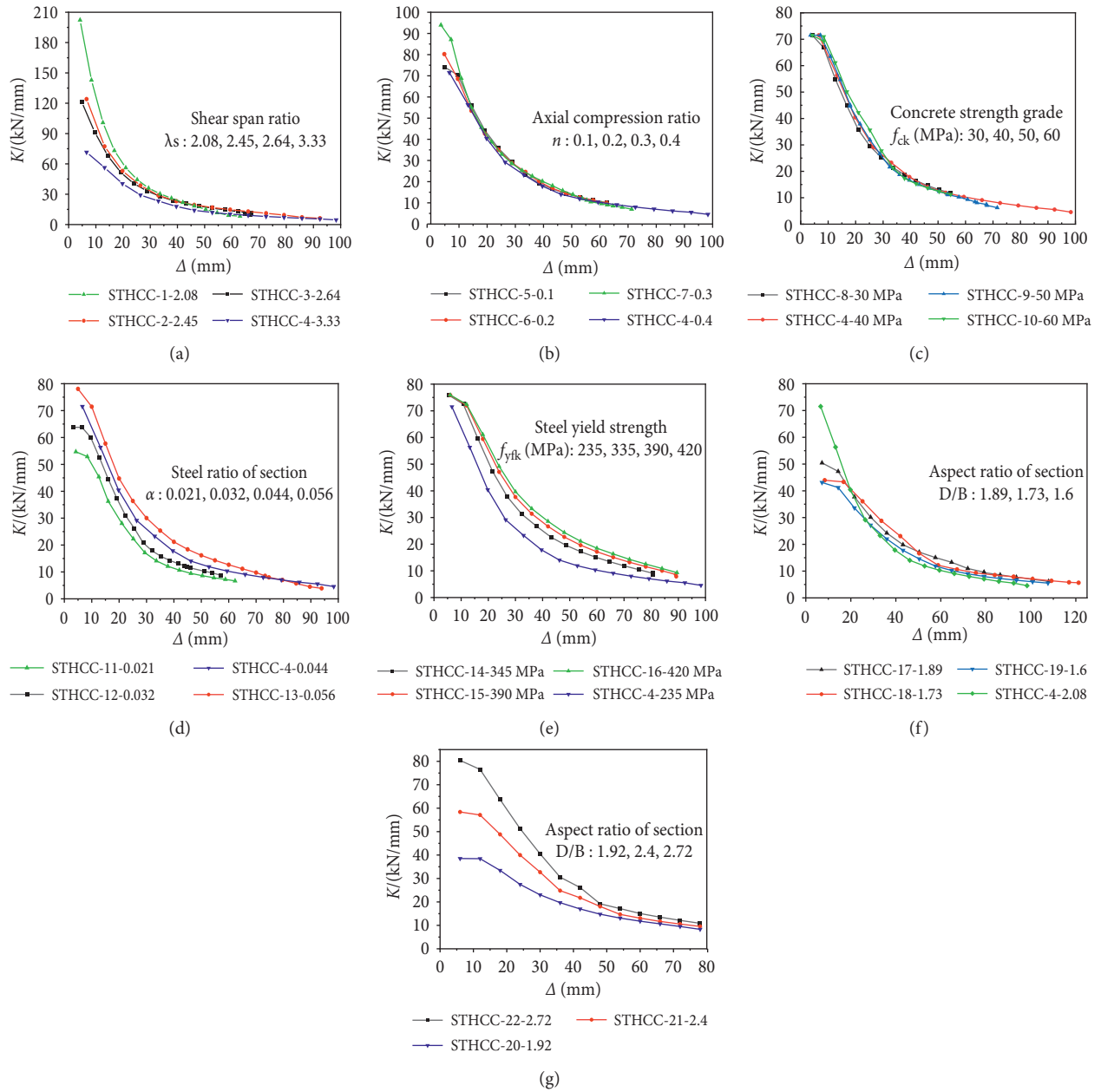


FIGURE 12: The relationships between K_i and Δ for STHCCs with different parameters. (a) λ_s : 2.08, 2.45, 2.64, 3.33. (b) f_{ck} : 30 MPa, 40 MPa, 50 MPa, 60 MPa. (c) n : 0.1, 0.2, 0.3, 0.4. (d) α : 0.021, 0.032, 0.044, 0.056. (e) f_{yk} : 235 MPa, 335 MPa, 390 MPa, 420 MPa. (f) D/B : 1.89, 1.73, 1.6. (g) D/B : 1.92, 2.4, 2.72.

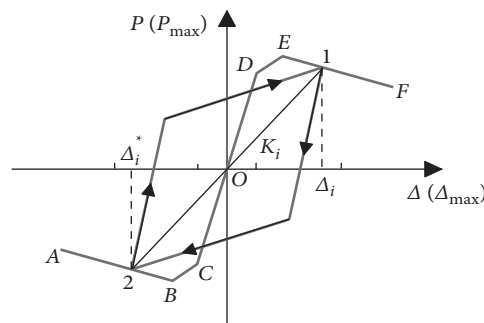


FIGURE 13: Stiffness degradation curve.

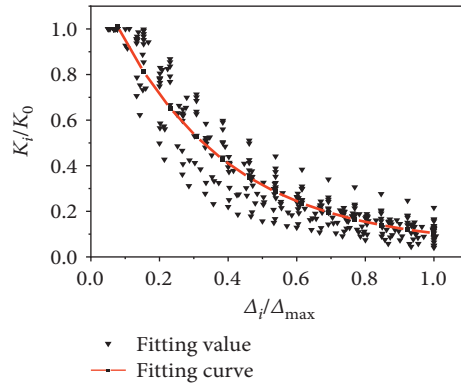


FIGURE 14: Relationships between K_i/K_0 and Δ_i/Δ_{max} .

TABLE 4: Ductility coefficients of STHCC specimens.

Specimens	λ_s	n	α	f_{ck} (MPa)	f_{yk} (MPa)	D/B	P_y (kN)	P_u (kN)	Δ_y (mm)	Δ_m (mm)	Δ_u (mm)	μ
STHCC1	2.08	0.4	0.044	40	235	2.08	1270.00	1079.50	4.33	12.60	29.40	6.78
STHCC2	2.45	0.4	0.044	40	235	2.08	1050.00	892.50	7.50	19.80	46.20	6.16
STHCC3	2.64	0.4	0.044	40	235	2.08	987.33	839.23	8.67	19.20	52.80	6.09
STHCC4	3.33	0.4	0.044	40	235	2.08	800.51	680.43	12.00	19.80	39.60	3.30
STHCC5	3.33	0.1	0.044	40	235	2.08	857.98	729.29	12.17	24.00	40.30	3.31
STHCC6	3.33	0.2	0.044	40	235	2.08	841.51	715.28	12.33	24.00	44.50	3.61
STHCC7	3.33	0.3	0.044	40	235	2.08	826.24	702.30	7.83	21.60	52.50	6.70
STHCC8	3.33	0.4	0.044	30	235	2.08	753.01	640.06	10.50	16.80	54.60	5.20
STHCC9	3.33	0.4	0.044	50	235	2.08	819.27	696.38	10.67	21.60	34.50	3.23
STHCC10	3.33	0.4	0.044	60	235	2.08	897.57	762.93	13.00	25.20	33.60	2.58
STHCC11	3.33	0.4	0.021	40	235	2.08	615.00	522.75	12.50	16.80	29.40	2.35
STHCC12	3.33	0.4	0.032	40	235	2.08	706.41	600.45	10.67	16.00	25.60	2.40
STHCC13	3.33	0.4	0.056	40	235	2.08	908.70	772.40	10.50	20.00	55.00	5.24
STHCC14	3.33	0.4	0.044	40	345	2.08	1022.73	869.32	15.17	27.00	64.80	4.27
STHCC15	3.33	0.4	0.044	40	390	2.08	1130.00	960.50	13.33	24.00	70.00	5.25
STHCC16	3.33	0.4	0.044	40	420	2.08	1200.00	1020.00	13.33	36.00	72.00	5.40
STHCC17	3.33	0.4	0.042	40	235	1.89	900.13	765.11	20.00	40.00	110.00	5.50
STHCC18	3.33	0.4	0.041	40	235	1.73	961.00	816.85	17.67	33.60	57.20	3.24
STHCC19	3.33	0.4	0.040	40	235	1.60	776.16	659.74	20.33	28.80	64.80	3.19
STHCC20	3.33	0.4	0.048	40	235	1.92	1030.00	875.50	25.63	18.00	68.43	2.67
STHCC21	3.33	0.4	0.031	40	235	2.40	1230.03	1045.53	14.00	24.00	45.00	3.21
STHCC22	3.33	0.4	0.034	40	235	2.72	714.09	606.97	9.00	21.00	40.00	4.44

Note. P_y denotes the yield load, Δ_y is the yield displacement corresponding to P_y , Δ_m denotes the peak displacement, P_u is the ultimate load, and Δ_u refers to the ultimate displacement corresponding to P_u .

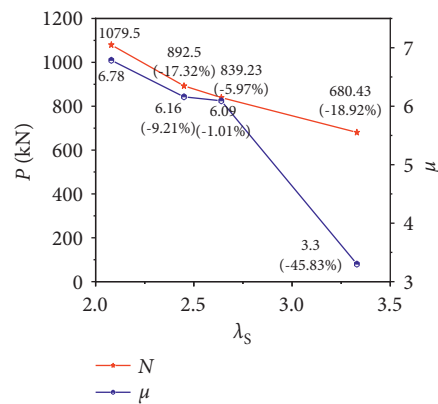


FIGURE 15: Relationships between P_u , μ , and λ_s .

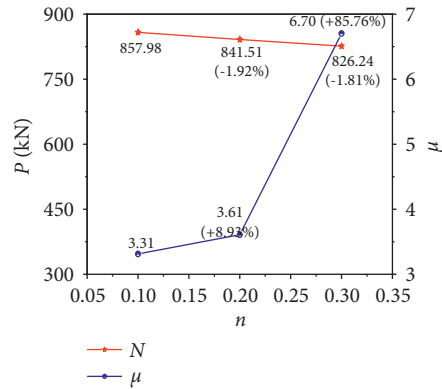


FIGURE 16: Relationships between P_u , μ , and n .

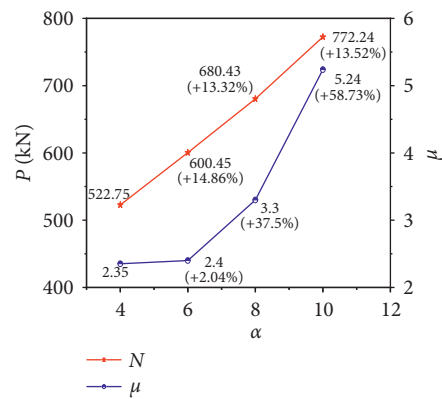


FIGURE 17: Relationships between P_u , μ , and α .

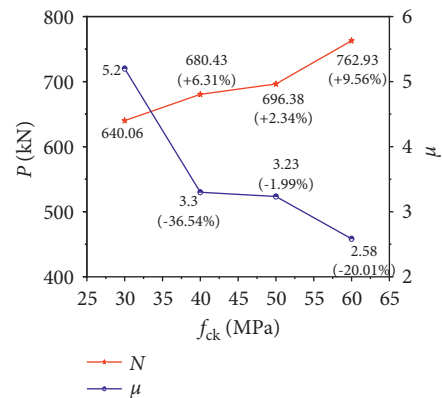


FIGURE 18: Relationships between P_u , μ , and f_{ck} .

With the further increase of n ($n > 0.7$) [12], μ of the STHCCs decreases obviously, so the limit value of n should be reasonably considered, which ensures that the STHCCs have good ductility [25, 30, 31].

13.52%, respectively, while μ increases by 2.04%, 37.5%, and 58.73%, respectively, which indicates that the influence of α on the ductility of the STHCCs is significant.

6.5.4. Steel Ratio of Section. The relationships between P_u , μ , and α of the STHCCs are illustrated in Figure 17. It can be seen from Figure 17 that when α increases from 4 to 6, 8, and 10, P_u of the STHCCs increases by 14.86%, 13.32%, and

6.5.5. The Compressive Strength of Concrete. Figure 18 shows the relationships between P_u , μ , and f_{ck} of the STHCCs. When f_{ck} increases from 30 MPa to 40 MPa, 50 MPa, and 60 MPa, P_u of STHCCs increases by 6.31%, 2.34%, and 9.56%, respectively, while μ decreases by 36.54%, 1.99%, and 20.01%,

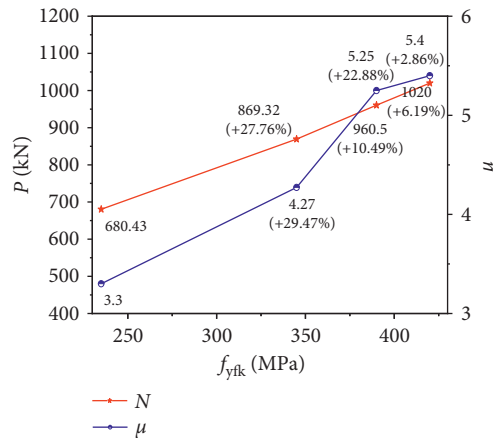


FIGURE 19: Relationships between P_u , μ , and f_{yfk} .

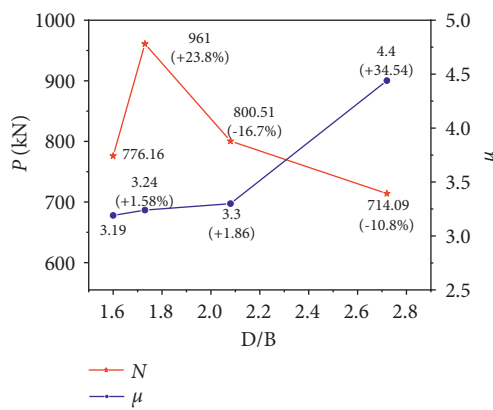


FIGURE 20: Relationships between P_u , μ , and D/B .

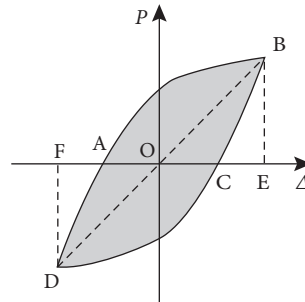


FIGURE 21: Calculation diagram of E .

respectively. With the increase of f_{ck} , P_u of the specimens increases but the ductility decreases, which indicates that the ductility of the STHCCs is significantly affected by f_{ck} .

6.5.6. The Yield Strength of Steel Tube. The relationships between P_u , μ , and f_{yfk} of the STHCCs are shown in Figure 19. When f_{yfk} increases from 235 MPa to 345 MPa, 390 MPa, and 420 MPa, P_u of the STHCCs increases by 27.76%, 22.88%, and 2.86%, respectively, and μ increases by 29.47%, 10.49%, and 6.19%, respectively, which indicates that P_u and deformation capacity of the STHCCs improve with the increase of f_{yfk} .

6.5.7. Section Aspect Ratio. The relationships between P_u , μ , and D/B of the STHCCs are shown in Figure 20. It can be seen from Figure 20 that when D/B increases from 1.6 to 1.73, 2.08, and 2.72, μ of the STHCCs increases by 1.58%, 1.86%, and 34.54%, respectively.

6.6. Energy Dissipation Capacity. The energy dissipation capacity is applied to evaluate the ability to absorb the energy released in the earthquake of the structure [9]. The energy dissipation coefficient (E) is used to evaluate the energy dissipation capacity of STHCC specimens, and the energy dissipation coefficient refers to the ratio of the shadow area to the

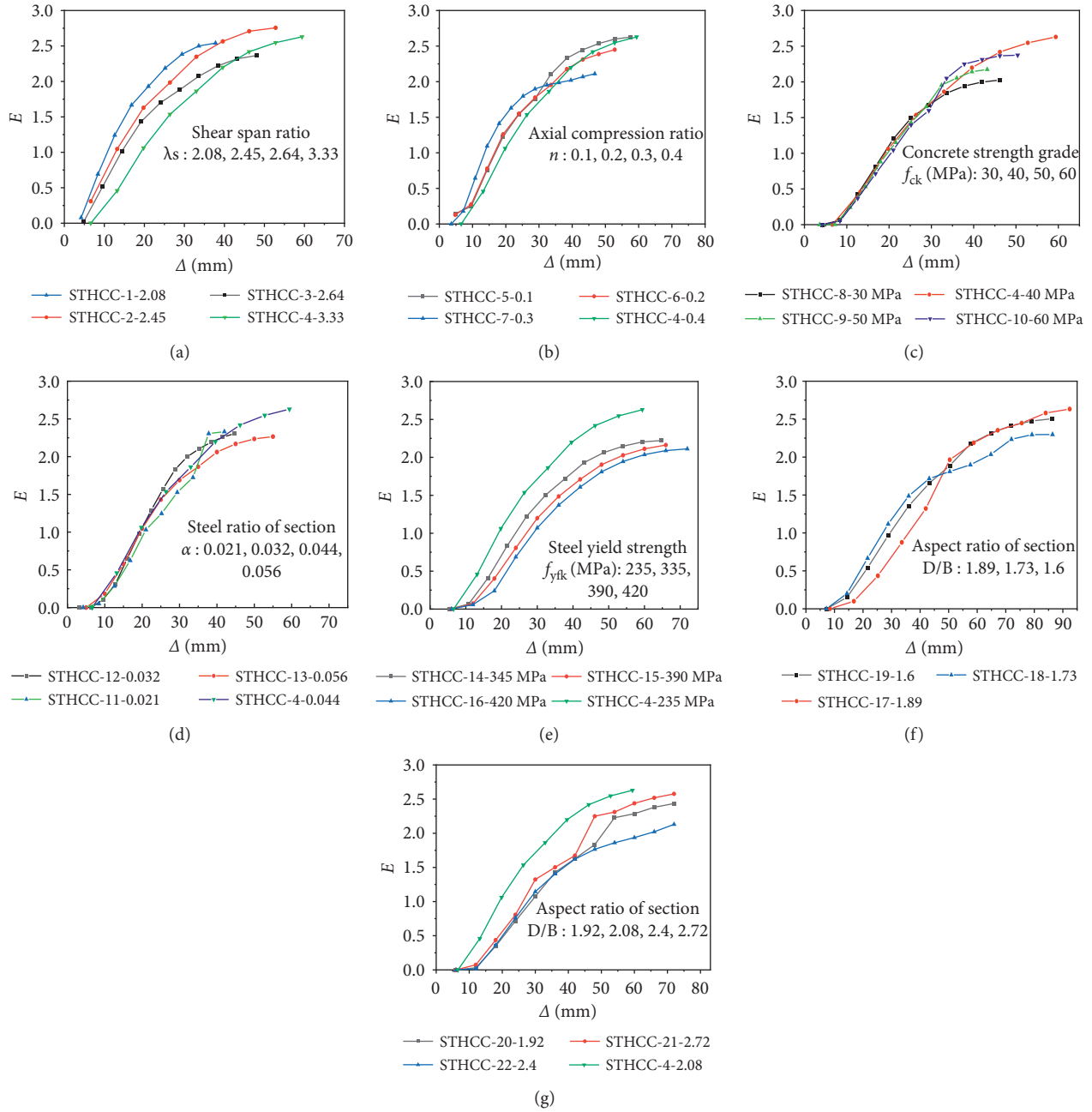


FIGURE 22: The relationship between E and Δ for STHCCs with different parameters. (a) λ_s : 2.08, 2.45, 2.64, 3.33. (b) n : 0.1, 0.2, 0.3, 0.4. (c) f_{ck} : 30 MPa, 40 MPa, 50 MPa, 60 MPa. (d) α : 0.021, 0.032, 0.044, 0.056. (e) f_{yk} : 235 MPa, 335 MPa, 390 MPa, 420 MPa. (f) D/B : 1.89, 1.73, 1.6. (g) D/B : 1.92, 2.08, 2.4, 2.72.

triangle DFO and the triangle BEO area, as shown in Figure 21. The energy dissipation coefficient can be calculated as follows:

$$E = \frac{S_{(ABC+CDA)}}{S_{(\Delta OBE+\Delta ODF)}} \quad (5)$$

Figure 22 shows the horizontal displacement (Δ) versus the energy dissipation coefficient (E) relationships of the 22 STHCCs under the first reciprocating load of each stage. It

can be found from Figure 22 that the energy dissipation capacity values of the 22 STHCCs are substantially similar.

The energy dissipation capacity of STHCCs is shown in Figure 22. With the increase of λ_s , n , f_{yk} , and D/B , E and the energy dissipation capacity of the specimens decrease gradually. It can be seen from Figures 22(c) and 22(d) that f_{ck} and α have little effect on the energy dissipation capacity of STHCCs. The existing research [32] shows that E of RC

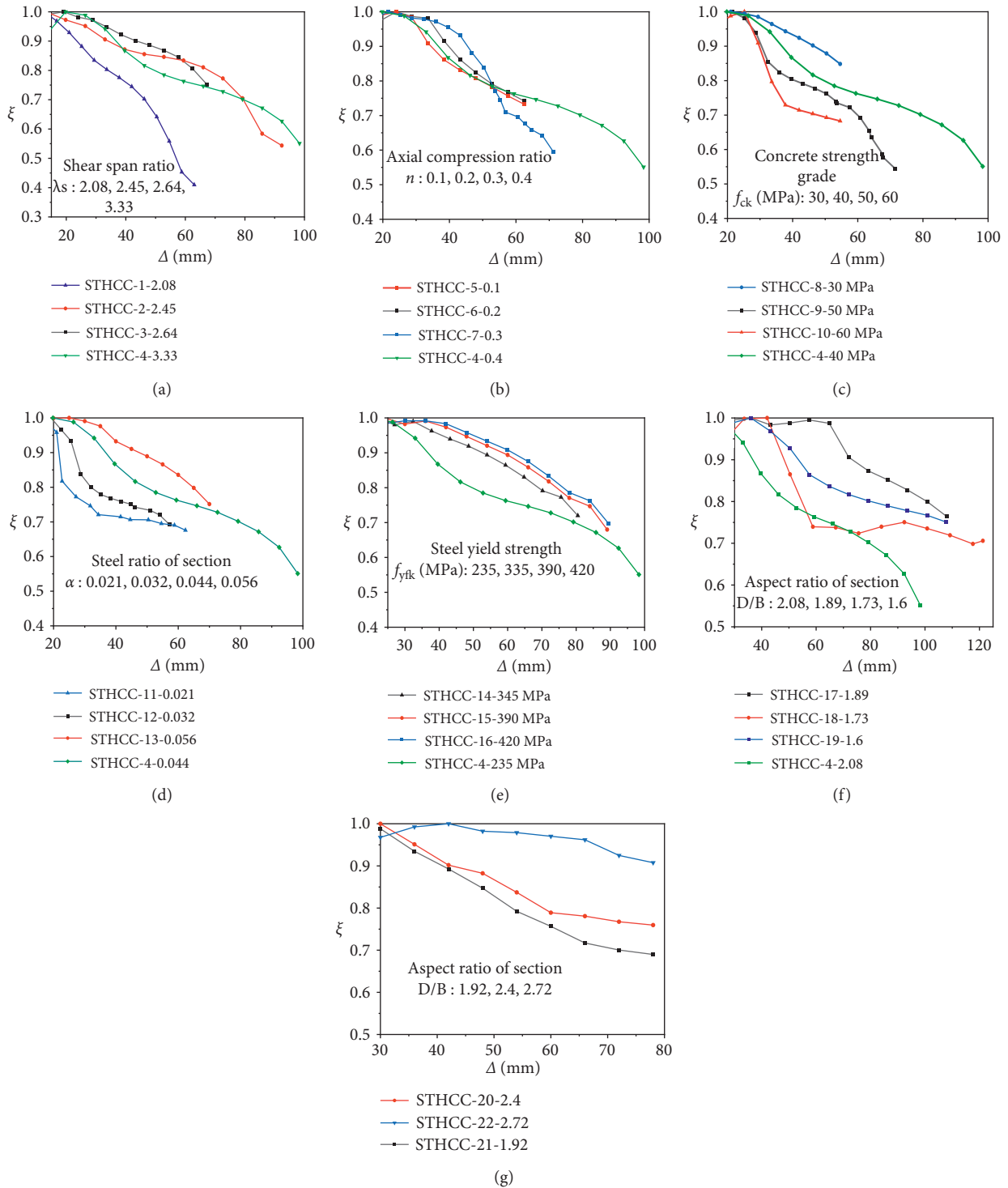


FIGURE 23: The relationships between ξ and Δ for STHCCs with different parameters. (a) λ_s : 2.08, 2.45, 2.64, 3.33. (b) n : 0.1, 0.2, 0.3, 0.4. (c) f_{ck} : 30 MPa, 40 MPa, 50 MPa, 60 MPa. (d) α : 0.021, 0.032, 0.044, 0.056. (e) f_{yk} : 235 MPa, 335 MPa, 390 MPa, 420 MPa. (f) D/B : 2.08, 1.89, 1.73, 1.6. (g) D/B : 2.4, 1.92, 2.72.

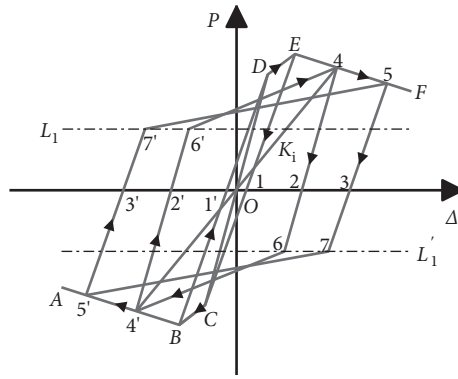


FIGURE 24: Restoring force model for STHCCs.

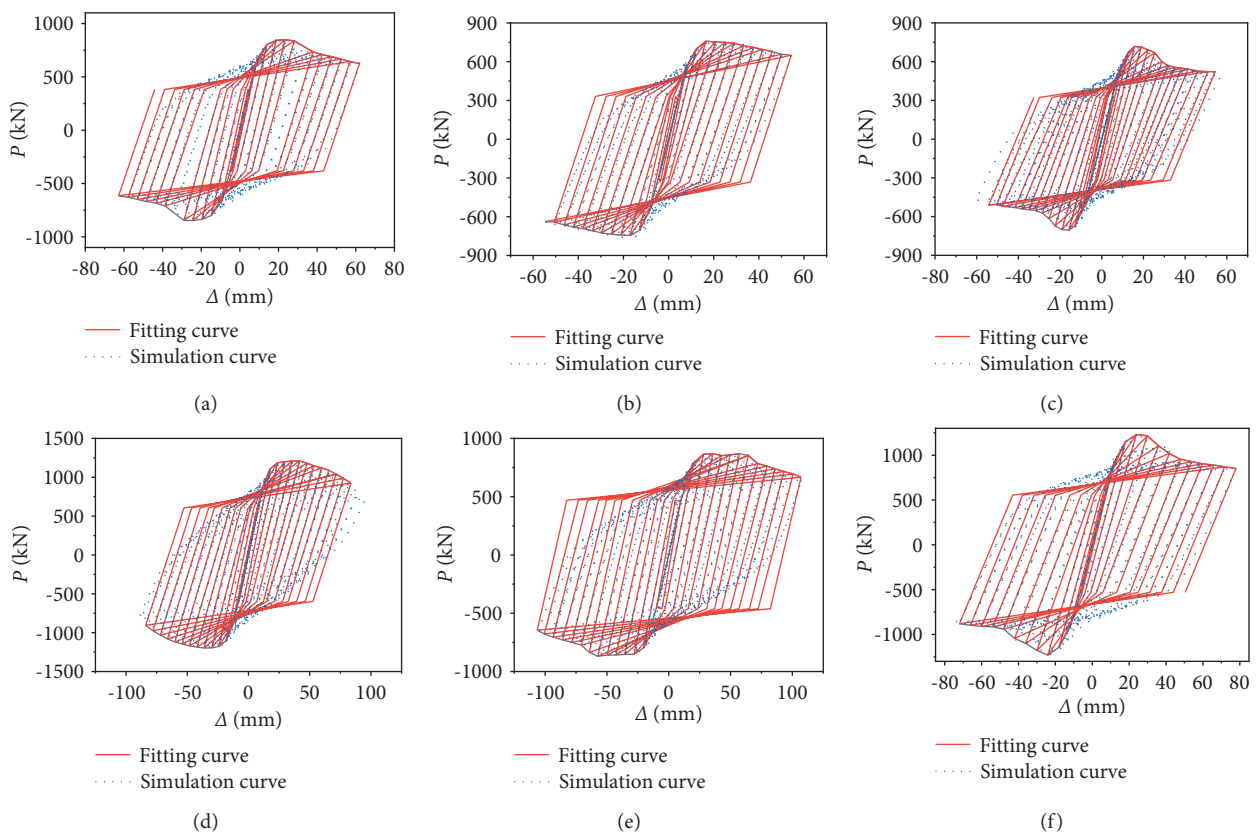


FIGURE 25: Comparisons of hysteresis curves between calculation and simulation. (a) STHCC5. (b) STHCC8. (c) STHCC12. (d) STHCC16. (e) STHCC17. (f) STHCC21.

columns is about 1.0 and E of SRC columns is about 2.4; E of specimens in this article can reach above 2.0, so it is indicated that the STHCCs have excellent energy dissipation capacity.

6.7. Resistance Degradation. The resistance degradation coefficient (ξ) is used to measure seismic action of STHCC specimens as shown in Figures 23(a), 23(b), 23(d), 23(e), and 23(g). With the increase of λ_s , n , α , f_{yk} , and D/B , ξ of the STHCCs increases and the resistance degradation rate gradually slows down. Figure 23(c) shows that with the increase of f_{ck} , the resistance degradation of the specimens

gradually decreases and the resistance degradation rate accelerates. It can be concluded that within a certain range, the increase of λ_s , n , α , f_{yk} , and D/B is conducive to improving the seismic performance of the structure.

6.8. Restoring Force Model. The restoring force model of STHCCs is established by statistical regression, as shown in Figure 24, in which points D and C represent the yield points of positive direction and negative direction. Points E and B represent the peak points. AB and EF represent the descent segment. The horizontal auxiliary line (L_1) represents the

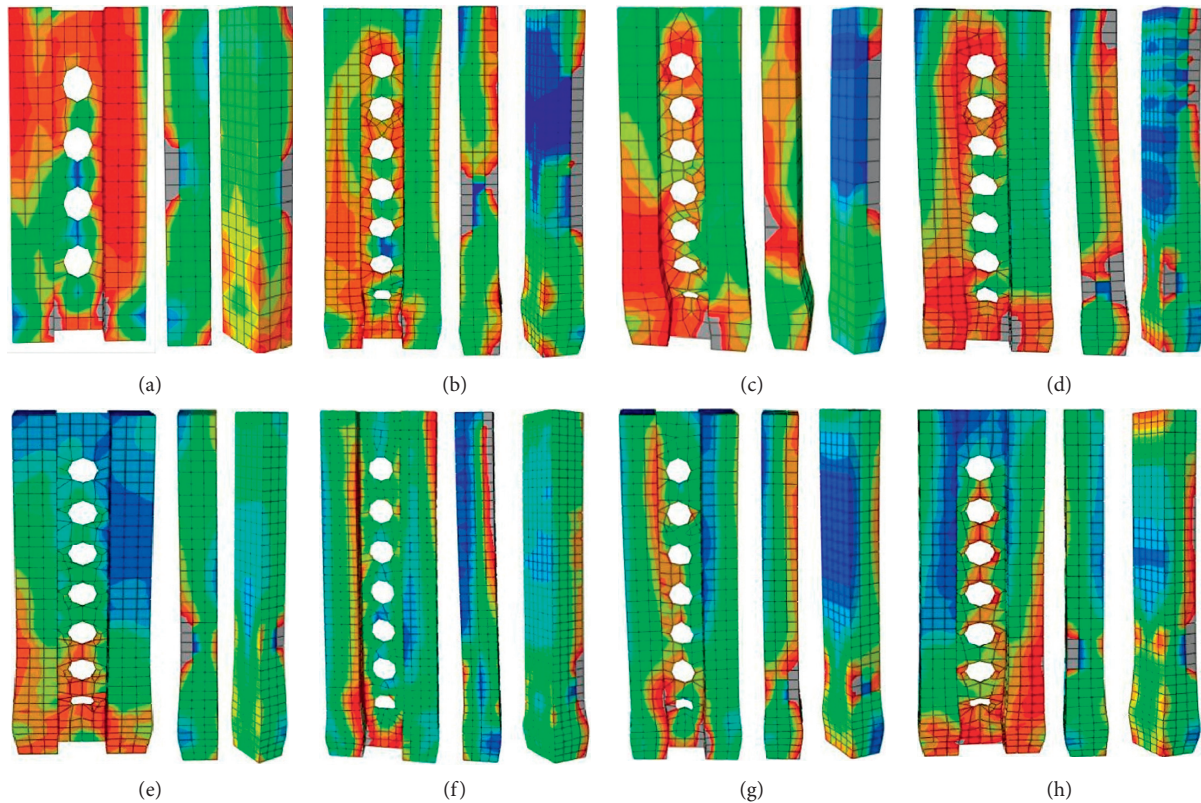


FIGURE 26: Failure modes of STHCCs. (a) STHCC2. (b) STHCC4. (c) STHCC6. (d) STHCC10. (e) STHCC13. (f) STHCC14. (g) STHCC19. (h) STHCC22.

straight line ($P = 0.45P_E$) [13], and L_1' represents the symmetric line of L_1 about horizontal coordinate axis.

The specimens are approximately at the elastic stage before yielding, and the paths of loading and unloading process are along the elastic stage of the skeleton curves; more specifically, the OD section is loaded forward, and the OC section is loaded backward after specimens unloading to the O point. It can be found that the loading stiffness and unloading stiffness are both the elastic stiffness of the skeleton curves.

After the specimens yielded, the loading path develops along the skeleton curves. Before reaching the peak load, the unloading and reverse loading are carried out according to the path of point E to the negative yield point C and then develop along the path of point C to point B. The overall loading path is D-E-1-C-B-1'-D.

After the peak load, the loading path develops along the skeleton curve from point E to point 4 (point 5). The unloading path is from point 4 (point 5) to point 2 (point 3), the reverse loading path is from point 2 (point 3) to point 4' (point 5'), the reverse unloading path is from point 4' (point 5') to point 2' (point 3'), and then the forward load is loaded to the path of the skeleton curve. The overall loading path is 4 (5)-2 (3)-6 (7)-4' (5')-2' (3')-6' (7')-4 (5).

6.9. Comparisons between Restoring Force Model and Simulation Results. The hysteretic curves of STHCCs calculated by the restoring force model are shown in Figure 25. By

comparing them with the simulation results, we can see that both are in good agreement; therefore, the restoring force model is feasible.

6.10. Destruction Form. The failure modes of STHCCs subjected to low cyclic loading are substantially the same, as shown in Figure 26. The column foot of the double-limb steel tube flange shows obvious outward expansion deformation. Due to the effect of axial force and horizontal force, the honeycomb steel web produces vertical compression deformation and transverse in-plane buckling deformation. The core concrete of the two-limb flange generates vertical compression deformation and bulging deformation of the upper column foot. The maximum stress of the steel tube appears in the inner side of the column foot, and the maximum bulging deformation is concentrated in the upper part of the column foot. The maximum stress of concrete occurs at the column foot and the outer side of the concrete columns. Therefore, it can be concluded that the steel tube exhibits confinement effect on the core concrete, which can effectively improve the strength of concrete and inhibit the damage of concrete. The honeycomb steel web also has a certain support for the CFST inside the flange, which can enhance the constraint effect of the inner steel tube on the concrete, the strength of the concrete, and the bearing capacity of the CFST flange. The core concrete in the steel tube effectively inhibits and delays buckling failure of the steel

tube and improves the deformation capacity and hysteretic behavior of the STHCCs.

7. Conclusions

Based on the simplified constitutive model of steel and the nonlinear constitutive model of concrete, 14 STHCCs are numerically simulated by ABAQUS software. By comparison, the maximum error between the simulation and test results is 5.58%, which can verify the rationality of the FE modeling method.

The hysteresis curves of all the specimens show full shuttle shape and strong energy dissipation capacity. α has a great influence on the hysteresis curves of STHCCs; with the increase of α , the ultimate displacement of the specimens gradually increases. After reaching the peak load, the decrease of the bearing capacity of the specimens gradually slows down, and the ductility becomes better. When $n < 0.4$ and $f_{ck} < 60$ MPa, the effects of n and f_{ck} on the bearing capacity of specimens are not remarkable. With the increase of α and f_{yk} , the bearing capacity and deformation capacity increase obviously. The stiffness degradation rate of specimens gradually slows down, and the E gradually decreases by increasing λ_s , α , and f_{yk} , but the energy dissipation capacity is still higher than that of ordinary concrete columns. With the increase of λ_s , α , f_{yk} , and D/B , the resistance degradation increases; the degradation rate decreases; and n , α , and f_{ck} have great influence on the ductility of specimens.

Based on the hysteresis curves obtained by the quasi-static analysis, the trilinear skeleton curve model and the restoring force model are established, and the hysteresis rules are proposed correspondingly.

By observing the failure mode of STHCCs, the steel tube has significant constraint on the core concrete and improves the compressive strength of concrete effectively. The honeycomb steel web provides effective support for the rectangular CFST flanges, and the core concrete delays the buckling failure of the steel tube validly, which can reflect the good overall hysteretic behavior of the STHCCs.

Data Availability

The data used to support the findings of this study are included within the article.

Conflicts of Interest

The authors declare that they have no conflicts of interest.

Acknowledgments

The authors are grateful for the financial support received from the Natural Science Foundation of Heilongjiang Province, grant no. LH2020E018; Scientific Research Fund of Institute of Engineering Mechanics, China Earthquake Administration, grant no. 2020D07; Opening Fund for Key Laboratory of the Ministry of Education for Structural Disaster and Control of Harbin Institute of Technology, grant no. HITCE201908; 2021 Social Science Development Research Project of Hebei Province, grant no. 20210301135;

Humanities and Social Science Research Project of Higher Education Institutions of Hebei Province, grant no. SQ2021115; General Research Project of Heilongjiang Higher Education Teaching Reform, grant no. SJGY20190096; and Northeast Petroleum University Guided Innovation Fund, grant no. 2020YDL-02.

References

- [1] K. Sakino, H. Nakahara, S. Morino, and I. Nishiyama, "Behavior of centrally loaded concrete-filled steel-tube short columns," *Journal of Structural Engineering*, vol. 130, no. 2, pp. 180–188, 2004.
- [2] Y. Essopjee and M. Dundu, "Performance of concrete-filled double-skin circular tubes in compression," *Composite Structures*, vol. 133, pp. 1276–1283, 2015.
- [3] B. Anupriya, B. K. Jagadeesa, and R. Baskar, "Experimental investigation of shear strength of castellated beam with and without stiffeners," *Journal of Structural Engineering*, vol. 42, no. 4, pp. 358–362, 2015.
- [4] J. Ji, Z. C. Xu, L. Q. Jiang et al., "Nonlinear buckling analysis of H-type honeycombed composite column with rectangular concrete-filled steel tube flanges," *Building Structure*, vol. 48, no. 15, pp. 50–55+70, 2018.
- [5] J. Ji, Z. C. Xu, L. Q. Jiang, Y. C. Liu, D. Y. Yu, and M. M. Yang, "Experimental study on compression behavior of H-shaped composite short column with rectangular CFST flanges and honeycombed steel web subjected to axial load," *Journal of Building Structures*, vol. 40, no. 9, pp. 63–73, 2019.
- [6] J. Ji, L. Jiang, L. Q. Jiang, Y. F. Zhang, Z. C. Teng, and Y. C. Liu, "Mechanic behavior of H-type honeycomb composite columns with rectangular concrete-filled steel tubes subjected to eccentric load," *Journal of Northeast Petroleum University*, vol. 44, no. 4, pp. 121–132, 2020.
- [7] A. H. Varma, J. M. Ricles, R. Sause, and L. W. Lu, "Seismic behavior and modeling of high-strength composite concrete-filled steel tube (CFT) beam-columns," *Journal of Constructional Steel Research*, vol. 58, no. 5, pp. 725–758, 2002.
- [8] P. Gajalakshmi and H. J. Helena, "Behaviour of concrete-filled steel columns subjected to lateral cyclic loading," *Journal of Constructional Steel Research*, vol. 75, pp. 55–63, 2012.
- [9] Z. Chen, C. Jing, J. Xu, and X. Zhang, "Seismic performance of recycled concrete-filled square steel tube columns," *Earthquake Engineering and Engineering Vibration*, vol. 16, no. 1, pp. 119–130, 2017.
- [10] Y.-C. Tang, L.-J. Li, W.-X. Feng, F. Liu, and B. Liao, "Seismic performance of recycled aggregate concrete-filled steel tube columns," *Journal of Constructional Steel Research*, vol. 133, pp. 112–124, 2017.
- [11] J. Wang, Q. Sun, and J. Li, "Experimental study on seismic behavior of high-strength circular concrete-filled thin-walled steel tubular columns," *Engineering Structures*, vol. 182, pp. 403–415, 2019.
- [12] F. Yin, S. D. Xue, W. L. Cao, H. Y. Dong, and H. P. Wu, "Experimental study on seismic behavior of specially-shaped multi-cell concrete-filled steel tubular columns loaded along different directions," *Journal of Building Structures*, vol. 40, no. 11, pp. 150–161, 2019.
- [13] Z. Q. Liu, J. Y. Xue, and Q. F. Yang, "Experimental study on restoring force of solid-web steel reinforced concrete T-shaped column," *Journal of Experimental Mechanics*, vol. 32, no. 6, pp. 800–810, 2017.
- [14] J. Ji, M. M. Yang, L. Q. Jiang, Y. C. Liu, and D. Y. Yu, "Research on seismic behavior of strength-gradient composite

- columns with built-in high-strength concrete filled steel tube," *Earthquake resistant engineering and Retrofitting*, vol. 42, no. 6, pp. 114–122, 2020.
- [15] J. B. Mander, M. J. N. Priestley, and R. Park, "Theoretical stress-strain model for confined concrete," *Journal of Structural Engineering*, vol. 114, no. 8, pp. 1804–1826, 1988.
- [16] J. G. Teng, T. Yu, Y. L. Wong, and S. L. Dong, "Hybrid FRP-concrete-steel tubular columns: concept and behavior," *Construction and Building Materials*, vol. 21, no. 4, pp. 846–854, 2006.
- [17] L. H. Han, Z. Tao, and W. Liu, "Concrete filled steel tubular Structures : Theory and practice," *Journal of Fuzhou University(Natural Science)*, vol. 29, no. 6, pp. 24–34, 2001.
- [18] M. Pagoulatou, T. Sheehan, X. H. Dai, and D. Lam, "Finite element analysis on the capacity of circular concrete-filled double-skin steel tubular (CFDST) stub columns," *Engineering Structures*, vol. 72, pp. 102–112, 2014.
- [19] Gb 50010-2010, *National Standard of the People's Republic of China Code for Design of Concrete Structures GB50010-2010*, China Architecture & Building Press, Beijing, China, 2010.
- [20] X. L. Cao, L. M. Wu, and Z. M. Li, "Behaviour of steel-reinforced concrete columns under combined torsion based on ABAQUS FEA," *Engineering Structures*, vol. 209, Article ID 109980, 2020.
- [21] W. Liu, "Research on mechanism of concrete-filled steel tubes subjected to local compression," Doctor dissertation, Fuzhou University, Fuzhou, China, 2005.
- [22] X. Dai and D. Lam, "Numerical modelling of the axial compressive behaviour of short concrete-filled elliptical steel columns," *Journal of Constructional Steel Research*, vol. 66, no. 7, pp. 931–942, 2010.
- [23] J. R. Qian and H. Z. Kang, "Experimental study on seismic behavior of high-strength concrete-filled steel tube composite columns," *Journal of Building Structures*, vol. 30, no. 4, pp. 85–93, 2010.
- [24] J. Xue, X. Zhang, R. Ren, L. Zhai, and L. Ma, "Experimental and numerical study on seismic performance of steel reinforced recycled concrete frame structure under low-cyclic reversed loading," *Advances in Structural Engineering*, vol. 21, no. 12, pp. 1895–1910, 2018.
- [25] Z. X. Guo, Z. W. Zhang, Q. X. Huang, and Y. Liu, "Experimental study on hysteretic model of SRC columns," *Earthquake Engineering and Engineering Vibration*, vol. 29, no. 5, pp. 79–85, 2009.
- [26] G. J. Zhang, X. L. Lu, and B. Q. Liu, "Study on resilience models of high-strength concrete frame columns," *Engineering Mechanics*, vol. 24, no. 3, pp. 83–91, 2007.
- [27] J. W. Zhang, W. B. Zheng, W. L. Cao, and M. Wang, "Seismic performance of composite walls with concrete-filled square steel-tube boundary element," *European Journal of Environmental and Civil Engineering*, vol. 25, no. 2, pp. 1–19, 2019.
- [28] H. Cai, L. H. Xu, Y. Chi, Y. X. Yan, C. L. Yu, and C. L. He, "Seismic performance of rectangular ultra-high performance concrete filled steel tube (UHPCFST) columns," *Composite Structures*, vol. 259, Article ID 113242, 2020.
- [29] Z. W. Cai, F. C. Liu, J. T. Yu, K. Q. Yu, and L. K. Tian, "Development of ultra-high ductility engineered cementitious composites as a novel and resilient fireproof coating," *Construction and Building Materials*, vol. 288, Article ID 123090, 2021.
- [30] X. G. Chen, Z. G. Mu, J. B. Zhang, C. K. Wang, C. H. Chen, and H. Z. Sun, "Experimental study on the seismic behavior of steel reinforced concrete columns," *Journal of University of Science and Technology Beijing*, vol. 31, no. 12, pp. 1516–1524, 2009.
- [31] Q. W. Wang, Q. X. Shi, W. S. Jiang, X. H. Zhang, W. Hou, and Y. Tian, "Experimental study on seismic behavior of steel reinforced concrete columns with new-type cross sections," *Journal of Building Structures*, vol. 34, no. 11, pp. 123–129, 2013.
- [32] Q. F. Wang, J. K. Zheng, B. Zhou, Y. Y. Xu, and L. Y. Wang, "Study on seismic behavior of HRBF500 RC column based on hysteretic energy," *China Civil Engineering Journal*, vol. 46, no. 11, pp. 22–28, 2013.

Research Article

Research on Integrated Design of Modular Steel Structure Container Buildings Based on BIM

Meng Su ¹, Bauer Yang ² and Xiaomin Wang ³

¹School of Architectural Science and Engineering, Yangzhou University, Yangzhou 225127, China

²Yangzhou Tonglee Reefer Container Co, Ltd., Yangzhou 225102, China

³Jiangsu Provincial Architectural D&R Institute Co, Ltd., Nanjing 210019, China

Correspondence should be addressed to Meng Su; 834157071@qq.com

Received 19 October 2021; Accepted 13 December 2021; Published 17 January 2022

Academic Editor: Qian Chen

Copyright © 2022 Meng Su et al. This is an open access article distributed under the Creative Commons Attribution License, which permits unrestricted use, distribution, and reproduction in any medium, provided the original work is properly cited.

Modular container buildings, as new modular steel structure buildings with the advantages of modular construction and transportation, fast construction speed, and conformance to the concept of sustainable development, have achieved rapid development in the field of civil engineering in recent years. However, in view of the incompatibility of the standards and systems between the traditional construction industry and the container manufacturing industry, contradictions between industrialization, standardization requirements and diversified demands of buildings, and the low integration of the design system of modular steel structure buildings, the further development of the modular container building industry has encountered a bottleneck. In this study, for resolving this problem, it was proposed to coordinate the modular sequence of the construction and container manufacturing, establish a modular system for modular steel structure buildings, establish a database of container building components and parts, and integrate BIM and PDM platforms, to strengthen professional coordination and improve the integrated design that can increase the integration of the whole process of design. The application and verification in pilot projects such as Huaduhui Commercial Street have approved that this design method can effectively improve the standardization, industrialization, and information levels of design, production, and construction, increase the diversity and overall quality of modular buildings, and promote the achievement of the integration target of the modular steel structure building system.

1. Introduction

Modular container buildings, as new modular steel structure buildings, have not been applied in civil engineering for a long time, and they have been used to civil buildings on a large scale for only more than ten years. At the end of the twentieth century, many Western architects started designing container buildings, most of which were the transformation of small modular buildings focusing on experimental trials [1]. In the twenty-first century, the new building type, “modular steel structure container building,” entered a period of development in the field of civil engineering and formed a unique architectural style and construction method [2, 3]. Since then, modular container buildings have been gradually applied as residences, stores, offices, hotels, etc. [4]. In 2019, for fighting against COVID-19, Huoshenshan and Leishenshan hospitals

were rapidly constructed, showing the unique advantages and development potential of modular steel structure container buildings [5].

In the past two decades, some companies and engineers have studied modular steel structure container buildings’ design and manufacture and made many achievements (Table 1). For example, SG Blocks (the USA) and Tempohousing (Netherlands) are good at building large-scale residential buildings such as barracks and dormitories; Urban Space Management (UK) and LOT-EK (the USA) have designed diversified and characteristic container buildings such as schools, offices, and business buildings [6]; Verbus Systems (UK) has obtained a patent for vertically stacked container buildings [7]; Shigeru Ban, the winner of the Pulitzer Prize, has successfully applied used containers in architectural design of the buildings such as the nomadic museum [8]. In recent years,

TABLE 1: Famous container design and manufacturing company and its works.

Company	Country	Representative projects	Awards or achievements
LOT-EK	America	Puma City Container City 2008 Apap Open School The CUBES at Socrates Sculpture Park	American National Design Award (2008) AIA Award (2011) PDC Annual Award (2018)
SG Blocks		U.S. Army Corps of Engineers Barracks	
Verbus Systems	UK	Travelodge Hotel Container City1, 2 Cuffley School	The Container City System
Urban Space Management		Fawood Children's Center	RIBA Stirling Prize (2009)
Tempohousing	Holland	Keetwonen Student Housing	
Addis Containers	New Zealand	Container RowBox	2010 Karapiro World Rowing Champs Promotional
CIMC	China	Sochi Winter Olympics Hotel Holiday Inn Express Hotel	

Jure Kotnik prepared the book *Container Architecture*, which introduces representative container buildings and theoretical research results. In *Prefab Architecture: A Guide to Modular Design and Construction*, the author conducts more in-depth analysis on the key points of the whole process, from components, panels, assembly to design and construction of the prefabricated container buildings. Eissa et al. investigate the development of a BIM governance framework (G-BIM) with the support of cloud technologies, identifying effectiveness factors that guarantee successful collaboration [9]. Ansah et al. extend the knowledge in automated BIM-based LCA by addressing specific characteristics of prefabrication and promotes the incorporation of comprehensive and detailed LCA data into BIM models for improved design robustness and holistic performances of buildings [10]. China International Marine Containers (Group) Co., Ltd., as the largest container manufacturer in the world, has made various achievements in the field of modular steel structure buildings. For example, it has developed the “seismic model analysis of modular building with self-stacking structure” technology with domestic universities [11]. The pioneered modular building technology has been applied in hotels for the Russian Winter Olympics.

However, there is a dilemma in the development of modular steel structure buildings at present: on the one hand, the industrialized mass production of modular steel structure buildings mainly depends on container manufacturers, and the facilities are primarily limited to low-end dormitories and stores consisting of a large number of repeated and straightforward units; on the other hand, as for modular steel structure buildings with higher quality requirements, although there are construction companies involved in the design and construction, the inconsistency of the standards with the container enterprises, the low system integration, and unfavorable transdisciplinary coordination have resulted in several problems such as common design integration, redundant types of modules and components, low production efficiency, and high cost, which have severely restricted the development of the industry of container buildings.

For resolving such a problem, in this paper, the author coordinated the related modulus and size restrictions in the traditional construction industry, container manufacturing

industry, and logistics industry based on the BIM platform and pilot projects and the advantages of BIM informatization, and then proposed a unified modular sequence and three-dimensional modular grid for modular container buildings. In addition, the author established a standardized and systematic database of components and parts characterized by “family” through the integration of building information modeling (BIM) and product data management (PDM) platforms and an integrated design method of container buildings led by architectural design based on a flexible modular combination and closely cooperated with structure and equipment, for realizing the standardization and digitization of the whole process of design, production, and construction. The completion and operation of the pilot projects such as Huaduhui Commercial Street (Figure 1) and Modular Fire Station have verified the feasibility and superiority of the integrated design of modular container buildings based on BIM.

The paper is organized as follows. Section 2 discusses the link between the goal of modular container building integration and BIM-based integrated design; Section 3 discusses a modular container building system based on BIM technology and components from the container logistics and conventional construction industries; Section 4 describes BIM database for modules, features, and parts of modular steel structure buildings; Section 5 describes integrated design and pilot projects for container buildings based on BIM and crossdisciplinary collaboration in design, production, and construction; and Section 6 provides conclusion.

2. Integration Target of Modular Steel Structure Container Buildings and Integrated Design Based on BIM

For resolving the contradiction between the diversified needs of modular container buildings and industrial production, there should be an integrated building system combining standardization with flexibility similar to KEP (Kodan Experimental Housing Project) and NPS (new plain system) in Japan [12]. Integrated buildings are assembled by building components in a manner of plant and social collaboration, which form a new building system that can



FIGURE 1: Pilot project-real aerial photo of Huaduhui Commercial Street.

provide ultimate perfect products for the market. The integrated building system can integrate building components and structural parts and provide optimized products that combine integration design, information-based production management methods, and high-performance materials and equipment. In order to establish the integration building system, Yangzhou University and CIMC Yangzhou Base jointly proposed the integration target for the container building system (Table 2).

Integrated design is the prerequisite and means for achieving the container building integration target. A multidisciplinary design method can be used to construct economic and high-quality facilities. A multidisciplinary design method can be used to construct economic and high-quality buildings by integrating various design elements in the design process. From a vertical perspective, integrated design runs through and leads the entire design, construction, and operation process and focuses on the whole life cycle of the building. From a horizontal perspective, different professional designers should work closely together and consider the form, function, performance, and cost to obtain high performance and various benefits at a lower price, thus realizing the sustainable development of the building. [13] BIM is the basis for the goal of integrated design. To realize the integration of different professional software and the mutual access between databases, all the professional data, system software, and application software must adopt the uniform model data expression and information exchange standards in the BIM system [14].

3. Establishment of a Modulus System for Modular Container Building Based on BIM

Integrated design should coordinate the size, positioning, and correlation of the main structure, components, and parts, and establish a unified and coordinated modular grid system through modular and serial design to realize the organic combination between structure, features, and equipment, and simplify the size and types of components. In other words, a modulus system is a prerequisite and foundation for establishing an integrated design system for container buildings. BIM technology has provided a platform for the establishment of such a system.

3.1. Modulus Coordination. For establishing a modulus system of modular container buildings, the building modulus system and container logistics modulus system in the

traditional construction industry should be first integrated. Specifically, in addition to the modulus based on the human scale, the modulus based on functional units, and building modules based on the size of the building components that should be integrated in the general building modulus system, the logistics modules, transportation size restrictions, container structural components, and material size modulus should also be deeply analyzed, so as to obtain the differences and mutual relations between different modulus systems. Then, the major constraint modulus and dimensions can be proposed on this basis to integrate and form a new container building modulus system (Figure 2).

Particular attention should be attached to the limitations on transportation dimensions because an essential feature of container buildings is the overall transportation of modules. It can be concluded through analyzing the Regulations on Transport Vehicles with Out-of-Gauge Goods and Limits of Outer Dimensions, Axle Loads and Mass of Automobiles, Trailers and Combination Vehicles (GB1589-2016) that there are limitations on transportation of large-size goods (2.5 M, 3M, 3.75 M, etc.) and also on height and length. Therefore, in the process of modulus coordination, the hierarchical modulus on width, height, and length of the module should be smaller than these values, respectively. The complexity of modulus may significantly increase the possibility of size combination. Since the cad plane, facade, and section cannot coordinate and control the varieties of modulus and modules in a 3D space, BIM was used to build a 3D model for simulated combination testing of modulus and modules. The method is first of all, find typical office, hotel, and residential architectural drawings, and use modules of different modulus sizes to puzzle in Revit. It must be ensured that (1) the outline of the module does not exceed the exterior wall of the building; (2) the module does not invade the stairwell; (3) no corner posts appear in the aisle; and (4) the size of the module meets the requirements of transportation and components; and secondly, when the module has basically completed the construction and modeling of the shape and space, use the collision check function of the Revit software to check. When the type is reduced, the building module often collides; then, by comparing the number of collisions in the collision check report with Revit, the ratio of the module types counted in the software, the modules with a lower ratio are selected; finally, there are correct validation and optimization of results. In the Revit system, the parameter adjustment and statistics of building components and parts are very convenient, which greatly improves the research efficiency. Thereby, the results of the

TABLE 2: Container modular building system integration target list.

Target	Rule	Index
Integration of architectural design	Modular system	Realize modular coordination, establish modular mesh, tolerance, and fit, connection, etc.
	General module, component	A large proportion of modules, prefabricated components, or components of the exact design specification
	Professional cooperation	BIM as a platform to achieve the architecture, structure, hydropower, HVAC professional close cooperation
Component parts production standardization, factory production	Prefabricated load-bearing member	Modules, columns, beams, floors
	Prefabricated non-load-bearing component	Interior wall, balcony, staircase, integral kitchen, integral bathroom, etc.
	Prefabrication rate of load-bearing components	Improve prefabricated volume ratio or prefabricated value ratio
	Prefabrication rate of non-load-bearing components	Improve prefabricated volume ratio or prefabricated value ratio
Assembly of building construction	Mode of transportation of components and parts	Prefabricated components and prefabricated parts shall be given priority to the size following transportation regulations, the integrated transportation mode shall be given priority, and the multimodal transportation mode shall be adopted for long-distance transportation.
	Technical equipment rate	Increase the ratio of the net value of enterprise-owned machinery and equipment to the total number of employees or workers at the end of the year
	Power equipment ratio	Increase the ratio of the total power of machinery and equipment to the average number of employees
	Degree of technology integration	Improve the degree of technical integration, upgrade the secondary design, complete set of the installation process
Production and management informatization	The phase of the design	Application of information technology (BIM, the Internet of Things, etc.)
	Component parts production stage	Application of information technology (BIM, the Internet of Things, etc.)
	Construction and installation stage	Application of information technology (BIM, the Internet of Things, etc.)
	Operational phase	Application of information technology (BIM, the Internet of Things, etc.)
	Life cycle information management	Integrated information technology approaches throughout life cycle management

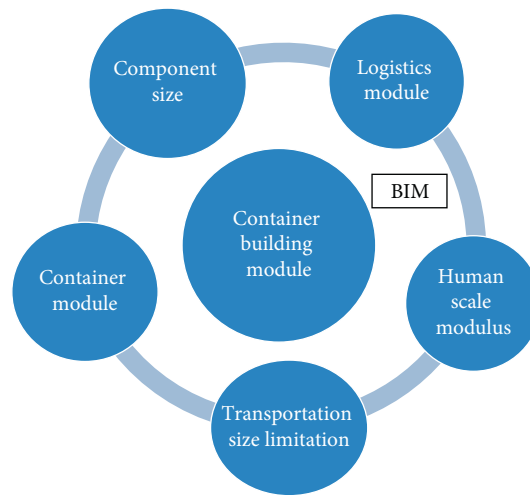


FIGURE 2: Modulus coordination of modular container buildings based on BIM.

first phase of the study can be verified, screened, and optimized, and the applicable modulus, module, and component size can be obtained.

3.2. Establishment of the Modulus System. Based on BIM simulation, screening, and optimization, the container building modulus system was initially proposed, based on which we designed the components, parts, and modules and then performed the trial installation. Through verification, adjustment, and improvement by several actual projects, the container building modulus system was initially established and included as essential parts into the internal standards of CIMC—*Standards for Container Modular Combination Barracks* and *Standards for Self-stacking Container Modular Hotel*.

The container modulus system consists of the following parts.

3.2.1. Determination of Modulus Sequence. In order to realize the standardization of the design of container buildings and offer greater versatility and interconvertibility to the structure and components in a facility, the limited sequence should be taken as actual working parameters in architectural design. Firstly, we determined (1) the basic modulus 1M, then determined (2) expanded modulus sequence (2M, 4M, 6M) based on the principle of superposition and multiple, and set (3) submodulus sequence: M/100, M/50, M/20, M/10, M/5, M/2, etc. The main range of expanded modulus and submodulus set here is different from that of ordinary buildings because it is determined by the modular features of prefabricated container buildings and the higher manufacturing and assembly accuracy of the machinery manufacturing industry than the traditional construction industry. Finally, (4) adjusted modulus based on English units was set to resolve the connection and conversion issues between the British and metric systems. Specifically, add an inserted value (insert segment) to the metric-based modulus series and the modulus grid. For example, the width of the international standard container is 8 feet, which is 2438 mm; then based on the metric module grid, add a 38 mm insert section; $2400 \text{ mm} + 38 \text{ mm} = 2438 \text{ mm}$ (8 ft), where 38 mm is the adjustment modulus M' . And $38 \text{ mm} \times 2 = 76 \text{ mm}$ (3 in) = i , where 76 mm happens to be the gap size i of the module splicing in the container module system, and its value is 3 inches, that is to say, the adjustment module $M' = i/2$. As a result, the international standard container module system based on the British system can be converted to the metric building module.

3.2.2. Establishment of a Modular Grid. For each container building, a modularized spatial grid composed of three-dimensional rectangular coordinates (modulus dimensions) should be established in BIM. The relevant modulus and parameters can be intuitively analyzed and adjusted; the expanded modulus and sun modulus are different in three directions. A final 3D modular grid of the container building system was established through optimization.

3.2.3. Principle of Positioning. In the modular grid, each component should be positioned by virtue of the boundary positioning of the centerline (or off-center line) in the three directions. Unlike conventional buildings, container buildings are constructed in a modular construction manner, so they are not applicable to the principle of positioning with the centerline (or off-center line) of column (beam) or wall but the code of placing with seam line as the positioning axis. At each end of the building, the modular grid lines can be set on the boundary surface of the module (Figure 3(a)).

3.2.4. Mark Dimensions, Production Dimensions, Seam, and Tolerance. In order to realize the size coordination between the design and installation of the containerized modular building and open up the data conversion between design and manufacturing, the relationship between the size of the logo and the size of the production needs to be handled. The size of the logo should be the modular size and meet the requirements of the modular sequence, usually indicating the distance between the building positioning lines (axis); the production size is the design size of the building module, parts, and components; the general production size plus the seam size or joint size is mark dimensions. The seam mainly refers to the gap between two or more modules in the container building modulus system. By optimizing the design and improving the production and installation process, the seam width of CIMC containers has been reduced to 10 mm from the original 20 mm (or 18 mm). Tolerance is the difference between two allowable limits, including manufacturing tolerance, installation tolerance, and positioning tolerance. The tolerance in the container construction system generally refers to the manufacturing tolerance, which is the difference between the production size and the actual part size. Considering the higher accuracy of container buildings compared to traditional buildings, we set the tolerance of container buildings at the millimeter level. For example, the manufacturing tolerances of container modules were controlled within the range of 0 to -5 mm. The sum of production dimensions, tolerance, and seam should be the marked dimensions, which can avoid recutting or rectifying (Figure 3(b)).

3.3. Application and Inspection of Modulus System in Actual Projects. The modulus system obtained through simulation, screening, and optimization based on the BIM platform should be inspected and improved throughout the entire process of the actual engineering projects. The pilot projects adopting the new modulus system are introduced below.

Huaduhui Tourist Service Center was designed based on the modulus of 3,000 mm in height, which can achieve higher indoor space while meeting the size permitted for road transportation; the modulus of the width of $2,438 \text{ mm} \times 2$ can meet the space requirements. The entire building was constructed by 17 modules of the same size (side panels were removed at the splicing). The size of every single module did not limit the shape and space of the building. The BIM 3D

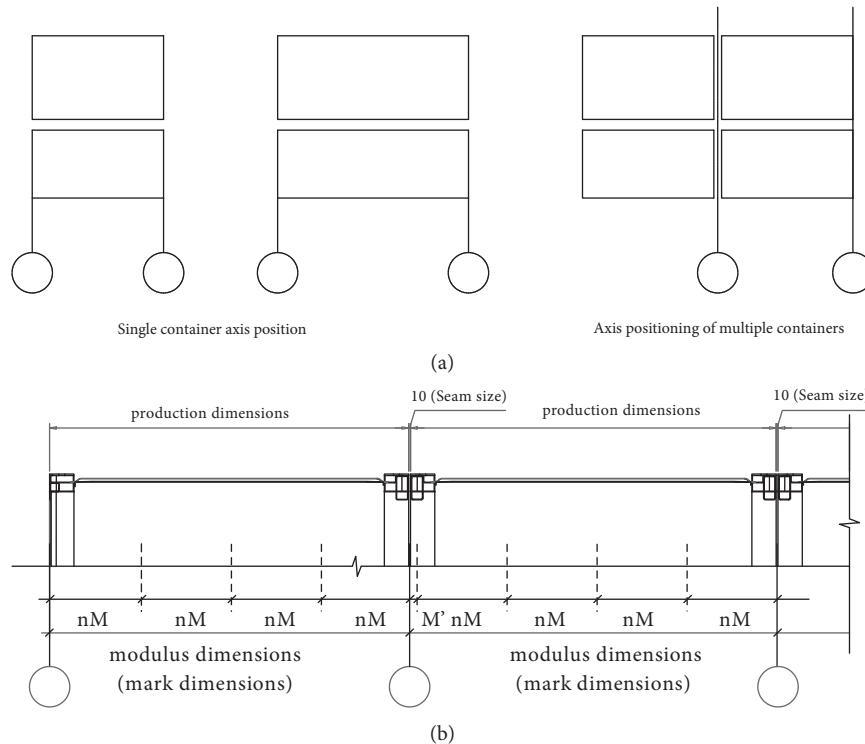


FIGURE 3: Principle of positioning. (a) Schematic diagram of axis positioning principles. (b) Schematic diagram of the seam, nominal dimensions, and structural dimensions.

modular grid can easily and intuitively generate different modular combinations in the 3D space grid. Finally, it forms the well-proportioned building rich in space and conforming to the principle of modularization (Figure 4).

In Huaduhui Commercial Street Project, the container splicing (opening the side walls) was adopted to meet the stores' requirements for space. As for module width, 2,438 mm was set for a spliced container and 3,000 mm for an independent container (structural dimension); as for height, 3,200 mm was selected as the significant modulus; as for length, 20, 30, and 40 feet were adopted.

The sizes and styles of components and parts were also simplified, but based on different combinations of interchangeable components and flexible application of orthogonal and oblique 3D modular grids (Figure 5), multiple combinations and spatial effects were obtained with fewer modules and components (Figure 1). The container building modulus system has also been applied in Yangzhou Suburb Park Maker Center, Modular Fire Stations, and other projects, all of which have made satisfactory achievements.

4. Establishment of a Database of BIM Modules and Components for Modular Steel Structure Container Buildings

The establishment of the database of BIM modules, components, and parts and the establishment of the modulus system are mutually complementary. In the database, the information

such as size and style of modules and features can be integrated; Autodesk Revit software was used to establish a "family" library of various prefabricated components (such as corner fittings, beams and columns, plates, doors, and windows) (Figure 6). In order to ensure quality, improve efficiency, and save cost, we used partial standard parts of container manufacturing enterprises in the architectural design of the projects, such as Huaduhui Tourist Service Center, and firstly established a high-precision standard component model library for coordinating the relevant standards in the construction industry and manufacturing industry based on modulus coordination; we also installed SECR software on the computer for mechanical manufacturing design and that for architectural design equipped with BIM software, and connected them with the server, to realize the compatibility between PDM data and BIM data [15].

Then, a database of nonstandard components and parts was established based on the database of standard features. After continuous accumulation and enrichment of the database, the "families" of the same type were compared to form the normal shape and modular dimensions of prefabricated building components. The modulus system has promoted standardization and serialization of the database, and the "family" library of prefabricated components has effectively promoted the optimization of the modulus system of prefabricated buildings and the establishment of design standards for container building enterprises. While the construction of the component model databased consumes massive time and energy, its establishment would be of great

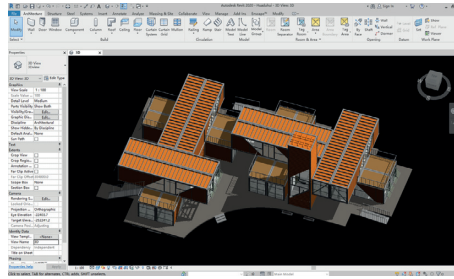


FIGURE 4: BIM model of the Tourist Service Center based on BIM platform (Autodesk Revit).

convenience for later project design to directly invoke the model from the database.

5. Design Integration of Modular Container Buildings Based on BIM and PDM

The establishment of the modulus system has formed a framework. The database has prepared the materials for the modular container building system. In contrast, the platform based on BIM and PDM has integrated data and software of different disciplines in the two industries and throughout the whole process of construction (Figure 7), forming the critical conditions for the design integration of the container building system.

BIM technology has provided strong support for architectural design, calculation analysis, cost management, and construction simulation, which have made it a core platform for information design and management in the construction industry. In contrast, as product data system of the manufacturing industry, PDM has become a core platform for digital design, manufacturing, and management of components and products throughout the life cycle. Therefore, in order to achieve a high degree of integration of container buildings, BIM should be integrated with PDM, and architectural design should be closely connected with factory production of parts and components [16], to realize the digital connection between architectural design and factory manufacturing design, and two-way synchronous design of architectural design and factory manufacturing, thus learning intelligent management and operation and maintenance [17].

BIM platforms can disclose and share design information. During design, the design plan of a container building can be uploaded to the “cloud” server for integrating the information such as dimensions and styles, accumulating and enriching basic modular combinations of prefabricated buildings with various standardized modules and “family” libraries, and saving design and adjustment time, thus increasing the varieties, improving the adaptability of prefabricated buildings, and better meeting the diversified needs. Integrated design based on BIM can better realize information sharing and coordination of various disciplines. For example, in the project of Shuangyu Island Hotel, the design model contained a large amount of design information (geometric information, material performance, and component properties); therefore, through introducing the model into performance analysis software, technical analysis

on sunshine and energy consumption can be carried out, which can improve the design plan. In particular, since modular buildings are different from ordinary ones in surface area and shape coefficient [18], the performance analysis can be conducted based on the BIM model in terms of energy conservation and other factors (Figure 8).

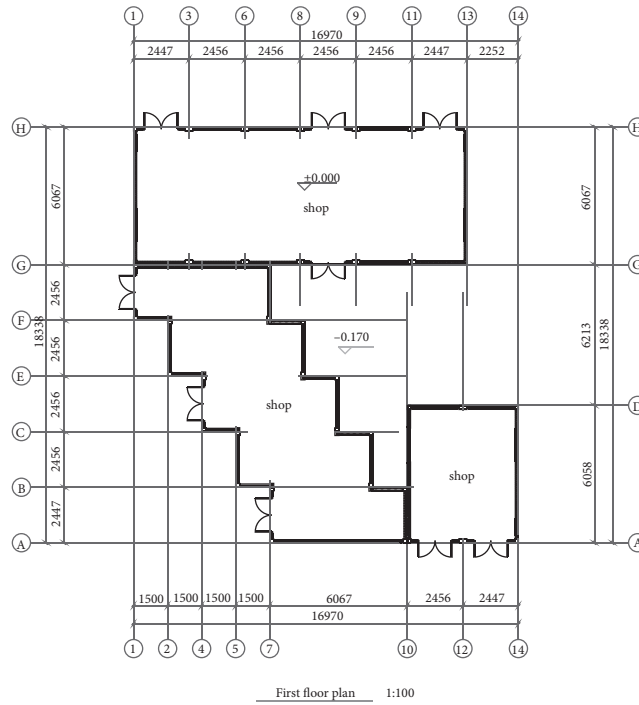
The integrated design of modular steel structure buildings should be conducted based on design coordination among different disciplines:

5.1. Modular Building Design Leading the Overall Direction.

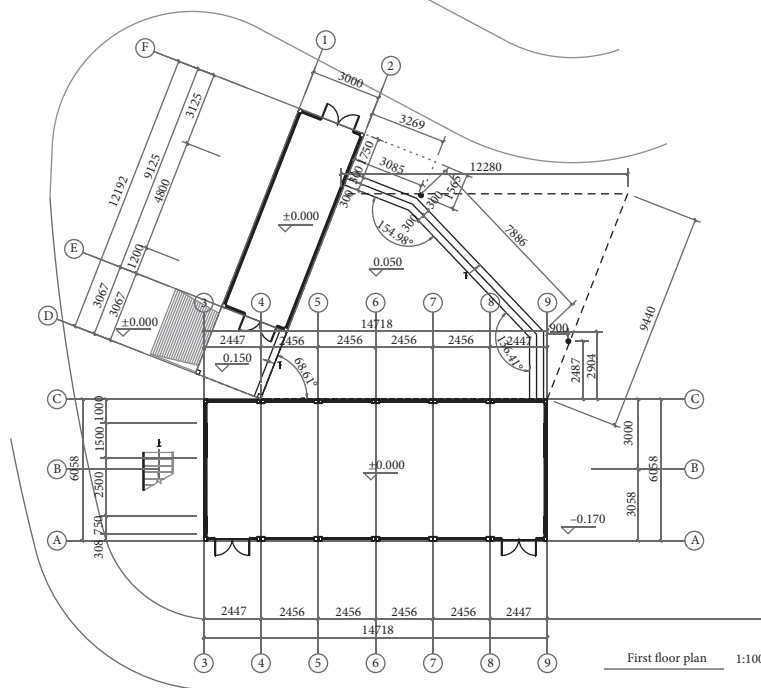
The integrated design of container buildings should be conducted based on coordination of various disciplines and whole process control, while architectural design plays the leading role. The successful container building design depends on the modular and standardized thinking from the phase of setting the architectural plan; the requirements of all disciplines should be comprehensively considered to create high-quality prefabricated buildings with unique shapes and applicable functions.

The pilot project “Modular Fire Station” is a modular firefighting duty building flexibly displayed in a city (Figure 9(a)). With the functions of fire command, fire garage, dormitory, kitchen and bathroom, and leisure, it can be placed in a key firefighting area for rapid response and rescue. This product is designed as a modular building, which can be expanded based on the 3D modular grid and standardized modular design, and the combination mode can also be adjusted, thus adapting to terrains of different sizes and shapes. The standardized and modular design can enable the plant to produce functional modules in batches, which can be assembled according to the actual needs of each project. In this project, a serialization design was performed, which can add or decrease functional modules according to the service radius and basic real needs, to adapt to different sizes of fire stations (one to five firefighting trucks). Such stations have been applied in cities such as Yangzhou, Langfang, and Shenzhen and have been well praised. Other pilot projects, such as “Xiangyu” Residence in Yangzhou Software Park [19] and Yangzhou Suburb Park Maker Center (Figures 9(b) and 9(d)), created functional and diverse architectural spaces and realized the integrated design and industrial production.

5.2. Design and Manufacture of Modular Steel Structure Buildings Based on BIM and PDM Coordination.



(a)



(b)

FIGURE 5: Modular grid plane (Huaduhui Commercial Street). (a) Orthogonal modular grid plane. (b) Oblique modular grid plane.

Container buildings are assembled in a modularized manner, which is not a conventional structural system, and may bring specific difficulties to the structural design [20]. The platform and structural component database based on BIM and PDM can bring convenience to the finite element analysis of the structure (Figure 10). With the BIM model, we can export IFC file with Revit and then import it into Tongji 3D3S, MIDAS

GEN, and other structural analysis software for finite element analysis so as to evaluate and analyze the seismic performance and stress of the main structure of modular buildings [21]; in addition, PKPM.STS based on building structural calculations and MSC Nastran (the structural CAE simulation analysis and calculation software of mechanical products) can be used for structural calculation on parts and components [22]; if the

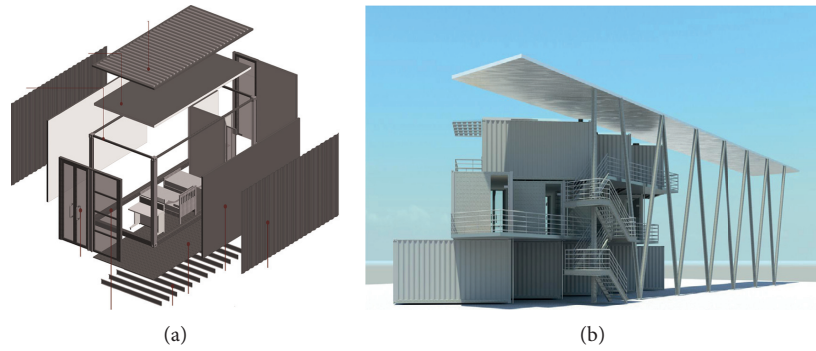


FIGURE 6: BIM model of modular steel structure buildings. (a) A single module. (b) Combination of modules, components, and parts of a modular steel structure building.

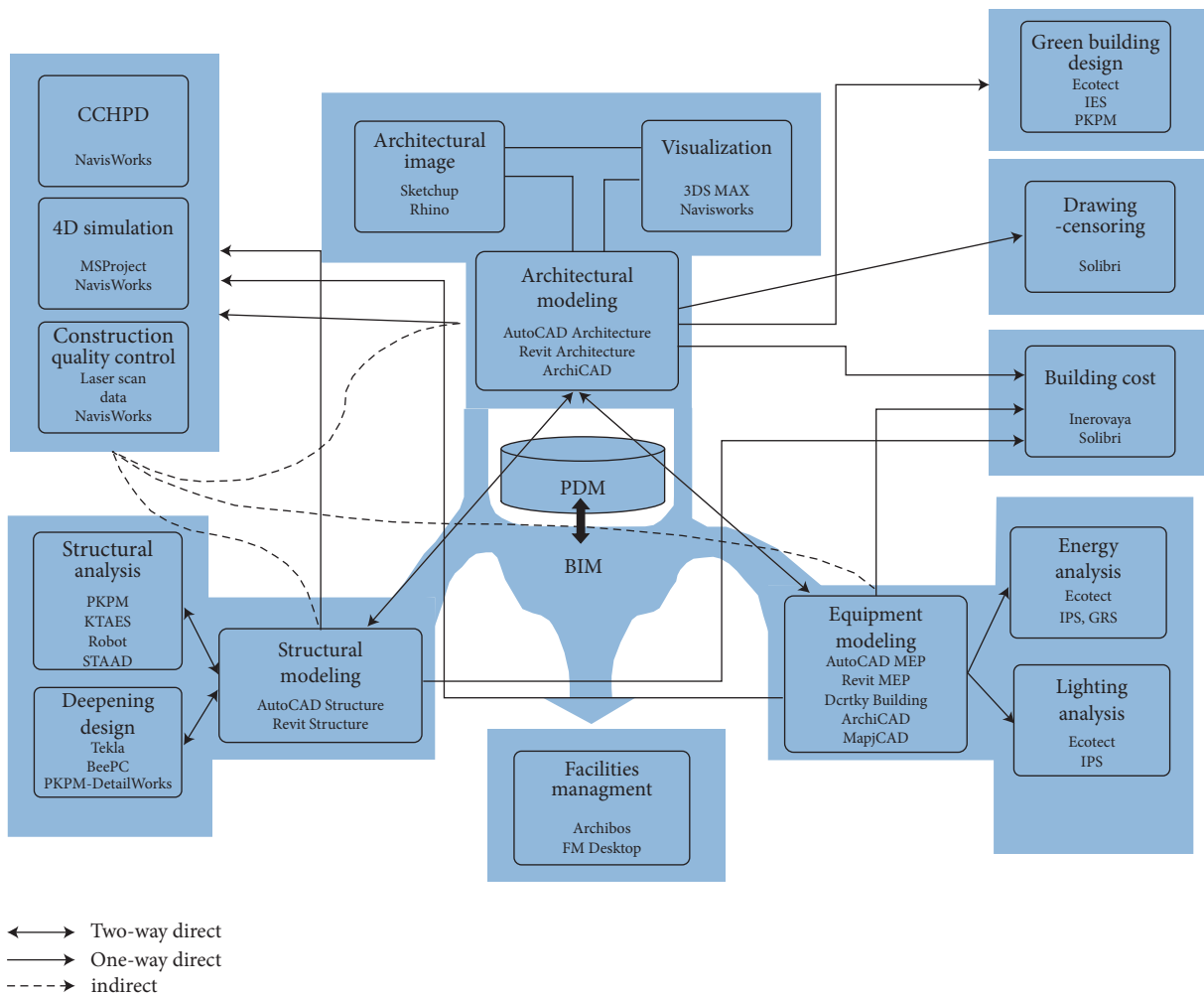


FIGURE 7: Analysis of greening of container buildings (Zhangzhou Shuangyu Island Hotel).

calculation results fail to meet the construction requirements, the relevant parameters of features and materials should be improved, until the calculation results meet the construction requirements. For example, in general, structural design software, the corrugated steel siding of the container module, cannot be used to establish the structural model directly. However, through analysis based on BIM platform with

architectural structure software and mechanical structure software, it can be found that the corrugated steel walls can be combined with the upper and lower side beams, diagonal bracing (Figure 11(a)) can be used, and inner metal keel and the corrugated steel plate can be welded, to effectively strengthen the overall strength of the structure. Therefore, the Tourist Service Center successfully reduced the downward

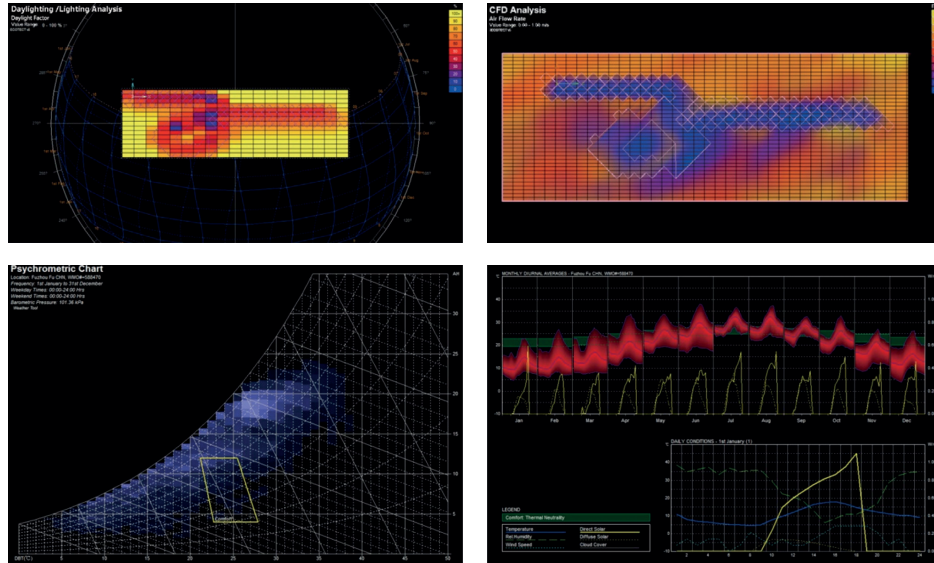


FIGURE 8: Photo of pilot projects. (a) Container modular fire station under construction. (b) Photo of “Xiangyu” Residence in Yangzhou Software Park. (c) Indoor photo of the container pilot project. (d) Photo of Yangzhou Suburb Park Maker Center.



FIGURE 9: Finite element stress analysis on modules of a container building.

deflection of the cantilever structure and applied the architectural scheme of the large cantilever (maximum cantilever: 3.6 M) and ample space (Figure 11(b)) successfully passed the inspection upon completion. Due to the integration between BIM and PDM platforms, the adjustment of structural design and mechanical manufacturing information of the components can realize real-time two-way intercommunication; as

thus, the component manufacturing drawing can be changed more efficiently, without mistakes; the parts can be conveniently classified, and their amount can be calculated, for facilitating the preparation of materials and fixtures by plants, thus promoting the factory production. As for the connection of nodes, the advanced module connection technology with independent intellectual property rights (patent number:

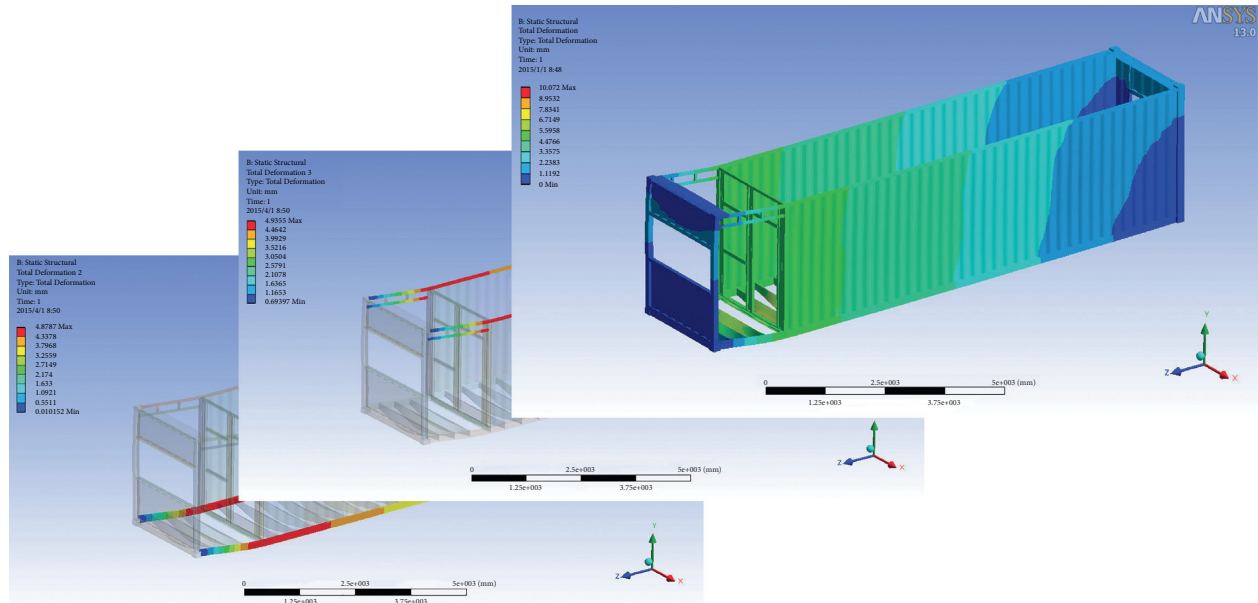


FIGURE 10: Integrated design information and software relationship based on BIM and PDM.



FIGURE 11: Photos of construction site. (a) Site installation of structurally strengthened modules. (b) Factory manufacturing and trial assembly of container building modules.

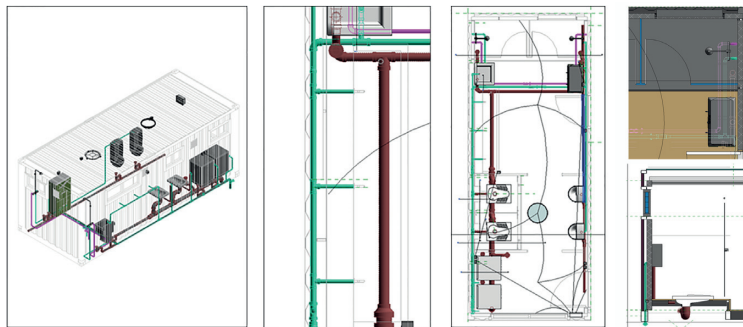


FIGURE 12: Comprehensive design of pipelines in bathroom based on BIM.

ZL2016 2 1236426.8) was adopted. The system consists of plug-in connectors, cover plates, and bolts. As proved by finite element analysis with Abaqus software and practice, it can provide sufficient rigidity and ensure structural integrity.

5.3. *Comprehensive Design and Construction of Pipelines in Container Buildings Based on BIM.* Prefabricated buildings have a high requirement for installation accuracy, and unlike traditional extensive wet construction methods, they have

higher standards for integration of electromechanical pipelines from design and construction to application and maintenance. From factory production to site assembly, the pipeline interfaces of all building modules should be accurately connected, and no holes and grooves should be prepared to not damage the paint and steel plate. Based on the BIM model shared among various disciplines and the analysis function of software such as Revit, the conflicts in design can be easily found in the three-dimensional virtual environment, thus significantly improving the comprehensive design ability work efficiency of the pipelines. It can timely avoid errors and conflicts that may be encountered during the construction and significantly reduce the application for changes; in addition, it can also considerably increase the efficiency of construction, reduce the cost increase and construction delay due to coordination, and reduce the construction waste and damage to the buildings caused by rework. Taking the bathroom module with robust pipelines in the “Maker Center” Project as an example, the collision detection and visualization optimization design of the channels, sanitary ware, equipment, and steel structure, and interior decoration based on the BIM model reduced the occurrence of multiple collisions and avoided rework. In the 3D model, it was found that pipelines can be arranged in gaps between the trim panels and corrugated steel wall panels, which could optimize the integrated design of channels and interior decoration (Figure 12); this module specifically designed the connection interfaces of pipelines and gradually improved them as standardized interface components. For some more complicated constructions, software such as Autodesk Navisworks can be used to perform visual 4D construction simulation based on the BIM platform to optimize the construction scheme. The construction personnel can also perform construction disclosure with Fuzor and Autodesk Navisworks Manage and get familiar with the construction process and site conditions by construction preview to improve the efficiency of assembly and quality of completion.

6. Conclusion

In this study, the low design integration and the contradiction between standardization and diversity were found to be the bottlenecks restricting further development of the modular container building system. To fix this problem, it was proposed to establish a modulus system for modular container buildings and a database of components and parts of modular steel structure buildings, to strengthen professional coordination based on BIM and PDM platforms and improve the integrated design method for modular container buildings.

In this study, the related modules in the traditional construction industry and container manufacturing industry and the restrictions on dimensions in the logistics industry were coordinated based on BIM; and the unified container building modulus sequence and 3D modulus grid were proposed. A standardized and systematic database of components and parts characterized by “family” through the integration of BIM and PDM platforms and an integrated design method of container buildings led by architectural design based on the flexible

modular combination and closely cooperated with structure and equipment, for realizing the standardization and digitization of the whole process of design, production, and construction were established.

The integrated design of modular steel structure container buildings based on BIM has been applied in several pilot projects, including Huaduhui Commercial Street and Modular Fire Station. As proved by practice, the application of this system has promoted the integration of the relevant standards in the two industries, strengthened the coordination of various disciplines, and improved the standardization, industrialization, and information levels of design, production, and construction. While adopting modules, prefabricated components, and components of the exact design specifications, the pilot projects also improved the buildings’ spatial relevance and artistic quality. At present, the integrated design has made phased achievements. In the next step, the versatility of modules and components will be further studied, the composability of modules will be expanded, and the cost will be further reduced. In addition, as compared with the proposed integration target, the integration of this design system should be strengthened in the operation and maintenance phase and complete life cycle information management. In the future, incorporating the Internet of Things into the integrated design system will further promote the development of container buildings.

Data Availability

The data used to support the findings of this study are available from the corresponding author upon request.

Conflicts of Interest

The authors declare that there are no conflicts of interest regarding the publication of this study.

Acknowledgments

This study was supported by the Science and Technology Program of the Ministry of Housing and Urban-Rural Development (Grant no. 2016-K5-021).

References

- [1] X. L. Gong and Y. K. Zhang, “Construction and modification of container-A sustainable development of construction trial,” *World Architecture*, vol. 57, no. 10, pp. 124-125, 2010.
- [2] P. C. H. Ling, C. S. Tan, Y. H. Lee, and Y. E. Tu, “Design consideration of container shelter in Malaysia,” *Jurnal Teknologi*, vol. 83, no. 5, pp. 1-7, 2021.
- [3] E. M. Grant, ““Pack ’em, rack ’em and stack ’em”: the appropriateness of the use and reuse of shipping containers for prison accommodation,” *Construction Economics And Building*, vol. 13, no. 2, pp. 35-44, 2013.
- [4] P. Zhao, *Study on Adaptive Design and Construction of Container Buildings*, Master’s Degree Thesis, Hunan University, Changsha, China, 2011.
- [5] L. L. Wong, “The new bud light steel system and the geometric shape evolution of light steel framework for COVID-19

- patients appointed hospital (Huoshenshan hospital),” *Journal of Intelligent and Fuzzy Systems*, vol. 39, pp. 9015–9026, 2020.
- [6] C. Kriston, “Studio visit lot-ek,” *Architect*, vol. 101, pp. 74–77, 2012.
- [7] M. J. Hough and M. Lawson, “Design and construction of high-rise modular buildings based on recent projects,” *Proceedings of the Institution of Civil Engineers- Civil Engineering*, vol. 172, no. 6, pp. 137–144, 2019.
- [8] J. Alread, “Shigeru ban,” *Journal of Architectural Education*, vol. 58, pp. 70–71, 2004.
- [9] A. Eissa, M. Monjur, and R. Yacine, “Factors for effective BIM governance,” *Journal of Building Engineering*, vol. 10, pp. 89–101, 2017.
- [10] M. K. Ansah, X. Chen, H. X. Yang, L. Lin, and L. Patrick, “Developing an automated BIM-based life cycle assessment approach for modularly designed high-rise buildings,” *Environmental Impact Assessment Review*, vol. 90, Article ID 106618, 2021.
- [11] Y. Lu, Q. Liu, Y. L. Chen, L. Yu, and S. S. Luo, “Research on structural design method of container house,” *Industrial Construction*, vol. 44, no. 10, pp. 130–136+97, 2014.
- [12] S. Qin, Z. C. Wu, and L. Yu, “Research on development of the interior system from KEP to KSI,” *Architectural Journal*, vol. 61, no. 7, pp. 17–23, 2014.
- [13] C. Zheng, *Research on Integrated Architecture Design Based on BIM*, Master’s Degree Thesis, Central South University, Changsha, China, 2012.
- [14] D. G. Guo, *Computer Aided Architectural Design and Construction Management Based on BIM*, Master’s Degree Thesis, Xiamen University, Xiamen, China, 2014.
- [15] M. Su and M. Gao, “A new exploration of prefabricated modular container buildings - design of Yangzhou Huaduhui Tourist Service Center,” *Jiangsu Construction*, vol. 38, no. 4, pp. 27–30, 2018.
- [16] S. Palos, A. Kiviniemi, and J. Kuusisto, “Future perspectives on product data management in building information Modeling,” *Construction Innovation*, vol. 14, no. 1, pp. 52–68, 2014.
- [17] S. Lemes and L. Lemes, “Blockchain in distributed cad environments,” *New Technologies, Development And Application II*, vol. 76, pp. 25–32, 2020.
- [18] M. Bertolini and L. Guardigli, “Upcycling shipping containers as building components: an environmental impact assessment,” *International Journal of Life Cycle Assessment*, vol. 25, no. 6, pp. 947–963, 2020.
- [19] M. Su and M. Gao, “Research on plant renovation and reuse based on container modular building,” *Industrial Construction*, vol. 50, no. 1, pp. 75–79, 2020.
- [20] K. Giriunas, H. Sezen, and R. B. Dupaix, “Evaluation, modeling, and analysis of shipping container building structures,” *Engineering Structures*, vol. 43, pp. 48–57, 2012.
- [21] J. Gu, “Structural design of modular container buildings,” *Building structure*, vol. 51, no. S1, pp. 1152–1156, 2021.
- [22] F. J. Luo, Y. Bai, J. Hou, and Y. Huang, “Progressive collapse analysis and structural robustness of steel-framed modular buildings,” *Engineering Failure Analysis*, vol. 104, pp. 643–656, 2019.

Research Article

Bearing Behavior of H-Shaped Honeycombed Steel Web Composite Columns with Rectangular Concrete-Filled Steel Tube Flanges under Eccentric Compression Load

Jing Ji,^{1,2} Chenyu Yu,¹ Liangqin Jiang,^{1,2} Jiedong Zhan,¹ Hongguo Ren ,³ Sixue Hao,³ Shaojie Fan ,³ Li Jiang,¹ Yubo Lin,¹ and Lingjie He¹

¹College of Civil and Architectural Engineering, Northeast Petroleum University, Heilongjiang Key Laboratory of Disaster Prevention, Mitigation and Protection Engineering, No. 99 Xuefu Road, Longfeng District, Daqing 163318, China

²Key Laboratory of Earthquake Engineering and Engineering Vibration, Institute of Engineering Mechanics, China Earthquake Administration, No. 29 Xuefu Road, Nangang District, Harbin 150000, China

³Handan Key Laboratory of Building Physical Environment and Regional Building Protection Technology, School of Architecture and Art, Hebei University of Engineering, No. 19 Taiji Road, Handan Economic and Technological Development District, Handan 056038, China

Correspondence should be addressed to Hongguo Ren; renhongguo771126@163.com and Shaojie Fan; fanshaojie2021@163.com

Received 2 November 2021; Accepted 15 December 2021; Published 5 January 2022

Academic Editor: Lingkun Chen

Copyright © 2022 Jing Ji et al. This is an open access article distributed under the Creative Commons Attribution License, which permits unrestricted use, distribution, and reproduction in any medium, provided the original work is properly cited.

In order to investigate the bearing capacity of H-shaped honeycombed steel web composite columns with rectangular concrete-filled steel tube flanges (STHCCs) subjected to eccentric compression load, 33 full-scale STHCCs were designed with the eccentricity (e), the slenderness ratio (λ), the cubic compressive strength of concrete (f_{cuk}), the thickness of the steel tube flange (t_1), the thickness of honeycombed steel web (t_2), diameter-depth ratio (d/h_w), space-depth (s/h_w), and the yield strength of the steel tube (f_y) as the main parameters. Considering the nonlinear constitutive model of concrete and simplified constitutive model of steel, the finite element (FE) model of STHCCs was established by ABAQUS software. By comparison with the existing test results, the rationality of the constitutive model of materials and FE modeling was verified. The numerical simulation of 33 full-scale STHCCs was conducted, and the influence of different parameters on the ultimate eccentric compression bearing capacity was discussed. The results show that the cross-sectional stress distribution basically conforms to the plane-section assumption. With the increase in e , λ , and d/h_w , the ultimate eccentric compression bearing capacity of the full-scale STHCCs decreases, whereas it gradually increases with the increase in f_{cuk} , t_1 , t_2 , s/h_w , and f_y . By introducing bias-stress stability coefficient (φ), the calculation formula of full-scale STHCCs under eccentric compression is proposed by statistical regression, which can lay a foundation for the popularization and application of these types of composite columns in practical engineering.

1. Introduction

H-shaped honeycombed steel web composite columns with rectangular concrete-filled steel tube flanges (STHCCs) are types of novel composite members formed by connecting two concrete-filled rectangular steel tubular flanges with a honeycombed steel web. The core concrete can prevent and delay the local buckling of the steel tube and the instability failure of the specimens effectively, and on the other hand,

the confinement of the steel tube makes the core concrete in a state of triaxial compression, which can effectively improve the capacity of resisting deformation and the compressive strength of the core concrete. In particular, the honeycombed steel web connects the two limbs into an organic whole, which can not only reduce the weight of the structure, but also improve the stiffness and bearing capacity of the composite columns. These types of composite columns are characterized by high ultimate bearing capacity, good

ductility, and excellent stability bearing capacity, which are superior to ordinary concrete-filled steel tube (CFST) columns and honeycombed columns [1].

Numerous research studies regarding CFST columns and honeycombed columns have been carried out at home and abroad. Jayaganesh et al. [2] conducted tests on 6 square and 6 circular CFST short columns to study the influence of concentric local compression on the structural behavior of CFST columns under axial compression. Ahmed et al. [3] proposed a simplified model of concrete-filled square steel tube columns subjected to axial compression and presented the interaction curve of high-strength square concrete-filled double steel tubular (CFDST) under eccentric loading by establishing the buckling model of CFDST under axial compression and uniaxial bending. Vatulia et al. [4] analyzed the deformation development regularity of concrete-filled rectangular steel tube columns with different lengths subjected to eccentric loading through the integral method and established the calculation mathematical model of eccentric compression bearing capacity for concrete-filled rectangular steel tube columns. Yu et al. [5] put forward the formula of eccentric compression bearing capacity of recycled coarse aggregate self-compacting CFST columns based on the experimental studies and analyzed the applicability of the formula in the United States, China, and Japan. Li et al. [6] conducted eccentric compression tests of L-shaped square CFST columns and established a finite element (FE) model to study the eccentric compression behavior of this type column and proposed a bearing capacity analysis method of the rectangular concrete-filled stainless steel tubular (CFSST) columns based on the stress yield criterion at the edge of the section base. Rong et al. [7] analyzed the eccentric compression behavior of concrete-filled square steel tube columns with I-shaped CFRP through experimental research and FE simulation, and derived the calculation formula of eccentric compression bearing capacity of composite columns. Sui et al. [8] investigated the failure mode of 19 multi-element composite T-shaped CFST columns under biaxial eccentric compression and proposed the simplified calculation formula of eccentric compression bearing capacity. Chen et al. [9] studied the influence regularity of different parameters on eccentric compression test of 18 concrete-filled square steel tube columns with spiral stirrups and derived the calculation formula of eccentric compression bearing capacity of these types of columns. Twenty-one recycled self-compacting concrete-filled circular steel tubular (RSCFCST) columns were tested subjected to eccentric compression by Yu et al. [10], and bearing capacity of these kinds of composite columns under eccentric compression was obtained systematically; finally, an analytical model for predicting the effective stiffness of RSCFCST columns under eccentric compression was proposed based on the moment magnifier method. In 2017, Ji et al. [11] investigated the eigenvalue buckling behavior of 29 STHCCs by ABAQUS software. Based on this, in 2018, Ji et al. [12] carried out the research on the overall nonlinear stability of STHCCs and derived the calculation expression of nonlinear stability bearing capacity of STHCCs. In the same year, in order to investigate the

influence regularity of different parameters on the axial compression bearing capacity of STHCCs, Ji et al. [13, 14] designed and conducted the axial compression tests of 16 short STHCCs and proposed the calculation expression of axial compression bearing capacity for STHCCs. In 2020, Ji et al. [15] studied the eccentric compression behavior of 17 reduced-scale STHCCs by ABAQUS software and derived the calculation expression of eccentric compression bearing capacity of reduced-scale STHCCs.

At present, the research on STHCCs is mainly aimed at axial compression and stability behavior, and few studies have been performed on the eccentric compression behavior of such full-scale columns. Based on the existing axial compression test and results of reduced-scale eccentric compression behavior of STHCCs, the numerical simulation analysis of 33 full-scale STHCCs is further carried out by ABAQUS software. The influence of different parameters on the ultimate bearing capacity of these types of full-scale composite columns under eccentric compression is discussed. The calculation formula of eccentric compression bearing capacity of these types of columns can be obtained by statistical regression based on the simulation results, which can provide technical support for the subsequent research and application of these types of columns.

2. Specimens Design

In order to investigate the mechanical behavior of full-scale H-shaped honeycombed steel web composite columns with rectangular concrete-filled steel tube flanges (STHCCs) under eccentric compression, 33 full-scale STHCCs were designed with the eccentricity (e), the slenderness ratio (λ), the cubic compressive strength of concrete (f_{cuk}), the thickness of the steel tube flange (t_1), the thickness of honeycombed steel web (t_2), diameter-depth ratio (d/h_w), space-depth (s/h_w), and the yield strength of the steel tube (f_y) as the main parameters. The schematic diagram and specific parameters of the specimens are shown in Figure 1 and Table 1, where h_w represents the width of webs, d refers to the diameter of the honeycombed holes on the web, and s represents the distance between two honeycombed holes.

3. Finite Element Model

3.1. Constitutive Model for Materials

3.1.1. Constitutive Model for Steel. The stress-strain curve of steel consists of five stages of elastic, elastic-plastic, plastic, strengthening, and second plastic flow. Thirty-three STHCCs designed are all medium-long columns; hence, the strengthening stage of steel can be neglected. The ideal elastoplastic constitutive model is applied to characterize the elastoplastic behavior of steel, as shown in Figure 2(a). Poisson's ratio of steel is set as 0.3.

3.1.2. Constitutive Model for Concrete. Han [16], Pagoulatou et al. [17], Teng et al. [18], Mander et al. [19], and Qian et al. [20] have successively given the constitutive models of confined concrete, and the constitutive model of unconfined

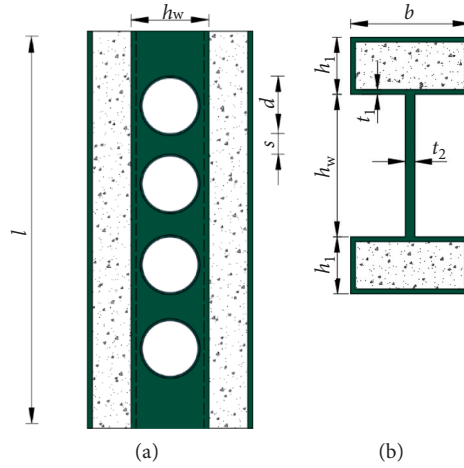


FIGURE 1: Physical meaning of all variables for STHCC specimens. (a) Longitudinal-section of STHCC specimens. (b) Cross section of STHCC specimens.

TABLE 1: Specific parameters of 33 STHCC specimens.

Specimens	$h_w \times h_1 \times b \times t_1 \times t_2$ (mm)	l (mm)	λ	e (mm)	ξ	f_{cuk} (MPa)	f_y (MPa)	d/h_w	s/h_w
STHCC-1	$400 \times 320 \times 500 \times 8 \times 10$	2240	19.40	80	0.73	40	345	0.6	0.4
STHCC-2	$400 \times 320 \times 500 \times 8 \times 10$	2240	19.40	160	0.73	40	345	0.6	0.4
STHCC-3	$400 \times 320 \times 500 \times 8 \times 10$	2240	19.40	240	0.73	40	345	0.6	0.4
STHCC-4	$400 \times 320 \times 500 \times 8 \times 10$	2240	19.40	320	0.73	40	345	0.6	0.4
STHCC-5	$400 \times 320 \times 500 \times 8 \times 10$	2240	19.40	400	0.73	40	345	0.6	0.4
STHCC-6	$400 \times 320 \times 500 \times 8 \times 10$	3040	26.33	240	0.73	40	345	0.6	0.4
STHCC-7	$400 \times 320 \times 500 \times 8 \times 10$	4640	40.18	240	0.73	40	345	0.6	0.4
STHCC-8	$400 \times 320 \times 500 \times 8 \times 10$	6240	54.04	240	0.73	40	345	0.6	0.4
STHCC-9	$400 \times 320 \times 500 \times 8 \times 10$	7040	60.97	240	0.73	40	345	0.6	0.4
STHCC-10	$400 \times 320 \times 500 \times 8 \times 10$	3040	26.33	240	0.98	30	345	0.6	0.4
STHCC-11	$400 \times 320 \times 500 \times 8 \times 10$	3040	26.33	240	0.59	50	345	0.6	0.4
STHCC-12	$400 \times 320 \times 500 \times 8 \times 10$	3040	26.33	240	0.49	60	345	0.6	0.4
STHCC-13	$400 \times 320 \times 500 \times 8 \times 10$	3040	26.33	240	0.42	70	345	0.6	0.4
STHCC-14	$400 \times 320 \times 500 \times 6 \times 10$	3040	26.33	240	0.54	40	345	0.6	0.4
STHCC-15	$400 \times 320 \times 500 \times 10 \times 10$	3040	26.33	240	0.93	40	345	0.6	0.4
STHCC-16	$400 \times 320 \times 500 \times 12 \times 10$	3040	26.33	240	1.14	40	345	0.6	0.4
STHCC-17	$400 \times 320 \times 500 \times 14 \times 10$	3040	26.33	240	1.35	40	345	0.6	0.4
STHCC-18	$400 \times 320 \times 500 \times 8 \times 8$	3040	26.33	240	0.73	40	345	0.6	0.4
STHCC-19	$400 \times 320 \times 500 \times 8 \times 12$	3040	26.33	240	0.73	40	345	0.6	0.4
STHCC-20	$400 \times 320 \times 500 \times 8 \times 14$	3040	26.33	240	0.73	40	345	0.6	0.4
STHCC-21	$400 \times 320 \times 500 \times 8 \times 16$	3040	26.33	240	0.73	40	345	0.6	0.4
STHCC-22	$400 \times 320 \times 500 \times 8 \times 10$	3040	26.33	240	0.73	40	345	0.1	0.4
STHCC-23	$400 \times 320 \times 500 \times 8 \times 10$	3040	26.33	240	0.73	40	345	0.3	0.4
STHCC-24	$400 \times 320 \times 500 \times 8 \times 10$	3040	26.33	240	0.73	40	345	0.475	0.4
STHCC-25	$400 \times 320 \times 500 \times 8 \times 10$	3040	26.33	240	0.73	40	345	0.75	0.4
STHCC-26	$400 \times 320 \times 500 \times 8 \times 10$	3040	26.33	240	0.73	40	345	0.6	0.15
STHCC-27	$400 \times 320 \times 500 \times 8 \times 10$	3040	26.33	240	0.73	40	345	0.6	0.6
STHCC-28	$400 \times 320 \times 500 \times 8 \times 10$	3040	26.33	240	0.73	40	345	0.6	0.9
STHCC-29	$400 \times 320 \times 500 \times 8 \times 10$	3040	26.33	240	0.73	40	345	0.6	1.4
STHCC-30	$400 \times 320 \times 500 \times 8 \times 10$	3040	26.33	240	0.73	40	235	0.6	0.4
STHCC-31	$400 \times 320 \times 500 \times 8 \times 10$	3040	26.33	240	0.73	40	390	0.6	0.4
STHCC-32	$400 \times 320 \times 500 \times 8 \times 10$	3040	26.33	240	0.73	40	420	0.6	0.4
STHCC-33	$400 \times 320 \times 500 \times 8 \times 10$	3040	26.33	240	0.73	40	460	0.6	0.4

concrete has been given in the Chinese Code for Design of Concrete Structures (GB50010-2010) [21]. The comparisons of different constitutive models are illustrated in Figure 2(b). Through comparative analysis, the constitutive model proposed by Han [16], which considered the confinement

effect, is applied in this article. It can be seen that the ductility of concrete is improved significantly; nevertheless, the strength of concrete remains unchanged.

The following formula represents the stress-strain curve of concrete under uniaxial compression:

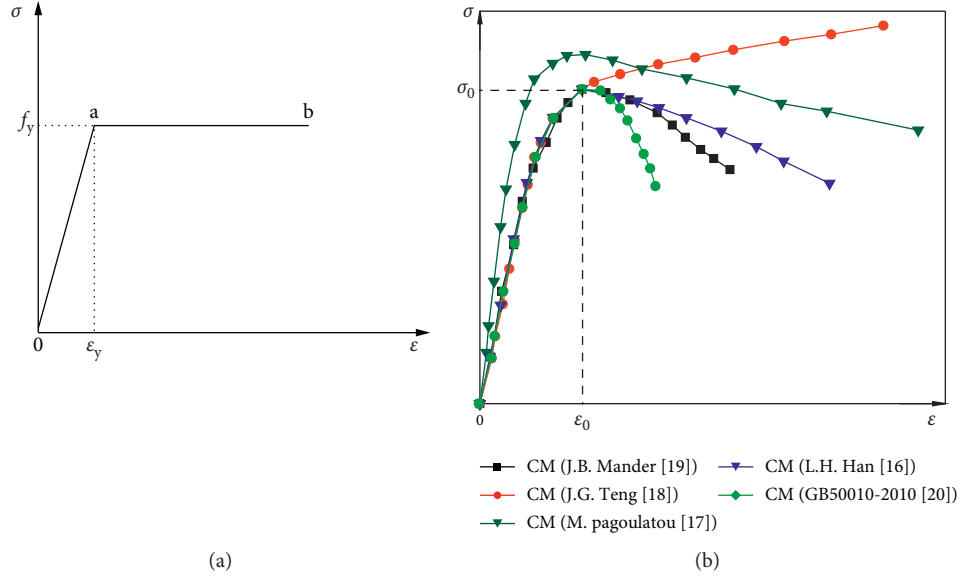


FIGURE 2: Constitutive models. (a) Constitutive model of steel. (b) Constitutive models of concrete.

$$y = \begin{cases} 2x - x^2, & (x \leq 1), \\ \frac{x}{\beta_0(x-1)^{(1.6+1.5/x)} + x}, & (x > 1), \end{cases} \quad (1)$$

where $x = \varepsilon/\varepsilon_0$, $y = \sigma/\sigma_0$, $\sigma_0 = f_c$, $\varepsilon_0 = (1300 + 12.5f_c) \times 10^{-6} + 800\xi^{0.2} \times 10^{-6}$.

The following formula represents the stress-strain curve of concrete under uniaxial tensile:

$$y = \begin{cases} 1.2x - 0.2x^6, & (x \leq 1), \\ \frac{x}{0.31\sigma_p^2 \cdot (x-1)^{1.7} + x}, & (x > 1), \end{cases} \quad (2)$$

where $x = \varepsilon_c/\varepsilon_p$, $y = \sigma_c/\sigma_p$, $\sigma_p = 0.26 \times (1.25f_c)^{2/3}$, $\varepsilon_p = 43.1\sigma_p$, and other variables can be found in reference [16].

3.2. Modeling Process and Boundary Conditions. The FE models of STHCCs were established by ABAQUS software [22], as shown in Figure 3. By adding material properties and then assigning material properties to the members, the constitutive model proposed by Han can be input into the material of ABAQUS. The eight-joint hexahedral element-type C3D8R was used to simulate the rectangular steel tube, honeycomb steel web, and concrete. The nonlinear symmetrical contact between steel tube and concrete was simplified as normal hard contact and tangential friction contact, and the Coulomb friction coefficient (μ) [23] was set as 0.25. Two reference points were set at the center of the upper and lower surfaces of the columns, namely, RP1 and RP2. The reference points were, respectively, coupled with the top end and the bottom end of the columns. The displacements (U_x , U_y , U_z) of the top end for columns were constrained by RP1, and the displacements (U_x , U_y , U_z ,

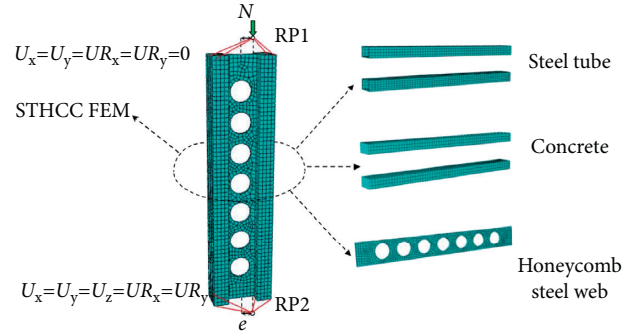


FIGURE 3: The FE models of STHCCs.

U_r_x , U_r_y) of the bottom end for columns were constrained by RP2.

4. Experimental Verification of FE Models

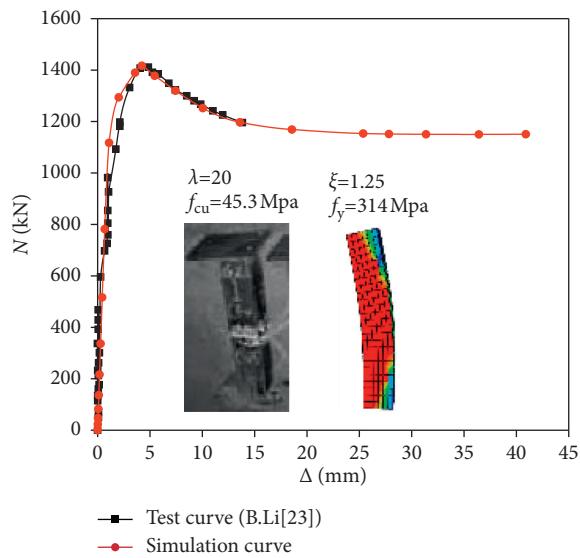
In order to verify the rationality of the FE models, numerical simulation analysis on 4 specimens selected from reference [24] and 11 specimens selected from references [25–28] was carried out, as shown in Table 2. The load-lateral deflection curves of the mid-span sections and failure modes were obtained. By the comparison, it could be seen from Figure 4 that the curves obtained by the simulation were consistent with the test curves. The comparisons of the bearing capacity obtained by simulation (N_a) and the bearing capacity by test (N_t) were shown in Figure 5. The maximum error was 8.74%, which could meet the requirements of engineering accuracy. The rationality of FE modeling proposed in this article was verified.

5. Parameter Analysis of Full-Scale STHCCs

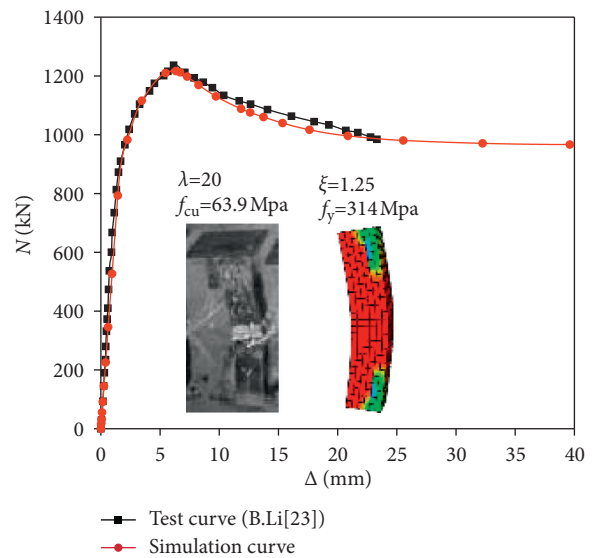
According to the proposed FE model, the load (N)-vertical displacement (Δ) curves, the load (N)-lateral deflection (Δ) curves of the mid-span sections, and the N/N_u - M/M_u curves

TABLE 2: : The specific parameters of 15 specimens.

Specimens	L (mm)	e (mm)	f_{cuk} (MPa)	f_y (Mpa)	N_t (kN)	N_a (kN)	$ N_a - N_t/N_t \times 100\%$	
The tests conducted by Li et al. [24]	GZ-1	866	25.0	45.3	314	1411	1416.8	0.41
	GZ-2	866	50.0	63.9	314	1236	1216.3	1.59
	GZ-3	1300	25.0	63.9	314	1365	1381.1	1.18
	GZ-4	1300	50.0	84.7	314	1150	1198.2	4.19
The tests conducted by Du et al. [25-28]	SC40-150-0.2	1180	13.0	43.2	488.4	2470	2576.11	4.30
	SC40-180-0.2	1180	18.5	43.2	488.4	2660	2520.53	5.24
	SC40-200-0.2	1180	20.0	43.2	488.4	2595	2445.86	5.75
	SC50-150-0.2	1180	15.0	55.3	488.4	2450	2664.10	8.74
	SC50-180-0.2	1180	18.0	55.3	488.4	2530	2684.80	6.12
	SC50-200-0.2	1180	19.0	55.3	488.4	2625	2608.31	0.64
	SC40-150-0.4	1180	31.5	43.2	488.4	2042	2032.09	0.49
	SC40-180-0.4	1180	37.0	43.2	488.4	2150	2074.93	3.49
	SC50-150-0.4	1180	32.5	55.3	488.4	2020	2127.70	5.33
	SC50-180-0.4	1180	41.0	55.3	488.4	2150	2104.70	2.11
	SC50-200-0.4	1180	41.5	55.3	488.4	2100	2091.91	0.39

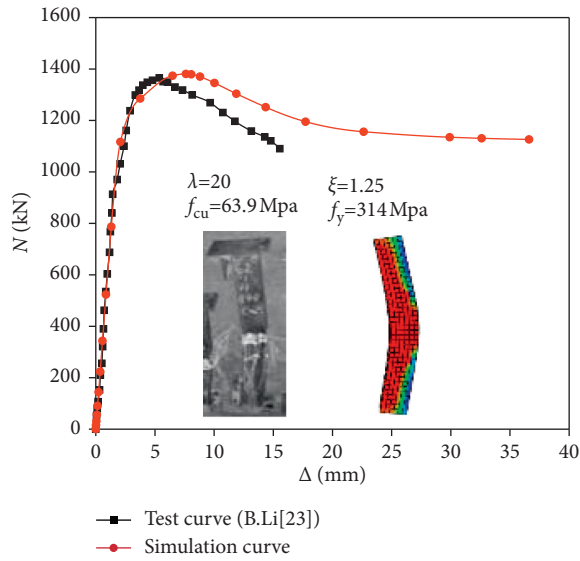


(a)

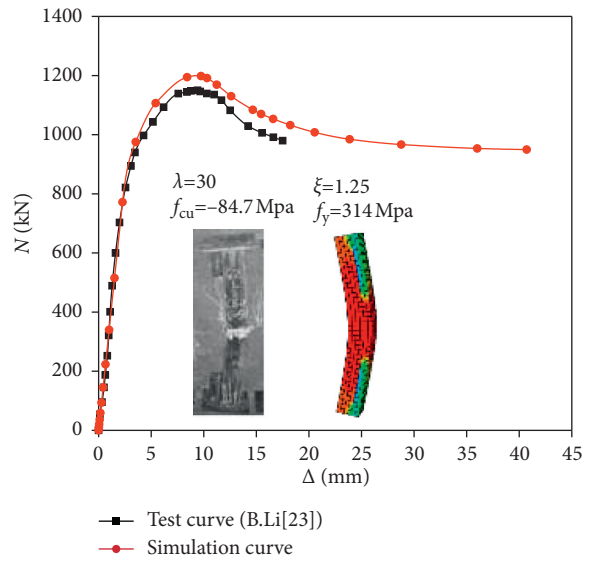


(b)

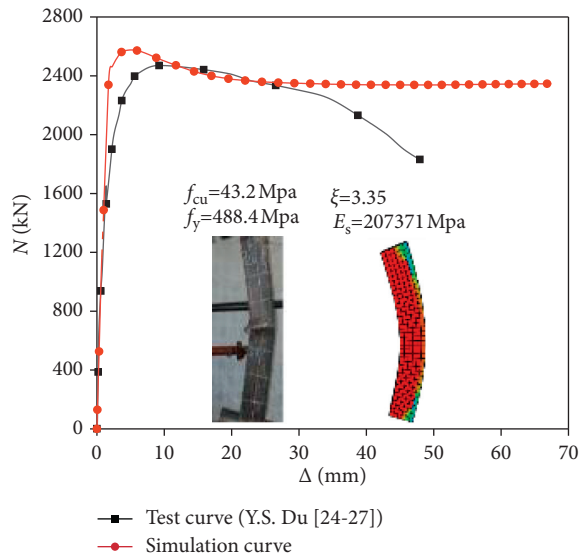
FIGURE 4: Continued.



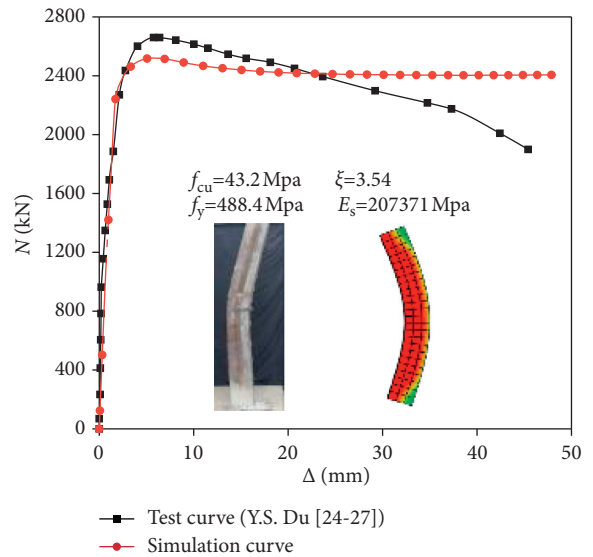
(c)



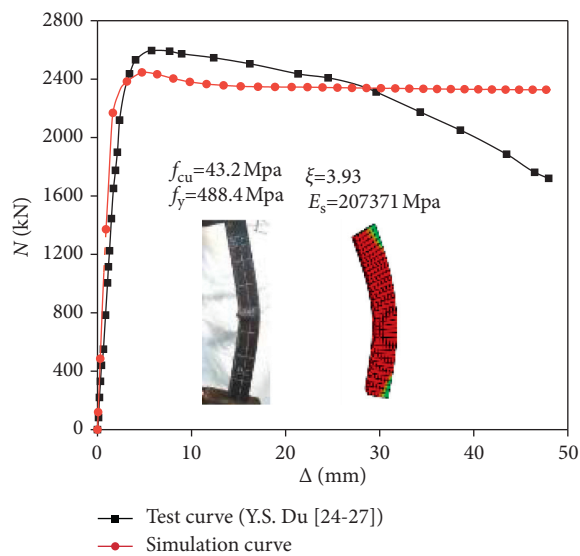
(d)



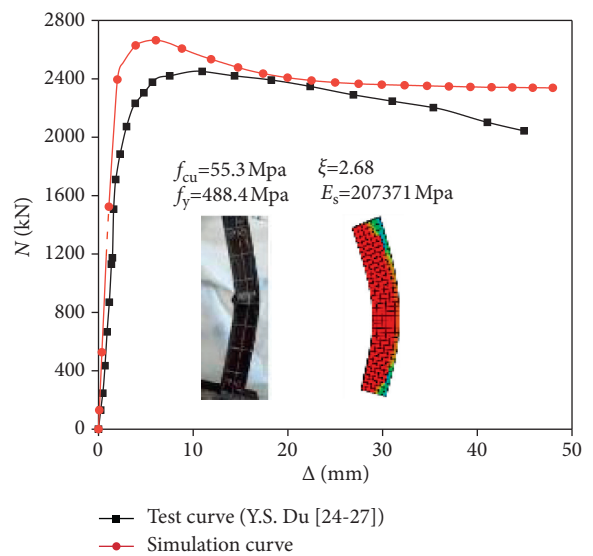
(e)



(f)

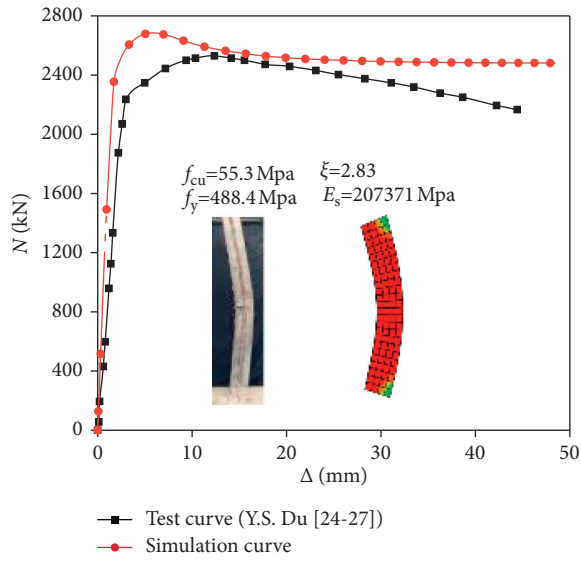


(g)

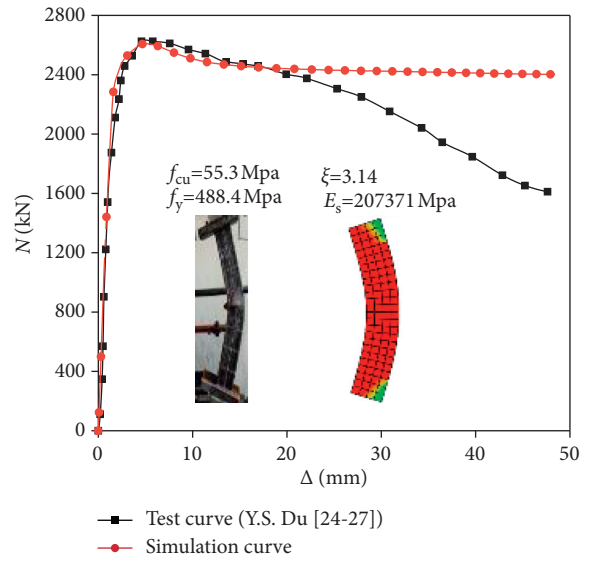


(h)

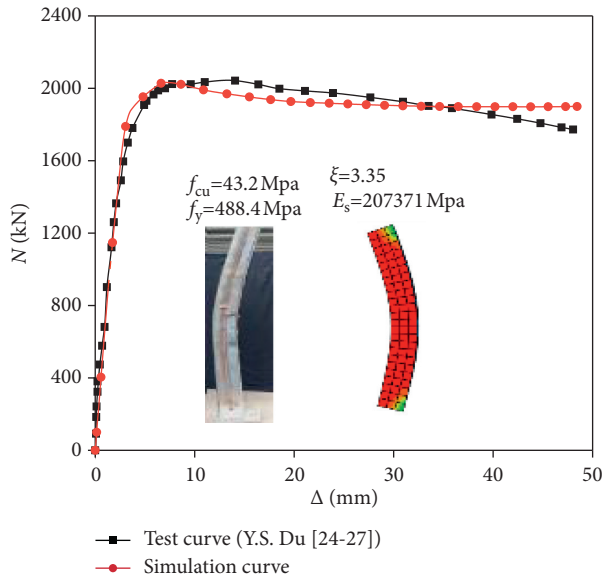
FIGURE 4: Continued.



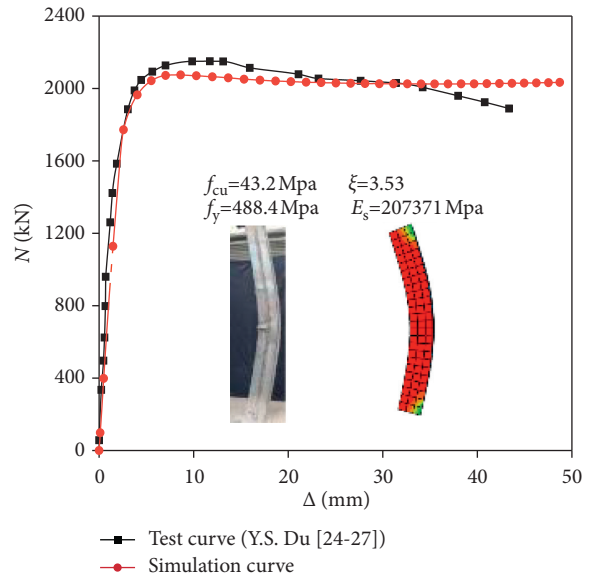
(i)



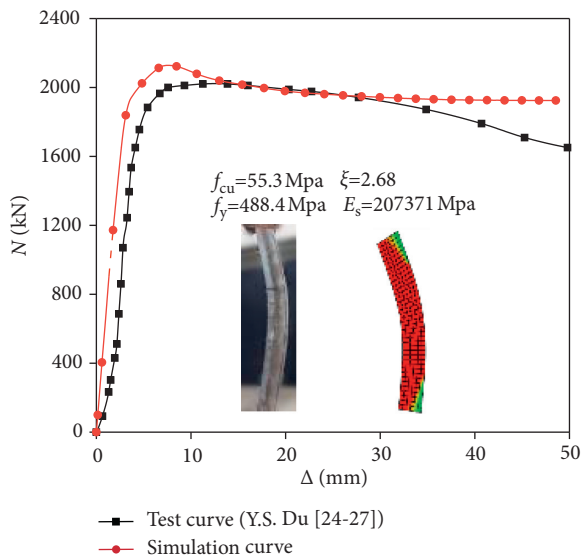
(j)



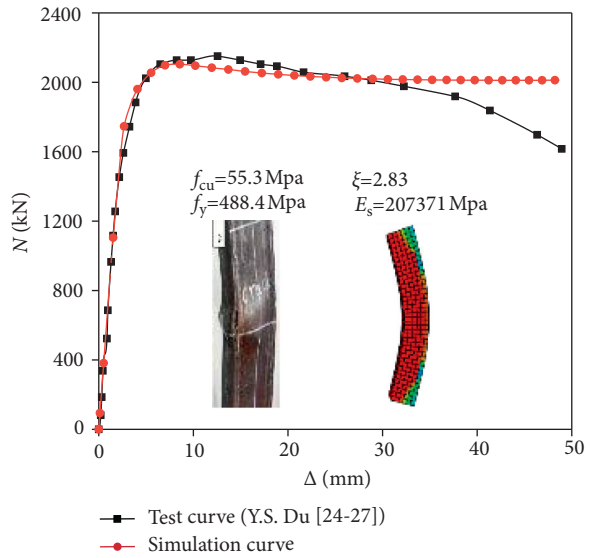
(k)



(l)



(m)



(n)

FIGURE 4: Continued.

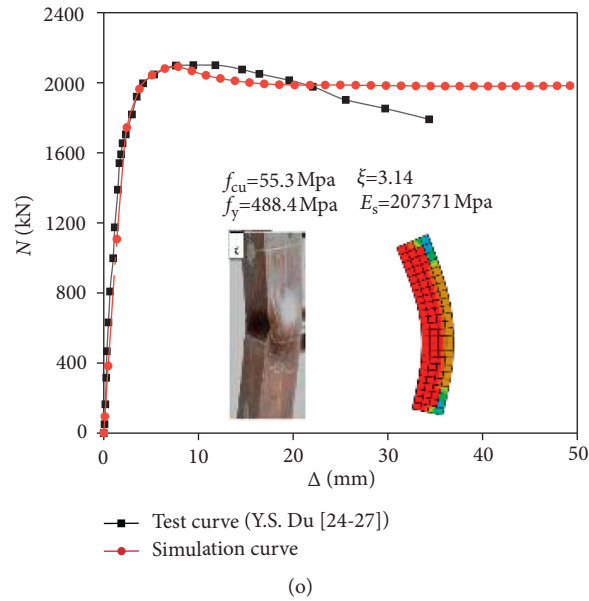


FIGURE 4: Comparisons for N - Δ curves between simulation and test results. (a) GZ-1. (b) GZ-2. (c) GZ-3. (d) GZ-4. (e) SC40-150-0.2. (f) SC40-180-0.2. (g) SC40-200-0.2. (h) SC50-150-0.2. (i) SC50-180-0.2. (j) SC50-200-0.2. (k) SC40-150-0.4. (l) SC40-180-0.4. (m) SC50-150-0.4. (n) SC50-180-0.4. (o) SC50-200-0.4.

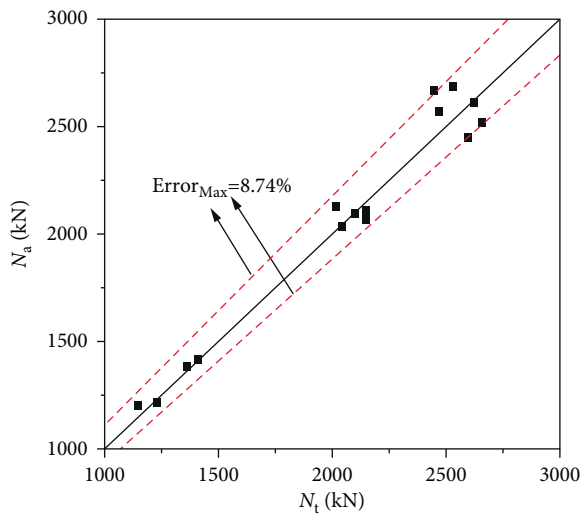


FIGURE 5: Comparison between N_a and N_t for 15 STHCCs under eccentric compression.

for full-scale STHCCs can be computed. Moreover, based on the proposed FE model, the effects of different parameters on the N - Δ curves were discussed. The main parameters can be summarized as eccentricity (e), the slenderness ratio (λ), the cubic compressive strength of concrete ($f_{cu,k}$), the thickness of the steel tube flange (t_1), the thickness of honeycombed steel web (t_2), diameter-depth ratio (d/h_w), space-depth (s/h_w), and the yield strength of the steel tube (f_y).

5.1. Load-Vertical Displacement Curves. The load (N)-vertical displacement (Δ) curves of the specimens with different eccentricity, slenderness ratio, and diameter-depth ratio are shown in Figure 6. It can be found that the load (N)-vertical displacement (Δ) curves can be classified into four

development stages: elastic stage, elastic-plastic ascending stage, descending stage, and gentle stage. With the increase in the eccentricity, the slenderness ratio, and diameter-depth ratio, the eccentric compression bearing capacity of the specimens gradually decreases. Figure 6(a) shows the load (N) versus the vertical displacement (Δ) relationships of the specimens with different eccentricity, and when the eccentricity of the specimens increases from 80 mm to 400 mm, the initial stiffness of the specimens decreases from 5.06×10^6 kN/m to 1.97×10^6 kN/m, which reduce by 61.1%. The eccentric compression capacity of the specimens decreases from 17.39×10^3 kN to 9.9×10^3 kN, which decreases by 42.6%. It indicates that with the increase in the eccentricity, the initial stiffness and eccentric compression capacity of the specimens decrease. Figure 6(b) shows the load (N) versus the vertical displacement (Δ) relationships of the specimens with different slenderness ratio, in which as the slenderness ratio of the specimens increases from 19.4 to 60.97, the initial stiffness of the specimens decreases from 3.62×10^6 kN/m to 1.17×10^6 kN/m, which reduces by 67.7%. The eccentric compression capacity of the specimens decreases from 12.86×10^3 kN to 10.88×10^3 kN, which decreases by 15.4%, while the decline section of the curves gradually slow down. It indicates that with the increase in the slenderness ratio, the initial stiffness and eccentric compression capacity of the specimens decrease, whereas the ductility increases. Figure 6(c) shows the load (N) versus the vertical displacement (Δ) relationships of the specimens with different diameter-depth ratio, and when the diameter-depth ratio of the specimens increases from 0.1 to 0.75, the eccentric compression capacity of the specimens decreases from 13.61×10^3 kN to 11.87×10^3 kN, which decreases by 12.8%, while the decline section of the curves gradually slow down. It can be seen that with the increase in the

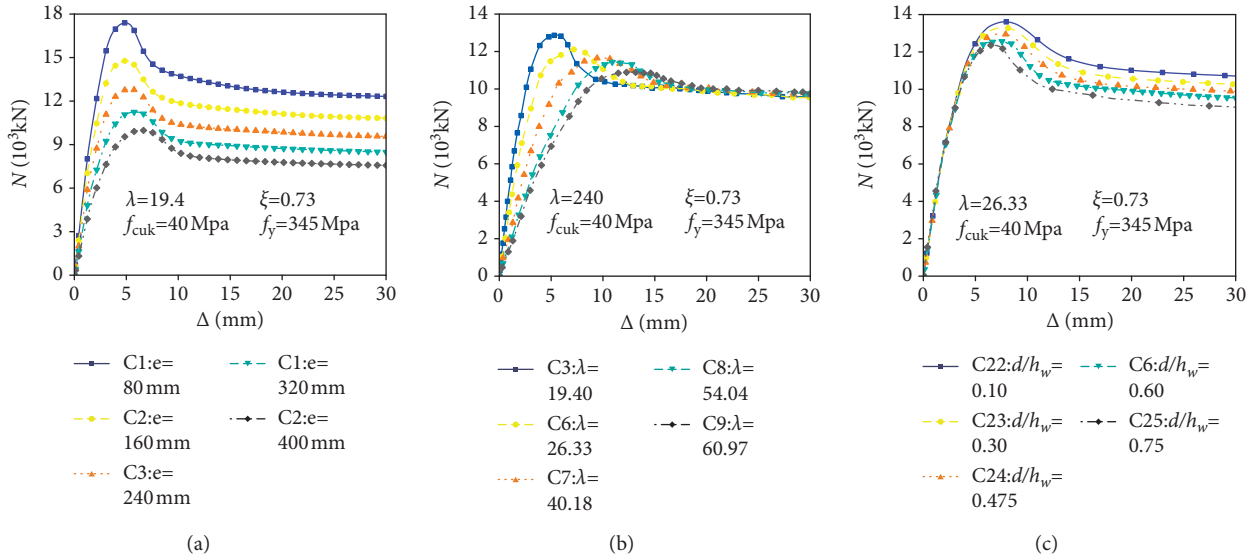


FIGURE 6: Comparisons of N - Δ curves of STHCCs with different parameters. (a) e . (b) λ . (c) d/h_w .

diameter-depth ratio, the eccentric compression bearing capacity of the specimens decreases gradually.

Figure 7 illustrates the load (N) versus the vertical displacement (Δ) relationships of the specimens with different parameters. Obviously, with the increase in the cubic compressive strength of concrete, the thickness of the steel tube flange, the thickness of honeycombed steel web, space-depth ratio, and the yield strength of the steel tube, the eccentric compression bearing capacity of the specimens increases gradually. Figure 7(a) shows the load (N) versus the vertical displacement (Δ) relationships of the specimens with different cubic compressive strength of concrete, and when the cubic compressive strength of concrete increases from 30 MPa to 70 MPa, the eccentric compression capacity of the specimens increases from 11.05×10^3 kN to 17.45×10^3 kN, which raises by 57.92%. It indicates that with the increase in the cubic compressive strength of concrete, the eccentric compression capacity of the specimens increases. Figure 7(b) shows the load (N) versus the vertical displacement (Δ) relationships of the specimens with different thickness of the steel tube flange, and when the thickness of the steel tube flange increases from 6 mm to 14 mm, the eccentric compression capacity of the specimens increases from 11.37×10^3 kN to 16.32×10^3 kN, which raises by 43.54%. It reflects that with the increase in the thickness of the steel tube flange, the eccentric compression capacity of the specimens increases. The load (N) versus the vertical displacement (Δ) relationships of the specimens with different thickness of honeycombed steel web are illustrated in Figure 7(c), and when the thickness of honeycombed steel web increases from 8 mm to 16 mm, the eccentric compression capacity of the specimens increases from 12.38×10^3 kN to 13.35×10^3 kN, which increases by 7.84%. It can be found that with the increase in the thickness of honeycombed steel web, the eccentric compression bearing capacity of the specimens increases gradually. Figure 7(d) shows the load (N) versus the vertical

displacement (Δ) relationships of the specimens with different space-depth ratio, and when the space-depth ratio increases from 0.15 to 1.4, the eccentric compression capacity of the specimens increases from 12.42×10^3 kN to 13.12×10^3 kN, which raises by 5.64%, which indicates that with the increase in the space-depth ratio, the eccentric compression capacity of specimens increases. The load (N) versus the vertical displacement (Δ) relationships of the specimens with different yield strength of the steel tube are illustrated in Figure 7(e), and when the yield strength of the steel tube increases from 235 MPa to 460 MPa, the eccentric compression capacity of the specimens increases from 10.86×10^3 kN to 14.51×10^3 kN, which increases by 33.61%. It can be found that with the increase in the yield strength of the steel tube, the eccentric compression bearing capacity of the specimens increases gradually.

5.2. Load-Lateral Deflection Curves of Mid-span Sections.

Figure 8 shows that with the increase in the eccentricity, the cubic compressive strength of concrete, the thickness of the steel tube flange, and diameter-depth ratio, the lateral deflection of mid-span sections of the specimens decreases gradually. The load-lateral deflection curves of the specimens with different parameters are illustrated in Figure 8. As the eccentricity of the specimens increases from 80 mm to 400 mm, the lateral deflection of mid-span sections decreases from 28.64 mm to 17.77 mm, which reduces by 37.94%, as shown in Figure 8(a). It can be found that the lateral deflection of mid-span sections of the specimens decreases gradually with the increase in eccentricity. Figure 8(b) illustrates the eccentric load (N) versus lateral deflection (Δ) relationships of specimens with different cubic compressive strength of concrete, and as the cubic compressive strength of concrete increases from 30 MPa to 70 MPa, the lateral deflection of mid-span sections decreases from 30.16 mm to 22.32 mm, which reduces by 25.92%. It

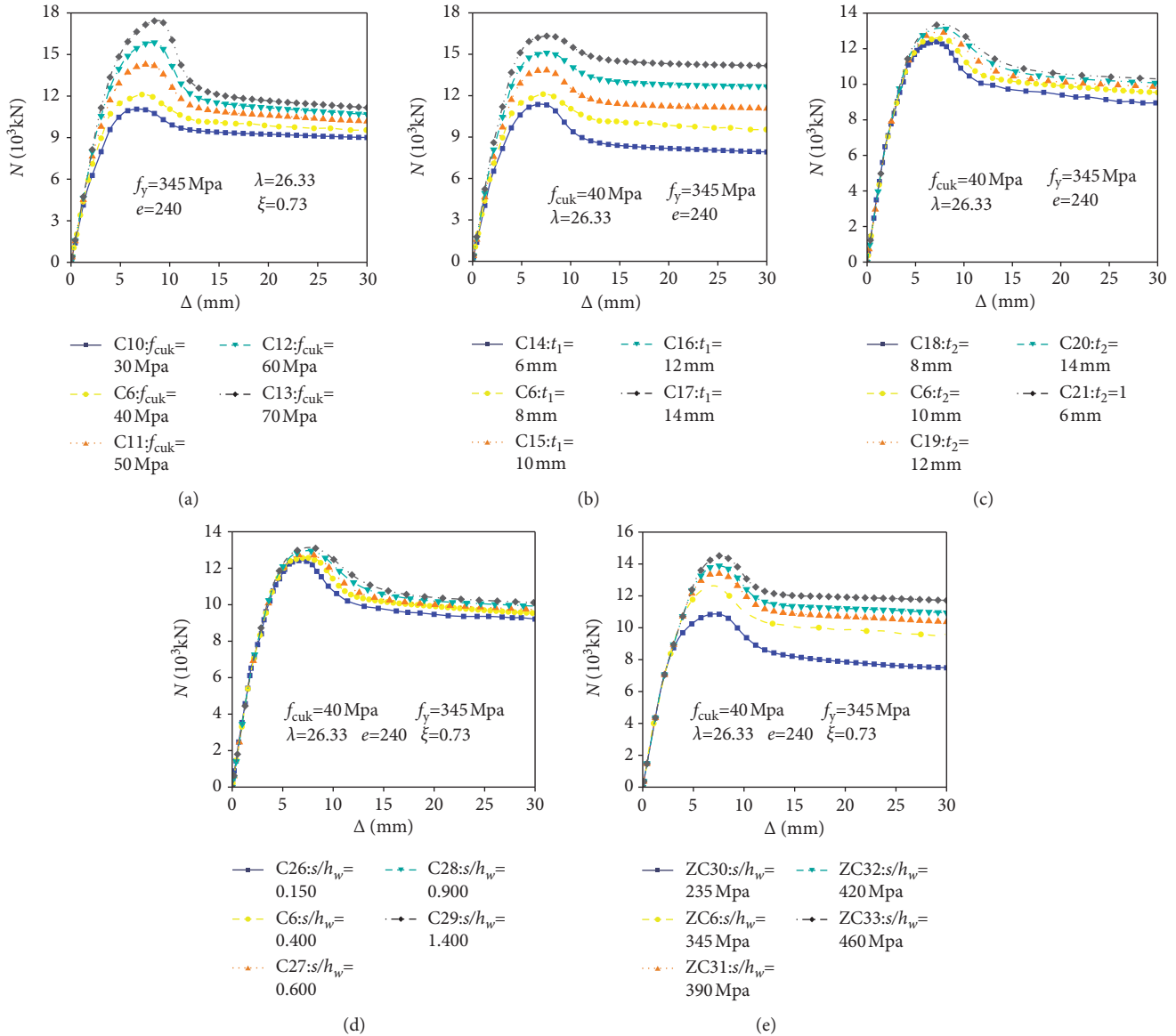


FIGURE 7: Comparisons of N - Δ curves of STHCCs with different parameters. (a) f_{cuk} . (b) t_1 . (c) t_2 . (d) s/h_w . (e) f_y .

can be found that with the increase in the cubic compressive strength of concrete, the lateral deflection of mid-span sections of the specimens decreases gradually.

Figure 8(c) shows that as the thickness of the steel tube flange increases from 6 mm to 14 mm, the lateral deflection of mid-span sections decreases from 29.56 mm to 23.00 mm, which reduces by 22.19%. This indicates that with the increase in the thickness of the steel tube flange, the lateral deflection of mid-span decreases. Figure 8(d) shows that as the diameter-depth ratio increases from 0.1 to 0.75, the lateral deflection of mid-span sections decreases from 31.21 mm to 23.83 mm, which reduces by 28.32%. This indicates that with the increase in the diameter-depth ratio, the lateral deflection of mid-span sections of the specimens decreases.

Figure 9 shows that with the increase in the slenderness ratio, the thickness of honeycombed steel web, space-depth

ratio, and the yield strength of the steel tube, the lateral deflection of mid-span sections of specimens gradually increases. As the slenderness ratio of the specimens increases from 19.4 to 60.97, the lateral deflection of mid-span section increases from 21.94 mm to 53.87 mm, which raises by 145.53%, as shown in Figure 9(a). It can be found that the lateral deflection of mid-span sections of the specimens increases gradually with the increase in the slenderness ratio. Figure 9(b) illustrates the eccentric load (N) versus lateral deflection (Δ) relationships of the specimens with different thickness of honeycombed steel web, in which as the thickness of honeycombed steel web increases from 8 mm to 16 mm, the lateral deflection of mid-span sections increases from 26.36 mm to 30.23 mm, which raises by 14.68%. It can be found that with the increase in the thickness of honeycombed steel web of the specimens, the lateral deflection of mid-span sections of the specimens decreases gradually.

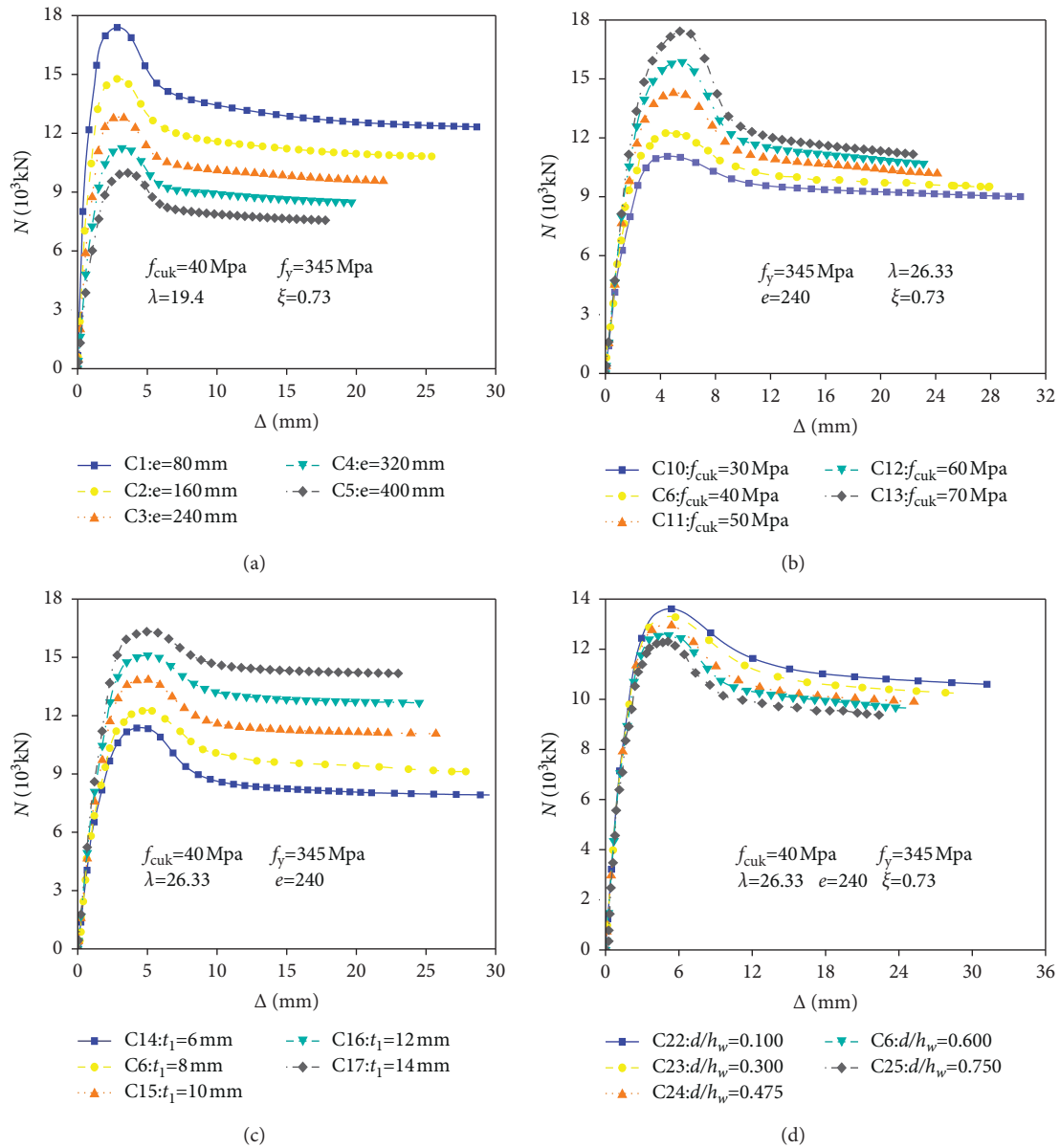


FIGURE 8: Comparisons of N - Δ curves of STHCCs with different parameters. (a) e . (b) f_{cuk} . (c) t_1 . (d) d/h_w .

Figure 9(c) shows that as the space-depth ratio of the specimens increases from 0.15 to 1.4, the lateral deflection of mid-span sections increases from 24.36 mm to 35.67 mm, which improves by 46.43%. It indicates that the lateral deflection of mid-span sections decreases with the increase in the space-depth ratio of the specimens. Figure 9(d) shows that as the yield strength of the steel tube increases from 235 MPa to 460 MPa, the lateral deflection of mid-span sections increases from 23.61 mm to 30.64 mm, which raises by 29.78%. This indicates that the lateral deflection of mid-span sections increases with the increase in the yield strength of the steel tube of the specimens.

5.3. N/N_u - M/M_u Curves. The numerical simulation results of the specimens reflect that with the increase in the slenderness ratio, the thickness of the steel tube flange, and diameter-depth ratio, the convexity of the N/N_u - M/M_u

curves of the specimens gradually decreases, as illustrated in Figure 10. With the increase in the cubic compressive strength of concrete, the thickness of honeycombed steel web, space-depth ratio, and the yield strength of the steel tube, the convexity of the N/N_u - M/M_u curves of the specimens gradually increases, as shown in Figure 11, and the load transfer capacity of honeycomb steel web increases.

Figure 10(a) illustrates that with the increase in the slenderness ratio of the specimens, the convexity of the N/N_u - M/M_u curves of the specimens gradually decreases, and the inflection points of the curves become inconspicuously. The curves basically show a trend to be straight lines, and with the increase in the slenderness ratio of the specimens, the intersection points of the curves and the longitudinal axis close to the origin gradually, which indicates that with the increase in the slenderness ratio of the specimens, the

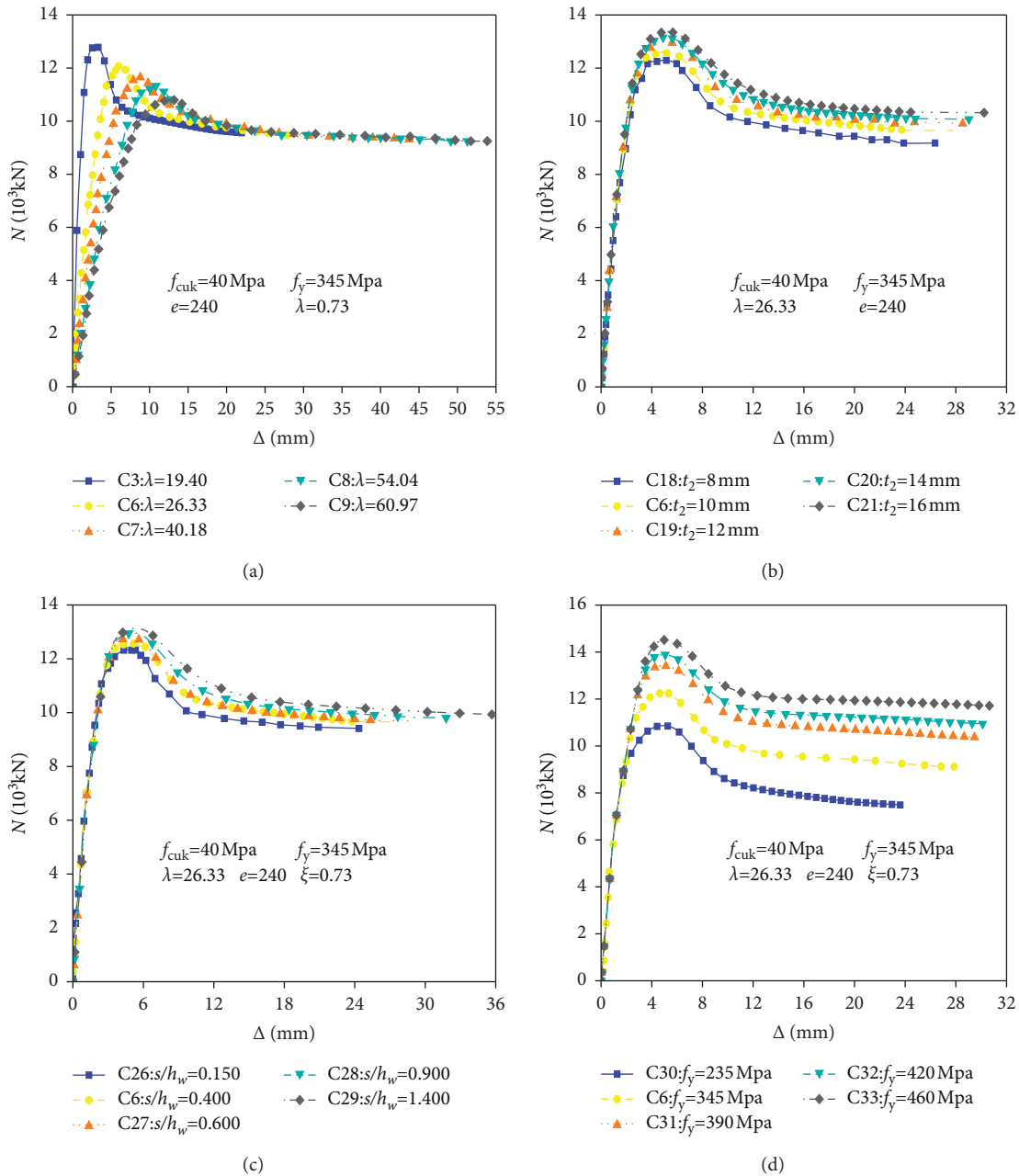


FIGURE 9: Comparisons of N - Δ curves of STHCCs with different parameters. (a) λ . (b) t_2 . (c) s/h_w . (d) f_y .

deformation of the specimens becomes larger, and the second-order bending moment caused by the geometric deformation of the specimens increases, and the eccentric compression bearing capacity of the specimens decreases. It can be found from Figure 10(b) that with the increase in the thickness of the flange steel tube, the convexity of the N/N_u - M/M_u curve of the specimens gradually decreases. It can also be found that with the increase in the thickness of the flange steel tube, the constraint effect of the steel tube on the core concrete increases. Figure 10(c) shows that with the increase in the diameter-depth ratio, the convex degree of the N/N_u - M/M_u curve of the specimens decreases gradually. It can be seen that with the increase in the diameter-depth ratio, the

inflection point of N/N_u - M/M_u curve moves left, which indicates that the load transfer capacity of honeycomb steel web decreases with the decrease in the diameter-depth ratio.

Figure 11(a) shows that with the increase in the cubic compressive strength of concrete, the convexity of the N/N_u - M/M_u curves of the specimens gradually increases. It can be seen that with the increase in the cubic compressive strength of concrete of the specimens, the constraint effect of the steel tube on the core concrete decreases. It can be found from Figure 11(b) that with the increase in the thickness of the honeycomb steel web of the specimens, the convexity of the N/N_u - M/M_u curves of the specimens gradually increases. It can also be found that with the increase in the thickness of

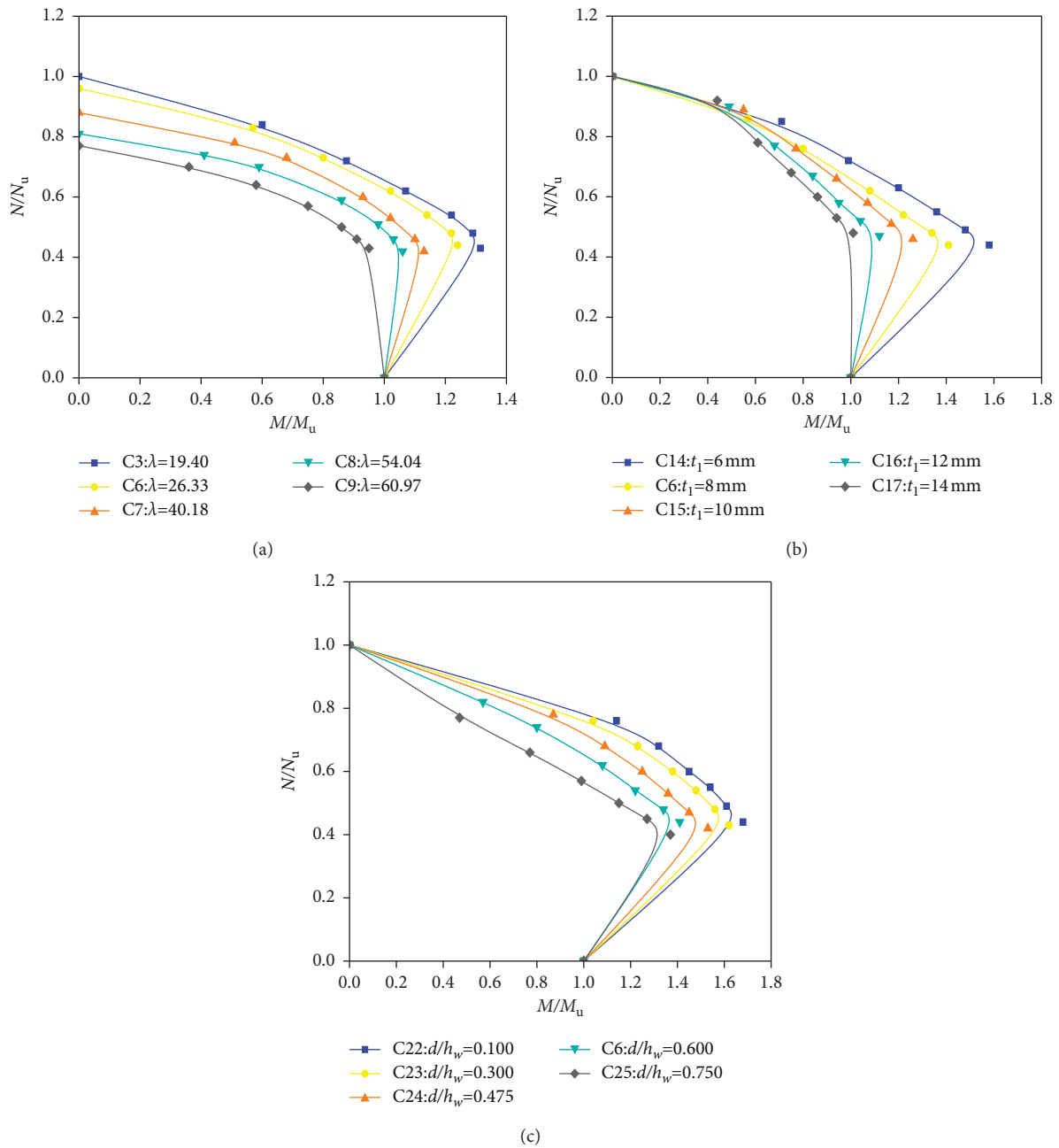


FIGURE 10: Comparisons of N/N_u - M/M_u curves of STHCCs with different parameters. (a) λ . (b) t_1 . (c) d/h_w .

the honeycomb steel web, the ability of load transfer of the honeycomb steel web increases, and the inflection points of the N/N_u - M/M_u curves move upward.

As can be seen from Figure 11(c), the convexity of the N/N_u - M/M_u curves of the specimens increases with the increase in the space-depth ratio, which shows that with the increase in the distance-to-height ratio, the capacity of load transfer of the honeycomb steel web increases. Figure 11(d) illustrates that with the increase in the yield strength of the steel tube, the convex degree of N/N_u - M/M_u curves of the specimens increases gradually, which indicates that with the increase in the yield strength of the steel tube, the constraint effect of the steel tube on concrete increases obviously.

6. Force Mechanism of Full-Scale STHCCs under Eccentric Compression

6.1. Lateral Deflection Curves. Five full-scale specimens are selected from 33 STHCCs as representative examples, and the representative specimens exhibit different eccentricity. The lateral (H)-deflection (Δ) curves of the five specimens subjected to eccentric compression are shown in Figure 12. It is noteworthy that the H - Δ curves of the specimens are basically symmetrical distribution. The maximum deflection appears at the mid-span sections of the specimens, and the increase in the deflection is proportional to the increase in the eccentricity.

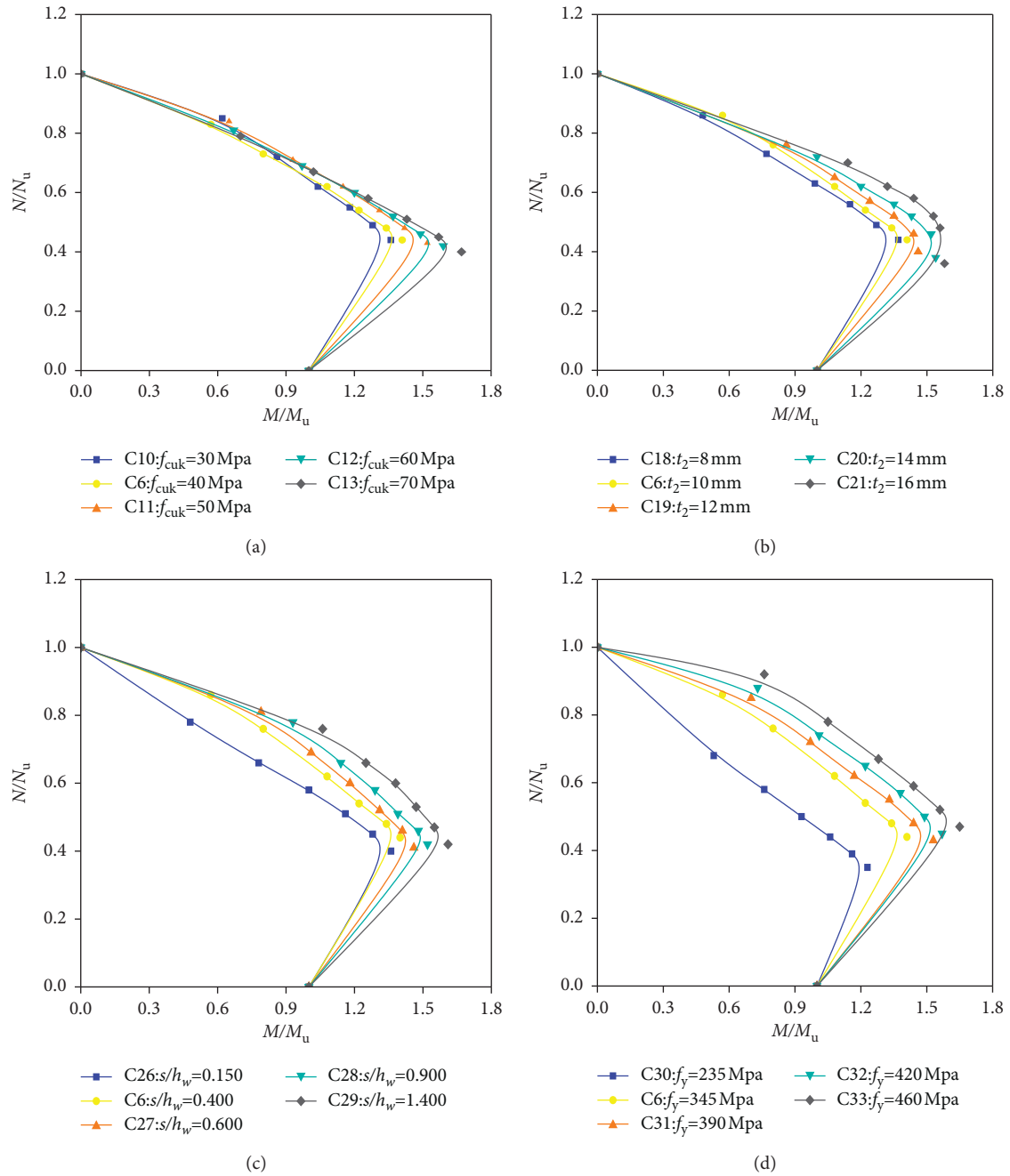


FIGURE 11: Comparisons of N/N_u - M/M_u curves of STHCCs with different parameters. (a) f_{cuk} . (b) t_2 . (c) s/h_w . (d) f_y .

When the load reaches $0.9N_u$, the deflection begins to rapidly increase, and eventually, the column destroys. The development regularity of the H - Δ curves of the STHCCs subjected to eccentric compression is obtained, which is consistent with the development regularity of the ordinary square CFST columns under eccentric compression [29].

6.2. *Strain Distribution on Sections.* Taking STHCC-1, STHCC-2, STHCC-3, STHCC-4, and STHCC-5 as representative examples, the longitudinal strain distribution of the mid-span section of the specimens under eccentric

compression is computed, as shown in Figure 13. During the loading process, the longitudinal strain of the mid-span section conforms to the plane-section assumption. At the early stage of the loading, namely, the elastic working stage, the longitudinal strain of the mid-span section is in good agreement with the plane-section assumption, which shows that the steel tube coordinated with the core concrete [30, 31].

When the load reaches $0.9 N_u$, the steel tube in the compression side yields firstly, and the obvious bulging appears on steel tube, simultaneously the concrete is crushed, which indicates that both cannot work in

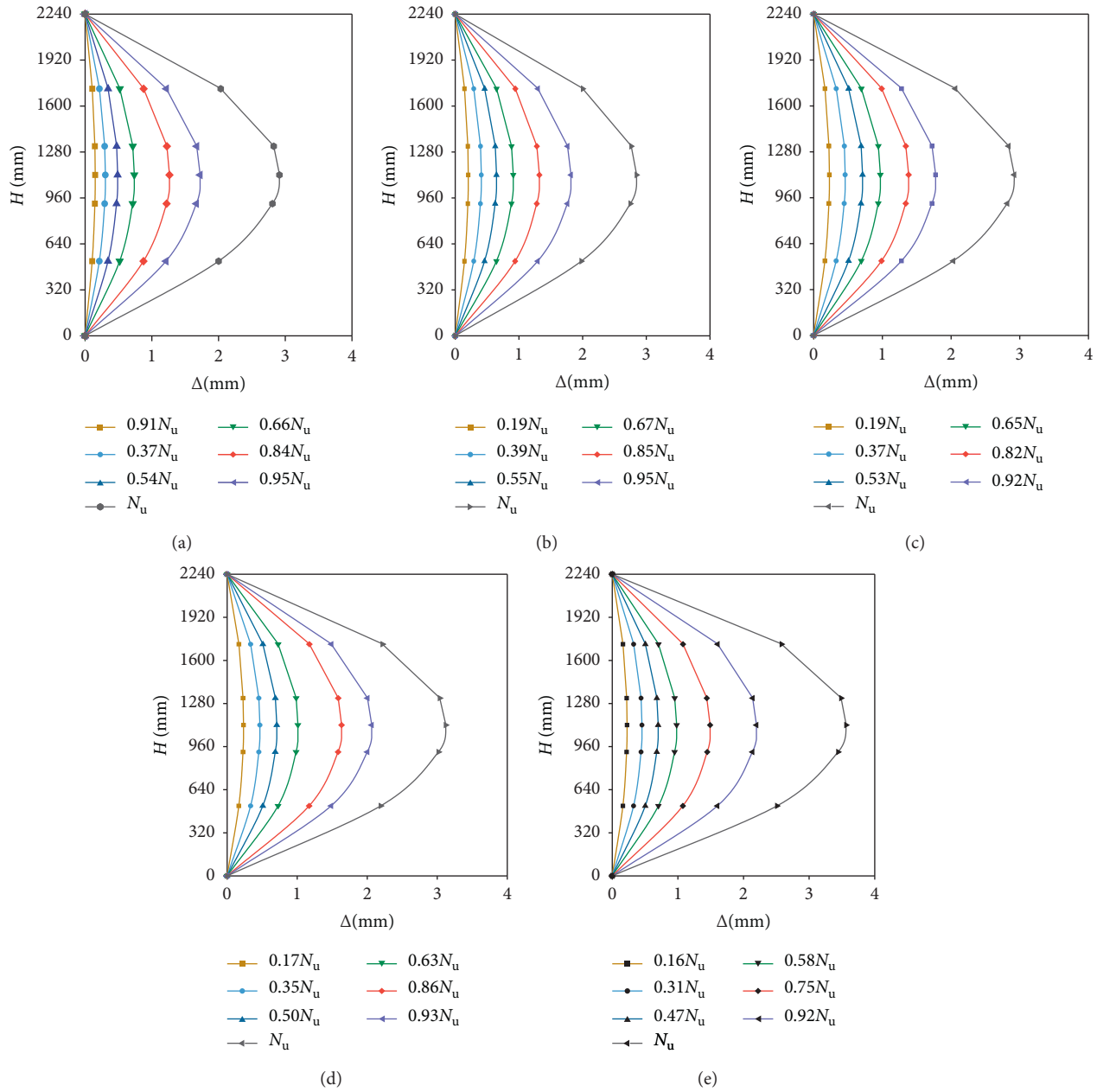


FIGURE 12: Comparisons of H - Δ curves of 5 specimens with different eccentricity. (a) STHCC-1. (b) STHCC-2. (c) STHCC-3. (d) STHCC-4. (e) STHCC-5.

coordination with each other. It is also found that with the increase in the eccentricity, the neutral axis of the mid-span section moves to the loading point gradually.

6.3. Load-Strain Curves. Figure 14 shows the load (N) versus strain (ϵ) relationships of point A and point E of specimen STHCC-1, and it can be seen from Figure 14 that at the initial stage of the loading, the strain and load of the tension and compression zone of STHCCs increase proportionally with the increase in the load. During the loading process, the longitudinal strain of the compression zone is greater than that of the tension side under the same load. When the load reaches about 95% of the ultimate load, the compression side

of the steel tube yields firstly, and the mutual coordination between the steel tube and the core concrete is destroyed, eventually the overall specimen is bent and unstable. The stress cloud diagram of each part of specimen STHCC-1 is illustrated in Figure 15.

7. Eccentric Compression Bearing Capacity of Full-Scale STHCCs

The simplified calculation method on eccentric compression bearing capacity for reduced-scale STHCCs has been proposed by Ji et al. [15], which can be expressed as (3). The specific meaning of variables is illustrated in reference [15].

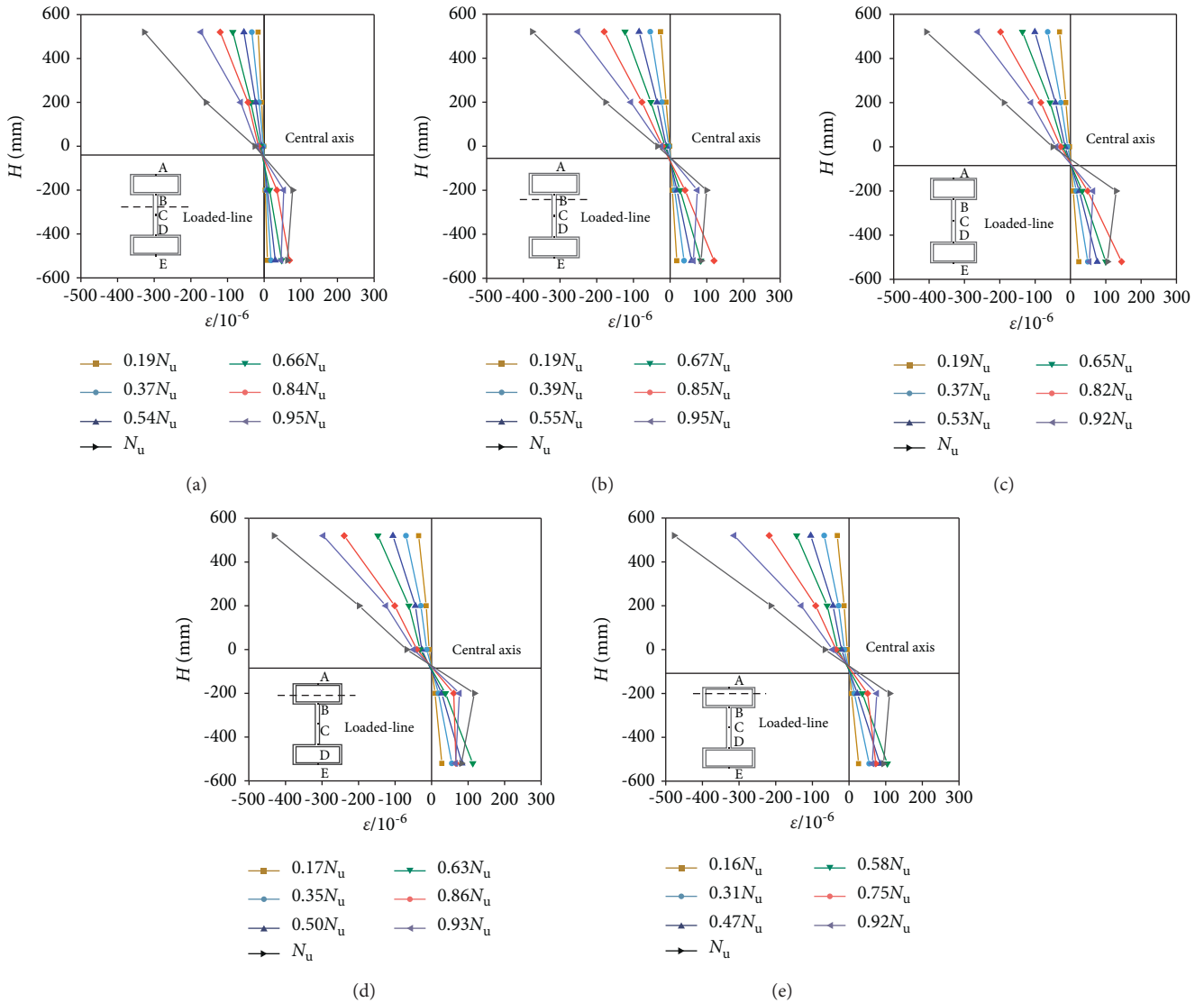


FIGURE 13: Longitudinal strain distribution of mid-span section of specimens with different eccentricity. (a) STHCC-1. (b) STHCC-2. (c) STHCC-3. (d) STHCC-4. (e) STHCC-5.

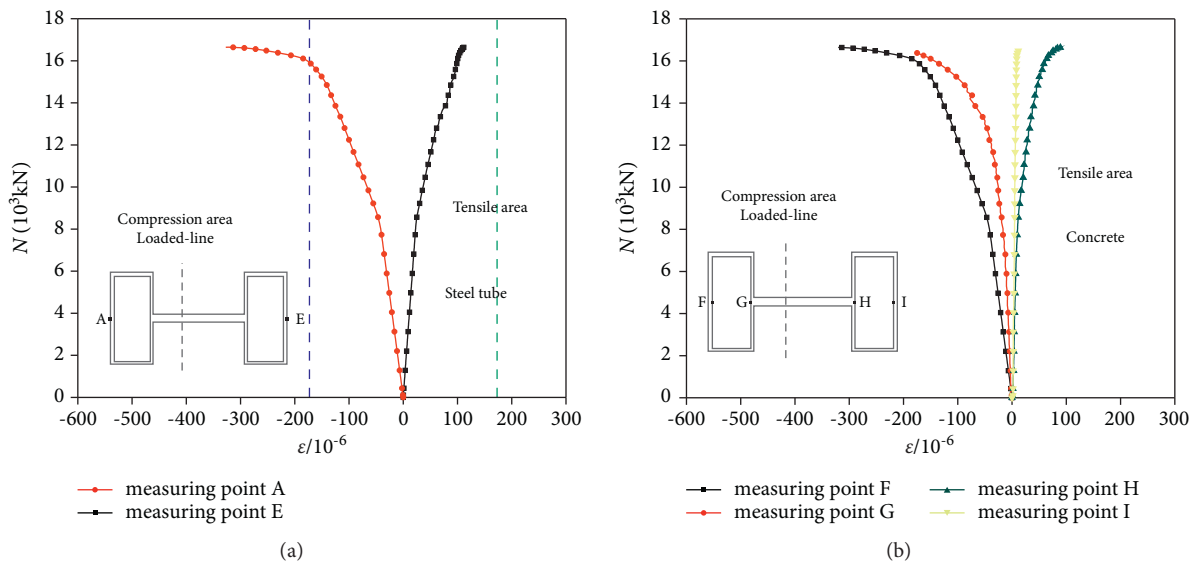


FIGURE 14: N - ϵ curves for STHCC-1. (a) N - ϵ curves for steel tube. (b) N - ϵ curves for concrete.

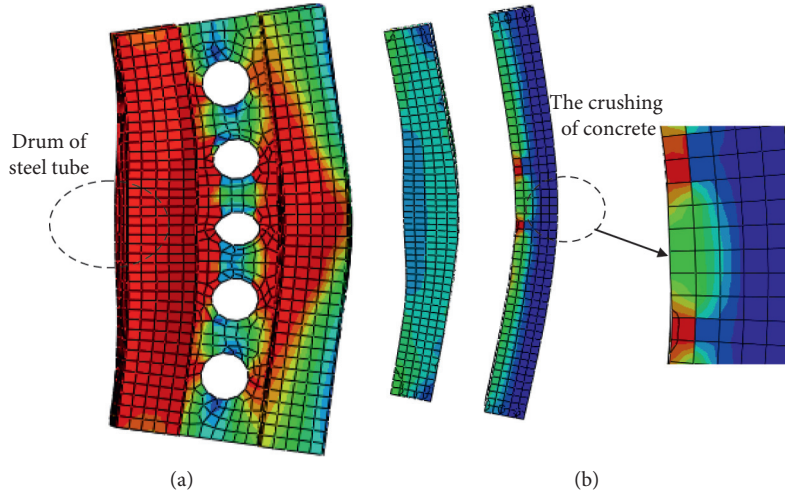


FIGURE 15: Stress cloud diagram of parts for specimen STHCC-1 in a state of failure. (a) The deformation of steel tube. (b) The deformation of concrete.

$$N_c^c = \varphi_e \varphi_1 \varphi_{f_{ck}} \varphi_{t_1} N_u \quad (3)$$

Equation (3) is adopted to calculate the eccentric compression bearing capacity (N_c^c) of 33 full-scale specimens, and the dispersion comparison between N_c^c and N_a for 33 specimens is shown in Figure 16. As can be seen in Figure 16, the maximum error is 43.24%. It is noteworthy that the calculation formula of eccentric compression bearing capacity obtained based on the reduced-scale model has certain limitations; thus, it is not suitable for calculating the eccentric compression bearing capacity of full-scale composite columns. So the calculation formula of eccentric compression bearing capacity of full-scale composite columns needs to be put forward.

The equation of the N/N_u - M/M_u curves for CFST composite columns proposed by Han [32, 33] can be expressed as follows:

$$\begin{cases} \frac{N}{N_u} + a \left(\frac{M}{M_u} \right) = 1, & \left(\frac{N}{N_u} \geq 2\eta_0 \right), \\ -b \left(\frac{N}{N_u} \right)^2 - c \left(\frac{N}{N_u} \right) + \left(\frac{M}{M_u} \right) = 1, & \left(\frac{N}{N_u} < 2\eta_0 \right), \end{cases} \quad (4)$$

where $a = 1 - 2\eta_0$, $b = (1 - \xi_0)/\eta_0^2$, $c = 2(\xi_0 - 1)/\eta_0$, and the significance of physical variables can be found in references [32, 33].

According to the unified theory deduced by Han [32], the axial compression capacity (N_u) on bearing and flexural bearing capacity (M_u) of CFST columns can be obtained, which are given by

$$\begin{aligned} N_u &= f_{scy} A_{sc}, \\ M_u &= \gamma_m W_{scm} f_{scy}, \end{aligned} \quad (5)$$

where $f_{scy} = (1.18 + 0.64\xi) \times f_{ck}$, $A_{sc} = A_s + A_c$, $\xi = A_s \times f_y / A_c \times f_{ck}$, $\gamma_m = 1.04 + 0.48 \ln(\xi + 0.1)$, and $W_{scm} = (2I/h)$. The significance of physical variables is shown in reference [32].

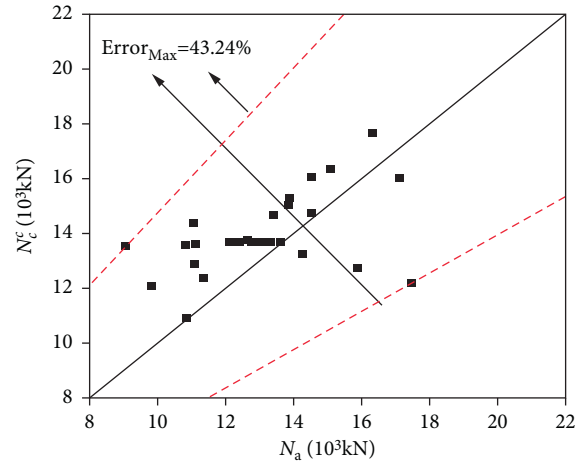


FIGURE 16: Comparison between N_c^c and N_a .

Considering the influence of the eccentricity, the slenderness ratio, the cubic compressive strength of concrete, the thickness of steel tube flange, the thickness of honeycombed steel web, diameter-depth ratio, space-depth, and the yield strength of the steel tube on the mechanical behavior of full-scale STHCCs, the bias stability coefficient (φ) [34] is subsequently introduced, and the influence of second-order bending moment [34] of the medium-long columns is considered. The related equation of N/N_u - M/M_u curves is summarized as follows:

$$\begin{cases} \frac{N}{\varphi N_u} + \frac{a}{d} \left(\frac{M}{M_u} \right) = 1, & \left(\frac{N}{N_u} \geq 2\eta_0 \right), \\ -b \left(\frac{N}{N_u} \right)^2 - c \left(\frac{N}{N_u} \right) + \frac{1}{d} \left(\frac{M}{M_u} \right) = 1, & \left(\frac{N}{N_u} < 2\eta_0 \right), \end{cases} \quad (6)$$

where $d = 1 - 0.25N/N_E$, $N_E = N_u \pi^2 E_{sc} / \lambda^2 f_y$, $E_{sc} = f_{scp} / \varepsilon_{scp}$, and $f_{scp} = [0.263 f_y / 235 + 0.365 \times$

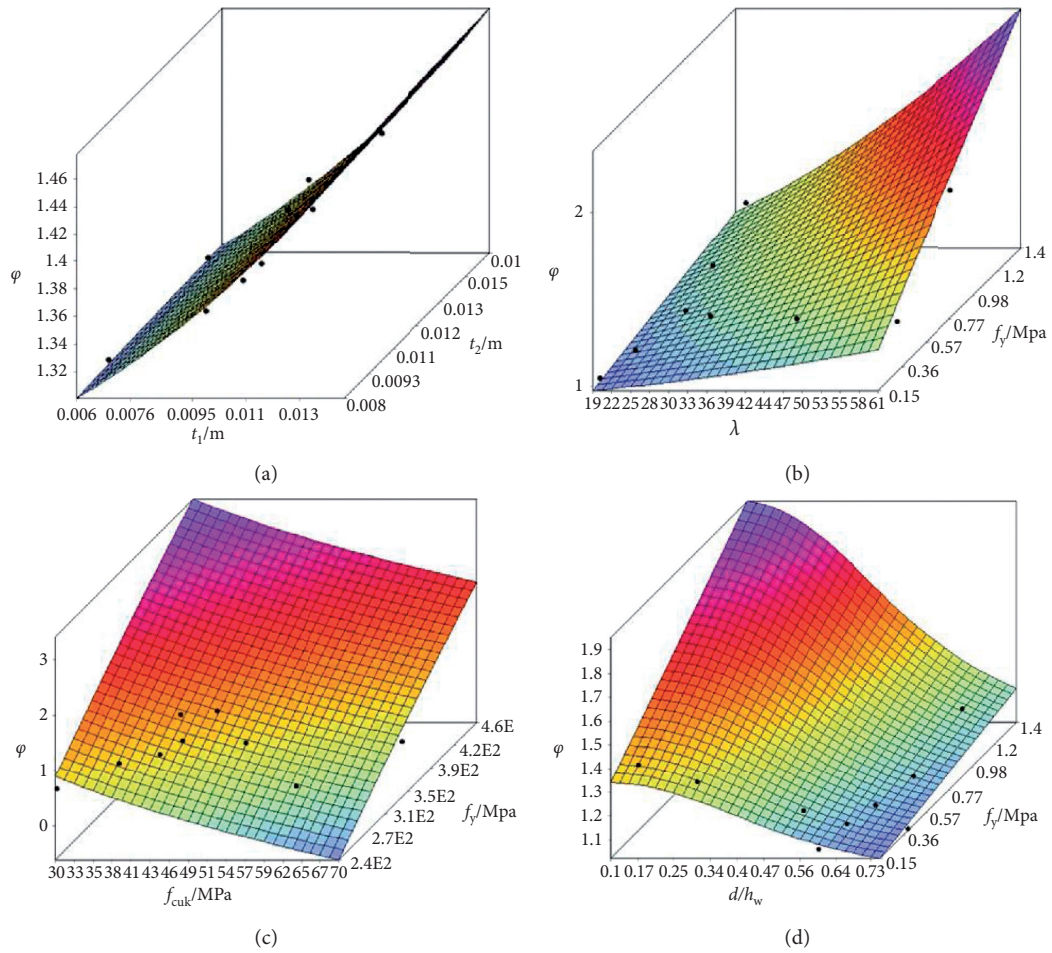


FIGURE 17: Effects of different parameters on ϕ . (a) t_1 and t_2 . (b) λ and e . (c) f_{cuk} and f_y . (d) d/h_w and s/h_w .

TABLE 3: The comparison between N_c and N_a .

Specimens	t_1 (mm)	t_2 (mm)	λ	E (mm)	d/h_w	s/h_w	N_c (10^3 kN)	N_a (10^3 kN)	N_c (10^3 kN)	$ N_a - N_c/N_c $ (%)	$ N_a - N_c/N_c $ (%)
STHCC-1	8	10	19.40	80	0.6	0.4	15.99	17.09	16.57	6.88	3.14
STHCC-2	8	10	19.40	160	0.6	0.4	14.74	14.53	14.25	1.42	1.96
STHCC-3	8	10	19.40	240	0.6	0.4	13.73	12.62	12.47	8.08	1.20
STHCC-4	8	10	19.40	320	0.6	0.4	12.85	11.07	11.06	13.85	0.09
STHCC-5	8	10	19.40	400	0.6	0.4	12.05	9.83	9.93	18.42	1.01
STHCC-6	8	10	26.33	240	0.6	0.4	13.69	12.11	12.24	11.54	1.06
STHCC-7	8	10	40.18	240	0.6	0.4	13.61	11.13	11.81	18.22	5.76
STHCC-8	8	10	54.04	240	0.6	0.4	13.54	10.84	10.16	19.94	6.69
STHCC-9	8	10	60.97	240	0.6	0.4	13.50	9.06	9.32	32.89	2.79
STHCC-10	8	10	26.33	240	0.6	0.4	14.38	11.06	11.01	23.09	0.45
STHCC-11	8	10	26.33	240	0.6	0.4	13.22	14.28	14.27	8.02	0.07
STHCC-12	8	10	26.33	240	0.6	0.4	12.72	15.87	15.91	24.76	0.25
STHCC-13	8	10	26.33	240	0.6	0.4	12.18	17.45	17.36	43.24	0.52
STHCC-14	6	10	26.33	240	0.6	0.4	12.32	11.37	12.11	7.71	6.11

TABLE 3: Continued.

Specimens	t_1 (mm)	t_2 (mm)	λ	E (mm)	d/h_w	s/h_w	N_c^c (10^3 kN)	N_a (10^3 kN)	N_c (10^3 kN)	$ N_a - N_c^c/N_c^c $ (%)	$ N_a - N_c/N_c $ (%)
STHCC-15	10	10	26.33	240	0.6	0.4	15.03	13.85	13.93	7.85	0.57
STHCC-16	12	10	26.33	240	0.6	0.4	16.34	15.10	15.49	7.59	2.52
STHCC-17	14	10	26.33	240	0.6	0.4	17.63	16.32	17.22	7.43	5.23
STHCC-18	8	8	26.33	240	0.6	0.4	13.69	12.29	12.61	10.23	2.54
STHCC-19	8	12	26.33	240	0.6	0.4	13.69	12.93	12.73	5.55	1.57
STHCC-20	8	14	26.33	240	0.6	0.4	13.69	13.14	12.63	4.02	4.04
STHCC-21	8	16	26.33	240	0.6	0.4	13.69	13.34	12.64	2.56	5.54
STHCC-22	8	10	26.33	240	0.10	0.4	13.69	13.60	13.41	0.66	1.42
STHCC-23	8	10	26.33	240	0.3	0.4	13.69	13.29	13.27	2.92	0.15
STHCC-24	8	10	26.33	240	0.475	0.4	13.69	12.96	12.93	5.33	0.23
STHCC-25	8	10	26.33	240	0.75	0.4	13.69	12.31	12.24	10.08	0.57
STHCC-26	8	10	26.33	240	0.6	0.15	13.69	12.41	12.47	9.35	0.48
STHCC-27	8	10	26.33	240	0.6	0.6	13.69	12.78	12.72	6.65	0.47
STHCC-28	8	10	26.33	240	0.6	0.9	13.69	12.94	12.89	5.48	0.39
STHCC-29	8	10	26.33	240	0.6	1.4	13.69	13.12	13.17	4.16	0.38
STHCC-30	8	10	26.33	240	0.6	0.4	10.86	10.86	11.79	0	7.89
STHCC-31	8	10	26.33	240	0.6	0.4	14.67	13.40	13.34	8.66	0.45
STHCC-32	8	10	26.33	240	0.6	0.4	15.27	13.88	13.71	9.10	1.24
STHCC-33	8	10	26.33	240	0.6	0.4	16.03	14.51	14.06	9.48	3.20

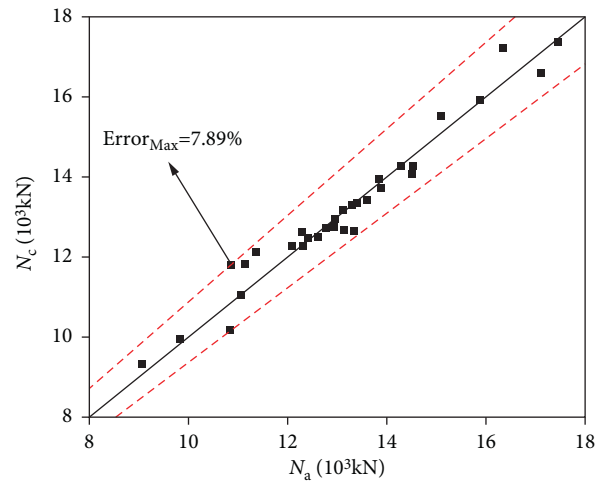
$30/f_{cu} + 0.104] \times f_{scy}$. The significance of physical variables is shown in reference [34].

The expression of φ is obtained by statistical regression as follows:

$$\varphi = 0.93 + \frac{-14f_{cuk}^{0.32} + t_2^{0.22} + 2.78s/h_w + f_y^{0.67}}{397\lambda^{1.38} - 106t_1 + 10(d/h_w)^3} \times e. \quad (7)$$

The effects of different parameters on φ are illustrated in Figure 17.

According to the (6), the eccentric compression bearing capacity (N_c) for 33 STHCCs can be calculated as shown in Table 3. By comparison, it can be seen from Figure 18 that the maximum error between N_c and N_a is 7.89%, which shows that both are in good agreement and can meet the requirements in actual engineering.

FIGURE 18: Comparison between N_c and N_a .

8. Conclusions

The eccentrical compression behavior analysis of 33 full-scale STHCCs was studied. The conclusions can be drawn as follows.

Based on the nonlinear constitutive model of concrete and simplified constitutive model of steel, the load-vertical displacement curves and load-lateral deflection curves of 15 square CFST columns were obtained by ABAQUS software. By comparison with the existing test data, both were in good agreement, which could verify the rationality of the material constitutive model and FE modeling method.

The development regularity of lateral deflection curves for full-scale STHCCs is consistent with that of lateral deflection curves for CFST columns, and the maximum deflection appears at the mid-span sections of the specimens. The stress distribution along the cross-sectional height of the mid-span sections for full-scale STHCCs subjected to eccentrical compression basically conforms to the plane-section assumption.

The influence of parameters on eccentrical compression bearing capacity and lateral deflection is systematically investigated. It can be concluded that with the increase in e , λ , and d/h_w , the eccentrical compression bearing capacity of specimens decreases gradually, whereas the eccentrical compression bearing capacity of specimens increases significantly with the increase in f_{cuk} , t_1 , t_2 , s/h_w , and f_y . It can be found that the lateral deflection of the mid-span section decreases gradually with the increase in e , f_{cuk} , t_1 , and d/h_w , whereas the lateral deflection of the mid-span section gradually increases as λ , t_2 , s/h_w , and f_y increase.

The calculation formula on eccentrical compression bearing capacity for STHCCs is proposed by statistical regression.

Data Availability

The data used to support the findings of this study are included within the article.

Conflicts of Interest

The authors declare that they have no conflicts of interest.

Acknowledgments

The authors are grateful for the financial support received from the Social Science Foundation of Hebei Province (Grant no. HB20GL055).

References

- [1] J. Ji, Z. C. Xu, L. Q. Jiang et al., "Nonlinear buckling analysis of H-type honeycombed composite column with rectangular concrete-filled steel tube flanges," *International Journal of Steel Structures*, vol. 18, no. 4, pp. 1153–1166, 2018.
- [2] S. Jayaganesh, J. R. Murugadoss, G. G. Prabhu, and J. Jegan, "Effects of concentric partial (local) compression on the structural behavior of concrete filled steel tubular column," *Advances in Materials Science and Engineering*, vol. 2015, Article ID 491038, 9 pages, 2015.
- [3] M. Ahmed, Q. Q. Liang, V. I. Patel, and M. N. S. Hadi, "Local-global interaction buckling of square high strength concrete-filled double steel tubular slender beam-columns," *Thin-Walled Structures*, vol. 143, Article ID 106244, 2019.
- [4] G. Vatulia, M. Rezunencko, D. Petrenko, Y. Balaka, and Y. Orel, "A statistical method for predicting the eccentric load capacity of rectangular concrete filled steel tubular columns," *MATEC Web of Conferences*, vol. 313, Article ID 00031, 2020.
- [5] Y. Feng, L. L. Yin, Y. Fang, and J. J. Jiang, "Mechanical behavior of recycled coarse aggregates self-compacting concrete-filled steel tubular columns under eccentric compression," *Structural Concrete*, vol. 20, no. 6, pp. 2000–2014, 2019.
- [6] Y. J. Li, W. H. Liu, and H. Han, "Analytical behaviour of rectangular concrete filled stainless steel tubular columns under Bi-axial eccentric compression," *Materials Science and Engineering*, vol. 490, no. 3, Article ID 032004, 2019.
- [7] B. Rong, C. X. Feng, R. Y. Zhang, G. C. You, and R. Liu, "Compression-bending behavior of L-shaped column composed of concrete filled square steel tubes under eccentric compression," *International Journal of Steel Structures*, vol. 17, no. 1, pp. 325–337, 2017.
- [8] Y. Sui, Y. Q. Tu, Q. Q. Guo, J. F. Zhang, and F. Ke, "Study on the behavior of multi-cell composite T-shaped concrete-filled steel tubular columns subjected to compression under biaxial eccentricity," *Journal of Constructional Steel Research*, vol. 159, pp. 215–230, 2019.
- [9] Z. P. Chen, J. Zhou, C. G. Jing, and Q. H. Tan, "Mechanical behavior of spiral stirrup reinforced concrete filled square steel tubular columns under compression," *Engineering Structures*, vol. 226, pp. 215–230, 2020.
- [10] F. Yu, P. C. Xu, Y. Fang, Y. Zhang, and J. J. Jiang, "Stiffness analysis of recycled self-compacting concrete-filled circular steel tubular columns under eccentric compression," *Advances In Civil Engineering*, vol. 2019, Article ID 2749587, 15 pages, 2019.
- [11] J. Ji, Z. C. Xu, W. F. Zhang et al., "Eigenvalue buckling analysis of H type honeycombed composite column with rectangular concrete-filled steel tube flanges," *Journal of Northeast Petroleum University*, vol. 41, no. 1, pp. 106–142, 2017.
- [12] J. Ji, Z. C. Xu, L. Q. Jiang et al., "Nonlinear buckling analysis of H-type honeycombed composite column with rectangular concrete-filled steel tube flanges," *Building Structure*, vol. 48, no. 15, pp. 50–55+70, 2018.
- [13] Z. C. Xu, "Axial compression and stability behavior of H-type honeycombed column with concrete-filled steel tube flanges(STHCC)," Master Dissertation, Northeast Petroleum University, Daqing, China, 2018.
- [14] J. Ji, Z. C. Xu, L. Q. Jiang, Y. C. Liu, D. Y. Yu, and M. M. Yang, "Experimental study on compression behavior of H-shaped composite short column with rectangular CFST flanges and honeycombed steel web subjected to axial load," *Journal of Building Structures*, vol. 40, no. 9, pp. 63–73, 2019.
- [15] J. Ji, L. Jiang, L. Q. Jiang, Y. F. Zhang, Z. C. Teng, and Y. C. Liu, "Mechanic behavior of H-type honeycomb composite columns with rectangular concrete-filled steel tubes subjected to eccentric load," *Journal of Northeast Petroleum University*, vol. 44, no. 4, pp. 121–132, 2020.
- [16] L. H. Han, *Concrete Filled Steel Tube Structure-Theory and Practice*, Science Press, Beijing, China, 2007.

- [17] M. Pagoulatou, T. Sheehan, X. H. Dai, and D. Lam, "Finite element analysis on the capacity of circular concrete-filled double-skin steel tubular (CFDST) stub columns," *Engineering Structures*, vol. 72, pp. 102–112, 2014.
- [18] L. Lam and J. G. Teng, "Design-oriented stress-strain model for FRP-confined concrete," *Construction and Building Materials*, vol. 17, no. 9, pp. 471–489, 2003.
- [19] J. B. Mander, M. J. N. Priestley, and R. Park, "Theoretical stress-strain model for confined concrete," *Journal of Structural Engineering*, vol. 114, no. 8, pp. 1804–1826, 1988.
- [20] J. R. Qian, L. R. Cheng, and D. L. Zhou, "Behavior of axially loaded concrete columns confined with ordinary hoops," *Journal of Tsinghua University Science and Technology*, vol. 10, pp. 1369–1373, 2002.
- [21] GB 50010-2010, *National Standard of the People's Republic of China Code for Design of Concrete Structures GB50010-2010*, China Architecture & Building Press, Beijing, China, 2010.
- [22] X. L. Cao, L. M. Wu, and Z. M. Li, "Behaviour of steel-reinforced concrete columns under combined torsion based on ABAQUS FEA," *Engineering Structures*, vol. 209, Article ID 109980, 2020.
- [23] L. Wang, "Numerical analysis of the bonding behavior of steel fiber-concrete interface," *Journal of water resources and architectural engineering*, vol. 17, no. 2, pp. 56–60, 2019.
- [24] B. Li, Y. C. Gao, B. Wang, and F. Zhang, "Research on the mechanics behavior of concrete-filled square steel tubular columns subjected to eccentric compression," *Building Structure*, vol. 40, no. S2, pp. 398–400, 2010.
- [25] Y. S. Du, Z. H. Chen, Y. B. Wang, and J. Y. Richard Liew, "Ultimate resistance behavior of rectangular concrete-filled tubular beam-columns made of high-strength steel," *Journal of Constructional Steel Research*, vol. 133, pp. 418–433, 2017.
- [26] Y. S. Du, Z. H. Chen, and M. X. Xiong, "Experimental behavior and design method of rectangular concrete-filled tubular columns using Q460 high-strength steel," *Construction and Building Materials*, vol. 125, pp. 856–872, 2016.
- [27] Y. S. Du, Z. H. Chen, J. Y. Richard Liew, and M. X. Xiong, "Rectangular concrete-filled steel tubular beam-columns using high-strength steel: experiments and design," *Journal of Constructional Steel Research*, vol. 131, pp. 1–18, 2017.
- [28] Y. S. Du, "Theoretical Analysis and Experimental Study on Rectangular Concrete-Filled Steel Tube Columns Using High-Strength Steel," Doctoral Dissertation, Tianjin University, Tianjin, China, 2017.
- [29] T. Zhao and L. B. Yan, "Bearing capacity studies on square steel tube confined steel reinforced concrete column under eccentric load," *Advances in Civil Engineering*, vol. 2020, Article ID 4212049, 11 pages, 2020.
- [30] K. Q. Yu, W. Mcgee, T. Y. Ng, H. Zhu, and V. C. Li, "3D-printable engineered cementitious composites (3DP-ECC): fresh and hardened properties," *Cement and Concrete Research*, vol. 143, Article ID 106388, 2021.
- [31] Z. W. Cai, F. C. Liu, J. T. Yu, K. Q. Yu, and L. K. Tian, "Development of ultra-high ductility engineered cementitious composites as a novel and resilient fireproof coating," *Construction and Building Materials*, vol. 288, Article ID 123090, 2021.
- [32] L. H. Han and Y. F. Yang, *Modern Concrete Filled Steel Tube Structure Technology*, Architecture & Building Press, Beijing, China, 2007.
- [33] L. H. Han, C. Hou, and Y. X. Hua, "Concrete-filled steel tubes subjected to axial compression: life-cycle based behavior," *Journal of Constructional Steel Research*, vol. 170, Article ID 106063, 2020.
- [34] Z.-B. Wang, Z. Tao, and Q. Yu, "Axial compressive behaviour of concrete-filled double-tube stub columns with stiffeners," *Thin-Walled Structures*, vol. 120, pp. 91–104, 2017.

Research Article

Experimental and Numerical Investigation on Dynamic Properties and Human-Induced Vibrations of an Asymmetric Steel-Plated Stress-Ribbon Footbridge

Yi Zhang ¹, Wei He ², Jiewen Zhang ² and Hua Dong ¹

¹China Construction Third Bureau First Engineering Co., LTD., Wuhan 430080, Hubei, China

²Faculty of Engineering, China University of Geosciences, Wuhan 430074, Hubei, China

Correspondence should be addressed to Hua Dong; donghua606@163.com

Received 3 October 2021; Accepted 13 November 2021; Published 22 December 2021

Academic Editor: Lingkun Chen

Copyright © 2021 Yi Zhang et al. This is an open access article distributed under the Creative Commons Attribution License, which permits unrestricted use, distribution, and reproduction in any medium, provided the original work is properly cited.

This paper presents a comprehensive study on dynamic properties and human-induced vibrations of a slender asymmetric steel-plated stress-ribbon footbridge via both experimental and analytical methods. Bridge modal test was conducted using both ambient vibration testing and impact methods. Modal properties of the bridge were identified based on stochastic subspace identification and peak-pick techniques. Results show that the bridge is characterized by closely spaced modes with low natural frequencies and small damping ratios (<0.002). A sophisticated finite element model that incorporates pretension of the stress ribbon and contribution of deck panels is developed and proven to be capable of reflecting the main dynamic characteristics of the bridge. Human-induced vibrations were measured considering synchronization cases, including single-person and small group walking as well as random walking cases. A theoretical model that takes into account human-structure interaction was developed, treating the single walking person as an SDOF system with biomechanical excited force. The validity of the model was further verified by measurement results.

1. Introduction

Structures are prone to have longer spans and become much flexible owing to the development of high strength and lightweight materials and innovation in construction methods [1]. This poses new challenges to structural design since slender structures are more susceptible to dynamic loadings such as human excitation or wind turbulence.

Many efforts have been made on human-induced vibrations of footbridges [1–12], long-span floors [13–16], and stadiums [17, 18]. These researches cover the aspect of human-induced load models (either deterministic [1] or stochastic [2–6]), human-structure interaction [7–9], vibration serviceability evaluation method [12–18], and vibration control countermeasures [10–12].

In recent years, the stress-ribbon footbridge has been increasingly preferred due to its elegant and simple shape, fewer components compared with traditional footbridges,

and low impact on surroundings [19–24]. Stress-ribbon footbridge, always formed by pretension catenary-shaped cables or steel plates with both ends anchored on the abutments, are characterized by closely spaced modes with low natural frequencies [19, 23, 24]. Hence, their dynamic performance under human excitation is often of great concern. A modal test is the most accurate and effective way to obtain the actual dynamic properties of the structure. In this regard, Hu et al. [23] tested a stress-ribbon footbridge in a campus in Portugal, which has two close spans of 30 m and 28 m. The bridge is formed by four pretensioned catenary-shaped cables embedded by a continuous concrete cast-in-situ slab. A modal test showed that the footbridge has low natural frequencies and closely spaced modes. The first eight natural frequencies are all below 6 Hz. Specifically, the first three natural frequencies are 0.951 Hz, 1.989 Hz, and 2.034 Hz, respectively. Soria et al. [24] reported a steel-plated stress-ribbon footbridge constructed in 2009 in Spain. The

bridge employs a singular catenary-shaped steel band with a single span of 85 m. A modal test reveals that the footbridge is so flexible and lightly damped. The modes are closely spaced with the first eight natural frequencies that are all less than 4 Hz. Specifically, the first three natural frequencies are 0.867 Hz, 1.408 Hz, and 1.541 Hz. The identified first eight damping ratios range from 0.3% to 0.6%. All these researches demonstrated that the stress-ribbon bridges are susceptible to dynamic excitation, and their dynamic performance needs careful evaluation. Arndt et al. [22] pointed out that stress-ribbon footbridges are the most slender and flexible structures. To date, application cases of stress-ribbon bridges or footbridges are still limited. The relevant experimental work, especially the dynamic performance under walking people, is rarely reported.

This paper reports a newly built slender asymmetric steel-plated stress-ribbon footbridge in China, where the stress ribbon is fabricated using the Chinese Q690D steel plate. This is the first time that the Q690D steel plate has been used in a real footbridge in China. The contribution of this study is twofold. On the one hand, this paper presents a comprehensive study of the footbridge's modal properties and dynamic performance under human excitation through combined experimental and analytical methods, which has rarely been reported before. On the other hand, it is beneficial to enrich the current experimental database of stress-ribbon footbridges. It would also be helpful for the future mechanical analysis and design of similar structures.

The paper is structured as follows: The concerned footbridge was briefly introduced in Section 2, followed by a modal test program in Section 3. Section 4 develops a detailed finite element model to capture the main dynamic characteristics of the footbridge. Section 5 gives the experimental results of human-induced vibrations, including synchronized walking and random walking cases. A theoretical model that takes into account moving human-structure interaction is developed in Section 6. Some conclusions are given in the closing Section 7.

2. Outline of the Test Footbridge

The stress-ribbon footbridge (see Figure 1(a)), constructed in 2020 and located in a park in Shenzhen, China, is a slender footbridge that links two mountains as part of a greenway. The bridge is an asymmetric stress-ribbon footbridge formed by a pretensioned catenary-shaped steel band with a main span of 63.8 m and a side span of 24.2 m. The net width of the bridge deck is 2.3 m, allowing for two-way pedestrian traffic. The top deck is 30 m above the bottom of the valley. The cross section of the bridge consists of two main stress-ribbon plates made of Chinese Q690D steel with a thickness of 40 mm and width of 750 mm at a spacing of 0.4 m, as shown in Figures 1(b) and 1(c). Both ends of the stress ribbons are anchored on the abutments. Precast concrete panels with dimensions of 2.7 m in length, 0.855 m in width, and 0.12 m in thickness were evenly paved on the stress ribbons along the longitudinal direction of the bridge (see Figures 1(c) and 1(d)). The space between two incident concrete panels is 0.02 m. Shear keys are evenly placed on top of the stress

ribbon to keep a reliable connection between the precast concrete panels and the main structure. The stress ribbon and deck panels are supported by a bracket comprising two inclined steel tube columns with variable cross-sections, as shown in Figure 1(e). The two columns are transversally braced by three horizontal steel pipes and three pairs of diagonal cables (see Figure 1(e)). Handrails made of stainless steel net with a height of 1.15 m are erected on both sides of the bridge deck (see Figure 1(d)). The abutments were cast in artificial digging piles using concrete and prestressed anchor cables.

3. Modal Test of the Stress-Ribbon Footbridge

3.1. Test Setup. A modal test was conducted to obtain the dynamic properties of the footbridge based on the ambient vibration testing (AVT) method [25, 26]. The bridge deck was divided into 30 grids along the longitudinal direction. 58 test points (TPs) were evenly spaced at an interval of 3 m on both sides of the bridge to obtain the spatial mode shapes, i.e., 29 at each side, as shown in Figure 2. The test program was divided into ten groups due to the limited number of accelerometers and cable length. TP 21, located near the east side of the main span, was chosen as the fixed reference point, while the other TPs were movable points. The classification of the setup of TPs is listed in Table 1. All accelerometers are in the vertical direction, and the bridge lateral modes were not considered due to the availability of test time. During the test, the bridge was temporarily closed to avoid the effect of pedestrians.

Accelerometers with the nominate frequency range from 0.25 Hz to 100 Hz and a measurement capacity of $2g$ (g is gravitational acceleration) were adopted. The DH9581 vibration data acquisition system, produced by Donghua company, China, was used for data recording. The sampling frequency was 200 Hz, which can cover the most concerned frequencies of the bridge. Figure 3 gives the photographs of the modal test.

For each setup, accelerometers were well fixed on the bridge deck according to the test protocol. A duration of 10 min was recorded for each setup. The test procedure is shown in Figure 4.

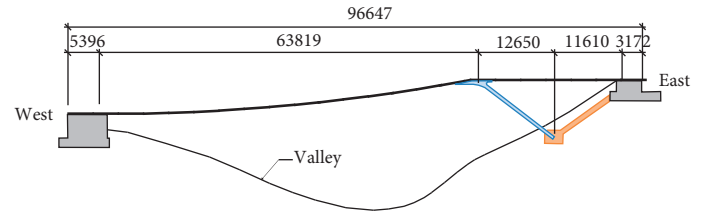
3.2. Test Results. Figure 5 illustrates part of the deck acceleration at the reference point (TP 21) under AVT. It is evident that the bridge deck was in small amplitude, and the vibration generally kept steady in the ambient vibration environment.

Figure 6 further gives the frequency spectrum below 6 Hz. Specifically, as shown in Figure 6(a), the test bridge has closely spaced modes with most natural frequencies below 4 Hz. Figures 6(b)~6(d) show the zoom-in view for the first three dominant frequencies at all test points. The measured first three natural frequencies are 0.95 Hz, 1.45 Hz, and 1.68 Hz, respectively.

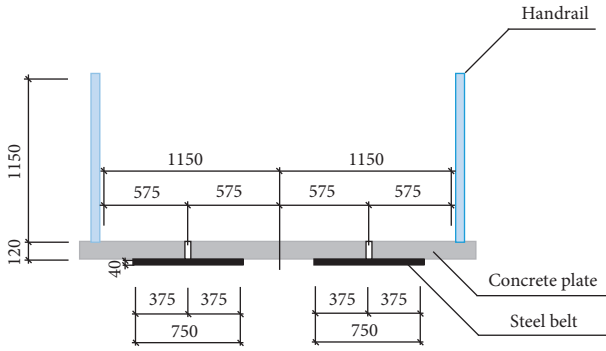
Meanwhile, the first three natural frequencies and corresponding mode shapes and damping ratios were identified



(a)



(b)



(c)



(d)



(e)

FIGURE 1: Schematic view and real pictures of the test bridge. (a) Real photograph, (b) elevation, (c) cross section, (d) bridge deck, and (e) columns. All dimensions are in mm.

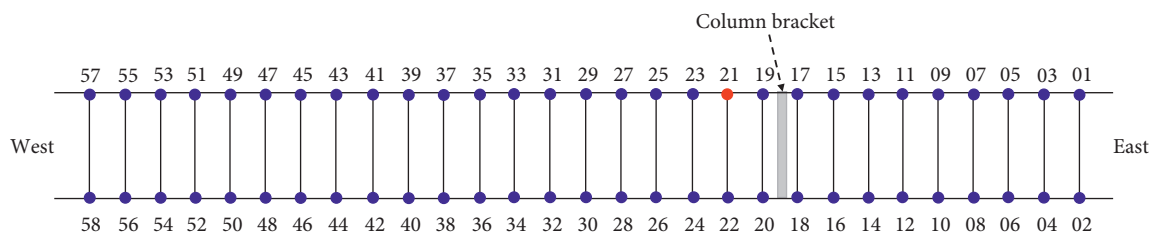


FIGURE 2: Schematic diagram of measurement grid. TP 21 in red is the reference point.

based on the stochastic subspace identification (SSI) method [27–30], given in Table 2. Figure 7 shows the first three mode shapes. Specifically, the first mode is a typical vertical

bending mode of the main span, the second mode is also a vertical bending mode, and the third mode corresponds to the first bending mode of the side span.

TABLE 1: Setup of measurement points.

Set number	Test point number	Reference point
1	07, 08, 09, 10, 11, 12, 13, 57, 58	21
2	14, 15, 16, 17, 18, 19, 20, 55, 56	21
3	01, 02, 03, 04, 05, 06, 53, 54	21
4	22, 23, 24, 25, 26, 27, 28, 51, 52	21
5	29, 30, 31, 32, 33, 34, 35, 49, 50	21
6	36, 37, 38	21
7	39, 43, 44	21
8	40, 41, 42	21
9	45, 46, 47	21
10	48	21

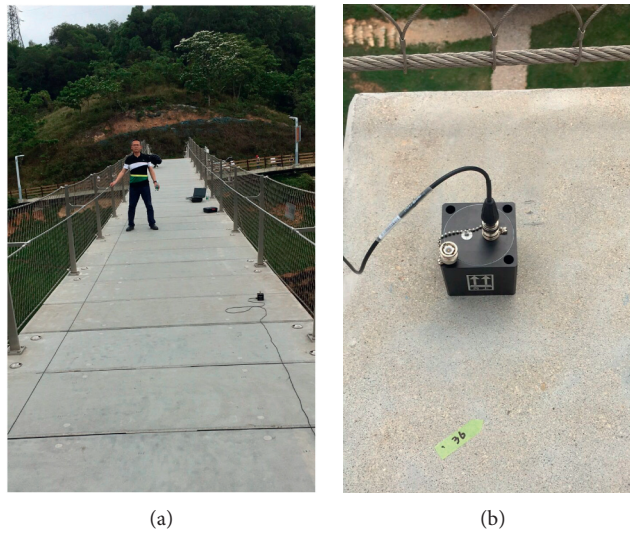


FIGURE 3: Photographs of the modal test. (a) Test scenario and (b) accelerometer.

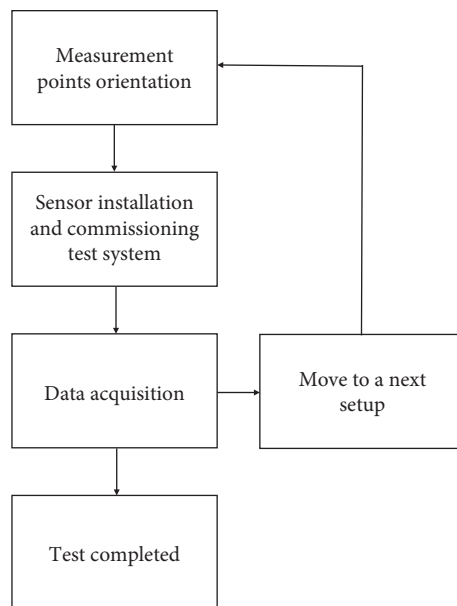


FIGURE 4: Flow chart of the test protocol.

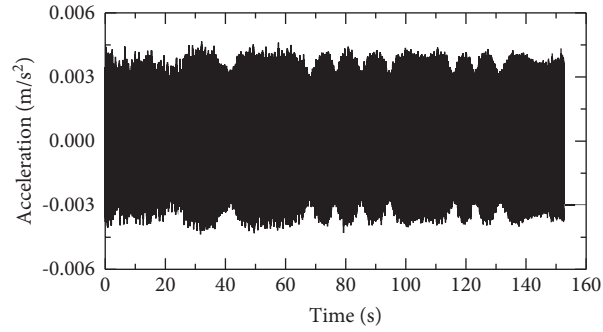


FIGURE 5: Bridge acceleration at reference point 23 under ambient vibration.

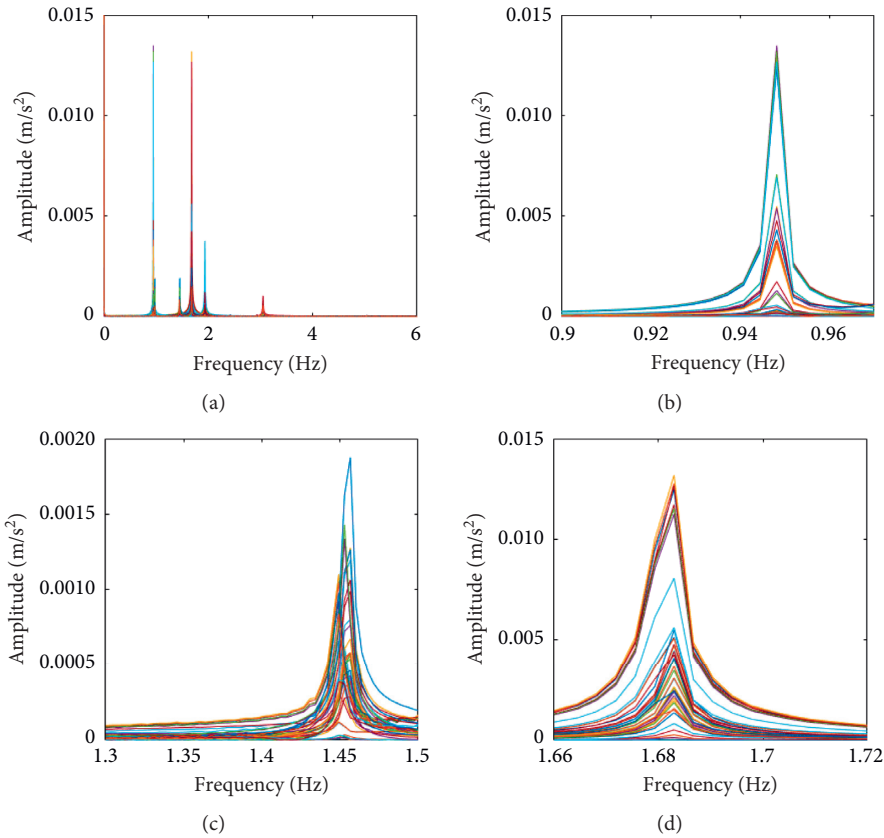


FIGURE 6: Frequency spectrum of the bridge: (a) overall view and (b-d) enlarged view.

TABLE 2: First three identified dynamic characteristics of the bridge.

Mode no.	Frequency (Hz)		Damping ratio		Modal description
	SSI	PP	SSI	PP	
1	0.95	0.95	0.0014	0.0018	1 st vertical bending
2	1.45	1.45	0.0020	0.0017	2 nd vertical bending
3	1.68	1.68	0.0006	0.0009	3 rd vertical bending

Note. SSI: stochastic subspace identification; PP: peak-picking.

A heel impact test was also conducted to check the accuracy of the identified results by the SSI method. The details of the heel-drop impact method can be found in

[8, 25]. The free decay time history of the bridge deck was truncated from the entire vibration record. Figure 8(a) shows the free decay response of the bridge deck, and

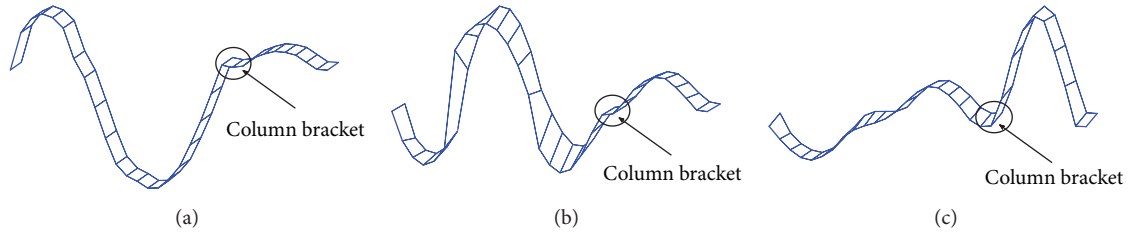


FIGURE 7: First three modes of the bridge. (a) 1st vertical bending, $f_{v,1} = 0.95$ Hz. (b) 2nd vertical bending, $f_{v,2} = 1.45$ Hz. (c) 3rd bending, $f_{v,3} = 1.68$ Hz.

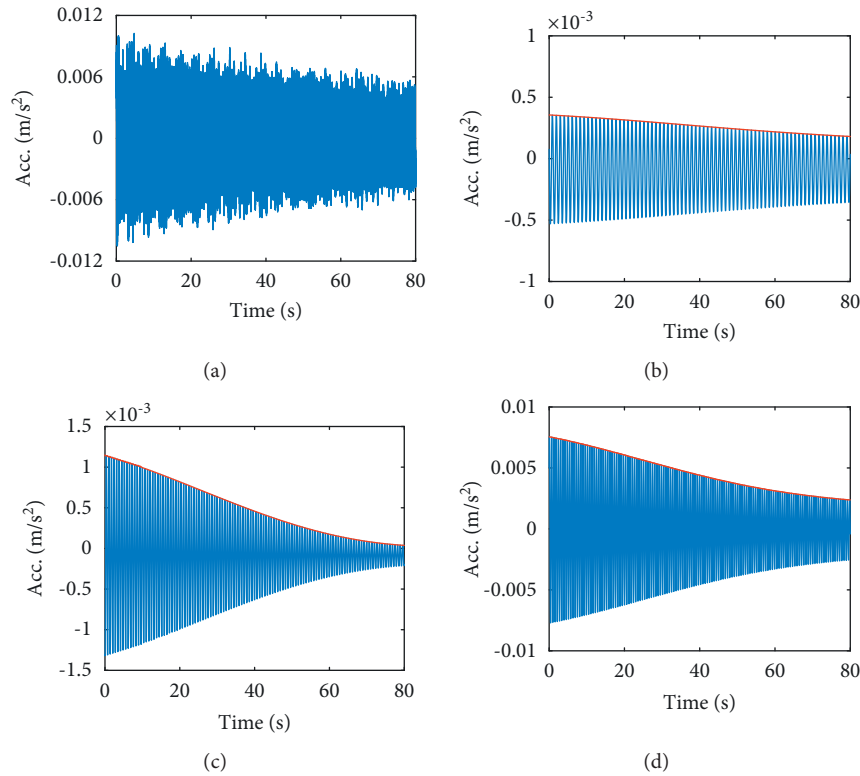


FIGURE 8: Free decay response of the bridge. (a) Overall response, (b) 0.8~0.96 Hz, (c) 1.4~1.5 Hz, and (d) 1.58~1.78 Hz.

Figures 8(b)–8(d) further give the filtering result using the fifth Butterworth filter with cut-off frequencies at 0.8~0.96 Hz, 1.4~1.5 Hz, and 1.58~1.78 Hz. Each individual component generally decreases in a free decay manner with a single vibration frequency. The corresponding spectrum of each individual is not presented here to keep the paper concise. As shown in Figures 8(b) to 8(d), each component can be regarded as a damped single-degree-of-freedom (SDOF) system.

For a damped SDOF, various damping estimation methods, such as the logarithmic decrement method and half-power spectrum methods [25, 30], could be employed to estimate the modal damping ratio. In this paper, the damping ratio was estimated using the ratio of the adjacent area formed by the free decay time series and the time axis, expressed as [31]

$$\xi = \frac{1}{2\pi} \ln \frac{S_i}{S_{i+1}}, \quad (1)$$

where ξ is the damping ratio; S_i and S_{i+1} are the i th and $(i+1)$ th area formed by acceleration time history and the time axis.

As shown in Figure 8, the damping of the ribbon bridge is so small that the bridge remains in remarkable motion even after 80 seconds. The identified natural frequencies and damping ratios are very close to those estimated from the SSI method (see Table 2), indicating that both methods are feasible and the identified results are reliable.

4. Finite Element Modeling

4.1. Overview of the Finite Element Model. In this section, a sophisticated finite element (FE) model of the stress-ribbon footbridge is established based on the ANSYS platform. The model considers the pretension of the stress ribbon and main nonstructural elements such as deck panels.

The stress-ribbon footbridge consists of three main components, including the precast concrete panels, stress ribbon, and support columns top down. The deck panels

are modeled as the Shell181 element with uniform thickness and evenly placed on the stress ribbon at a spacing of 0.02 m. The stress ribbon is also considered as the Shell 181 element according to the construction configuration in which the whole curved stress ribbon is divided into several straight plates. The column bracket, consisting of the top plate, bottom plate, and transverse stiffeners, is also modeled by the Shell181 element, as shown in Figure 9(b). The columns are modeled as the Beam188 element with variable cross sections. The three horizontal steel pipes are also modeled as beam elements with uniform cross sections, as shown in Figure 9(c). The three pairs of diagonal cables are modeled by link elements. Only the mass effect of handrails was included in the model since their constraint to the main structure is weak (see Figure 1(d)).

4.2. Material Parameters. The whole bridge mainly consists of two types of steel plates and concrete deck panels. The material parameters of each component were determined through a mechanical test of specimens in the laboratory and are summarized in Table 3.

4.3. Boundary Conditions. The relative linear displacements and rotations between the stress ribbons and the abutments at the contacting area are restrained to zero. The bottom of the columns is treated as fixed boundary conditions (BCs).

According to the construction method, the bridge deck and stress ribbons are well bonded via shear keys, as shown in Figure 1(b). Hence, coupling pairs are set for these points to ensure no relative displacements among them. Similarly, the coupling pairs are set between stress ribbons and the column bracket at the contacting area to ensure they are well coupled.

The boundary conditions (BCs) in the finite element model were firstly determined according to the construction drawings. Then, a trial-and-error method was employed to update the mode based on the principle that the first three natural frequencies as well as mode shapes approach the measured ones. A refined modal test incorporating more vertical modes and lateral modes will be conducted later, and then, a detailed model updating would be implemented to obtain more reasonable BCs.

4.4. Application of Pretension to the Footbridge. The static analysis of the footbridge was firstly conducted only considering its gravity. The stress obtained from the static analysis was further used as the initial pretension forces applied to the stress ribbons before modal analysis. The whole structure has 1291 elements in total. Figures 9(a)–9(c) show the overview and details of the FE model developed here.

4.5. Simulated Modal Properties. Modal analysis was conducted for the pretensioned structure using the block Lanczos method. The first ten modes and natural frequencies were obtained, as shown in Table 4. For comparison, the

measured results are also listed in the table. Note that the natural frequencies are presented according to similar mode shapes since some modes are unidentified from the field measurement.

For clarity, Figure 10 further depicts the first ten-mode shapes. Clearly, the stress-ribbon footbridge is characterized by closely spaced modes with the first ten simulated natural frequencies well below 4 Hz. The first ten modes are dominated by vertical bending modes and bending and torsion coupled modes. Since the stress ribbons are asymmetric supported, the main span is more prone to vibrate owing to the larger span length.

The simulated mode shapes showed satisfactory agreement with the measured ones with modal assurance criterion (MAC) value greater than 0.9. The simulated natural frequencies for the first (corresponding to the first measurement, see Table 4) and fifth modes (corresponding to the 3rd measurement) are very close to the measured ones except for the fourth mode (corresponding to the second measurement). This may be attributed to the complex BCs between the stress ribbons and the abutments as well as the contact relationship between the stress ribbons and the column bracket. In fact, the proper modeling of these contacts is challenging since it is hard to quantify the stiffness (rigid or semirigid) and the effective anchorage length in such cases. In general, the FE model developed here can reflect the actual dynamic properties of the test footbridge and thus can be applied in subsequent analysis.

5. Human-Induced Vibration Test

5.1. Experimental Setup. This section reports a human-induced vibration test of the stress-ribbon footbridge to further evaluate the dynamic performance under normal operating conditions. Test cases consisted of a controlled synchronized walking test of both single-person and multiple-person cases as well as random walking. Besides, an unexpected case such as group running was also considered. A total of seven participants was recruited for the test. The basic information, including gender, age, height, and body mass, is given in Table 5. Table 6 summarizes the detailed test cases. In the single-person walking test, four individuals were considered in the test to account for the intersubject variability [8]. For the multiple-person case, seven TSs formed in a line (7×1) as a small group were considered. Walking frequencies at 1.44 Hz and 1.67 Hz were selected to excite the structural resonant response. During the controlled test, test subjects (TSs) were instructed by a metronome to realize the target frequency.

5.2. Results. All measured data were firstly filtered using a Butterworth band-pass filter. The cut-off frequency is 0.1 to 10 Hz. Components below 0.1 Hz are mainly trend items and components above 10 Hz are not pronounced since the main structural frequencies and excitation frequencies all fall within 10 Hz. The measured data were analyzed in both time and frequency domains.

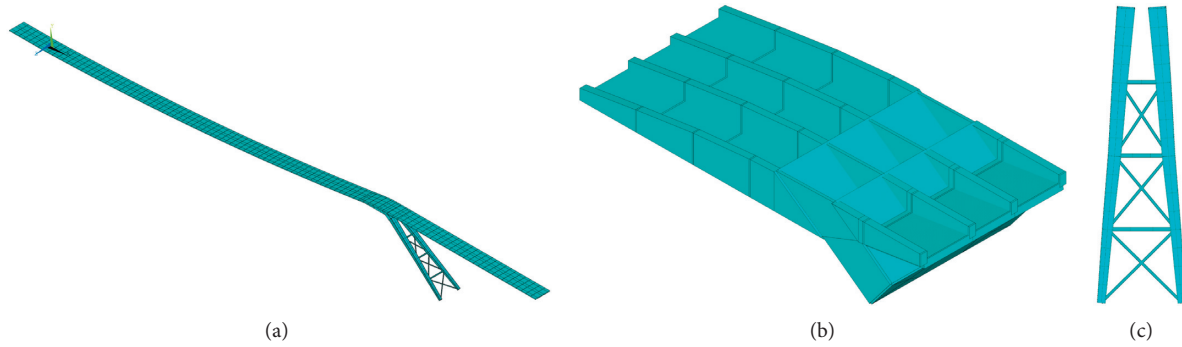


FIGURE 9: FE model of the bridge. (a) Overall FE model; (b) configuration of column bracket (without a top plate for clarity); (c) configuration of columns.

TABLE 3: Material parameters.

Component type	Material	Density (kg/m ³)	Elastic modulus (MPa)	Poisson's ratio
Stress ribbon	Q690 steel	7698	2.06×10^5	0.3
Column	Q420 steel	7850	2.06×10^5	0.3
Bridge deck	C30 concrete	2500	3.00×10^4	0.2

TABLE 4: Dynamic characteristics of the bridge.

Modal no.	Frequency (Hz)		Modal description
	Simulated	Measured	
1	0.95	0.95	1 st vertical bending (main span)
2	0.97	—	1 st lateral bending + torsion (main span)
3	1.09	—	2 nd vertical bending (main span)
4	1.65	1.45	3 rd vertical bending (main span) + 1 st vertical bending (side span) + lateral (column)
5	1.71	1.68	3 rd vertical bending (main span) + 1 st vertical bending (side span)
6	2.20	—	1 st torsion (main span)
7	2.27	—	4 th vertical bending (main span)
8	2.89	—	5 th vertical bending (main span)
9	3.15	—	2 nd lateral bending + torsion (main span)
10	3.47	—	6 th vertical bending (main span)

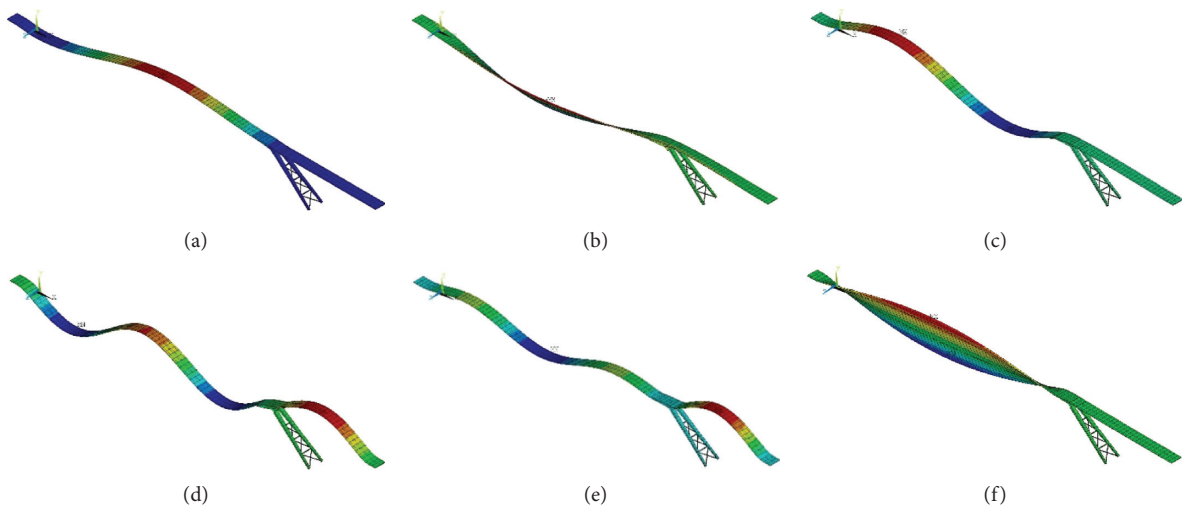


FIGURE 10: Continued.

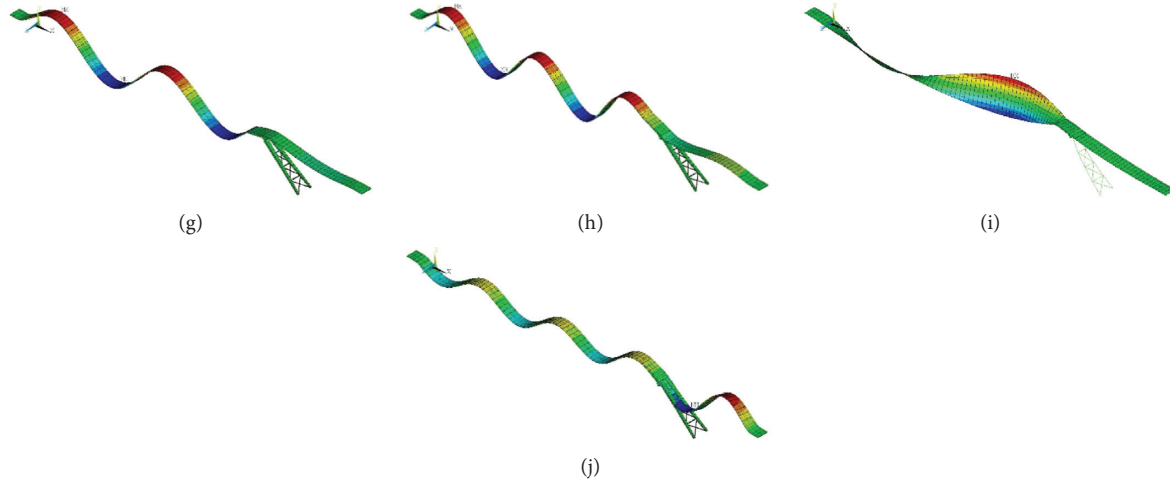


FIGURE 10: First ten simulated modes of the footbridge. (a) 1st vertical bending (main span), 0.95 Hz. (b) 1st lateral bending + torsion (main span), 0.97 Hz. (c) 2nd vertical bending (main span), 1.09 Hz. (d) 3rd vertical bending (main span) + 1st vertical bending (side span) + lateral (column), 1.65 Hz. (e) 3rd vertical bending (main span) + 1st vertical bending (side span), 1.71 Hz. (f) 1st torsion (main span), 2.20 Hz. (g) 4th vertical bending (main span), 2.27 Hz. (h) 5th vertical bending (main span), 2.89 Hz. (i) 2nd lateral bending + torsion (main span), 3.15 Hz. (j) 6th vertical bending (main span), 3.47 Hz.

TABLE 5: Basic information of the test subject.

Test subject no.	Gender	Age (years)	Height (m)	Body mass (kg)
S1	M	25	170	55.0
S2	M	23	183	70.0
S3	M	37	174	80.0
S4	M	24	177	100.0
S5	M	34	171	67.0
S6	F	23	167	58.5
S7	F	22	167	56.0
[Mean, std]	—	[26.9, 6.0]	[172.7, 5.8]	[69.5, 16.1]

Note. M: male; F: female; std: standard deviation.

TABLE 6: Summary of all test cases.

Case no.	Case description
1	S1 walking at 1.67 Hz
2	S2 walking at 1.67 Hz
3	S3 walking at 1.67 Hz
4	S4 walking at 1.67 Hz
5	Group (7 × 1, S1~S7) walking at 1.44 Hz
6	Group (7 × 1, S1~S7) walking at 1.67 Hz
7	Group (7 × 1, S1~S7) running at 3.0 Hz
8	Random walking (7 × 1, S1~S7)

In time-domain analysis, both the peak value and root-mean-square (RMS) acceleration were considered. Compared with the peak value, the RMS value, which considers the average energy during the vibration period (defined as equation (2)), gives more stable estimates.

$$a_{\text{RMS}} = \sqrt{\int_0^T a(t)^2 dt}, \quad (2)$$

where $a(t)$ is the time history, and T is the time duration of the vibration event. It should be noted that a_{RMS} largely

depends on the selection of T . The time duration of 1 s is adopted here according to ISO 10137(2007) [32].

Table 7 summarizes the peak and 1 s-RMS values of the bridge acceleration under walking pedestrians. Clearly, the maximum bridge acceleration is 2.14 m/s^2 for the group (7 × 1) walking at 1.67 Hz; however, for random group walking, the peak acceleration reduces to 0.43 m/s^2 .

Figures 11(a)–11(f) show an example of bridge acceleration and its spectrum at the center of the side span (TP12) under different walking cases. The 1s-RMS acceleration is also plotted in the time-domain figures. As

TABLE 7: Peak acceleration and maximum 1 s-RMS (m/s^2).

Case no.	Peak acceleration				RMS ($T=1$ s)			
	Main span 1/2	Main span 1/4	Side span 1/4	Side span 1/2	Main span 1/2	Main span 1/4	Side span 1/4	Side span 1/2
1	0.07	0.13	0.22	0.31	0.04	0.07	0.12	0.20
2	0.07	0.19	0.37	0.53	0.03	0.12	0.21	0.34
3	0.09	0.20	0.39	0.62	0.05	0.14	0.25	0.40
4	0.21	0.33	0.46	0.67	0.11	0.17	0.28	0.46
5	0.63	0.95	0.44	0.48	0.38	0.58	0.23	0.35
6	0.60	0.86	1.17	2.14	0.35	0.49	0.86	1.40
7	0.67	1.20	2.12	0.72	0.39	0.70	1.38	0.28
8	0.36	0.43	0.28	0.33	0.18	0.21	0.12	0.14

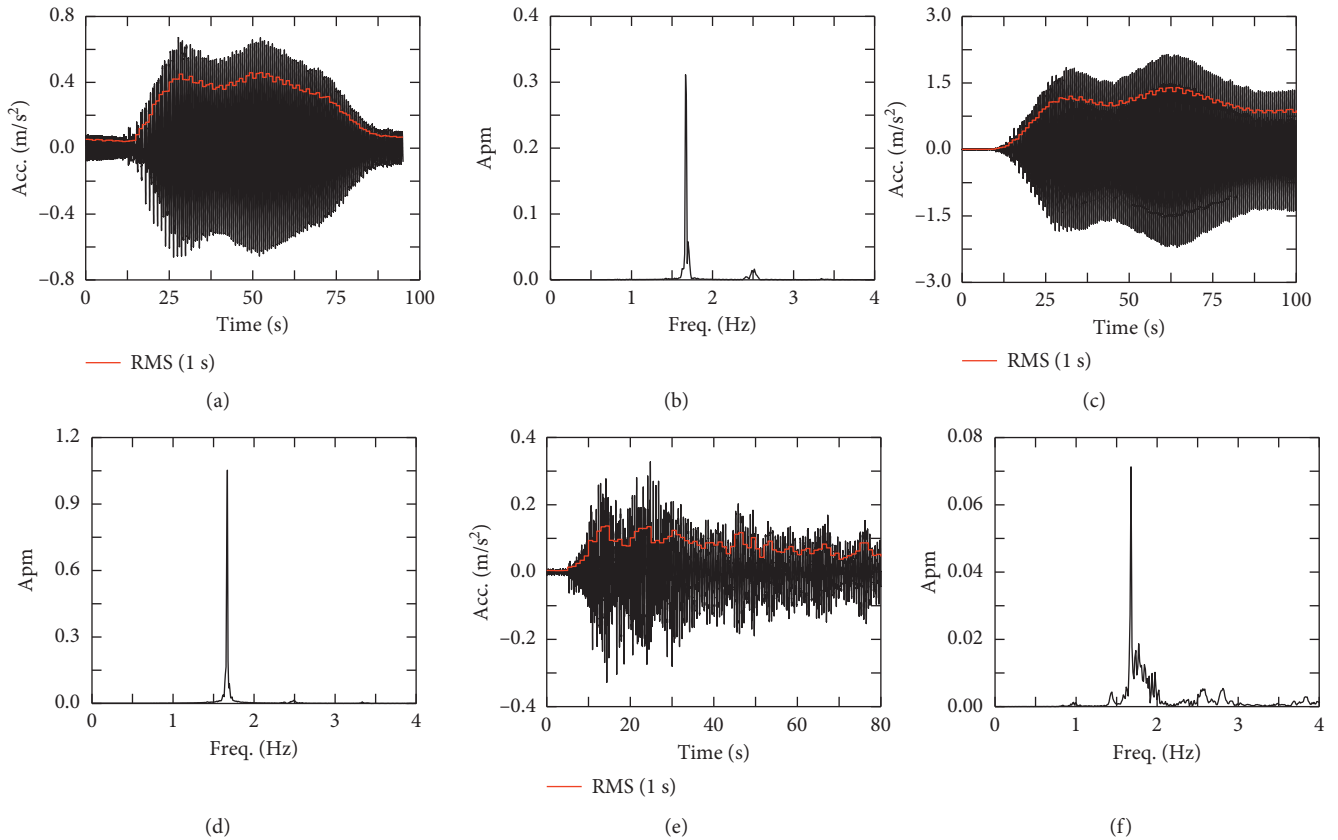


FIGURE 11: Measured bridge acceleration at TP12 (center of side span) in both time and frequency domains. (a) S4 walking at 1.67 Hz, time domain. (b) S4 walking at 1.67 Hz, frequency domain. (c) Group (7×1) walking at 1.67 Hz, time domain. (d) Group (7×1) walking at 1.67 Hz, frequency domain. (e) Random walking (7×1), time domain. (f) Random walking (7×1), frequency domain.

expected, the resonant response was observed when walking frequency approaches bridge natural frequency. The bridge response consists of both excitation frequencies and the first few structural frequencies, as shown in Figures 11(b), 11(d), and 11(f). The bridge acceleration at TP 12 is 0.67 m/s^2 for single-person S4 walking at 1.67 Hz (corresponding to the first vertical bending mode of side span). It reaches 2.14 m/s^2 for the group (7×1) synchronized walking at 1.67 Hz; however, it reduces to 0.33 m/s^2 under random group walking.

A comparison of bridge acceleration between single-person and multiperson walking cases indicates that pedestrian numbers do not linearly amplify the bridge response

under multiple-person. A comparison of bridge acceleration between single-person, group synchronized walking, and random walking cases implies that the bridge response is most sensitive to step frequency. This is also in accordance with a previous study by He and Xie [8]. Moreover, the acceleration spectrum curve under random walking is much wider than synchronized walking, showing the narrow-band and stochastic features of random walking [1].

Figures 12(a)–12(d) further compare the bridge acceleration spectrum at the center of the side span (TP12) for all test cases. It is evident that the human-induced bridge responses show obvious forced vibration features. The bridge response consists of both excitation frequencies and structural frequencies.

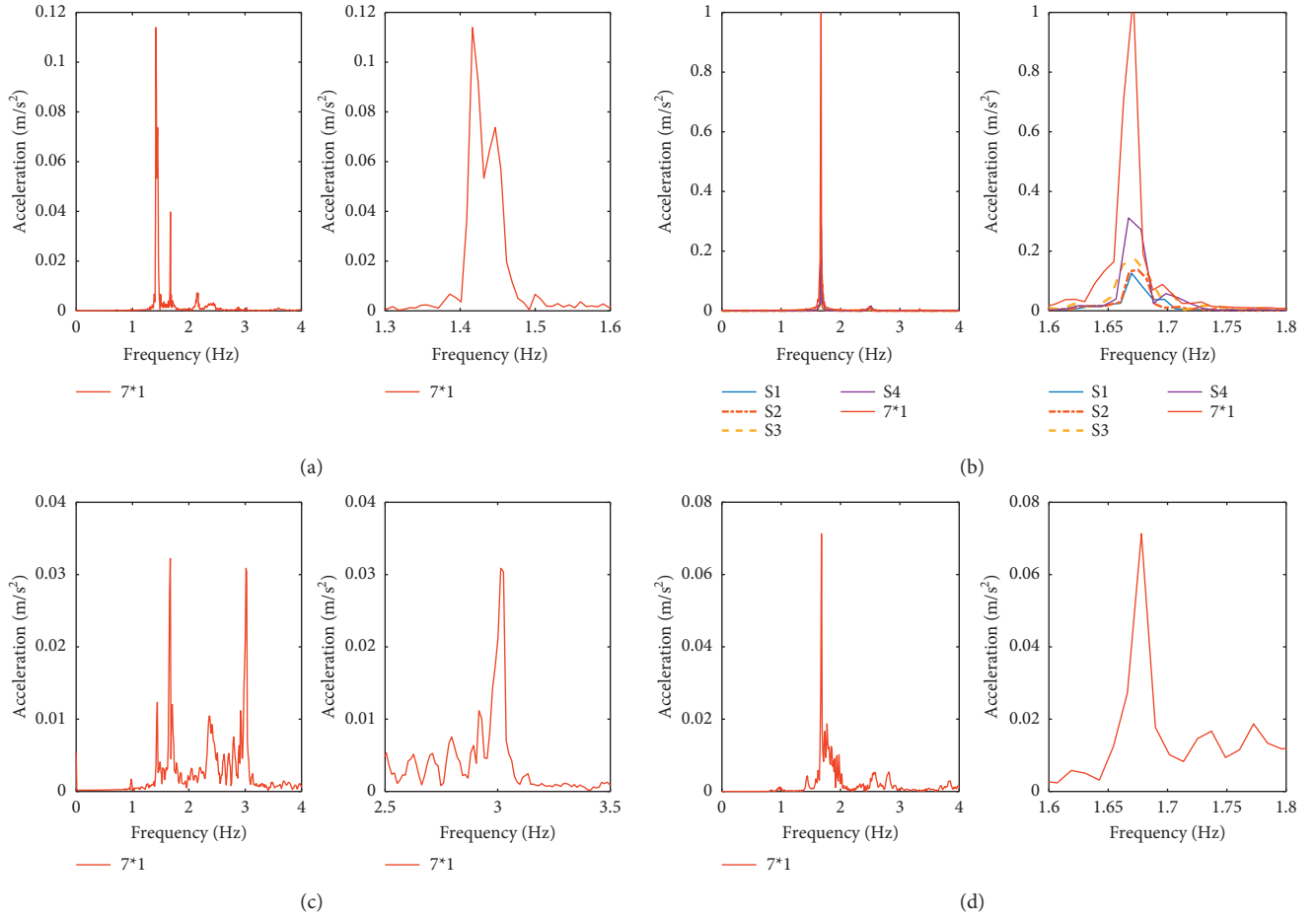


FIGURE 12: Frequency spectrum: (a) Group (7×1) walking at 1.44 Hz; (b) single-person and multiperson (7×1) walking at 1.67 Hz; (c) group (7×1) running at 3.0 Hz; (d) group (7×1) random walking.

As shown in Figure 12(b), the bridge acceleration spectrum under different single-person walking cases is similar but varies in magnitude. The normalized spectrum (acceleration spectrum divided by body weight) for each individual also varies, implying the intersubject variability [1, 2]. The spectrum gets wider for group walking at 1.67 Hz compared with single-person cases, which may attribute to the increase of system damping owing to more pronounced human-structure interaction at a larger mass participant ratio. This is in accordance with experimental finds in [8]. Compared with single-person walking, the bridge response under multiple-person is not linearly amplified by pedestrian number.

Figure 12(c) also exhibits a typical forced vibration feature. Both structural frequencies and excitation frequencies were observed. There is some leakage for frequencies between 2.5 and 3.0 Hz. This may be attributed to the imperfect synchronization among group people when running along a sloped deck at 3.0 Hz.

Figures 13(a) and 13(b) give the correlation between bridge peak acceleration, 1s-RMS, and step frequency. The bridge reaches maximum acceleration for step frequencies at 1.67 Hz and 3.0 Hz. This is reasonable since 1.67 Hz corresponds to the first vertical bending mode of the side span (see Table 4). The 3.0 Hz may also be close to the vertical bending

frequency of the side span (a clear peak was observed at 3.0 Hz, as shown in Figure 6(a)). A comparison of bridge acceleration between single-person and group random walking cases implies that the bridge response is more sensitive to step frequency rather than the number of pedestrians.

6. Analytical Verification

6.1. Mathematical Formulation. Consider a simply supported Euler beam with span length L and constant cross-section A subjected to a walking pedestrian. The beam has bending stiffness EI , mass per unit length m_b , and damping ratio c . The walking pedestrian is considered an SDOF system with biomechanical excited force [33]. Figure 14 gives the schematic illustration of the bridge-walking pedestrian coupled system.

The motion equation of the beam under a walking excitation is given by

$$EI \frac{\partial^4 w}{\partial x^4} + m_b \frac{\partial^2 w}{\partial t^2} + \frac{\partial w}{\partial t} = F_p(x, t), \quad (3)$$

where w is the beam deflection and $F_p(x, t)$ is the contact force between the bridge and walking people:

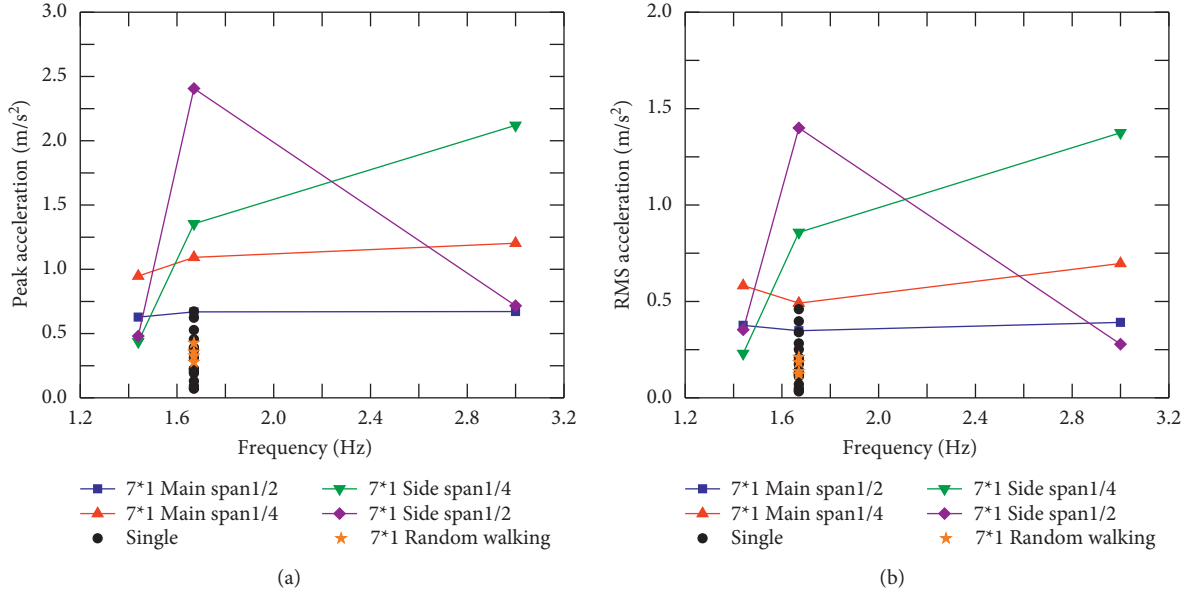


FIGURE 13: Correlation between bridge (a) peak acceleration, (b) 1 s RMS, and step frequency.

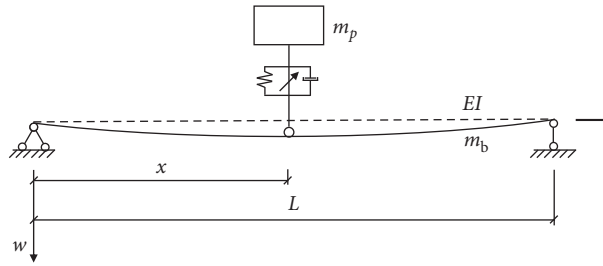


FIGURE 14: Schematic view of the human-structure interaction model.

$$F_p(x, t) = f_p(t) \cdot \delta(x - xp(t)), \quad (4)$$

in which $\delta(\cdot)$ is the Dirac delta function, and $f_p(t)$ is the human-structure interaction force, which could be represented using the body motion as follows:

$$f_p(t) = -m_p g - m_p a_c(t), \quad (5)$$

where m_p is the human body mass and $a_c(t)$ is the acceleration at the center of mass (CoM).

The CoM acceleration $a_c(t)$ consists of two parts, namely, the relative acceleration with respect to the bridge $a_{cr}(t)$ and the associated acceleration with respect to the bridge $a_{ce}(t)$; that is,

$$a_c(t) = a_{cr}(t) + a_{ce}(t). \quad (6)$$

The associated bridge acceleration where the human located, $a_{ce}(t)$, is given by

$$a_{ce}(t) = \frac{\partial^2 w(x_p, t)}{\partial t^2}. \quad (7)$$

Assume that the bridge vibration has little impact on the human walking pattern; we have

$$a_{cr}(t) = \frac{\hat{f}_p(t) - m_p g}{m_p}, \quad (8)$$

where $\hat{f}_p(t)$ is the ground reaction force (GRF) on the rigid floor.

Substituting equations (4)~(8) into equation (3) yields

$$\begin{aligned} EI \frac{\partial^4 w}{\partial x^4} + m_b \frac{\partial^2 w}{\partial t^2} + c \frac{\partial w}{\partial t} \\ = - \left(\hat{f}_p(t) - m_p \frac{\partial^2 w(x_p, t)}{\partial t^2} \right) \delta(x - x_p(t)). \end{aligned} \quad (9)$$

Note that equation (9) treats the human-structure interaction force as a summation of GRF on the rigid floor, $\hat{f}_p(t)$, and the inertial force of the human body owing to bridge oscillation.

Based on the mode superposition method, the beam displacement is rewritten as

$$w(x, t) = \sum_{i=1}^{\infty} q_i(t) \phi_i(x), \quad (10)$$

in which $\phi_i(x)$ and $q_i(t)$ are the i th mode shape and corresponding generalized coordinate, respectively. In practice, using only a few modes can give satisfactory predictions since the contribution of higher modes to the total structural response is not pronounced.

For a simply supported beam, the mode shape $\phi_j(x)$ is

$$\phi_j(x) = \sin \frac{j\pi x}{L}. \quad (11)$$

Substituting equation (10) into equation (9) yields

$$\begin{aligned} EI \sum_{i=1}^{\infty} \dot{q}_i(t) \phi_i^{(4)}(x) + m_b \sum_{i=1}^{\infty} \phi(x) \ddot{q}_i(t) + c \sum_{i=1}^{\infty} \phi_i(x) \dot{q}_i(t) \\ = -\delta(x - x_p(t)) \left[\hat{f}_p(t) + m_p \sum_{i=1}^{\infty} \phi(x_p) \ddot{q}_i(t) \right]. \end{aligned} \quad (12)$$

Multiplying $\phi_j(x)$ on both sides of equation (12) and integrating along the beam length within $[0, L]$ leads to

$$\begin{aligned} \dot{q}_j(t) + \frac{2}{m_b L} m_p \phi_j(x_p) \sum_{i=1}^{\infty} \phi(x_p) \ddot{q}_i(t) \\ + 2\zeta_n w_n \dot{q}_j(t) + w_n^2 q_j(t) \\ = \frac{-2}{m_b L} \hat{f}_p(\phi_j)(x_p(t)). \end{aligned} \quad (13)$$

If N modes are considered for the bridge, the bridge-moving pedestrian coupled system could be rewritten in a discrete matrix form as

$$\mathbf{M}\ddot{\mathbf{U}} + \mathbf{C}\dot{\mathbf{U}} + \mathbf{K}\mathbf{U} = \mathbf{F}, \quad (14)$$

where \mathbf{M} , \mathbf{C} , and \mathbf{K} are the $N \times N$ mass, damping, and stiffness matrix, respectively; \mathbf{U} , $\dot{\mathbf{U}}$, and $\ddot{\mathbf{U}}$ are the N -vectors for independent displacement, velocity, and acceleration, respectively. That is,

$$\mathbf{M} = \begin{bmatrix} 1 + p_M \phi_{11} & p_M \phi_{12} & \cdots & p_M \phi_{1N} \\ p_M \phi_{21} & 1 + p_M \phi_{21} & \cdots & p_M \phi_{2N} \\ \cdots & \cdots & \cdots & \cdots \\ p_M \phi_{N1} & p_M \phi_{N1} & \cdots & 1 + p_M \phi_{NN} \end{bmatrix}, \quad (15a)$$

$$\mathbf{C} = \begin{bmatrix} 2\zeta_1 w_1 & & & \\ & 2\zeta_2 w_2 & & \\ & & \ddots & \\ & & & 2\zeta_n w_n \end{bmatrix}, \quad (15b)$$

$$\mathbf{K} = \begin{bmatrix} w_1^2 & & & \\ & w_2^2 & & \\ & & \ddots & \\ & & & w_n^2 \end{bmatrix}, \quad (15c)$$

$$\mathbf{U} = \{\mathbf{q}_1, \mathbf{q}_2, \dots, \mathbf{q}_N\}^T, \quad (15d)$$

$$\mathbf{F} = [p_F \phi_1, p_F \phi_2, \dots, p_F \phi_N]^T. \quad (15e)$$

$$\begin{aligned} \rho_m &= \frac{2m_p}{m_b L}, \\ \rho_F &= -\frac{2}{m_b L} \hat{f}_p, \\ \phi_n &= \sin \frac{n\pi x_p}{L}, \\ \Phi_{nm} &= \phi_n \phi_m. \end{aligned} \quad (15f)$$

Note that equation (14) is a time-varying system since the mass, damping, and stiffness matrix all change with the human location. One GRF \hat{f}_p is given, equation (14) could be solved (e.g., using the Newmark- β method).

6.2. GRF of a Walking Pedestrian. Previous studies showed that the GRF under human walking has a strong periodical character owing to the unique walking pattern of human beings [1]. The GRF could mathematically be represented as the summation of several Fourier series, expressed as [1]

$$F_v(t) = G \left(1 + \sum_{i=1}^n \alpha_i \sin(2\pi i f_n t + \varphi_i) \right), \quad (16)$$

where $F_v(t)$ is the vertical footfall force, G is the bodyweight, n is the number of harmonics to be considered, α_i is the i th dynamic load factor (DLF), f_n is the fundamental step frequency, and φ_i is the i th phase angle.

The formula is simple and has a clear physical meaning, but the parameters such as DLFs and phase angles may vary from person to person [1]. To this end, TSs involved in the walking test on the stress-ribbon bridge were tested on a rigid floor to obtain their GRF directly. The wireless pressure insoles (see Figure 15(a)) produced by Loadsol were employed for footfall force measurement. The smartphone (iPhone 7 plus, see Figure 15(b)), which has built-in accelerometers and gyroscopes, was used to record the body acceleration during walking. Previous studies [34, 35] showed that the C7, sternum, and lower back are satisfactory candidates to present body motion. In this study, the smartphone was well fastened on the lower back (see Figure 15(d)) to capture body motion since it is easy to fasten and has little effect on human movement.

Before the measurement, the insoles were calibrated via standing with a single foot since the supporting foot is expected to have total static weight. The resolution of the smartphone in acceleration capture was also checked by comparing it with a high-resolution wireless inertial measurement unit (IMU) produced by Xsense. Figure 16 shows an example of the comparison between the smartphone and IMU in both time and frequency domains. Results show that the smartphone has satisfactory resolution and can be used in the subsequent measurement.

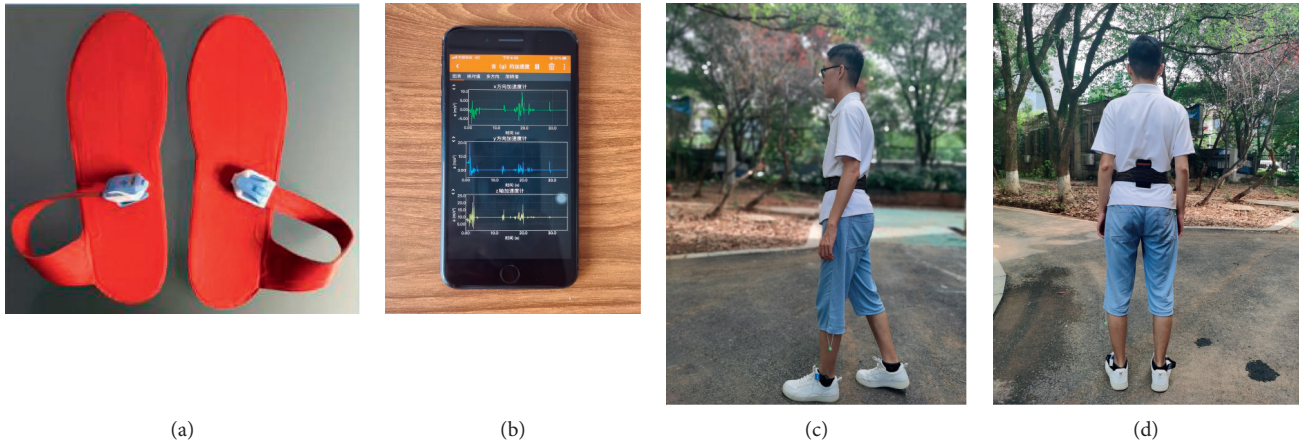


FIGURE 15: Test instruments and test scenario: (a) wireless pressure insoles; (b) smartphone; (c) and (d) installation of test instruments.

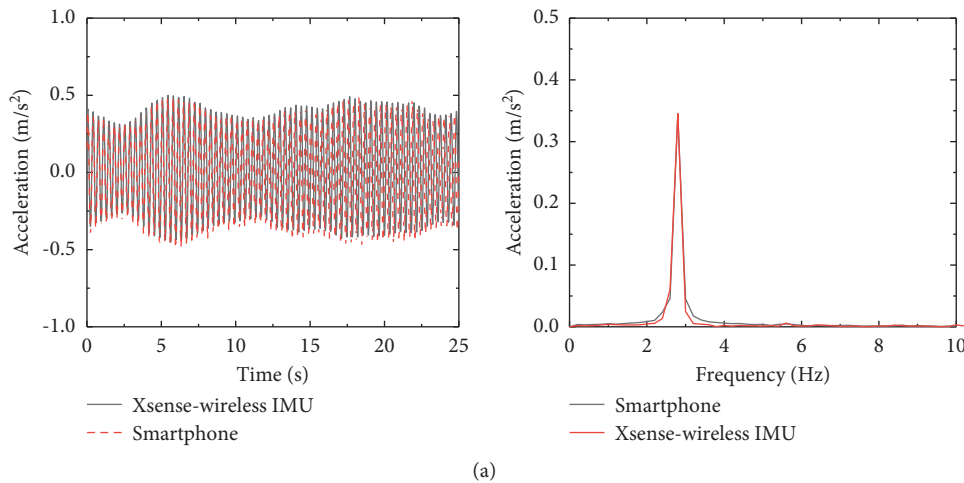


FIGURE 16: Comparison of human body acceleration (lower back) obtained from wireless IMU and smartphone (iPhone 7 plus). (a) Time domain and (b) frequency domain.

Figure 17 gives the continuous vertical GRF for single-person walking at 1.6 Hz, 1.8 Hz, 2.0 Hz, 2.2 Hz, and 2.4 Hz in both time and frequency domains. It is evident that the GRF shows prominent periodical features for all step frequencies. The GRF consists of several primary harmonics and subharmonics. The DLF generally attenuates as the order increases. The contribution of primary harmonics is generally more significant than subharmonics. However, for some cases (i.e., 2.2 Hz), the subharmonic is so pronounced and cannot be ignored. This is in accordance with a previous study by Zivanovic et al. [1].

Figure 18 illustrates the corresponding body acceleration in the vertical direction for single-person walking at various step frequencies. Clearly, the body motion also shows typical periodical characteristics. The spectrum of body acceleration is similar to that of GRF, demonstrating that the inertial of body motion is the leading cause of footfall force oscillation.

Since all measured footfall forces have similar features, GRF that consists of both primary harmonics and subharmonics was used for the subsequent numerical modeling.

6.3. Comparison of the Theoretical Results with Experimental Data. Based on the FE model developed in Section 4 and the measured GRF of all involved individuals in the walking test, the methodology developed in Section 6.1 was applied to the stress-ribbon footbridge to check its validity.

Equations (14) and (15a)–(15f) show that the coupled system is time-varying since the mass, damping, and stiffness matrix changes with the human location. In this study, an iteration procedure is developed to solve the problem based on the combination of MATLAB and ANSYS platforms. The basic procedure of the iteration process is shown in Figure 19.

Figures 20 and 21 compare the simulated and measured bridge acceleration time history and Fourier spectrum at the center of the main span and side span, respectively, under a single-person walking at 1.67 Hz. The simulated time history and spectrum distribution are very close to the measured ones. The magnitude of the simulated acceleration is slightly greater than the measured one for both the center of the main span and side span. This may be attributed to the fact that GRF measured on the rigid floor is

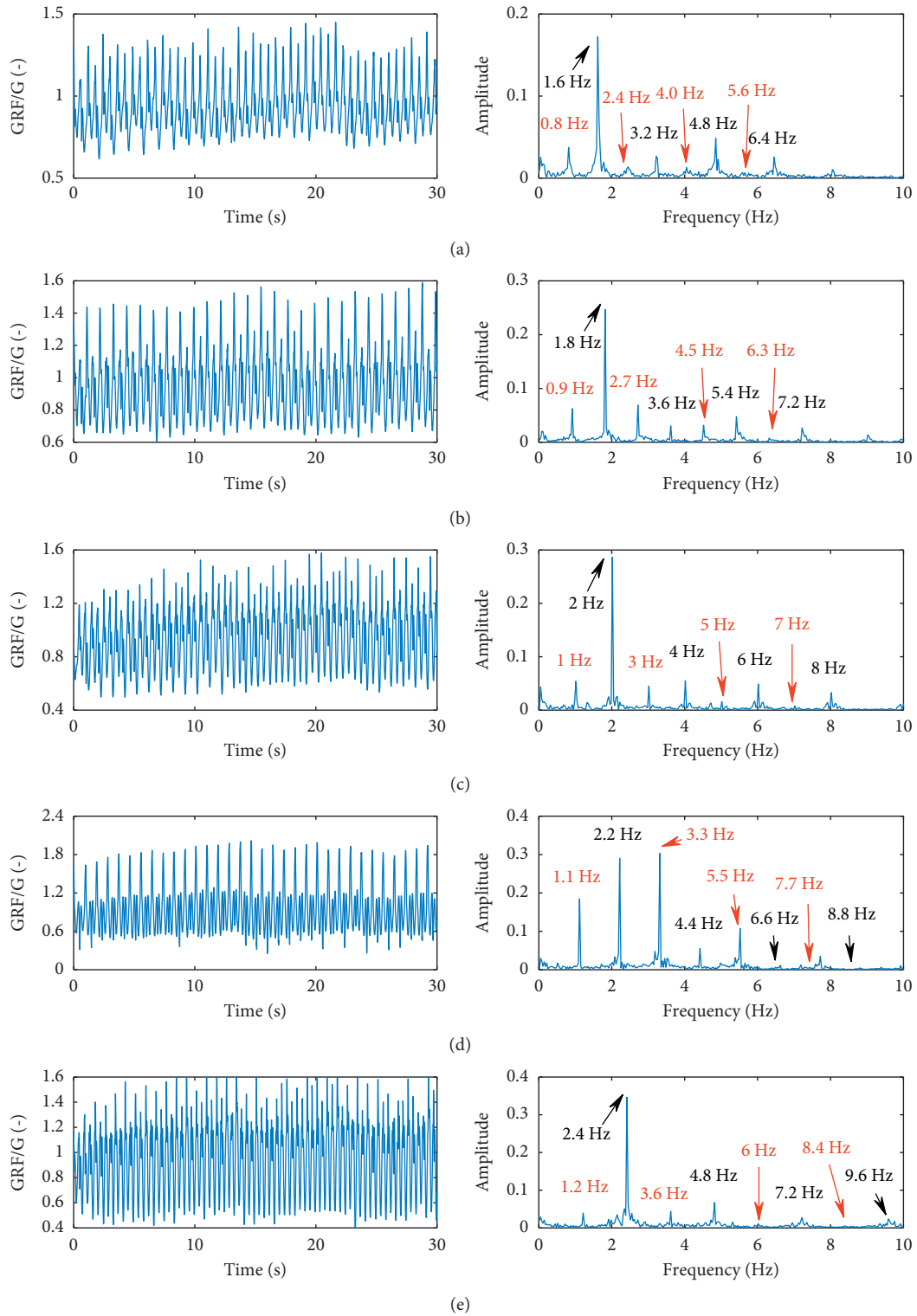


FIGURE 17: Vertical GRF for a single-person walking at step frequencies of (a) 1.6 Hz, (b) 1.8 Hz, (c) 2.0 Hz, (d) 2.2 Hz, and (e) 2.4 Hz in time and frequency domains.

used in the present study. In fact, the footfall force would be smaller on a flexible footbridge than on a rigid floor owing to human-structure interaction. The simulated results

generally show satisfactory agreement with the measured ones, demonstrating that the proposed analytical model is valid and effective.

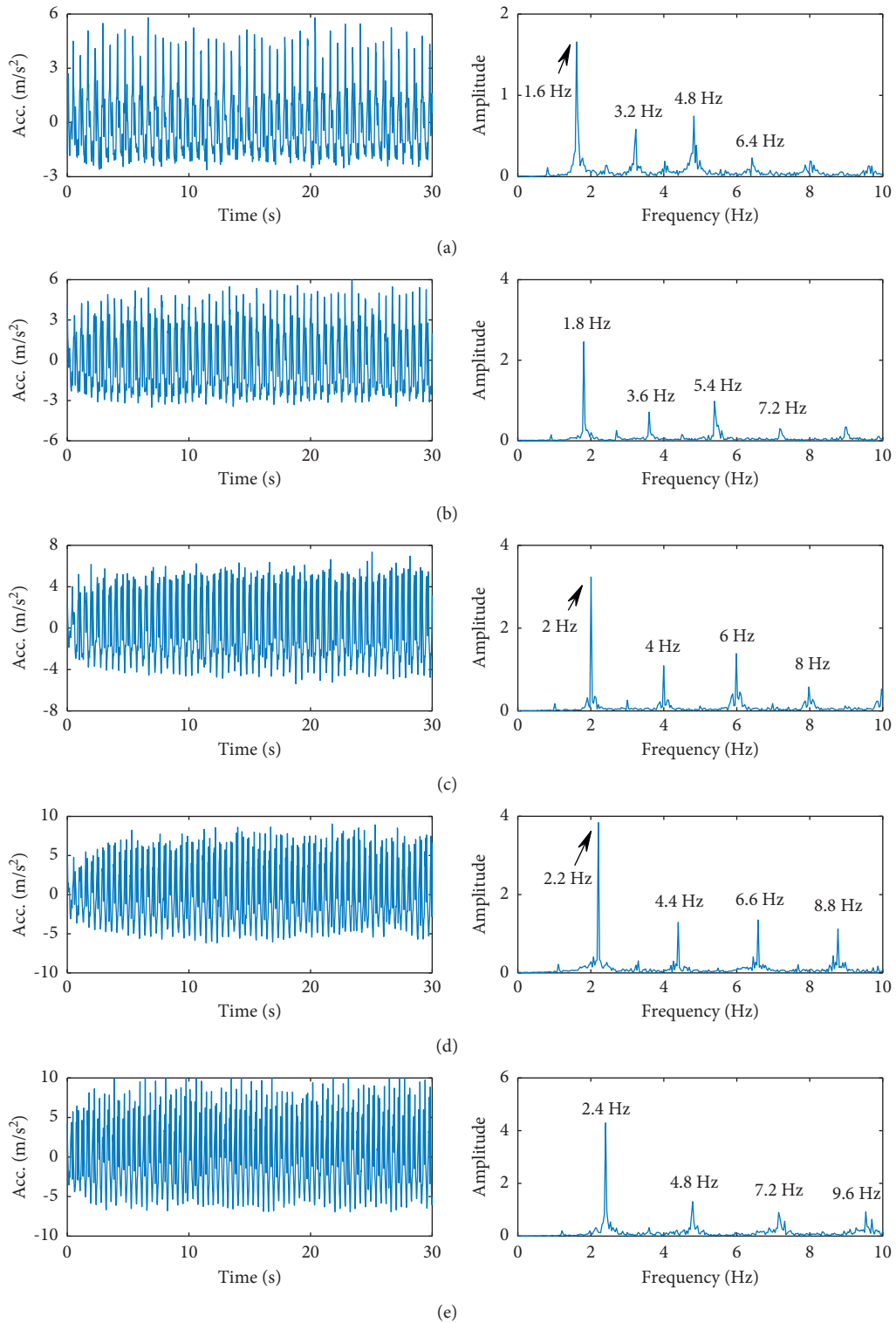


FIGURE 18: Vertical body acceleration for a single-person walking at step frequencies of (a) 1.6 Hz, (b) 1.8 Hz, (c) 2.0 Hz, (d) 2.2 Hz, and (e) 2.4 Hz in time and frequency domains.

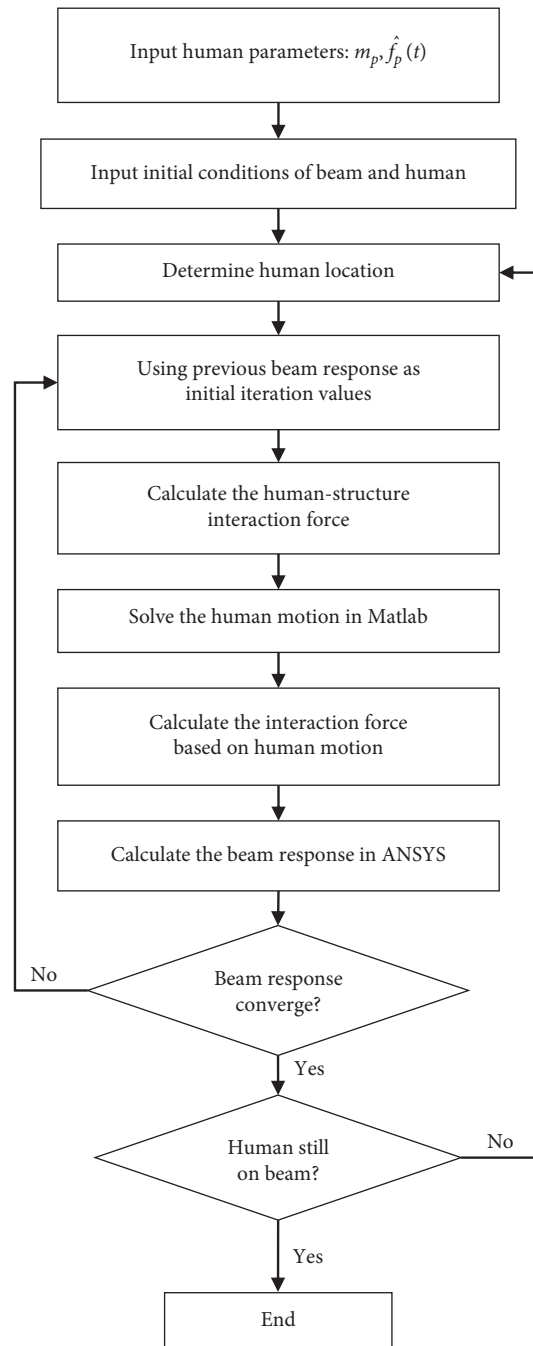


FIGURE 19: Solution procedure of the bridge-walking human coupled system.

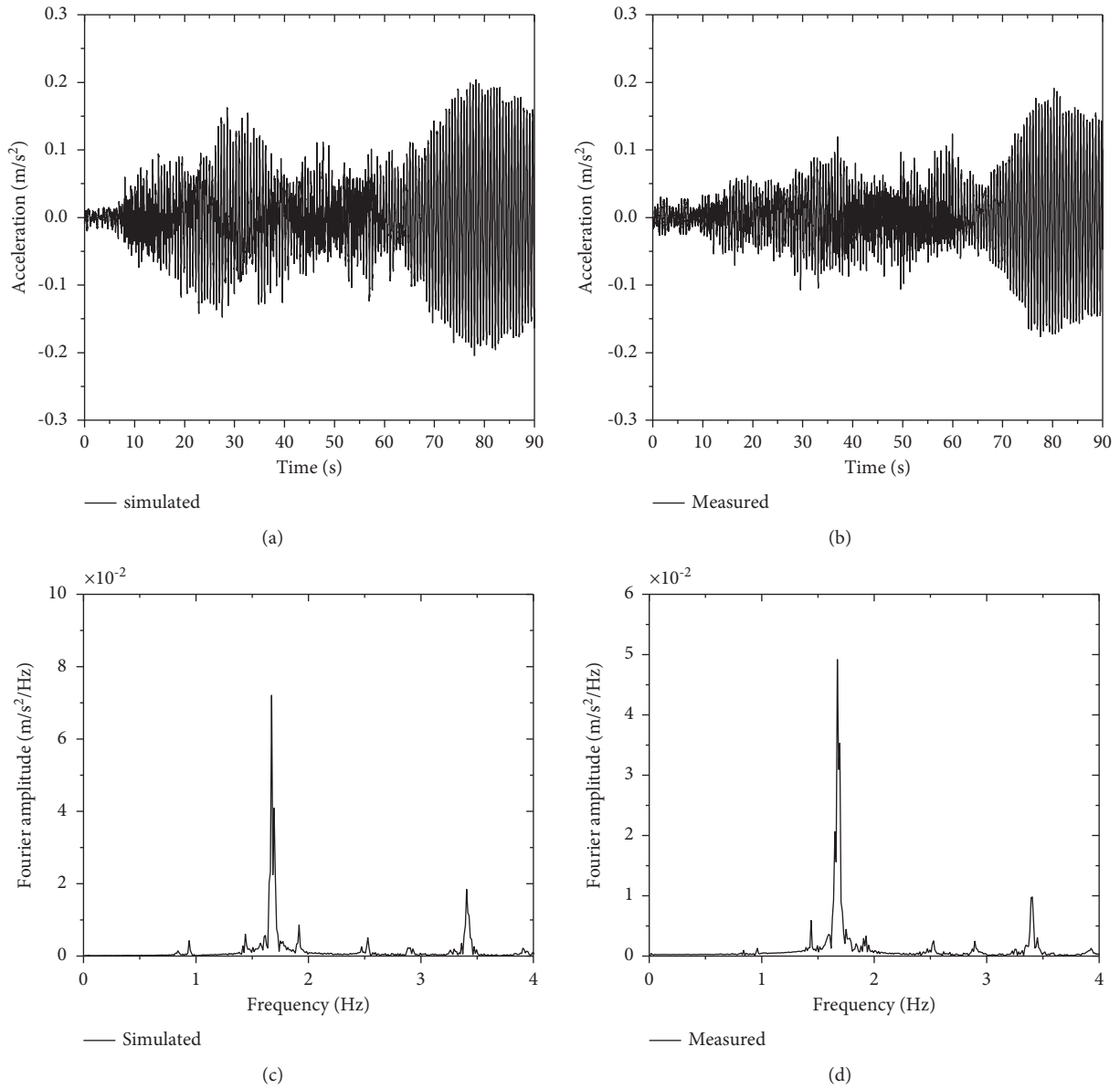


FIGURE 20: Comparison between simulated and measured bridge acceleration at the center of the main span: (a) simulated time history; (b) measured time history; (c) simulated spectrum; (d) measured spectrum.

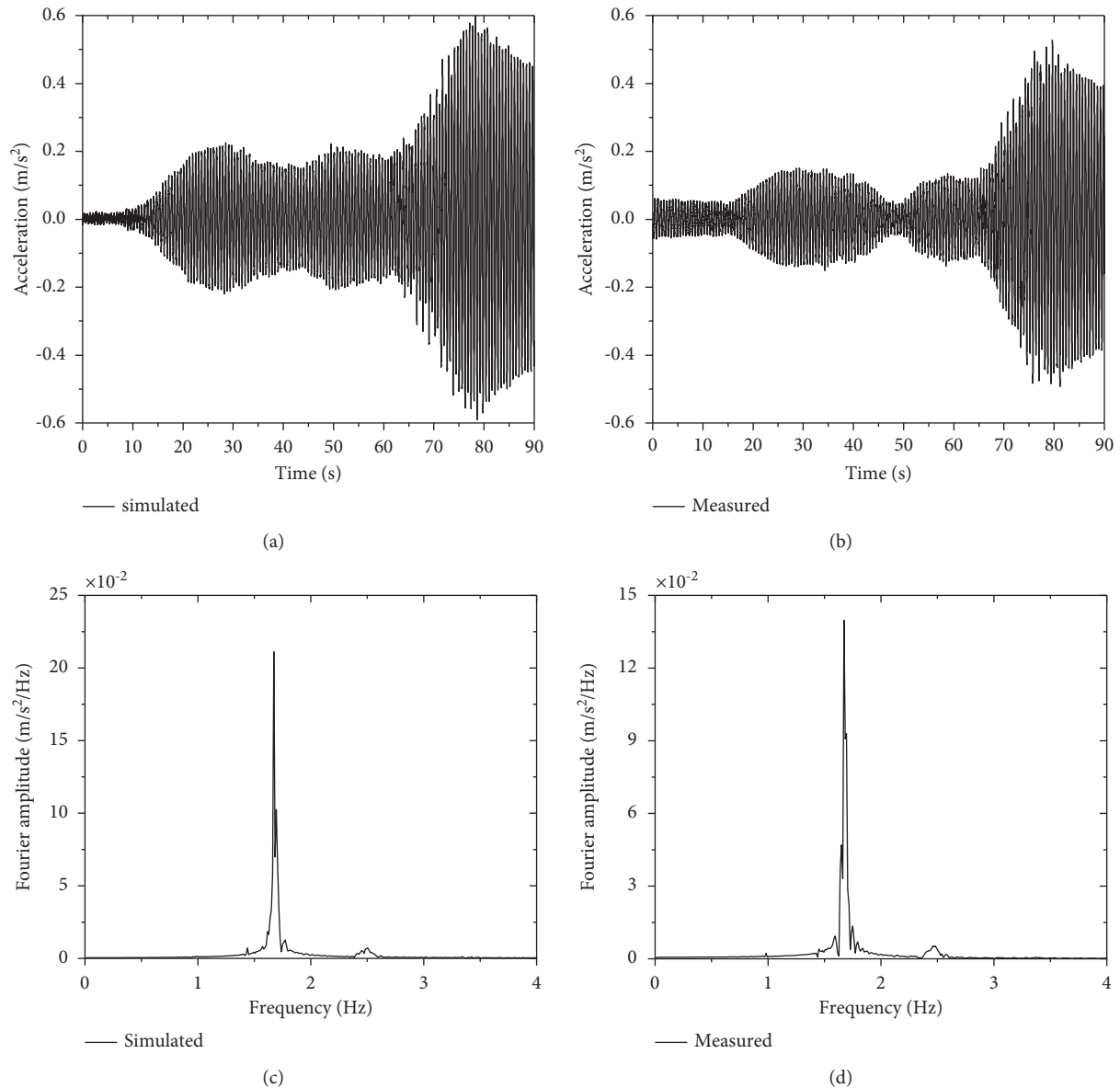


FIGURE 21: Comparison between simulated and measured bridge acceleration at the center of side span: (a) simulated time history; (b) measured time history; (c) simulated spectrum; (d) measured spectrum.

7. Concluding Remarks

This study has presented a flexible asymmetric stress-ribbon pedestrian bridge's modal properties and dynamic performance via both experimental and analytical methods. The following conclusions could be drawn:

- (1) Modal test showed that the stress-ribbon footbridge has closely spaced modes, low natural frequencies, and small damping ratios (<0.002). The measured first three natural frequencies are 0.95 Hz, 1.45 Hz, and 1.68 Hz, respectively. A numerical model that considers the pretension of the stress ribbon and contribution of deck panels is developed and proven capable of reflecting the main dynamic properties of the actual bridge.
- (2) The maximum bridge acceleration reaches 2.14 m/s^2 for small group synchronized walking; however, it reduces to 0.43 m/s^2 under random group walking.
- (3) The bridge response is more sensitive to step frequency rather than the pedestrian number. Compared with single-person walking, the bridge response under multiple-person synchronized walking is not linearly amplified by pedestrian number.
- (4) A theoretical model considering the human-structure interaction is developed by treating the single walking person as an SDOF system with biomechanical excited force. The validity of the model was verified by field measurement results.

Further extensions of the present study may include mechanic property and its influence factors of the stress-ribbon bridge. Besides, mitigation measures against excessive bridge vibration should be considered in the future to improve the vibration serviceability of the footbridge.

Data Availability

Relevant data used in this paper can be accessed upon request to the corresponding author.

Conflicts of Interest

The authors declare that they have no conflicts of interest.

Acknowledgments

This work was supported by the National Natural Science Foundation of China (51508431) and the Fundamental Research Funds for the Central Universities (CUG190637).

References

- [1] S. Zivanovic, A. Pavic, and P. Reynolds, "Vibration serviceability of footbridges under human-induced excitation: a literature review," *Journal of Sound and Vibration*, vol. 279, no. 1-2, pp. 1-74, 2005.
- [2] S. Zivanovic, A. Pavic, and P. Reynolds, "Probability-based prediction of multi-mode vibration response to walking excitation," *Engineering Structures*, vol. 29, no. 6, pp. 942-954, 2007.
- [3] J. M. W. Brownjohn, A. Pavic, and P. Omenzetter, "A spectral density approach for modelling continuous vertical forces on pedestrian structures due to walking," *Canadian Journal of Civil Engineering*, vol. 31, no. 1, pp. 65-77, 2004.
- [4] F. Venuti and F. Tubino, "Human-induced loading and dynamic response of footbridges in the vertical direction due to restricted pedestrian traffic," *Structure and Infrastructure Engineering*, vol. 17, no. 10, pp. 1431-1445, 2021.
- [5] C. C. Caprani, J. Keogh, P. Archbold, and P. Fanning, "Enhancement factors for the vertical response of footbridges subjected to stochastic crowd loading," *Computers & Structures*, vol. 102-103, pp. 87-96, 2012.
- [6] W. He, C. Zou, Y. Pang, and X. Wang, "Environmental noise and vibration characteristics of rubber-spring floating slab track," *Environmental Science and Pollution Research*, vol. 28, no. 11, Article ID 13671, 2021.
- [7] L. Bruno and F. Venuti, "Crowd-structure interaction in footbridges: modelling, application to a real case-study and sensitivity analyses," *Journal of Sound and Vibration*, vol. 323, no. 1-2, pp. 475-493, 2009.
- [8] W. He and W. P. Xie, "Characterization of stationary and walking people on vertical dynamic properties of a lively lightweight bridge," *Structural Control and Health Monitoring*, vol. 25, no. 3, p. e2123, 2018.
- [9] F. Venuti, V. Racic, and A. Corbetta, "Modelling framework for dynamic interaction between multiple pedestrians and vertical vibrations of footbridges," *Journal of Sound and Vibration*, vol. 379, pp. 245-263, 2016.
- [10] F. Ricciardelli and C. Demartino, "Design of footbridges against pedestrian-induced vibrations," *Journal of Bridge Engineering*, vol. 21, no. 8, Article ID C4015003, 2016.
- [11] F. Venuti and A. Reggio, "Mitigation of human-induced vertical vibrations of footbridges through crowd flow control," *Structural Control and Health Monitoring*, vol. 25, no. 12, Article ID e2266, 2018.
- [12] S. E. T. R.A. Footbridge, *Assessment of Vibrational Behaviour of Footbridge under Pedestrian Loading*, Setra, Paris France, 2006.
- [13] J. Chen, R. Xu, and M. Zhang, "Acceleration response spectrum for predicting floor vibration due to occupant walking," *Journal of Sound and Vibration*, vol. 333, no. 15, pp. 3564-3579, 2014.
- [14] A. S. Mohammed, A. Pavic, and V. Racic, "Improved model for human induced vibrations of high-frequency floors," *Engineering Structures*, vol. 168, pp. 950-966, 2018.
- [15] Z. O. Muhammad and P. Reynolds, "Vibration serviceability of building floors: performance evaluation of contemporary design guidelines," *Journal of Performance of Constructed Facilities*, vol. 33, no. 2, Article ID 04019012, 2019.
- [16] B. M. Basaglia, J. Li, R. Shrestha, and K. Crews, "Response prediction to walking-Induced vibrations of a long-span timber floor," *Journal of Structural Engineering*, vol. 147, no. 2, Article ID 04020326, 2021.
- [17] K. A. Salyards and L. M. Hanagan, "Evaluation of vibration assessment criteria and their application to stadium serviceability," *Journal of Performance of Constructed Facilities*, vol. 24, no. 2, pp. 100-107, 2010.
- [18] N. T. Do, M. Gül, O. Abdeljaber, and O. Avci, "Novel framework for vibration serviceability assessment of stadium grandstands considering durations of vibrations," *Journal of Structural Engineering*, vol. 144, no. 2, Article ID 04017214, 2018.
- [19] J. Strasky, *Stress Ribbon and cable-supported Pedestrian Bridges*, Thomas Telford, London England UK, 2005.
- [20] R. Agrawal, "Stress ribbon bridges," *Structural Engineer*, vol. 87, no. 22, pp. 22-27, 2009.
- [21] D. C. D. Arco, A. C. Aparicio, and A. R. Mañá, "Preliminary design of prestressed concrete stress ribbon bridge," *Journal of Bridge Engineering*, vol. 6, no. 4, pp. 234-242, 2001.
- [22] G. Arndt, M. Schlaich, and M. Meiselbach, "Stress ribbon bridges: mechanics of the stress ribbon on the saddle," *Journal of Bridge Engineering*, vol. 21, no. 5, Article ID 04015089, 2016.
- [23] W. H. Hu, E. Caetano, and Á. Cunha, "Structural health monitoring of a stress-ribbon footbridge," *Engineering Structures*, vol. 57, pp. 578-593, 2013.
- [24] J. M. Soria, I. M. Díaz, H. Jaime, G. Palacios, and N. Ibán, "Vibration monitoring of a steel-plated stress-ribbon footbridge: uncertainties in the Modal Estimation," *Journal of Bridge Engineering*, vol. 21, no. 8, Article ID C5015002, 2016.
- [25] S. S. Ivanovic, M. D. Trifunac, and M. I. Todorovska, "Ambient vibration test-a review," *ISSET Journal of Earthquake Technology*, vol. 37, no. 4, pp. 165-197, 2000.
- [26] B. Jaishi and W. X. Ren, "Structural finite element model updating using ambient vibration test results," *Journal of Structural Engineering*, vol. 131, no. 4, pp. 617-628, 2005.
- [27] B. Peeters and G. D. Roeck, "Reference-based stochastic subspace identification for output-only modal analysis," *Mechanical Systems and Signal Processing*, vol. 13, no. 6, pp. 855-878, 1999.
- [28] W. X. Ren, X. L. Peng, and Y. Q. Lin, "Experimental and analytical studies on dynamic characteristics of a large span cable-stayed bridge," *Engineering Structures*, vol. 27, no. 4, pp. 535-548, 2005.
- [29] P. V. Overschee and D. B. Moor, *Subspace Identification for Linear System: Theory-Implementation-Applications*, Kluwer

- Academic Publishers, Alphen aan den Rijn, Netherlands, 1996.
- [30] F. Magalhães, E. Caetano, Á Cunha, O. Flamand, and G. Grillaud, “Ambient and free vibration tests of the Millau Viaduct: evaluation of alternative processing strategies,” *Engineering Structures*, vol. 45, pp. 372–384, 2012.
 - [31] F. L. Huang, X. H. He, and Z. Q. Chen, “A new approach for identification of modal damping ratios for a structure,” *China Civil Engineering Journal*, vol. 35, no. 6, pp. 20–24, 2002, (in Chinese).
 - [32] *Bases for Design of Structures—Serviceability of Buildings and Walkways against Vibrations*, ISO (International Organization for Standardization), Geneva, Switzerland, 2007.
 - [33] M. S. Zhang, C. T. Georgakis, and J. Chen, “Biomechanically excited SMD model of a walking pedestrian,” *Journal of Bridge Engineering*, vol. 21, no. 8, Article ID C4016003, 2016.
 - [34] J. M. W. Brownjohn, J. Chen, M. Bocian, V. Racic, and E. Shahabpoor, “Using inertial measurement units to identify medio-lateral ground reaction forces due to walking and swaying,” *Journal of Sound and Vibration*, vol. 426, pp. 90–110, 2018.
 - [35] Z. Han, J. M. W. Brownjohn, and J. Chen, “Structural modal testing using a human actuator,” *Engineering Structures*, vol. 221, Article ID 111113, 2020.

Research Article

Sandy Soil Liquefaction Prediction Based on Clustering-Binary Tree Neural Network Algorithm Model

Yu Wang and Jiachen Wang 

School of Civil Engineering, Beijing Jiaotong University, Beijing 100044, China

Correspondence should be addressed to Jiachen Wang; wangjiachen@bjtu.edu.cn

Received 19 September 2021; Accepted 25 October 2021; Published 13 December 2021

Academic Editor: Zhiyong Chen

Copyright © 2021 Yu Wang and Jiachen Wang. This is an open access article distributed under the Creative Commons Attribution License, which permits unrestricted use, distribution, and reproduction in any medium, provided the original work is properly cited.

The neural network algorithm is a small sample machine learning method built on the statistical learning theory and the lowest structural risk principle. Classical neural network algorithms mainly aim at solving two-classification problems, making it infeasible for multiclassification problems encountered in engineering practice. According to the main factors affecting sand liquefaction, a sand liquefaction discriminant model based on a clustering-binary tree multiclass neural network algorithm is established using the class distance idea in cluster analysis. The model can establish the nonlinear relationship between sand liquefaction and various influencing factors by learning limited samples. The research results show that the hierarchical structure based on the clustering-binary tree neural network algorithm is reasonable, and the sand liquefaction level can be categorized accurately.

1. Introduction

Earthquake-induced sand liquefaction is a very destructive phenomenon of geological disasters, which can bring about damages to the farmland, roads, bridges, various civil buildings, and water conservancy facilities, causing great harm to the social economy and human life safety. Therefore, sand liquefaction under the action of earthquake has always been one of the hot issues in the field of geotechnical engineering and disaster geology. As earthquakes are inevitable, the possibility of seismic liquefaction assessment and prediction of the site are the focus of the research on this issue [1–4].

The current discrimination methods for seismic liquefaction are mainly divided into two categories: the empirical analysis method based on the investigation data of the sand liquefaction disaster at the earthquake site and the experimental analysis method based on the field or indoor test.

The commonly used empirical analysis methods mainly include the standard penetration method, the critical void ratio, and the energy discrimination method [5]. The experimental analysis methods mainly include the Seed–Idriss

simplification method [6], shear wave velocity method [7], static cone penetration method [8], dynamic simple shear test, shaking table test [9, 10], and dynamic triaxial test [11, 12].

In recent years, the application of machine learning-based research methods in the field of earth sciences has gained a lot of attention [13–20]. Traditional geological research is gradually moving closer to the fields of data deep mining, big data, and artificial intelligence, such as in coal mine water inrush prediction [21] and research on landslides [22, 23].

In the study of seismic liquefaction, Xue and Yang examined the potential of support vector machines (SVMs) for assessing liquefaction potential based on cone penetration test (CPT) field data [24]. A hybrid model based on a combination of SVMs and particle swarm optimization (PSO) was proposed in the study to improve the forecasting performance. Chou and Thedja proposed a novel classification system integrating swarm and metaheuristic intelligence, i.e., a smart firefly algorithm (SFA), with a least-square support vector machine (LSSVM), to provide decision-makers with timely warnings of geotechnical hazards

[25]. Xue and Liu presented two optimization techniques: genetic algorithm (GA) and particle swarm optimization (PSO), to improve the efficiency of the backpropagation (BP) neural network model for predicting liquefaction susceptibility of soil [26]. Yang et al. established a new liquefaction evaluation formula based on the 156 SPT data from the liquefaction investigation in China mainland [27]. Ali and Jahanpour applied the evolutionary polynomial regression technique and provided a new model for predicting the liquefaction potential [28]. Rahbarzare and Azadi used hybrid particle swarm optimization and genetic algorithms with a fuzzy support vector machine (FSVM) as the classifier for the soil liquefaction prediction problem [29]. Hu and Liu attempted to reduce the parameter and model uncertainties of the Bayesian network model for predicting earthquake-induced soil liquefaction. In their work, 31 candidate intensity measures were investigated by the analyses of correlation, efficiency, proficiency, and sufficiency based on a large database of historical ground motion records [30]. Hu and Liu constructed two new Bayesian network (BN) models for predicting the probability of the occurrence of soil liquefaction and then compared them with four simplified procedures and a Bayes classifier for soil liquefaction evaluation [31].

At present, in the field of geotechnical engineering, machine learning methods are often used to consider problems such as binary classification. In contrast, the problems encountered in geotechnical practice are often multiclassification problems. To date, multiclassification research is still in its infancy. The application of neural network algorithms in geotechnical engineering is rarely reported in the literature. This paper introduces multiple types of neural networks into the evaluation of sand liquefaction for the first time, analyses the factors affecting sand liquefaction, extracts characteristic parameters, and adopts the cluster analysis method of class distance to establish a sand soil based on the cluster-binary tree multiclass neural network algorithm. The liquefaction discriminant model has achieved satisfactory evaluation results.

2. Neural Network Algorithm

2.1. Introduction to Neural Network Algorithm. The neural network algorithm is a typical supervised machine learning algorithm, which is composed of a large number of nodes connected to each other by imitating the transmission of electrical signals between biological neurons in the natural world. Among them, multilayer perceptron (MLP) is one of the most popular feedforward artificial neural networks. A typical MLP neural network usually contains an input layer, a hidden layer (one or more layers), and an output layer. The input layer and the input variables have the same number of nodes; the hidden layer contains the weight values of the connections between neurons and the corresponding threshold function, which are used to transmit and process the signal; and the output value is the final data to be obtained.

The mathematical representation of the feedforward neural network is as follows:

$$\begin{aligned} y_k(x) &= \sum_{i=1}^M \omega_{ih} \times T_r(z) + b_{ih}, \\ z &= \sum_{i=1}^D \omega_{ho} \times x_i + b_{ho}, \end{aligned} \quad (1)$$

where x is the input parameter, ω_{ih} and ω_{ho} are the input layer-hidden layer weight and hidden layer-output layer weight, respectively, b_{ih} and b_{ho} are the deviation parameter, M is the number of nodes in the hidden layer, d is the number of nodes in the input layer, and $T_r(z)$ is the transfer function that performs a nonlinear transformation on the summation input.

The goal of the algorithm is to reduce the error between the calculated value and the true value through a series of training. The error E can be defined as follows:

$$E = \frac{1}{p} \sum_{p=1}^p E_p, \quad (2)$$

where p is the total number of training modes and E_p is the error of P -th training mode that is obtained by the following formula:

$$E_p = \frac{1}{2} \sum_{k=0}^N (O_k - t_k)^2, \quad (3)$$

where N is the total number of output nodes, k is the output of P -th time output node, and t_k is the target output of the P -th output node.

2.2. Neural Network Algorithm Method of Multiclassification Based on Clustering-Binary Tree. The basic neural network algorithm is aimed at two-classification problems, and the multiclassification problem is more common in engineering practice. The multiclass neural network algorithm method based on the binary tree is one of the effective methods to solve the multiclassification problem. As shown in Figure 1, the binary tree structure classifier solves a complex multiclass problem into multiple two-class problems. A multiclass problem can be transformed into multiple two-category problems in various forms with various corresponding binary tree structures. For a k -category problem, the number of binary trees that can be constructed is $N_k = \prod_{i=1}^{k-1} 2 * i - 1$, $k > 2$. As shown from Figure 1, the classification performance of the neural network algorithm subclassifier of the upper node has a greater impact on the generalization of the entire classification model. If a classification error occurs at a node, the error will continue, resulting in a phenomenon of "error accumulation," making the next-level node lose its classification meaning. It can be seen that constructing a reasonable binary tree structure is essential to the correct classification of the model. In order to make the binary decision tree have the optimal level of performance and construct a reasonable binary tree hierarchy, the samples must be divided into two groups at the decision point in an approximate optimal level method even if the separability between the two type sample types in the

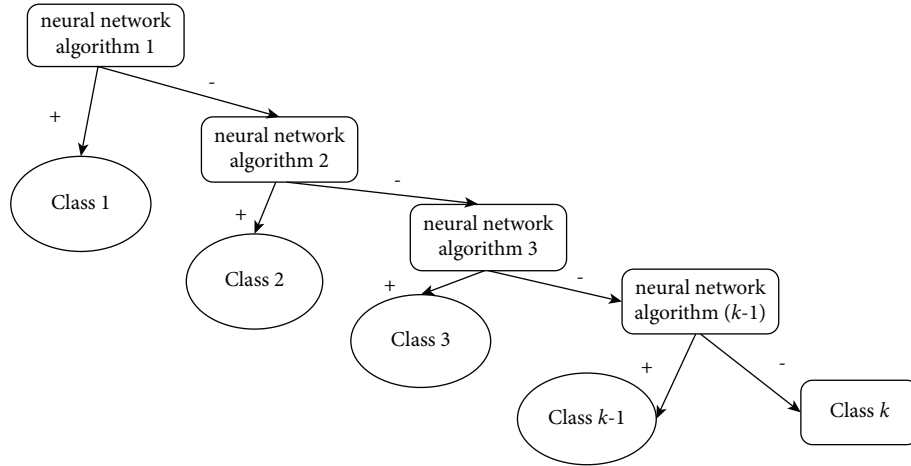


FIGURE 1: Classification map based on clustering-binary tree.

upper layer is strong. In so doing, the distance between the cluster centers of the two groups of samples is the largest, and the divergence of each group of samples is the smallest.

2.2.1. Definition of Distance. For given A class and B class ($x_a \in A, x_b \in B$), the distance between two samples can be expressed as $d(x_a, x_b)$. In the linear case, the distance between the two samples x_a and x_b is defined as follows:

$$d(x_a, x_b) = \|x_a - x_b\| = \sqrt{\sum (x_a^i - x_b^i)^2}. \quad (4)$$

In the case of nonlinearity, the distance between the two samples x_a and x_b is defined as follows:

$$d(x_a, x_b) = \sqrt{K(x_a, x_a) - 2(x_a, x_b) + K(x_b, x_b)}. \quad (5)$$

This paper adopts the idea of class distance in cluster analysis as the algorithm for generating binary trees. First, the class farthest from others is segmented, and the optimal hyperplane constructed at this time has good generalization.

Algorithm flow of multiclass neural network based on clustering-binary tree is as follows:

- (1) Calculate the distance between classes according to formulas (4) or (5): $d_{i,j}$ ($i, j = 1, 2, \dots, k, i \neq j$).
- (2) For each class, there are $(k - 1)$ class spacing values from other classes, and the class spacing values of each class are sorted in ascending order from small to large and renumbered. For example, the spacing $d_{i,j}$ ($i, j = 1, 2, \dots, k, i \neq j$) between the i -th class and other classes is sorted as $d_i^1 \leq d_i^2 \leq \dots \leq d_i^{k-1}$.
- (3) Compare the minimum class spacing of each category d_i^1 ($i = 1, 2, \dots, k$), and sort them in descending order from largest to smallest. When there are two or more categories with the same minimum category spacing d_i^1 , the sizes d_i^2 can be compared again and so on. For example, when $d_q^1 > d_p^1$, sort the q -th category in front of the p ; if the first $d_q^1 = d_p^1$, then compare d_q^2 and d_p^2 ; if $d_q^2 < d_p^2$, sort the p -th category in front of the q -th category so that the larger the difference, the

more the category partition. Thus, one can get the arrangement of all categories n_1, n_2, \dots, n_k .

- (4) According to the generated binary tree, a binary neural network training algorithm is used to construct the optimal hyperplane of the binary node. Take the n_1 -th sample as the positive sample set and other samples as the negative sample set. The neural network training algorithm is used to construct the binary neural network subclassifier at the root node. The i -th subclassifier takes the i -th sample as a positive sample and uses the $i + 1, i + 2, \dots, k$ -th sample as a negative sample to train the neural network i subclassifier until $(k - 1)$ -th subclassifier separates the $(k - 1)$ -th category from the k -th category. In this way, the recognition of multiple types of problems can be completed.
- (5) The multicategory classification ends and outputs the result.

3. Sand and Soil Discriminant Model Based on the Neural Network Algorithm

3.1. Analysis of Influencing Factors and Model Establishment. Sand liquefaction is a form of foundation failure caused by earthquake damages. It is an important content of geological engineering evaluation in earthquake areas. The liquefaction of saturated sand is a very complicated process with many influencing factors.

It can be roughly divided into three categories:

- (i) The nature of the sand layer, such as the type of soil, particle composition, and degree of compaction
- (ii) The buried depth of the soil layer and the groundwater level
- (iii) Seismic factors, such as earthquake intensity, epicenter distance, and earthquake duration

This paper proposes representative parameters from many influencing factors as the distinguishing index of sand liquefaction, including the seismic intensity I , epicenter

TABLE 1: Samples of training for sand earthquake liquefaction.

Serial number	Intensity I/grade	Epicenter distance $R \text{ (km)}$	Sand buried depth $d_s \text{ (m)}$	Groundwater level $d_w \text{ (m)}$	Number of hammers N/strike	Average particle size $D_{50} \text{ (mm)}$	Nonuniformity coefficient C_u	Dynamic shear stress ratio τ_d/σ'_v	Measured category	Machine learning result
1	8	87	3.1	1.6	2.3	0.12	1.54	0.123	II	II
2	7	78	3.9	0.9	4.2	0.08	3.21	0.132	I	I
3	8	79	2.3	1.2	3.2	0.17	1.32	0.112	II	II
4	8	81	1.8	0.8	2.5	0.18	2.33	0.185	I	I
5	9	82	2.3	0.6	1.8	0.12	4.12	0.156	II	II
6	7	79	8.2	1.8	5.6	0.31	2.45	0.125	III	III
7	7	108	11.9	1.6	20.0	0.12	7.12	0.175	III	III
8	8	82	3.6	1.6	17.0	0.13	1.75	0.132	IV	IV
9	9	86	8.8	1.3	17.0	0.16	1.62	0.175	IV	IV
10	8	92	4.0	0.9	13.0	0.14	1.32	0.164	III	III
11	7	111	5.8	2.8	8.0	0.12	1.42	0.124	II	II
12	7	98	9.2	1.5	10.0	0.14	2.12	0.266	II	II
13	9	65	5.3	1.5	8.0	0.12	2.62	0.232	I	I
14	8	64	2.0	0.8	9.0	0.12	1.36	0.212	II	II
15	7	45	2.6	1.6	6.0	0.32	2.12	0.111	II	II
16	8	35	2.61	0.6	12.0	0.25	1.75	0.325	I	I
17	8	75	1.8	1.2	7.0	0.15	2.12	0.133	III	III
18	9	106	8.5	3.0	28.0	0.23	3.01	0.285	III	III
19	7	32	3.8	0.9	6.0	0.16	1.74	0.325	II	II
20	8	25	6.8	0.9	9.0	0.12	4.11	0.311	I	I
21	7	109	13.8	2.8	15.0	0.18	2.65	0.162	III	III
22	9	42	4.5	3.2	25.0	0.32	5.41	0.156	IV	IV
23	9	45	1.3	0.9	13.0	0.19	2.65	0.132	III	III
24	8	120	5.1	2.8	12.0	0.21	2.23	0.174	II	II
25	7	110	3.3	3.1	1.2	0.16	2.45	0.133	II	II
26	7	46	4.3	2.9	13.0	0.22	1.98	0.173	III	III
27	8	23	14.8	3.9	35.0	0.15	2.31	0.284	IV	IV
28	8	110	14.5	1.2	21.0	0.13	1.93	0.122	III	III
29	8	65	5.3	3.7	20.0	0.20	1.85	0.186	IV	IV
30	8	25	3.6	2.3	16.0	0.25	2.65	0.196	III	III

distance R , sand buried depth d , groundwater level d_w , standard penetration number N , average particle size D_{50} , nonuniformity coefficient C_u , and the dynamic shear stress ratio $(\tau_d/\sigma'_v)d$. The eight variables are used as classification indicators. Such selection helps avoid that attributes with a large value range are more dominant than those with a small value range.

First, by performing normalization preprocess on each attribute of the sample data and adjusting linearly to $[-1, +1]$, the sand liquefaction evaluation can be divided into 4 grades, which are severe liquefaction (I), moderate liquefaction (II), slight liquefaction (III), and no liquefaction (IV).

The use of neural network algorithms to discriminate sand liquefaction is to find the nonlinear relationship between influencing factors and sand liquefaction. Assuming that n samples are collected, the problem is abstracted as the mapping from attribute set X to classification set Y ; that is, the index matrix is $X_{n \times 8}$, $Y = \{I, II, III, IV\}$. This paper sorts out 40 typical examples from the literature of the Wenchuan Earthquake and divides them into training sample sets and test sample sets. Among them, 30 samples are used for learning machine learning, as shown in Table 1, and the other 10 samples are used to test the model performance.

3.2. Sample Learning. There are 4 levels of sand liquefaction, indicating a 4-classification problem. A decision binary tree with 3 classifiers needs to be established to divide the sample into 4 subsets. Through the learning of 30 samples, various classification functions are obtained, and the sand liquefaction discriminant model is established based on the neural network algorithm of the clustering-binary tree.

The parameters of the neural network algorithm are mainly kernel function parameters and penalty factor C . In the research, it is found that for different training parameters, the learning efficiency and generalization ability of neural network algorithms are different. In this paper, the radial basis function is selected as the kernel function through a trial algorithm, namely:

$$K(x, x_i) = \exp \left\{ -\frac{|x - x_i|^2}{\sigma^2} \right\}, \quad (6)$$

where x_i and x_j are the training input and σ is the width of the kernel function.

In this way, the training parameters of the support vector machine in this paper are σ and C . The size of σ affects the output response interval of the sample. When σ is small, the response interval is narrow, leading to less risky

TABLE 2: Samples of testing for sand earthquake liquefaction.

Serial number	Intensity I/grade	Epicenter distance $R \text{ (km)}$	Sand buried depth $d_s \text{ (m)}$	Groundwater level $d_w \text{ (m)}$	Number of hammers N/strike	Average particle size $D_{50} \text{ (mm)}$	Nonuniformity coefficient C_u	Dynamic shear stress ratio τ_d/σ'_v	Measured category	Machine learning result
1	8	78	5.2	1.2	8.0	0.16	2.15	0.15	III	III
2	8	21	4.2	1.3	6.0	0.13	2.89	0.275	I	I
3	7	68	3.2	1.5	5.0	0.11	1.95	0.135	III	III
4	9	49	2.8	1.2	6.0	0.14	2.13	0.135	II	II
5	7	52	6.5	2.6	9.0	0.18	2.30	0.121	III	III
6	9	52	4.2	1.8	9.0	0.28	2.13	0.153	IV	IV
7	8	32	3.9	1.3	8.0	0.13	2.07	0.265	II	II
8	8	68	2.6	1.1	7.0	0.15	0.63	0.165	III	III
9	9	57	4.8	1.2	7.0	0.10	4.89	0.356	II	II
10	8	75	10.2	1.9	10.0	0.15	2.35	0.165	III	III

classification. The penalty factor C , which represents the degree of punishment for errors, is a compromise between training error and promotion ability by controlling training accuracy. The larger the C is, the greater the penalty for misclassification is.

The value of σ and C can be determined according to the samples during the training process. This paper uses the variable increment iteration method based on the number of misclassified samples to obtain $\sigma=0.28$ and $C=300$. Through the learning of 30 samples, the error-free classification of the sample is given in Table 1.

3.3. Sample Prediction. When using the clustering-binary tree neural network algorithm for classification, starting from the root classifier, the attributes of the unknown samples are substituted into the classification function to test their values one by one.

When the test value is 1, it reaches the leaf node and stops moving forward, indicating that the sample is the class represented by the leaf node. When the test value is -1 , one must go down the branch until reaching a certain leaf node. The other 10 samples are input as test samples into the decision binary tree, and the classification of each sample is shown in Table 2. One can see that the learning results are consistent with the actual ones. Therefore, the method in this paper can correctly distinguish multiple types of problems, indicating that the promotion performance of the support vector machine is good.

4. Conclusion

In this paper, a multiclass neural network is introduced into the discrimination of sand liquefaction. During the modelling process, it was found that the promotion performance of the multiclass neural network model based on the binary tree is related to the binary tree structure. The learning efficiency and promotion performance vary with the binary tree structure and the model parameter. This paper adopts the idea of class distance in cluster analysis as the algorithm of generating binary tree and establishes a multiclass neural network to predict the sand liquefaction based on cluster-

binary tree. The model establishes the nonlinear relationship between sand liquefaction and various influencing factors through the learning of limited samples. The research results show that the required number of classifiers in the clustering-binary tree neural network is small (only 3 classifiers are needed for 4 types of problems), the repetitive training samples are few, the binary tree hierarchy is reasonable, the classification accuracy is high, and the generalization is good. Thus, the proposed model predicts the liquefaction level accurately and can be used for sandy soil.

The neural network algorithm method is based on the VC theory of statistical theory and the principle of minimum structural risk. It seeks the best compromise between complexity and learning ability based on limited sample information and has a good generalization ability. As a new machine learning method, the neural network algorithm has broad application prospects in geotechnical engineering and other fields because of its unique advantages.

Data Availability

The data are generated from the field and can be available from the corresponding author upon request.

Conflicts of Interest

The authors declare that there are no conflicts of interest regarding the publication of this paper.

Acknowledgments

This work was supported by Beijing Jiaotong University.

References

- [1] Y. Zhang, Y. Xie, Y. Zhang, J. Qiu, and S. Wu, "The adoption of deep neural network (DNN) to the prediction of soil liquefaction based on shear wave velocity," *Bulletin of Engineering Geology and the Environment*, vol. 80, no. 6, pp. 5053–5060, 2021.
- [2] Y.-g. Zhang, J. Qiu, Y. Zhang, and Y. Wei, "The adoption of ELM to the prediction of soil liquefaction based on CPT," *Natural Hazards*, vol. 107, no. 1, pp. 539–549, 2021.

- [3] Y. Zhang, J. B. Qiu, Y. G. Zhang, and Y. L. Xie, "The adoption of a support vector machine optimized by GWO to the prediction of soil liquefaction," *Environmental Earth Sciences*, vol. 80, 2021.
- [4] Y. Zhang, J. Qiu, Y. Zhang, and R. Liao, "The establishment of a constitutive model of sand under monotonic loading by adopting the support vector machine (SVM)," *Arabian Journal for Science and Engineering*, vol. 25, pp. 1–15, 2021.
- [5] M. Ishac and A. Heidebrecht, "Energy dissipation and seismic liquefaction in sands," *Earthquake Engineering & Structural Dynamics*, vol. 10, no. 1, pp. 59–68, 2010.
- [6] J. Wang, T. Zuo, X. Li, Z. Tao, and J. Ma, "Study on the fractal characteristics of the pomegranate Biotite Schist under impact loading," *Geofluids*, vol. 2021, Article ID 1570160, 8 pages, 2021.
- [7] R. Dobry, R. Ladd, and D. Powell, *Prediction of Pore Water Pressure Buildup and Liquefaction of Sands during Earthquakes by the Cyclic Strain Method*, National Bureau of Standards Building Science Series, Annapolis, MA, USA, 1982.
- [8] P. Robertson and C. Wride, "Evaluating cyclic liquefaction potential using the cone penetration test," *Canadian Geotechnical Journal*, vol. 35, no. 3, pp. 442–459, 1988.
- [9] X. Ling, C. Wang, and Z. Wang, "Study on large-scale shaking table proportional model test for free-ground liquefaction arisen from earthquake," *Earthquake Engineering & Engineering Vibration*, vol. 23, no. 6, pp. 138–143, 2003.
- [10] I.-S. Ha, S. M. Olson, M.-W. Seo, and M.-M. Kim, "Evaluation of reliquefaction resistance using shaking table tests," *Soil Dynamics and Earthquake Engineering*, vol. 31, no. 4, pp. 682–691, 2011.
- [11] H. Yu, W. Mao, and M. Huang, "Triaxial tests on the fluidic behavior of post-liquefaction sand," *Environmental Earth Sciences*, vol. 67, no. 8, pp. 2325–2330, 2012.
- [12] H. Qing, L. Heng, and Y. Zhang, "Liquefaction evaluation based on dynamic triaxial test and soil seismic response," *Journal of Geodesy & Geodynamics*, vol. 242017, in Chinese.
- [13] Y. Zhou, D. Zhao, and B. Li, "Fatigue damage mechanism and deformation behaviour of granite under ultrahigh-frequency cyclic loading conditions," *Rock Mech Rock Eng*, vol. 54, 2021.
- [14] A. I. Lawal, S. Kwon, O. S. Hammed, and M. Adebayo Idris, "Blast-induced ground vibration prediction in granite quarries: an application of gene expression programming, ANFIS, and sine cosine algorithm optimized ANN," *International Journal of Mining Science and Technology*, vol. 31, no. 2, pp. 265–277, 2021.
- [15] V. A. Temeng, Y. Y. Ziggah, and C. K. Arthur, "A novel artificial intelligent model for predicting air overpressure using brain inspired emotional neural network," *International Journal of Mining Science and Technology*, vol. 30, no. 5, pp. 683–689, 2020.
- [16] R. Kumar, P. K. Mandal, A. Narayan, and A. J. Das, "Evaluation of load transfer mechanism under axial loads in a novel coupler of dual height rock bolts," *International Journal of Mining Science and Technology*, vol. 31, no. 2, pp. 225–232, 2021.
- [17] X. Sun, C. Zhao, Y. Zhang, F. Chen, S. Zhang, and K. Zhang, "Physical model test and numerical simulation on the failure mechanism of the roadway in layered soft rocks," *International Journal of Mining Science and Technology*, vol. 31, no. 2, pp. 291–302, 2021.
- [18] L. Adam, "Proactive interburden fracturing using UIS drilling with validation monitoring," *International Journal of Mining Science and Technology*, vol. 31, no. 1, pp. 3–7, 2021.
- [19] X. Li, Q. Li, J. Wang, Z. Wang, H. Wang, and Z. Tao, "Influence of hole arrangement on the section of cavity formed by cutting blast," *Geofluids*, vol. 21, 2021.
- [20] J. Ma, X. Li, J. Wang et al., "Experimental study on vibration reduction technology of hole-by-hole presplitting blasting," *Geofluids*, vol. 15, 2021.
- [21] Y. Zhang and L. Yang, "A novel dynamic predictive method of water inrush from coal floor based on gated recurrent unit model," *Natural Hazards*, vol. 105, no. 2, pp. 2027–2043, 2020.
- [22] Y.-g. Zhang, J. Tang, R.-p. Liao et al., "Application of an enhanced BP neural network model with water cycle algorithm on landslide prediction," *Stochastic Environmental Research and Risk Assessment*, vol. 35, no. 6, pp. 1273–1291, 2020.
- [23] Y.-g. Zhang, J. Tang, Z.-y. He, J. Tan, and C. Li, "A novel displacement prediction method using gated recurrent unit model with time series analysis in the Erdaohe landslide," *Natural Hazards*, vol. 105, no. 1, pp. 783–813, 2020.
- [24] X. Xue and X. Yang, "Seismic liquefaction potential assessed by support vector machines approaches," *Bulletin of Engineering Geology and the Environment*, vol. 75, no. 1, pp. 153–162, 2016.
- [25] J.-S. Chou and J. P. P. Thedja, "Metaheuristic optimization within machine learning-based classification system for early warnings related to geotechnical problems," *Automation in Construction*, vol. 68, no. 8, pp. 65–80, 2016.
- [26] X. Xue and E. Liu, "Seismic liquefaction potential assessed by neural networks," *Environmental Earth Sciences*, vol. 76, no. 5, p. 192, 2017.
- [27] Y. Yang, L. Chen, R. Sun, Y. Chen, and W. Wang, "A depth-consistent SPT-based empirical equation for evaluating sand liquefaction," *Engineering Geology*, vol. 221, pp. 41–49, 2017.
- [28] G. Ali and R. Jahanpour, "Evaluation of liquefaction potential of marine sandy soil with piles considering non-linear seismic soil-pile interaction; a simple predictive model," *Marine Georesources & Geotechnology*, vol. 38, pp. 1–22, 2019.
- [29] A. Rahbarzare and M. Azadi, "Improving prediction of soil liquefaction using hybrid optimization algorithms and a fuzzy support vector machine," *Bulletin of Engineering Geology & the Environment*, vol. 78, 2019.
- [30] J. Hu and H. Liu, "Identification of ground motion intensity measure and its application for predicting soil liquefaction potential based on the Bayesian network method," *Engineering Geology*, vol. 248, pp. 34–49, 2019.
- [31] J. Hu and H. Liu, "Bayesian network models for probabilistic evaluation of earthquake-induced liquefaction based on CPT and vs databases," *Engineering Geology*, vol. 11, 2019.

Research Article

Influence of Water-Structure and Soil-Structure Interaction on Seismic Performance of Sea-Crossing Continuous Girder Bridge

Jie Guo,^{1,2} Kunpeng Wang ,³ Hongtao Liu,⁴ and Nan Zhang ¹

¹School of Civil Engineering, Beijing Jiaotong University, Beijing 100044, China

²China Railway 14th Bureau Group Co. LTD., Jinan 250101, China

³CCCC Highway Bridges National Engineering Research Centre Co., Ltd., Beijing 100120, China

⁴Beijing University of Civil Engineering and Architecture, Beijing 102612, China

Correspondence should be addressed to Nan Zhang; nzhang@bjtu.edu.cn

Received 11 October 2021; Revised 27 October 2021; Accepted 11 November 2021; Published 7 December 2021

Academic Editor: Qian Chen

Copyright © 2021 Jie Guo et al. This is an open access article distributed under the Creative Commons Attribution License, which permits unrestricted use, distribution, and reproduction in any medium, provided the original work is properly cited.

Based on the Hong Kong-Zhuhai-Macao project, considering the fluid-structure interaction and soil-structure interaction, the seismic response of a sea-crossing continuous girder bridge is analyzed. Three-dimensional nonlinear numerical bridge model is developed, in which the hydrodynamic force is represented by added mass and pile-soil interaction is represented by p - y elements. Meanwhile, stratification of soil is considered in the free field analysis. Through the comparison of responses of the bridge cases, the effects of earthquake-induced hydrodynamic force and pile-soil interaction are studied. For the influence of hydrodynamic force, the results show that it is relatively slight as compared with pile-soil interaction; moreover pile foundation is more sensitive to it than other bridge components. The influence of pile-soil interaction is relatively significant. When both of the interactions are considered, the influence is not a simple superposition of acting alone, so it is recommended to consider both factors in dynamic analysis.

1. Introduction

With the development of economy and the necessity of coastal regional linkages, a certain number of sea-crossing bridges have been constructed around the world in the last few decades. Earthquake risk is usually very high in coastal areas, due to movement and collisions between continental and oceanic plate margins [1]. Earthquake brings great challenge to the safety of bridge structure [2]. In addition, compared with the bridge on land, the sea-crossing bridge is always in deep water. The complex environment of the sea-crossing bridge also means that the seismic response and design of the bridge are quite different from those of the conventional bridge [3]. However, most previous studies focused on the seismic response of bridges constructed on onshore sites [4, 5]; a comprehensive study on the seismic response of sea-crossing continuous girder bridge is rarely reported in the literature.

In the seismic analyses and design of bridge, how to consider pile-soil interaction is always involved [6]. Currently, the following two methods are mostly adopted in the seismic design [7]. One is connecting the foundation and the soil with a simple spring; another is more simply assuming that the foundation and the soil are consolidated. All the above assumptions ignore dynamic soil-structure interaction (SSI) [8], and a large number of seismic disaster data show that this assumption is unreasonable [9, 10]. In addition, Makris et al. [11] analyzed the response of the Painter Street Bridge located in California, and results showed the significance of reasonable consideration of the pile-soil interaction. Hutchinson et al. [12] studied the seismic response of viaduct structure supported by expanded bored pile considering soil-pile interaction. Soneji and Jangid [13] studied the influence of soil-structure interaction on seismic performance of seismic-isolated cable-stayed bridge. The results showed that the soil had a significant impact on the dynamic response of bridge, and ignoring the pile-soil

interaction effect might underestimate the displacement of the bridge. Using the improved Penzien model to simulate the soil-structure interaction, Chen et al. [14] set up bridge models of high-speed railway of multispan simply supported. The seismic responses of the models show that the influence of the SSI on seismic responses of the bridge cannot be ignored.

There is also a need for special consideration of interaction between the submerged structure and fluid under seismic excitation. The dynamic force is called earthquake-induced hydrodynamic force [15]. The study of the hydrodynamic force started from the dam-water interaction [16]. With the continuous development of deep-water bridges, researchers began to pay attention to the hydrodynamic force on cylinders [17]. The interaction force is related to the structures, fluid, ground motions, and boundary conditions, so accurate hydrodynamic force can be obtained by fluid-structure coupling analysis [18]. However, the calculation cost is too high, which is not suitable for engineering. The simplified hydrodynamic calculation method based on the radiation wave theory proposed by Liaw and Chopra [19] can meet the requirements and accuracy of engineering [20]. According to the radiation wave theory, when considering the compressibility of water, earthquake-induced hydrodynamic force is a frequency dependent function. Du et al. [21] proposed an accurate and efficient time-domain model to transform while many researchers find that water compressibility can be ignored in problems for relatively flexible and slender structures such as bridge piers and piles [19, 22]. Later, Li and Yang [23], Jiang et al. [24], and Wang et al. [25] studied the fitting calculation formulas for circular cylinders in incompressible and nonviscous fluid based on the radiation wave theory. In bridge engineering, most of the underwater components are columns with noncircular cross sections. Zhao et al. [26] established a simplified formula for the hydrodynamic force of rectangular column by curve fitting numerical solution. Huang and Li [27] studied the influence of water on the dynamic response of bridge pier. Based on the above researches, the influences of pile-soil and water-structure interaction on deep-water continuous rigid frame bridge in reservoir area was analyzed by Wu et al. [28].

However, there still lack of research which discusses the effect of water-structure and pile-structure interaction on the dynamic response of actual sea-crossing engineering projects, especially for the most commonly and widely used continuous girder bridge [29]. Therefore, in this paper, on the foundation of previous researchers, based on the Hong Kong-Zhuhai-Macao bridge engineering, the influences of the water-structure interaction and pile-structure interaction on the response of multispan continuous girder bridge are examined.

2. Seismic Analysis Methodology

2.1. Hydrodynamic Force. For slender columns such as bridge piers, it is reasonable that compressibility and viscosity of water and the free surface waves can be neglected when calculating the earthquake-induced hydrodynamic

force. Thus, based on the radiation hydrodynamic theory, the water-cylinder interaction force can be expressed as product of an added mass of water and the acceleration of the cylinder. Namely, when considering water-structure interaction, the dynamic equation of the structure is expressed as

$$[M_s + M_w]\{\ddot{u}_s\} + [C_s]\{\dot{u}_s\} + [K_s]\{u_s\} = -[M_s + M_w]\{\ddot{u}_g\}, \quad (1)$$

where M_s is the mass matrix of structure; M_w is the added mass matrix of hydrodynamic force, as it is related to the elastic deformation of the structure; it is a spatially coupled off-diagonal mass matrix; \ddot{u}_s is the acceleration vector of structure; C_s is the damping matrix of structure; \dot{u}_s is the velocity vector of structure; K_s is the stiffness matrix of structure; u_s is the displacement vector of structure; and \ddot{u}_g is the ground motion acceleration vector.

Due to the off-diagonal of M_w , there are difficulties in engineering calculation. In the present literature, the precision of the centralized diagonalization method with rigid column assumption meets the engineering requirement [20]. Therefore, this paper adopts the above simplified method to obtain the added mass of interaction.

The cross section of the bridge pier is nearly rectangular. The two sides of the rectangular section are a and b , respectively, where a is the length of the side perpendicular to the direction of the ground motion. The simplified formula of the added mass at height y from the bottom of the water can be expressed as [26]

$$m_w = 4\rho a^2 d_1 \left[1 - \frac{y}{h} e^{d_2 (y/h - 1)} \right], \quad (2)$$

in which ρ is the density of water; h is the depth of water; d_1 and d_2 are fitting coefficients, and the expressions are as follows:

$$\begin{aligned} d_1 &= m_1 \left(\frac{2a}{h} \right)^{m_2} + 0.412 \left(\frac{a}{b} \right)^{-1.012} + 0.952. \\ d_2 &= n_1 \left(\frac{2a}{h} \right)^{-1.26} + n_2. \\ m_1 &= -0.35 \left(\frac{a}{b} \right)^{-1.092} - 0.198. \\ m_2 &= 0.766 e^{0.0471a/b} - 0.782 e^{-1.401a/b}. \\ n_1 &= -0.0157 \left(\frac{a}{b} \right)^2 + 0.194 \frac{a}{b} + 0.846. \\ n_2 &= 0.004 \left(\frac{a}{b} \right)^2 - 0.0533 \frac{a}{b} + 2.143. \end{aligned} \quad (3)$$

2.2. Pile-Soil Interaction. Numerical analysis and simplified method are commonly used to analyze pile-soil dynamic interaction [30]. Using 2D or 3D continuum numerical simulation tends to be much more computationally consuming and the result is not easy to converge [31]. As this

paper mainly focuses on the dynamic response of bridge structure, simplified method is adopted to consider the pile-soil interaction. Most simplified models are put forward based on beam on nonlinear Winkler foundation, among which p - y method is the most widely used and has relatively high accuracy [32]. The method of p - y curves generally refers to the general terms including p - y element (simulating the lateral pile-soil action), t - z element (simulating the axial friction), and q - z element (simulating the pile tip resistance).

The formula of p - y curve of the same pile foundation is different for different soils. Here is a brief introduction to formulas for clay and sand, respectively, which are used in this paper. For clay under cyclic loading, the ultimate soil resistance (p_u) per unit length of pile is [33]

$$p_u = \min \left(\begin{array}{c} \left(3 + \frac{r'}{c_u} x + \frac{J}{D} x \right) c_u D \\ 9c_u D \end{array} \right), \quad (4)$$

where r' is the effective weight of soil; c_u is the undrained shear strength of soil; x is the depth of pile node; J is a constant and is taken as 0.5 according to recommendation. D is the diameter of pile. The force-displacement curve of p - y element is expressed as

$$\begin{aligned} y \leq 3y_{50}: \quad \frac{p}{p_u} &= 0.5 \left(\frac{y}{y_{50}} \right)^{1/3} \\ &\cong 3y_{50} < y < 15y_{50}: \quad p = 0.72p_u \left(\frac{x}{x_r} \right) \\ x < x_r: \\ y > 3y_{50}: \\ &\cong y \geq 15y_{50}: \quad \text{The same constant} \\ x \geq x_r: \quad p &= 0.72p_u \end{aligned} \quad (5)$$

where y is pile deformation; y_{50} is the lateral displacement of pile at half of the ultimate soil resistance, and $y_{50} = 2.5\varepsilon_{50}D$, ε_{50} is the strain of soil at half of the maximum theoretical stress; p is the soil resistance; x_r is the critical depth and defined as [34]

$$x_r = \left(\frac{6c_u D}{\gamma' D + Jc_u} \right), \quad (6)$$

For the p - y curve of sand under cyclic load, the ultimate soil resistance (p_u) is also determined first. Combining the simple wedge-type failure model and flow-through type failure model, p_u is given by

$$p_u = \min \left(\begin{array}{c} \left(\frac{C_1}{D} + C_2 \right) r' x \\ C_3 r' x \end{array} \right), \quad (7)$$

where C_1 C_2 C_3 are the coefficients that change with the friction angle, and the values are referenced to American Petroleum Institute (API) recommendations [34]; the meanings of the same parameters are as above.

The force-displacement curve of p - y element is expressed as

$$p = ap_u \tanh \left(\frac{kx}{ap_u} y \right), \quad (8)$$

where a is the correction coefficient, with a value of 0.9; k is the initial modulus of subgrade reaction.

The t - z curve of clay used in this paper is briefly described as follows. The ultimate friction resistance (f_{\max}) is

$$f_{\max} = \alpha_z c_u \leq 263kPa. \quad (9)$$

The force-displacement curve is defined as follows:

$$\frac{f}{f_{\max}} = \begin{cases} 0.593157 * \frac{R}{0.12}, & R \leq 0.12 \\ \frac{R}{(0.095155 + 0.892937 * R)}, & R \leq 0.74 \\ 0.978929 - 0.115817 * (R - 0.74), & R \leq 2.0 \\ 0.833, & R > 2.0 \end{cases} \quad (10)$$

where f is the soil resistance; R is relative deformation, and $R = 100 * z/D$, where z is the deformation of pile [35].

The t - z curve of sand is described as follows. The ultimate friction resistance is [32]

$$f_{\max} = K\sigma'_v \tan \left(\frac{3}{4} \phi \right), \quad (11)$$

where K is pressure coefficient of soil; σ'_v is the effective vertical stress of soil; ϕ is the friction angle of soil [36].

The force-displacement curve is defined as follows:

$$f = f_{\max} \left(2\sqrt{\frac{z}{0.51}} - \frac{z}{0.51} \right). \quad (12)$$

The q - z curve of sand at pile top is briefly described as follows. The ultimate resistance is [31]

$$q_{\max} = \frac{1.27}{D} q'_{\max}$$

$$q'_{\max} = \begin{cases} 57.5 * N_{SPT} & 0 \leq N_{SPT} \leq 50 \\ 2900 & N_{SPT} > 50 \end{cases} \quad (13)$$

$$\frac{q}{q_{\max}} = -1.079 \times 10^{-4} \times R^4 + 3.558 \times 10^{-3} \times R^3 - 4.512 \times 10^{-2} \times R^2 + 0.349 \times R, \quad (14)$$

where q is the resistance of soil.

For pile group foundation, when pile spacing is less than eight times the pile diameter, the so-called pile group effect needs to be considered generally [37]. Pile group effect refers to the phenomenon that the bearing capacity of pile group is less than the sum of the capacity of single pile [30]. In this paper, the widely used “p-multiplier” method is applied to consider the pile group effect [38], and the parameter values are determined by referring to the experiment conducted by Brown et al. [39].

3. Bridge Model and Analysis Cases

3.1. Prototype and Numerical Model of Bridge. A six-span continuous girder bridge at the nonnavigable spans of the Hong Kong-Zhuhai-Macao link is adopted as the example in this study. Actually, the site conditions, heights of pile foundation, and bridge piers have some differences along the longitudinal direction of the bridge. Here the differences are ignored, and the soil is simplified as layered soil. For the influence of adjacent bridge spans, only the weight of girder is considered. The bridge has six spans of 85 m each, so the total length is 510 m. The dimensions of the bridge and its main sections are shown in Figure 1. The main girder is arranged in two parts with the cross section of steel-concrete composite box, the steel deck is the Q345qD steel [40], and the concrete is the C60 concrete [41]. The bearing is the lead rubber bearing (LRB). The bridge pier is rectangular hollow with one longitudinal web, the longitudinal reinforcement is HRB335 [42], and the concrete is C50 [41]. The bridge cap is connected with 2×3 reinforced concrete pile foundation, and the pile is made of C35 concrete [41].

The pier is located in an environment where the normal water level is about 20 m. The site conditions of the soil layers where the pile foundation is located are shown in Figure 2, and the main mechanical parameters of soil are shown in Table 1. The three-dimensional finite element model of the bridge is implemented in the commercial finite element software ABAQUS, as shown in Figure 3. Beam elements are used for main girders, piers, and pile foundations, among which elastoplastic damage model is used for concrete material and elastic model is used for reinforcement. The bearings are simulated by bilinear connection elements. The pile-soil interaction is represented by nonlinear springs based on the p - y method described above.

where N_{SPT} is the blow count of standard penetration test (SPT).

The force-displacement curve is defined as follows:

3.2. Ground Motions and Analysis Cases. According to Figure 2 and Table 1, the average velocity of shear wave in the top 30 m of soil (v_s) in the bridge construction site is 103 m/s. Three ground motion records are selected from the PEER Strong Motion Database [42], and v_s of the records ranges from 114 m/s to 133 m/s. The three records are the EW component of Chuetsu-oki seismic record measured at MYG017 station in 2007, the 90° component of Yountville seismic record measured at APEEL 2-Redwood City station in 2000, and the EW component of Niigata seismic record measured at KNG002 station in 2004. Besides, the peak ground accelerations of the above records are uniformly adjusted to 2 m/s^2 . The time history of acceleration and the Fourier amplitude spectrum of Chuetsu-oki record are shown in Figure 4.

The free ground seismic response of layered soil is obtained by EERA analysis. Here, only the longitudinal bridge response is considered, so the free field response at the corresponding soil depth is input at the free end of the p - y elements.

Four cases are considered in the paper, as shown in Table 2. When pile-soil interaction is not considered, the model is consolidated at the bottom of the piers.

4. Numerical Results and Discussions

4.1. Influence of Water-Structure Interaction. By comparing the responses of Case 1 and Case 2 in Table 2, the influence of water-structure interaction which neglects pile-soil interaction is obtained. Figure 5 shows the time history of absolute displacement of pier No. 4 at top under Chuetsu-oki record. It can be found that the hydrodynamic force slightly changes the dynamic response of the structure. The periodic characteristics, the amplitudes, and time of the peak response are all changed. Combining with Table 3 (the fundamental periods and corresponding change rates of bridge under cases), the elongation ratio of hydrodynamic force to the fundamental period is 1.8%.

Figure 6 shows the bending moment envelopes of piers No. 1 and No. 4 under the excitation of Chuetsu-oki records. As can be seen, the responses of bending moment along the whole height are slightly increased by the hydrodynamic force. In order to reflect the influence more intuitively, the discrepancy rate of response is defined as follows. The average value of maximums of the envelopes under the three seismic excitations is denoted as the peak response value

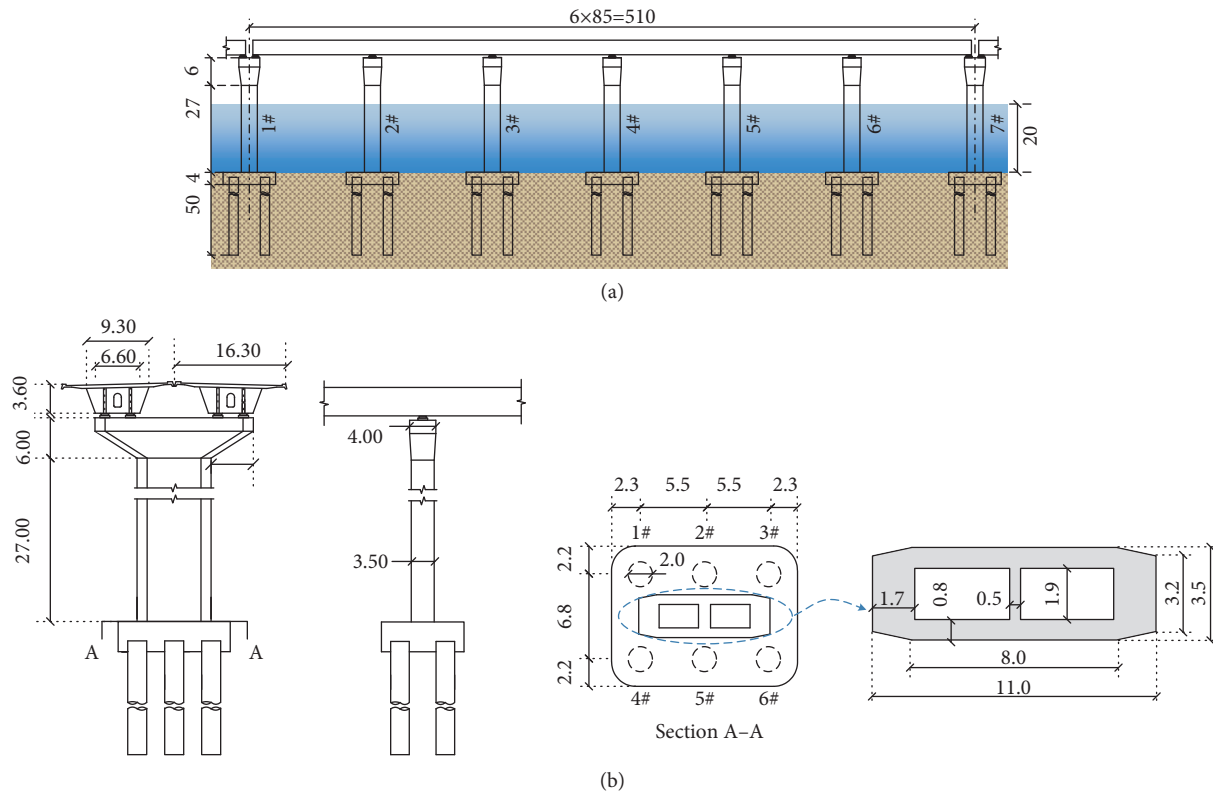


FIGURE 1: Schematic diagram of bridge and the main sections (unit: m): (a) elevation view and (b) schematic diagram of component dimensions.

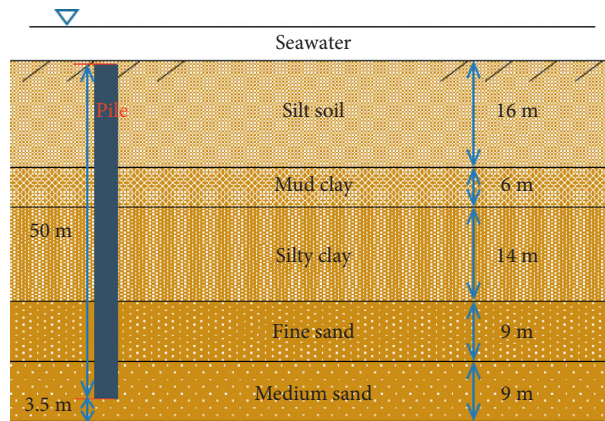


FIGURE 2: Schematic diagram of the soil layers.

TABLE 1: Main parameters of soil layers.

Soil layer	Soil type	Effective heavy (kN/m^3)	Shear wave velocity (m/s)	Frictional angle ($^\circ$)	Undrained shear strength (kPa)
Silt soil		9.4	80	—	9
Mud clay	Clay	12.2	110	—	21
Silty clay		12.8	210	—	28
Fine sand	Sand	14.0	250	32	—
Medium sand		16.0	340	36	—

(Re_p) of the case. The response discrepancy rate for Case- i and Case- j is defined as $(Re_p \text{ of Case-}i - Re_p \text{ of Case-}j)/(Re_p \text{ of Case-}j)$. If the rate is positive, it means the response of Case- i

is larger than that of Case- j ; if the rate is negative, it means the response of Case- i is smaller. The discrepancy rates for Case 2 and Case 1 are shown in Table 4. Due to the symmetry

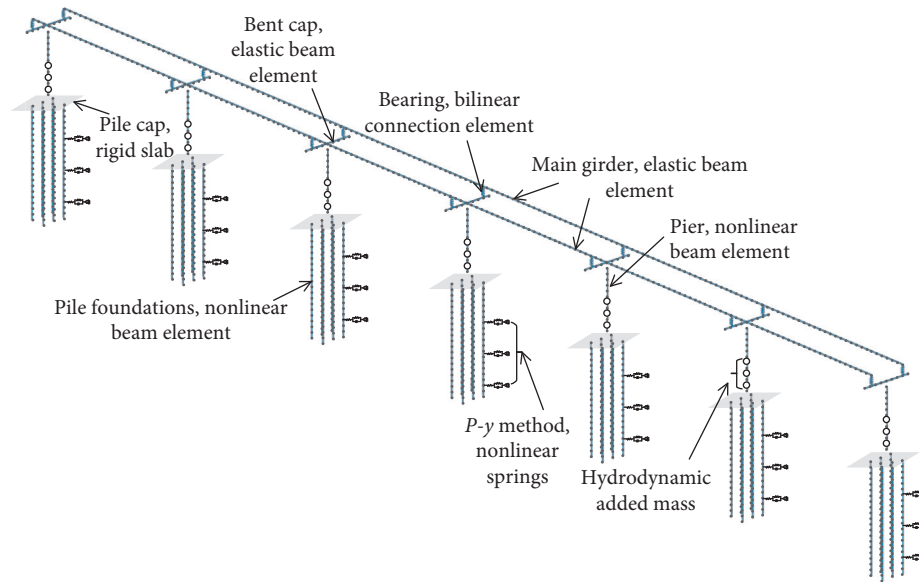


FIGURE 3: Finite element model of the example.

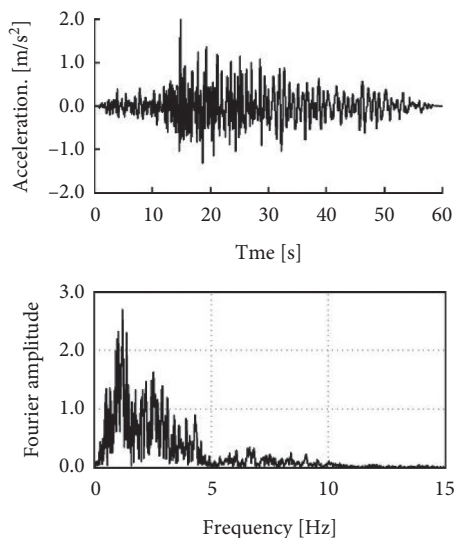


FIGURE 4: Ground motion acceleration of Chuetsu-oki and its Fourier amplitude spectrum.

of the structure, the rates of pier Nos. 1 and 5, pier Nos. 2 and 6, and pier Nos. 3 and 7 are similar, so only the rates of pier Nos. 1 to 4 are listed in the table. The discrepancy rates of displacement and bending moment are both within 5%, and the rates of bending moment are slightly less than those of displacement.

By comparing the responses of Case 3 and Case 4 in Table 2, the influence of water-structure interaction is obtained when pile-soil interaction is considered. According to Table 3, the elongation ratio of hydrodynamic force to the fundamental period is 1.6%, which is slightly lower than that when pile-soil interaction is ignored.

Figure 7 shows the envelopes of relative displacement of pier Nos. 1 and 4, and Figure 8 shows the displacement of corresponding pile No. 1. The pile foundation numbers are

shown in Figure 1. As can be seen, the hydrodynamic force slightly reduces the deformation of the piers along the whole height, while moderately increases the deformation of the piles. The response discrepancy rates for Case 4 and Case 3 are listed in Table 5. It can be seen that the reduction effect of water-structure interaction on pier deformation is within 5%; meanwhile the enlargement effect on pile is in a range of 7%~14%.

Figure 9 shows the envelopes of bending moment of pier Nos. 1 and 4, and Figure 10 shows the bending moment of corresponding pile No. 1. As can be seen, the hydrodynamic force changed the response of piers and piles which may increase or decrease in the height range of the components. Combined with Table 5, the change rates of piers are all positive and within 5%; that of pile foundation could be positive or negative, and the absolute value is less than 10%.

By comparing the responses of displacement and bending moment, it can be found that the influence of hydrodynamic force on displacement is greater than that of bending moment. By comparing the responses of bridge pier and pile foundation, it can be found that the effects of water-structure interaction on the two are not consistent; that is, hydrodynamic force may increase the responses of piles while decreasing the responses of piers, and the opposite is also true. However, the influence on pile response is greater in the degree than that of bridge pier. Through the above two comparisons, it is apparent that, considering pile-soil interaction, the influence of hydrodynamic force on bridge response is greater.

4.2. Influence of Pile-Soil Interaction. Based on the responses of Case 1 and Case 3, the influence of pile-soil interaction without water surrounded is studied. Figure 11 is the time history of bending moment at the bottom of pier No. 4. It can be seen that pile-soil interaction significantly changed the bending moment response of the structure. And the

TABLE 2: Cases analyzed.

Case number	Depth of water (m)	Pile-soil interaction
1	0.0	None
2	20.0	None
3	0.0	Being
4	20.0	Being

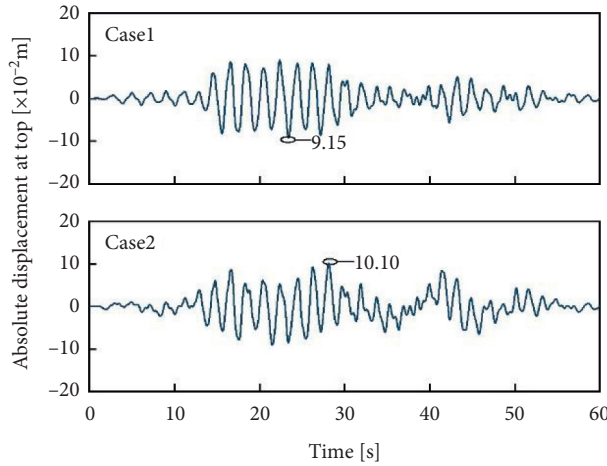


FIGURE 5: Absolute displacement time histories of pier No. 4 in Cases 1 and 2.

TABLE 3: Fundamental periods and the elongation ratios.

Item	Case 1	Case 2	Case 3	Case 4
Fundamental period (s)	1.71	1.74	3.18	3.23
Change rate (%)	—	1.8 (relative to Case 1)	86.0 (relative to Case 1)	1.6 (relative to Case 3)

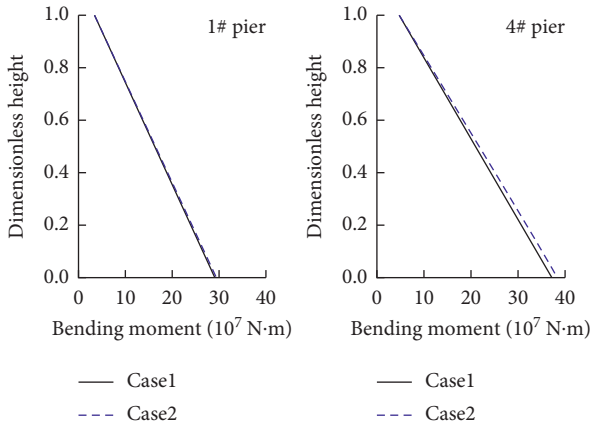


FIGURE 6: Bending moment envelopes of piers in Cases 1 and 2.

periodic characteristics, the amplitude, and time of the peak response are all changed dramatically: the period increases while the peak value decreases significantly. Combining with Table 3, the elongation ratio of pile-soil interaction to the fundamental period is 86%.

Figure 12 shows the deformation envelopes of pier Nos. 1 and 4 relative to bottom of respective pier. It can be observed that there are some differences in the displacement distribution of the piers in the two cases. The displacement

distribution of Case 1 is closer to the first-order mode shape, while that of Case 3 is partly closer to a line distribution. The response discrepancy rates for Case 3 and Case 1 are listed in Table 6. It can be seen that pile-soil interaction significantly reduces the peak response values of deformation and bending moment of bridge pier, and the absolute values of discrepancy rates of displacement are less than 30%, while those of the bending moment are nearly 70%.

According to the displacement time histories of the main girder relative to the pier top, as shown in Figure 13, it appears that the peak response of Case 3 is slightly smaller than that of Case 1, and the vibration periods are significantly different. It seems pile-soil interaction slightly reduces the relative displacement response of the main girder.

Based on the response of Case 2 and Case 4, the influence of pile-soil interaction with the consideration of hydrodynamic force is analyzed. The envelopes of bending moment under earthquake are drawn in Figure 14. Apparently, pile-soil interaction still significantly changes the response of the piers. Furthermore, the response discrepancy rates for Case 4 and Case 2 are listed in Table 7. The reduction rates of deformation and bending moment are as high as 35% and 67%, respectively. Combined with Table 6, it is recognized that hydrodynamic force moderately intensified the reduction effect of pile-soil interaction, and the influence on displacement is more obvious.

TABLE 4: Response discrepancy rates for Case 1 and Case 2 (%).

Rate	1#	2#	3#	4#
Displacement	1.3	2.4	2.8	3.4
Bending moment	1.4	2.2	2.7	3.0

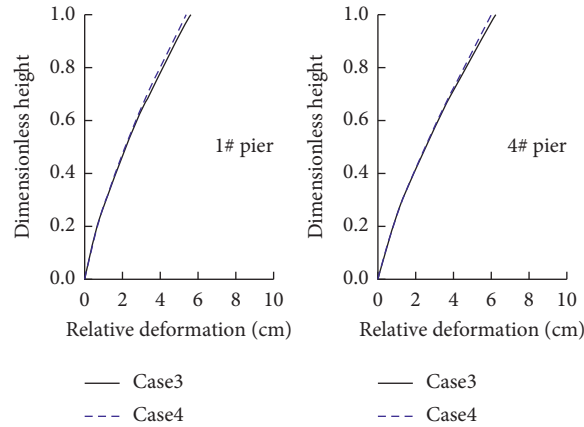


FIGURE 7: Displacement envelopes of piers in Cases 3 and 4.

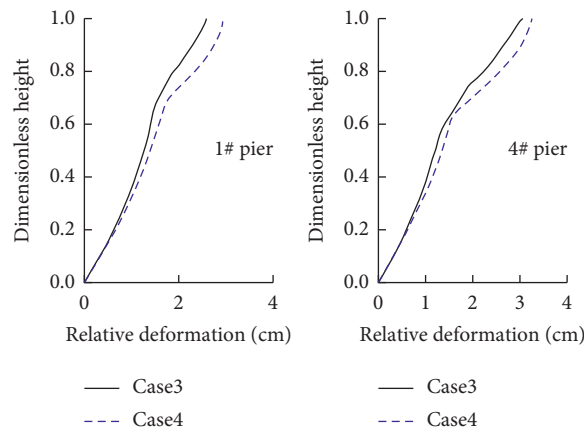


FIGURE 8: Displacement envelopes of pile No. 1 in Cases 3 and 4.

TABLE 5: Response difference rates for Case 3 and Case 4 (%).

Item		1#	2#	3#	4#
Pier	Displacement	-4.6	-4.2	-3.9	-3.7
	Bending moment	2.8	2.9	3.1	3.0
Pile	Displacement	13.1	11.2	11.0	7.3
	Bending moment	2.7	-3.0	3.9	-8.4

The above results suggest that the pile-soil interaction significantly changes the seismic response of the bridge: the vibration period of the structure is significantly prolonged; the maximum values of the pier displacement and bending moment are significantly reduced, and the change of bending moment is more prominent than the displacement. While the influence on the peak value of relative displacement of the girder is limited, the reason may be related to the use of LRB. When water-structure interaction is ignored, the influence of pile-soil

interaction will be underestimated, especially for structural deformation.

Both the hydrodynamic force and pile-soil interaction prolong the period of structural vibration, and the pile-soil interaction has much greater influence. When the soil-structure interaction is neglected, water-structure interaction will increase the structure response; when soil-structure interaction is considered, the influence of hydrodynamic force is complex. From the perspective of pile-soil interaction, hydrodynamic force may increase the influence.

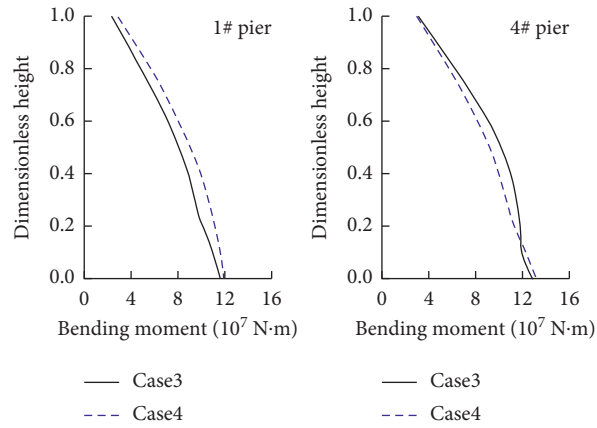


FIGURE 9: Bending moment envelopes of pier No. 4 in Cases 3 and 4.

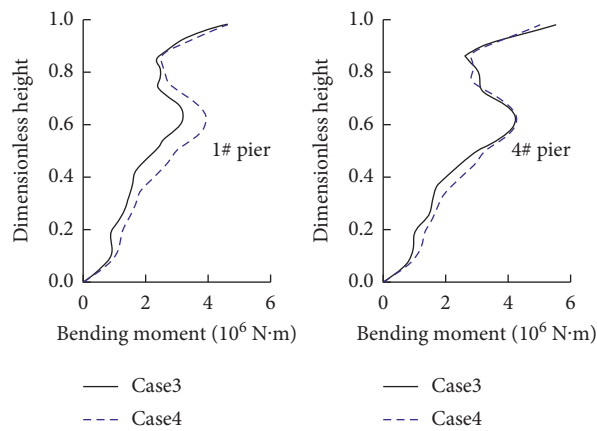


FIGURE 10: Bending moment envelopes of pile No. 1 in Cases 3 and 4.

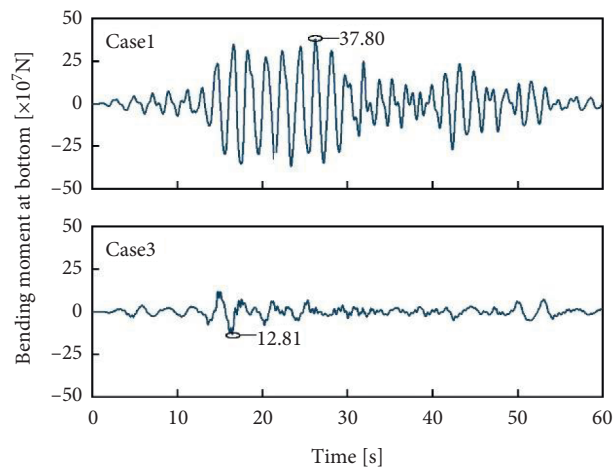


FIGURE 11: Bending moment time histories of pier No. 4 in Cases 1 and 3.

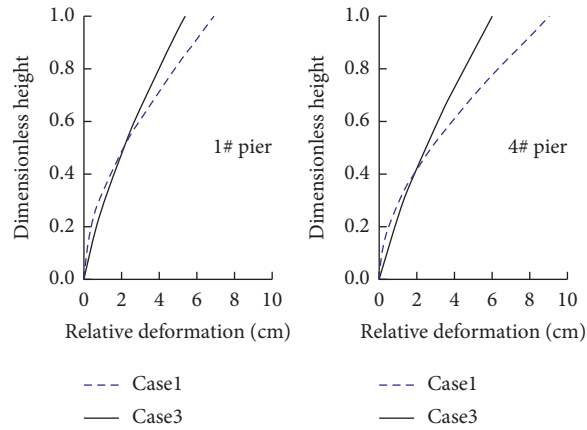


FIGURE 12: Displacement envelopes of piers in Cases 1 and 3.

TABLE 6: Response difference rates for Case 1 and Case 3 (%).

Item	1#	2#	3#	4#
Displacement	-17.8	-22.7	-24.3	-29.4
Bending moment	-59.1	-62.9	-63.2	-66.1

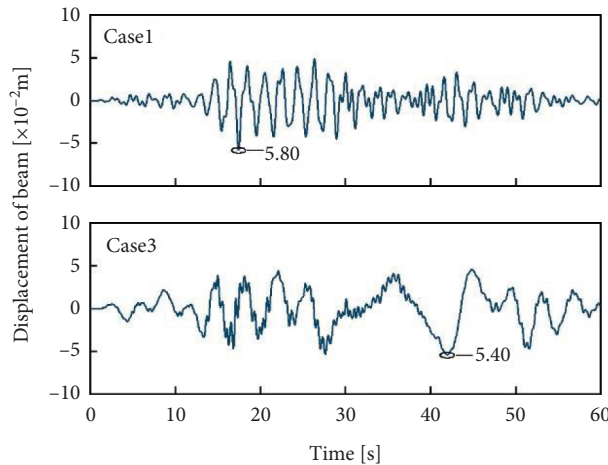


FIGURE 13: Displacement time histories of beam relative to pier No. 4 in Cases 1 and 3.

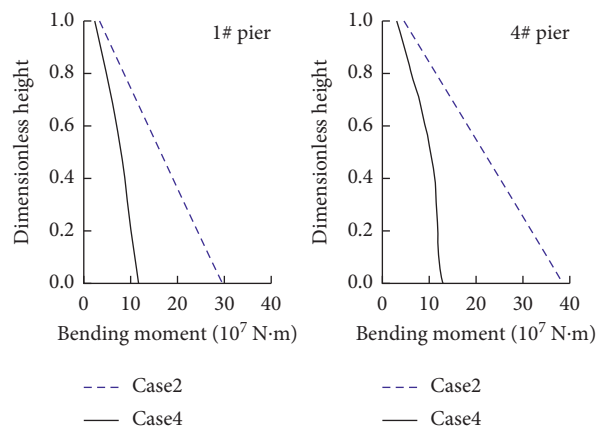


FIGURE 14: Bending moment envelopes of piers in Cases 2 and 4.

TABLE 7: Response difference rates for Case 2 and Case 4 (%).

Rate	1#	2#	3#	4#
Displacement	-22.7	-23.0	-26.6	-34.3
Bending moment	-60.7	-59.3	-62.2	-66.5

5. Conclusions

This paper presents a study on the dynamic response of sea-crossing continuous girder bridge. By comparing the numerical results obtained from different cases, the influences of water-structure interaction and pile-soil interaction are preliminary investigated and discussed. The main conclusions are drawn.

The vibration periods and dynamic responses of the structure are slightly affected by water-structure interaction. This effect could be increased when pile-soil interaction is considered simultaneously. Compared with the pier, the influence of hydrodynamic force on pile is more significant. Compared with the bending moment, the displacement response is more influenced.

The vibration periods and dynamic responses of the structure are severely affected by pile-soil interaction. The vibration periods are obviously prolonged. The responses of deformation and force are reduced, and the bending moment is more affected than the displacement. The usage of isolation bearings may lead to slight impact on main girder.

The influence of pile-soil interaction is much more significant than that of hydrodynamic force. Meanwhile, the effect of coaction of the two is not a simple superposition of action alone, so the seismic analysis of such bridge should consider both effects.

The pile-soil interaction has obvious reducing effect in this study. Combined with the existing research, the pile-soil interaction may magnify the seismic response of structure. Therefore, the influence of pile-soil interaction is complex, and the effect cannot be generalized.

It should be noted that the difference of ground motion intensity, near-field earthquake, and vertical seismic excitation are not considered in this paper. As the notable influences of these factors have been proved for on-land bridge, they will be considered in the subsequent studies on the seismic responses of the offshore bridge.

Data Availability

All the raw data used to support the findings of this study are included within the article. All the raw data are available from the corresponding author upon request.

Conflicts of Interest

The authors declare that they have no conflicts of interest.

Acknowledgments

This work was supported by the National Natural Science Foundations of China (Grant no. 52178101) and the Open Project of Key Laboratory of Urban Security and Disaster

Engineering of Beijing University of Technology (Grant no. 2020B05). The support is gratefully acknowledged.

References

- [1] M. A. Gutscher, J. Malavieille, S. Lallemand, and J. Y. Collot, "Tectonic segmentation of the north andean margin: impact of the carnegie ridge collision," *Earth and Planetary Science Letters*, vol. 168, no. 3, pp. 255–270, 1999.
- [2] C. Zhang, C. Wu, and P. Wang, "Seismic fragility analysis of bridge group pile foundations considering fluid-pile-soil interaction," *Shock and Vibration*, vol. 2020, Article ID 8838813, 17 pages, 2020.
- [3] J. Zhang, K. Wei, and J. Qin, "Resilience and economic loss assessment of highway bridges in deep reservoir under near-fault ground motions," *Journal of Bridge Engineering*, vol. 26, no. 3, 2021.
- [4] R. S. Jangid, "Seismic response of isolated bridges," *Journal of Bridge Engineering*, vol. 9, no. 2, pp. 156–166, 2004.
- [5] J. Yi Meng and E. M. Lui, "Seismic analysis and assessment of a skew highway bridge," *Engineering Structures*, vol. 22, no. 11, pp. 1433–1452, 2000.
- [6] M. Dicleli, "Seismic design of lifeline bridge using hybrid seismic isolation," *Journal of Bridge Engineering*, vol. 7, no. 2, pp. 94–103, 2002.
- [7] M. Mallick and P. Raychowdhury, "Seismic analysis of highway skew bridges with nonlinear soil-pile interaction," *Transportation Geotechnics*, vol. 3, no. 3, pp. 36–47, 2015.
- [8] C. C. Spyrakos, "Seismic behavior of bridge piers including soil-structure interaction," *Computers & Structures*, vol. 43, no. 2, pp. 373–384, 1992.
- [9] L. Di Sarno, F. Da Porto, G. Guerrini, P. M. Calvi, G. Camata, and A. Prota, "Seismic performance of bridges during the 2016 central Italy earthquakes," *Bulletin of Earthquake Engineering*, vol. 17, no. 10, pp. 5729–5761, 2019.
- [10] Q. Han, X. Du, J. Liu, Z. Li, L. Li, and J. Zhao, "Seismic damage of highway bridges during the 2008 Wenchuan earthquake," *Earthquake Engineering and Engineering Vibration*, vol. 8, no. 2, pp. 263–273, 2009.
- [11] N. Makris, D. Badoni, E. Delis, and G. Gazetas, "Prediction of observed bridge response with soil-pile-structure interaction," *Journal of Structural Engineering*, vol. 120, no. 10, pp. 2992–3011, 1994.
- [12] T. C. Hutchinson, Y. H. Chai, R. W. Boulanger, and I. M. Idriss, "Inelastic seismic response of extended pile-shaft-supported bridge structures," *Earthquake Spectra*, vol. 20, no. 4, pp. 1057–1080, 2004.
- [13] B. B. Soneji and R. S. Jangid, "Influence of soil-structure interaction on the response of seismically isolated cable-stayed bridge," *Soil Dynamics and Earthquake Engineering*, vol. 28, no. 4, pp. 245–257, 2008.
- [14] L. Chen, L. Jiang, L. Tao, and Z. Yu, "Seismic response analysis of high-speed vehicle-bridge considering soil-structure interaction," *Rock and Soil Mechanics*, vol. 33, no. 10, pp. 3162–3170, 2012.
- [15] P. Wang, P. Long, M. Zhao, C. Zhang, and X. Du, "Analytical solution of earthquake-induced hydrodynamic pressure on arrays of circular cylinders considering high-order scattered waves," *Journal of Engineering Mechanics*, vol. 147, no. 9, 2021.
- [16] A. Løkke and A. K. Chopra, "Direct finite element method for nonlinear analysis of semi-unbounded dam-water-foundation rock systems," *Earthquake Engineering & Structural Dynamics*, vol. 46, no. 8, pp. 1267–1285, 2017.

- [17] W. Yang and Q. Li, "The expanded Morison equation considering inner and outer water hydrodynamic pressure of hollow piers," *Ocean Engineering*, vol. 69, pp. 79–87, 2013.
- [18] W. L. Yang, Q. Li, and H. Yeh, "Calculation method of hydrodynamic forces on circular piers during earthquakes," *Journal of Bridge Engineering*, vol. 22, no. 11, Article ID 04017093, 2017.
- [19] C.-Y. Liaw and A. K. Chopra, "Dynamics of towers surrounded by water," *Earthquake Engineering & Structural Dynamics*, vol. 3, no. 1, pp. 33–49, 1974.
- [20] J. Guo, M. Zhao, P. Wang, and N. Zhang, "Comparative assessment of simplified methods for hydrodynamic force on cylinder under earthquakes," *Ocean Engineering*, vol. 234, Article ID 109219, 2021.
- [21] X. Du, P. Wang, and M. Zhao, "Simplified formula of hydrodynamic pressure on circular bridge piers in the time domain," *Ocean Engineering*, vol. 85, pp. 44–53, 2014.
- [22] M. Greenhow and L. Yanbao, "Added masses for circular cylinders near or penetrating fluid boundaries-review, extension and application to water-entry, -exit and slamming," *Ocean Engineering*, vol. 14, no. 4, pp. 325–348, 1987.
- [23] Q. Li and W. Yang, "An improved method of hydrodynamic pressure calculation for circular hollow piers in deep water under earthquake," *Ocean Engineering*, vol. 72, pp. 241–256, 2013.
- [24] H. Jiang, B. X. Wang, X. Y. Bai, C. Zeng, and H. D. Zhang, "Simplified expression of hydrodynamic pressure on deep-water cylindrical bridge piers during earthquakes," *Journal of Bridge Engineering*, vol. 22, no. 6, Article ID 04017014, 2017.
- [25] P. Wang, M. Zhao, X. Du, J. Liu, and J. Chen, "Simplified evaluation of earthquake-induced hydrodynamic pressure on circular tapered cylinders surrounded by water," *Ocean Engineering*, vol. 164, pp. 105–113, 2018.
- [26] M. Zhao, Y. Huang, and P. Wang, "Simplified model for the earthquake induced hydrodynamic pressure on rectangular cylinder," *Journal of Beijing University of Technology*, vol. 45, no. 12, pp. 1212–1217, 2019.
- [27] X. Huang and Z. X. Li, "Influence of hydrodynamic pressure on seismic response of bridge piers in deepwater," *China Civil Engineering Journal*, vol. 44, no. 1, pp. 65–73, 2011.
- [28] W. P. Wu, S. S. Liang, P. Liang, and S. G. Long, "Journal of disaster prevention and mitigation engineering influence of hydrodynamic pressure and pile-soil interaction (PSI) on seismic performance of high pier bridges in deep water," *Journal of Disaster Prevention and Mitigation Engineering*, vol. 41, no. 1, pp. 67–74, 2021.
- [29] Y. Deng, Q. Guo, Y. I. Shah, L. Xu, and F. Paolacci, "Study on modal dynamic response and hydrodynamic added mass of water-surrounded hollow bridge pier with pile foundation," *Advances in Civil Engineering*, vol. 2019, Article ID 1562753, 23 pages, 2019.
- [30] M. B. Adeel, M. A. Jan, M. Aaqib, and D. Park, "Development of simulation based p-multipliers for laterally loaded pile groups in granular soil using 3D nonlinear finite element model," *Applied Sciences*, vol. 11, no. 1, p. 26, 2021.
- [31] S. Carbonari, F. Dezi, and G. Leoni, "Seismic soil-structure interaction in multi-span bridges: application to a railway bridge," *Earthquake Engineering & Structural Dynamics*, vol. 40, no. 11, pp. 1219–1239, 2011.
- [32] Q. Han, J. Wen, X. Du, Z. Zhong, and H. Hao, "Nonlinear seismic response of a base isolated single pylon cable-stayed bridge," *Engineering Structures*, vol. 175, pp. 806–821, 2018.
- [33] H. Matlock, "Correlations for design of laterally loaded piles in soft clay," pp. 77–94, 1970, Offshore technology in civil engineering's hall of fame papers from the early years OTC-1204-MS.
- [34] *Recommended Practice for Planning, Designing and Constructing Fixed Offshore Platforms—Working Stress Design*, American Petroleum Institute (API), Washington, DC, USA, 20th ed. edition, 1993.
- [35] Y. Bin, *Study on Simplified Models of Bridge Pile-Foundation Subjected to Earthquake* Tongji University, Shanghai, China, 2007.
- [36] X. J. Duan, *A Soil Structure -Interaction Analysis of Tall Buildings*, University of Southern California, Los Angeles, CA, USA, 1999.
- [37] O. Maeso, J. J. Aznárez, and F. Garcia, "Dynamic impedances of piles and groups of piles in saturated soils," *Computers & Structures*, vol. 83, no. 10-11, pp. 769–782, 2005.
- [38] D. A. Brown, L. C. Reese, and M. W. O'Neill, "Cyclic lateral loading of a large-scale pile group," *Journal of Geotechnical Engineering*, vol. 113, no. 11, pp. 1326–1343, 1987.
- [39] D. A. Brown, C. Morrison, and L. C. Reese, "Lateral load behavior of pile group in sand," *Journal of Geotechnical Engineering*, vol. 114, no. 11, pp. 1261–1276, 1988.
- [40] Gb50017-2017, *Standard for Design of Steel Structures* Ministry of Housing and Urban-Rural Development of the People's Republic of China, Beijing, China, 2017.
- [41] GB 50010-2010, *Code for Design of concrete Structures* Ministry of Housing and Urban-Rural Development of the People's Republic of China, Beijing, China, 2015.
- [42] PEER, *Pacific Earthquake Engineering Research center Ground Motion Database-Ngawest2*, Pacific Earthquake Engineering Research. (PEER), Berkeley, CA, USA, 2013, <http://ngawest2.berkeley.edu/>.

Research Article

“Relief-Retaining” Control Technology of Floor Heave in Mining Roadway with Soft Rock: A Case Study

Ai Chen ^{1,2}, Xuebin Li ¹, Xuesheng Liu ¹, Yunliang Tan ¹, Ke Xu ¹
and Honglei Wang ¹

¹School of Energy and Mining Engineering, Shandong University of Science and Technology, Qingdao 266590, China

²Ningxia Coal Industry Co., Ltd., of China Energy Group, Yinchuan 750000, China

Correspondence should be addressed to Xuesheng Liu; xuesheng1134@163.com

Received 1 October 2021; Revised 28 October 2021; Accepted 5 November 2021; Published 23 November 2021

Academic Editor: Lingkun Chen

Copyright © 2021 Ai Chen et al. This is an open access article distributed under the Creative Commons Attribution License, which permits unrestricted use, distribution, and reproduction in any medium, provided the original work is properly cited.

The floor heave problem is one of the important factors affecting the stability and safety of surrounding rocks of roadways, especially in deep high-stress mining roadway with soft rock. The return airway of no. 130203 working face in Zaoquan Coal Mine of Ningdong Mining Area in Northwest China is the research object in this study. Firstly, an innovative “relief-retaining” control scheme of floor heave is proposed, which is the comprehensive measure of “cutting groove in floor + drilling for pressure relief at roadway side + setting retaining piles at the junction of roadway side and floor.” Then, the specific parameters suitable for floor heave control of no. 130203 return airway are determined using numerical simulation method. Finally, the yield monitoring results show that both the deformation of surrounding rocks and the cable force are significantly reduced. The roof falling capacity, floor heave displacement, and thickness increasing value of 0–2 m floor strata are 596 mm, 410 mm, and 82 mm, respectively, which are 43.67%, 67.49%, and 75.38% less than those of the control section. The maximum force of cables at roadway sides is 140.13 kN, about 32.54% less than that of the control section. The results verify the reliability of the proposed “relief-retaining” control scheme and can provide some reference for the floor heave control of similar roadways.

1. Introduction

After excavation of mining roadway, the phenomenon of upward heave of roadway floor is called floor heave. Floor heave will reduce the roadway section, hinder pedestrians and transportation, and hinder the mine ventilation. Many mines have to invest a lot of manpower and material resources to do temporary processing work such as “digging the bottom.” Seriously, it will cause the whole roadway to be scrapped and affect the safety of mine production [1–5]. Therefore, it is of great significance to study the floor heave control of mining roadway.

In order to control the floor heave problem effectively, many scholars have conducted a lot of exploration, and many floor heave prevention and control technologies are proposed. For example, He et al. [6] proposed the bolt, steel mesh, and anchor coupling support technology for the floor heave of deep coal roadway, which controlled the large deformation and floor heave of deep coal roadway

effectively. Sun and Wang [7] studied the control method of floor heave by the way of roadway cutting groove to relieve pressure, which improved the stress state of the floor effectively. Aiming at the deformation and failure characteristics of mining roadway, Bai et al. [8] put forward to strengthen the floor and reduce the stress environment of surrounding rocks for the control measures of floor heave, and the control effect is remarkable. Li [9] proposed reinforcement floor and bottom angle control method for floor heave of roadway, which laid the foundation for further study of floor heave control. Wang et al. [10] studied the floor heave control method of high-stress soft rock roadway, took the triple roadway of the main belt conveyor roadway in the west wing of Panyidong Mine as the research object, and proposed the floor heave control scheme based on end anchor cable bundle, which provided solutions and ideas for the floor heave problem of high-stress soft rock roadway. Chen et al. [11] proposed the floor heave control technology of soft rock roadway with “floor anchor + floor

hardening + relief groove + roof and side anchor (cable supplement)" and achieved good engineering application results. Wang et al. [12] proposed the support concept of strong bottom reinforcement and modified the support parameters in a timely manner by dynamic analysis according to the degree of floor heave, which provided a theoretical basis for the treatment of floor heave. Stankus and Peng [13] proposed the supporting theory of coupling of yielding support and rigid support and designed and applied the retractable floor beam, which achieved good economic and technical results. Many scholars have done a lot of research on floor heave control, mainly focused on the aspects of reducing surrounding rocks stress [14–17] and increasing floor integrity [18–23], and achieved good control results.

However, due to the complex diagenetic conditions of Ningdong Mining Area in northwest China, the cohesion of coal and rock is low, the internal friction angle is small, the stress level of surrounding rocks is high, the roadway floor has continuous deformation, and the floor heave is very large [24–27]. The application effect of the existing floor heave control method in Ningdong Mining Area is limited. The method of floor heave control suitable for high-stress roadway with soft rock needs further exploration, especially in Ningdong Mining Area.

Based on the typical large deformation roadway with soft rock in Zaoquan Coal Mine of Ningdong Mining Area, this paper puts forward the innovative "relief-retaining" control scheme of floor heave, and the specific parameters suitable for floor heave control of no. 130203 return airway are determined using numerical simulation method. Field monitoring results verify the reliability of the proposed "relief-retaining" control scheme and can provide some reference for the floor heave control of similar roadways.

2. Engineering Background

Zaoquan Coal Mine in Ningdong Mining Area, as the main production mine of Ningmei Group with an annual output of 8 million tons, is located at the edge of Maowusu Desert 62 km southeast of Lingwu City, Ningxia, and the specific geographical location is shown in Figure 1. The length of the minefield is 13 km from north to south, and the width from east to west is about 4 km on average. The minefield area is 56.6982 km², and the geological reserves are 10.6574 million tons.

The research object of this paper is no. 130203 return airway in Zaoquan Coal Mine. The depth of roadway is 670 m, the vertical stress is about 16.75 MPa, the recoverable length of strike is 2832 m, and the inclined length is 198~225 m. There are 5~15 m coal pillars on the east side of the working face adjacent to the goaf of no. 130202 working face. The west side is the no. 130205 preparation face under excavation, the south side is the undeveloped area, and the north side is the extension section of 13 mining areas. Through the in situ stress test of the return airway in 130203 working face, the results show that the maximum horizontal principal stress of the roadway is 11.65 MPa, which belongs to the area of medium stress value.

The strata of no. 130203 working face coal seam are Middle Jurassic Yan'an Formation. The floor is a typical soft stratum, which is mainly the carbonaceous mudstone and argillaceous sandstone, and the uniaxial strength is between 17 MPa and 23 MPa. The soft strata of the floor lead to the serious floor heave problem of the roadway under the influence of the high surrounding rocks stress of the floor during the tunneling and mining of the no. 130203 roadway, which affects the normal mining of the mine. The floor heave deformation of the roadway is shown in Figure 2.

3. "Relief-Retaining" Control Scheme of Floor Heave

3.1. Control Scheme

3.1.1. Cutting Groove in the Floor. The loose pressure relief groove is arranged near the center of roadway floor in the test area. In order to minimize the disturbance of surrounding rocks outside the pressure relief groove, the pressure relief groove is produced by smooth blasting, and the sectional drawing and vertical view are as shown in Figure 3.

3.1.2. Setting Retaining Piles at the Junction of Roadway Side and Floor. The retaining pile is inclined to the outside of the roadway at a certain angle in the horizontal direction. The retaining pile is made of steel pipe, cement, and sodium silicate slurry. By drilling a hole at a predetermined position, installing a steel pipe in the hole and installing an anchor cable inside the steel pipe, injecting cement and water glass, and then applying a certain preload to the anchor cable after solidification, the fabrication of retaining pile can be completed. The sectional drawing and vertical view are as shown in Figure 4.

3.1.3. Drilling for Pressure Relief at Roadway Side. Large-diameter pressure relief boreholes are arranged in the solid coal side to transfer the peak value of lateral abutment pressure to the deep coal side. At a certain height from the floor of the roadway, two rows of large-diameter boreholes are constructed along the roadway direction, which are arranged in three-flower-hole layout. For the convenience of site construction, a certain elevation angle can be brought in the borehole construction. The borehole diameter is generally 130 mm, and the sectional drawing and vertical view are as shown in Figure 5.

3.2. Parameter Selection

3.2.1. Simulation Scheme and Modeling. The "relief-retaining" control scheme of floor heave mainly involves the following parameters: the depth and width of pressure relief grooves, the length and spacing of retaining pile, and the depth and spacing of large-diameter pressure relief boreholes in solid coal side. By comparing the construction examples of mines with similar geological conditions, the numerical simulation scheme is shown in Table 1. Physical

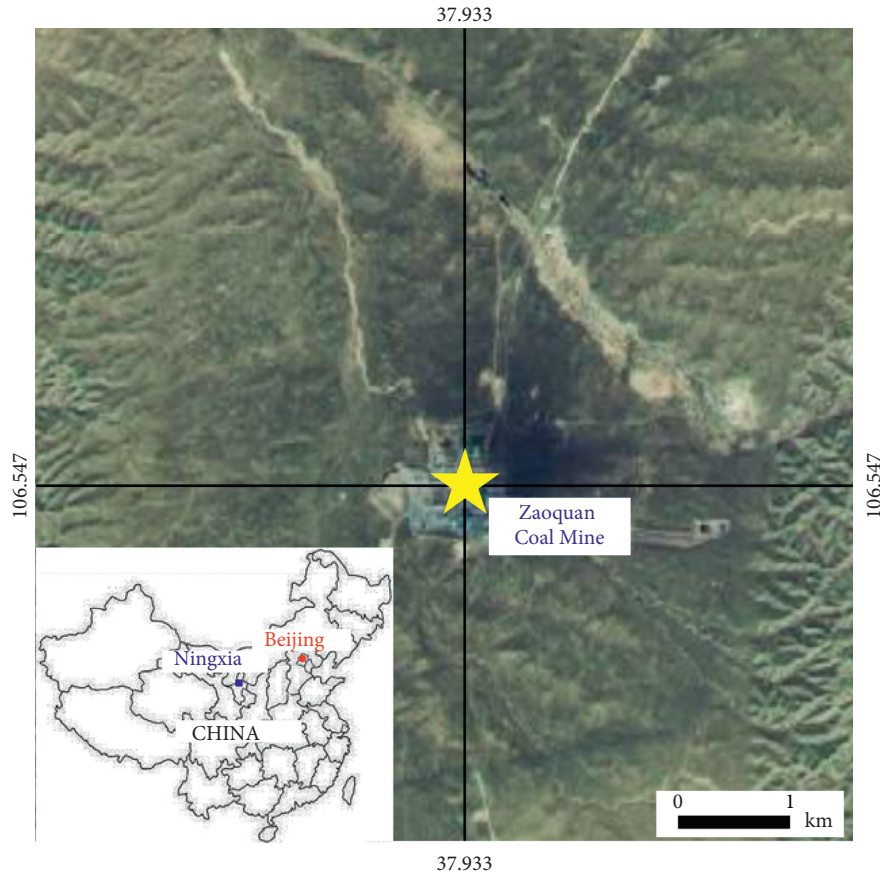


FIGURE 1: Floor heave of return airway in no. 130203 working face.

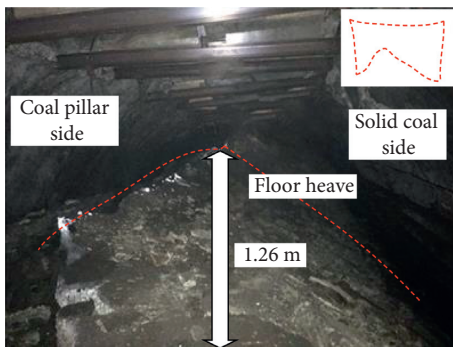


FIGURE 2: Floor heave of return airway in no. 130203 working face.

and mechanical parameters of retaining pile are shown in Table 2.

This section takes the geological and mining conditions of no. 130203 return airway in Zaoquan Coal Mine as the background, adopts FLAC3D numerical software, selects no. 130203 working face as the engineering prototype, and selects the length of X horizontal direction 200 m, the length of Y horizontal direction 50 m, and the length of Z vertical direction 150 m to establish the numerical calculation model. The coarse sandstone is the upper boundary of the model, and the medium sandstone is the lower boundary of the model. The strata from top to bottom are coarse sandstone, siltstone, coal, mudstone, fine sandstone, and

medium sandstone. The buried depth of field roadway is about 700 m, and 17.5 MPa uniform compressive stress is applied on the upper boundary of the model. The specific shape of roadway section is selected as rectangular roadway, and the roadway size is 5.0 m × 4.0 m. The specific model is shown in Figure 6.

The left and right, front and back, and lower boundaries of the model are displacement boundaries, and the top of the model is stress boundary conditions. The mechanical parameters of coal and rock in the model are shown in Table 3.

3.2.2. Modeling Results

(1) *Cutting Groove in the Floor.* The deformation and stress distribution of roadway surrounding rocks with different width of cutting grooves in the floor are shown in Figure 7.

It can be seen from Figure 7 that when the depth of cutting groove is constant, with the increase of the width of cutting groove, the deformation compensation space of the floor surrounding rocks increases, and the floor heave displacement of the roadway decreases gradually. In particular, when the width of cutting groove is not more than 0.6 m, the floor heave displacement decreases rapidly. When the width of cutting groove is more than 0.6 m, the floor heave displacement decreases slowly with the increase of the width of cutting groove. It can be seen that when the cutting

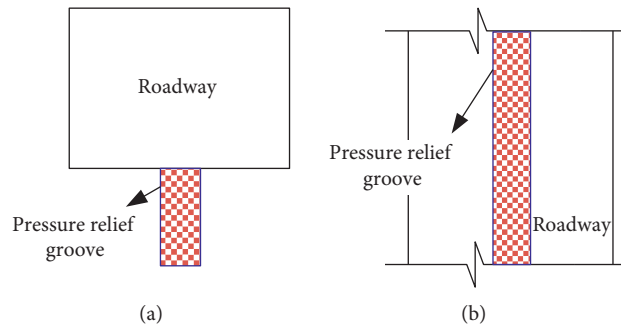


FIGURE 3: Schematic diagram of cutting groove in the floor. (a) Sectional drawing; (b) vertical view.

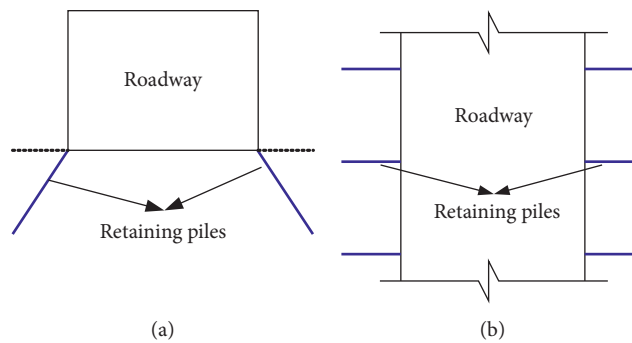


FIGURE 4: Indication diagram of retaining pile arrangement. (a) Sectional drawing; (b) vertical view.

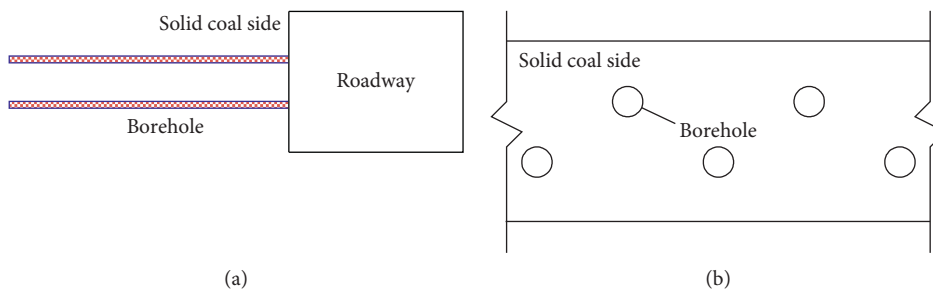


FIGURE 5: Large-diameter pressure relief drilling schematic diagram of solid coal side. (a) Sectional drawing; (b) vertical view.

TABLE 1: Numerical simulation scheme for control scheme of floor heave.

Control technologies and parameters		Scheme 1	Scheme 2	Scheme 3
Pressure relief grooves	Depth (m)	2.0	2.0	2.0
	Width (m)	0.4	0.6	0.8
Retaining piles	Depth (m)	3.0	3.0	3.0
	Spacing (m)	0.5	1.0	1.5
Large-diameter pressure relief boreholes	Depth (m)	10	10	10
	Spacing (m)	0.8	1.0	1.2

groove is set to control the floor heave, the width of cutting groove should not exceed 0.6 m.

(2) *Setting Retaining Piles at the Junction of Roadway Side and Floor.* The deformation and stress nephogram of roadway surrounding rocks with different spacings of retaining piles are shown in Figure 8.

From Figure 8, it can be seen that the floor heave displacement increases with the increase of the spacing of retaining piles, and the increase trend decreases gradually. When the spacing of retaining piles exceeds 1.0m, the increase of the spacing of retaining piles has little effect on the improvement of floor heave control. From the economic point of view, too small spacing of retaining piles will also

TABLE 2: Physical and mechanical parameters of retaining pile.

Name	Diameter (mm)	Density ($\text{kg}\cdot\text{m}^{-3}$)	Elastic modulus (GPa)	Poisson ratio
Retaining piles	50	2500	35	0.2

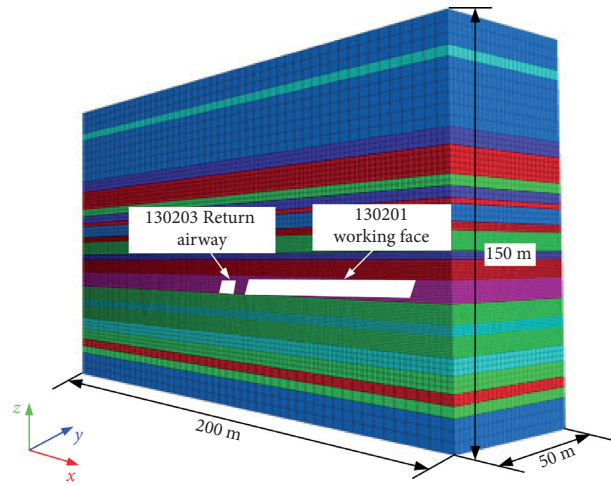


FIGURE 6: Numerical calculation model diagram of no. 130203 working face.

TABLE 3: Physical and mechanical parameter table of numerical model materials.

Lithology	Density ($\text{kg}\cdot\text{m}^{-3}$)	Compressive strength (MPa)	Tensile strength (MPa)	Elastic modulus (GPa)	Internal cohesion (MPa)	Internal friction angle ($^{\circ}$)	Poisson ratio
Medium grained sandstone	2300	21.76	0.61	11.73	1.62	32	0.25
Gritstone	2360	28.39	0.83	21.35	1.83	36	0.21
Siltstone	2860	27.62	0.71	19.04	1.24	37	0.23
Mudstone	2620	17.36	0.56	9.60	0.86	34	0.24
Fine-sandstone	2510	23.30	0.96	14.37	1.36	47	0.21
Carbon mudstone	2650	17.36	0.56	8.03	0.47	27.25	0.24
Coal	1310	11.65	0.47	8.71	0.50	26.36	0.23
Siltstone	2860	27.62	0.71	19.04	1.42	37	0.23

cause the increase of floor heave control cost. Therefore, the simulation of the spacing of retaining piles in the no. 130203 working face of Zaoquan Coal Mine in Ningdong Mining Area shows that the spacing of retaining piles is 1.0 m.

(3) *Drilling for Pressure Relief at Roadway Side.* The deformation and stress nephogram of surrounding rocks of roadway with different spacings of pressure relief boreholes are shown in Figure 9.

Figure 9 shows that the floor heave displacement increases with the increase of the spacing of pressure relief boreholes, and the increasing trend decreases gradually. When the spacing of pressure relief boreholes exceeds 1.0 m, the effect of pressure relief boreholes on floor heave control is not obvious. At the same time, when the spacing is reduced, the setting of dense drilling will further increase the control cost. Therefore, considering the control cost and control effect, the spacing of pressure relief boreholes in no. 130203 working face of Zaoquan Coal Mine in Ningdong Mining Area is 1.0 m.

In summary, the main parameters for determining the “relief-retaining” control scheme of floor heave are as follows: the depth and width of pressure relief groove are 2.0 m and 0.5 m, respectively. The length and spacing of retaining piles are 3.0 m and 1.0 m, respectively. The depth and spacing of large-diameter pressure relief boreholes at the roadway side are 10.0 m and 1.0 m, respectively.

4. Analysis of Result

The scheme is implemented outside 200 m of advanced working face, and the roadway with similar geological structure, surrounding rocks property, and coal pillar sizes should be selected for test. The length of the test area is 200 m. The test area division and the corresponding station layout are shown in Figure 10. The original support scheme was used as the control section in the first 100 m, and the last 100 m was the test section of the “relief-retaining” control scheme of floor heave in this paper. The monitoring results are as follows.

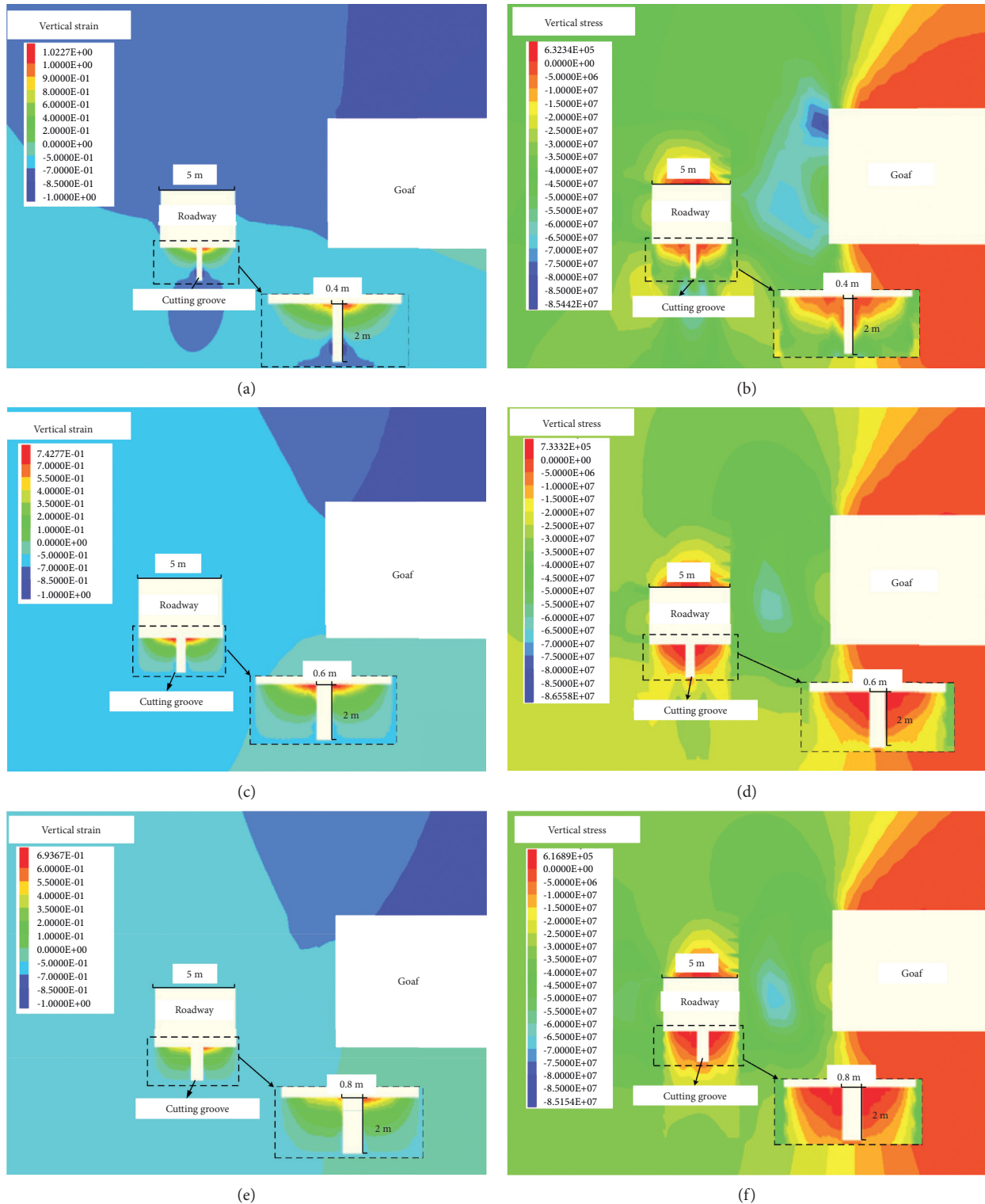


FIGURE 7: Deformation and stress distribution of roadway surrounding rock with different floor cutting groove width. (a) Vertical strain of 0.4 m; (b) vertical stress of 0.4 m; (c) vertical strain of 0.6 m; (d) vertical stress of 0.6 m; (e) vertical strain of 0.8 m; (f) vertical stress of 0.8 m.

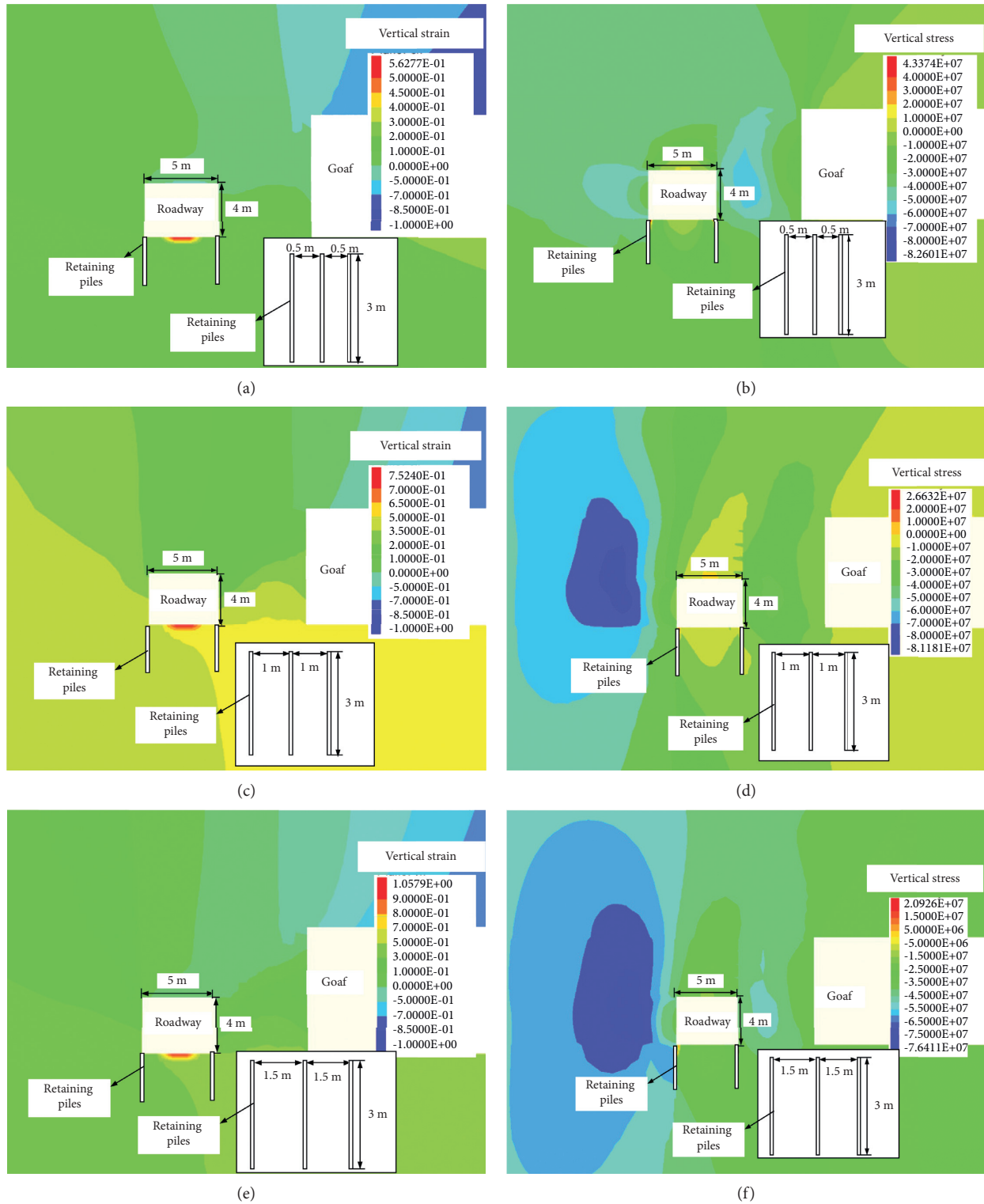


FIGURE 8: Deformation and stress distribution of roadway surrounding rocks with different spacings of retaining piles. (a) Vertical strain of 0.5 m; (b) vertical stress of 0.5 m; (c) vertical strain of 1.0 m; (d) vertical stress of 1.0 m; (e) vertical strain of 1.5 m; (f) vertical stress of 1.5 m.

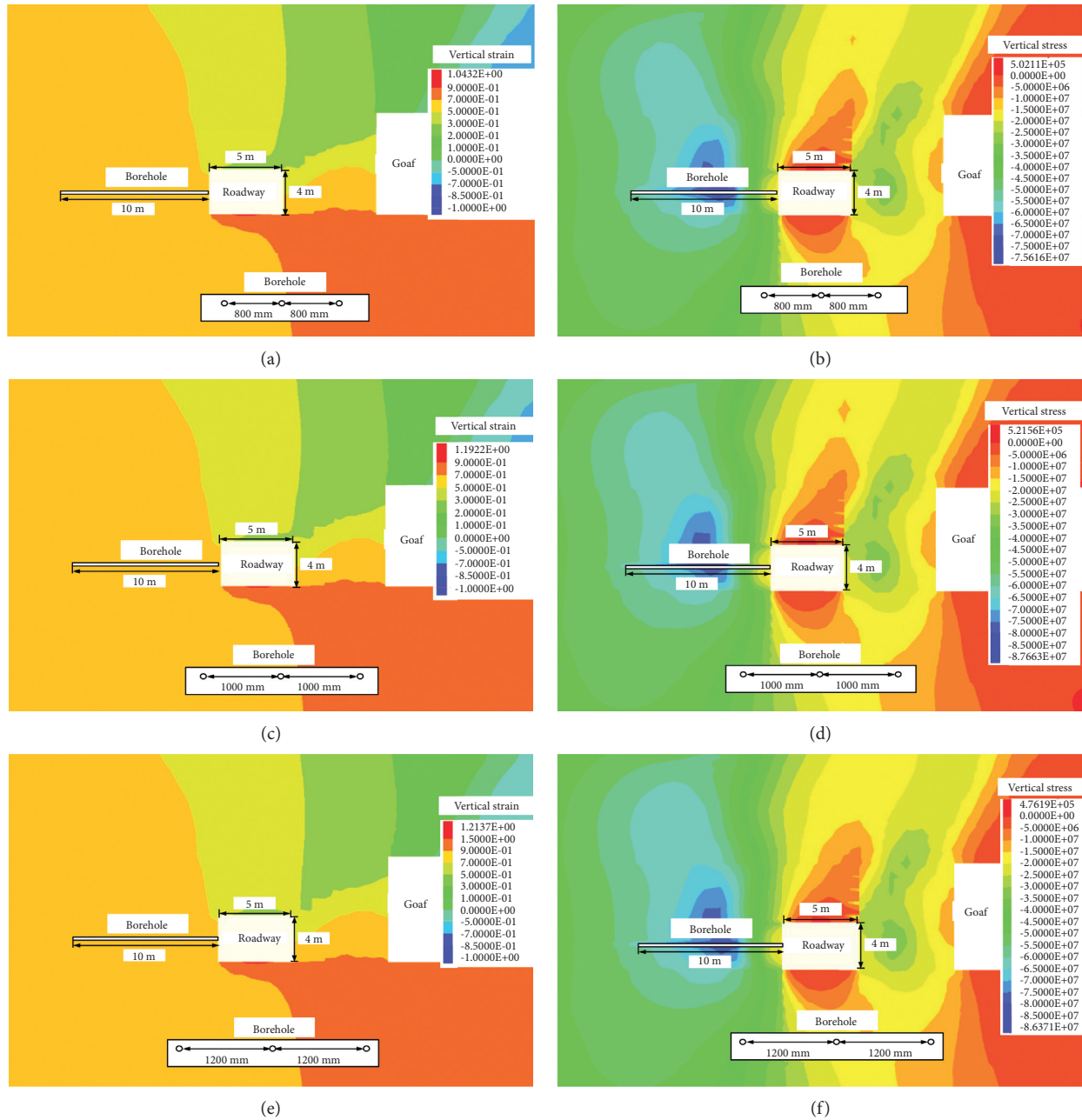


FIGURE 9: Deformation and stress distribution of surrounding rocks in mining roadway with different spacings of pressure relief boreholes. (a) Vertical strain of 0.8 m; (b) vertical stress of 0.8 m; (c) vertical strain of 1.0 m; (d) vertical stress of 1.0 m; (e) vertical strain of 1.2 m; (f) vertical stress 1.2 m.

4.1. Deformation Law of Roadway Surrounding Rocks.

The “cross-bonded method” was used to observe the surface displacement of roadway surrounding rocks, the multipoint displacement meter was used to observe the deep displacement of roadway surrounding rocks, and the roof and floor of roadway are the main monitoring object. The main monitoring results are as follows.

(1) Deformation law of roadway roof and floor

With the mining of no. 130203 working face, the surrounding rocks deformation of return airway shows different changes. The monitoring results of roof falling capacity and floor heave displacement of each station are shown in Figures 11 and 12, respectively. In order to facilitate data comparison, the

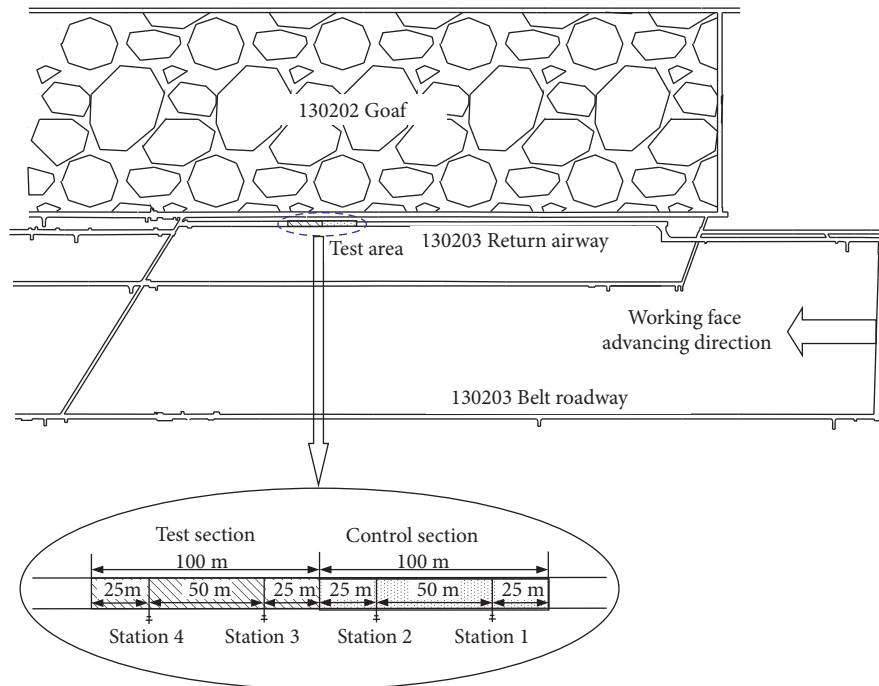


FIGURE 10: Test area and station layout diagram.

data of each station are recorded at 120 m from the working face.

It can be seen from Figure 11 that when the measuring point is 80 m away from the working face, the roof falling capacity of roadway is small. Within the range of 80–30 m from the working face, the surrounding rocks of the roadway are affected by the advanced abutment pressure, and the roof falling capacity begins to increase significantly. When the distance from the working face is within 30 m, the roof falling capacity of the control section is still increased, and the speed of the roof falling capacity of the test section is gradually slowed down. Thus, the mining roadway is less affected by the mining of the working face outside 80 m and is in the slow deformation stage. The influence range of the advanced abutment pressure of the working face is 80 m ahead of the working face.

At the same time, by comparing the change of roof falling capacity of each station, the maximum values of the control section are 1366 mm and 1364 mm, respectively, with an average of 1365 mm. The maximum values of roof falling capacity in the test section were 598 mm and 594 mm, respectively, with an average of 596 mm, which were 43.67% lower than those in the control section, and the control effect was obvious.

By comparing the change of floor heave displacement of each station, it can be seen from Figure 12 that the deformation of floor heave in the initial test section is slightly larger than that in the control section, which is because the integrity of the floor is

reduced due to the initial construction. In the process of approaching the working face, the floor heave displacement of the control section increases rapidly, while the increase of the test section is slow, indicating that the measures of the test section begin to play a key role. In addition, compared with the monitoring data of each station, the maximum values of the control section were 1257 mm and 1267 mm, with an average of 1262 mm. The maximum floor heave displacement of the test section was 414 mm and 406 mm, with an average of 410 mm, which was 852 mm lower than that of the control section, and the decrease was 67.49%, indicating that the floor heave displacement of the test section was significantly lower than that of the control section.

At the same time, it can be seen from the control section that the floor heave displacement accounts for a large proportion in the deformation of roadway roof and floor. When the deformation of roadway roof and floor is the largest, the floor heave displacement accounts for about 48.16% of the roof to floor convergence, while the floor heave displacement of the test section accounts for about 40.99% of the deformation of roadway, indicating that the floor heave displacement of the test section is effectively reduced due to the implementation of the “relief-retaining” control scheme of floor heave, which has a good control effect on the floor heave of roadway.

- (2) Deformation law of thickness increasing value of 0–2 m floor strata

With the mining of working face, the deformation of surrounding rocks of roadway floor has different

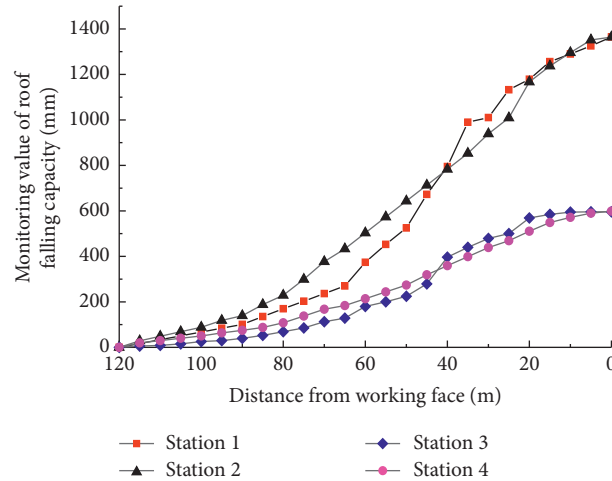


FIGURE 11: Curve diagram of roof falling capacity of each station.

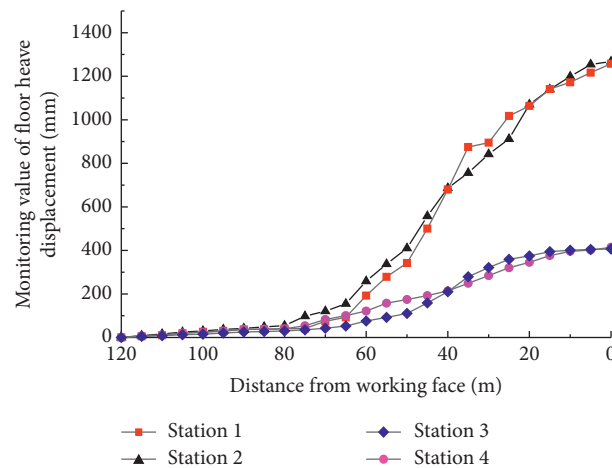


FIGURE 12: Curve diagram of floor heave displacement at each station.

changes. The monitoring results of the average deformation of the surrounding rocks of the roadway floor in the control section and the test section are shown in Figure 13. Because the depth of the cable claw at the deepest point of the multipoint displacement meter of the roadway floor is 2 m, the monitoring data of the deep 2 m position of the roadway floor are compared and analyzed. At the same time, in order to facilitate data comparison, the data of each station are recorded from 120 m away from the working face.

Comparing the average change of surrounding rocks of roadway floor between the control section and the test section, it can be seen that before 80 m from the working face, the deformation trend of surrounding rocks of roadway floor in the test section and the control section is similar, but the deformation speed of the test section is slightly smaller than that of the control section. In the range of 80–50 m from the working face, the deformation of the test section is still very stable, but the deformation of the control

section increases sharply, and the deformation of the surrounding rocks of the roadway floor in the test section is much smaller than that of the control section. Within 50 m, the deformation of the control section slightly slowed down, while the deformation of the test section was still relatively stable and maintained at a low growth state.

From the monitoring data, it can be seen that during the period from 120 m from the measuring station to the working face until the working face is pushed past the measuring station, the deformation of roadway floor surrounding rocks in the test section was significantly reduced compared with that in the control section. The maximum deformation value of roadway floor surrounding rocks in the control section was 333 mm, and the deformation value of roadway floor surrounding rocks in the test section was 82 mm, which was reduced by 75.38%, indicating that the effect of the “relief-retaining” control scheme of floor heave was significant.

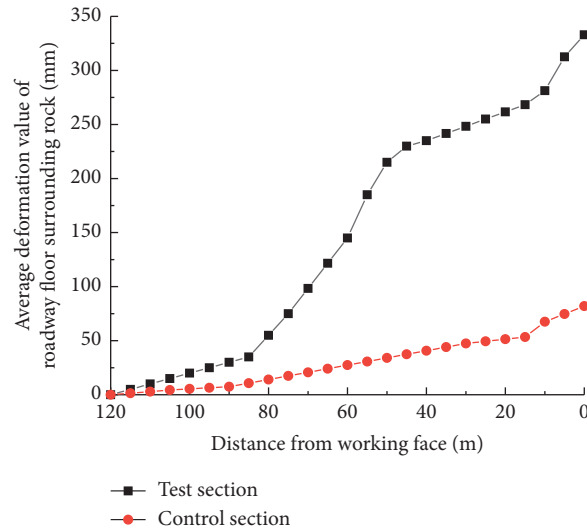


FIGURE 13: The average deformation curves of 0–2 m floor strata of control section and test section.

After monitoring the station, the deformation of surrounding rocks in different layers of roadway floor is counted, and the deformation of surrounding rocks in different layers of roadway floor is shown in Figure 14. It can be seen from Figure 14 that whether the test section or the control section, the deformation of surrounding rocks of roadway floor gradually decreases with the increase of depth. By comparing the deformation of surrounding rocks in different layers of the test section and the control section, it is found that the deformation of the test section in each layer is smaller than that in the corresponding layer of the control section. The shallower the layer is, the more obvious the reduction effect of the test section scheme is. In particular, the effect is the most obvious when the shallow part is 0–0.5 m. The deformation reduction of the test section is 155 mm, which is 75.61% lower than that of the control section.

4.2. Stress Variation Law of Roadway Surrounding Rocks.

In the mining process of no. 130203 working face, the stress of roadway surrounding rocks shows a certain change rule. The MSC-400 cable dynamometer is used to monitor the average stress of roadway surrounding rocks. The monitoring results of the control section and the test section are shown in Figure 15. In order to facilitate data comparison, the data of each station are recorded from 190 m away from the working face.

It can be seen from the monitoring data that within the range of 30–35 m from the working face, the cable force in the control section and the test section appears to be the maximum. The maximum force of cable in the control section appears at about 35 m from the working face, which is about 206.06 kN. The maximum force of the cable in the test section appears at about 30 m from the working face, which is about 140.13 kN. Compared with the control

section, the test section is reduced by 32.54%, indicating that the “relief-retaining” control scheme of floor heave has a certain effect on reducing the force of surrounding rocks.

4.3. Discussion. The analysis of the above monitoring results shows that the deformation of the surrounding rocks of the mining roadway is effectively controlled after the “relief-retaining” control scheme of floor heave. The floor heave displacement is reduced by 67.49%, and the cable force is reduced by 32.54%. The stress environment and stability of the surrounding rocks are significantly improved, which has played a good demonstration role. The main reason is that the “relief-retaining” control scheme of floor heave liberates the deformation of floor, reduces the stress of surrounding rocks, and effectively blocks the transmission of horizontal stress, which will greatly reduce the deformation and stress of floor.

Many studies have been carried out by many scholars on the floor heave control of roadways with similar conditions [4, 16, 28–31]. For example, Gu et al. [28] proposed the combined support of bolt grouting and grooving to control floor heave for the floor of return airway in 2407 working face of high-stress roadway with soft rock in Yuhua Coal Mine, Tongchuan, and the field monitoring showed that the floor heave displacement was reduced by 61.5%. This not only reduces the impact of horizontal stress but can also lead to difficulty in repairing the floor. Compared with the above scheme, the “relief-retaining” control scheme of floor heave proposed in this paper can effectively reduce the stress concentration degree of roadway side and resist the transmission of horizontal stress of floor, so as to reduce the influence of horizontal stress on floor strata. At the same time, it can provide certain free space for floor deformation and liberate the deformation of roadway floor, so the control effect is better than the above scheme.

In summary, it can be seen that the mechanism of floor heave is likely to be related to the horizontal stress and the

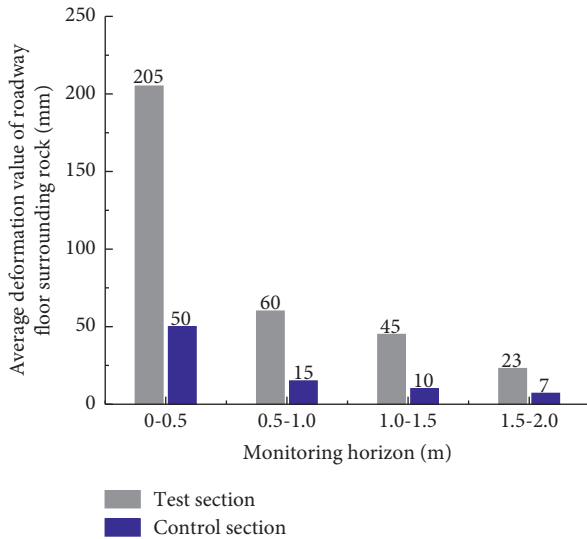


FIGURE 14: Histogram of average deformation value of roadway floor surrounding rocks in different layers.

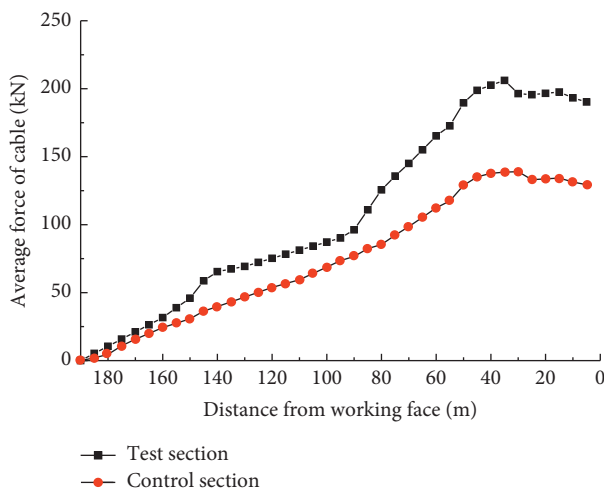


FIGURE 15: Average stress curve of anchor of surrounding rocks of solid coal side of roadway in control section and test section.

stress concentration degree of roadway side and floor. For example, the floor heave can be reduced to a certain extent by reducing the stress concentration by implementing the pressure relief of large-diameter boreholes on roadway side. The next step will focus on these three factors to carry out the related research on the mechanism of floor heave in high-stress roadway with soft rock.

5. Conclusions

Based on the serious floor heave problem of no. 130203 working face return airway in Zaoquan Coal Mine of Ningdong Mining Area, an innovative “relief-retaining” control scheme of floor heave is designed, and the specific parameters suitable for floor heave control of no. 130203 return airway are determined; then the feasibility of the

technical scheme is verified by engineering practice in the field. The main conclusions are as follows.

- (1) Taking the typical high-stress soft rock roadway with large deformation in Zaoquan Coal Mine of Ningdong Mining Area as the background, the “relief-retaining” control scheme of floor heave is proposed, which is the comprehensive measure of “cutting groove in floor+drilling for pressure relief at roadway side + setting retaining piles at the junction of roadway side and floor.”
- (2) The specific parameters suitable for floor heave control of no. 130203 return airway are determined using numerical simulation method. The depth and width of pressure relief groove are 2.0 m and 0.5 m, respectively. The length and spacing of retaining piles are 3.0 m and 1.0 m, respectively. The depth and spacing of large-diameter pressure relief boreholes are 10.0 m and 1.0 m, respectively.
- (3) By conducting “relief-retaining” control scheme, field monitoring results show that the average roof falling capacity is 596 mm, and the average floor heave displacement is 410 mm, which are, respectively, 43.67% and 67.49% less than the control section. The maximum force of cable is about 140.13 kN, which is 32.54% less. The deformation and failure of roadway surrounding rocks, especially floor heave, are well controlled.

Data Availability

The data used to support the findings of this study are available from the corresponding author upon request.

Conflicts of Interest

The authors declare no conflicts of interest.

Acknowledgments

The authors would like to thank reviewers and editors for their kind work. The authors gratefully acknowledge financial support from the National Natural Science Foundation of China (nos. 51804181, 51874190, and 52074168) and the Climbing Project of Taishan Scholar in Shandong Province (no. tspd20210313).

References

- [1] J. Shi and D. Kong, “Floor heave mechanism and anti-slide piles control technology in deep and large-span chamber,” *Applied Sciences*, vol. 11, no. 10, p. 4576, 2021.
- [2] H. Jia, L. Wang, K. Fan, B. Peng, and K. Pan, “Control technology of soft rock floor in mining roadway with coal pillar protection: a case study,” *Energies*, vol. 12, no. 15, p. 3009, 2019.
- [3] C. Wang, Y. P. Wu, S. J. Chen et al., “Analysis and application on inverted arch support of cross-cut floor heave,” *Journal of Physics: Conference Series*, vol. 2002, no. 1, pp. 713–720, 2021.
- [4] X. Kang, D. Guo, and Z. Lu, “Mechanism of roadway floor heave controlled by floor corner pile in deep roadway under

- high horizontal stress,” *Advances in Civil Engineering*, vol. 2021, Article ID 6669233, 10 pages, 2021.
- [5] W. Zheng, Y. Zhao, Q. Bu, and S. I. Kundalwal, “The coupled control of floor heave based on a composite structure consisting of bolts and concrete antiarches,” *Mathematical Problems in Engineering*, vol. 2018, Article ID 3545423, 14 pages, 2018.
- [6] M. C. He, G. F. Zhang, G. L. Wang, Y. L. Xu, C. Z. Wu, and Q. D. Tang, “Research on mechanism and application to floor heave control of deep gateway,” *Chinese Journal of Rock Mechanics and Engineering*, vol. 28, pp. 2593–2598, 2009.
- [7] J. Sun and L. Wang, “Numerical simulation of grooving method for floor heave control in soft rock roadway,” *Mining Science and Technology (China)*, vol. 21, no. 1, pp. 49–56, 2011.
- [8] J. B. Bai, W. F. Li, X. Y. Wang, X. U. Ying, and L. J. Huo, “Mechanism of floor heave and control technology of roadway induced by mining,” *Journal of Mining and Safety Engineering*, vol. 28, pp. 1–5, 2011.
- [9] Y. J. Li, “Study on mechanism analysis and control technology of roadway floor heave,” *Coal Chemical Industry*, vol. 40, pp. 31–33, 2017.
- [10] X. Q. Wang, J. G. Kan, and J. K. Jiao, “Mechanism of floor heave in the roadway with high stress and soft rock and its control practice,” *Journal of Mining and Safety Engineering*, vol. 38, pp. 215–226, 2021.
- [11] G. M. Chen, Y. T. Zhang, H. H. He, and H. W. Zhang, “Research on mechanism and control technology of floor heave in soft rock roadway in Dafosi mine,” *China Coal*, vol. 39, pp. 59–61, 2013.
- [12] C. Wang, Y. Wang, and S. Lu, “Deformational behaviour of roadways in soft rocks in underground coal mines and principles for stability control,” *International Journal of Rock Mechanics and Mining*, vol. 37, 2000.
- [13] J. C. Stankus and S. S. Peng, “Floor bolting for control of mine floor heave,” *Mining Engineering*, vol. 46, pp. 1099–1102, 1994.
- [14] P. T. Xie, “Reinforcement design and application on close roadway below mined - out area,” *Shanxi Coking Coal Science Technology*, vol. 37, pp. 8–10+14, 2013.
- [15] X. S. Liu, D. Y. Fan, Y. L. Tan et al., “Failure evolution and instability mechanism of surrounding rock for close-distance parallel chambers with super-large section in deep coal mines,” *International Journal of Geomechanics*, vol. 21, 2021.
- [16] L. Shi, H. D. Zhang, and P. Wang, “Research on key technologies of floor heave control in soft rock roadway,” *Advances in Civil Engineering*, vol. 2020, Article ID 8857873, 13 pages, 2020.
- [17] W. X. Zheng, Q. W. Bu, and Y. Q. Hu, “Plastic failure analysis of roadway floor surrounding rocks based on unified strength theory,” *Advances in Civil Engineering*, vol. 2018, Article ID 7475698, 10 pages, 2018.
- [18] X. Liu, S. Song, Y. Tan et al., “Similar simulation study on the deformation and failure of surrounding rock of a large section chamber group under dynamic loading,” *International Journal of Mining Science and Technology*, vol. 31, no. 3, pp. 495–505, 2021.
- [19] X. S. Liu, D. Y. Fan, Y. L. Tan et al., “New detecting method on the connecting fractured zone above the coal face and a case study,” *Rock Mechanics and Rock Engineering*, vol. 54, no. 8, pp. 4379–4391, 2021.
- [20] H. Zhang, H. P. Kang, and Y. L. Xu, “Study on rapid reinforced technology with pre-stressed anchor for floor of mine roadway in deep mine,” *Coal Science and Technology*, vol. 41, pp. 16–19+23, 2013.
- [21] L. Z. Xu and S. J. Wei, “Control technology and simulation study of floor heave in high stress soft rock roadway,” *Geotechnical & Geological Engineering*, vol. 38, pp. 1–14, 2020.
- [22] H. P. Kang, J. H. Wang, and J. Lin, “Study and applications of roadway support techniques for coal mines,” *Journal of China Coal Society*, vol. 35, pp. 1809–1814, 2010.
- [23] T. Yang and J. Zhang, “Research on the treatment technology of soft rock floor heave based on a model of pressure-relief slots,” *Arabian Journal Geosciences*, vol. 14, 2021.
- [24] D. Y. Fan, X. S. Liu, Y. L. Tan et al., “Roof cutting parameters design for gob-side entry in deep coal mine: a case study,” *Energies*, vol. 12, 2019.
- [25] M. G. Qian, P. W. Shi, and J. L. Xu, *Ground Pressure and Strata Control*, China University Min Techno Press, Beijing, China, 2010.
- [26] S. G. Liu, J. B. Bai, X. Y. Wang, B. W. Wu, W. D. Wu, and Z. X. Li, “Mechanisms of floor heave in roadways adjacent to a goaf caused by the fracturing of a competent roof and controlling technology,” *Shock and Vibration*, vol. 2020, Article ID 5632943, 17 pages, 2020.
- [27] D. Y. Fan, X. S. Liu, Y. L. Tan, S. L. Song, J. G. Ning, and Q. Ma, “Numerical simulation research on response characteristics of surrounding rock for deep super-large section chamber under dynamic and static combined loading condition,” *Journal of Central South University*, vol. 27, no. 12, pp. 3544–3566, 2020.
- [28] S. C. Gu, X. M. Wang, R. B. Huang, and H. W. He, “Analysis on mechanism and control technique of floor heave deformation in high stress roadway,” *Journal Safety Science and Technology*, vol. 16, pp. 57–63, 2020.
- [29] J. Yang, K. Zhou, Y. Cheng, Y. Gao, Q. Wei, and Y. Hu, “Mechanism and control of roadway floor heave in the paleogene soft rock surroundings,” *Geotechnical & Geological Engineering*, vol. 37, no. 6, pp. 5167–5185, 2019.
- [30] G. Y. Yu, J. Wang, J. Z. Hu et al., “Innovative control technique for the floor heave in goaf-side entry retaining based on pressure relief by roof cutting,” *Mathematical Problems in Engineering*, vol. 2021, Article ID 7163598, 17 pages, 2021.
- [31] G. R. Feng, S. Y. Li, P. F. Wang et al., “Study on floor mechanical failure characteristics and stress evolution in double predriven recovery rooms,” *Mathematical Problems in Engineering*, vol. 2020, Article ID 9391309, 13 pages, 2020.

Research Article

Equivalent Resilient Modulus Inversion and Calculation of Different Asphalt Pavement Structures

Mingming Cao ¹, Wanqing Huang,¹ Yiwen Zou,² and Zhiyong Wu¹

¹Sichuan Communication Surveying and Design Institute Co., Ltd., Chengdu 610041, China

²School of Civil Engineering, Southwest Jiaotong University, Chengdu 610031, China

Correspondence should be addressed to Mingming Cao; 707360021@qq.com

Received 9 October 2021; Accepted 9 November 2021; Published 22 November 2021

Academic Editor: Lingkun Chen

Copyright © 2021 Mingming Cao et al. This is an open access article distributed under the Creative Commons Attribution License, which permits unrestricted use, distribution, and reproduction in any medium, provided the original work is properly cited.

Based on the modulus inversion theory and the equivalent principle of deflection basin, by analyzing the deflection basin data of each structure layer measured by the FWD, the obtained equivalent resilient moduli of different structural layers in three different structures (a semirigid type Asphalt pavement and two inverted asphalt pavements) were compared. At the same time, the calculated equivalent resilient modulus of the top surface of the structural layer based on the inversion method was used to modify the existing theory formula. The results show that, with the inversion method and the theoretical calculation method, the calculated equivalent resilient modulus of the top surface of the cushion layer has a small error, but the theoretical calculation method overestimates the equivalent resilient modulus of the top surface of the cement stabilized crushed stone layer and the top surface of the graded crushed stone transition layer, especially for the inverted asphalt pavement; by contrast, the corresponding result of the inversion method is closer to the value in actual engineering. While determining the equivalent resilient modulus of the cushion layer, the influence of the thickness of the cement stabilized crushed stone layer needs to be considered, and the inverted asphalt pavement structure should adopt a thicker asphalt layer to reduce the modulus deviation; at the same time, the more the structural layers and the larger the difference in the interlayer modulus ratio, the larger the deviation of equivalent resilient modulus of the top surface of the base layer; for the inverted asphalt pavement and semirigid asphalt pavement, the correction coefficients of the calculation formula of the equivalent resilient modulus of the top surface of cement stabilized gravel layer are 0.35~0.55 and 0.65~0.75, respectively. The inversion method can be used to determine the equivalent resilient modulus of each structural layer of the inverted asphalt pavement and semirigid asphalt pavement, and its results can provide a basis for the design of the structure reconstruction of asphalt pavement.

1. Introduction

During the road reconstruction design of pavement, it is necessary to know the equivalent resilient modulus of the existing pavement or the top surface of the foundation. In fact, the equivalent resilient modulus is characterized by the ability to resist the load of a multilayer system composed of soil foundation, graded crushed stone, and cement stabilized crushed stone; these materials have different modulus and thicknesses. Therefore, it is necessary to transform the multilayer structure system into a 2-layer or 3-layer equivalent semi-infinite homogeneous space system according to the equivalent physical principle of deflection value and flexural stress [1–3]. At present, most studies

mainly focus on solving the equivalent resilient modulus of the foundation or the cement concrete. The conversion formula of the equivalent resilient modulus of the foundation was modified according to the equivalent principle of deflection and introduced the correction coefficient of the influence of the load action radius; this formula is suitable for conversion of equivalent resilient modulus of the top surface of the base layer [4–6]. A method to calculate the equivalent resilient modulus of the top surface of the cement concrete pavement base layer was proposed based on different equivalence principles such as deflection, flexural stress, and temperature [7–11]. Besides, the influence of the contact situation between layers on the calculation results was also considered, but the calculation result based on the

bending-tension stress and temperature was poor; particularly, it is difficult to effectively monitor bending-tension stress, and the equivalent principle based on the deflection value has a wide range of applications. Jiang and Yao [12] and Tan et al. [13] proposed the approximate conversion formula of the multilayer structure under different load forms (single circle, double circle wheel load) and regressed the calculation formula of the equivalent modulus of the top surface of the double-layer structure under different inter-layer contact conditions (smooth, continuous). Vakili [14] established an equivalent modulus calculation model for simple pavement structure layer (the pavement structure layer on the subgrade is regarded as a two-layer elastic layered system) and verified the accuracy of the model using the inversion method (the ratio of pavement equivalent modulus to subgrade modulus).

In the structure design of cement concrete pavement, the equivalent resilient modulus of the top surface of the structural layer needs to be solved; the existing research mainly focuses on the equivalent resilient modulus of the top surface of the cement concrete pavement or soil foundation [15–20], but the asphalt material pavement has obvious viscoelastic properties; the influence of temperature must be considered in calculation or correction; besides, due to the high complexity of structural and material properties, there are relatively few studies on the equivalent resilient modulus of asphalt pavement. Based on the design method of the overlay layer, Guo et al. [21] calculated the minimum equivalent resilience modulus of the top surface of the crushed layer under different structural combinations and did not study the calculation method of the equivalent resilience modulus. According to the theory of section bending stiffness, Tan and Yu [22] studied the equivalent resilient modulus of asphalt surface layer and considered the contact conditions between different layers. In addition, by comparing the inverse calculated modulus of the indoor dynamic triaxial test, rotary compaction molding, and the test road structure, Xu et al. [23] studied the correction coefficient of the modulus inversion value. Cao et al. [24] research showed that the structure of the inverse asphalt pavement was more complex, and the traditional modulus inversion error was larger than the inversion value of the semirigid asphalt pavement; besides, the layer-by-layer inversion method can improve the accuracy of the modulus inversion. Considering the current equivalent resilience modulus research is mainly based on the theoretical calculation and analysis of semirigid asphalt pavement, without too much field verification, in this paper, by testing the dynamic deflection of three pavement structures by layer, the equivalent resilient modulus of the top surface of the cushion layer, the top surface of the base layer, and the top surface of the transition layer was determined using the inversion method, which was also used to correct theoretical calculation formula, providing the basis for the road overlay design of the semirigid asphalt pavement and inverted asphalt pavement.

2. The Test Pavement Structure and Equivalent Resilient Modulus Inversion Method

2.1. The Test Pavement Structure. The test section of Sui-Guang Expressway adopted two kinds of structural forms, the semirigid asphalt pavement (S1) and inverted asphalt pavement (S2 and S3), as shown in Table 1. The traffic grade of Sui-Guang Expressway is heavy traffic grade.

2.2. Theoretical Calculation Method for Determining Equivalent Resilient Modulus. While using the theoretical calculation method to calculate the equivalent resilient modulus, firstly, the structural layer is converted into an equivalent single-layer structure (Figure 1); then, the equivalent resilient modulus of the top surface of the cement stabilized crushed stone layer is calculated as follows [1]:

$$E_t = ah_x^b E_0 \left(\frac{E_x}{E_0} \right)^{1/3},$$

$$a = 6.22 \left[1 - 1.51 \left(\frac{E_x}{E_0} \right)^{-0.45} \right],$$

$$b = 1 - 1.44 \left(\frac{E_x}{E_0} \right)^{-0.55},$$
(1)

where E_t represents the equivalent resilient modulus of the top surface of the cement stabilized crushed stone layer (MPa), E_x represents the modulus of cement stabilized crushed stone layer (MPa), H_x represents the thickness of cement stabilized crushed stone layer (m), E_0 represents the resilient modulus of the top surface of the graded crushed stone cushion layer (MPa), and a and b are regression coefficients relating to E_x/E_0 .

In addition, the equivalent modulus of the top surface of the graded crushed stone cushion layer is calculated using formulas (2) and (3) in the “Standard for Design of Highway Cement Concrete JTG D40-2011.”

$$E_{2t} = \left(\frac{E_3}{E_4} \right)^\alpha E_4,$$
(2)

$$\alpha = 0.86 + 0.26 \ln h_3,$$
(3)

where E_{2t} represents the equivalent modulus of the top surface of the graded crushed stone cushion layer (MPa), E_3 and h_3 represent the modulus (MPa) and thickness (m) of the graded crushed stone cushion layer, respectively, E_4 represents the modulus of the soil foundation (MPa), and a is the regression coefficient. Besides, while calculating the equivalent modulus of the top surface of the graded gravel transition layer using (2) and (3), the lower structure is used as the base.

TABLE 1: The structure of the test section.

Pavement structure	S1 (semirigid structure)	S2 (inverted structure 1)	S3 (inverted structure 2)
The asphalt mastic macadam SMA upper surface layer (cm)		4	
The SBS modified asphalt AC-20C middle surface layer (cm)		6	
The lower surface layer	The type Asphalt AC-20C	The SBS modified asphalt AC-20C	ATB-25
The type			
The thickness (cm)	8	8	12
The graded crushed stone transition layer (cm)	—		12
The cement stabilized crushed stone base (cm)	28		20
The cement stabilized crushed stone subbase (cm)	28	24	20
The graded crushed stone cushion layer (cm)	15	15	15
The total pavement thickness (cm)	89	89	89

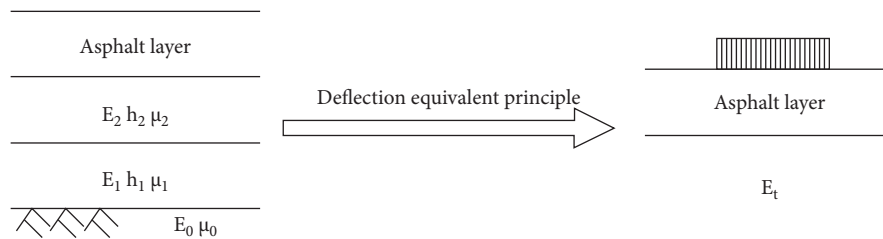


FIGURE 1: Conversion model of equivalent principle of deflection.

2.3. *The Method of Determining the Equivalent Resilient Modulus Based on Deflection.* During the calculation of the equivalent resilient modulus, the calculated theoretical equivalent modulus through multiple double-layer conversion is greater than the result of one double-layer conversion [8, 25], and it was believed that the deviation of the calculation results of these two conversion methods is mainly due to the difference in load distribution on the top surface of different structural layers, which means the actual load effect is smaller and the load distribution on the top surface of each structural layer is mostly in the shape of bell rather than the uniform distribution. Therefore, in order to prevent the overestimation of equivalent modulus using multiple double-layer conversions and to make it conform to the actual field value, the inversion method was proposed in this paper. Based on the theory of elastic layered system, the inversion method adopts the tested deflection of the top surface of each structural layer by FWD as the basic data and regards the modulus of each structural layer calculated with the aid of the inversion program as the structural layer modulus; moreover, the designated structural layer and lower structural layer are considered as one layer, to determine the equivalent resilient modulus of the top surface of the designated structural layer using the inversion method again. While using the inversion method to determine the equivalent resilient modulus, the variable is only the equivalent resilient modulus, which avoids the tedious process of multiple double-layer conversions, reduces the variable number, and improves inversion accuracy. The existing pavements are often unable to test the top surface

deflection and sink of the top surface of each structural layer, and the modulus can be inverted based on the deflection and sink of road surface.

A more advanced iteration method was adopted, in which based on the assumed structural layer modulus, the theoretical deflection basin is calculated using the mechanical calculation method. By analyzing the difference in deflection basin between the actual measurement and the theoretical calculation, the new assumed combination of structural layer modulus is determined; then, the calculation is repeated until the mean square error between the measured and the theoretical deflection basin reached the minimum value, and the ending condition is set as the iterations number or the preassumed convergence accuracy [26].

3. Deflection Data of Different Pavement Structures

Following the “Field Test Regulations of Highway Subgrade and Pavement” (JTGE60-2008), the PRIMAX1500 FWD (Figure 2) was used to test the dynamic deflection basin of the top surface of the base layer, the graded crushed stone transition layer, the lower layer, the middle layer, and the upper layer. The distance between the sensor and the center of the loading plate is shown in Table 2. The FWD test of the cement stabilized crushed stone base layer is performed 30 days after its construction is completed, and the subsequent test intervals of each layer are within 48h.



FIGURE 2: FWD field testing.

TABLE 2: The distance between the sensor and the center of the loading plate.

The distance between the sensor and the center of the loading plate (cm)											
0	20	30	40	50	60	90	120	150	180	210	

4. Comparison of Calculated Equivalent Modulus of Different Structures

4.1. Calculation and Comparison of Equivalent Resilient Modulus of Top Surface of Cushions with Different Structures. Based on the deflection basin data of the top surface in the FWD test, the inversion method and theoretical calculation method were used to determine the equivalent resilient modulus of the cushion top surface, as shown in Tables 3 and 4. For the three test sections, the roadbed and graded crushed stone cushions layers all adopt the same construction technology, raw materials, and construction team. The tested roadbed is uniformly compacted, and its compaction is greater than 96%, with a maximum of 98.3%, and an average of 97.4%. The compaction of graded crushed stone cushions layer is greater than 97%, with a minimum of 97.9%, a maximum of 108.4%, and an average of 102%. In theory, the equivalent resilience modulus of the top surface of any cushion in the test section should be basically the same. However, the equivalent resilience modulus determined by the inversion method or theoretical calculation method is not the same, structure S3 < structure S2 < structure S1. At the same time, the thickness values of the cement stabilized crushed stone layer of structure S1, structure S2, and structure S3 are 56 cm, 44 cm, and 40 cm, respectively. It can be inferred that the thickness of the cement stabilized crushed stone layer affects the inversion result of the equivalent resilient modulus. With the theoretical calculation method, the calculated equivalent modulus of the top surface of structure S1 cushion layer is 1.11 times that of structure S2 and 1.28 times that of structure S3; at the same time, with the inversion method, the determined equivalent modulus of the top surface of structure S1 cushion layer determined is 1.16 times that of structure S2

and 1.40 times that of structure S3; it can be seen that when the thickness of the cement stabilized crushed stone layer is thin, for the same decrease of the thickness of the cement stabilized crushed stone layer, the reduction in the equivalent modulus of the cushion top surface is greater than that of thick cement stabilized crushed stone layer. Besides, the decrease of the equivalent modulus of the cushion top surface determined by the inversion method is more than the result of the theoretical calculation method, suggesting it is important to accurately test the thickness of the cement stabilized gravel layer for using the inversion method to determine the equivalent modulus of the top surface of cushion layer.

The difference in the determined equivalent resilient modulus of the cushion top surface between the theoretical calculation method and the inversion method was structure S3 < structure S2 < structure S1, but the absolute values of the deviation were all within 10%, so it can be concluded that the equivalent resilient moduli determined by these two methods are basically the same, and they can be used to determine the equivalent resilient modulus of the top surface of cushion layer of semirigid asphalt pavement and inverted asphalt pavement.

4.2. Calculation and Comparison of Equivalent Resilient Modulus of the Top Surface of Different Base Structures. Based on the FWD deflection basin data, the equivalent resilient modulus of the top surface of the base layer was determined using the inversion method and theoretical calculation method, as shown in Tables 5 and 6. It can be seen that the equivalent resilient modulus of the top surface of the base layer of structure S1 was greater than that of structures S2 and S3, and the value of structure S3 was the smallest. When FWD is subjected to the top surface of the asphalt layer, the thickness and characteristics of the asphalt layer (such as temperature) will affect the equivalent resilient modulus value of the top surface of the base layer. According to Table 6, for structure S1, based on the deflection basin data of the top surface of the lower layer tested by FWD, the equivalent resilient modulus of the base layer top surface determined by the inversion method was 1.38 and 1.37 times that based on deflection basin data of the top surface of the middle layer and the upper layer; at the same time, its value determined by the theoretical calculation method was 1.64 times and 1.59 times that based on deflection basin data of the top surface of the middle layer and the upper layer.

In addition, compared with the theoretical calculation method, the deviation value of the equivalent resilient modulus of the top surface of the cushion determined by the inversion method (Table 3) is significantly smaller than that of the equivalent resilient modulus of the base layer top surface (Tables 5 and 6). The equivalent resilient modulus of the top surface of the cushion is the equivalent of the modulus of the subgrade and the graded crushed stone cushion layer, their modulus ratio was less than 3, and the thickness of the cushion layer was small. The subgrade is a half-space infinite elastic body, and the equivalent resilience modulus of the top surface of the cushion layer is

TABLE 3: The calculation of equivalent resilient modulus of the top surface of the cushion layer when FWD is loaded on the top surface of the base layer.

Structural layer	Determined method		Base layer	Cushion layer	Roadbed
S1	Equivalent resilient modulus	Inversion modulus value (MPa)	8417	309	206
		Theoretical calculation method (MPa)	—	239	
		Inversion method (MPa)	—	243	
		Deviation value (%)	—	-2	
S2	Equivalent resilient modulus	Inversion modulus value (MPa)	6330	309	175
		Theoretical calculation method (MPa)	—	216	
		Inversion method (MPa)	—	206	
		Deviation value (%)	—	5	
S3	Equivalent resilient modulus	Inversion modulus value (MPa)	4762	309	139
		Theoretical calculation method (MPa)	—	186	
		Inversion method (MPa)	—	174	
		Deviation value (%)	—	7	

TABLE 4: Determination of equivalent resilient modulus of cushion top surface based on road surface deflection.

Structural layer	Determined method		Cushion layer	Roadbed
S1	Equivalent resilient modulus	Inversion modulus value (MPa)	309	141
		Theoretical calculation method (MPa)		188
		Inversion method (MPa)		195
		Deviation value (%)		-4
S2	Equivalent resilient modulus	Inversion modulus value (MPa)	309	138
		Theoretical calculation method (MPa)		185
		Inversion method (MPa)		197
		Deviation value (%)		-6
S3	Equivalent resilient modulus	Inversion modulus value (MPa)	309	152
		Theoretical calculation method (MPa)		197
		Inversion method (MPa)		181
		Deviation value (%)		9

mainly determined by the subgrade modulus; while determining the equivalent resilience modulus of the top surface of the base layer, the thickness of the cement stabilized crushed stone layer is large, its modulus is more than 10 times that of the subgrade or graded crushed stone, and the load is mainly borne by the roadbed and the cement stabilized crushed stone layer. Therefore, the determined equivalent resilient modulus of the top surface of the base layer is far greater than the subgrade modulus and smaller than the modulus of the cement stabilized crushed stone layer, and thicker cement-stabilized crushed stone layer or larger subgrade modulus can improve the equivalent resilience modulus of the top surface of the base layer. At the same time, while calculating the equivalent resilient modulus of the top surface of the base layer with the theoretical calculation method, the three-layer system of cement-stabilized crushed stone layer, cushion layer, and subgrade is transformed into a one-layer system, and more conversion times will increase the deviation of the calculated equivalent resilient modulus of the top surface of the base layer. Besides, the more the structural layers in the inversion or calculation of the equivalent resilient modulus, the greater the modulus ratio of the interlayer, and the greater the deviation of the equivalent modulus of elasticity determined by the inversion method compared with the theoretical calculation method.

4.3. Comparison and Calculation of Equivalent Resilient Modulus of the Top Surface of Transition Layer with Different Structure. Based on the FWD test deflection basin data of asphalt upper layer, middle surface layer, and lower layer of structure S2 and structure S3, the inversion method and theoretical calculation method were used to determine the equivalent resilient modulus of the top surface of the graded gravel transition layer, as shown in Table 7. It can be seen that the equivalent resilient modulus obtained by the theoretical calculation method was about 1.7~2.4 times that of the inversion method. Based on the FWD test deflection basin data of the lower layer of the asphalt, compared to the result of the theoretical calculation method, the deviation of equivalent resilient modulus of structure S2 determined by the inversion method was greater than that of structure S3, and this deviation value decreased with the increase of the number of asphalt surface layers; besides, a thick asphalt layer can reduce this deviation. Therefore, while determining the equivalent resilient modulus of the top surface of the transition layer, it is better to use FWD to test the deflection basin data of the asphalt upper layer. This is because the increase of the thickness of the asphalt layer increases the weight of the superstructure so as to improve the confining pressure of the loaded part of the graded crushed stone, making the modulus of the graded crushed stone layer become higher and the internal force of the graded crushed

TABLE 5: The calculation of the equivalent resilient modulus of the top surface of the base layer when FWD is loaded on the top surface of the transition layer.

Structural layer	Inversion modulus value (MPa)	S2			S3			
		Equivalent resilient modulus			Equivalent resilient modulus			
		Theoretical calculation method (MPa)	Inversion method (MPa)	Deviation value (%)	Inversion modulus value (MPa)	Theoretical calculation method (MPa)	Inversion method (MPa)	Deviation value (%)
Transition layer	243	—	—	—	243	—	—	—
Base layer	6330				4762			
Cushion layer and roadbed	134	1121	762	47	101	780	360	117

TABLE 6: Calculation of equivalent resilient modulus of the top surface of structure S1.

Load layer	Determined method			Base layer	Cushion layer and roadbed
Lower layer	Equivalent resilient modulus	Inversion modulus value (MPa)		8417	489
		Theoretical calculation method (MPa)			3039
		Inversion method (MPa)			1845
Middle layer	Equivalent resilient modulus	Deviation value (%)			65
		Inversion modulus value (MPa)		8417	185
		Theoretical calculation method (MPa)			1858
Upper layer	Equivalent resilient modulus	Inversion method (MPa)			1336
		Deviation value (%)			39
		Inversion modulus value (MPa)		8417	195
Upper layer	Equivalent resilient modulus	Theoretical calculation method (MPa)			1913
		Inversion method (MPa)			1344
		Deviation value (%)			42

TABLE 7: Calculation of the equivalent resilient modulus of the top surface of the graded gravel transition layer.

Structural layer	Inversion modulus value (MPa)	S2			S3			
		Equivalent resilient modulus			Equivalent resilient modulus			
		Theoretical calculation method (MPa)	Inversion method (MPa)	Deviation value (%)	Inversion modulus value (MPa)	Theoretical calculation method (MPa)	Inversion method (MPa)	Deviation value (%)
FWD loading on the top surface of the lower layer								
Transition layer	243				243			
Base layer	6330	837	351	138	4762	546	270	102
Cushion layer and roadbed	212				102			
FWD loading on the top surface of the middle layer								
Transition layer	243				243			
Base layer	6330	684	356	92	4762	578	278	108
Cushion layer and roadbed	127				117			
FWD loading on the top surface of the upper layer								
Transition layer	243				243			
Base layer	6330	813	467	74	4762	685	358	91
Cushion layer and roadbed	197				181			

TABLE 8: Determination of the equivalent resilient modulus of the top surface of the structural layer.

Structure	Structural layer	Equivalent resilient modulus (MPa)		
		Theoretical calculation method	Corrected theoretical calculation method	Inversion method
Semirigid structure	Base layer	835	585	535
	Base layer	483	217	211
Inverted structure	Transition layer	532	239	233

stone layer more uniform; furtherly, the effect of the error on the equivalent resilient modulus is reduced, and the accuracy of the inversion of the equivalent resilient modulus of the top surface of the transition layer is improved.

5. Modification of the Theoretical Calculation Formula of Equivalent Resilient Modulus

According to the analysis above, it can be known that the determination of the equivalent resilient modulus of the top surface of the cushion layer is less affected by the pavement structure, and the existing calculation method has high accuracy. Formulas (2) and (3) are recommended. For the equivalent resilient modulus of the top surface of the base layer, when $E_d/E_s \approx 47$, the deviation of the resilient modulus of structure S3 determined by theoretical calculation method and the inversion method is up to 117%, while the deviation of structure S2 is 47%, so except the modulus ratio, factors such as the type of pavement structure and the FWD loading layer position should also be considered while deriving the calculation formula of the equivalent modulus of the base layer. Due to the different structure types and the different FWD loading position, the equivalent resilient modulus of the top surface of each structural layer determined by the calculation method and the inversion method is different. Therefore, by regressively and comparatively analyzing the equivalent resilient modulus of the top surface of each structural layer determined by the theoretical calculation and inversion, their difference is eliminated by introducing the correction coefficient k_1 to formula (1), which is 0.65~0.75 for semirigid asphalt pavement, and 0.35~0.55 for inverted asphalt pavement. The large difference in structural characteristics results in a significant difference in the correction coefficient of equivalent modulus theoretical calculation formula of semirigid asphalt pavement and inverted asphalt pavement. The specific value of k_1 depends on the thickness of the asphalt layer and the FWD loading position; the closer the FWD loading position to the top surface of the base layer, the closer the value to the upper limit. After the correction, the calculation of the equivalent modulus of the top surface of the base is shown in formula (2), in which the regression parameters a and b are calculated as before. Compared to the inversion method, the deviation of the equivalent resilient modulus of the top surface of the base layer determined by the corrected calculation method is within 20%, with a maximum value of 19%.

$$E_t = k_1 a h_x^b E_0 \left(\frac{E_x}{E_0} \right)^{1/3} \quad (4)$$

While using modified formulas (2)–(4) to calculate the equivalent resilient modulus of the top surface of the graded crushed stone transition layer, k_1 was taken as 0.35 to obtain the deviation within 20% compared with the inversion method, and the maximum deviation is 16%; this calculation accuracy meets the requirements of engineering applications.

In order to verify the reliability of the calculation formula for the equivalent resilience modulus of the top surface of the structural layer based on the corrected measured deflection basin data, two kinds of asphalt pavement structures in Sichuan were selected [27], and the determined equivalent resilient modulus of the top surface of the base layer with different methods is shown in Table 8. The correction coefficient k_1 of the semirigid structure was 0.7, and the correction coefficient k_1 of the inverted structure was 0.45. Compared with the inversion method, the deviation of using the corrected theoretical calculation method is within 10%, which is much decreased. It can be seen that using the modified theoretical calculation formula to calculate the equivalent resilient modulus of the top surface of the structure layer is more in line with the actual value.

6. Conclusions

- (1) The equivalent resilient modulus is influenced by factors such as pavement structure characteristics (thickness of adjacent layers, structure type, etc.), material characteristics, and loading layer position. The thin cement stabilized crushed stone layer or asphalt surface layer in the inverted asphalt pavement is not conducive to accurately determining the equivalent resilient modulus value of the structural layer.
- (2) Generally, in terms of the deviation of the equivalent resilient modulus of the top surface of the cushion layer determined by the theoretical calculation method and the inversion method, the semirigid asphalt pavement is smaller than the inverted asphalt pavement, and the deviation using these two methods is less than 10%. However, for the equivalent resilience modulus of the top surface of the base layer and the equivalent resilience modulus of the top surface of the transition layer, this deviation is larger than 40% and 70%, respectively. Therefore, these two methods can be used to determine the equivalent resilience modulus of the top surface of the cushion layer, but the inversion method should be preferred while determining the equivalent resilient modulus under other working conditions.

- (3) With using the corrected calculation formula of the equivalent resilient modulus of the top surface of the cement stabilized crushed stone layer, the calculated equivalent resilient modulus of the top surface of the transition layer is close to that obtained by the inversion method, which means the distortion of equivalent resilient modulus calculated by theoretical calculation method comes from the calculation formula of equivalent modulus of the top surface of cement-stabilized crushed stone layer; based on this, the correction coefficient of structure type is introduced.
- (4) The accuracy of the equivalent resilient modulus determined by the inversion method is higher than that of the theoretical calculation method and more in line with the actual value. While determining the equivalent resilient modulus of the asphalt pavement structure, the inversion method is more suitable; when the test conditions are insufficient, the modulus of the structural layer of similar engineering can be considered to be substituted into the correction formula to calculate the equivalent resilient modulus of the top surface of the structural layer.

Data Availability

The data used to support the findings of this study are available from the corresponding author upon request.

Conflicts of Interest

The authors declare that they have no conflicts of interest.

Acknowledgments

This study was supported by the Sichuan Transportation Science and Technology Project (Grant nos. 4-1, 2015) and the Sichuan Province Science and Technology Planning Project (Application Fundamental Research) (Grant no. 2020YFS0362).

References

- [1] Z. H. Wang, L. C. Cai, Q. K. Gu, X. J. Liu, and A. H. Wu, "Modified calculation method of equivalent modulus of elasticity of foundation," *Journal of Air Force Engineering University (Natural Science Edition)*, vol. 10, no. 6, pp. 23–27, 2009.
- [2] X. S. Mao and X. L. Zhi, "Checking method of construction deflection of semi-rigid base," *Journal of Xi'an Highway University (Natural Science Edition)*, vol. 23, no. 2, pp. 37–40, 2003.
- [3] X. Liu, S. Song, Y. Tan et al., "Similar simulation study on the deformation and failure of surrounding rock of a large section chamber group under dynamic loading," *International Journal of Mining Science and Technology*, vol. 31, no. 3, pp. 495–505, 2021.
- [4] Y. J. Jiang, J. L. Dai, and Z. D. Chen, "Calculation method of equivalent modulus of elasticity of foundation under principles of different equivalence," *Journal of Chang'an University (Natural Science Edition)*, vol. 25, no. 3, pp. 1–6, 2005.
- [5] Y. Zhou, D. Zhao, B. Li, H. Wang, and Q. Zhang, "Fatigue damage mechanism and deformation behaviour of granite under ultrahigh-frequency cyclic loading conditions," *Rock Mechanics and Rock Engineering*, vol. 54, no. 9, pp. 4723–4739, 2021.
- [6] X. Liu, D. Fan, Y. Tan et al., "New detecting method on the connecting fractured zone above the coal face and a case study," *Rock Mechanics and Rock Engineering*, vol. 54, no. 8, pp. 4379–4391, 2021.
- [7] H. P. Wang, "Research on the revised coefficient of the recommended value for earth subgrade rebound modulus in the design of rigid pavement," *China Journal of Highway and Transport*, vol. 11, no. 4, pp. 1–20, 1998.
- [8] Z. M. Tan and L. Wang, "Equivalent resilient modulus of subgrade based on principle of flexural-tensile stress equivalence," *Journal of Highway and Transportation Research and Development*, vol. 32, no. 3, pp. 46–50, 2015.
- [9] Y. J. Jiang, C. L. Hou, X. F. Qin, and Z. D. Chen, "Calculation method of composite resilient modulus of foundation under cement concrete pavement," *Journal of Highway and Transportation Research and Development*, vol. 22, no. 5, pp. 38–42, 2005.
- [10] Y. J. Jiang and J. L. Dai, "Calculation method of equivalent modulus of elasticity of foundation under principles of thermal stress equivalence," *Journal of Highway and Transportation Research and Development*, vol. 23, no. 7, pp. 10–13, 2006.
- [11] Y. Sun, G. Li, N. Zhang, Q. Chang, and J. Zhang, "Development of ensemble learning models to evaluate the strength of coal-grout materials," *International Journal of Mining Science and Technology*, vol. 31, no. 2, pp. 153–162, 2021.
- [12] A. F. Jiang and Z. K. Yao, "Calculation of surface equivalent modulus of subgrade in the pavement structure," *Journal of Tongji University: Natural Science Edition*, vol. 29, no. 5, pp. 536–540, 2001.
- [13] Z. M. Tan, Z. K. Yao, and B. Y. Liu, "Approximate calculation of equivalent modulus of end face of layered structures," *Highways*, vol. 48, no. 8, pp. 5–8, 2003.
- [14] J. Vakili, "A simplified method for evaluation of pavement layers moduli using surface deflection data," *Proceedings of the 12th International Conference of International Association for Computer Methods and Advances in Geomechanics (IAC-MAG)*, vol. 16, pp. 4314–4319, 2008.
- [15] Q. K. Gu, R. Y. Zhang, B. Qu, and Y. Li, "Method on the calculation of compressive modulus based on loading test," *Journal of Chang'an University (Natural Science Edition): Natural Science Edition*, vol. 35, no. 1, pp. 56–60, 2015.
- [16] J. M. Wu, R. Y. Du, and X. F. Wang, "Design method of asphalt pavement's overlay based on valid modulus," *Journal of Chang'an University (Natural Science Edition)*, vol. 32, no. 4, pp. 1–6, 2012.
- [17] S. Shao, C. Wu, M. Hao et al., "A novel coating technology for fast sealing of air leakage in underground coal mines," *International Journal of Mining Science and Technology*, vol. 31, no. 2, pp. 313–320, 2021.
- [18] Y. Zhang, Y. Xie, Y. Zhang, J. Qiu, and S. Wu, "The adoption of deep neural network (DNN) to the prediction of soil liquefaction based on shear wave velocity," *Bulletin of Engineering Geology and the Environment*, vol. 80, no. 6, pp. 5053–5060, 2021.
- [19] H. Rafezi and F. Hassani, "Drilling signals analysis for tricone bit condition monitoring," *International Journal of Mining Science and Technology*, vol. 31, no. 2, pp. 187–195, 2021.

- [20] X. S. Liu, D. Y. Fan, Y. L. Tan et al., "Failure evolution and instability mechanism of surrounding rock for close-distance parallel chambers with super-large section in deep coal mines," *International Journal of Geomechanics*, vol. 21, no. 5, 2021.
- [21] L. Guo, Y. Zhou, and Z. Tan, "Loading stress of asphalt overlay on rubblized cement concrete pavement and related resilient modulus," *Journal of Highway and Transportation Research and Development*, vol. 5, no. 1, pp. 7–12, 2012.
- [22] Z. M. Tan and X. H. Yu, "Calculation of sectional flexural stiffness equivalent modulus of asphalt pavement," *China Journal of Highway and Transport*, vol. 25, no. 6, pp. 37–42, 2012.
- [23] Y. L. Xu, B. M. Tang, G. D. Xie, and S. Chen, "Back calculated modulus correction coefficient for asphalt concrete layer based on fwd," *Journal of Chang'an University (Natural SciEnce Edition)*, vol. 32, no. 3, pp. 24–29, 2012.
- [24] M. Cao, W. Huang, Y. Zou, and Y. Liu, "Modulus inversion layer by layer of different asphalt pavement structures," *Advances in Civil Engineering*, vol. 2021, pp. 1–10, Article ID 1928383, 2021.
- [25] Z. M. Tan, "Simplified calculation of bi-layer plate bending with semi-continue condition," *Highways*, vol. 4, pp. 25–26, 2001.
- [26] P. Li, "Study of the pavement modulus backanalysis using the database of FWD" Qingdao: Master's degree thesis of Shandong University of Science and Technology, 2007.
- [27] C. Xiao, Y. J. Qiu, J. Zeng, and B. X. Li, "Measured dynamic response of asphalt pavement under fwd load," *Journal of Highway and Transportation Research and Development*, vol. 8, no. 4, pp. 1–9, 2012.

Research Article

Research on Hysteretic Models for Prestressed and Non-Prestressed Steel Reinforced Concrete Frames

Huihui Luo ¹ and Kun Wang ^{2,3}

¹College of Guangling, Yangzhou University, Yangzhou 225127, China

²College of Civil Science and Engineering, Yangzhou University, Yangzhou 225127, China

³Jiangsu Hanjian Group Company Limited, 225000, China

Correspondence should be addressed to Huihui Luo; 060137@yzu.edu.cn

Received 3 July 2021; Accepted 24 September 2021; Published 12 October 2021

Academic Editor: Zhiyong Chen

Copyright © 2021 Huihui Luo and Kun Wang. This is an open access article distributed under the Creative Commons Attribution License, which permits unrestricted use, distribution, and reproduction in any medium, provided the original work is properly cited.

The beam-column fibre model is used to simulate the entire hysteretic process of the prestressed and non-prestressed steel reinforced concrete frame, and the results are compared with the test results. Based on the analysis of a large number of parameters, the hysteretic curve characteristics of this kind of composite frame are discussed, and the load-displacement hysteretic models of single-storey and single-span composite frame are established. The models can comprehensively consider the influence of axial compression ratio and column slenderness ratio and can predict the hysteretic behaviour of this kind of composite frame under horizontal loads. The load-displacement hysteretic models are consistent with the numerical simulation results. Relevant research can provide reference for simplifying the elastic-plastic dynamic analysis of structures.

1. Introduction

Prestressed steel reinforced concrete structures have the advantages of high bearing capacity and good seismic performance, which have been widely used in practical engineering, especially in the super-span and out-jacketing frame structure [1–4]. However, due to the uneven distribution of lateral stiffness and bearing capacity along the height of the out-jacketing building, it is necessary to have a comprehensive grasp of its overall seismic performance under rare earthquakes [5, 6]. As mathematical models of the relationship between restoring force and deformation obtained after abstraction and simplification, the hysteretic models can better reflect the seismic performance of structures or components and have been extensively studied.

At present, at the level of components, Xue et al. [7] established the $M-\varphi$ hysteretic models of prestressed steel reinforced concrete beams. Zheng et al. [8] proposed the $M-\varphi$ hysteretic models of angle-steel concrete columns based on the experimental results and numerical simulations. At the level of frame structure, Wang et al. [9] built a practical

hysteretic model for concrete filled steel tubular frame, which can effectively predict the mechanical behaviour of the frame. Hu et al. [10] presented the hysteretic models of steel frames infilled with the reinforced concrete deep beam with the skeleton curves as a three-fold line based on the test results. Wang et al. [11] developed a simplified hysteretic model based on the analysis of experimental results, which can better describe the hysteretic performance of the frame under repeated loads. It can be seen that almost of the above studies involve the hysteretic characteristics of the combined frame proposed in this paper, and the idea and method of establishing the hysteretic model provide an important reference basis for the study in this paper.

For this reason, a numerical model of a single-storey and single-span frame was proposed for prestressed and non-prestressed steel reinforced concrete frames, which was compared with the tested results. Through the analysis of a large number of parameters by using the numerical model, the characteristics of hysteretic curves of this type of the composite frame were analysed, and the horizontal load-displacement hysteresis models of this type of single-storey

and single-span composite frame were obtained by statistical regression and compared with the results of numerical calculation, which provided a reasonable basis for the elastoplastic dynamic analysis of simplified structure.

2. Numerical Models

2.1. The Establishment of the Models. In this paper, a numerical analysis model of a single-storey and single-span frame was established for both prestressed and non-prestressed steel reinforced concrete frame structures based on the seismic analysis platform OpenSees [12]. The prestressed tendons in the frame beams were arranged in the form of three-segment parabola and each cross section had a certain variation, so the lumped plastic hinge fibre element named Beam with Hinges Element was used to simulate the beams. Since the cross section was the same in the axial direction for frame columns, the distributed plastic hinges beam-column fibre element named Nonlinear Beam Column Element was adopted in this paper. Reference [13] describes the two-stage principle of prestressing: in the first stage, the concentrate forces and moments at two beam ends and the equivalent load on beam between joints are conceived as external loads when effective prestressing stress is built through tensioning the tendons; in the second stage, the redundant strength exceeding the effective prestressing stress in tendons is used to resist the additional external loads, and thus the tendons with redundant strength could be thought as materials. The node arrangement and section division of the prestressed steel concrete frame model as well as loading patterns are presented in Figure 1. In the figure, the frame beam is divided into 6 elements according to the prestressed equivalent load, the vertical load distribution, and the midspan point. The nodes were, respectively, set at the beam end, the middle span, the point of inflection for prestressed reinforcement, and the vertical concentrated load points. Each frame column was divided into one element, and the bottom of the frame column was rigidly connected to the foundation. The horizontal cyclic load P was imposed on node 3 at the left end of the frame beam, the vertical concentrated forces N_1 were applied on nodes 3 and 4, and concentrated loads N_2 were exerted on nodes 5 and 6 on the beam. When the cross-sectional area of the prestressed tendons was zero, the model can be transformed into a non-prestressed steel reinforced concrete frame. For the beams and columns, the cross-sectional concrete was divided into two portions due to the confinement effect of stirrups, which were concrete cover and concrete confined by stirrups. In addition, the connection of beams and columns in the numerical model is rigidly connected.

3. Material Constitutive Relationship

The concrete adopted the model Concrete01 provided in OpenSees (see Figure 2). In the figure, f_c is the compressive strength of concrete cylinder, K is the coefficient of strength increase due to constraint consideration, ε_0 is the peak strain, ε_p is the compressive strain after unloading, ε_u is the compressive strain at the unloading point, and $\varepsilon_{u'}$ is the ultimate

compressive strain. No influence of concrete under tension was considered in this model, and the stress-strain relationship of uniaxial compression was from the Kent–Park model modified by Scott [14–16]. The hysteretic rule of Concrete01 model was based on the hysteretic model provided by Karsan and Jirsa. To simplify the analysis, the confinement effect of the steel embedded in the beam and column was not considered in the modelling. Therefore, beam and column sections were only divided into concrete core and concrete cover without stirrup confinement, and confined and unconfined concrete models were adopted, respectively.

The steel adopted the steel02 model in OpenSees, which was a bilinear kinematic hardening model considering the Bauschinger effect. The prestressed reinforcement adopted the Elastic Perfectly Plastic Material model in OpenSees. According to the two-stage principle of prestressing, the residual strength of the prestressed tendons took the stress-strain relationship displayed in Figure 3, and unloading and reloading were carried out along a straight line, after the effective prestress was deducted from the second-stage prestressed tendons of the external load. In the figure, $f_{p0.2}$ is the conditional yield strength, σ_{pe} is the effective prestress of prestressed reinforcement, and E_p is the initial stiffness.

3.1. Test Verification. Fu et al. [3] fabricated one specimen of ordinary steel reinforced concrete frame and one of prestressed steel reinforced concrete frame according to the scale of 1/3 on the basis of practical engineering. The two specimens were named SRCF and PSRCF, respectively, and the reinforcements are described in Figures 4(a) and 4(b). Figure 4(c) gives the loading patterns, where two vertical concentrate loads of 40 kN were imposed on the beam, and a horizontal cyclic load $\pm P$ was applied at left end of the beam. The two frame specimens were designed according to “strong column and weak beam” and “strong joints and weak members.” The column cross section dimensions of the two frame specimens were the same, both were 230 mm \times 230 mm, and welded H-shaped steel HN130 \times 110 \times 4 \times 10 was arranged in the columns. The cross section size of the frame beam of the specimen SRCF was 150 mm \times 230 mm, and the size of the H-shaped steel placed in the centre was HN130 \times 50 \times 4 \times 14. The frame beam section size of the prestressed specimen PSRCF was 150 mm \times 230 mm, and the size of the embedded welded H-shaped steel was HN130 \times 50 \times 4 \times 8. In order to facilitate the arrangement of the prestressed tendons, the section steel web was offset on one side, and a steel strand with grade of 1860 and a diameter of 12.7 mm was taken as the prestressed reinforcement. By measurement, the tension control stress was 1395 MPa and the actual effective prestress was 970 MPa.

The strength grade of stirrups of beams and columns was HPB235, while the strength grade of longitudinal reinforcements was HRB400 and the structural steels were welded with Q235 steel plates. The specimens were poured on-site and made of commercial fine stone concrete. The measured compressive strength f_{cu} of concrete cube was

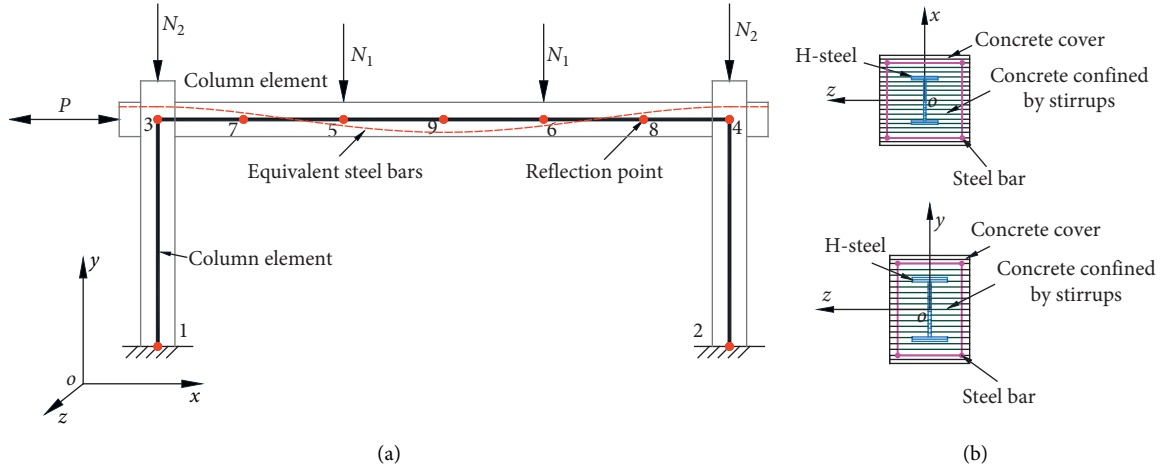


FIGURE 1: Node layout and element section division. (a) Node distribution. (b) Division of cross section.

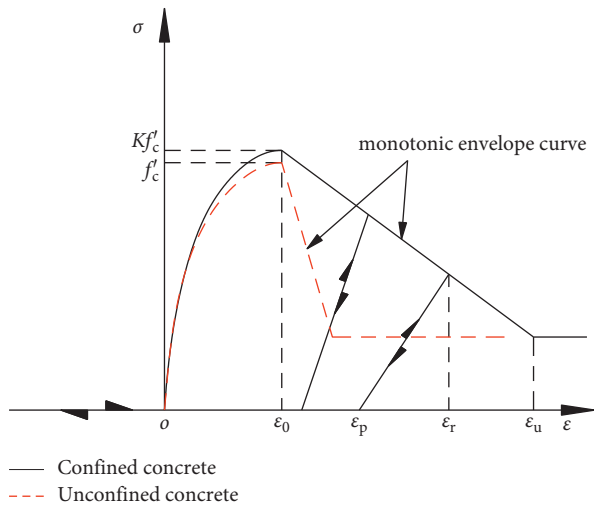


FIGURE 2: Constitutive model of concrete.

41 MPa, and the modulus of elasticity E_c was 3.17×10^4 MPa. The tested yield strength f_y of $\Phi 25$, $\Phi 14$, $\Phi 12$, and $\Phi 6$ steel bars was 412 MPa, 398 MPa, 487 MPa, and 305 MPa, respectively. In the test, the horizontal load and displacement were measured. The hysteretic properties of two steel concrete frame specimens under low horizontal cyclic loading were studied, and the hysteretic curves, skeleton curves, and energy dissipation capacities of the specimens were investigated.

The comparison between the numerical calculation and the experimental hysteresis curves was described (see Figure 5). It can be seen that the calculated curves and the experimental curves generally agree with each other in bearing capacity, stiffness degradation, and hysteresis loop shape, reflecting the correctness of the model built.

4. Hysteresis Curve Characteristics

4.1. Impact Parameters. In order to further study the hysteretic characteristics of prestressed and non-prestressed steel reinforced concrete frames, parameter analysis was

conducted to observe the main influence factors on the seismic performance in this paper, which include the column slenderness ratio (β), axial compression ratio (n_0), compressive strength of concrete cube (f_{cu}), sectional resistance moment of shaped steel in beams and columns (W_{ss-c} and W_{ss-b}), ratio of longitudinal reinforcement in beams and columns (ρ_{s-b} and ρ_{s-c}), yield strength of shaped steel in beams and columns (f_{ss-b} and f_{ss-c}), yield strength of longitudinal bars in beams and columns (f_{y-b} and f_{y-c}), and prestressing degree (λ).

Neglecting the contribution of steel web, the prestressing degree (λ) could be computed as follows:

$$\gamma = \frac{A_p f_{py} h_p}{A_p f_{py} h_p + A_{sf-b} f_{ss-b} h_{ss-b} + A_{s-b} f_{y-b} h_{s-b}}, \quad (1)$$

where A_p , A_{sf-b} , and A_{s-b} represent the cross-sectional areas for tendons, tensile flange of shaped steel, and tensile longitudinal rebars in beam, respectively; f_{py} is the tensile yielding strength for tendons; and h_p , h_{ss-b} , and h_{s-b} represent the distances from centroid of tendons, tensile flange of shaped steel, and tensile longitudinal rebars to extreme compressive fibre, respectively.

The hysteretic analysis parameters of prestressed and non-prestressed steel reinforced concrete frames are presented in Table 1.

4.2. Parameter Analysis. The influences of different slenderness ratios, axial compression ratios, cubic concrete strengths, sectional resistance moment of shaped steel in column, longitudinal reinforcement ratios, and prestressed degrees on the horizontal load-displacement hysteretic curves of prestressed steel reinforced concrete frames are described in Figure 6. The corresponding skeleton curves are provided in Figure 7, and Table 2 gives the critical values of the skeleton curves in the positive direction. It could be observed that

- (1) The peak load of prestressed frame decreased with the increase of column slenderness ratio, but the

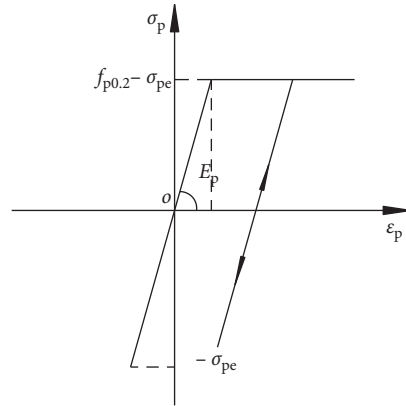


FIGURE 3: Model of prestressed reinforcement.

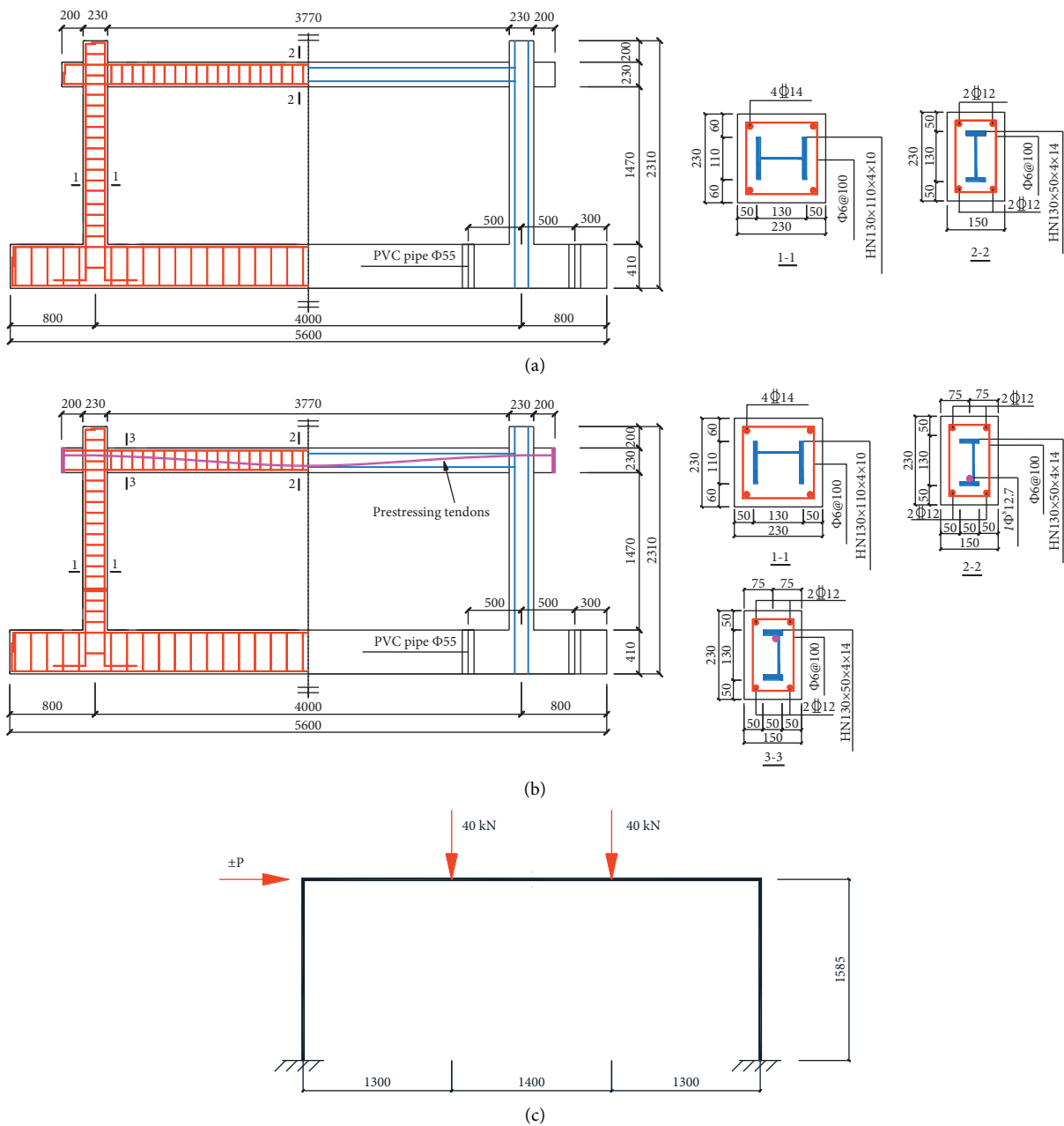


FIGURE 4: Size of frame specimen. (a) Specimen SRCF. (b) Specimen PSRCF. (c) Loading sketch.

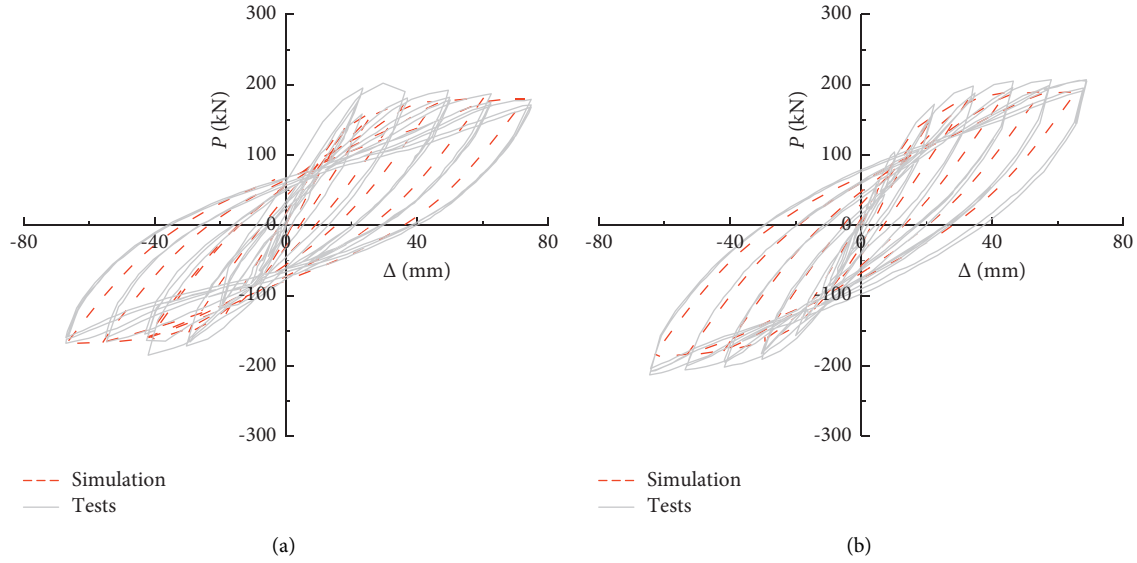


FIGURE 5: Comparison of hysteretic curves for specimens obtained from test and calculation. (a) Specimen SRCF. (b) Specimen PSRCF.

TABLE 1: Analysis parameters.

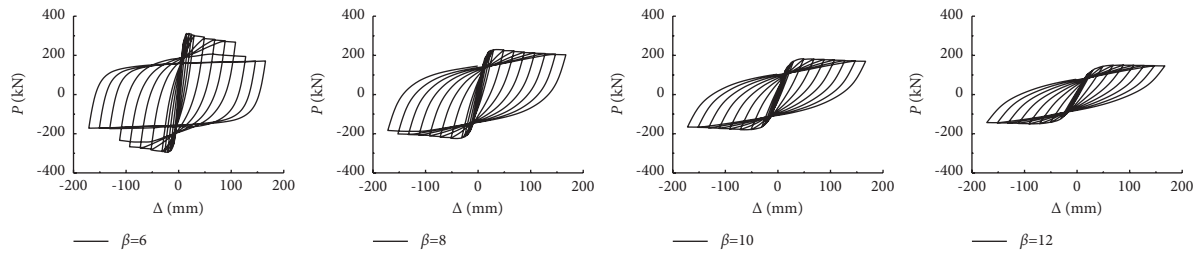
Parameter category	PSRCF		SRCF	
	Parameter change range	Remarks	Parameter's range	Remarks
Column slenderness ratio β	6; 8; 10; 12	Corresponding column height: 1500 mm; 2000 mm; 2500 mm; 3000 mm	6; 8; 10; 12	Corresponding column height: 1500 mm; 2000 mm; 2500 mm; 3000 mm
Axial compression ratio n_0	0.1; 0.2; . . . ; 0.8	—	0.1; 0.2; . . . ; 0.8	—
Concrete strength f_{cu} (MPa)	30, 40, 50	—	30, 40, 50	—
Sectional resistance moment of shaped steel in beam W_{ss-b} (mm^3)	82.126, 64.521	Corresponding H-shaped steel: H180 \times 50 \times 4 \times 8; H150 \times 50 \times 4 \times 8	82.126, 64.521	Corresponding H-shaped steel: H180 \times 50 \times 4 \times 8; H150 \times 50 \times 4 \times 8
Sectional resistance moment of shaped steel in column W_{ss-c} (mm^3)	256.281, 206.098	H180 \times 150 \times 4 \times 10 H150 \times 150 \times 4 \times 10	256.281, 206.098	H180 \times 150 \times 4 \times 10 H150 \times 150 \times 4 \times 10
Reinforcement ratio of longitudinal steel bars in beam ρ_{s-b}	0.785%, 1.131%, 1.539%	4 Φ 10, 4 Φ 12, 4 Φ 14	0.785%, 1.131%, 1.539%	4 Φ 10, 4 Φ 12, 4 Φ 14
Reinforcement ratio of longitudinal steel bars in column ρ_{s-c}	0.724%, 0.985%, 1.287%	4 Φ 12, 4 Φ 14, 4 Φ 16	0.724%, 0.985%, 1.287%	4 Φ 12, 4 Φ 14, 4 Φ 16
Yield strength for shaped steels f_{ss-b} and f_{ss-c} (MPa)	235, 345, 390	Q235, Q345, Q390	235, 345, 390	Q235, Q345, Q390
Yield strength of longitudinal steel bars f_{y-b} and f_{y-c} (MPa)	300, 335, 400	HPB300, HRB335, HRB400	300, 335, 400	HPB300, HRB335, HRB400
Prestressed degree λ	0.31, 0.45, 0.54	1 Φ^s 9.5, 1 Φ^s 12.7, 1 Φ^s 15.2	—	—

displacement corresponding to the peak load increased; after the skeleton curves reached the peak loads, the descending segment gradually became gentle and the ductility was improved obviously; the hysteretic curves of the frame behaved plump and no pinching occurred.

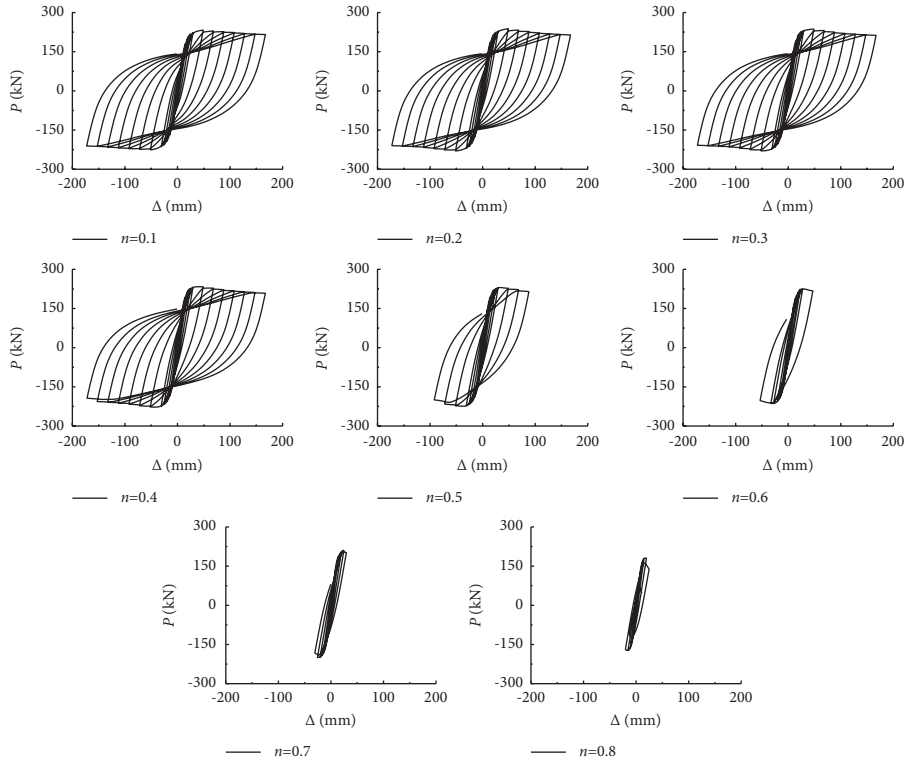
- (2) When the axial compression ratio was relatively small, the hysteretic curves were plump and the hysteretic loops had shuttle shape; as the axial compression ratio increased, the horizontal peak load first increased and

then decreased; when the axial compression ratio was greater than 0.5, the horizontal displacement at peak load was decreased, and the ductility of the frame was obviously reduced. At this time, the hysteresis loops pinched a certain amount.

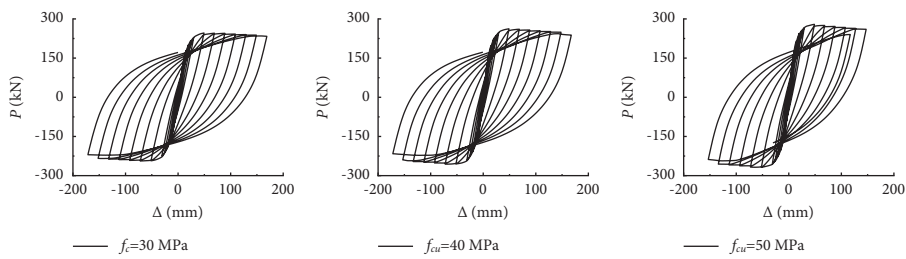
- (3) With the increase of cubic concrete strength, the peak loads of the skeleton curves were enhanced, the displacement corresponding to the peak load had almost no changes, and the stiffnesses of the descending segments were the same.



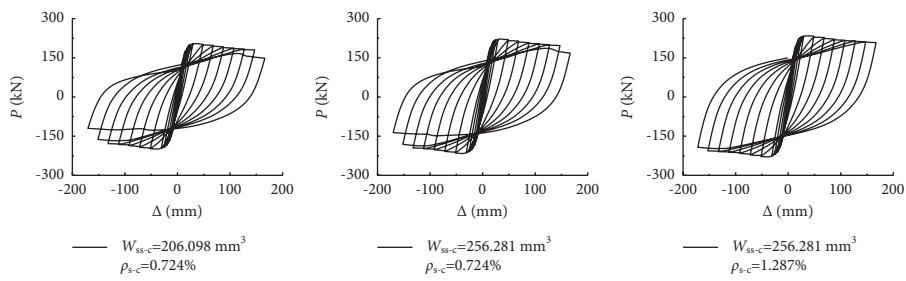
(a)



(b)



(c)



(d)

FIGURE 6: Continued.

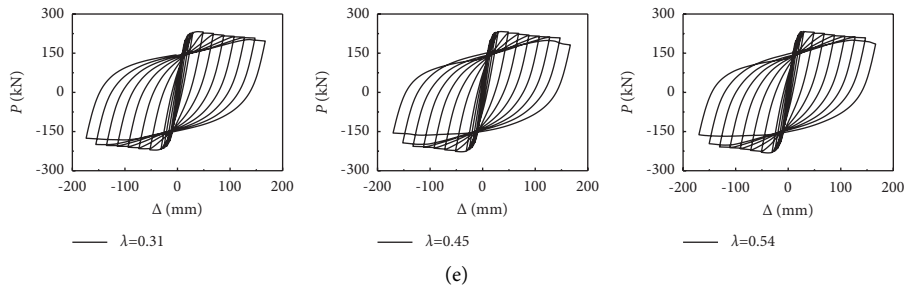


FIGURE 6: The influence of different parameters on the hysteresis curves. (a) Column slenderness ratio. (b) Axial compression ratio. (c) Cubic concrete strength. (d) Sectional resistance moment of shaped steel and longitudinal reinforcement ratio in the column. (e) Prestressing degree.

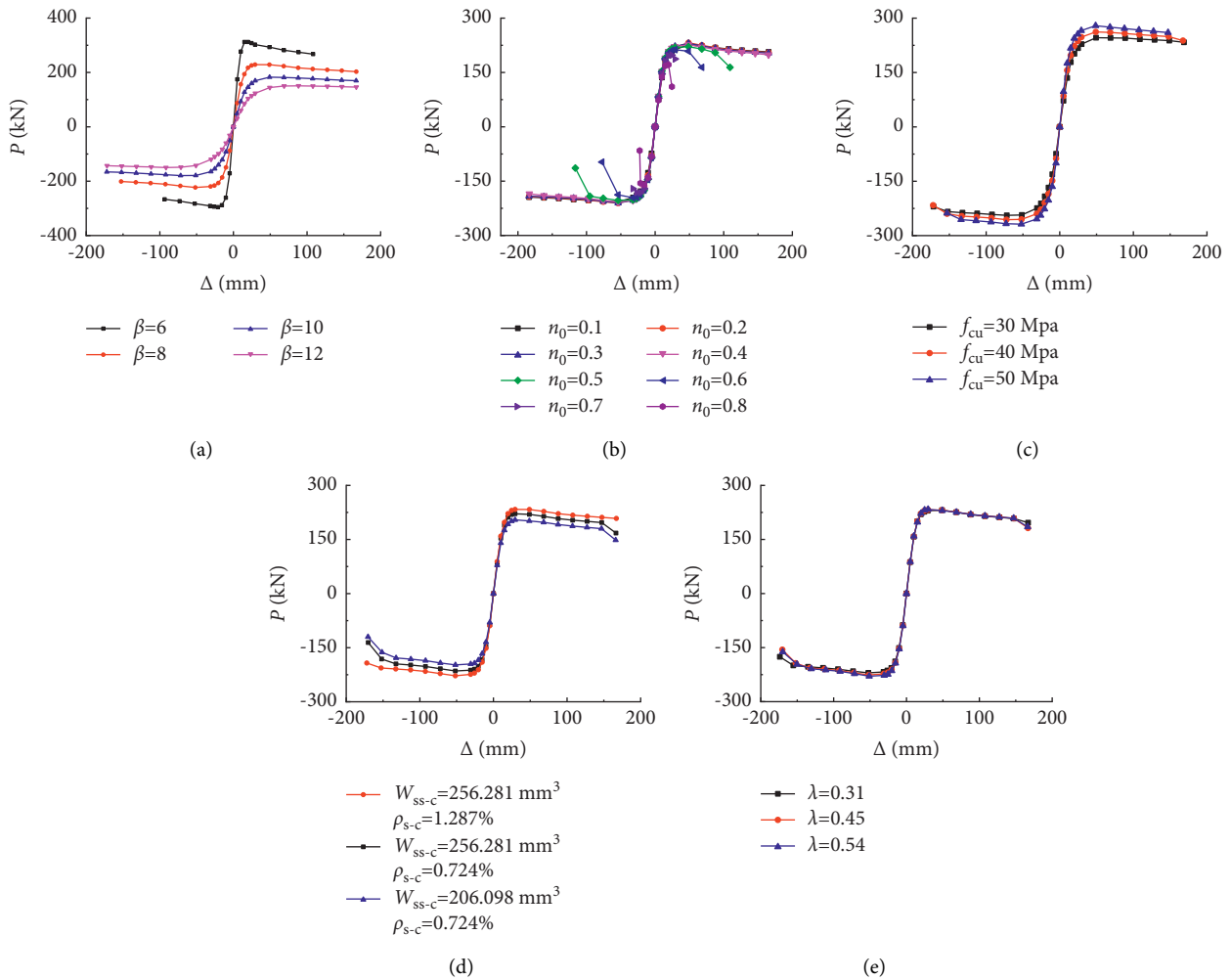


FIGURE 7: The influence law of different parameters on the skeleton curves. (a) Column slenderness ratio. (b) Axial compression ratio. (c) Cubic concrete strength. (d) Sectional resistance moment of shaped steel and longitudinal reinforcement ratio in the column. (e) Prestressed degree.

(4) With the increase of the sectional resistance moment of shaped steel and longitudinal reinforcement ratio in columns, the hysteretic curves became fuller, and the horizontal peak load increased, while the displacements corresponding to the peak loads as well as the stiffnesses of descending segments kept almost unchanged.

(5) Due to the existence of internal shaped steels, the hysteretic curves with varying prestressed degree showed no apparent distinction. The increase of prestressed degree can only slightly increase the horizontal bearing capacity of the frame; however, it had little influence on the initial stiffness, the

TABLE 2: Characteristics of skeleton curves under different analytical parameters in positive direction.

Analytical parameters	K_y (kN/mm)	Δ_y (mm)	Δ_m (mm)	P_m (kN)	K_d (kN/mm)
$\beta = 6$	27.3	10.2	19.7	312.1	0.503
$\beta = 8$	12.4	16.3	29.5	228.7	0.187
$\beta = 10$	6.5	24.7	49.2	182.8	0.110
$\beta = 12$	3.8	34.3	88.4	150.7	0.058
$n_0 = 0.1$	9.7	20.6	48.7	226.6	0.171
$n_0 = 0.3$	11.0	18.4	48.6	230.4	0.230
$n_0 = 0.5$	12.2	16.2	48.6	221.2	0.660
$n_0 = 0.7$	12.7	14.0	24.2	197.8	2.135
$f_{cu} = 30$ MPa	9.1	23.6	49.4	246.0	0.106
$f_{cu} = 40$ MPa	10.6	21.5	49.0	262.1	0.203
$f_{cu} = 50$ MPa	12.2	20.1	48.8	279.2	0.192
$W_{ss-c} = 256.281$; $\rho_{s-s} = 1.287\%$	12.2	16.0	29.5	221.2	0.263
$W_{ss-c} = 268.281$; $\rho_{s-c} = 0.724\%$	12.6	16.3	29.5	233.3	0.182
$W_{ss-c} = 206.098$; $\rho_{s-c} = 0.724\%$	11.2	16.2	29.5	204.3	0.247
$\lambda = 0.31$	12.7	16.2	49.1	233.3	0.314
$\lambda = 0.45$	12.6	16.2	29.5	232.1	0.270
$\lambda = 0.54$	12.6	16.4	29.7	233.3	0.259

displacement at peak load, and the stiffness of the descending branch of the skeleton curves.

Other factors, such as the sectional resistance moment of shaped steel and longitudinal reinforcement ratio in the beam, the yield strength of the shaped steel, and the longitudinal reinforcement both in beams and columns, had the same effects as the sectional resistance moment of shaped steel in the columns. In addition, the influence of various analysis parameters on the hysteretic and skeleton curves for the non-prestressed steel reinforced concrete frame was analogous to that of the prestressed ones, which were omitted here.

4.3. Characteristics of Hysteresis Curves. As can be seen by calculated hysteretic curves, in the initial stage of loading, the hysteretic curves behaved as a straight line passing through the origin in two directions, and the loading and unloading curves coincided, which means that the composite frame is in the elastic working stage; as the loading displacement increased, the skeleton curves gradually deviated from the straight line, and a certain unloading deformation appeared, and as the unloading displacement increases, the unloading stiffness decreases slightly. When the axial compression ratio did not exceed the value of 0.5, the calculated hysteretic curves were relatively plump, showing a stable shuttle shape, and no obvious pinch formed.

It can be found from the skeleton curves that the column slenderness ratio and axial compression ratio had significant influence on the initial stiffness, displacement at peak load, and the stiffness of the descending segment, while the other factors had almost no impact on the shape of the skeleton curves.

5. Horizontal Load-Displacement Hysteretic Models

Based on the analysis of a large number of parameters, the horizontal load-displacement hysteretic models of single-storey and single-span prestressed and non-prestressed steel

reinforced concrete frames were regressed in this paper, which were suitable for such frame structure.

5.1. Skeleton Curves. The skeleton curves of the hysteretic model adopt a degenerate trilinear model shown in Figure 8, where five parameters are needed to be determined, namely, the yield stiffness K_y , the horizontal yield load P_y , the horizontal peak load P_m , the peak point displacement Δ_m , and the descending branch stiffness K_d . It is demonstrated from the foregoing analysis that prestressing degree had a certain effect on the peak load of the skeleton curves. Due to the fact that the peak load was mainly related to the flexural capacity of beam and the influence of prestressing tendons had been considered to compute the flexural capacity of beam, to simplify the analysis, the axial compression ratio and slenderness ratio are taken as the major factors to establish the skeleton curve model, and the influence of prestressing degree was not considered repeatedly.

- (1) According to the initial bending stiffness of the beam and column section, the size of the specimen, and the load distribution patterns, elastic theory and numerical regression can be used to establish the expression of the initial frame stiffness K_y as follows:

$$K_y = (1.412 + 0.39n_0 - 0.043\beta - 0.69n^2 + 0.066n_0\beta)K_e. \quad (2)$$

Among them,

$$K_e = \frac{3EI_c}{L_2^3} \cdot \frac{12 + 36k}{3(4 + 3k)}, \quad (3)$$

$$k = \frac{EI_b/0.5L_1}{EI_c/L_2},$$

where n_0 is the axial compression ratio; K_e is the elastic lateral stiffness of the composite frame under horizontal load; EI_c and EI_b represent the sectional

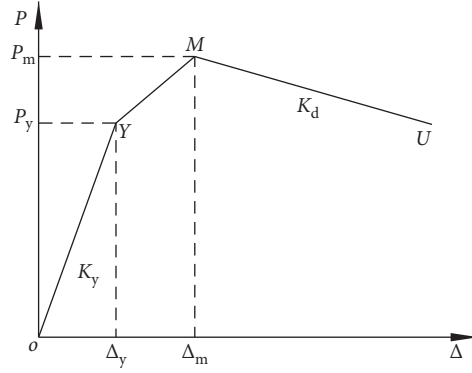


FIGURE 8: Skeleton curve model.

stiffness of the column and beam, respectively; L is the beam length; and H is the total height of the column.

- (2) The expression of the regressed horizontal yield load P_y is taken as

$$P_y = (1.35 - 1.17n_0 - 0.0181\beta + 1.66n_0^2 + 0.044n_0\beta)P_e, \quad (4)$$

where

$$P_e = \frac{M_{bu1} + M_{bu2} + M_{cu1} + M_{cu2}}{L_2 - 0.5H_b}, \quad (5)$$

where M_{bu1} and M_{bu2} represent, respectively, the flexural capacity at the two ends of the beam in the direction of bending deformation and M_{cu1} and M_{cu2} represent, respectively, the flexural capacity at the bottom of the two columns.

- (3) By the analysis, the expression of peak load P_m is given as

$$P_m = (1.39 - 1.02n_0 - 0.0071\beta + 1.62n_0^2 + 0.033n_0\beta)P_e. \quad (6)$$

- (4) Through regression analysis, the expression of the displacement Δ_m corresponding to the peak load is as follows:

$$\Delta_m = (-2.692 + 4.314n_0 + 0.997\beta - 4.788n_0^2 - 0.171n_0\beta + 0.05\beta^2)\Delta_y. \quad (7)$$

- (5) The expression of the stiffness of the descending section K_d is given below by regression.

$$K_d = (0.516n_0^2 - 0.169n_0 + 0.0242)K_e. \quad (8)$$

6. Hysteresis Rules

The horizontal load-displacement (P - Δ) hysteretic model of the frames is provided in Figure 9. The numbers from small to large in this figure indicate the walking route of the hysteretic models during forward and reverse loading and unloading [17, 18]. The hysteresis rule is stated as follows:

- (1) Loading and unloading rules for elastic segment: before the horizontal load reaches the yield load P_y , loading and unloading are carried out along the skeleton curves; the unloading stiffness is taken as the initial stiffness, regardless of the stiffness degradation and residual deformation.
- (2) Loading and unloading rules for elastoplastic stage: the loading stiffness is the incremental stiffness after yielding when the restoring force exceeds the positive or negative yield load P_y and does not reach the ultimate bearing capacity P_u in the positive or

negative directions. According to a large number of calculated results and statistical regression, the unloading stiffness K_{un} is reduced from the initial stiffness, which can be obtained as follows:

$$K_{un} = 0.925 \left(\frac{\Delta_{un}}{\Delta_y} \right)^{-0.162} K_y. \quad (9)$$

- (3) Unloading rules for descending segment: when the restoring force exceeds the limit horizontal load P_u in the positive or negative direction, the loading stiffness is taken as the stiffness of the descending segment of the skeleton curves, and the unloading stiffness of the descending segment is still computed in accordance with equation (9).
- (4) Reverse reloading rules: after unloading in the forward direction and subsequent loading in the reverse direction, when the maximum displacement experienced in the reverse direction does not exceed the yield displacement Δ_y , the loading curve will directly point to the reverse yield point from $P = 0.2P_{un}$. When the maximum displacement experienced in the reverse direction exceeds the yield displacement

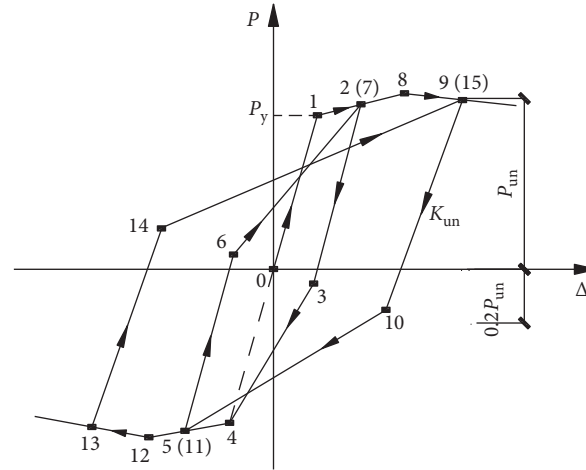
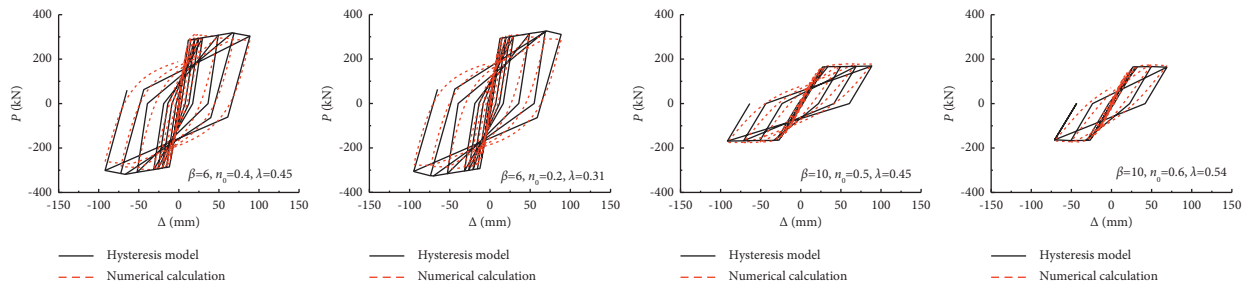
FIGURE 9: (P)- Δ hysteretic model.

FIGURE 10: Comparison between numerical calculation and hysteretic models.

Δ_y , loading curve points directly from $P = 0.2P_{un}$ to the maximum displacement point experienced in the reverse direction; when unloading in the reverse direction and reloading in the forward direction, the loading curve will point from $P = 0.2P_{un}$ to the maximum displacement point experienced in the forward direction.

6.1. Hysteresis Model Validation. The comparison between the hysteretic curves obtained by numerical calculation and the P - Δ hysteretic models established in this paper is presented in Figure 10. The results indicate that the hysteretic curves of numerical calculation are close to the hysteretic model. It can be found that the hysteretic models established in this paper are reliable and can be used to predict the hysteretic performance of prestressed and non-prestressed steel reinforced concrete frames under horizontal loads.

7. Conclusions

The numerical simulation of the whole hysteretic process of the prestressed steel reinforced concrete frame under

horizontal low cyclic loading is conducted, and the following conclusions are obtained:

- (1) The single-storey and single-span prestressed and non-prestressed steel reinforced concrete frame numerical models established can appropriately reflect the test results and have high reliability.
- (2) The calculation results of the numerical model showed that the prestressed and non-prestressed steel reinforced concrete frames had full hysteretic loop area and stable shuttle shape without obvious pinching, which showed good energy dissipation capacity.
- (3) With the increase of column slenderness ratio, the frame stiffness and peak load decreased while the ductility increased; with the increase of axial compression ratio, the frame displacement ductility decreased, showing that its deformation ability is reduced.
- (4) According to the parameter analysis, the hysteresis model of single-storey and single-span prestressed and non-prestressed steel reinforced concrete frames was established, which can better predict the hysteretic performance of such composite frame under horizontal load.

Data Availability

The data used to support the findings of this study are available from the corresponding author upon request.

Conflicts of Interest

The authors declare that they have no conflicts of interest.

Acknowledgments

The authors appreciate the support of the National Natural Science Foundation of China (51878589), China Postdoctoral Science Foundation (2019M651762), Six Talent Peaks Project of Jiangsu Province (2017-JZ-038), Science and Technology Planning Project of Yangzhou City (YZ2018068), and Project of Innovation and Entrepreneurship Plan of Jiangsu Province (2019). The authors also appreciate the contribution of Guanpu Xu, Zaixian Chen, Xinyu Li, Jinyu Shi, and Ahmed Ahmad Omar.

References

- [1] X. Xiong, G. Yao, and X. Su, "Experimental and numerical studies on seismic behavior of bonded and unbonded prestressed steel reinforced concrete frame beam," *Engineering Structures*, vol. 167, pp. 567–581, 2018.
- [2] X. Xiong and G. Yao, "Studies on the static behaviors of unbonded prestressed steel reinforced low-strength concrete rectangular frame beams," *Engineering Structures*, vol. 171, pp. 982–991, 2018.
- [3] C. G. Fu, Y. Y. Li, X. B. Sun, and J. Xu, "Experimental study on seismic performance of pre-stressed and non-prestressed steel reinforced concrete frames," *Journal of Building Structures*, vol. 31, no. 8, pp. 15–21, 2010, (in Chinese).
- [4] K. Wang, Sh. F. Yuan, D. F. Cao, and W. Zh. Zheng, "Experimental and numerical investigation on frame structure composed of steel reinforced concrete beam and angle-steel concrete column under dynamic loading," *International Journal of Civil Engineering*, vol. 13, no. 2, pp. 137–147, 2015.
- [5] W. Zh. Zheng and X. J. Sun, "Methods and practice on adding storeys around an existing building," *Concrete Engineering International*, vol. 12, no. 3, pp. 62–63, 2008.
- [6] Z. Y. Liu, W. Chen, and P. F. Li, "The technique of seismic isolation in story-adding buildings using light-weight steel structure and its application," *Applied Mechanics and Materials*, vol. 174, pp. 2119–2121, 2012.
- [7] W. Xue, L. Li, B. Cheng, and J. Li, "The reversed cyclic load tests of normal and pre-stressed concrete beams," *Engineering Structures*, vol. 30, no. 4, pp. 1014–1023, 2008.
- [8] W. Zheng and J. Ji, "Dynamic performance of angle-steel concrete columns under low cyclic loading-II: parametric study," *Earthquake Engineering and Engineering Vibration*, vol. 7, no. 2, pp. 137–146, 2008.
- [9] W.-D. Wang, L.-H. Han, and X.-L. Zhao, "Analytical behavior of frames with steel beams to concrete-filled steel tubular column," *Journal of Constructional Steel Research*, vol. 65, no. 3, pp. 497–508, 2009.
- [10] L. I. Hu, H. Zheng, and F. Xiao, "Restoring force model of steel frames infilled with the reinforced concrete deep beam," *China Civil Engineering Journal*, vol. 43, no. 9, pp. 49–54, 2010.
- [11] K. Wang, X.-F. Lu, S.-F. Yuan, D.-F. Cao, and Z.-X. Chen, "Analysis on hysteretic behavior of composite frames with concrete-encased CFST columns," *Journal of Constructional Steel Research*, vol. 135, pp. 176–186, 2017.
- [12] S. Mazzoni, F. McKenna, and M. H. Scott, *Open System for Earthquake Engineering Simulation User Command-Language Manual*, pp. 14–105, University of California, Berkeley, CA, USA, 2006.
- [13] W. Zh. Zheng and Y. Wang, *Uniform Design Method and Examples for Pre-stressed concrete Building Structures*, Harbin: Hei long jiang Science and Technology Press, Harbin, China, 1998, in Chinese.
- [14] R. Park, M. J. N. Priestley, and W. D. Gill, "Ductility of square-confined concrete columns," *Journal of the Structural Division*, vol. 108, no. 4, pp. 929–950, 1982.
- [15] B. D. Scott, R. Park, and M. J. N. Priestley, "Stress-strain behavior of concrete confined by overlapping hoops at low and high strain rates," *Aci Journal*, vol. 79, no. 1, pp. 13–27, 1982.
- [16] I. D. Karsan and J. O. Jirsa, "Behavior of concrete under compressive loadings," *Journal of the Structural Division*, vol. 95, no. 12, pp. 2543–2564, 1969.
- [17] Y. Fukada, "A Study on the Restoring Force Characteristics of Reinforced concrete Buildings," in *Proceedings of the Kanto District Symposium of AIJ*, Tokyo, Japan, 1969.
- [18] O. Kustu and J. G. Bouwkamp, "Behavior of Reinforced concrete Deep Beam-Columns Subassemblages under Cyclic Loads," UCB/EERC Report 73~82, University of California, Berkeley, CA, USA, 1973.

Research Article

Numerical Analysis for Dynamic Response of In Situ Blasting Expansion of Large Cross-Section Tunnel with Small Net Distance

Min Zhang 

Department of Geotechnical Engineering College of Civil Engineering, Tongji University, Shanghai 200092, China

Correspondence should be addressed to Min Zhang; 2041916@tongji.edu.cn

Received 18 July 2021; Accepted 1 September 2021; Published 11 October 2021

Academic Editor: Zhiyong Chen

Copyright © 2021 Min Zhang. This is an open access article distributed under the Creative Commons Attribution License, which permits unrestricted use, distribution, and reproduction in any medium, provided the original work is properly cited.

Based on the Damaoshan Highway Tunnel Reconstruction and Expansion Project, the dynamic response of adjacent tunnels during the blasting excavation of existing tunnels is analyzed by using the LS_DYNA finite element software, and the blasting vibration response and lining stress change in the blasting process are studied. Taking the particle peak vibration speed as the criterion, the traffic safety of the adjacent operating tunnels is determined. Moreover, the stress changes of the adjacent tunnel lining caused by blasting excavation are studied through the maximum principal stress. The results show that the particle peak vibration speed on the front explosion side is significantly greater than that on the back explosion side, and the maximum particle peak vibration speed on the road surface is 13 cm/s, which is greater than the allowable safety standard. Besides, the maximum principal stress on the front explosion side is about 1.5 times of that on the back explosion side, showing a “quasi-bias” phenomenon. Therefore, it is recommended to control the operation of the tunnel during the blasting process and especially focus on monitoring the vibration responses and stress changes of the lining of the operating tunnel during the construction period.

1. Introduction

With the rapid economic development of China, the traffic volume of highway tunnels is gradually increasing. Due to the saturation of traffic volume in some economically developed areas, more and more expressway tunnels are expanded into two-way six-lane or even eight-lane road tunnels [1, 2]. The reasons of tunnel reconstruction mainly include structure of the tunnel constructed long time ago is too old or the tunnel structure is damaged by external forces. Moreover, due to the increase of traffic volume and disaster prevention limits, the requirements of the existing tunnels cannot be met [3, 4]. Although there are many tunnel reconstruction forms, the tunnel extension can only be carried out in situ by expanding the tunnel section and increasing the number of traffic lanes, in order to adapt to the growth of traffic volume. This is mainly due to the limitation of topography, geology, and construction conditions. The in situ extension of the tunnel has three commonly used forms: unilateral extension, bilateral extension, and peripheral extension [5, 6].

The span of the Damaoshan Highway Tunnel Reconstruction and Expansion Project is the largest in similar reconstruction projects of China. The characteristics of this project lie in the following: the tunnel section is large, the net distance between the new tunnel and the original tunnel is small, and the original tunnel will be kept in operation during the construction period [7, 8]. At present, Chinese researchers have carried out a series of studies on the reconstruction and expansion project of Damaoshan Tunnel. For example, Liu et al. [9] analyzed the cumulative damage effect of rock in the Damaoshan Tunnel Group based on the dynamic damage theory. Besides, Lin et al. [10–13] studied the vibration characteristics and regularities of the wall and middle rock of the existing operating tunnel through insite blasting tests. In addition, Sun et al. [14] studied characteristics of the deformation evolution of surrounding rock and the stress of supporting structure in the construction process of the new tunnel through the insite monitoring measurements. Moreover, Yang et al. [15] compared the deformation and mechanical properties of surrounding rock during the construction of new and expanded tunnels

through numerical simulation. Furthermore, Chen et al. [16] proposed the maximum blasting charge insitu for the largest section of the Damoshan Tunnel by analyzing the influence of in situ blasting on the structural safety of adjacent operating tunnels. What is more, Li et al. [17] proposed an analytical algorithm for calculating the mechanical properties of surrounding rock during the in situ tunnel expansion, which was verified by the monitoring data of surrounding rock deformation during the expansion project in Damaoshan.

The LS-DYNA program is a fully functional geometric nonlinearity (large displacement, large rotation and large strain), material nonlinearity (more than 140 material dynamic models), and contact nonlinearity (more than 50) program. It is based on the Lagrange algorithm, combined with ALE and Euler algorithms, based on explicit solution, with implicit solution function, based on structural analysis, combined with thermal analysis and fluid-structure coupling function, and nonlinear dynamic analysis, mainly with static analysis functions (such as prestress calculation before dynamic analysis and springback calculation after sheet stamping and forming).

In the construction process of in situ tunnel expansion, the adjacent tunnels are planned to maintain normal traffic operation, so it is very important to ensure their operation and structural safety under the blasting load. In this study, the dynamic response of adjacent tunnels during the blasting excavation of existing tunnels is analyzed by using the LS-DYNA finite element software, which is based on the Fujian Quan-Xia Expressway Damoshan Tunnel Expansion Project, and the blasting vibration response and lining stress change in the blasting process are studied. According to these analyses, relevant suggestions are put forward to ensure the traffic safety of the operating tunnels, and it is expected to provide valuable references for similar tunnel reconstruction and expansion projects.

2. Project Overview

Damaoshan Tunnel is located in the Xiamen section of Quan-Xia Expressway which is called as the "First Road of Fujian" in Fujian Province of China. The original tunnel is a two-hole and four-lane separated tunnel with a total length of 600 m. The tunnel reconstruction and expansion project is to build a four-lane tunnel between the two original tunnels and expand the right tunnel into a four-lane tunnel in situ. The net distance between the original two-lane tunnel and the newly built four-lane tunnel is 5.89 m and that between the newly built and the expanded four-lane tunnel is 8.83 m, which is a typical tunnel with small net distance. After the completion of the expansion, the tunnel can meet the traffic requirements of a single hole with four lanes, a span of 22 m, and a cross section area of 255 m², of which the span is the largest in China. A rare tunnel group with large cross-section and small net distance is formed by the original tunnel, the newly built tunnel, and the expanded tunnel [18–33]. The cross-section layout of the tunnel group is shown in Figure 1.

According to the tunnel reconstruction and expansion plan, the tunnel group from left to right is two-lane tunnel

(the original tunnel, which maintains traffic during construction and will be abandoned or used for other purposes after construction completed), newly built four-lane tunnel, and the in situ expanded four-lane tunnel (the expansion begins after the completion of the newly built four-lane tunnel). The illustration of the reconstruction and expansion of the tunnel is shown in Figure 2.

3. Numerical Calculation Scheme

3.1. Numerical Calculation Model. Large-scale dynamic finite element calculation software LS-DYNA is used to carry out the simulation of in situ blasting expansion. According to the construction plan of the in situ tunnel expansion, the original secondary lining is dismantled first; then, blasting excavation is carried out on the left guide pit, but this plan produces the most negative effect on adjacent operating tunnels. Therefore, in the numerical simulation, the typical section of IV class perimeter rock is selected, and the explosive is set in the left guide pit of the in situ expanding tunnel, while the equivalent TNT explosive is simplified into a cube loading. The model size of surrounding rock is 150 m × 100 m, and a single-layer mesh is taken for the tunnel axial. The partial diagram of the numerical model is shown in Figure 3.

The calculation algorithms of LS-DYNA mainly include the Lagrange algorithm, Euler algorithm, and ALE algorithm. In order to avoid calculation errors caused by grid distortion, the ALE algorithm is used for blasting simulation. The surrounding rock, primary support, and secondary lining are connected by common nodes, and Lagrange algorithm is used, while the ALE algorithm is also applied for explosives and air. The propagation of blast wave in the surrounding rock and its interaction with primary support and secondary lining are realized by the fluid-solid coupling method. In order to improve the calculation accuracy, regular quadrilateral SOLID164 element and hexahedral mapping grid are employed in the model, and the surrounding rock grid size is about 20 cm. The nonreflective boundary condition is adopted to avoid the reflection of shock wave around the surrounding rock.

3.2. Material Model and Parameter Settings. The explosive material is modeled by a high-energy explosive material defined in the numerical software (*Mat_high_Explosive_Burn), and it is described by the JWL state equation (*Eos_Jwl). The explosive detonates at the center of charge, with the explosive density of 1300 kg/m³ and detonation velocity of 4000 m/s. The equation of explosive state is defined as

$$P = A \left(1 - \frac{\omega}{R_1 V} \right) e^{-R_1 V} + B \left(1 - \frac{\omega}{R_2 V} \right) e^{-R_2 V} + \frac{\omega E}{V}, \quad (1)$$

where P is the pressure, V is the relative volume, E is the internal energy density, and A , B , R_1 , R_2 , and ω are the explosive constants. Wherein, $A = 214$ GPa, $B = 0.18$ GPa, $\omega = 0.15$, $R_1 = 4.2$, and $R_2 = 0.9$.

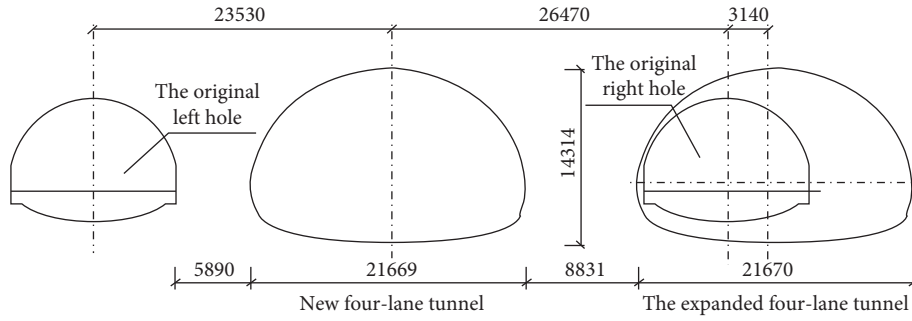


FIGURE 1: Layout of tunnel section (unit: mm).



FIGURE 2: Illustration of reconstruction and expansion of tunnel.

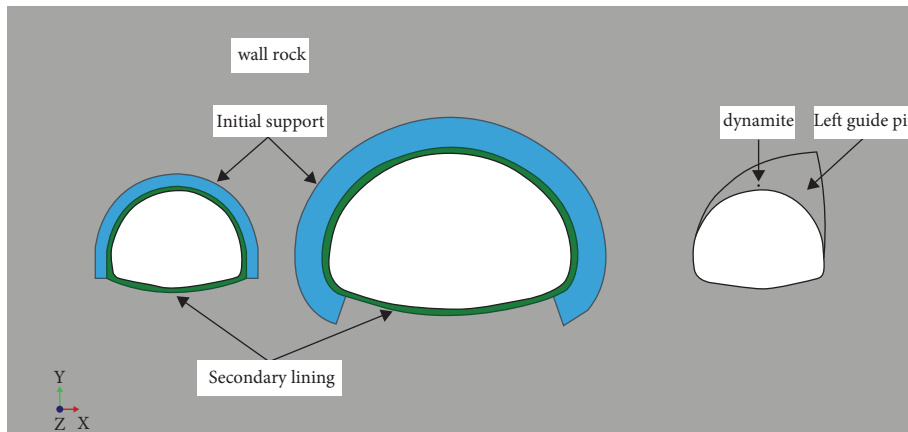


FIGURE 3: Partial diagram of the numerical calculation model.

Air is simplified as a nonviscous ideal gas, and the *Mat_Null material model is adopted for the air. The expansion process of the shock wave is assumed to be an isentropic adiabatic process, and the linearly polynomial state equation (*Eos_Linear_Polynomial) is used to describe this process. The state equation of air is defined as

$$P = C_0 + C_1\mu + C_2\mu^2 + C_3\mu^3 + (C_4 + C_5\mu + C_6\mu^2)E, \quad (2)$$

where $C_0, C_1, C_2, C_3, C_4, C_5,$ and C_6 are the constants related to gas properties, $C_0 = C_1 = C_2 = C_3 = C_6 = 0,$ and $C_4 = C_5 =$

$\gamma - 1; \mu = \rho / \rho_0 - 1; \rho_0, \rho, \gamma,$ and E are the initial density, density, adiabatic index, and internal energy density, respectively. Wherein, $\rho_0 = 1.293 \text{ kg/m}^3, \gamma = 1.4,$ and $E = 0.25 \text{ MPa}.$

The ideal elastoplastic model is used for the surrounding rock and initial support (*Mat_Plastic_Kinematic). The parameters of initial support are represented by the increased surrounding rock properties, such as the 50% increased elastic modulus or yield stress. The secondary lining uses the J-H-C material model (*Mat_Johnson_Holmquist_Concrete). According to the geological survey report of the Damaoshan Tunnel and the reference of “the Road Tunnel

Design Specification,” the physical and mechanical parameters of the surrounding rock, initial support, and secondary lining are determined and given in Table 1.

4. Calculation Results and Analysis

4.1. Vibration Control Analysis of Operating Tunnels

4.1.1. Blasting Vibration Velocity Control Threshold. Vibration caused by tunnel blasting has a negative effect on the surrounding rock and adjacent structures, and the in situ expansion blasting-induced vibration will affect the traffic safety of adjacent operating tunnels. Therefore, research studies on the vibration control of the tunnel in situ expansion blasting process should be conducted. The current promulgated “Blasting Safety Regulations” (GB6722-2014) of China regards the peak particle vibration velocity as the index of the allowable safety standard for blasting vibration, and the allowable safety standard is set at 10–20 cm/s for traffic tunnels.

By analyzing available literature, the blasting vibration velocity control thresholds of some tunnels with small net distance in China are summarized in Table 2. Through the combination of engineering practice and literature analysis, the maximum vibration speed of the surrounding rock and lining of existing tunnel is 15 cm/s due to the blasting construction of the new tunnel. Therefore, when the road vibration speed is less than 10 cm/s, no noticeable vibration will be aware when the car passes the tunnel in a quick speed. In the particular view of the Damaoshan Tunnel Reconstruction and Expansion Project, in order to ensure the traffic and structural safety of the adjacent operating tunnel, the secondary lining vibration threshold of the operating tunnel is set as 15 cm/s and the road vibration threshold is set as 10 cm/s.

4.1.2. Vibration Analysis of Adjacent Tunnels. During the numerical simulation process, monitoring points are set in the vaults, arch shoulders, arch waists, arch feet, and arch bottoms of the newly built four-lane operating tunnel to monitor the vibration effect of blasting expansion on the operation tunnel. The full section peak vibration velocity envelope of the original two-lane operating tunnel and the newly built four-lane operating tunnel is shown in Figures 4 and 5, respectively.

As can be seen from Figures 4 and 5, the peak vibration velocities at the arch shoulder and waist are the largest, followed by the vault and arch foot, and the arch bottom is the lowest. The peak vibration velocity of the side near the explosion is obviously higher than that of the side away from the explosion. Due to the long distance from the explosion point, the power response of the support structure of the original operating tunnel is smaller than that of the newly built operating tunnel. Therefore, when the construction of blasting expansion is carried out, the traffic and structural safety of the adjacent newly built four-lane operating tunnel should be paid more attention.

According to the simulation analysis of several blasting groups, the peak vibration velocity at the tunnel shoulder is

about 1.5–4 times of that at the tunnel bottom, and the peak vibration velocity at the side near the explosion is about 5–10 times of that at the side away from the explosion. Therefore, the in situ expansion blasting has a great influence on the adjacent operating tunnel, and the shoulder and waist of the operating tunnel are the weak links during the blasting excavation. Thus, in the construction process, special attention should be paid to the blasting vibration response of the arch shoulder and waist at the side near the explosion in the adjacent operating tunnel.

Through numerical simulation, the maximum value of the mass point vibration speed of road is 13 cm/s, which is greater than the allowable safety value stipulated in “the Blast Safety Regulations.” Therefore, during the construction of the expansion tunnel, temporary traffic control should be implemented in adjacent operating tunnels until the completion of the blasting and safety inspection. Thus, it is recommended that the blasting operations should be carried out at night or in the early morning with low traffic volumes, in order to avoid causing traffic jams. During the construction of tunnel expansion, the safety monitoring of the lining structure of adjacent operating tunnels should be strengthened, so as to provide timely and early warning.

4.2. Stress Analysis of Tunnel Lining in Operation. In order to analyze the influence of blasting expansion on the lining structure of adjacent operation tunnels, the monitoring points are set in the vaults, arch shoulders, arch waists, arch feet, and arch bottoms of the newly built four-lane operating tunnel, and the stress distribution of the lining structures is monitored, as shown in Figure 6.

It can be seen from Figure 6 that the stresses at the arch shoulder and waist of the lining structure are the largest, followed by the vault and arch foot, and the stress at the arch bottom is the smallest. The stress of the lining structure is asymmetrically distributed and that on the side near the explosion is obviously greater than that on the side away from the explosion. The maximum stress of the lining structure of the newly built four-lane operating tunnel is 1.76 MPa, which appears at the arch waist of the side near the explosion. The maximum principal stress of the arch waist of the side away from the explosion is 1.17 MPa; thus, the former is 1.5 times of the latter, showing a “quasi-bias” phenomenon.

The pressure distribution of the newly built four-lane operating tunnel is shown in Figure 7, and it is found that the surrounding rock pressure shows a side extrusion characteristic of “larger on both sides and smaller on vault” in the spatial distribution. The pressure of the side near the explosion of the surrounding rock is greater than the side away from the explosion, and the pressure distribution of the surrounding rock is in consistence with the stress distribution of the lining structure, which shows a “quasi-bias” phenomenon. Therefore, in the construction process of blasting expansion, the stress distribution of the explosion side lining structure adjacent to the operating tunnel should be paid more attention.

TABLE 1: Physical-mechanical parameters of materials.

Material	Density ($\text{kg}\cdot\text{m}^{-3}$)	Elastic modulus (GPa)	Poisson's ratio	Yield stress (MPa)
Surrounding rock	2300	3.0	0.35	10
Initial support	2400	4.5	0.30	15
Secondary lining	2700	30.0	0.20	20

TABLE 2: Control thresholds of the blasting vibration velocity for some tunnels with small net distance.

Project	Net distance (m)	Threshold of vibration velocity ($\text{cm}\cdot\text{s}^{-1}$)
Zhaobaoshan Highway Tunnel	0.95	10
Xiaoyangshan Tunnel	9.34	10
Bantao Tunnel	6.14	1.8
Wutong Mountain Tunnel	13.5	6
Sanfu Expressway Tunnel	5	10
Dongjiashan Tunnel	3.75	15
Shishi Tunnel	8.2	15

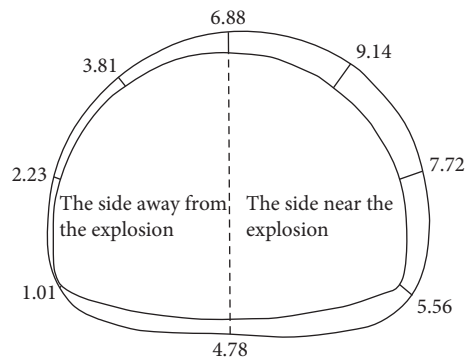


FIGURE 4: Envelope of full section peak vibration velocity of the original two-lane operating tunnel (unit: cm/s).

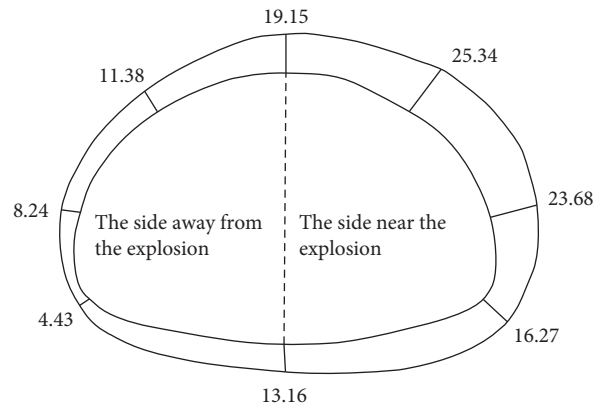


FIGURE 5: Envelope of full section peak vibration velocity of the new four-lane operating tunnel (unit: cm).

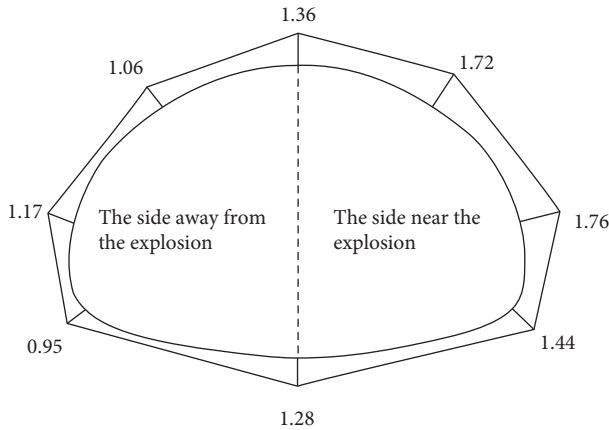


FIGURE 6: Stress distribution of the lining structure of the newly built four-lane operating tunnel (unit: MPa).

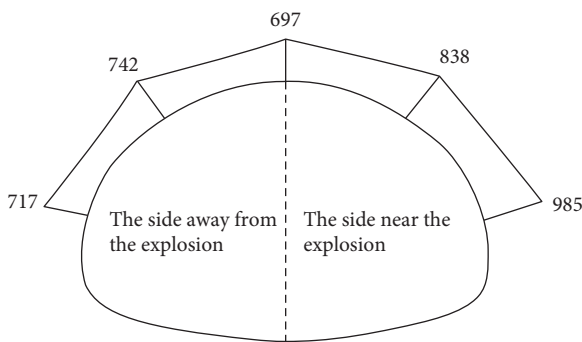


FIGURE 7: Pressure distribution of surrounding rock of the newly built four-lane operating tunnel (unit: kPa).

5. Conclusion

In this study, the numerical model for blasting expansion of the large section tunnel with small net distance in situ was established by LS_DYNA power finite element software; the vibration responses and lining stress changes of adjacent operating tunnels under blasting load of the Damaoshan Tunnel expansion project were simulated. The results of the present work can provide references and guidances for the construction problems of similar tunnel expansion projects. The main conclusions and recommendations are listed as follows.

- (1) In situ expansion by blasting excavation has a great impact on adjacent operating tunnels, and the shoulder and waist of the operating tunnel are the weak links during the blasting excavation. The peak vibration velocity at the arch shoulder of the tunnel is about 1.5–4 times of the tunnel bottom and that on the side near the explosion is about 5–10 times of the side away from the explosion.
- (2) Under the blasting loads during tunnel expansion, the peak particle vibration speed of the newly built four-lane operating tunnel reaches 13 cm/s, which exceeds the allowable safety value. Therefore, it is recommended that during the blasting construction

of the expanded tunnel, traffic control should be implemented temporarily in the adjacent operating tunnels. It is also suggested that the blasting operations arranged at night or early morning during which the traffic volume is small.

- (3) Under the blasting loads of the newly built four-lane operating tunnel, the stress of the lining of the near blast side arch waist is about 1.5 times of the side away from the blasting, showing a “bias-like” phenomenon, and the pressure distribution of surrounding rock presents similar trends.
- (4) On the explosion side of the adjacent operating tunnel, the mass point vibration and stress distribution of the lining structure are in an unfavorable state. Dynamic monitoring should be carried out during the expansion process to ensure the traffic safety of the adjacent operating tunnels.

Data Availability

The data used to support the findings of this study are available from the corresponding author upon request.

Conflicts of Interest

The authors declare that there are no conflicts of interest.

Authors' Contributions

Min Zhang carried out the experiments, analyzed the results, conducted the theoretical explanations, and wrote the manuscript.

Acknowledgments

The authors would like to express appreciation to Department of Geotechnical Engineering, College of Civil Engineering, Tongji University, for providing the laboratory.

References

- [1] N. Mojtabei and S. G. Beattie, “Empirical approach to prediction of damage in bench blasting,” *Transactions of the Institution of Mining and Metallurgy Section a-Mining Industry*, vol. 105, pp. A75–A80, 1996.
- [2] X. Xia, H. B. Li, J. C. Li, B. Liu, and C. Yu, “A case study on rock damage prediction and control method for underground tunnels subjected to adjacent excavation blasting,” *Tunnelling and Underground Space Technology*, vol. 35, pp. 1–7, 2013.
- [3] T. R. Yu and S. Vongpaisal, “New blast damage criteria for underground blasting,” *CIM Bulletin*, vol. 89, no. 998, pp. 139–145, 1996.
- [4] M. H. Mussa, A. A. Mutalib, R. Hamid, and S. N. Raman, “Blast damage assessment of symmetrical box-shaped underground tunnel according to peak particle velocity (PPV) and single degree of freedom (SDOF) criteria,” *Symmetry-Basel*, vol. 10, no. 5, 2018.
- [5] C. Shi, Q. Zhao, M. Lei, and M. Peng, “Vibration velocity control standard of buried pipeline under blast loading of adjacent tunnel,” *Soils and Foundations*, vol. 59, no. 6, pp. 2195–2205, 2019.

- [6] J. P. Liu, R. Wang, G. Lei, Y. T. Si, S. D. Xu, and Y. H. Li, "Studies of stress and displacement distribution and the evolution law during rock failure process based on acoustic emission and microseismic monitoring," *International Journal of Rock Mechanics and Mining Sciences*, vol. 132, p. 10, 2020.
- [7] T. Sato, T. Kikuchi, and K. Sugihara, "In-situ experiments on an excavation disturbed zone induced by mechanical excavation in Neogene sedimentary rock at Tone mine, central Japan," *Engineering Geology*, vol. 56, no. 1-2, pp. 97-108, 2000.
- [8] L. M. Duan, W. S. Lin, J. X. Lai, P. Zhang, and Y. B. Luo, "Vibration characteristic of high-voltage tower influenced by adjacent tunnel blasting construction," *Shock and Vibration*, vol. 2019, Article ID 8520564, 2019.
- [9] P. Bossart, P. M. Meier, A. Moeri, T. Trick, and J. C. Mayor, "Geological and hydraulic characterisation of the excavation disturbed zone in the opalinus clay of the mont terri rock laboratory," *Engineering Geology*, vol. 66, no. 1-2, pp. 19-38, 2002.
- [10] Y. Fan, J. W. Zheng, X. Z. Cui, Z. D. Leng, F. Wang, and C. C. Lv, "Damage zones induced by in situ stress unloading during excavation of diversion tunnels for the Jinping II hydropower project," *Bulletin of Engineering Geology and the Environment*, vol. 80, no. 6, pp. 4689-4715, 2021.
- [11] T. T. Minh and N. Q. Huy, "Effect of blasting on the stability of lining during excavation of new tunnel near the existing tunnel," *Civil Engineering Journal*, vol. 30, no. 1, pp. 47-62, 2021.
- [12] G. Luan, Z. Wang, Z. Song, and H. Yu, "Analysis of the influence of lately excavated tunnel blasting on the vibration of early excavated tunnel in small-space tunnel," *Earth and Environmental Science*, vol. 643, no. 1, p. 6, 2021.
- [13] W. Wang, Q. Yuan, H. Jiang, and P. S. Chen, "Influence and safety control of blasting vibration on existing lining for closely tunnel expansion," *Earth and Environmental Science*, vol. 351, no. 1, p. 13, 2019.
- [14] Q. H. Sun, F. S. Ma, J. Guo et al., "Excavation-induced deformation and damage evolution of deep tunnels based on a realistic stress path," *Computers and Geotechnics*, vol. 129, Article ID 103843, 2021.
- [15] B. Yang, C. M. Lin, Z. C. Zhang, R. Yin, and Z. Wen, "Mechanical characteristics analysis of surrounding rock of unilateral expansion tunnels in situ," *Chinese Journal of Underground Space and Engineering*, vol. 14, no. 6, pp. 1458-1465, 2018.
- [16] F. Chen, Z. Li, S. Ren et al., Powerchina Road Bridge Group Co Ltd, 2016.
- [17] X. D. Li, S. P. Jiang, Y. X. Liu, and L. H. Huang, "Numerical simulation of blasting dynamic response of small spacing tunnel expansion," *China Earthquake Engineering Journal*, vol. 36, no. 4, pp. 784-789, 2014.
- [18] X. D. Li, S. P. Jiang, Y. X. Liu, and L. H. Huang, "Blasting vibration control of local expansion of large section tunnel with small cycle distance," *Blasting*, vol. 31, no. 3, pp. 85-90, 2014.
- [19] X. D. Li, S. P. Jiang, Y. X. Liu, and L. H. Huang, "Blasting effect and control of new tunnel with small clear space on existing operation tunnel," *Chinese Journal of Underground Space and Engineering*, vol. 12, no. 6, pp. 1631-1636, 2016.
- [20] J. R. Zhang, J. Wu, C. W. Yan, X. Gou, L. Ye, and J. Feng, "Construction technology of super-large section of highway tunnels with four or more lanes in China," *China Journal of Highway and Transport*, vol. 33, no. 1, pp. 14-31, 2020.
- [21] M. C. Liu, "Impact analysis on construction of large section and small spacing road tunnel," *Journal of Shanghai University of Engineering Science*, vol. 49, no. 4, pp. 78-85, 2019.
- [22] M. Zhao and Z. H. Zhou, "Study on damage laws of subway tunnel under explosive load," *Journal of Safety Science and Technology*, vol. 15, no. 8, pp. 118-123, 2019.
- [23] Y. Q. Zhong, "Field monitoring and analysis of in-situ tunnel extension by three-bench method," *Modern Tunnelling Technology*, vol. 56, no. 5, pp. 170-179, 2019.
- [24] Y. X. Chen, G. Q. Cui, and L. Song, "Back analysis of the internal force on the supporting structure of a multi-centered circular arch tunnel," *Modern Tunnelling Technology*, vol. 55, no. 1, pp. 85-91, 2018.
- [25] Y. Z. Shi, J. F. Chai, J. C. Ruan, and S. Lin, "The influence of zonal multiple blasting of a large-span tunnel on its surrounding rock and antecedent tunnel," *Acta Scientiarum Naturalium Universitatis Sunyatseni*, vol. 57, no. 5, pp. 72-80, 2018.
- [26] Z. Y. Sun, D. L. Zhang, Q. Fang, and W. Su, "Distribution of surrounding rock pressure of shallow highway tunnels with small spacing," *China Journal of Highway and Transport*, vol. 31, no. 9, pp. 84-94, 2018.
- [27] C. M. Lin, Z. C. Zhang, Q. Zheng, H. Zheng, and M. Li, "Study on the soft surrounding rocks stability and supporting parameters of two-to-fourlane tunnel of small clear-distance by CD method," *China Civil Engineering Journal*, vol. 46, no. 7, pp. 124-132, 2013.
- [28] F. Cao, S. Zhang, and T. H. Ling, "Blasting-induced vibration response of the transition section in a branching-out tunnel and vibration control measures," *Advances in Civil Engineering*, vol. 2020, Article ID 6149452, 2020.
- [29] E. Ghasemi, M. Ataei, and H. Hashemolhosseini, "Development of a fuzzy model for predicting ground vibration caused by rock blasting in surface mining," *Journal of Vibration and Control*, vol. 19, no. 5, pp. 755-770, 2013.
- [30] X. Gu and Q. Zhang, "Progress in numerical simulation of dam failure under blast loading," *Journal of Hohai University. Natural Sciences*, vol. 45, no. 1, pp. 45-55, 2017.
- [31] Z. S. Shao and Y. Y. Xiong, "Study on site dynamic monitoring of soft rock tunnel with large span," *Chinese Journal of Underground Space and Engineering*, vol. 13, no. 3, p. 779, 2017.
- [32] Q. Fang, W. Su, D. L. Zhang, and F. Yu, "Tunnel deformation characteristics based on on-site monitoring data," *Chinese Journal of Rock Mechanics and Engineering*, vol. 35, no. 9, pp. 1884-1897, 2016.
- [33] Y. Hu, J. F. Zhu, and K. Zhu, "Numerical simulation study for the internal explosion effect on the structure of the public buildings," *Journal of Safety and Environment*, vol. 16, no. 2, pp. 184-188, 2016.

Research Article

Girder Longitudinal Movement and Its Factors of Suspension Bridge under Vehicle Load

Guoping Huang ^{1,2}, Jianhua Hu ^{1,3}, Haibo Liu,³ and Xiugui Sun^{1,4}

¹Key Laboratory for Wind and Bridge Engineering of Hunan Province, College of Civil Engineering, Hunan University, Changsha 410082, China

²College of Civil Engineering, Hunan City University, Yiyang 413000, China

³Hunan Communication & Water Conservancy Group Ltd., Changsha 410008, China

⁴Hunan Provincial Communications Planning Survey & Design Institute Co, Ltd., Changsha 410200, China

Correspondence should be addressed to Guoping Huang; gphuang@hnu.edu.cn

Received 6 August 2021; Accepted 9 September 2021; Published 1 October 2021

Academic Editor: Zhiyong Chen

Copyright © 2021 Guoping Huang et al. This is an open access article distributed under the Creative Commons Attribution License, which permits unrestricted use, distribution, and reproduction in any medium, provided the original work is properly cited.

Vehicle load may not only cause vertical deformation and vibration of suspension bridge but also lead to longitudinal deformation and vibration. And the longitudinal behavior is closely related to the durability of the girder end devices and the bending fatigue failure of suspenders. In this study, the longitudinal deformation behavior and longitudinal vibration of suspension bridge under vehicles, as well as the related influencing factors, are investigated. The underlying mechanism of girder longitudinal movement under the moving vehicles is revealed. Based on the simplified vehicle model of vertical concentrated force, the characteristics of main cable deformation and girder longitudinal displacement under vertical loads are analyzed first. Then, the longitudinal motion equation of the girder under vertical moving loads is derived. Finally, a single long-span suspension bridge is employed in the case study, and the girder longitudinal response and influencing factors are investigated based on both numerical simulation and field monitoring. Results indicate that the asymmetric vertical load leads to cable longitudinal deflection owing to the geometrically nonlinear characteristic of the main cable, leading to longitudinal movement of the girder. The results of field monitoring and numerical simulation indicate that the girder moves quasi-statically and reciprocates longitudinally with centimeter amplitude under normal operational loads.

1. Introduction

The suspension bridge with great spanning ability is increasingly used in projects of spanning grand Canyons, seas, and islands [1]. However, such bridges are flexible and vibration sensitive, and the stiffness and vibration of the suspension bridges are major topics in research on structural dynamics. The previous studies showed that the fatigue and durability of girder end ancillary facilities such as the expansion joints, dampers, and bearing are related to the reciprocating longitudinal movement characteristics of the stiffening girders. The huge accumulative displacement caused by traffic or wind loads during the operational stage is an important reason for the damage of the end attached

facilities [2–5]. The reciprocating longitudinal movement may also induce fatigue failure of short suspenders for suspension bridge [6–9] and oil leakage of hydraulic damper [10]. Meanwhile, the vehicle load can cause excessive rotation angle to the girder ends, which will affect driving safety and comfort [11, 12].

In early studies concerning girder end displacement and girder longitudinal vibration for the suspension bridges, majority of researchers were concerned with overlarge girder end displacement or pounding between adjacent components at the girder ends of the bridge [13–15]. However, for vehicle load, related to vertical moving loads, vertical vibration and deflection are directly and mostly investigated [16–19]. The longitudinal vibration caused by vehicles only

involves the braking force, which is the longitudinal load excitation applied to the deck [14, 20]. The longitudinal response of the girder caused by earthquake is much larger than that caused by vehicle load, and the longitudinal vibration and control under operational actions were relatively less concerned.

An increasing number of investigators are paying attention to the issues of girder longitudinal movement and its factors under vehicle load for the suspension bridge at present, owing to increasing cases that the girder end devices fail prematurely due to operational actions. The vehicle-girder longitudinal movement relationship is mainly investigated qualitatively via statistical regression based on bridge health monitoring data [21–25], or numerical analysis based on finite element (FE) [26–28]. For example, Guo et al. [22] utilized the long-term monitoring data of two long-span suspension bridges and a long-span cable-stayed bridge in China to comparatively investigate the response characteristics of girder longitudinal movements. Sun et al. [23] also utilized the long-term monitoring data to evaluate the condition of girder end expansion joints for suspension bridge during the operational stage. Hu et al. [24] further investigated the frequency spectrum of longitudinal girder end displacement and quantitative contribution of longitudinal girder end cumulative displacement due to various load excitations.

Scholars also used the FE to analyze longitudinal vibration and control for the suspension bridges. For instance, Zhao et al. [26] established a bridge FE model to investigate the dynamic response of suspension bridge under random traffic load and influence of fluid viscous damper. Gao et al. [28] developed two bridge FE models to simulate interaction of traffic excitations and suspension bridges for evaluating the effect of the rigid central clamps on the longitudinal deformation of suspension bridges. However, the above-mentioned investigation ignored the underlying mechanical mechanism on longitudinal behavior of suspension bridges under vehicle load, which is often covered by huge monitoring data and numerical analysis.

This study is devoted to investigating the longitudinal deformation and vibration of suspension bridge under traffic loads by combining field measurement, theory analysis, and numerical simulation with two specific aims: (1) to reveal the underlying mechanisms of girder longitudinal behavior caused by vehicles through comparative analysis and (2) to discuss influencing factors and propose control measures of girder longitudinal displacement during normal operation period.

2. Engineering Background

2.1. Bridge Description. The Aizhai bridge (Figure 1), a single-span steel suspension bridge, crossing the Dehang Grand Canyon with deep steep and complex geology along the highway between Jishou and Chadong in Hunan Province, carries the Changsha to Chongqing Expressway. As shown in Figure 1(b), the layout of the main cable is $242\text{ m} + 1176\text{ m} + 116\text{ m}$; meanwhile, the total length of the bridge is 1073.65 m. The bridge also has the longest main

span crossing Grand Canyon in the world when it was opened to traffic in 2012.

The two bridge towers, namely, the Jishou and Chadong towers, are made of reinforced concrete and constructed in situ. They are 130 m high with two crossbeams and 62 m high with one crossbeam, respectively. Thus, the suspension cable has a sag ratio of 1 : 9.6. The double main cables, which are paralleled to each other with the central distance of 27 m, are supported by the four saddles installed at the top of the tower. Then, they are fixed to gravity anchorage and tunnel anchorage on the Jishou and Chadong sides, respectively. The steel truss girder with a total length of 1000.5 m is adopted for the bridge stiffening girder, which consists of main trusses, top and bottom bracings, and transverse trusses. The main trusses are of Warren type and have a height of 7.5 m and a width of 27 m. The stiffening girder is made of Q345 steel with an elastic modulus of 210 GPa, axial allowable stress of 200 MPa, bending allowable stress of 210 MPa, and shear allowable stress of 120 MPa. And the parameters for the main components of the bridge are shown in Table 1.

2.2. Displacement Monitoring System. The girder end displacement monitoring system was installed specifically on the Aizhai Bridge and began operation on February 25, 2016, to clearly understand the longitudinal behavior of the suspension bridge during normal operation period. Overall, a total of 10 sensors including four ultrasonic displacement sensors, four draw-wire displacement sensors, and two temperature sensors were installed to monitor the stiffening girder longitudinal movement and structural temperature. They were located at the truss-girder sections of the main girder ends. At each monitoring section, two ultrasonic displacement sensors were symmetrically located at two ends of the top chord, two draw-wire displacement sensors were symmetrically located at two ends of the bottom chord, and a temperature sensor was placed at middle of the bottom chord. The detailed location of the displacement and temperature sensors is shown in Figure 2, and the sampling frequency and the serial number of the sensors are listed in Table 2.

2.3. FE Model. A 3D FE model of the Aizhai Suspension Bridge is established by ANSYS, as shown in Figure 3. The tower, pier, and stiffening girder are simulated by space beam-column elements, and the main cables and suspenders are simulated as the link element (Link 10) that only bears tension. The gravity stiffness and large deformation nonlinear characteristics of the main cable are considered. In view of the rigid tower foundation, the tower bottom is modeled in the form of consolidation without regard to the pile-soil effect. The end of the stiffening girder is provided with lateral wind-resistant bearing, which would permit movement in the longitudinal direction and rotation about the transverse direction. The Rayleigh damping model is adopted in dynamic analysis, and the damping ratios that were associated with the first two longitudinal drift modes are 0.005. The first seven vibration modes of the bridge are

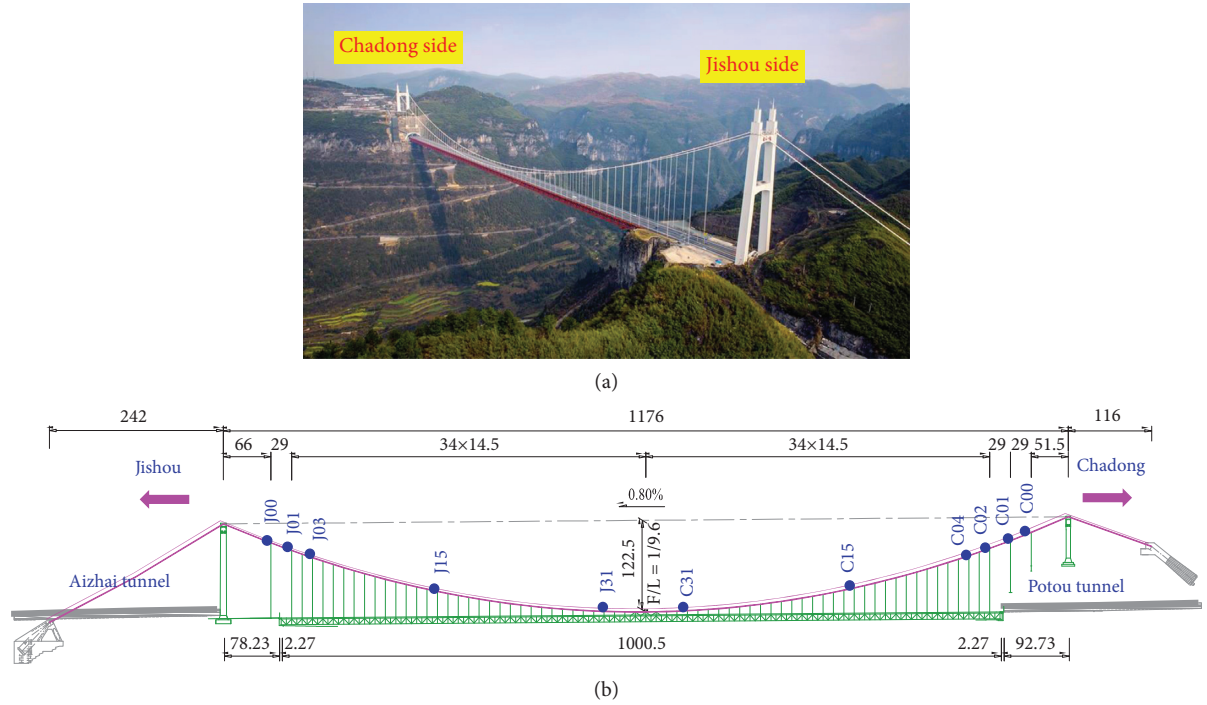


FIGURE 1: Aizhai Suspension Bridge (m): (a) realistic scene; (b) general layout.

TABLE 1: Parameters for the main components of the bridge.

Member	Detailed location	A (m ²)	I_{yy} (m ⁴)	I_{zz} (m ⁴)	I_{xx} (m ⁴)	E (GPa)	P (kg/m ³)
Stiffening girder truss	Top chords	0.06797	0.00458	0.00654	0.00804	210	8673
	Bottom chords	0.05032	0.00326	0.00323	0.00482	210	8673
	Bottom chord end	0.06000	0.00384	0.00381	0.00569	210	8673
	Web member	0.02141	0.00134	0.00013	2.3983×10^{-6}	210	8673
	Web member end	0.05472	0.00339	0.00225	0.00391	210	8673
	Diagonal webs	0.02451	0.00184	0.00021	1.658×10^{-6}	210	8673
	Diagonal web end	0.04560	0.00299	0.00156	0.00293	210	8673
Main cable	Main span and Chadong bank	0.46462	—	—	—	200	8043
	Jishou bank	0.48112	—	—	—	200	8043
Suspenders	J00/C01	0.02386	—	—	—	115	8680
	J01/C00/C02	0.01591	—	—	—	115	8680
	J02 ~ C03	0.00779	—	—	—	115	8680

A , sectional area; I_{yy} , longitudinal bending moment inertia; I_{zz} , transverse bending moment inertial; I_{xx} , torsional moment inertial; E , elastic modulus; ρ , density.

listed in Table 3, and the first two-order asymmetric vertical bending with longitudinal floating mode diagram that is closely related to the girder longitudinal displacement is shown in Figure 4.

3. Field Monitoring Data Analysis

Figure 5 displays displacement and temperature records from the six sensors installed in different positions at the truss-girder sections, which were obtained from March 1, 2016, to October 31, 2017. During this monitoring period, the measure displacement and temperature varied significantly with the seasonal alternation; moreover, the amplitude of displacement and temperature variation were

418 mm and 37.2°C, respectively, at Jishou side. Meanwhile, they were 452 mm and 40.1°C at Chadong side. In fact, several load factors contribute to girder end longitudinal displacement including temperature, traffic, or wind loading in the operational stage. Figure 3 can only superficially reflect the qualitative relationship between the temperature variation and the girder longitudinal movement.

In detail, daily monitoring data (e.g., August 15, 2017) were randomly selected to reveal daily longitudinal movement characteristic of the girder (Figure 6). Figure 6 plots a typical daily time-history curve of girder end longitudinal displacement for a suspension bridge, which is similar to a sinusoidal-shaped fluctuation curve with many small burrs and also been observed in other related studies [3,22,24].

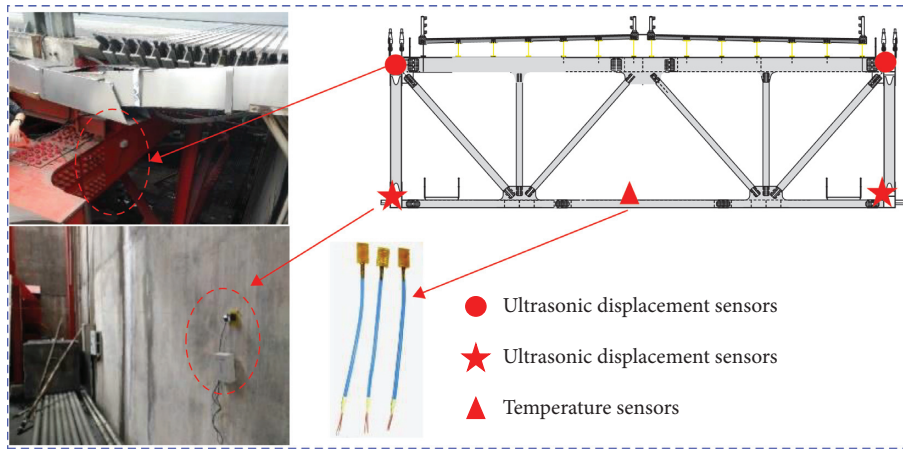


FIGURE 2: Monitoring sensors in the truss-girder section at the girder ends.

TABLE 2: Instrumentations applied on Aizhai Bridge.

Monitoring section	Serial number	Location details	Sampling frequency	Unit
Jishou side	ULDJ1	Top chord (south)	5	mm
	ULDJ2	Top chord (north)	5	mm
	DWDJ1	Bottom chord (south)	5	mm
	DWDJ2	Bottom chord (north)	5	mm
	TEMJ	Bottom chord (central)	2	°C
Chadong side	ULDC1	Top chord (south)	5	mm
	ULDC2	Top chord (north)	5	mm
	DWDC1	Bottom chord (south)	5	mm
	DWDC2	Bottom chord (north)	5	mm
	TEMC	Bottom chord (central)	1	°C

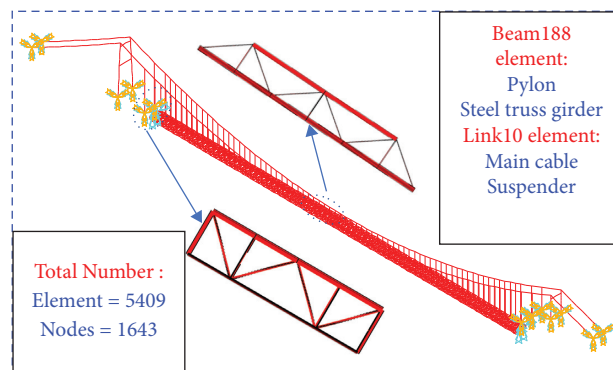


FIGURE 3: FE model of the Aizhai Bridge.

TABLE 3: The vibration modes of the Aizhai Bridge.

Mode no.	Frequency (Hz)		Mode shape
	FEM res.	Field test res [29]	
1	0.0562	Not available	1st symmetric lateral
2	0.1158	0.1005	1st antisymmetric vertical + longitudinal floating
3	0.1408	0.1443	1st antisymmetric lateral
4	0.1595	0.1759	1st symmetric vertical
5	0.2126	0.2030	2st symmetric vertical
6	0.2540	0.2822	2st antisymmetric vertical + longitudinal floating
7	0.2939	0.3189	1st symmetric torsional

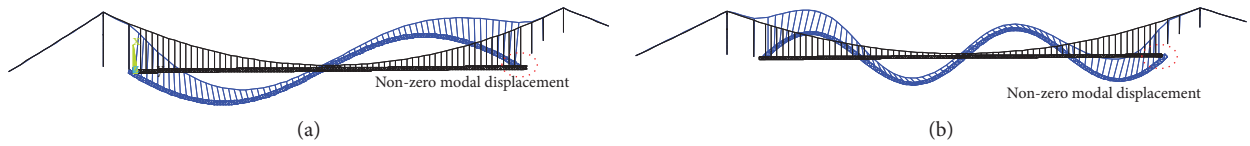


FIGURE 4: First two-order asymmetric vertical bending with longitudinal mode: (a) first order; (b) second order.

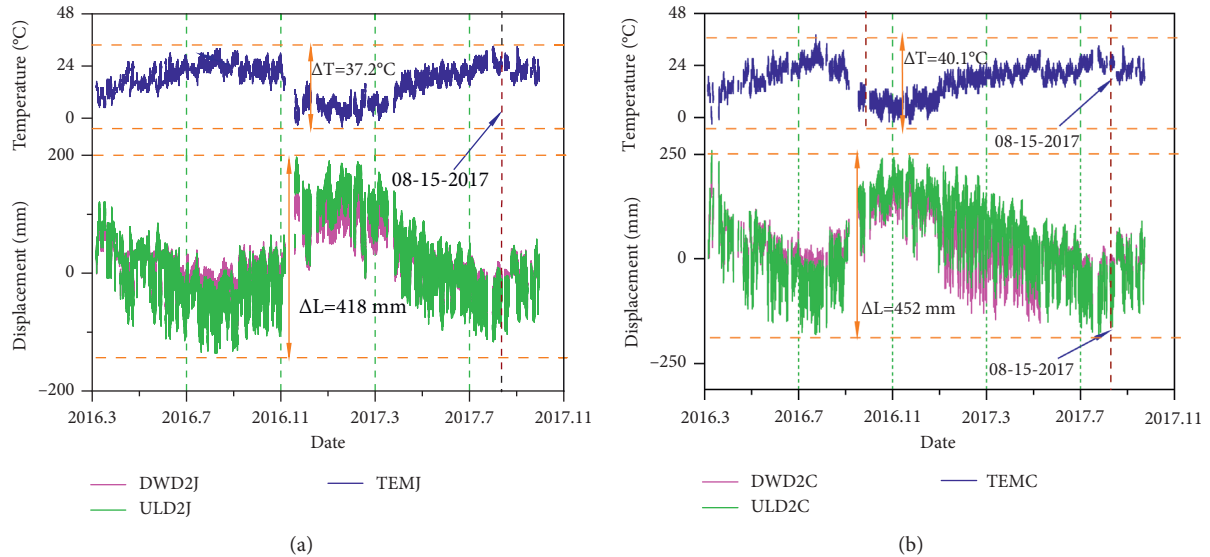


FIGURE 5: Displacement and temperature measured during monitoring period: (a) Jishou side; (b) Chadong side.

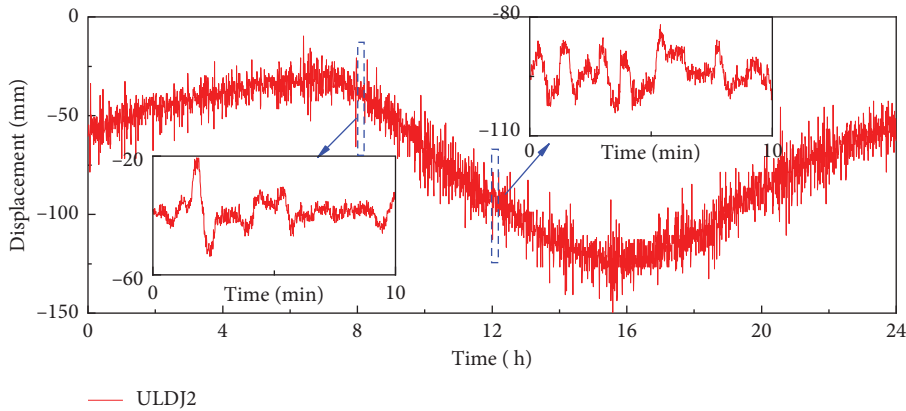


FIGURE 6: Time-history curve of daily longitudinal displacement at the girder end.

Meanwhile, these investigations all emphasized that the fluctuation trend of displacement time-history curve is caused by the slowly varying temperature, while the burr displacement is induced by the rapidly changing dynamic loads such as wind and vehicle load. This view can be confirmed in Figure 7, and the Fourier spectrum of the girder end longitudinal displacement of the bridge, which is obtained by the fast Fourier transform (FFT) from the daily time-history curve of the girder end longitudinal displacement, is shown in Figure 6.

Temperature-induced girder longitudinal displacement has been extensively researched. And this study focuses on the girder longitudinal movement caused by the vehicle load. Several 10 min displacement data were selected for vehicle-induced response analysis, where the temperature changes slightly and the wind speed is less than 2 m/s, so that the selected displacement responses are approximately assumed to be caused only by vehicles.

As observed from the partial view in Figure 6, the traffic loads may cause several centimeters of girder end

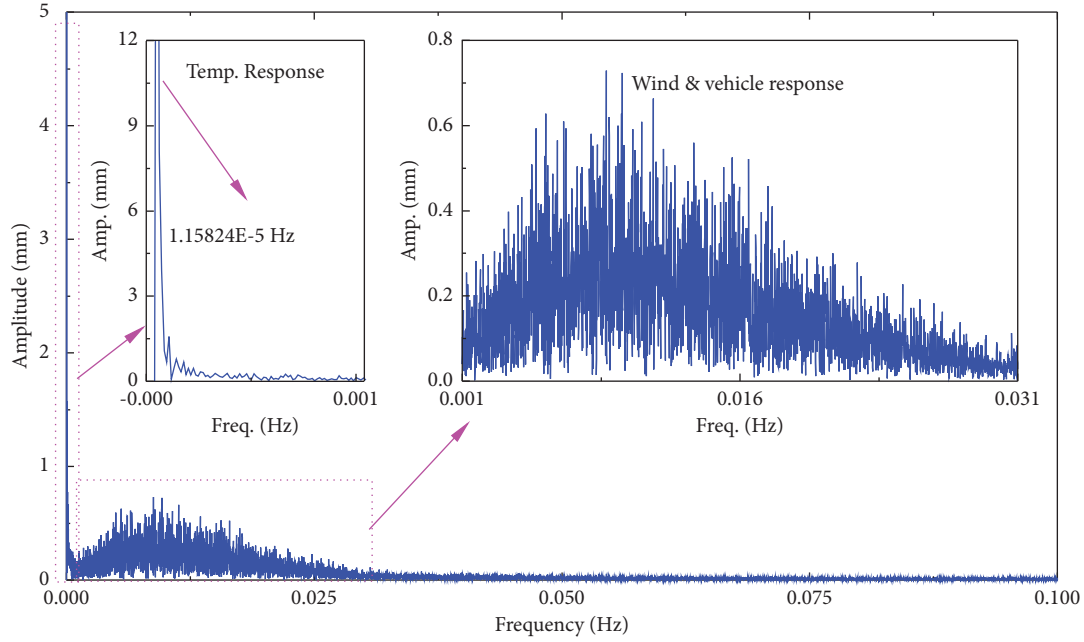


FIGURE 7: Fourier spectrum curve of daily longitudinal displacement at the girder end.

longitudinal displacement. Moreover, the Fourier spectrum curve of 10 min longitudinal displacement is plotted in Figure 8 by FFT. It indicates that the frequency band of girder end displacement response is mainly concentrated in 0–0.03 Hz, which is far less than the frequency of first-order asymmetric vertical bending with longitudinal mode in Table 2 (0.116 Hz).

4. Theoretical Analysis

4.1. Static Longitudinal Behavior under Vertical Loads. To investigate the longitudinal girder movement mechanism of the suspension bridge under the moving vehicle load, the static deformation behavior of the structure under vehicle load (i.e., the vertical loads) should be researched before considering the dynamic displacement response under moving vehicle. Figure 9 shows a two-hinge single-span suspension bridge considered in this study. There is no longitudinal support at either end of the girder, and the girder longitudinal movement is allowed to reduce the internal force effect under loads, especially seismic excitation.

The displacement, which reflects the total stiffness of the bridge system, is a macroscopic manifestation of structural deformation behavior characteristics. For suspension bridges, the structural behavior of the whole bridge depends on the mechanical properties of the main cables. When the vertical load is applied to the deck of suspension bridge, the main cables will undergo flexural deformation. Many scholars have conducted relevant research on this issue [30–33], but they all focused on the vertical flexural deformation instead of horizontal deflection.

In fact, when the displacement at the top of the tower and the elastic elongation of the cable are ignored, the cable geometric configuration will change due to the applied

unbalanced loads (or the asymmetric loads). The deformation diagrams of suspension bridge under vertical asymmetric loads are presented in Figure 10. And the coupling relationship between vertical deflection and longitudinal displacement of the cable is analyzed on the basis of deflection theory as follows.

The ds micro-element section of the main cable (Figure 11) is taken as the research object to analyze the deflection characteristic. The horizontal projection of change in cable length of a differential cable element dw is given by the compatibility equation [34]:

$$dw = \frac{Hp}{EcA\cos^3 \psi} dx + \frac{\alpha T}{\cos^2 \psi} dx - \frac{dy}{dx} d\eta, \quad (1)$$

where Hp = horizontal cable force component due to live load; $EcAc$ = cable axial stiffness; T = temperature change in suspension cable; α = coefficient of thermal expansion; Ψ = cable inclination angle; η = cable deflection under live load; y = cable ordinate under dead load; and x = the horizontal coordinate along the axis of the deck.

Equation (1) indicates that dw consists of three parts. The first two are the elastic elongation deformation displacement caused by vertical live loads and temperature, respectively. Meanwhile, the last is the longitudinal deformation displacement induced by the cable vertical deflection η , and this reveals the cable deformation characteristics that the vertical displacement is coupling with the longitudinal. Without regard to temperature and the elastic elongation induced by live loads [35], Equation (1) can be written more simply as

$$dw = -\frac{dy}{dx} d\eta. \quad (2)$$

Then, the cable horizontal displacement $u(x)$ can be written as

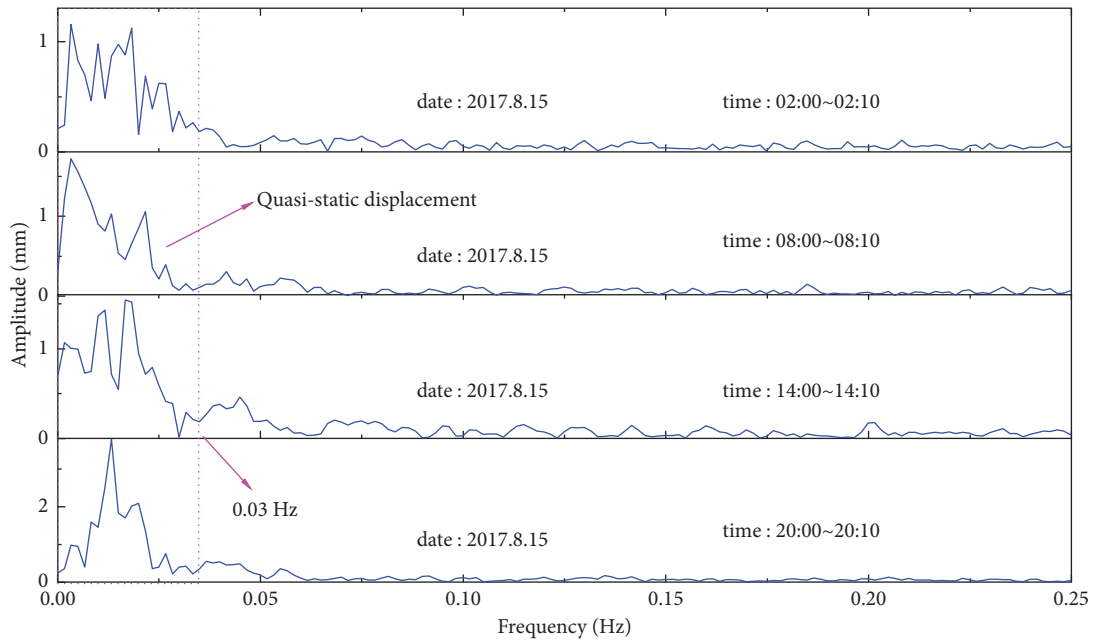


FIGURE 8: Fourier spectrum curve of 10 min longitudinal displacement at the girder end.

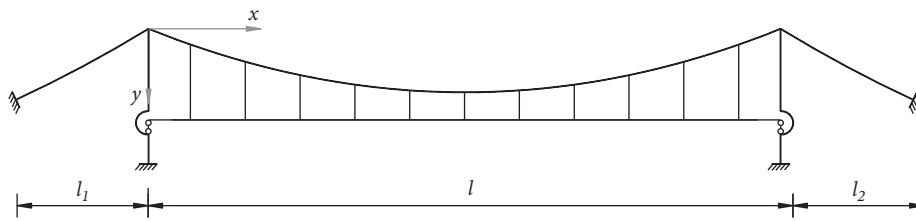


FIGURE 9: Geometry and coordinate system of a single-span suspension bridge.

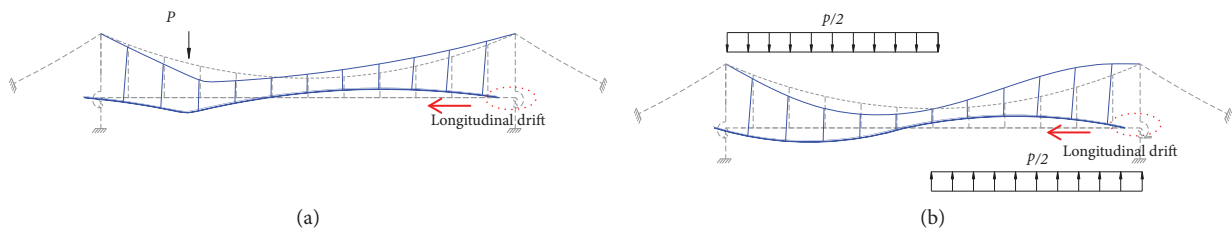


FIGURE 10: Deformation of a suspension bridge under asymmetric load: (a) a single vertical load case; (b) antisymmetric uniformly distributed load case.

$$w(x) = - \int_0^x \frac{dy}{dx} d\eta = - \int_0^x \frac{dy}{dx} \frac{d\eta}{dx} dx. \quad (3)$$

Equations (2) or (3) shows that the vertical deflection of the cable induced by vertical live loads is accompanied by the longitudinal horizontal displacement. Notably, any form of loads can be decomposed into symmetrical and antisymmetrical loads based on mechanical theory, and it is only the asymmetric vertical loads applied to the deck that may cause the girder longitudinal displacement. However, symmetrical vertical loads may cause symmetrical deformation of the

suspension bridge, which fails to contribute to the girder longitudinal movement. When asymmetric vertical loads, especially the antisymmetric vertical loads, are applied to the deck of the suspension bridge, then the girder and cable undergoes approximately antisymmetric vertical deflection accompanied by longitudinal drift, which result in the static displacement response of the girder, as shown in Figure 10(b).

An exact analytic solution is difficult to obtain from Equation (2) due to the complex function expression of η . However, $u(x)$ can be solved in some ideal cases with

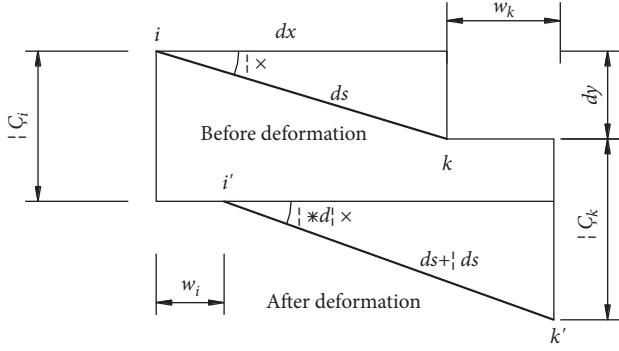


FIGURE 11: Deformation and displacement of the main cable microelement.

appropriate approximation assumptions, such as the load case shown in Figure 10(b).

The cable geometry under dead load is parabolic and can be written as

$$y = \frac{4f}{l^2} x(l-x), \quad (4)$$

and the cable deflection under antisymmetric uniformly distributed load is a sine curve that can be expressed as

$$\eta = A \sin \frac{2\pi x}{l}, \quad (5)$$

where A is the maximum of cable vertical deflection.

Substituting Equations (4) and (5) to Equation (3), Equation (3) will be rewritten as

$$u(x) = -\frac{4Af}{\pi L} \left[\left(1 - \frac{2x}{L}\right) \pi \sin\left(\frac{2\pi x}{L}\right) - \cos\left(\frac{2\pi x}{L}\right) + 1 \right]. \quad (6)$$

The cable longitudinal displacement curve is drawn as shown in Figure 12. And the figure shows that the cable longitudinal displacement varies with its horizontal coordinates and presents an analogous double wave peak curve with its maximums occurring at approximately $l/4$ and $3l/4$. This homodromous but unequal cable longitudinal displacement causes the suspenders to incline; as a result, the girder moves longitudinally as a whole. Notably, the cable longitudinal displacement determines that of the girder but not the same, and the correlation between them is affected by several factors, such as gravity stiffness, load cases, and the connection between the cables and girder. Consequently, the analytical solution of the girder longitudinal displacement induced by vertical loads is difficult to obtain and is generally solved by numerical methods.

4.2. Under Vertical Moving Loads. Without considering longitudinal vibration temporarily, the linear vibration equation of suspension bridge system under vertical load $p(x, t)$ can be expressed as

$$EI \frac{d^4 \eta}{dx^4} - H_0 \frac{d^2 \eta}{dx^2} + C\dot{\eta} + m\ddot{\eta} = p(x, t), \quad (7)$$

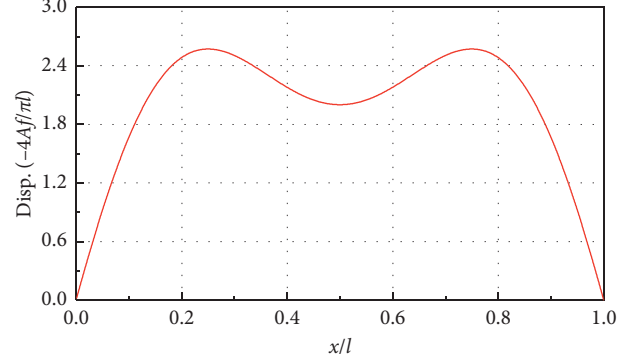


FIGURE 12: Longitudinal displacement of the main cable under antisymmetric uniformly distributed load.

where EI is the flexural rigidity of stiffening girder, H_0 is the horizontal cable force component at the static equilibrium position, C is the structural damping coefficient, and m is the mass per unit deck length.

The dynamic deflection of the flexural vibration of the suspension bridge is assumed to be

$$\eta(x, t) = \sum_{n=1}^{\infty} q_n(t) \cdot \varphi_n(x), \quad (8)$$

where $q_n(t)$ denotes the n th modal coordinate and $\varphi_n(x)$ denotes the n -order vibration mode vector.

Substituting Equations (8) to (7) and using mode shape orthogonality, the n -order equation of motion without the effect of structural damping in modal coordinate system can be expressed as

$$\ddot{q}_n(t) + \omega_n^2 q_n(t) = Q(t), \quad (9)$$

where $\omega_n^2 = EI \int_0^l \varphi_n^{(4)} \varphi_n dx - H_0 \int_0^l \varphi_n'' \varphi_n dx / m \int_0^l \varphi_n^2(x) dx$ is n -order natural vibration frequency of the suspension bridge, and the generalized load is

$$Q(t) = \frac{\int_0^l p(x, t) \varphi_n dx}{m \int_0^l \varphi_n^2(x) dx}. \quad (10)$$

For long-span suspension bridges, the vehicle mass and the body length are far less than the bridge structural system mass and the bridge span, respectively. This study aims to reveal the mechanism of the displacement response of the girder and grasp its overall response characteristics under vehicle load without considering the vibration effect of the vehicle itself and the influence of coupling effects between the moving loads and bridge deformations temporarily. Thus, the moving vehicle is approximately simulated as moving constant load, and then, the generalized load can be expressed as

$$Q(t) = \frac{\int_0^l p \delta(x-vt) \varphi_n dx}{m \int_0^l \varphi_n^2(x) dx} = \frac{p \varphi_n(vt)}{m \int_0^l \varphi_n^2(x) dx}, \quad (11)$$

where p is the moving constant load and δ , which is the Dirac delta function, is defined as

$$\delta(x - vt) = \begin{cases} 0, & x \neq vt, \\ 1, & x = vt. \end{cases} \quad (12)$$

Substituting Equations (11) to (9), Equation (9) can be rewritten as

$$\ddot{q}_n(t) + \omega_n^2 q_n(t) = \frac{P\varphi_n(vt)}{m \int_0^l \varphi_n^2(x) dx}. \quad (13)$$

Note that only longitudinal drift modes are concerned for the girder longitudinal displacement or longitudinal vibration under moving load, and these modes are always accompanied by the asymmetric vertical flexural modes for suspension bridge, as shown in Figure 4. Moreover, the antisymmetric vertical bending mode function of the girder is assumed as

$$\varphi_n = \sin\left(\frac{2\pi nx}{l}\right). \quad (14)$$

Substituting Equations (14) to (13), the solution of the equation can be obtained as

$$q(t) = \frac{2P}{ml} \sum_{n=1}^N \frac{1}{\omega_n^2 - \Omega_n^2} \left(\sin \Omega_n t - \frac{\Omega_n}{\omega_n} \sin \omega_n t \right), \quad (15)$$

where the generalized disturbance frequency $\Omega_n = 2\pi nv/l$.

As shown in Figure 4, the antisymmetric vertical bending modes are always coupled with longitudinal drift, and longitudinal nonzero displacement (i.e., modal coordinates) of the girders is assumed to be equal to φ_{xn} . Then, the corresponding girder longitudinal displacement $u_b(t)$ can be expressed as

$$u_b(t) = \frac{2P}{ml} \sum_{n=1}^N \frac{1}{\omega_n^2 - \Omega_n^2} \left(\sin \Omega_n t - \frac{\Omega_n}{\omega_n} \sin \omega_n t \right) \varphi_{xn}. \quad (16)$$

Therefore, the longitudinal vibration of suspension bridge under moving loads is presented as simple harmonic forced vibration at generalized disturbance frequency $2\pi nv/l$ in the modal coordinate system.

If the moving speed is very small, then Ω_n is far less than the natural frequency of the structure ω_n and the structure response is quasi-static under moving load. If only the first mode is considered, then the longitudinal displacement of the girder can be expressed as

$$u_b(t) = u_{b0}(t) \sin \frac{2\pi}{l} x, \quad (17)$$

where u_{b0} is the static longitudinal displacement amplitude of the girder and l is the displacement wavelength of sinusoidal curve, and it is also equal to the span of the main girder of a single-span suspension bridge.

When the generalized longitudinal disturbance frequency, $f_p = v/l$, is equal to the bending-longitudinal coupling vibration frequency f_n of some order of the system, the longitudinal resonance phenomenon will occur, and the resonance speed required is $v_{br} = lf_n$.

5. Numerical Study

5.1. Quasi-Static Response. The quasi-static response of the suspension bridge under a single slowly moving load with a magnitude of 550 kN, the standard value of vehicle weight in bridge design code in China, is first investigated on the basis of the FE model of the Aizhai Bridge. The longitudinal displacement response of the girder end under that load case is obtained, as shown in Figure 13. As observed, the shapes of the curves on the figure are similar to the sinusoids and the influence line of longitudinal displacement at the girder end of suspension bridge [2]. When the load is applied to the middle of the span, the displacement of the girder end is approximately equal to zero, while in the 1/4 of the span, it approximately reaches the maximum.

As shown in Figure 13(a), the longitudinal displacement curves at different positions of the girder ends are similar but not the same, and the slight differences of the curves are caused by the vertical bending (elastic deformation) of the girder. If that longitudinal displacement induced by flexural deflection is ignored, then the longitudinal displacement of the girder (i.e., rigid body longitudinal displacement) can be calculated by averaging the four curves in Figure 13(a). In this way, the girder displacement curve is closer to the sinusoid (the idealized displacement curve in Figure 13(b), which is adopted by Equation (17)).

5.2. Dynamic Response. The simulation analysis of a single moving load at different speeds traveling across the bridge is conducted to investigate the influence of the speed effect of moving load on the girder longitudinal of the suspension bridge. Meanwhile, the dynamic amplification factor (DAF) is introduced to assess the dynamic effect caused by moving loads, and it is defined as

$$DAF = \frac{R_{D\max}}{R_{S\max}}, \quad (18)$$

where $R_{D\max}$ and $R_{S\max}$ are the absolute maximum dynamic and static responses, respectively, including displacement, stress, and internal force of the bridge, and the response in this study is the girder longitudinal displacement.

Figure 14 illustrates the longitudinal displacement response of the girder under a single moving load at different speeds (0–140 m/s). The DAFs for the longitudinal displacement at the girder end of the suspension bridge are shown in Figure 15. Figures 14 and 15 indicate that the longitudinal displacement response is extremely sensitive to the speed of the moving load, and the dynamic displacement response is magnified with the increasing speed. In particular, when the speed reaches about the resonance speed, $v_{br} = lf_1 = 1000.5 \times 0.116 = 116$ m/s, the vertical coupling longitudinal resonance occurs; the displacement response reaches the maximum and subsequently decreases gradually (Figure 15).

5.3. Analysis of Influencing Factors. Several factors, including structural damping ratio, dampers installed at the girder ends, and bearing friction resistance, are investigated to analyze their effect on vehicle-induced

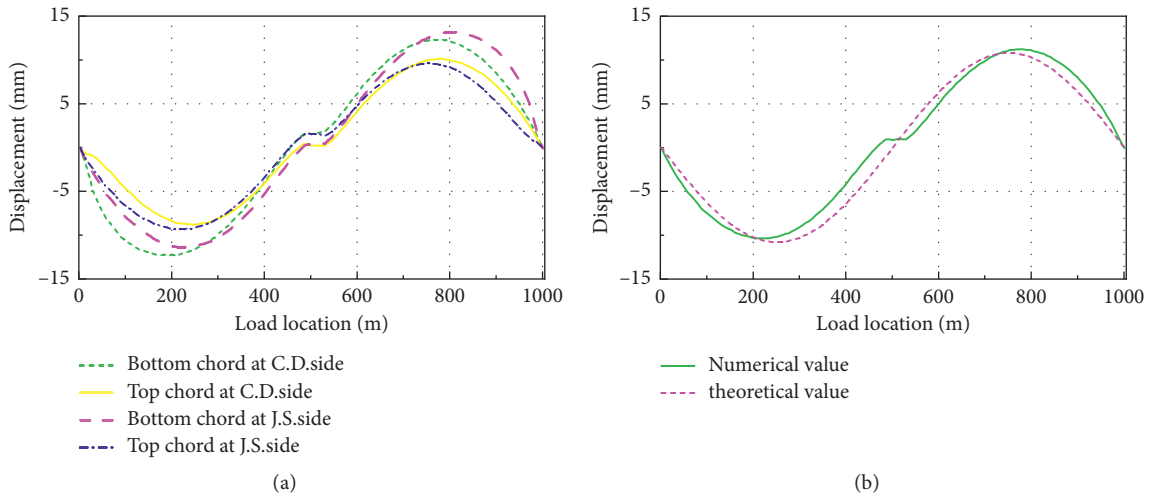


FIGURE 13: Longitudinal displacement at the end of the girder induced by a load at a slow speed moving on the bridge: (a) longitudinal displacement at different positions of girder ends; (b) average longitudinal displacement and equivalent longitudinal displacement at the ends.

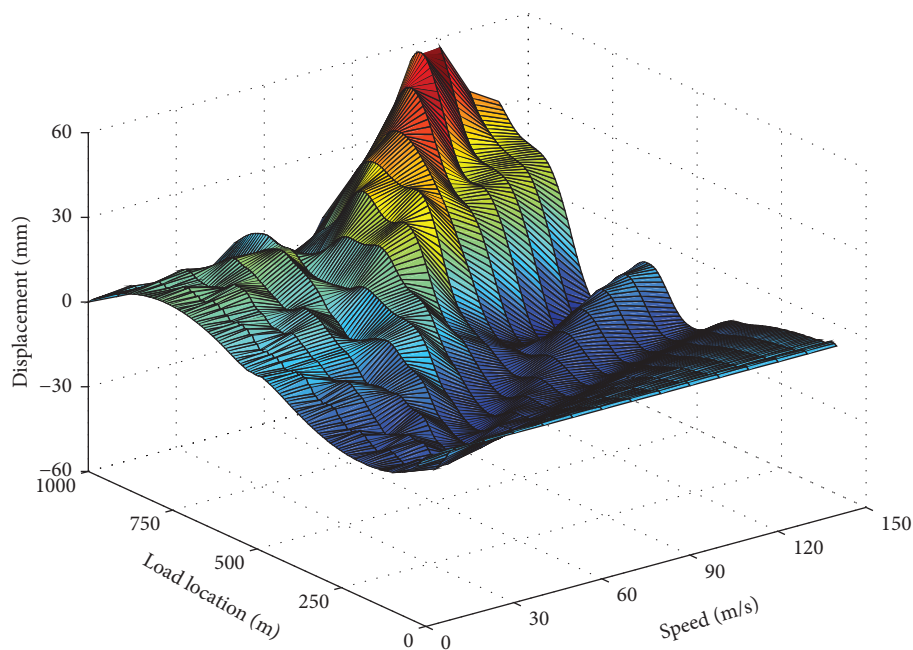


FIGURE 14: Longitudinal displacement at the end of the girder of the suspension bridge under a single moving load.

longitudinal vibration under different moving load cases and to further explore the response characteristics of vehicle-induced girder longitudinal displacement response. Table 4 lists the various combinations of factors considered, while Table 5 displays different moving load cases, including single moving load, moving load series, and uniform load flow.

Figures 16 and 17 present the longitudinal displacement response caused by the three different moving load cases in consideration of different influencing factors in Table 4. The plots in the figures indicate that the displacement response of girder end consists of quasi-static and dynamic effects under moving loads. However, the dynamic effect rather

than the quasi-static effect can be reduced to some certain extent as a result of the damper installed on the girder ends or the structure damping and the bearing friction resistance. In particular, only the quasi-static effect displacement is left, while the dynamic effect is completely suppressed due to the synergistic effect of damper and bearing friction (the curves of $\xi = 0.005 + \text{damper} + \text{friction}$ in Figure 16).

The single moving load case is taken as an example for further illustration, as shown in Figure 16(b). The figure indicates that the first-order dominant frequency of displacement response is approximately equal to the generalized longitudinal disturbance frequency of moving load across the bridge, $f_p = 30/1000.5 = 0.030$ Hz. Meanwhile, the

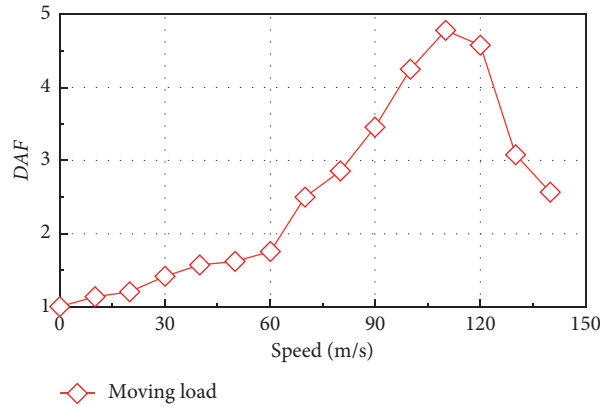


FIGURE 15: DAFs for longitudinal displacement at the end of the girder under a single moving load.

TABLE 4: Cases for calculation of different damping conditions.

Factor no.	Damping ratio	Damper parameters	Friction
1	0.005	Ignored	Ignored
2	0.005	$C = 5000 \text{ kN}/(\text{m/s})^\alpha, \alpha = 0.4$	Ignored
3	0.005	$C = 5000 \text{ kN}/(\text{m/s})^\alpha, \alpha = 0.4$	Counted
4	0.03	Ignored	Ignored

TABLE 5: Cases of different moving loads.

Load cases	Load value (kN)	Load number	Load space (m)	Speed (m/s)
Single moving load	550	1	—	30
Moving load series	550	10	100	25
Uniform load flow	550	—	100	25

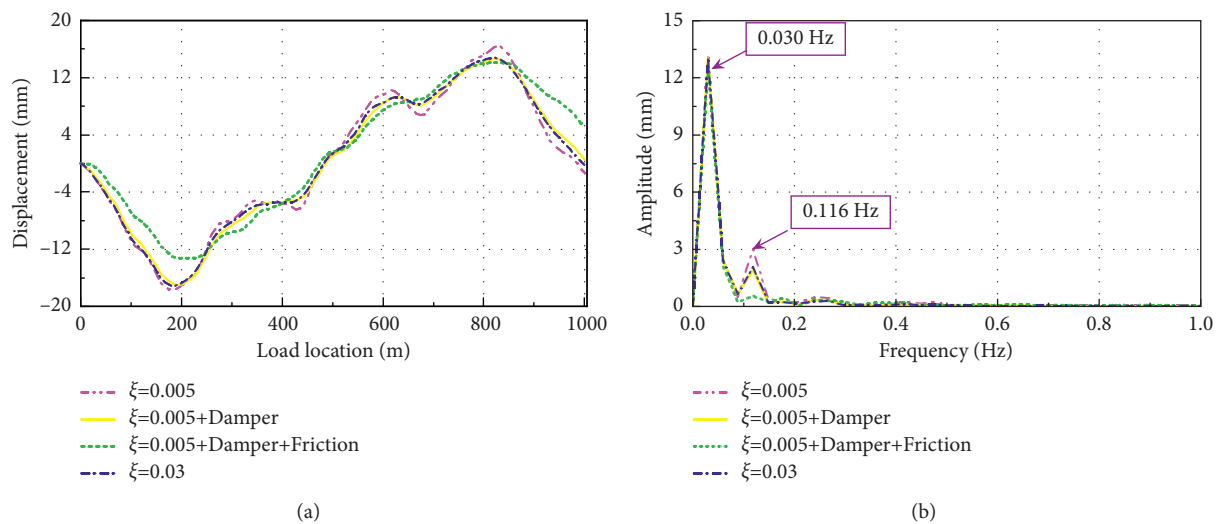


FIGURE 16: Girder end longitudinal displacement of the suspension bridge under a single moving load at 30 m/s: (a) time history of longitudinal displacement; (b) Fourier spectrum of longitudinal displacement.

second-order dominant frequency of displacement response is approximately equal to the first-order asymmetric vertical bending coupling longitudinal drift modal frequency (0.116 Hz). The structural damping and installed

longitudinal damper have a little restraining effect on the dynamic displacement. However, no first-order asymmetric vertical bending vibration mode is observed under the combined effect of damper and bearing friction. Therefore,

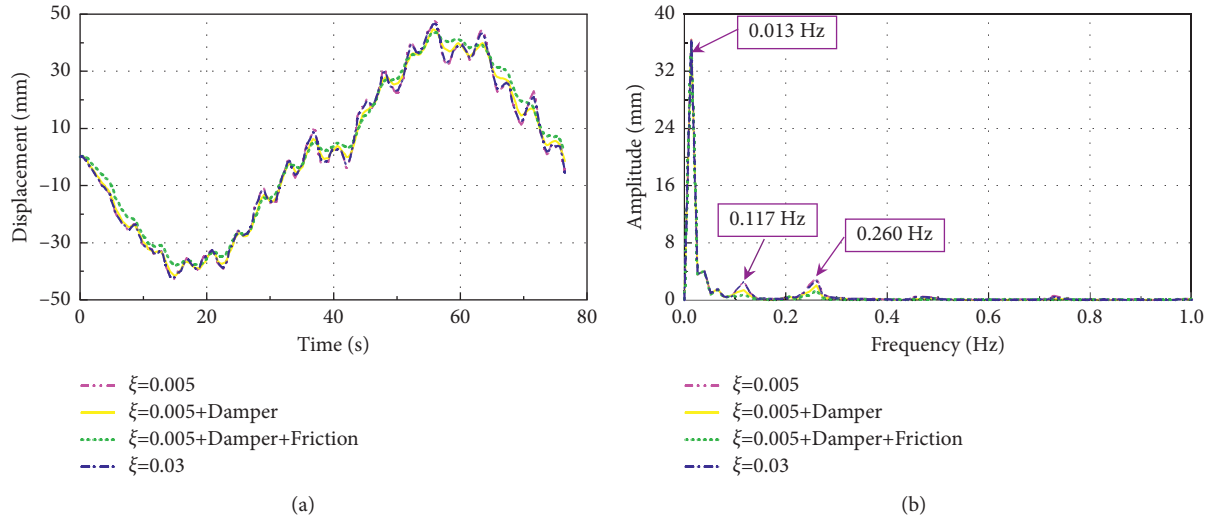


FIGURE 17: Girder end longitudinal displacement of the suspension bridge under a series of moving loads at 25 m/s: (a) time history of longitudinal displacement; (b) Fourier spectrum of longitudinal displacement.

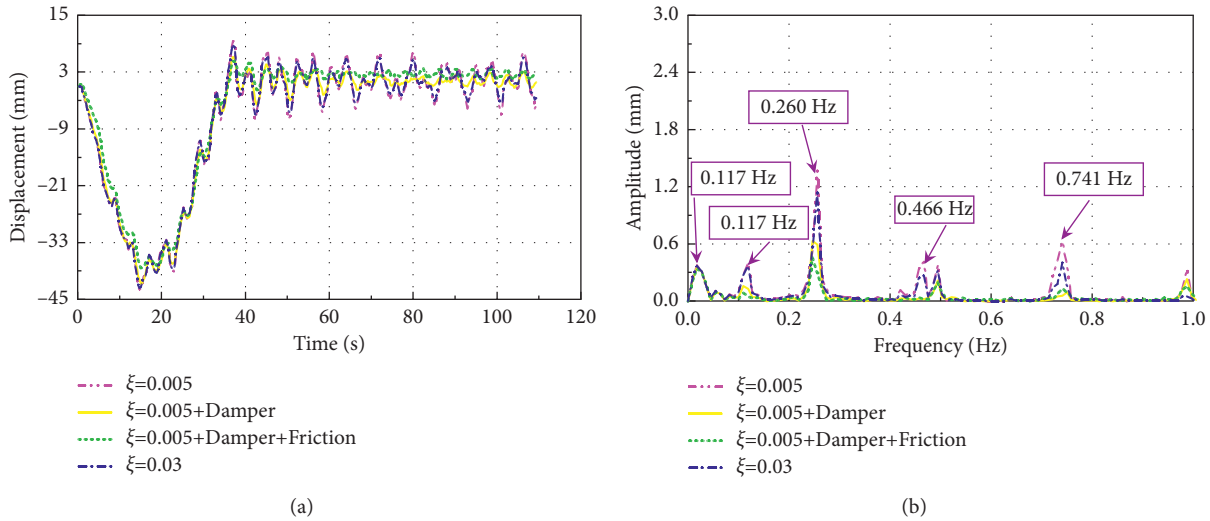


FIGURE 18: Girder end longitudinal displacement of the suspension bridge under a series of moving loads at 25 m/s: (a) time history of longitudinal displacement; (b) Fourier spectrum of longitudinal displacement.

the influence of friction resistance on dynamic displacement cannot be ignored.

For the normal speed of the driving vehicles on highway bridge (no more than 40 m/s in general), the corresponding generalized excitation frequency of moving load is often far less than the natural frequency of the structure. That is, the forced vibration is far from the first-order longitudinal drift resonance region of the bridge, as shown in Figure 16(b).

The displacement response characteristic under moving load series is similar to that under single moving load. However, that is not the same for the uniform load flow case (Figure 18). The dynamic response is magnified due to that the idealized traffic flow forms periodic excitation on the bridge, while quasi-static effect is largely counterbalanced by uniformly distributed loads on the deck. In fact, uniform load flow case is rare in engineering.

6. Conclusions

On the basis of the background of Aizhai Bridge, this study analyzes the response characteristics and influencing factors of girder longitudinal displacement of the suspension bridge under moving vehicle load.

- (1) The analysis results both in time domain and frequency domain based on field measured data indicate that the girder of the Aizhai Bridge moves quasi-statically and reciprocates longitudinally with centimeter amplitude under normal operational loads, which is verified by finite element numerical simulation.
- (2) The coupling relationship between the vertical and longitudinal displacements of the main cable is deduced based on the cable geometric deformation

theory. The imposed vertical load will contribute to the configuration change of the cable, that is, the deformation with vertical deflection and longitudinal drift, which leads to the girder longitudinal displacement and movement.

- (3) The vehicle is modeled as a moving concentrated load, and the numerical simulation analysis for vehicle-induced vibration is carried out. Then, the longitudinal displacement response characteristic of the girder is obtained, which reveals the mechanical mechanism of the girder longitudinal movement of suspension bridge caused by moving load. However, the numerical results cannot be directly applied to practical projects given that the vehicle-bridge coupling and random vehicle flow effects are ignored. In view of this, more reliable girder longitudinal displacement will be further investigated in the future.
- (4) The moving load induces the longitudinal vibration of the floating girder of suspension bridge. When the speed of the moving load is small, the longitudinal behavior of the girder is quasi-static; however, the dynamic response of that is magnified with the increase of moving speed in a certain range of moving speed. There is a theoretically possible resonance speed, $v_{br} = lf_1$, which is generally far greater than the speed of the driving vehicles on the highway bridge.
- (5) Under moving vehicle with normal speed, the forced quasi-static longitudinal movement of the girder is accompanied by the dynamic effects, which may induce excessive cumulative girder displacement. However, the dynamic effects can be eliminated to a great extent, as a result of the combined influence of damping, installed longitudinal damper, and bearing friction.

Data Availability

The data used to support the findings of this study are available from the corresponding author upon request.

Conflicts of Interest

The authors declare no conflicts of interest.

Acknowledgments

This study was sponsored by the Hunan Provincial Natural Science Foundation of China (Grant No. 2021JJ50143) and Hunan Science and Technology Talent Promotion Project in China (Grant No. 2019TJ-Y08), which are greatly acknowledged.

References

- [1] Y. L. Xu and Y. Xia, *Structural Health Monitoring of Long-Span Suspension Bridges*, CRC Press, Boca Raton, FL, USA, 2011.
- [2] G. Li, W. Han, X. Chen, and T. Guo, "Wear evaluation on slide bearings in expansion joints based on cumulative displacement for long-span suspension bridge under monitored traffic flow," *Journal of Performance of Constructed Facilities*, vol. 34, no. 1, Article ID 04019106, 2020.
- [3] T. Guo, J. Liu, and L. Huang, "Investigation and control of excessive cumulative girder movements of long-span steel suspension bridges," *Engineering Structures*, vol. 125, pp. 217–226, 2016.
- [4] T. Guo, L. Huang, J. Liu, and Y. Zhou, "Damage mechanism of control springs in modular expansion joints of long-span bridges," *Journal of Bridge Engineering*, vol. 23, no. 7, Article ID 04018038, 2018.
- [5] Z. Sun and Y. Zhang, "Failure mechanism of expansion joints in a suspension bridge[J]," *Journal of Bridge Engineering*, vol. 21, no. 10, Article ID 05016005, 2016.
- [6] Z. Sun, S. Ning, and Y. Shen, "Failure investigation and replacement implementation of short suspenders in a suspension bridge," *Journal of Bridge Engineering*, vol. 22, no. 8, Article ID 05017007, 2017.
- [7] Z. Liu, T. Guo, L. Huang, and Z. Pen, "Fatigue life evaluation on short suspenders of long-span suspension bridge with central clamps," *Journal of Bridge Engineering*, vol. 22, no. 10, Article ID 04017074, 2017.
- [8] Z. Liu, T. Guo, M. H. Hebdon, and W. Han, "Measurement and comparative study on movements of suspenders in long-span suspension bridges," *Journal of Bridge Engineering*, vol. 24, no. 5, Article ID 04019026, 2019.
- [9] X. Liu, W. Han, Y. Yuan, X. Chen, and Q. Xie, "Corrosion fatigue assessment and reliability analysis of short suspender of suspension bridge depending on refined traffic and wind load condition," *Engineering Structures*, vol. 234, Article ID 111950, 2021.
- [10] Z. Sun, Z. Zou, and Y. Zhang, "Utilization of structural health monitoring in long-span bridges: case studies," *Structural Control and Health Monitoring*, vol. 24, no. 10, p. e1979, 2017.
- [11] Y. Li, M. Wu, Y. Zang, and S. Qing, "Effects of vertical rotation angle at girder ends on train running performance for large-span suspension bridges," *China Civil Engineering Journal*, no. 8, pp. 122–128, 2012.
- [12] D. Wang, Y. Deng, and Y. Liu, "Influence of central buckle on suspension bridge dynamic characteristics and driving comfort," *Journal of Central South University*, vol. 22, no. 8, p. 3115, 2015.
- [13] S. Arzoumanidis, A. Shama, and F. Ostadan, "Performance-based seismic analysis and design of suspension bridges," *Earthquake Engineering & Structural Dynamics*, vol. 34, no. 4-5, pp. 349–367, 2010.
- [14] M.-G. Yang and C. S. Cai, "Longitudinal vibration control for a suspension bridge subjected to vehicle braking forces and earthquake excitations based on magnetorheological dampers," *Journal of Vibration and Control*, vol. 22, no. 17, pp. 3659–3678, 2016.
- [15] L. Liang, Z. Feng, and Z. Chen, "Seismic control of SDOF systems with nonlinear eddy current dampers[J]," *Applied Sciences*, vol. 9, no. 16, p. 3427, 2019.
- [16] M. Zribi, N. B. Almutairi, and M. Abdel-Rohman, "Control of vibrations due to moving loads on suspension bridges," *Nonlinear Analysis Modelling and Control*, vol. 11, no. 11, pp. 293–318, 2006.
- [17] B. S. Xing and X. F. Wang, "The singular function method based on the moving load deformation of suspension bridge," *Advanced Materials Research*, vol. 403–408, pp. 3059–3062, 2012.

- [18] S. H. Ju, H. T. Lin, C. C. Hsueh, and S. L. Wang, "A simple finite element model for vibration analyses induced by moving vehicles," *International Journal for Numerical Methods in Engineering*, vol. 68, no. 12, pp. 1232–1256, 2006.
- [19] N. B. Almutairi, M. F. Hassan, M. Abdel-Rohman, and M. J. Terro, "Control of suspension bridge nonlinear vibrations due to moving loads," *Journal of Engineering Mechanics*, vol. 132, no. 6, pp. 659–670, 2006.
- [20] M. G. Yang and Z. Q. Yang, "Longitudinal vibration control of floating system bridge subject to vehicle braking force with viscous dampers," *Advanced Materials Research*, vol. 446–449, pp. 1256–1260, 2012.
- [21] A. Q. Li, Y. Ding, H. Wang, and T. Guo, "Analysis and assessment of bridge health monitoring mass data—progress in research/development of "Structural Health Monitoring,"" *Science China*, vol. 55, no. 8, pp. 134–146, 2012.
- [22] T. Guo, J. Liu, Y. Zhang, and S. Pen, "Displacement monitoring and analysis of expansion joints of long-span steel bridges with viscous dampers," *Journal of Bridge Engineering*, vol. 20, no. 9, Article ID 04014099, 2015.
- [23] Z. Sun and H. Sun, "Jiangyin bridge: an example of integrating structural health monitoring with bridge maintenance," *Structural Engineering International*, vol. 28, no. 3, pp. 353–356, 2018.
- [24] J. Hu, L. Wang, X. Song, Z. Sun, J. Cui, and G. Huang, "Field monitoring and response characteristics of longitudinal movements of expansion joints in long-span suspension bridges," *Measurement*, vol. 162, Article ID 107933, 2020.
- [25] Y. Zhang, H. Wang, Y. Baib, X. J. Mao, X. Y. Changa, and L. B. Wang, "Switching Bayesian dynamic linear model for condition assessment of bridge expansion joints using structural health monitoring data," *Mechanical Systems and Signal Processing*, vol. 160, Article ID 107879, 2021.
- [26] Y. Zhao, P. Huang, G. Long, Y. Yuan, and Y. Sun, "Influence of fluid viscous damper on the dynamic response of suspension bridge under random traffic load," *Advances in Civil Engineering*, vol. 2020, Article ID 1857378, 19 pages, 2020.
- [27] F. Petrini, P. Olmati, and F. Bontempi, "Coupling effects between wind and train transit induced fatigue damage in suspension bridge," *Structural Engineering & Mechanics*, vol. 70, pp. 311–324, 2019.
- [28] W. Gao, G. Li, Q. Su, and W. Han, "Impact of rigid central clamps on longitudinal deformation of long-span suspension bridges under vehicle excitations," *Structure and Infrastructure Engineering*, pp. 1–15, 2021.
- [29] D. Yan, H. Xu, Q. Pan, and K. Zhang, *Technical Report: Field Load Test of Aizhai Bridge*, Changsha University of Science and Technology, Changsha, China, 2012, In Chinese.
- [30] L. T. Stavridis, "A simplified analysis of the behavior of suspension bridges under live load," *Structural Engineering & Mechanics*, vol. 30, no. 5, pp. 559–576, 2008.
- [31] R. A. Dorton, "Cable supported bridges: concept and design," *Canadian Journal of Civil Engineering*, vol. 13, no. 6, p. 401, 2012.
- [32] J. M. W. Brownjohn, K.-Y. Koo, and A. Scullion, "Operational deformations in long-span bridges," *Structure and Infrastructure Engineering*, vol. 11, no. 4, pp. 556–574, 2015.
- [33] D. Arco and C. Aparicio, "Preliminary static analysis of suspension bridges," *Engineering Structures*, vol. 23, no. 9, pp. 1096–1103, 2001.
- [34] G. P. Wollmann, "Preliminary analysis of suspension bridge," *Journal of Bridge Engineering*, vol. 6, no. 4, pp. 227–233, 2001.
- [35] P. Clemente, G. Nicolosi, and A. Raithele, "Preliminary design of very long-span suspension bridges," *Engineering Structures*, vol. 22, no. 12, pp. 1699–1706, 2000.

Research Article

Experimental and Numerical Study on Ultimate Shear Load Carrying Capacity of Corroded RC Beams

Zhanzhan Tang ¹, Zhixiang He,¹ Zheng Chen,¹ Lingkun Chen ¹, Hanyang Xue,¹
and Hanqing Zhuge²

¹College of Civil Science and Engineering, Yangzhou University, Yangzhou 225127, China

²College of Civil Engineering and Architecture, Zhejiang University of Science & Technology, Hangzhou 310023, China

Correspondence should be addressed to Lingkun Chen; lkchen@yzu.edu.cn

Received 24 July 2021; Accepted 14 September 2021; Published 27 September 2021

Academic Editor: André Furtado

Copyright © 2021 Zhanzhan Tang et al. This is an open access article distributed under the Creative Commons Attribution License, which permits unrestricted use, distribution, and reproduction in any medium, provided the original work is properly cited.

For an RC beam, the strength of steel rebar, the bonding strength between the concrete and reinforcement, and the bite action between the aggregates will deteriorate significantly due to corrosion. In the present study, 10 RC beams were designed to study the impact of corrosion on the shear bearing capacity. The mechanism of corrosion for stirrups and longitudinal bars and their effects were analyzed. Based on the existing experimental data, the correlation between the stirrup corrosion factor and the cross section loss rate was obtained. An effective prediction formula on the shear bearing capacity of the corroded RC beams was proposed and validated by the experimental results. Moreover, a numerical analysis approach based on the FE technique was proposed for the prediction of the shear strength. The results show that corrosion of the reinforcements could reduce the shear strength of the RC beams. The corrosion of stirrups can be numerically simulated by the reduction of the cross section. The formulae in the literature are conservative and the predictions are very dispersed, while the predictions by the proposed formula agree very well with the experiment results.

1. Introduction

Most of the infrastructures, e.g., buildings and bridges, are exposed to the natural environment for decades and unavoidably be corroded due to the corrosive environments around them. The corrosion of a reinforced concrete (RC) beam always leads to the strength loss of the reinforcement, the degradation of material mechanical properties, the descending of the bond strength between the reinforcements and concrete, and the decrease of biting force between the inclined crack of the aggregates, which are the main factors decreasing the durability of an RC structure. At present, most studies focused on the deterioration of bending strength of RC beams caused by corrosion, rather than the decrease of the shear strength. Therefore, it is very significant to study the influence of corrosion on the shear performance of the RC beams and to propose effective formulae to facilitate the shear bearing capacity evaluation process.

A series of studies have been carried out on the shear failure mechanism of the corroded RC beams. Corrosion is a continuous process, and the extension of cracks produced by structural corrosion is related to the loss of cross section [1–3]. Usually, the corrosion of reinforcement induces the crack initiation and propagation, and in turn, the development of cracks accelerates the corrosion [4]. Corrosion cracking also leads to the decrease of the bond strength between the reinforcement and concrete [5]. Khan et al. [6], Ye et al. [7], Zhao et al. [8], and Xu et al. [9] conducted experimental studies on the shear strength of corroded beams using the rapid electrochemical corrosion method. However, the effect of the longitudinal reinforcement corrosion was not involved. Sola et al. [3], Higgins et al. [10], Huo [11], and Wang et al. [12] investigated experimentally the shear performance of RC beams with consideration of the longitudinal reinforcement corrosion and the reduction of bond strength, while stirrup corrosion was ignored in

these studies. Dai et al. [13] and Xue et al. [14] discussed the effect of longitudinal reinforcement corrosion on the shear performance of RC beams through a targeted method. The abovementioned studies focused on the influences of either the longitudinal reinforcement corrosion or the stirrup corrosion. However, the combined effect of them on the shear bearing capacity was not analyzed.

Various improved prediction formulae and theoretical models were proposed after the establishment of the classical truss model, e.g., the variable angle truss model, the fixed pressure field theory, the truss-arch model, the pull-rod model, the limit equilibrium theory, the plasticity theory, and the statistical analysis. Based on the limit equilibrium theory, Xu et al. [9] analyzed the contribution proportions of the concrete and reinforcement to shear bearing capacity of the RC beams, in which the correlation coefficient of stirrup corrosion was introduced. El-Sayed [15] and Alaskar et al. [16] proposed a shear bearing capacity evaluation model for the corroded RC beams, in which the effective width of the member and the reduction of reinforcement cross section were considered. Zhao et al. [8] introduced the fitting empirical coefficient P_v to reduce the shear bearing capacity of noncorroded RC beams using the equivalent truss theory. Li et al. [17] considered the effective width of the geometrical dimension of the member after corrosion and the reduction of the yield strength of the longitudinal reinforcements when evaluating the shear bearing capacity of the corroded RC beams. Yu et al. [18] proposed a precise prediction formula which includes the angle of the critical inclined crack and the reduction of the cross section. However, most of the proposed formulae ignore either the impact of the longitudinal reinforcement corrosion or the deterioration of the stirrup and the decrease of the bonding strength. Therefore, the predictions are very conservative. Although the prediction of the formula proposed by Yu et al. [18] agrees well with the experiments, the method is very complicated when applying in engineering practice. Finite element analysis was carried out to study the mechanical performance of RC beams in recent years. Hawileh et al. [19] examined the critical parameters that influence the effectiveness of side-bonded EB-FRP systems through a newly developed finite element (FE) model. Naser et al. [20] discussed an advanced finite element simulation as a mean to understand and predict the performance of FRP-strengthened structures.

In this study, the influences of stirrups and longitudinal reinforcement corrosion on the shear bearing capacity of RC beams were experimentally and theoretically studied. A short-time test was adopted to facilitate the experiment, in which the longitudinal reinforcements were wrapped by a thin Teflon insulated film with perfect nonadhesion property to simulate the nonbonding effect, and the axial rust swelling crack was simulated by filling an acrylic plate. A more practical formula for the shear bearing capacity evaluation of corroded RC beams was proposed, whose effectiveness was validated by the experimental results. Moreover, numerical analysis based on the FE method was carried out and compared with the test results.

2. Structural Tests and Discussions

2.1. Shear Strength Test. A series of experimental studies on the shear bearing capacity of corroded RC beams have been carried out in the literature. However, the time costs of these experiments are extremely high; thus, in this study, a short-time test was adopted. The mechanical cutting method was adopted to simulate the stirrup corrosion, the wrapping of insulated Teflon film was adopted to simulate the unbonding effect of the corroded longitudinal reinforcements, and the filling of acrylic plate was adopted to simulate the rust expansion cracks. Sufficient bending reinforcements were utilized so that only shear failure could occur. The steel and concrete materials specified by the Japan JIS-G-3112-2004 standard [21] and the Japan Architectural Institute JASS5 standard [22] were used. In the test, 10 beams were designed. The specimens were divided into two groups, in which 2 specimens were designed for the stirrup corrosion and 2 specimens were designed with consideration of the bonding strength and 1 ordinary RC beam for comparison purpose in Group A. In Group B, 2 specimens were designed for simulating the combined effects of bond strength and rust swelling crack and 2 specimens were designed to simulate rust swelling crack and 1 ordinary beam for comparison. Table 1 lists the design parameters of the specimens, where η_1 and η_w are the cross section loss rates due to corrosion of the longitudinal reinforcements and stirrups, respectively. s and λ are the stirrup spacing and the shear span ratio, respectively.

The extent of the bond strength degradation can be determined by the corrosion level [23]. The unbonded longitudinal reinforcements can be converted to a mass loss rate. The relationship between the reduction factor of bond strength ξ and the mass corrosion rate of the reinforcement η_m is [24]

$$\xi = \begin{cases} 1.0 + 0.125 \times \eta_m, & \eta_m \leq 2.0\%, \\ 1.59 \times \eta_m^{-0.35}, & \eta_m > 2.0\%. \end{cases} \quad (1)$$

Similarly, the simulated rust swelling crack can be transformed into the corresponding area loss rate η_s ($\eta_s = \Delta A_{sm}/A_s$, where ΔA_{sm} and A_s are the average area loss and the original area of reinforcement, respectively). The relationship between ΔA_{sm} and the corrosive crack width w is [25]

$$w = 0.1916\Delta A_{sm} + 0.164. \quad (2)$$

Before the structural test, material tests were conducted. Figure 1(a) shows the tensile test of the reinforcements, in which a 50 kN universal testing machine was used. Four types of reinforcements with different diameters, including D6 (SD295), D10 (SD295), D13 (SD345), and D22 (SD490), were tested. The specimen ID of D6 indicates the nominal diameter of the steel bar, and SD295 in the parenthesis represents the strength grade of steel bar, which indicates the yield point or 0.2% guaranteed strength is greater than 295 MPa. Standard tensile tests were carried out on the steel bars in the same batch. Different mass loss rates of 0%, 20%, and 40% were considered by the cutting

TABLE 1: Specimen design parameters.

Group	No.	Dimension (mm)	s (mm)	λ	Corrosion	η_1 (%)	η_w (%)
A	A1	125 × 200 × 1500	125	2.94	No corrosion	0	0
	A2	125 × 200 × 1500	125	2.94	Stirrup corrosion	0	25.2
	A3	125 × 200 × 1500	125	2.94	Stirrup corrosion	0	44.2
	A4	125 × 200 × 1500	125	2.94	Longitudinal bar corrosion	23.1	0
	A5	125 × 200 × 1500	125	2.94	Longitudinal bar corrosion	41.1	0
B	B1	150 × 235 × 2200	180	2.93	No corrosion	0	0
	B2	150 × 235 × 2200	180	2.93	Longitudinal bar corrosion	20.0	0
	B3	150 × 235 × 2200	180	2.93	Longitudinal bar corrosion	26.0	0
	B4	150 × 235 × 2200	180	2.93	Longitudinal bar corrosion	44.1	0
	B5	150 × 235 × 2200	180	2.93	Longitudinal bar corrosion	69.4	0

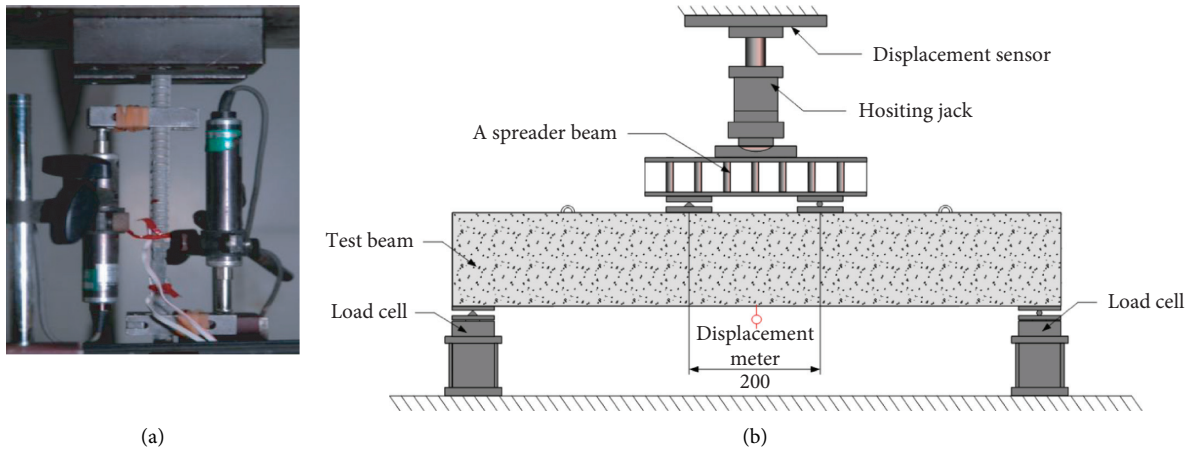


FIGURE 1: Material and structural tests. (a) Tensile tests of reinforcements. (b) Shear bearing capacity tests of beams.

TABLE 2: Mechanical properties of reinforcements.

Type	Grade	Effective yielding strength (MPa)	Effective ultimate strength (MPa)	Effective elastic modulus (GPa)
D6-0% mass loss rates	SD295	356	499	193
D6-20% mass loss rates	SD295	305	418	155
D6-40% mass loss rates	SD295	220	297	97
D10-0% mass loss rates	SD295	374	519	200
D13-0% mass loss rates	SD345	391	565	199
D22-0% mass loss rates	SD490	533	712	192

treatment for D6 steel bars. Table 2 shows the mechanical properties of the tested reinforcements. As it can be seen, the effective elastic modulus, the effective yielding strength, and ultimate strength decrease due to the cross section loss. Moreover, ordinary Portland cement was used to get a target compressive strength of 21 MPa for the concrete. Standard material tests were conducted using the cylinder blocks ($\phi 100 \text{ mm} \times 200 \text{ mm}$), and the measured compressive and tensile strengths are 24.1 MPa and 2.28 MPa, respectively. Figure 1(b) shows the shear strength test of the corroded RC beams, in which a 2 MN mechanical universal testing machine and a TDS-7130 (version 1.3) recorder were used. The midspan vertical displacement, the longitudinal strain at the midspan of the beam bottom, and the stirrup strain in the shear-compression zone were measured during the test.

2.2. Effect of Corrosion on Shear Bearing Capacity. A typical shear failure mode was observed from the tests. The shear bearing capacity declines due to the corrosion of the stirrup and the longitudinal reinforcements. Figure 2 shows the relationship between the shear bearing capacity V_u of each beam and the corrosion ratio of the steel bars, in which the effects of the corrosion ratios of the stirrup η_w and the longitudinal reinforcement η_1 were revealed. It can be seen from the tests of Group A that the shear bearing capacities of A2 and A3 beams with corroded stirrups decrease remarkably. At the early stage of the corrosion, the shear capacity decreases slightly. As the corrosion level becomes severe, the shear strength decreases significantly. The shear bearing capacity of A3 beam with a stirrup mass loss rate of 44.2% is 62.35 kN, which is 21.4% lower than that of the noncorroded beam. Likewise, the shear strength of A5 beam

with a longitudinal reinforcement corrosion rate of 41.1% is only 58.25 kN, which is 26.6% lower than its original strength. The tests of Group B show that except for beam B4, the shear bearing capacity decreases with the increase of the corrosion level.

3. Shear Bearing Capacity Evaluation of Corroded RC Beams

3.1. Models in the Codes. In the Chinese and American specifications, the shear resistances of the longitudinal reinforcements and the concrete are separately considered for the RC beams, indicating the classical truss model is adopted. The shear strength prediction formula of RC beams under a concentrated load stipulated by the Chinese specifications is [26]

$$V_{cs} = \frac{1.75}{\lambda + 1.0} f_t b_w h_0 + \frac{h_0}{s} A_{sw} f_{yw}, \quad (3)$$

where V_{cs} is the shear strength of the beam, f_t is the concrete tensile strength, b_w and h_0 are the width and effective height of the cross section, respectively, A_{sw} is the cross section area of the stirrup, and f_{yw} is the yield strength of the stirrup.

The shear strength prediction formula of an RC beam with stirrups in the American standard is [27]

$$V_{Rd} = V_{Rd,c} + V_{Rd,s} = \frac{1}{\beta} [C_{Rd,c} k (100\rho_l f_{ck})^{(1/3)} b_w h_0] + \frac{1}{\beta} \left[\frac{0.9h_0 f_{yw} A_{sw}}{s} (\cot \theta + \cot \alpha) \sin \alpha \right], \quad (5)$$

$$\beta = \begin{cases} 0.25, & a_v < 0.5h_0, \\ \frac{a_v}{2h_0}, & 0.5h_0 \leq a_v \leq 2h_0, \\ 1, & a_v > 2h_0, \end{cases}$$

where V_{Rd} is the shear strength of RC beams, $V_{Rd,c}$ and $V_{Rd,s}$ are shear strength provided by concrete and stirrups, respectively. $C_{Rd,c} = 0.18/\gamma_c$, in which γ_c ($=1.5$) is the material coefficient of concrete. $k = 1 + \sqrt{200}/h_0 \leq 2$, and ρ_l is the longitudinal reinforcement ratio. f_{ck} is the characteristic compressive strength of concrete, $f_{ck} = f_{cu,k}/1.226$ [29]. $f_{cu,k}$ is the standard value of the cubic concrete compressive strength. β is the coefficient of the shear span ratio, and a_v is the horizontal distance between the concentrated load point and the bearing support.

The partial factor of the shear resistance contributed by the stirrups is taken as 1.0 in the Chinese and American specifications, indicating the angle between the diagonal compressive bar and the longitudinal axis is a constant value of 45° . Table 3 shows the shear strength errors between the experimental results and the predictions by the formulae in the standards [29], where K_p is the ratio of the experimental strength to the prediction by the formulae and μ_{kp} and σ_{kp} are, respectively, the average value and discrete coefficient of

$$V_{cs} = \varphi (V_c + V_s) = \varphi \left(0.17\omega \sqrt{f'_c} b_w h_0 + \frac{A_{sw} f_{yw} h_0}{s} \right), \quad (4)$$

where φ is the strength reduction coefficient of 0.85, V_c and V_s are shear strength provided by concrete and stirrups, respectively, ω is the concrete correction coefficient of 1.0, and f'_c is the compressive strength of the standard concrete cylinder.

The variable angle truss model is adopted by the European standard, in which the concrete is treated as a diagonal compressive bar. The angle between the equivalent diagonal bar and the longitudinal axis of the beam is variable within a prescribed range [28]. Figure 3 shows the variable angle truss model, where θ is the inclination angle between the effective compressive rod of the concrete and the longitudinal axis and α is the angle between the effective tension rod caused by the stirrups and the longitudinal axis. F_{cs} is the compression force of the equivalent compression rod caused by concrete, and F_{sw} is the tensile force of the equivalent tension rod caused by the stirrup. z ($=0.9h_0$) is the inner lever arm corresponding to the maximum bending moment in the element under consideration.

According to the specifications, $\cot \theta$ ranges from 1.0 to 2.5, and the shear strength of the RC beam can be predicted by

K_p . It is found that the prediction of the European standard is more accurate due to the consideration of the angle θ , while the predictions based on the Chinese and American standards are very conservative.

4. Proposed Formula for Prediction of Shear Bearing Capacity

As the variable angle truss theory is more effective, the contributions of the concrete and stirrups to the shear resistance are discussed in this section. In the theory, the concrete between the diagonal cracks is treated as a pressure rod to resist the compressive force, while the stirrups are equivalent to an upper chord, and the bottom longitudinal bars are considered as a lower chord to resist the tensile force. In order to ensure that the stirrups can reach their yield strength before the concrete crushing, the EC2 stipulates that $21.8^\circ < \theta < 45^\circ$ ($1.0 \leq \cot \theta \leq 2.5$) [28]. Supposing that $\alpha = 90^\circ$, then

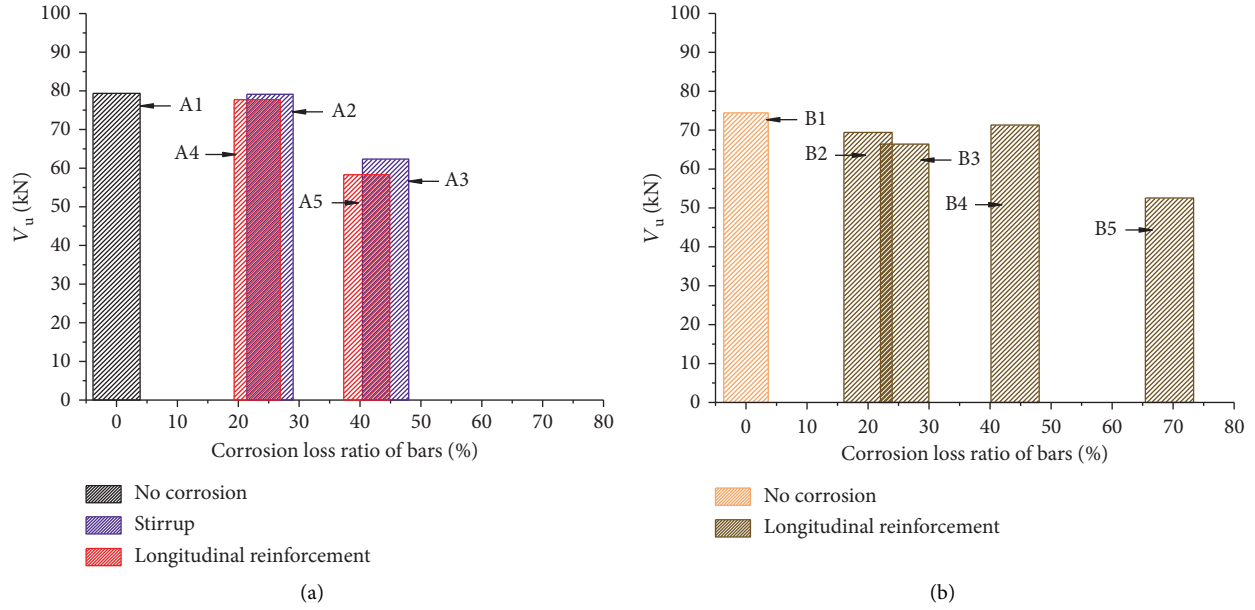


FIGURE 2: Shear strength versus the corrosion ratio. Test results of (a) Group A and (b) Group B.

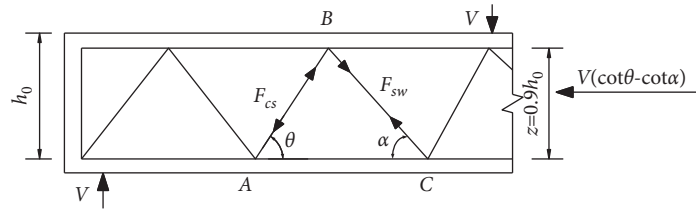


FIGURE 3: Variable angle truss model in Eurocode 2.

TABLE 3: Statistical parameters of K_p .

Parameters	Chinese standard	American standard	European standard
μ_{kp}	1.4403	1.8403	0.9697
σ_{kp}	0.2319	0.3008	0.2297

$$\cot \theta = \sqrt{\frac{\alpha_{cv} v_1 f_{cd}}{\rho_w f_{yw}}} - 1, \quad (6)$$

$$v_1 = \begin{cases} 0.6, & f_{ck} \leq 60 \text{MPa}, \\ 0.9 - \frac{f_{ck}}{200} > 0.5, & f_{ck} > 60 \text{MPa}, \end{cases}$$

where α_{cv} is a coefficient considering the stress state of the compression rod, and $\alpha_{cv} = 1$ for nonprestressed structures. ρ_w is the stirrup ratio, v_1 is the reduction factor with consideration of the concrete cracking strength, and f_{cd} ($=\alpha_{cc} f_{ck} / \gamma_c$) is the design value of the concrete compression force in the direction of the longitudinal member axis. α_{cc} is

the influencing factor of the long-term action effect of concrete, which can be taken as 0.85 [28].

As surface spalling of the concrete may occur due to severe corrosion of the reinforcements, the width of the beam should be reduced. According to the suggestions of Higgins et al. [10], the effective width b_{wc} can be calculated by

$$b_{wc} = \begin{cases} b_w, & \eta_w \leq 30\%, \\ b_w - 2(c + d_{sw}) + \frac{s}{5.5}, & \eta_w > 30\%, s \leq 5.5c, \\ b_w - \frac{5.5}{s}(c + d_{sw})^2, & \eta_w > 30\%, s > 5.5c, \end{cases} \quad (7)$$

where c is the thickness of the concrete cover and d_{sw} is the diameter of the stirrups. The relationship between the mass loss rate η_m and the area loss rate η_s is

$$\eta_s = \begin{cases} 0.015 + 0.97\eta_m, & \eta_m \leq 10\%, \\ 0.062 + 0.95\eta_m, & \eta_m > 10\%. \end{cases} \quad (8)$$

A theoretical prediction formula for shear strength evaluation of the corroded RC beams is proposed, in which the factors of ϕ and γ to, respectively, consider the corrosion impacts of the longitudinal reinforcements and the stirrups are involved:

$$V_{Rc} = \phi V_{Rd,c} + \gamma V_{Rd,s} \\ = \frac{1}{\beta} \left[\phi C_{Rd,c} k (100\rho_l f_{ck})^{(1/3)} b_{wc} h_0 + \gamma \frac{0.9h_0 f_{ywc} A_{sw}}{s} \cot \theta \right], \quad (9)$$

where V_{Rc} is the shear strength of corroded RC beams, b_{wc} and f_{ywc} ($=f_{yw}(1 - 1.077\eta_s)/(1 - \eta_s)$) are, respectively, the effective width of the section and the nominal yield strength of the steel bars after corrosion. $\cot \theta$ can be calculated using equation (6), in which ρ_w and f_{yw} can be replaced by ρ_{wc} and f_{ywc} in consideration of corrosion. The corrosion factors of ϕ can be obtained by [11]

$$\phi = \begin{cases} 1.0, & \eta_l \leq 5\%, \\ 1.098 - 1.96\eta_l, & \eta_l > 5\%. \end{cases} \quad (10)$$

As the conditions of the stirrups have a significant effect on the shear performance of the corroded RC beams, the correlation between parameters γ and η_w is discussed. Thus, 10 tests in this study and 118 tests in the literature are selected for further analysis [9–12, 30–34]. Table 4 lists the summary of the experimental results on shear strength of the RC beams with corroded stirrups, in which f_c is the design value of the concrete axial compressive strength and N is the number of tests in each literature.

Figure 4 shows the collection of the experimental data and the fitting relation between the parameters γ and η_w . The experimental results show that the shear strength is almost unaffected when the corrosion rate is relatively small. Therefore, γ is taken as 1.0 in this study when η_w is less than 10%, indicating the shear strength of the corroded RC beam can retain the original strength as the noncorroded one. When the corrosion rate becomes larger, the shear strength decreases gradually, and a linear fitting relation between parameters γ and η_w is adopted:

$$\gamma = \begin{cases} 1.0, & \eta_w \leq 10\%, \\ 1.076 - 0.76\eta_w, & \eta_w > 10\%. \end{cases} \quad (11)$$

4.1. Verification of Prediction Formula. The ratio K_p ($=V_{u,exp}/V_u$) between the experimental strength $V_{u,exp}$ and the predicted value V_u is obtained. Meanwhile, the mean value and the dispersion coefficient of the ratio are calculated. Figure 5 shows the comparison between the experimental and the predicted shear strengths using different

theoretical models, where μ_{kp} is the mean value of the ratio K_p and σ_{kp} is the corresponding coefficient of variation. The predicted strengths obtained from the theoretical models are different from each other. The formula proposed by Yu is based on the modified pressure field theory, in which the influence of corrosion on the angle of critical inclined crack, geometric reduction, and the stirrup ratio is considered. Therefore, the predictions are in a good agreement with the test values. The mean value of K_p is 1.0785 with a dispersion coefficient of 0.2834. However, complicated iterative computation is required in Yu's model, making it very difficult for engineering practice. Huo's model is based on the truss arch theory, and the accuracy of the prediction is lower than Yu's model. The model proposed by El-Sayed is based on the American standard, which considers the reduction of the cross section and the effective shear section caused by corrosion. Nevertheless, the inclination of the crack in this model is assumed as a fixed value of 45° , so the predictions are rather conservative. The strength is a sum of the shear resistances of the stirrup and the concrete in the Xu and Li's models. The angle between the bar and the longitudinal axis is also a constant value, and the corrosion of the longitudinal reinforcement is not considered. Thus, conservative predictions are obtained. Noticeably, the average value of K_p is 1.0027 with a dispersion coefficient of 0.172 in the proposed model, indicating the highest precision with a relatively small dispersion can be achieved by the proposed formula in this study.

4.2. Numerical Simulation of Shear Capacity of Corroded Beams. Finite element analysis is carried out to study the shear failure of the corroded RC beam in this section. Figure 6 shows the three-dimensional FE model of the RC beam. Commercial software ABAQUS was adopted for the numerical analysis. The concrete beam was modeled by 3D solid element (C3D8). The longitudinal reinforcements and stirrups were modeled by truss elements (T3D2). The plastic-damage constitutive model was adopted for the simulation of the concrete material, and the bilinear plastic constitutive model was used for the mechanical behavior of the reinforcements [35–37]. The cross section reduction method was adopted for the simulation of the reinforcement corrosion [38–41]. The coupling interaction between the longitudinal reinforcement and the concrete was utilized to control they were fully bonded or disconnected [42]. The meshing of the structure was carried out using the structured meshing method during the FE modelling.

Figure 7 shows the comparison of the load-deflection curves obtained from the numerical and the test results. It can be seen that the numerical results of both the test beams in Group A and Group B (FEM) are in good agreement with the experimental results (EXP). The effect of the corrosion can be well simulated by the section reduction of the rebar and the coupling interaction between the reinforcement and concrete beam.

128 models of the corroded RC beams in the literature with stirrups were created, and the shear bearing capacity was computed. Figure 8 shows the comparison between the

TABLE 4: Summary of experimental data on shear capacity of corroded beams with stirrups.

Data source	N	Beam no.	f_c (MPa)	b_w (mm)	h_0 (mm)	ρ_l (%)	ρ_w (%)	f_{yw} (MPa)	A_{sw} (mm ²)	s (mm)	λ
This study	10	A1~A5	14.3	125	170	3.6	0.41	360	63.4	125	2.94
		B1~B5	14.3	150	205	2.5	0.23	360	63.4	180	2.93
Xu et al. [9]	21	A/B/A2~C2	15.06~16.25	120	200	1.92	0.32	275	57	150	2.00
		A3~C3/A5~C5	15.06~16.25	120	200	1.92	0.32	275	57	150	2.00
		C/A1~A3	15.06~16.25	120	200	1.92	0.32	275	57	150	1.00
		A4~C4/A6~C6	15.06~16.25	120	200	1.92	0.32	275	57	150	1.00
		8RA/8RD	17.58	254	521	1.9	0.196	585	101	203	2.04
Higgins et al. [10]	8	10RA~10RD	20.04	254	521	1.9	0.157	585	101	254	2.04
		12RA/12RD	17.76	254	521	1.9	0.13	585	101	305	2.04
Huo [11]	14	L1~L14	9.6	100	170	1.94	0.44	324	66	150	1.50
Wang et al. [12]	10	BC2.0-1~5	18.29~26.74	150	150	1.29	0.31	441.5	57	150	2.00
		BC3.0-1~5	18.29~26.74	150	150	1.29	0.31	441.5	57	200	3.00
Xia et al. [30]	18	A-0~A-5	12.97	120	200	2.68	0.253	321.8	67.2	100	1.50
		B-0~B-5	12.97	120	200	2.68	0.19	321.8	67.2	100	1.50
		C-0~C-5	12.97	120	200	2.62	0.475	463.9	92	150	1.50
Yang et al. [31]	8	1.5-1~1.5-4	21.27	150	260	2.62	0.475	482	101	150	1.50
		L1-1~L1-4	21.27	150	260	2.62	0.561	482	101	150	1.00
Wang et al. [32]	7	0#~6#	16.91~18.32	250	455	2.34	0.447	337.9	66	200	1.74
Yu [33]	8	JL-L0~JL-L5	11.02~12.83	180	260	2.34	0.447	280	57	120	2.22
		HJL-L1/L3/L5	11.02~12.83	180	260	1.63	0.12	280	57	120	2.22
Lu et al. [34]	24	X1/X2	19.49	200	275	2.15	0.19/0.14	339	57	150/200	2/2.5
		X3/X4	19.49	200	275	2.15	0.2/0.25	373	101	250/200	3/3.5
		X5/X6	19.49	200	275	2.15	0.19/0.14	458	57	150/200	2/2.5
		X7/X8	19.49	200	275	2.15	0.2/0.25	433	101	250/200	3/3.5
		X9/X10	19.49	200	275	2.15	0.19/0.14	476	57	150/200	2/2.5
		X11/X12	19.49	200	275	2.15	0.2/0.25	524	101	250/200	3/3.5
		Y1/Y2	23.86	200	275	2.15	0.19/0.14	339	57	150/200	2/2.5
		Y3/Y4	23.86	200	275	2.15	0.2/0.25	373	101	250/200	3/3.5
		Y5/Y6	23.86	200	275	2.15	0.19/0.14	458	57	150/200	2/2.5
		Y7/Y8	23.86	200	275	2.15	0.2/0.25	433	101	250/200	3/3.5
		Y9/Y10	23.86	200	275	2.15	0.19/0.14	476	57	150/200	2/2.5
		Y11/Y12	23.86	200	275	2.15	0.2/0.25	524	101	250/200	3/3.5

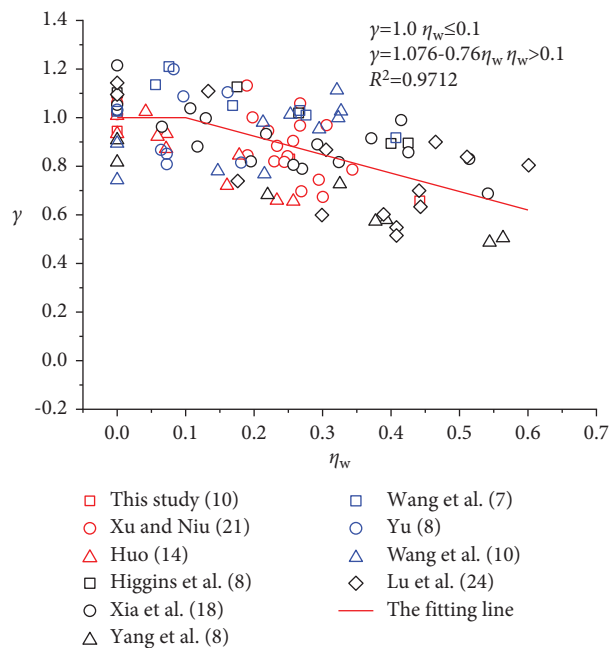


FIGURE 4: Correlation between γ and η_w .

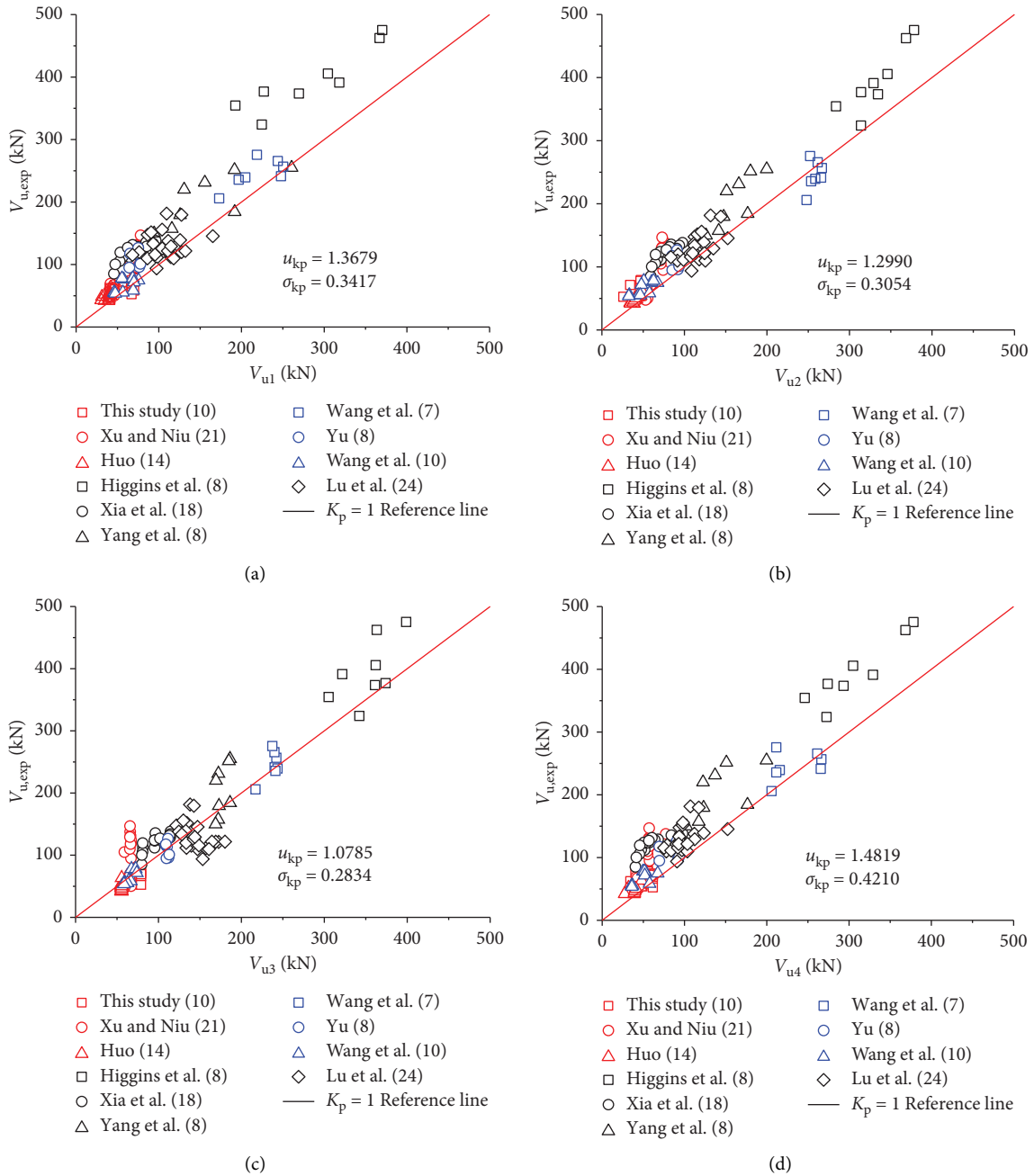


FIGURE 5: Continued.

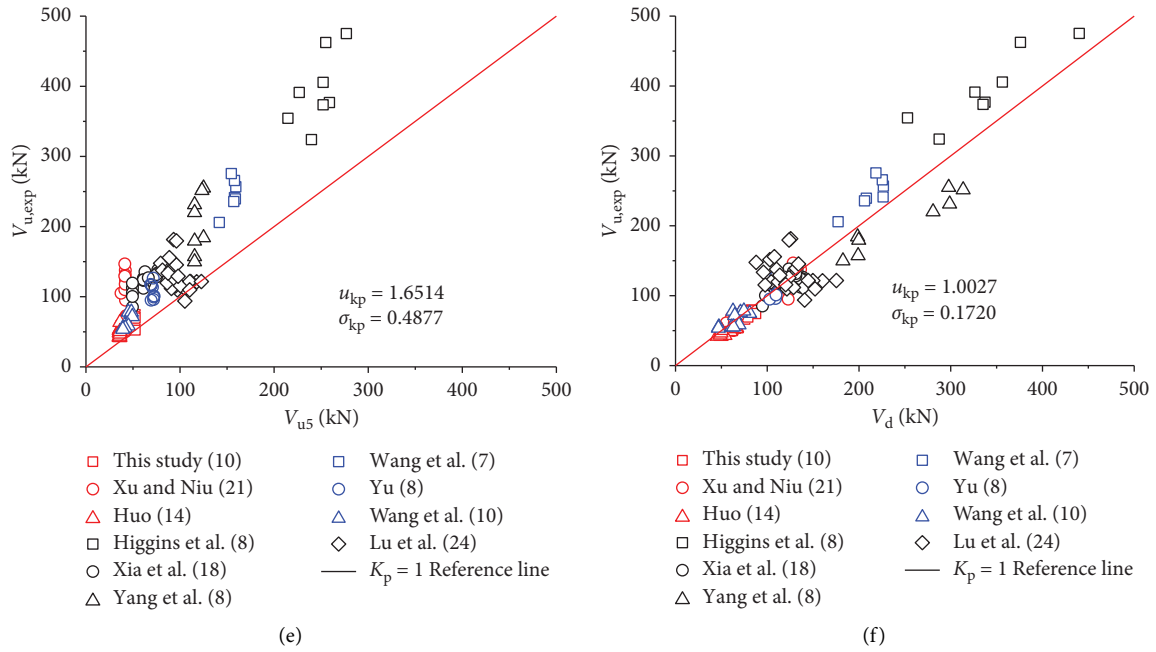


FIGURE 5: Comparison between the experimental and theoretical shear strength of the corroded RC beams. (a) V_{u1} predicted by Xu’s model. (b) V_{u2} predicted by Huo’s model. (c) V_{u3} predicted by Yu’s model. (d) V_{u4} predicted by Li’s model. (e) V_{u5} predicted by El-Sayed’s model. (f) V_d predicted by the proposed model in this study.

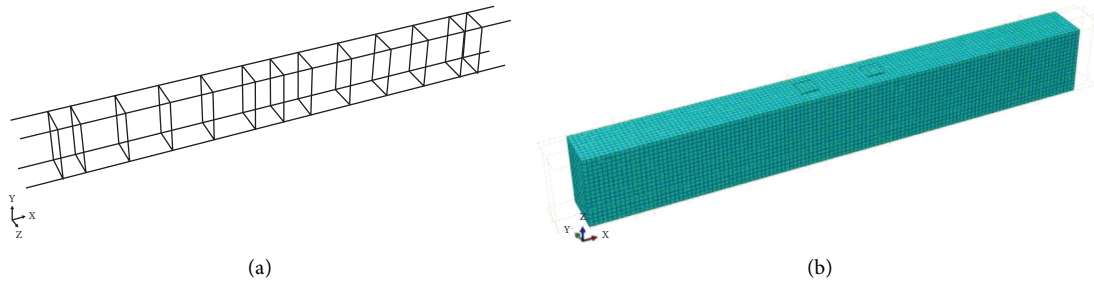


FIGURE 6: FE model of the corroded RC beam. (a) Framework of the reinforcement. (b) Mesh of the model.

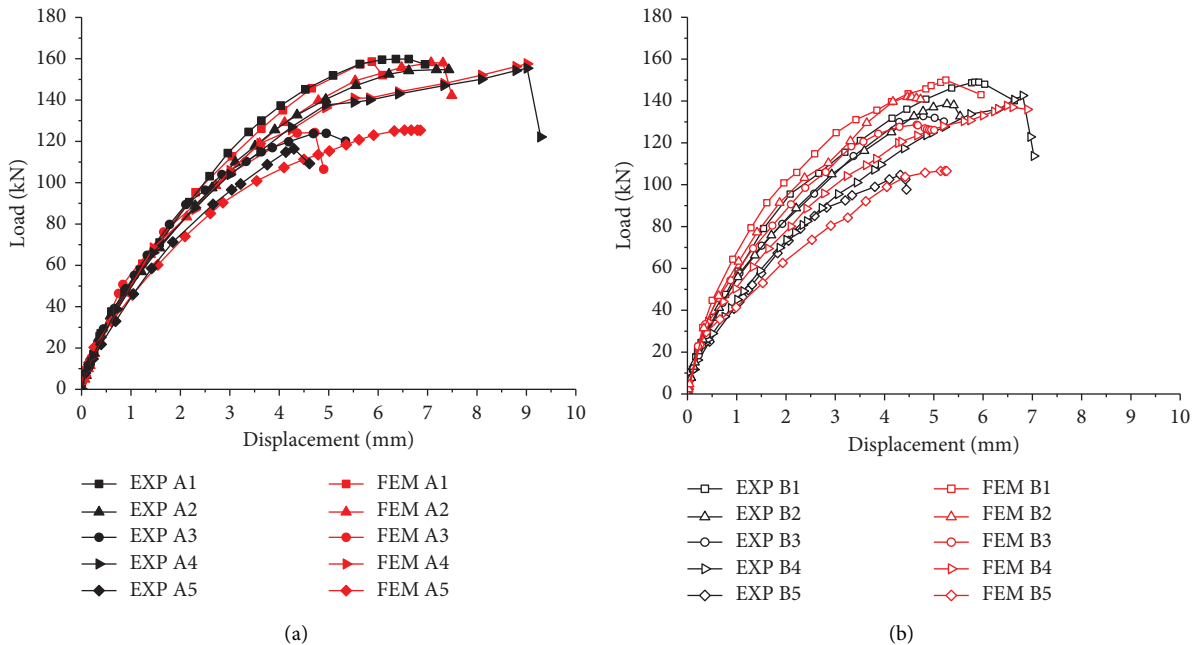


FIGURE 7: Comparison between the numerical and experimental results. Load-deflection curves of beams in (a) Group A and (b) Group B.

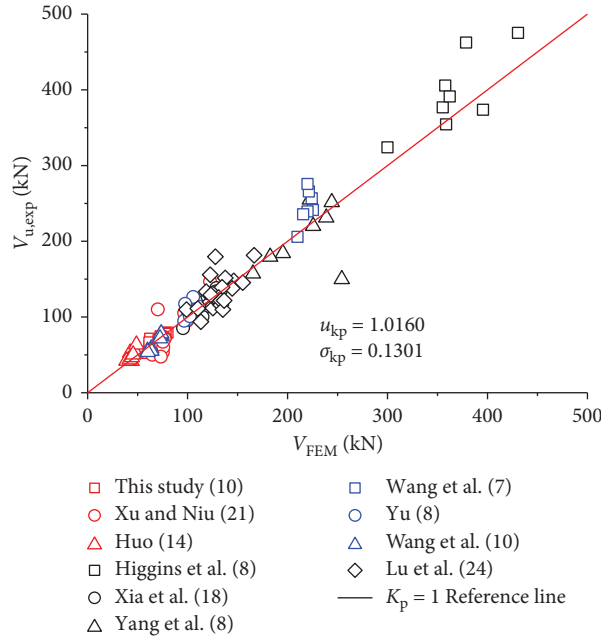


FIGURE 8: Comparison between numerical and experimental results for 128 specimens.

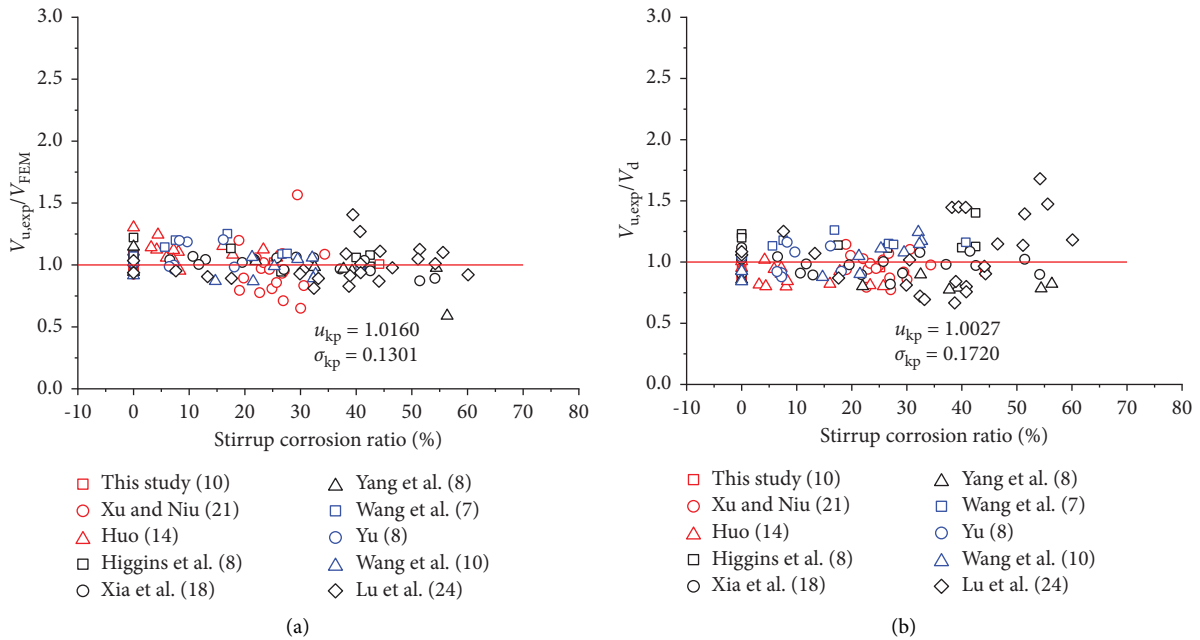


FIGURE 9: Comparison of the numerical results and the experimental or theoretical results. Ratios of (a) $V_{u,exp}/V_{FEM}$ and (b) $V_{u,exp}/V_d$.

numerical and the experiment results of the shear strength. Electrochemical corrosion or other fast corrosion methods were adopted by most of tests in the literature. Therefore, the corroded reinforcement was computed using the cross section reduction technique during the numerical analysis. As it can be seen, the mean value of the ratio $K_p (= V_{FEM}/V_{u,exp})$ is 1.0160 and the corresponding dispersion coefficient is 0.1301.

K_p is higher than the mean value predicted by the proposed formula, but the dispersion coefficient is lower, indicating that the numerical results using the FE method are more accurate than the proposed theoretical method.

Figure 9 shows the comparison of the numerical results and the experimental or theoretical results. It can be found that it is feasible to evaluate the shear strength of the

corroded beam by the cross section reduction method and the interaction technique. Moreover, the effectiveness of the proposed formula is verified by the numerical analysis.

5. Conclusions

The shear bearing capacity of the corroded RC beams was experimentally and numerically studied. A short-time test was adopted to facilitate the experimental study, and a more practical formula for the shear strength evaluation was proposed and validated by the experimental data. Moreover, numerical analysis based on the FE method was carried out and compared with the test results. The following conclusions can be drawn:

- (1) Stirrup corrosion has a significant effect on the shear strength of the RC beams, and the shear strength decreases gradually along with the increase of the corrosion rate. The axial rust swelling crack and the degradation of the bond strength due to longitudinal reinforcement corrosion can also decrease the shear strength. Moreover, the wrapping of the thin Teflon insulated film on the longitudinal reinforcements is an effective way to simulate the nonbonding effect, and the filling of an acrylic plate is feasible for the simulation of rust swelling crack in the short-time test.
- (2) Most of the existing theoretical models for the shear strength estimation of the corroded RC beams are conservative and the predicted results are very dispersed, while the models with relatively higher accuracy are complicated in application. As the corrosion effects of the longitudinal reinforcement and the stirrup are both considered, the predictions by the proposed formula in this study are in good agreement with the experimental results, and the formula is very simple and easy for engineering application.
- (3) The numerical results based on the FE technique agree very well with the experimental results, which indicates that the corrosion effect can be well simulated by the cross section reduction of the reinforcements and the coupling interaction between the reinforcement and the concrete beam. Moreover, the proposed prediction formula is validated by the numerical simulations.

Data Availability

The data are included within the article.

Conflicts of Interest

The authors declare that there are no conflicts of interest regarding the publication of this paper.

Acknowledgments

This research was funded by the National Natural Science Foundation of China (51708485) and the China Postdoctoral Science Foundation (2017M611925).

References

- [1] T. Vidal, A. Castel, and R. François, "Analyzing crack width to predict corrosion in reinforced concrete," *Cement and Concrete Research*, vol. 34, no. 1, pp. 165–174, 2004.
- [2] Y. X. Zhao, J. Chen, and W. L. Jin, "Design of shear strengths of corroded reinforced concrete beams," *International Journal of Modelling, Identification and Control*, vol. 7, no. 2, pp. 190–198, 2009.
- [3] E. Sola, J. Ožbolt, G. Balabanić, and Z. M. Mir, "Experimental and numerical study of accelerated corrosion of steel reinforcement in concrete: transport of corrosion products," *Cement and Concrete Research*, vol. 120, pp. 119–131, 2019.
- [4] L. Huang, H. Ye, X. Jin, N. Jin, and Z. Xu, "Corrosion-induced shear performance degradation of reinforced concrete beams," *Construction and Building Materials*, vol. 248, Article ID 118668, 2020.
- [5] Y. Moodi, M. R. Sohrabi, and S. R. Mousavi, "Corrosion effect of the main rebar and stirrups on the bond strength of RC beams," *Structure*, vol. 32, pp. 1444–1454, 2021.
- [6] I. Khan, R. François, and A. Castel, "Experimental and analytical study of corroded shear-critical reinforced concrete beams," *Materials and Structures*, vol. 47, no. 9, pp. 1467–1481, 2014.
- [7] Z. Ye, W. Zhang, and X. Gu, "Deterioration of shear behavior of corroded reinforced concrete beams," *Engineering Structures*, vol. 168, pp. 708–720, 2018.
- [8] Y. X. Zhao and W. L. Jin, "Analysis of the shear capacity of corroded stirrup concrete beams," *Journal of Zhejiang University*, vol. 42, no. 1, pp. 19–24, 2008, in Chinese.
- [9] S. H. Xu and D. T. Liu, "The shear behavior of corroded simply supported reinforced concrete beam," *Journal of Building Structures*, vol. 25, pp. 98–104, 2004.
- [10] C. Higgins and W. C. Farrow, "Tests of reinforced concrete beams with corrosion-damaged stirrups," *ACI Structural Journal*, vol. 103, pp. 133–141, 2006.
- [11] Y. H. Huo, "Study on shear capacity of corroded reinforced concrete beam," *Industrial Building*, vol. 36, no. S1, pp. 910–912, 2006, in Chinese.
- [12] X. H. Wang, X. H. Gao, B. Li, and B. R. Deng, "Effect of bond and corrosion within partial length on shear behaviour and load capacity of RC beam," *Construction and Building Materials*, vol. 25, no. 4, pp. 1812–1823, 2011.
- [13] M. Dai, O. Yang, Y. Xiao, and F. Li, "Influence of longitudinal bar corrosion on impact behavior of RC beams," *Materials and Structures*, vol. 49, no. 9, pp. 3579–3589, 2016.
- [14] X. Xue and H. Seki, "Influence of longitudinal bar corrosion on shear behavior of RC beams," *Journal of Advanced Concrete Technology*, vol. 8, no. 2, pp. 145–156, 2010.
- [15] A. K. El-Sayed, "Shear capacity assessment of reinforced concrete beams with corroded stirrups," *Construction and Building Materials*, vol. 134, pp. 176–184, 2017.
- [16] A. Alaskar, A. S. Alqarni, G. Alfalah, A. K. E. Sayed, H. Mohammadhosseini, and R. Alyousef, "Performance evaluation of reinforced concrete beams with corroded web reinforcement: experimental and theoretical study," *Journal of Building Engineering*, vol. 35, Article ID 102038, 2021.
- [17] S. B. Li, X. Zhang, and L. D. Jia, "Analysis of the shear capacity of reinforced concrete beams with stirrup corrosion," *Journal of Engineering Mechanics*, vol. 28, no. S1, pp. 60–63, 2011, in Chinese.
- [18] B. Yu and B. Chen, "A probabilistic model for calculating shear capacity of corroded reinforced concrete beams,"

- Journal of Engineering Mechanics*, vol. 35, no. 11, pp. 115–124, 2012, in Chinese.
- [19] R. A. Hawileh, H. A. Musto, J. A. Abdalla, and M. Z. Naser, “Finite element modeling of reinforced concrete beams externally strengthened in flexure with side-bonded FRP laminates,” *Composites Part B: Engineering*, vol. 173, Article ID 106952, 2019.
- [20] M. Z. Naser, R. A. Hawileh, and J. Abdalla, “Modeling strategies of finite element simulation of reinforced concrete beams strengthened with frp: a review,” *Journal of Composites Science*, vol. 5, no. 1, 2021.
- [21] JIS-G-3112, *Japanese Industrial Standard: Steel Bars for Concrete Reinforcement*, Japanese Standard Association, Tokyo, Japan, 2004.
- [22] JASS5, *Japanese Architectural Standard Specification for Reinforced Concrete Work JASS5*, Architectural Society of Japan, Tokyo, Japan, 2009.
- [23] W. Zhu, R. François, D. Coronelli, and D. Cleland, “Effect of corrosion of reinforcement on the mechanical behaviour of highly corroded RC beams,” *Engineering Structures*, vol. 56, pp. 544–554, 2013.
- [24] B. Zhang, H. Zhu, J. Chen, and O. Yang, “Evaluation of bond performance of corroded steel bars in concrete after high temperature exposure,” *Engineering Structures*, vol. 198, Article ID 109479, 2019.
- [25] R. J. Zhang, A. Castel, and R. François, “Concrete cover cracking with reinforcement corrosion of RC beam during chloride-induced corrosion process,” *Cement and Concrete Research*, vol. 40, no. 3, pp. 415–425, 2009.
- [26] GB 50010-2010, *Code for Design of Concrete Structures*, China Building Industry Press, Beijing, China, 2010.
- [27] ACI 318-08, “Building code requirements for structural concrete and commentary,” *Farmington Hills: ACI Committee*, vol. 318, 2008.
- [28] EN 1992-1-1, “Eurocode2: Design of Concrete Structures,” *Part 1-1: General Rules and Rules for Buildings*, British Standards, Brussels, Belgium, 2004.
- [29] W. W. Wei, J. X. Gong, and L. Tian, “Comparative analysis of shear bearing capacity of reinforced concrete members,” *Journal of Building Science and Engineering*, vol. 27, no. 2, pp. 25–37, 2010, in Chinese.
- [30] J. Xia, W. L. Jin, and L. Y. Li, “Shear performance of reinforced concrete beams with corroded stirrups in chloride environment,” *Corrosion Science*, vol. 53, no. 5, pp. 1794–1805, 2011.
- [31] X. M. Yang, T. Wu, and Y. Y. Wang, “Experimental study on shear behavior of reinforced concrete beams with small shear span ratio corroded,” *Journal of Building Structures*, vol. 40, no. 12, pp. 147–154, 2019, in Chinese.
- [32] L. Wang, X. Zhang, J. Zhang, Y. Ma, and Y. Liu, “Effects of stirrup and inclined bar corrosion on shear behavior of RC beams,” *Construction and Building Materials*, vol. 98, pp. 537–546, 2015.
- [33] F. J. Yu, *Experimental Study and Analysis on Performance of the Inclined Section of Corroded Reinforced concrete Beams*, Hohai University, Nanjing, China, 2005, in Chinese.
- [34] Z. H. Lu, Y. B. Ou, Y. G. Zhao, and C. Q. Li, “Investigation of corrosion of steel stirrups in reinforced concrete structures,” *Construction and Building Materials*, vol. 127, pp. 293–305, 2016.
- [35] J. Lubliner, J. Oliver, S. Oller, and E. Oñate, “A plastic-damage model for concrete,” *International Journal of Solids and Structures*, vol. 25, no. 3, pp. 299–326, 1989.
- [36] B. Alfarah, F. A. López, and S. Oller, “New methodology for calculating damage variables evolution in plastic damage model for RC structures,” *Engineering Structures*, vol. 132, pp. 70–86, 2017.
- [37] J. Yu, W. Zhang, Z. Tang, X. Guo, and S. Pospíšil, “Seismic behavior of precast concrete beam-column joints with steel strand inserts under cyclic loading,” *Engineering Structures*, vol. 216, Article ID 110766, 2020.
- [38] D. Li, C. Xiong, T. Huang, R. Wei, N. Han, and F. Xing, “A simplified constitutive model for corroded steel bars,” *Construction and Building Materials*, vol. 186, pp. 11–19, 2018.
- [39] C. Zeng, J. H. Zhu, C. Xiong, Y. Li, D. Li, and J. Walraven, “Analytical model for the prediction of the tensile behaviour of corroded steel bars,” *Construction and Building Materials*, vol. 258, Article ID 120290, 2020.
- [40] L. Berto, S. Paola, and A. Saetta, “Numerical modelling of bond behavior in RC structures affected by reinforcement corrosion,” *Engineering Structures*, vol. 30, no. 5, pp. 1375–1385, 2007.
- [41] T. Potisuk, C. C. Higgins, T. H. Miller, and S. C. Yim, “Finite element analysis of reinforced concrete beams with corrosion subjected to shear,” *Advances in Civil Engineering*, vol. 2011, Article ID 706803, 14 pages, 2011.
- [42] Dassault Systèmes Simulia Corporation, *ABAQUS/Analysis User’s manual*, Dassault Systèmes Simulia Corporation, Johnston, RI, USA, 2014.

Research Article

Analysis on the Influence of Increasing Seismic Fortification Intensity on Seismic Performance of Underground Station

Ying Zeng ¹, Shiguang Xu ^{1,2} and Shiqian Yin¹

¹School of Land and Resources Engineering, Kunming University of Science and Technology, Kunming 650093, China

²Yunnan Geological and Mineral Bureau of Exploration & Exploitation, Kunming 650041, China

Correspondence should be addressed to Shiguang Xu; xushiguang828@qq.com

Received 27 July 2021; Accepted 26 August 2021; Published 13 September 2021

Academic Editor: Lingkun Chen

Copyright © 2021 Ying Zeng et al. This is an open access article distributed under the Creative Commons Attribution License, which permits unrestricted use, distribution, and reproduction in any medium, provided the original work is properly cited.

China Earthquake Parameter Zoning (2016) has increased the seismic fortification intensity in Chengdu from VII to VIII. It is necessary to conduct in-depth discussion on the impact of the seismic performance of the built underground station structure. In this paper, a stratum-structure finite element model is established with a Chengdu subway station as an example. The model boundary adopts viscoelastic boundary, and the ground motion is input in the form of equivalent nodal force. The equivalent linearization method is used to consider the nonlinearity of soil materials. The time-history analysis of seismic fortification intensity of VII and VIII degrees is carried out, respectively. By comparing the calculation results of the two seismic fortification intensity ground motion conditions, it is concluded that the connection between the side wall and the floor is the weakest position of the station structure under the action of the earthquake; the seismic fortification intensity is increased from VII to VIII to the internal force of the structure. It has a relatively large impact, especially the most obvious impact on the bending moment. The results of the verification of the seismic time-history analysis show that the increase of fortification intensity will have a more obvious impact on the structural deformation, and the structural design of the station can meet the safety performance requirements of VII and VIII degrees of seismic fortification. The research has certain reference significance for the seismic safety evaluation of the built underground station structure in Chengdu area.

1. Introduction

With the development of science and technology and productivity in China, more and more underground structure projects are emerging and the research on their seismic performance is paid more and more attention [1]. Hashash et al. [2, 3], respectively, summarized the earthquake disaster phenomena, model test, and theoretical research results, as well as the present situation of earthquake-resistant analysis and design of underground structures at home and abroad; the results can be used to guide the seismic design of underground structures.

Wang et al. [4, 5] adopted the finite element numerical simulation method, respectively, to establish an analysis model and discuss the influence law of seismic response of underground structures. Zou et al. [6] proposed an improved finite element method, NewPSA, to predict the

nonlinear behavior of underground frame structures under horizontal seismic action and a new one-dimensional seismic analysis method to calculate the distribution of displacement and shear stress along the depth in the free field with the increase of the movement of bedrock. Jiang et al. [7] proposed an improved pushover analysis method (I-PAM) and proved that I-PAM could accurately predict the maximum axial force, bending moment, and displacement of the structure. Shi et al. [8] and Yu and Yuan [9], respectively, adopted the response displacement method to discuss the applicability of the seismic analysis of underground integrated pipe corridor and complex underground large space structure, as well as the selection of foundation spring stiffness and the simulation method. Al Agha et al. [10] used ABAQUS to create soil media and used the El Centro acceleration time-history record input by seismic load to analyze the difference of the influence of buildings on

soft soil and hard soil in strong earthquakes, and the research results have good engineering guiding significance.

Zhou et al. [11, 12] combined engineering examples, compared the differences of inertial force method, time-history analysis method, and response displacement method in seismic analysis of underground structures, and put forward the applicability and suggestions of different calculation formulas. Deng and Liang [13] selected five calculation methods including the inertia force method, reaction displacement method, and dynamic time-history method and evaluated the adaptability of the five calculation methods. Xu et al. [14] discussed the forced reaction displacement method and the reaction acceleration method on the basis of the reaction displacement method. When the forced reaction displacement method was used, it was suggested that the side distance should be twice the width of the structure, while when the reaction acceleration method was used, the side distance should be more than three times the width of the structure. Li et al. [15] and Liu et al. [16], respectively, improved the seismic pushover analysis method of underground structures, and the two improved methods can better evaluate the seismic performance of underground structures after being verified by examples. The pushover analysis [17] was proposed for the large difference in seismic response characteristics of surface structures. It has been proved that the pushover analysis can be effectively applied to seismic design and damage assessment of underground structures.

Belostotsky et al. [18] introduced the classification and brief overview of force-based methods, displacement-based methods, and numerical methods for seismic analysis of the coupling system of soil-underground structures, providing methods and means for seismic design of underground structures. Yu et al. [19] proposed a VHS method for seismic analysis of soil-structure system using a multiaxis test device and applied it to practical projects, verifying its rationality and accuracy. Li et al. [20] set up a 3D simulation analysis model to study the seismic characteristics of cross-transfer subway station under the action of horizontal seismic waves in soft soil layer. Qiu et al. [21], based on the dynamic equilibrium characteristics of the aboveground building-soil-subway station integral model, proposed a simplified calculation method for the structural internal forces of subway stations.

The aseismic design of underground structure always lags behind that of aboveground structure, but underground structure is often very important; once destroyed, it is difficult to repair. Especially for underground stations, failure to do a good seismic design will cause serious danger to people's lives and property safety. Also, the cost of the underground station is high; once destroyed, the loss is very huge. Starting from June 1, 2016, new buildings in Chengdu located in the seismic fortification intensity zone of VII will be upgraded to VIII. The higher the seismic fortification intensity in an area, the stronger the overall seismic resistance of the building, which represents the requirement of an area. Therefore, it is necessary to analyze and study the impact of the increase in seismic fortification intensity on the seismic safety performance of the built subway.

This paper takes an underground station of the Chengdu Metro as an example, adopts the viscoelastic boundary and equivalent nodal force input method of ground motion, uses the equivalent linearization method to simulate its non-linearity in the soil material, and, respectively, calculates the VII and VIII earthquake response under the conditions of high seismic fortification intensity, combined with national standards to check the seismic performance of the station structure, discuss the impact of the increase in seismic fortification intensity on the seismic performance of the built subway, and evaluate the seismic safety of the built subway project.

2. Engineering Background

A certain line of the Chengdu Metro was built in 2013, with a total length of 41 km, of which the underground line is 36 km. This study selects a typical two-storey three-span structure of the station.

The main structure of the station is 17.41 m high, the left and right track areas are overlapping stations, and the standard section structure has a net width of 25.50 m. The main enclosure structure of the station adopts a 1.2 m thick underground continuous wall. The bottom of the station structure floor is about 21 m below the ground. According to the structural design, the components of the station structure that are in contact with the soil, such as the top slab (including beams), bottom plates, and side walls (including the inner columns of the wall), use C35 concrete and the components that do not contact the soil, such as the partition wall and the middle slab, use C35 concrete for the center beam and C45 concrete for the center column.

According to the geological survey report, the soil layer where the station is located is mainly silty clay and silt soil. The physical properties of the materials on the station site are sorted out as shown in Table 1. According to the "Code for Seismic Design of Buildings (GB50011-2010)" [22], the soil type of the site is comprehensively determined to be medium soft soil and the site category is Class III. The specific soil layer is shown in Table 1.

3. Calculation Model

The paper uses the finite element software ABAQUS to establish a two-dimensional stratum-structure model. ABAQUS is a piece of powerful universal finite element software, which includes a very rich material model, element model, load, and boundary conditions, and can solve static, dynamic, and other issues, in particular, the ability to solve nonlinear problems is very excellent for seismic dynamic analysis. The model is shown in Figure 1. The model is 100 m high and 200 m long (the distance from the structure boundary to the model boundary is more than three times the width of the structure). The grid is divided into plane strain units, in which the soil is divided into 37621 units, and the station structure is divided into 3236 units.

The calculation model in this paper adopts the viscoelastic boundary, and the ground motion input adopts the equivalent nodal force, that is, the spring-damping system

TABLE 1: Soil material parameters.

Soil layer number	Soil	Layer thickness (m)	Density (kg·m ³)	Wave speed (m·s ⁻¹)	Poisson's ratio
1	Plain fill	1.50	1916.2	107.0	0.429
2	Silty clay	3.50	1953.7	138.0	0.429
3	Clay	5.85	1909.6	126.5	0.410
4	Silty clay	3.45	1966.3	165.0	0.429
5	Clay	1.40	2019.5	206.0	0.418
6	Silty clay	4.25	2033.9	240.0	0.425
7	Silty clay	2.35	2020.6	266.0	0.417
8	Clay	4.65	2053.1	257.3	0.412
9	Clay	1.50	2060.4	250.0	0.339
10	Clay	2.75	2045.3	267.5	0.402
11	Silty clay	8.10	2005.8	243.0	0.411
12	Clay	2.85	2056.3	367.0	0.412
13	Silty clay	2.50	2018.5	250.0	0.428
14	Clay	10.45	2001.6	376.5	0.422
15	Clay	10.30	2045.3	312.0	0.412
16	Clay	7.00	2091.2	318.0	0.412
17	Silty clay	7.50	2074.1	334.0	0.412
18	Clay	4.00	2065.3	329.0	0.422
19	Silty clay	4.50	2077.4	339.0	0.432
20	Silty clay	4.00	1957.2	450.0	0.422



FIGURE 1: Finite element meshing of the formation-structure model.

and the equivalent nodal force are applied at the model boundary. The spring element is used to simulate the elastic recovery ability of the soil, and the damping element is used to absorb the scattered wave energy at the boundary, as shown in Figure 2. The equivalent nodal force is calculated from the velocity, displacement, and stress of the free field, which is used to simulate the input of ground motion.

In this paper, the equivalent linearization method is used to simulate the nonlinear characteristics of soil materials. According to the geological survey report, the relationship between the dynamic shear modulus ratio, damping ratio, and shear strain of soil materials is shown in Table 2.

The ground motion input of the calculation model adopts the VII degree fortified ground motion of the station design and the VIII degree fortified ground motion of the adjacent project. The ground motion time-history curve is shown in Figures 3(a) and 3(b). The peak ground accelerations of E_1 , E_2 , and E_3 are 0.052 g, 0.178 g, and 0.314 g for VII degree and 0.042 g, 0.148 g, and 0.380 g for VIII degree, respectively.

4. Result Analysis

The impact of the increase in seismic fortification intensity on the seismic performance of underground stations is

reflected in three aspects: structural internal force, seismic performance index check calculations, and suggested measures.

4.1. Internal Force of Structure. Taking the E_3 seismic condition calculated by the seismic fortification intensity of VIII degree as an example, the displacement and strain cloud diagrams at the moment of maximum bending moment of the station structure are given in Figures 4(a) and 4(b).

It can be seen from Figure 4(a) that the horizontal displacement of the station structure is relatively large, reaching about 0.66 m, which is the result of coordinated deformation with the soil. However, the relative displacement of the top and bottom of the station is not large. At the moment of maximum bending moment, the maximum relative displacement of the top and bottom of the station is 12.4 mm. Figure 4(b) shows that the location of the most adverse effect of ground motion on the station structure is at the connection between the side wall and the bottom plate, which needs to be paid attention to in the seismic design. Generally, the side wall and bottom plate of the station can be thickened or the concrete strength level can be increased.

The axial force, shear force, and bending moment of the station structure at the maximum moment of the bending moment of the station structure under the action of E_2 and

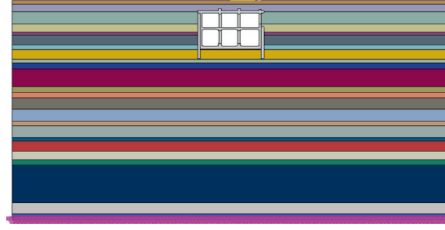


FIGURE 2: The viscoelastic boundary in the formation-structure model.

TABLE 2: Relationship between dynamic shear modulus ratio, damping ratio, and shear strain.

Soil	Depth (m)	Experimental results	Shear strain							
			5×10^{-6}	1×10^{-5}	5×10^{-5}	1×10^{-4}	5×10^{-4}	1×10^{-3}	5×10^{-3}	1×10^{-2}
Silty clay	9.2	G/G_0	0.9859	0.9958	0.9652	0.9235	0.777	0.5478	0.1744	0.1075
		λ_d	0.0245	0.0383	0.0554	0.0694	0.117	0.137	0.1759	0.1755
Silty clay	20.5	G/G_0	0.9969	0.9988	0.9654	0.9248	0.7070	0.5480	0.1752	0.1081
		λ_d	0.0185	0.0282	0.04542	0.0478	0.1001	0.1176	0.1519	0.1550
Silt sand	32.5	G/G_0	0.9973	0.9986	0.9543	0.941	0.7277	0.5775	0.2129	0.1155
		λ_d	0.0177	0.0285	0.0453	0.0594	0.0973	0.1778	0.1485	0.1559
Silty clay	46.3	G/G_0	0.9866	0.9982	0.957	0.9361	0.7474	0.5941	0.2266	0.1577
		λ_d	0.0187	0.0287	0.0453	0.0609	0.1076	0.1279	0.1687	0.1665
Silt	65.3	G/G_0	0.9864	0.9988	0.9548	0.932	0.7726	0.577	0.216	0.1206
		λ_d	0.0288	0.0288	0.0559	0.065	0.1073	0.1284	0.1616	0.1668
Silty clay	78.0	G/G_0	0.986	0.982	0.9655	0.9258	0.7179	0.5571	0.1996	0.1106
		λ_d	0.0188	0.0282	0.0415	0.0561	0.1037	0.1771	0.1666	0.1644

$E3$ seismic fortification intensity of VII and VIII degrees are extracted, respectively, as shown in Table 3.

Table 3 compares the influence of the increase in seismic fortification intensity on the internal force of the station structure. Under the action of $E2$ ground motion, the increase in seismic fortification intensity increased the internal force of the structure by 16%~23%; under the action of $E3$ ground motion, the increase in seismic fortification intensity had a more obvious impact on the internal force of the structure, and the internal force of the structure increased by 20%~30%. The increase in seismic fortification intensity has a greater impact on the bending moment of the structure, which is more obvious in the working conditions of $E3$ ground motion. The comparison of the structural internal forces of the seismic fortification intensity of VII and VIII degrees shows that the influence of seismic fortification intensity on the structure of the built underground station cannot be ignored, and attention should be paid to the design of seismic safety performance.

4.2. Checking Calculation of Seismic Performance Index.

According to the "Standard for Seismic Design of Underground Structures" [23], the calculation results are checked for cross-sectional bearing capacity and seismic deformation. Among them, the cross-sectional bearing capacity is reflected by the area of cross-sectional reinforcement and the seismic deformation is reflected by the displacement angle between floors.

It can be seen from Table 4 that, (1) in the case of fortification of degree VII, compared with the calculation results under the action of moderate earthquake $E2$, the

effect of large earthquake $E3$ increased the area of reinforcement by 18.1% and the displacement angle between floors increased by 15.2%; (2) in the case of fortification of degree VIII, compared with the results of the calculation under the action of the moderate earthquake $E2$, the effect of the large earthquake $E3$ increased the reinforcement area by 11.3% and the interstorey displacement angle by 30.5%. The effect of the strong earthquake $E3$ has increased the displacement angle between floors more than the increase of the reinforcement area, indicating that the structure has entered the elastoplastic stage under the effect of the strong earthquake $E3$. The increase in fortification intensity has significantly improved the internal force and deformation check calculation indicators, so the impact of the increase in seismic fortification intensity on the seismic performance of underground stations should be given sufficient attention. (3) The increase in seismic fortification intensity increased the area of reinforcement under the action of moderate earthquake $E2$ by about 33.8%, and the displacement angle between floors increased by about 47.8%; the area of reinforcement under the action of large earthquake $E3$ needed to be increased by about 26.1%. The displacement angle between layers increased by about 67.4%. The reinforcement area reflects the change in the internal force of the structure, and the displacement angle between floors reflects the change in the structural deformation. It is not difficult to see that the increase in seismic fortification intensity has a considerable impact on the structural deformation, which deserves special attention in future engineering practice.

The checked calculation results show that the structural design of the station can meet the safety performance requirements of degree VII and degree VIII seismic fortification.

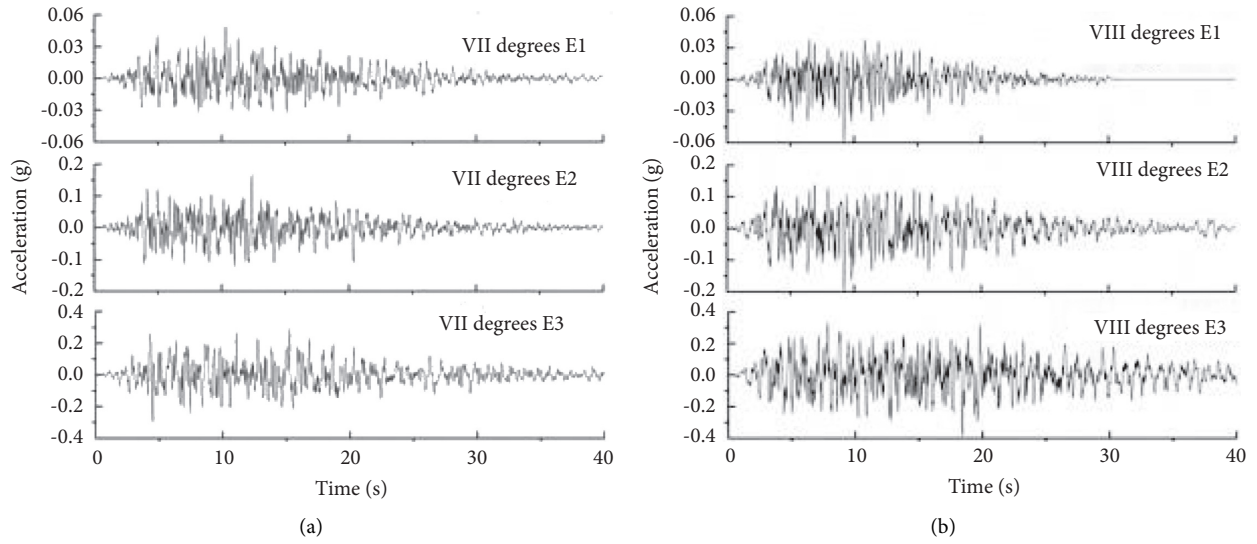


FIGURE 3: The time-history curve of bedrock motion with seismic fortification intensity. (a) VII degree. (b) VIII degree.

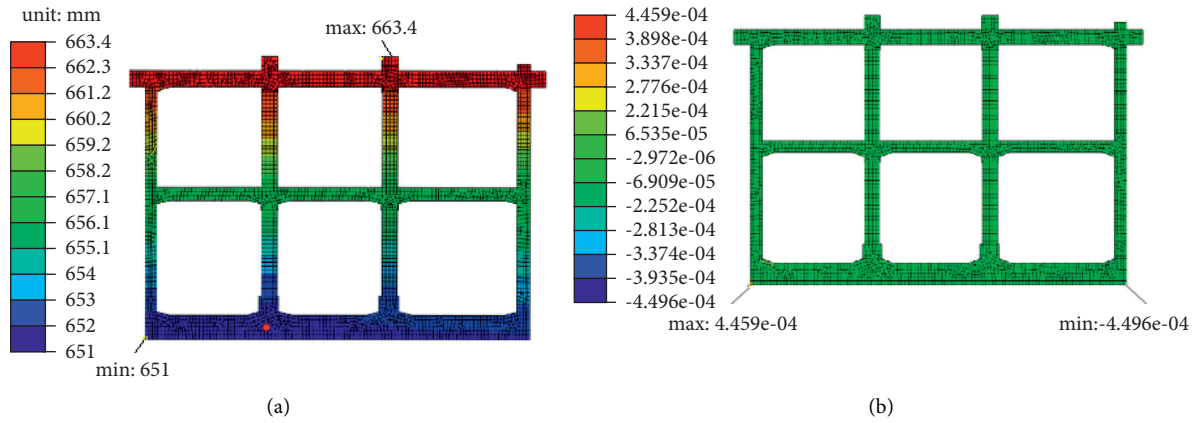


FIGURE 4: (a) The horizontal displacement and (b) the shearing strain of the station with the E3 earthquake motion of degree VIII.

TABLE 3: Internal forces of the station structure with different earthquake motions.

Type	E2			E3		
	VII degree fortification	VIII degree fortification	Difference %	VII degree fortification	VIII degree fortification	Difference %
Axial force (kN)	991.3	1182.5	19	1296.5	1687.1	30
Shear force (kN)	968.7	1123.8	16	1212.8	1451.4	20
Bending moment (kN-m)	1542.3	1896.5	23	1968.7	2469.2	25

TABLE 4: Checking calculation results of section bearing capacity and deformation.

Type	Design value	E2		E3	
		VII degree fortification	VIII degree fortification	VII degree fortification	VIII degree fortification
Reinforcement area (mm ²)	4765.6	2213.4	2961.5	2614.8	3296.8
Layer displacement angle	E2 < 1/600 E3 < 1/300	1/1360	1/920	1/1180	1/705

5. Conclusion

In this paper, a stratum-structure model is established by taking the structure of a certain subway station in Chengdu as an example. The nonlinearity of soil materials is simulated by using the equivalent linearization method, the finite element analysis model is based on viscoelastic boundary, and the ground motion is input in the form of equivalent nodal force. Through seismic time-history analysis, the effect of the increase in seismic fortification intensity on the seismic performance of the station is comparatively studied, and the calculation results are checked according to the national standards, and the following conclusions are drawn:

- (1) The most unfavorable position of the effect of ground motion on the structure of the underground station is at the connection between the side wall and the bottom plate. At the stage of seismic design, attention should be paid to the strengthening design of this position. Generally, the side wall and bottom plate of the station can be thickened or the concrete strength level can be increased.
- (2) The impact of the increase in seismic fortification intensity on the internal force of the built underground station structure cannot be ignored, especially the impact on the structural bending moment is more obvious. According to the data analysis in this paper, the increase of seismic fortification intensity has a considerable impact on the structural deformation, such as in the E3 earthquake, the reinforcement rate increased by 26.1%, increasing the material consumption and cost of underground construction.
- (3) The calculation results checked according to the national standards show that the increase in fortification intensity will have a more obvious impact on structural deformation; the structural design of the station can meet the safety performance requirements of degree VII and degree VIII seismic fortification.

Data Availability

The data are generated from experiments and can be made available by the corresponding author upon request.

Conflicts of Interest

The authors declare that there are no conflicts of interest regarding the publication of this paper.

Authors' Contributions

Ying Zeng carried out the experiments, analyzed the results, conducted the theoretical explanations, and wrote the manuscript. Shiguang Xu provided constructive suggestions and performed significant review and editing of the technical paper. Shiqian Yin provided rigor and fluency in the language of the academic paper.

References

- [1] Y. M. A. Hashash, "Seismic behavior of underground structures and site response," in *Earthquake Engineering Frontiers in the New Millennium*, pp. 243–249, CRC Press, Beijing, China, 2000.
- [2] Y. M. A. Hashash, J. J. Hook, B. Schmidt, and J. I-Chiang Yao, "Seismic design and analysis of underground structures," *Tunnelling and Underground Space Technology*, vol. 16, no. 4, pp. 247–293, 2001.
- [3] X. Yao, "Seismic response analyses method of underground structures in China," in *Proceedings of the 2015 International Forum on Energy, Environment Science and Materials*, pp. 309–314, Shenzhen, China, September 2015.
- [4] X. J. Wang, H. Y. Zhuang, G.-X. Chen, and R. Wang, "Effect of diaphragm wall on earthquake responses of an underground subway station," *Journal of Geotechnical Engineering*, *Chinese Journal of Geotechnical Engineering*, vol. 39, no. 8, pp. 1435–1443, 2017.
- [5] W. H. Gao and X. Ji, "A three-dimensional finite element dynamic model for seismic behavior of rail transit structures in the urban underground space," *China Earthquake Engineering Journal*, vol. 41, no. 2, pp. 347–352, 2019.
- [6] Y. Zou, H. Liu, L. Jing, and J. Cui, "A pseudo-static method for seismic responses of underground frame structures subjected to increasing excitations," *Tunnelling and Underground Space Technology*, vol. 65, pp. 106–120, 2017.
- [7] J. W. Jiang, C. S. Xu, H. M. El Naggar, X. Du, Z. Xu, and J. Assaf, "Improved pushover method for seismic analysis of shallow buried underground rectangular frame structure," *Soil Dynamics and Earthquake Engineering*, vol. 140, 2021.
- [8] Y. Z. Shi, J. B. Hua, and X. F. Li, "Application of response displacement method in seismic design of underground utility tunnels," *Journal of Jilin University. Earth Science Edition*, vol. 48, no. 6, pp. 1785–1796, 2018.
- [9] H. T. Yu and Y. Yuan, "Application of response displacement method on seismic design of a complex underground structure," *Chinese Journal of Underground Space and Engineering*, vol. 7, no. 5, pp. 857–862, 2011.
- [10] W. Al Agha, W. Alozzo Almorad, N. Umamaheswari, and A. Alhelwani, "Study the seismic response of reinforced concrete high-rise building with dual framed-shear wall system considering the effect of soil structure interaction," *Materials Today: Proceedings*, vol. 43, no. 1, pp. 2182–2188, 2021.
- [11] J. Zhou, P. Zhong, and Y. Chi, "Research on seismic soil pressure of underground structures in soft soils," *Rock and Soil Mechanics*, vol. 25, no. 4, pp. 554–559, 2004.
- [12] Z. F. Dong, B. Z. Cai, and Y. C. Yao, "Accuracy of the response acceleration method and response displacement method considering different imbedding depths of underground structures," *Journal of Vibration and Shock*, vol. 36, no. 14, pp. 216–220, 2017.
- [13] Y. J. Deng and F. Y. Liang, "Comparison of calculation methods for seismic response of underground structures in design codes," *China Earthquake Engineering Journal*, vol. 40, no. 5, pp. 996–1003, 2018.
- [14] K. P. Xu, L. P. Jing, and J. Bin, "A comparative analysis of forced displacement and response acceleration methods for underground structures," *China Earthquake Engineering Journal*, vol. 42, no. 4, pp. 967–972, 2020.
- [15] S. T. Li, J. B. Liu, X. Bao, D. Wang, and F. Wang, "Seismic analysis of underground structures based on local deformation of the free field via the pushover analysis method," *China*

- Earthquake Engineering Journal*, vol. 41, no. 6, pp. 1472–1481, 2019.
- [16] J. B. Liu, X. Q. Liu, and B. Li, “A pushover analysis method for seismic analysis and design of underground structures,” *China Civil Engineering Journal*, vol. 41, no. 4, pp. 73–80, 2008.
- [17] J. Liu, W. Wang, and G. Dasgupta, “Pushover analysis of underground structures: method and application,” *Science China Technological Sciences*, vol. 57, no. 2, pp. 423–437, 2014.
- [18] A. M. Belostotsky, P. A. Akimov, and D. D. Dmitriev, “About methods of seismic analysis of underground structures,” *International Journal for Computational Civil and Structural Engineering*, vol. 14, no. 3, pp. 14–25, 2018.
- [19] H. T. Yu and Y. X. Li, “Virtual hybrid simulation method for underground structures subjected to seismic loadings,” *Tunnelling and Underground Space Technology*, vol. 110, 2021.
- [20] Y. Li, H. Di, S. Zhou, and Q. Gong, “Seismic analysis for cross transfer subway stations in soft soil stratum,” *Ksce Journal Of Civil Engineering*, vol. 25, no. 5, pp. 1732–1745, 2021.
- [21] Y. Qiu, H. Zhang, and Z. Yu, “A seismic design method of subway stations affected by surrounding buildings,” *Rock and Soil Mechanics*, vol. 42, no. 5, pp. 1443–1452, 2021.
- [22] GB50011-2010, *Code for Seismic Design of Building*, China Architecture and Building Press, Beijing, China, 2016.
- [23] GB/T51336-2018, *Standard for Seismic Design of Underground Structures*, China Architecture and Building Press, Beijing, China, 2018.

Research Article

Stability Analysis of the Shiliushubao Landslide Based on Deformation Characteristics and External Trigger Factors in the Three Gorges Reservoir

Guilin Luo ^{1,2}, Guangming Ren,¹ Xiaojun Bao,² Xili Yang,¹ and Teng Liu¹

¹State Key Laboratory of Geo-Hazard Prevention and Geoenvironment Protection, Chengdu University of Technology, No. 1 Erxianqiao East Road, Chengdu 610059, China

²School of Civil Engineering and Mechanics, Lanzhou University, Lanzhou 73000, China

Correspondence should be addressed to Guilin Luo; luogl15@lzu.edu.cn

Received 8 July 2021; Accepted 18 August 2021; Published 6 September 2021

Academic Editor: Zhiyong Chen

Copyright © 2021 Guilin Luo et al. This is an open access article distributed under the Creative Commons Attribution License, which permits unrestricted use, distribution, and reproduction in any medium, provided the original work is properly cited.

There exists the problem of landslide reactivation due to the seasonal fluctuation of rainfall and reservoir water level annually. Based on a large number of GPS monitoring data of the landslide mass after impoundment of the Three Gorges Reservoir in Shiliushubao landslide area, the relationship between the external trigger factors and slope stability could be obtained. A finite element calculation model has been established for the stability analysis of the Shiliushubao landslide after impoundment from January 2004 to October 2009. Through the deformation characteristics of the landslide, it is shown that the landslide exhibited a stepwise pattern on the whole, which developed faster after impoundment and slowed down in rainy seasons. The trend of the curve kept roughly opposite to the fluctuation of the safety factor. It suggested that the stability of the landslide mass was closely related to the seasonal fluctuation of the rainfall and the reservoir level, and the landslide deposits demonstrated to be reactive with them. The subject provides a certain reference value on the landslide stability analysis and the risk assessment within a similar engineering geological condition.

1. Introduction

Landslide and floods in China are a large amount of socioeconomic disruptions, property damages, and casualties, and they are caused by multiple factors including the geography [1, 2], the geological tectonism [3–5], hydraulic alteration [6], flood alluvial [7], earthquake [8, 9], climate change [10, 11], and anthropogenic engineering constructions [12]. The Three Gorges Dam has provided huge hydropower resources and mitigated the devastating effects of deluges with time tested for the past decades ago [13, 14], while there exists some geological disasters owing to the drastic fluctuation of the reservoir water level.

In the recent years, the researchers have found that the changes of the water level would affect the safety of the reservoir bank via numerical simulation [15, 16] and/or field

investigation [17, 18]. The hydraulic conductivity and the rate of the water level changes dominate the transient flow response which directly controls the stability of the landslide [19, 20]. The pore pressures and the water surface pressure can also affect the stability of the landslide [21, 22] in the form of drag force outside the slope and impair the soil shear strength and the geophysical characteristics [23, 24]. Furthermore, the study of the rainfall diffusion in the soil also reveals the mechanisms of the landslide to eventually result in slope failure [25, 26].

All experimental works have their limitations, either due to the difficulties or ambiguity in filed investigations or measuring some quantities [27, 28], mainly due to the complexity of the test process. Numerical simulations and field investigations are widely used to study the deformation and the stability mechanism of the landslide [29], and there are a few research studies attending to apply the integrated

monitoring system to a single landslide and combine the numerical model results [30, 31].

In the present study, a generalized model was selected to represent the landslide on the north bank of the Yangtze River, and the nonlinear seepage field of the bank was considered to realize the real-time changes. Combined with the field investigation data, the numerical analysis using Comsol Multiphysics was conducted to investigate the dynamic failure process of the landslide mass under the fluctuation of the reservoir water level and precipitations. In the whole process, this subject attended on the evolution of the changes of the safety factors to determine the changes of the stability of the reservoir bank with the grey relational grade. The results of the numerical modeling and the surface deformation were able to accurately explain why the stability of the Shiliushubao landslide increased as the reservoir water level rose, whereas it decreased as the reservoir water level dropped during the flood season.

2. Description of the Shiliushubao Landslide

The Shiliushubao landslide is a part of the Huanglashi landslide, situated in 1.5 km downstream of Badong Country and 66 km upstream of the Three Gorges Dam. Along the north bank of the Yangtze River, the planar shape of the landslide mass approximates a square of length 500–550 m and a width of 350–470 m. The average thickness of the sliding mass has an average of about 40–50 m, and an area of $25.2 \times 10^4 \text{ m}^2$ with an estimated volume of $12 \times 10^6 \text{ m}^3$. The sliding direction is 25°N , which is approximately perpendicular to the Yangtze River. The vertical height of the landslide is about 320 m, and its elevation ranges from 40 to 320 m, with an average slope angle of about 28° . The right and left sides are bounded by the gully, and the trailing edge is bounded by a group of steep walls. In addition, the field survey indicated that two secondary shallow sliding blocks have developed near the river (Figure 1).

There are totally fifteen GPS stations on the landslide mass monitoring the surface deformation, and these station distributions are all shown in Figure 2. In order to monitor the deformation of the whole area, the GPS stations were roughly uniformly placed near the three survey lines. These three survey lines were established for borehole distributions which could directly and accurately identify stratigraphic. Different from other projects, five GPS stations were placed at the leading edge, which may be more comprehensive to reflect the fluctuations of the landslide stability. Besides, there exists three points for the reservoir water level and rainfall in the upper part of the landslide.

The geological units and structures of the landslide mass were analyzed on the early materials which were obtained from field investigations and explorations. The engineering geological profile proved that the sliding deformation occurred along the contact surface between the deposits and the bedrock (Figure 2). The landslide mass consists of the full weathering or strong weathering red broken calcareous with some clastic rock, and the bedrock mainly consists of grey, thin to medium-thick layer of interbedded dolomitic limestone and partially the purple-red mudstone of Badong

Formation from the Triassic. From the formal lecture, the stratum of the Badong Formation was always called the “easiest sliding strata” in China due to its special geophysical characteristics and low strength. The geophysical characteristics and hydraulic properties are given in Table 1.

As the erosion of the strong weathering deposits, long-term water softening, and rainfall infiltration, there are numerous cracks and subsidence features observed at the slippery tongue and the trailing edge of landslide of the landslide body, especially those in the rear part are turned out to form a continuous crack within the landslide deposit. From the field explorations, the largest crack was around 344 m long with an opening width of 1–45 cm, a roughly depth of 10–110 cm, and a dip-slip dislocation of 2–150 cm until 2009. The maximum accumulated surface deformation from January 2004 to December 2009 reached 1485 mm. These cracks and apertures proved good tunnels for seepages and may cause extra pore pressures to the slides.

The special topography, lithology, and geological structure of the landslide area are the pivotal factors of landslide formation and control the deformation and evolution of the prestable landslide. In addition, the project finally compared the deformation and the landslide stability results and summarized the dominant factors which drove landslide reactivation, i.e., the seasonal fluctuation of rainfall and reservoir level of the Three Gorges Reservoir. The water level change will induce the growth of landslide mass, and the rainfall will accelerate the deformation of the landslide mass. The seasonal fluctuations of the water level during the operation of the reservoir and the increase of the rainfall capacity dramatically change the hydrogeological conditions of the landslide mass and reduce the strength of the soil.

3. Monitoring Data and Analysis of Deformation Characteristics

3.1. Monitoring Data. In early years, the slope was confirmed to undergo noticeable deformation and cracks, and this information was reported to government by local people. Therefore, the special monitor area was established for deformation and rainfall of the landslide slope. The accumulated displacement and water level fluctuation versus time curve is plotted in Figure 3 along with the surface deformation, reservoir water level, and rainfall capacity monitoring data since January 2004 to October 2009.

As seen from the curves of the reservoir water level, the reservoir water level remained approximately constant over 135 m, and its variation tendency is essentially synchronous to the rainfall capacity. In the large rainfall months, especially rainy seasons, the water level is always on the rise, and the highest water level was 169.7 m in December 2006. With the period of low precipitations, the reservoir water level fluctuation is in base volatility, and the water level changes are in the range of 1–2 m. In 2007–2009, the rainfall was much larger than the other years, and the water level fluctuations were at around 12–20 m. Based on the data comparison of the average velocity of the impoundment and drawdown of per month, the trend of water level changing can be observed by their difference to some extent (Figure 4).

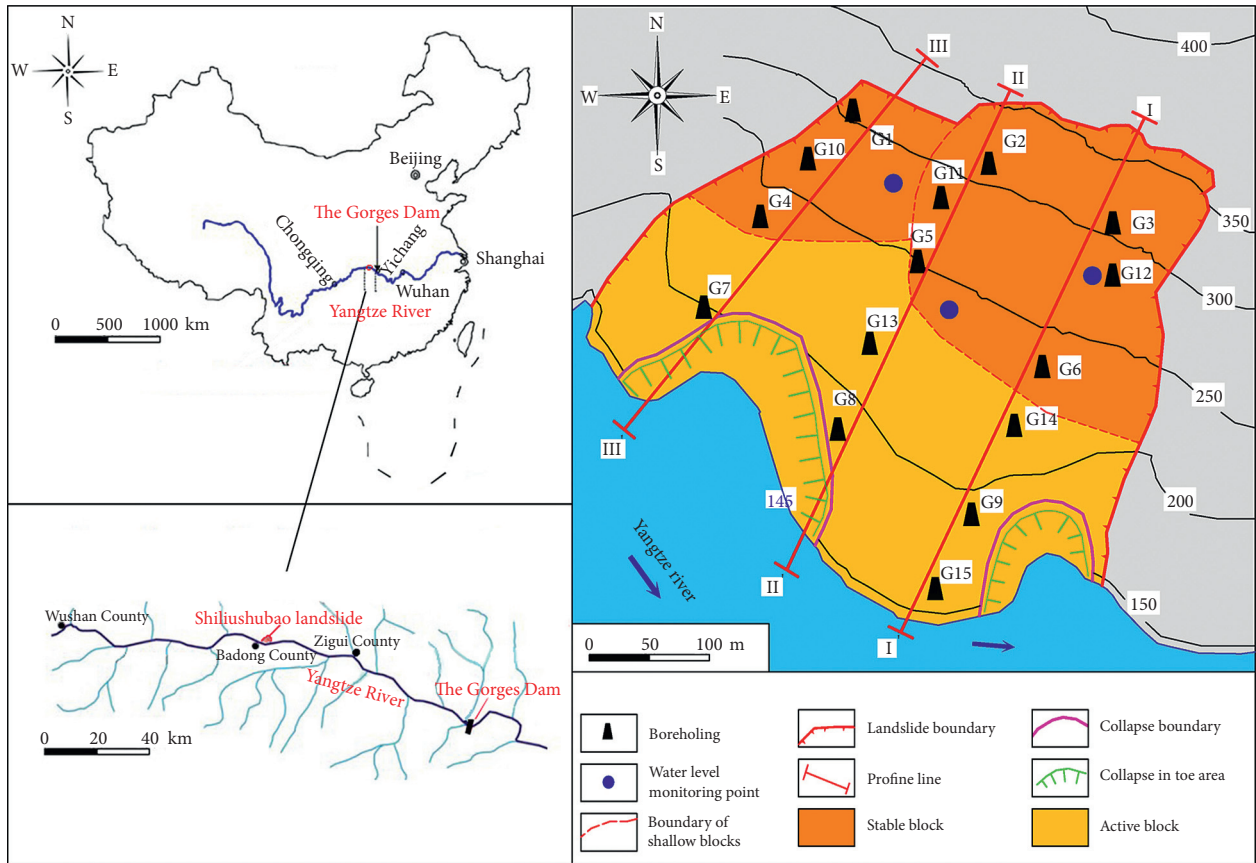


FIGURE 1: Location distribution and geological map of the Shiliushubao landslide.

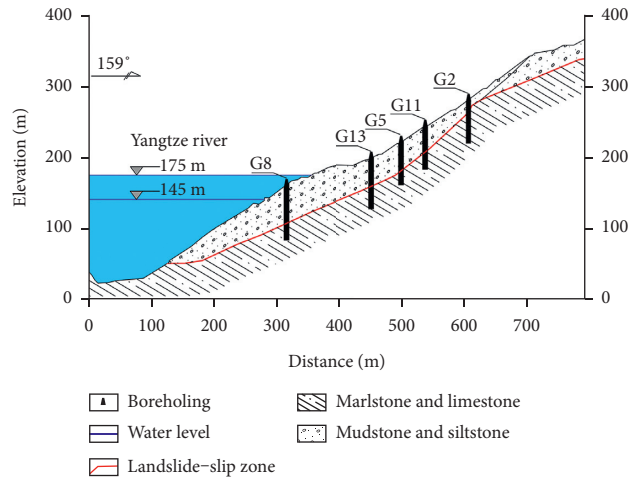


FIGURE 2: Geological map of the section II-II' of the landslide.

TABLE 1: Geophysical characteristics and hydraulic properties of the study area.

Rock category	ρ (g/cm ³)	E (GPa)	μ	φ (°)	c (MPa)	K ($\times 10^{-4}$ m/s)
Landslide deposit	2.61	0.45	0.27	38	0.15	0.067
Bedrock	2.75	12.5	0.25	45	0.8	0.048

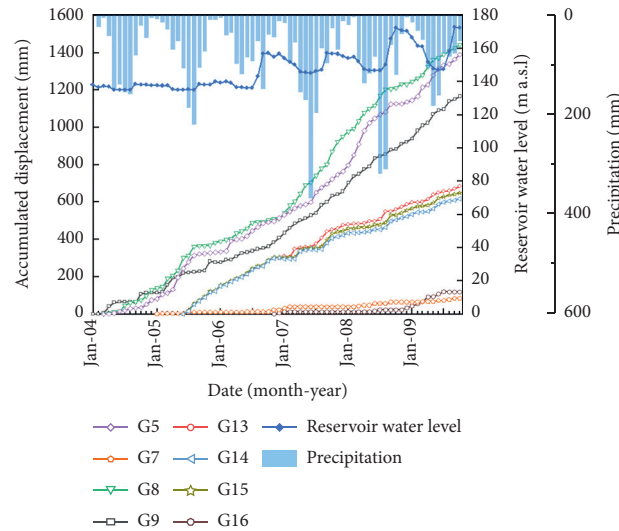


FIGURE 3: Accumulated displacement of GPS stations, reservoir water level, and precipitations from January 2004 to October 2009.

It roughly reveals that the landslide mass exhibited a stepwise deformation characteristic, especially occurred on the active blocks since the implementation of the professional monitoring in 2004 which can be reflected by the accumulated displacement curve of the GPS station points of the landslide mass (Figure 4(a)). The total displacement of G5, G7, and G8 was placed in front of the landslide maintain sustained growth from 2004 to 2009, which suggests that the slope was marginally stable or unstable and maybe revival for complexity external trigger factors (Figure 5). In 2004, there are few GPS stations effected by these factors, and the average daily deformation is lower than 4 mm/d that suggested that the middle and rear parts of the landslide remained stable. During 2007–2009, the reservoir water level changed substantially at the elevation of 145–169 m, and the accumulated deformation increased significantly.

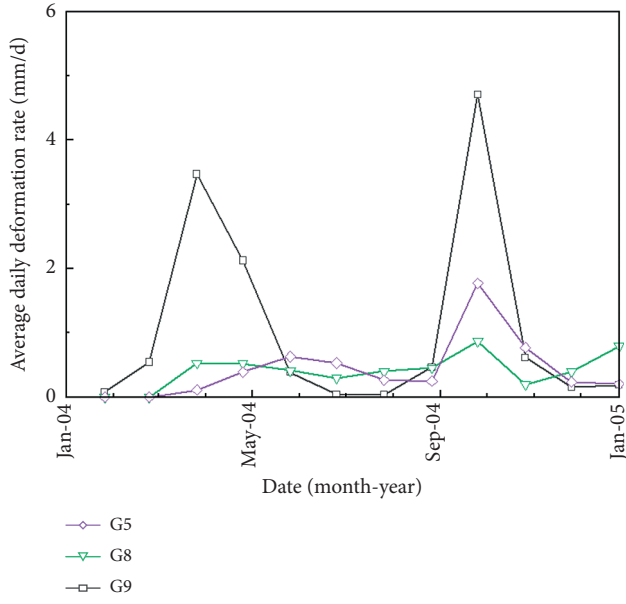
It is clear that the accumulated surface displacement curves always increase sharply after drawdown in May–July every year and remain or increase relatively slowly after impoundment from September to April. Correlated to the collapses, precipitations, and reservoir water level fluctuations at the leading edge of the landslide, the accumulated surface displacement near these stations grows continually, in which the stepwise growth is not as clear as before from 2007 to 2008, showing prominently at the station of G7, G8, and G9. In the heterogeneity and anisotropic stratum, the groundwater level rise at a slower rate than the reservoir water level. There exist some progressive cracks in the landslide, such as the shear cracks at the leading edge and tension cracks at the trailing edge. Everytime the reservoir water level rises, the leading edge of the landslide may be submerged. The hydrostatic pressure increases on the landslide surface which directed inside the slope, and the overall landslide remains steady and the monthly deformation is relatively stable [32]. On its reverse side, the groundwater level would always lag behind the reservoir

water level, and the hydrodynamic pressure would directly act in the sliding section, directed outside the slope (Figure 6). Furthermore, the rainfall infiltration may weaken the mechanical properties of the rock mass that may also decrease the landslide stability.

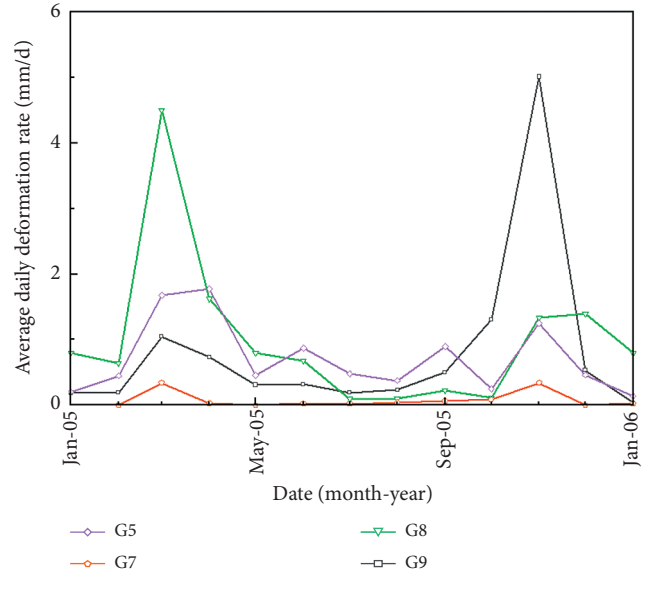
3.2. Analysis of the Deformation Characteristics of the Landslide Mass. According to the results shown in Figure 4, these deduced that the increase of the accumulated displacement was relatively large. Based on the field investigations, the internal deformation mainly rose parallel to the sliding direction. The closer to the collapse boundary, the larger the displacement is, while the increase of the displacement of the other station points is relatively small [33–35].

It is reflected in Figure 4 that the annual displacement of G5, G8, G9, and G13 is much larger than other GPS station points, in which the average displacement rate of these fluctuated between 0.89 and 3.65 mm/d, and the rate of GPS-3 and GPS-6 fluctuated between 0.55 and 1.68 mm/d. The other station points were under 0.55 mm/d or nearly unchanged.

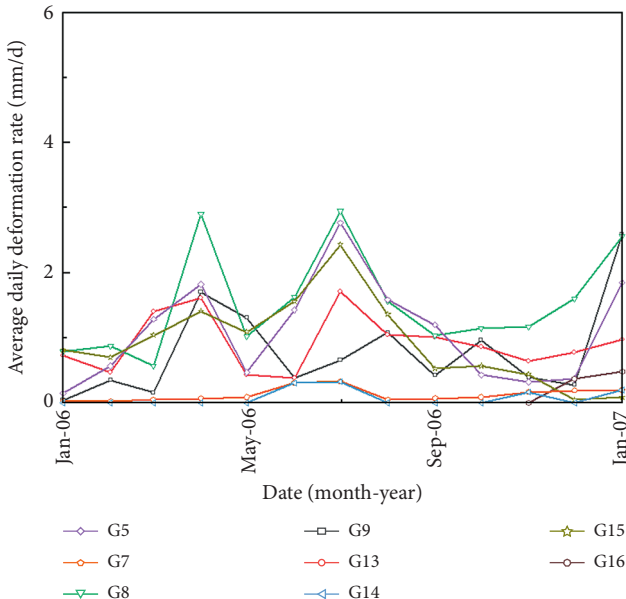
Combining Figure 5, it could be seen that the fluctuation of the reservoir water level in 2004, 2005, and 2006 were stable, and the rate of the annual displacement changed significantly after drawdown. Especially in 2006, the rainfall was little higher than 2004 and 2005, and the increase of the displacement of the landslide was smaller. However, in 2007, the displacement of the landslide changed not as that in 2004–2006, while the rainfall was much bigger than the past three years in the flood season, in which the highest precipitation reached to 367.9 mm in June 2007. Too much rainfall caused the rate of the annual displacement of the landslide increased; but unlike the formal, the accumulated displacement in 2007 grew consistently, in which the maximum displacement rate of the



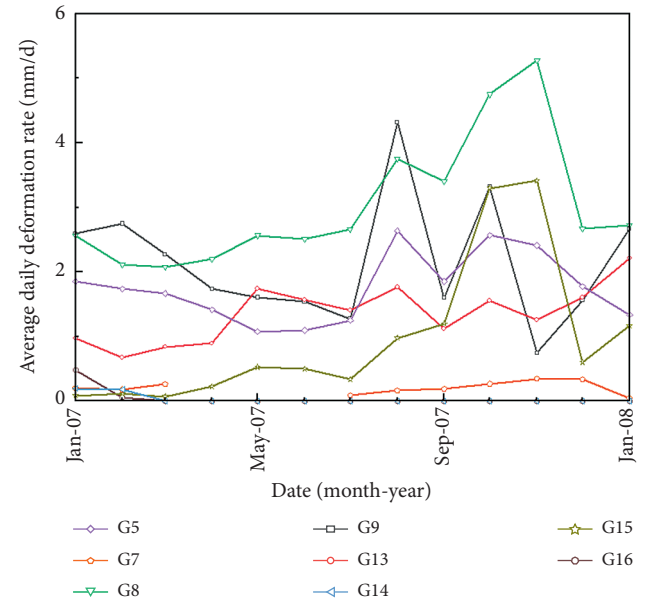
(a)



(b)



(c)



(d)

FIGURE 4: Continued.

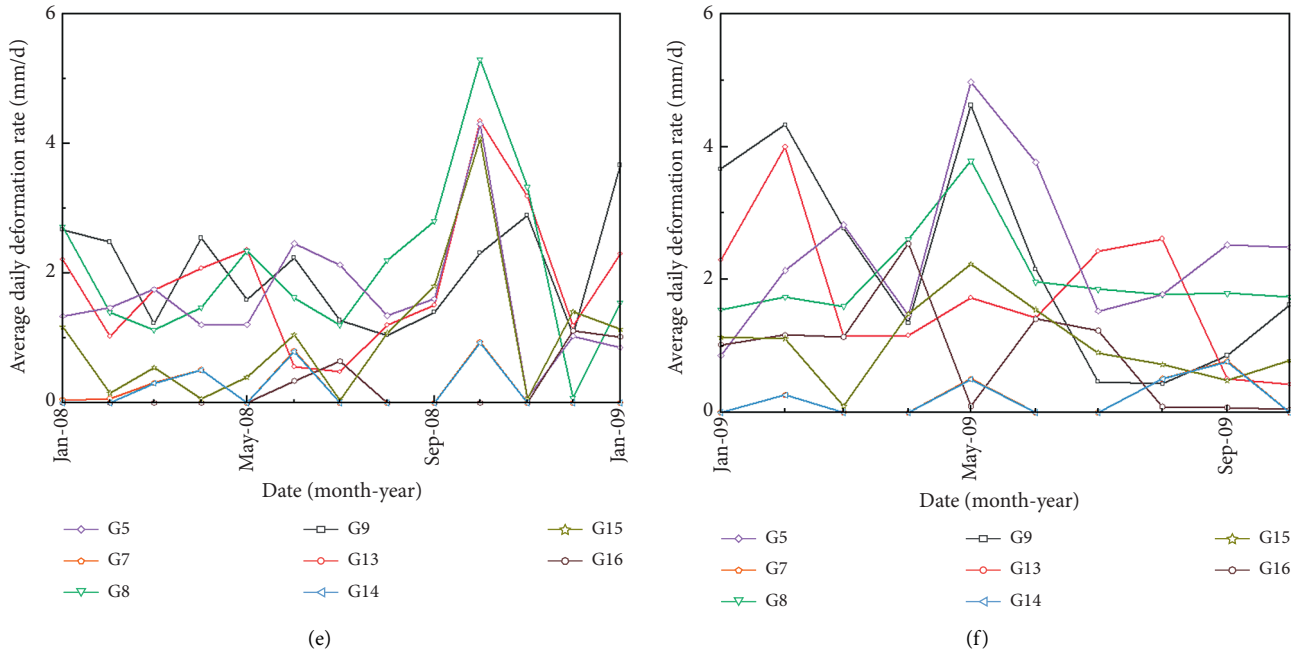


FIGURE 4: Curves of daily mean displacement rate of each month from January 2004 to September 2009. (a) From January 2004 to January 2005; (b) from January 2005 to January 2006; (c) from January 2006 to January 2007; (d) from January 2007 to January 2008; (e) from January 2008 to January 2009; (f) from January 2009 to October 2009.

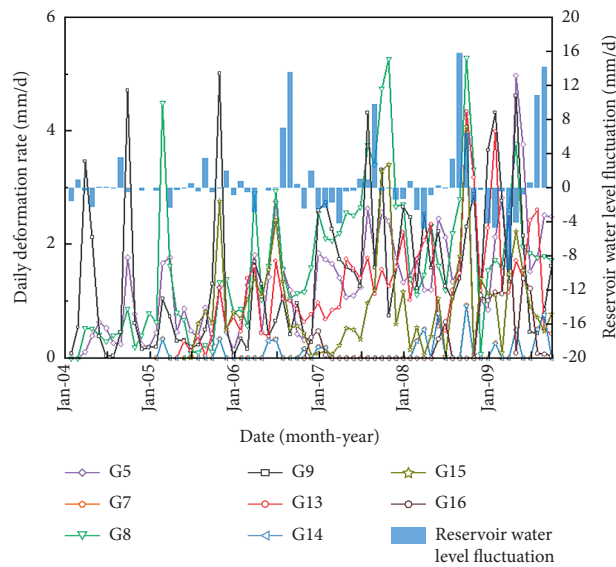


FIGURE 5: Accumulated daily deformation rate of GPS stations and reservoir water level fluctuation from January 2004 to October 2009.

monitoring points reached 4.46 and 5.31 mm/d. Therefore, the rate of the annual displacement of these stations to the collapse boundary increased substantially. There were two months in which the precipitation was over 300 mm in 2008, and the displacement rate decreased relatively after impoundment, with rapid increase after drawdown. Everytime the reservoir water level is rising high, the rate of the deformation would increase significantly after the reservoir water level dropped, and the accumulated displacement would become steps in several months. As the

reservoir water level rose too high in 2008, there were several months for reservoir water dropping at the beginning of 2009, and the displacement rate of these monitoring stations was kept elevated.

Based on the monitoring materials, the sliding process only progressed to the mediocre part; the back part of the landslide mass was merely slightly deformed. Following this trend, if the landslide was not reinforced, the rear part would have to fail when the sliding of the average part supplied sufficient space to move.

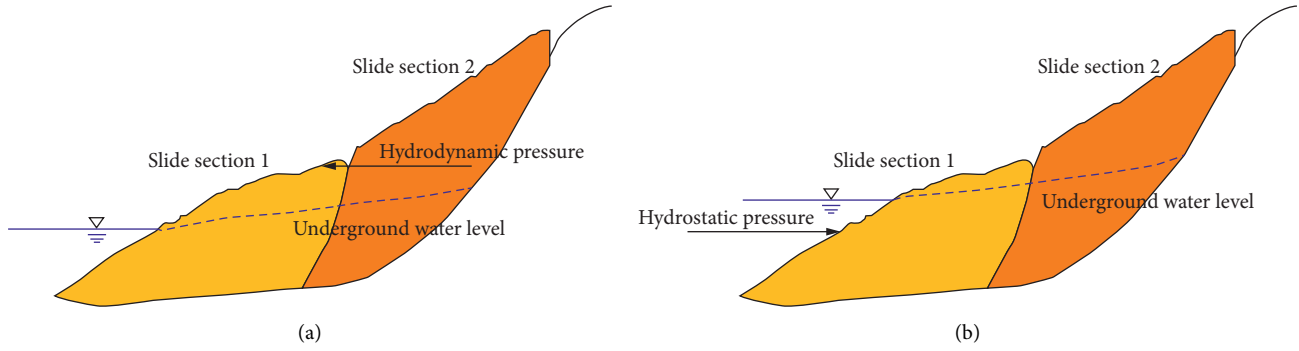


FIGURE 6: The schematic diagram of hydraulic action acting on the slide of Shiliushubao landslide.

4. Stability Analysis of Water Level Fluctuation

4.1. Numerical Modeling and Calculation Conditions. A numerical calculation model of the slope had been established based on the geological engineering section II-II' (denoted in Figure 7). The boundary of the model could be given as this: the bottom periphery elevation of the model is approximately 0 m, the height of the right periphery is around 368 m, the left periphery is around 42 m, and the horizontal distance is around 794 m. There has been set two kinds of materials in the model, the bedrock and the landslide body, which are all assumed as elastoplastic material that the yield conditions satisfied the Mohr–Coulomb criterion [36].

When simulating the two-dimensional finite element seepage in the Multiphysics, the progress of the subsurface flow first adopts the two-phase Darcy's law model and then combines the soil mechanics [37]. The transient seepage analysis is conducted based on the actual reservoir water level (Figure 3) parallel to the monthly precipitation (equation (1)) [38]. Then, the pore pressure calculations join up the stability analysis with the shear strength reduction, which is realized by reducing the variables c and ϕ while defining the parameter SRF and accumulating the results till the critical state (equation (2)). Also, there are two parameters to define the saturated area and unsaturated area with its built-in function Hp , which defines the pore pressure in the soil.

$$\begin{cases} \frac{\partial}{\partial x} \left[K_x \frac{\partial H}{\partial x} \right] + \frac{\partial}{\partial y} \left[K_y \frac{\partial H}{\partial y} \right] + \frac{\partial}{\partial z} \left[K_z \frac{\partial H}{\partial z} \right] + W = S_s \frac{\partial H}{\partial t}, \\ H(x, y, z, t)|_{t=0} = H_0(x, y, z), \quad (x, y, z) \in \Omega, \\ K \frac{\partial H}{\partial n} \Big|_{\Gamma_2} = q(x, y, z, t), \quad (x, y, z) \in \Gamma_2, \end{cases} \quad (1)$$

where K_x , K_y , and K_z are the values of hydraulic conductivity along the x , y , and z coordinate axes, which are assumed to be parallel to the major axes of hydraulic conductivity; H is the potentiometric head; W is a volumetric flux per unit volume representing sources and/or sinks of water; S_s is the

specific storage of the porous material; t is the time; q is the flux.

$$\begin{cases} c' = \frac{c}{\text{SRF}}, \\ \tan \phi' = \frac{\tan \phi}{\text{SRF}}. \end{cases} \quad (2)$$

During the numerical computing process, c is the cohesion; ϕ is the internal friction angle; and Fr is the factor of safety. The trail of Fr incrementally increases until the convergent criterion is not satisfied.

For boundary conditions, the interface, i.e., the sliding surface of this landslide, which is between the landslide mass and the bedrock, is taken as impermeable, for it is nearly three orders of magnitudes of hydraulic conductivity larger than other materials. To fit the reality, there establishes a subordinate landslide-slip zone. The saturated hydraulic conductivity k_s of the landslide mass in the Gorges Reservoir region could vary from 1×10^{-4} m/s to 1×10^{-7} m/s, and this subject finally uses those given in Table 1 combining with the velocity of impoundment and drawdown. The other physical and mechanism parameters are all obtained from early in situ tests and laboratory experiments, such as the packer permeability test, specific gravity test, and consolidated drained triaxial compression test.

4.2. Numerical Simulation Results for Stability. Figure 8 illustrates the results of the variations of the safety factor from January 2004 to October 2009, as obtained from the fluid-soiled coupling analysis. From Figure 8, the fluctuation of the landslide stability could be approximately divided into two parts with the factor of safety. One part is from January 2004 to October 2006, the fluctuation is slight, and it keeps relatively high. The other is from November 2006 to October 2009, the fluctuation decreases sharply, and it keeps relatively low. The increase of the external trigger factors may cause disequilibrium and large deformation in the slope.

The precipitations during January 2004 to July 2006 were around 42–80 mm/month; thus, the reservoir water level was maintained at 135–138 m. And the factor of safety was between 1.12 and 1.2, which demonstrates that there was no trend to slide in the landslide mass, and the slope is primarily

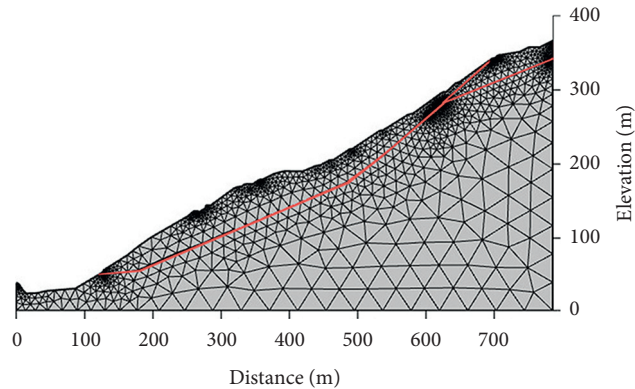


FIGURE 7: Numerical model of the section II-II' for slope stability analysis.

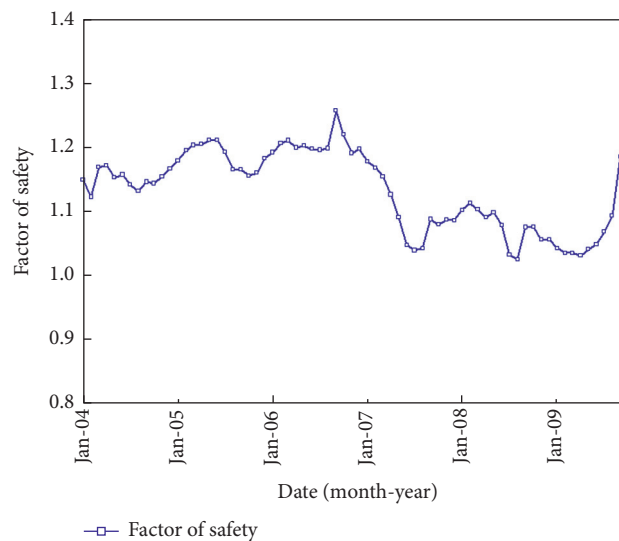


FIGURE 8: Factor of safety of section II-II' from January 2004 to October 2009.

kept stable. While the precipitations grew obviously in rainy seasons in 2006, the factor of safety grew parallel to the reservoir water level from 1.17 to 1.26. On the contrast, the factor of safety fluctuated sharply after impoundment until the next rainy season and reached the minimum of 1.04. The accumulated displacement grew constantly in the whole process, and there existed an acceleration phase in 2006 after impoundment (Figure 3). It suggests that there was some insurance that the landslide might become disequilibrium. After the lower peak of this curve, the factor of safety grew corresponded to the rainy season in 2007, conforming to the general change of fluctuations of the factor of safety. While the increase of the factor of safety was not as much as the formal one in 2006, the reservoir water level kept high between 147 and 172 m, which just kept from 1.04 to 1.15. The accumulated displacement assumed stepwise growth more obviously, and the rate of displacement was higher and more periodical. Generally speaking, the rate of surface landslide deformation decreased as the reservoir water level rose after the reservoir impoundment, whereas it increased with the water level fell.

4.3. Sensitivity Analysis for Stability. The curve of the safety factor is approximately synchronous with the water level change, but always lags behind compared with the reservoir water level. The water level fluctuations may assist to predict the stability of the slope which is mainly driven by the seepage field in a sense (Figure 9), but it could not directly represent the variation of stability which requests actual external trigger factors.

Figure 9 shows the relationship between the rate of factors of safety with the velocity of water level change, which represented the different stages the landslide mass might have experienced. The reservoir water level fluctuations could be approximately divided into four types throughout the calculation process with its velocity. Same as the variation of the water level, these curves could not directly respect the relationship between the factor of safety with the reservoir water level. Since the impoundment of the reservoir, the leading edge of the landslide may be submerged by the water level that would increase the hydrostatic pressure, which is conducive to the landslide stability. In the process of the reservoir impoundment, the faster the velocity

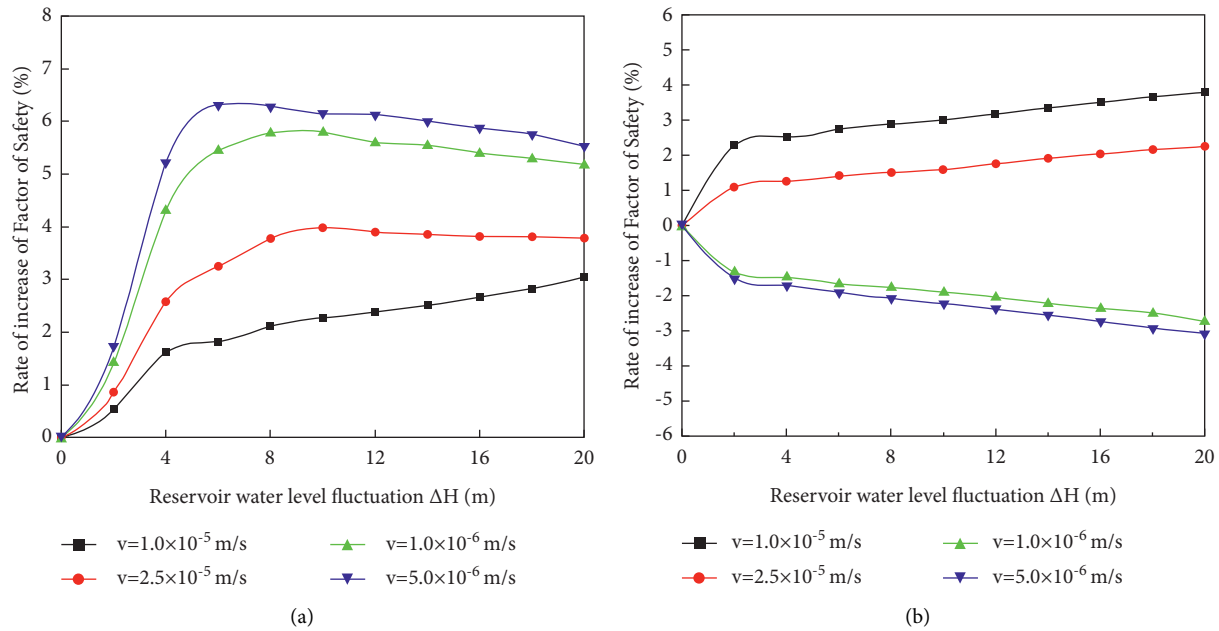


FIGURE 9: Sensitivity analysis of slope stability conditions. (a) Reservoir storage; (b) reservoir water level drawdown.

is, the faster the safety factor would increase. However, if the velocity is too much bigger than the hydraulic conductivity, the increase rate would gradually slow down as the water level rises. The closer the values are, the greater the height of the water level where the incremental slowdown occurs. It suggests that the impoundment would improve the stability of the landslide mass [39, 40].

The drawdown of the reservoir water level may cause the hydrodynamic pressure in the rear edge of crack particularly prominent. On the contrast, it shows two different types in the process of drawdown. As the hydraulic conductivity is closed to the velocity of the water level fluctuation, the factor of safety was not just decreased. When the velocity of the water level fluctuation is less than the hydraulic conductivity, the safety factor increases and the rate is small. However, these kinds of conditions would not actually occur, and this analysis is only based on theoretical exploration. The further reason may be the lagging drainage of the groundwater, inducing the excretion of the water in the landslide mass lags behind the reservoir water. It suggests that the drawdown would reduce the stability of the landslide mass at some extent.

5. Discussion

After the analysis of the landslide deformation characteristics and numerical model calculating, the seasonal fluctuation of rainfall and reservoir level plays significant roles in the landslide stability. The characteristics of the landslide deformation could guide the analysis of the stability, and it may be the tight data for the field research work [28, 41].

These figures have shown the relationships between the surface accumulated displacement, the stability of the landslide mass and the fluctuation of the reservoir water level, as all of them have an important correlation. The

surface accumulated displacement curves has a palpable stepwise increment in rainy seasons each year, and the safety factor keeps relatively similar. If the slope keeps marginally stable, the slightest changes of the external trigger factors may lead to disequilibrium and significant deformations [42]. Table 2 summarizes the input items for the factor of safety and the displacement of G5 station.

Based on the grey relation analysis, the grey relation grade (GRG) is useful to evaluate the degree of relationship between the input and extra factors. The GRG ranges from 0 to 1; according to the assumption of the method, a value of 0.6 or higher proves a strong relationship towards these. Table 2 provides the mainly factors influencing the safety factor and the landslide deformation. They both correspond to the rainfall and water level fluctuations and always lag behind the precipitations. When the water level rises, the accumulated surface displacement curve is relatively stable or grows slowly, and the landslide mass will keep steady or the stability might be limited increasing [43]. At this time, the water level of the Gorges region drops rapidly or runs at a low elevation, and the rate of the surface displacement changes significantly, with the stability of the landslide decreasing.

Upon combining the factor of safety with the surface displacement monitoring results obtained after the reservoir water level fluctuated (Figure 10), it is suggested that the numerical modeling results demonstrate why the deformation rate of the Shiliushubao landslide decreased as the reservoir water level increased, and the deformation rate was negatively correlated with the reservoir filling. The permeability limited the excretion and replenishment of water in the soil. Everytime there is the reservoir water level drawdown, it causes the seepage force and extra pore pressure to the landslide. And if the reservoir water level remains relatively constant after increased, the extra pore water pressure

TABLE 2: The grey relational grade (GRG) between the influencing factor with factor of safety and displacement.

Input	Influencing factors	GRG
Factory of safety	Input 1, the 1-month cumulative antecedent rainfall	0.626
	Input 2, the 2-month cumulative antecedent rainfall	0.605
	Input 3, reservoir level change in the 1-month period	0.681
	Input 4, reservoir level change in the 2-month period	0.703
	Input 5, the average elevation of the reservoir level in the current month	0.610
	Input 6, the displacement of G8 over the past 1 month	0.604
	Input 7, the displacement of G5 over the past 1 month	0.608
The displacement of G5	Input 8, the 1-month cumulative antecedent rainfall	0.664
	Input 9, the 2-month cumulative antecedent rainfall	0.662
	Input 10, reservoir level change in the 1-month period	0.672
	Input 11, reservoir level change in the 2-month period	0.662
	Input 12, the average elevation of the reservoir level in the current month	0.761
	Input 13, the displacement of G8 over the past 1 month	0.941

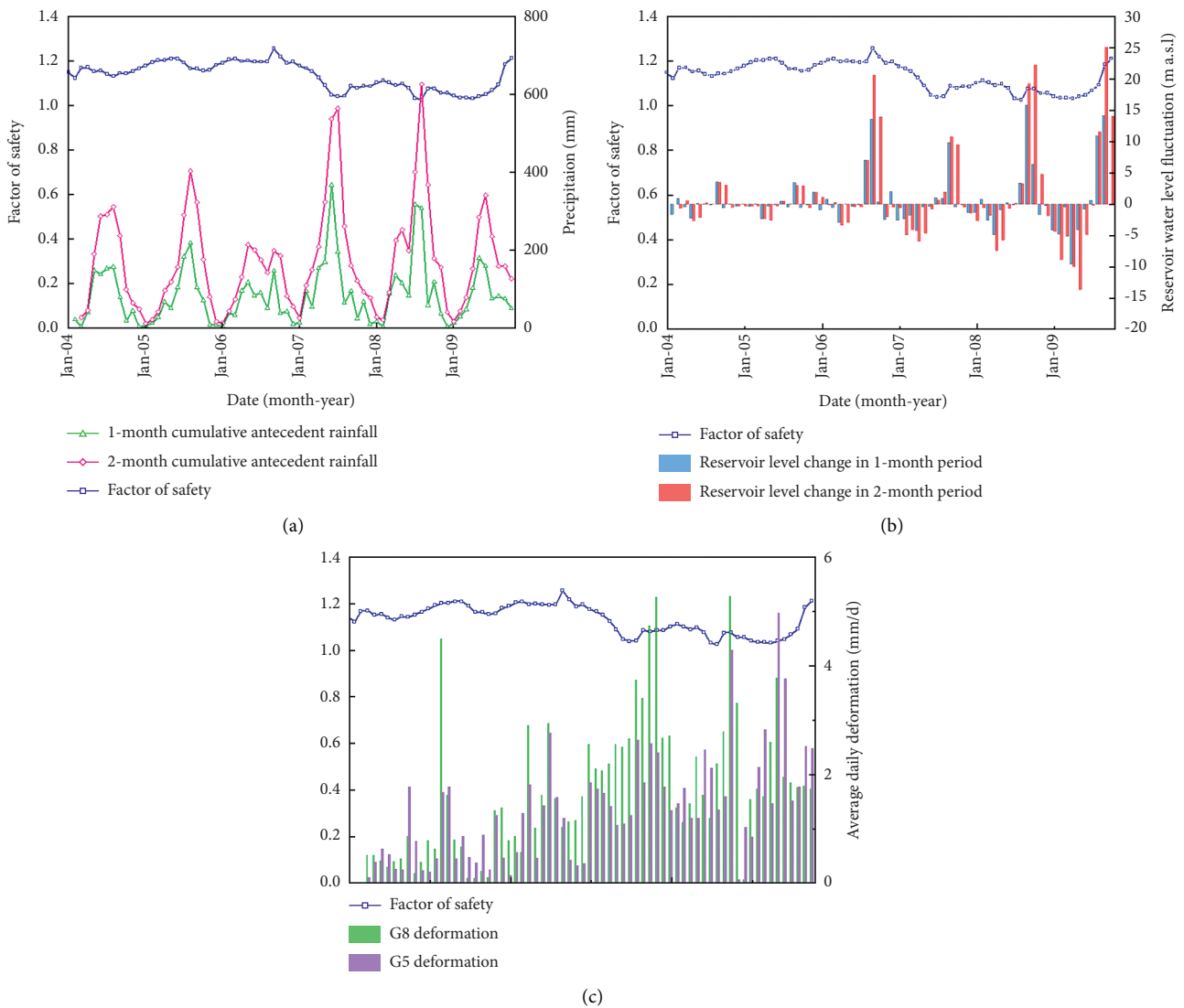


FIGURE 10: External trigger factor analysis with the factor of safety. (a) Accumulated antecedent rainfall; (b) reservoir water level fluctuation; (c) average daily deformation.

would dissipate progressively, which may improve the stability of the landslide and the rate of the deformation would imperceptibly keep steady [44]. From accumulated displacement curves, there exists a stepwise character. Compared with numerical simulation, a simple deformation feature analysis has lower accuracy in determining slope stability.

After calculating the transient safety factor of the slope with multiple rainfall combinations, it is suggested that with the infiltration of the rainwater and its movement within the slope body, the safety factor changes, indicating that in addition to the time effect, there is also a spatial effect. While it is difficult to assess the stability of the landslide mass with numerical simulation on a scene, the external performance becomes necessary then. And the behavior of slopes subjected to water level fluctuations and landslide deformation are increasingly the subject of scientific attention and research.

6. Conclusion

The Shiliushubao landslide is an emblematic slope failure in Huanglashi landslide which is influenced evidently by the water level in Three Gorges Reservoir region. Based on investigation and simulation analyses, these following conclusions were made.

- (1) According to the analysis of GPS surface deformation monitoring of the landslide, the displacements obtained by these GPS stations on the active blocks were relatively large and escalated with time, while the increase of the displacements on the other stations was approximately small in the whole monitoring process. With this trend, if the landslide is not reinforced, the rear part would fail when the sliding of the middle part supplies sufficient space to move.
- (2) The calculation results for landslide stability show that the reactivation triggering factors are mainly corresponded to the water level variations and precipitations. While the process of the reservoir drawdown, the decrease of the groundwater level of landslide lags behind the reservoir water level, which is a typical deterioration of the slope conditions, and increases the accumulated deformation. It shows that the stability is sensitive to the velocity of water level fluctuation.

Discussing the deformation and stability of the landslide, we quantify the importance of each factor on landslide occurrences, and we find that the drawdown of the water level of the Three Gorges Reservoir region could be summarized as the main controlling factor of the deformation of the landslide mass.

Data Availability

The data used to support the findings of this study are included within the article.

Disclosure

Chengdu University of Technology has bought the right for use of Comsol Multiphysics.

Conflicts of Interest

The authors declare that they have no conflicts of interest.

Acknowledgments

The authors sincerely thank Huang Bangzhi, Sun Renxian, and Xia Min for providing facilities for the field survey and their assistance in collecting the data.

References

- [1] M. S. Kim, Y. Onda, J. K. Kim, and S. W. Kim, "Effect of topography and soil parameterisation representing soil thicknesses on shallow landslide modelling," *Quaternary International*, vol. 384, pp. 91–106, 2015.
- [2] L. Liucci, L. Melelli, C. Suteanu, and F. Ponziani, "The role of topography in the scaling distribution of landslide areas: a cellular automata modeling approach," *Geomorphology*, vol. 290, pp. 236–249, 2017.
- [3] A. Agostini, V. Tofani, T. Nolesini et al., "A new appraisal of the ancona landslide based on geotechnical investigations and stability modelling," *The Quarterly Journal of Engineering Geology and Hydrogeology*, vol. 47, pp. 29–43, 2014.
- [4] C. Mark, "An updated empirical model for ground control in u.S. Multiseam coal mines," *International Journal of Mining Science and Technology*, vol. 31, pp. 163–174, 2021.
- [5] H. Rafezi and F. Hassani, "Drilling signals analysis for tricone bit condition monitoring," *International Journal of Mining Science and Technology*, vol. 31, pp. 187–195, 2021.
- [6] J. M. Chang, H. Chen, B. J. D. Jou, N. C. Tsou, and G. W. Lin, "Characteristics of rainfall intensity, duration, and kinetic energy for landslide triggering in taiwan," *Engineering Geology*, vol. 231, pp. 81–87, 2017.
- [7] S. Segoni, A. Rosi, D. Lagomarsino, R. Fanti, and N. Casagli, "Brief communication: using averaged soil moisture estimates to improve the performances of a regional-scale landslide early warning system," *Natural Hazards and Earth System Sciences*, vol. 18, pp. 807–812, 2018.
- [8] K. Roback, M. K. Clark, A. J. West et al., "The size, distribution, and mobility of landslides caused by the 2015 m(w)7.8 gorkha earthquake, Nepal," *Geomorphology*, vol. 301, pp. 121–138, 2018.
- [9] T. Wang, S. R. Wu, J. S. Shi, P. Xin, and L. Z. Wu, "Assessment of the effects of historical strong earthquakes on large-scale landslide groupings in the wei river midstream," *Engineering Geology*, vol. 235, pp. 11–19, 2018.
- [10] M. Alvioli, M. Melillo, F. Guzzetti et al., "Implications of climate change on landslide hazard in central Italy," *The Science of the Total Environment*, vol. 630, pp. 1528–1543, 2018.
- [11] D. J. Peres and A. Cancelliere, "Modeling impacts of climate change on return period of landslide triggering," *Journal of Hydrology*, vol. 567, pp. 420–434, 2018.
- [12] S. Mohammadi and H. Taiebat, "Finite element simulation of an excavation-triggered landslide using large deformation theory," *Engineering Geology*, vol. 205, pp. 62–72, 2016.
- [13] X. Q. Luo, F. W. Wang, Z. H. Zhang, and A. L. Che, "Establishing a monitoring network for an impoundment-

- induced landslide in three gorges reservoir area, China," *Landslides*, vol. 6, pp. 27–37, 2009.
- [14] M. Wang and J. P. Qiao, "Reservoir-landslide hazard assessment based on gis: a case study in wanzhou section of the three gorges reservoir," *Journal of Mountain Science*, vol. 10, pp. 1085–1096, 2013.
- [15] J. C. Cai, N. P. Ju, R. Q. Huang et al., "Mechanism of toppling and deformation in hard rock slope: a case of bank slope of hydropower station, qinghai province, China," *Journal of Mountain Science*, vol. 16, pp. 924–934, 2019.
- [16] X. R. Wang, Q. G. Rong, S. L. Sun, and H. Wang, "Stability analysis of slope in strain-softening soils using local arc-length solution scheme," *Journal of Mountain Science*, vol. 14, pp. 175–187, 2017.
- [17] S. Alemdag, A. Akgun, A. Kaya, and C. Gokceoglu, "A large and rapid planar failure: causes, mechanism, and consequences (mordut, gumushane, Turkey)," *Arabian Journal of Geoscience*, vol. 7, pp. 1205–1221, 2014.
- [18] J. Zhuang, J. Peng, G. Wang, I. Javed, Y. Wang, and W. Li, "Distribution and characteristics of landslide in loess plateau: a case study in shaanxi province," *Engineering Geology*, vol. 236, pp. 89–96, 2018.
- [19] H. Hong, W. Chen, C. Xu, A. M. Youssef, B. Pradhan, and B. T. Dieu, "Rainfall-induced landslide susceptibility assessment at the chongren area (China) using frequency ratio, certainty factor, and index of entropy," *Geocarto International*, vol. 32, pp. 139–154, 2017.
- [20] Z. L. Wei, Y. Q. Shang, H. Y. Sun, H. D. Xu, and D. F. Wang, "The effectiveness of a drainage tunnel in increasing the rainfall threshold of a deep-seated landslide," *Landslides*, vol. 16, pp. 1731–1744, 2019.
- [21] A. A. E. Zehairy, M. M. Nezhad, V. N. Joekar, I. Guymmer, N. Kourra, and M. A. Williams, "Pore-network modelling of non-Darcy flow through heterogeneous porous media," *Advances in Water Resources*, vol. 131, 2019.
- [22] G. H. Wang and K. Sassa, "Pore-pressure generation and movement of rainfall-induced landslides: effects of grain size and fine-particle content," *Engineering Geology*, vol. 69, pp. 109–125, 2003.
- [23] S. Matsuura, S. Asano, and T. Okamoto, "Relationship between rain and/or meltwater, pore-water pressure and displacement of a reactivated landslide," *Engineering Geology*, vol. 101, pp. 49–59, 2008.
- [24] J. Zhao, J. Chen, X. Zhan, J. Ning, and Y. Zhang, "Distribution characteristics of floor pore water pressure based on similarity simulation experiments," *Bulletin of Engineering Geology and the Environment*, vol. 79, 2020.
- [25] E. Conte and A. Troncone, "A performance-based method for the design of drainage trenches used to stabilize slopes," *Engineering Geology*, vol. 239, pp. 158–166, 2018.
- [26] Y. G. Zhang, J. Qiu, Y. Zhang, and Y. Wei, "The adoption of elm to the prediction of soil liquefaction based on cpt," *Natural Hazards*, vol. 107, pp. 539–549, 2021.
- [27] S. Shao, "A novel coating technology for fast sealing of air leakage in underground coal mines," *International Journal of Mining Science and Technology*, vol. 31, 2021.
- [28] Y. Zhang, Z. Zhang, S. Xue, R. Wang, and M. Xiao, "Stability analysis of a typical landslide mass in the three gorges reservoir under varying reservoir water levels," *Environmental Earth Science*, vol. 79, 2020.
- [29] L. K. Chen, L. Z. Jiang, H. X. Qin et al., "Nonlinear seismic assessment of isolated high-speed railway bridge subjected to near-fault earthquake scenarios," *Structure and Infrastructure Engineering*, vol. 15, pp. 1529–1547, 2019.
- [30] L. K. Chen, A. Kurtulus, Y. F. Dong, E. Taciroglu, and L. Z. Jiang, "Velocity pulse effects of near-fault earthquakes on a high-speed railway vehicle-ballastless track-benchmark bridge system," *Vehicle System Dynamics*, vol. 25, 2021.
- [31] L. K. Chen, P. Liu, L. M. Zhu, J. B. Ding, Y. L. Feng, and F. Moreu, "A simplified iterative approach for testing the pulse derailment of light rail vehicles across a viaduct to near-fault earthquake scenarios," *Proceedings of the Institution of Mechanical Engineers - Part F: Journal of Rail and Rapid Transit*, 2021.
- [32] Y. G. Zhang, J. Tang, R. P. Liao et al., "Application of an enhanced bp neural network model with water cycle algorithm on landslide prediction," *Stochastic Environmental Research and Risk Assessment*, vol. 35, pp. 1273–1291, 2021.
- [33] L. K. Chen, H. X. Qin, L. Z. Jiang, and L. Xu, "A vertical near-fault scenario earthquakes-based generic simulation framework for elastoplastic seismic analysis of light rail vehicle-viaduct system," *Vehicle System Dynamics*, vol. 59, pp. 949–973, 2021.
- [34] W. Hou, H. Wang, L. Yuan, W. Wang, Y. Xue, and Z. Ma, "Experimental research into the effect of gas pressure, particle size and nozzle area on initial gas-release energy during gas desorption," *International Journal of Mining Science and Technology*, vol. 31, pp. 253–263, 2021.
- [35] Y. Zhang, J. Qiu, Y. Zhang, and Y. Xie, "The adoption of a support vector machine optimized by gwo to the prediction of soil liquefaction," *Environ Earth Sci*, vol. 80, 2021.
- [36] M. Xia, G. M. Ren, S. S. Zhu, and X. L. Ma, "Relationship between landslide stability and reservoir water level variation," *Bulletin of Engineering Geology and the Environment*, vol. 74, pp. 909–917, 2015.
- [37] G. Wang, X. Qin, D. Han, and Z. Liu, "Study on seepage and deformation characteristics of coal microstructure by 3d reconstruction of ct images at high temperatures," *International Journal of Mining Science and Technology*, vol. 31, pp. 175–185, 2021.
- [38] A. Corsini and M. Mulas, "Use of roc curves for early warning of landslide displacement rates in response to precipitation (piagneto landslide, northern apennines, Italy)," *Landslides*, vol. 14, pp. 1241–1252, 2017.
- [39] Z. Dai, S. Chen, and J. Li, "Physical model test of seepage and deformation characteristics of shallow expansive soil slope," *Bulletin of Engineering Geology and the Environment*, vol. 79, 2020.
- [40] Y. Zhang, Y. Xie, Y. Zhang, J. Qiu, and S. Wu, "The adoption of deep neural network (dnn) to the prediction of soil liquefaction based on shear wave velocity," *Bulletin of Engineering Geology and the Environment*, vol. 80, pp. 5053–5060, 2021.
- [41] L. K. Chen, R. P. Yuan, X. J. Ji et al., "Modular composite building in urgent emergency engineering projects: a case study of accelerated design and construction of wuhan thunder god mountain/leishenshan hospital to covid-19 pandemic," *Automation in Construction*, vol. 124, 2021.
- [42] B. Yang, K. Yin, S. Lacasse, and Z. Liu, "Time series analysis and long short-term memory neural network to predict landslide displacement," *Landslides*, vol. 16, pp. 677–694, 2019.
- [43] Y. Zhang, S. Zhu, J. Tan, L. Li, and X. Yin, "The influence of water level fluctuation on the stability of landslide in the three gorges reservoir," *Arabian Journal of Geoscience*, vol. 13, 2020.
- [44] Y. Zhang, S. Zhu, W. Zhang, and H. Liu, "Analysis of deformation characteristics and stability mechanisms of typical landslide mass based on the field monitoring in the three gorges reservoir, China," *Journal of Earth System Science*, vol. 128, 2018.

Research Article

Modulus Inversion Layer by Layer of Different Asphalt Pavement Structures

Mingming Cao ¹, Wanqing Huang,¹ Yiwen Zou,² and Guomin Liu³

¹Sichuan Communication Surveying and Design Institute CO., LTD, Chengdu 610041, China

²School of Civil Engineering, Southwest Jiaotong University, Chengdu 610031, China

³School of Civil Engineering, Sichuan Vocational and Technical College of Communications, Chengdu 611130, China

Correspondence should be addressed to Mingming Cao; 707360021@qq.com

Received 25 July 2021; Accepted 25 August 2021; Published 3 September 2021

Academic Editor: Zhiyong Chen

Copyright © 2021 Mingming Cao et al. This is an open access article distributed under the Creative Commons Attribution License, which permits unrestricted use, distribution, and reproduction in any medium, provided the original work is properly cited.

In order to improve the accuracy of modulus inversion of the pavement structure layer, a layer-by-layer inversion method was proposed to be compared with the traditional inversion method by inverting the modulus of each structural layer of the inverted asphalt pavement and semirigid asphalt pavement. The results show that the influence of cushion modulus on the modulus of inverted subgrade and modulus of cement-stabilized crushed stone is restricted by the cushion modulus and pavement structure characteristics, and the thicker cement-stabilized crushed stone layer is beneficial for improving inverted modulus of subgrade; besides, for the inverted asphalt pavement, the modulus of the graded crushed stone transition layer has a significant influence on the modulus inversion of cement-stabilized crushed stone. The modulus of the graded gravel transition layer inverted by these two methods is underestimated, the modulus of cement-stabilized gravel is overestimated using the traditional inversion method, and the inversion result of the inverted asphalt pavement is more significantly affected by the inversion method than the semirigid base asphalt pavement. Moreover, the modulus of the pavement structural layer is determined by the material and structural characteristics, and its recommended empirical value or the value in the indoor test does not conform to the actual value of the site; by contrast, the inversion modulus obtained using the layer-by-layer inversion method is closer to the actual value, which can be used in the design of similar pavement structures to accumulate data for determining the material modulus or the pavement structure adjustment coefficient in the pavement structure.

1. Introduction

The deflection basin can comprehensively reflect the structural characteristics (thickness, layer position), material characteristics (modulus, etc.) of each structural layer of the pavement, and external factors (temperature, humidity, and traffic conditions), and it can also indirectly evaluate the operation duration of the road, etc. [1–3]. Research on the modulus inversion of pavement structure layer mainly focuses on the following aspects: (1) the influence of the thickness of pavement structure layer, interlayer contact, and the temperature on the inverted modulus [4–7]; (2) the establishment of the correction coefficient between the modulus of each pavement structure layer material in indoor test and the inverted modulus to characterize the

relationship between the inverted modulus and the actual modulus of the pavement structure [8–10]; besides, the research subject mainly includes semirigid base asphalt pavement and flexible base asphalt pavement, but inverted structure asphalt pavement is few studied.

The traditional inversion method is to substitute the initial value directly, maximum value, and minimum value of the modulus of each structural layer into the inversion software, in which the deflection value is the dynamic deflection of the pavement surface. It has been found that using the dynamic deflection makes the deviation coefficient of the inverted modulus large, especially for the base layer and the subbase layer, their deviation coefficient is mostly between 60 and 90%, and the system error of 1%~2% of the deflection sensor may lead to 10%~20% inversion modulus error

[11, 12]. In addition, so far, FWD is mostly used to test deflection basins of the pavement surface to evaluate the bearing characteristics, during which 95% of FWD load acts on the pavement surface and spreads to the underlying structural layer, and 5% is directly loaded on the roadbed. There are few studies on testing the distribution of deflection basins in each layer and inverting the modulus of each structural layer [13, 14].

RN Stubstad [15] emphasized the feasibility of controlling the quality of applying FWD to the pavement construction; the dynamic deflection value of the main layers was tested layer by layer, and the equivalent pavement modulus was solved using the empirical formula, but the evaluation of the modulus inversion of each layer was not carried out layer by layer. Based on the Wisdom Road project in Virginia, Nassar et al. [16] used FWD to test the dynamic deflection of each layer during the construction of flexible pavement to invert the modulus of the main structural layers, and the modulus of each structural layer was inverted layer by layer. Solanki et al. [17] analyzed the difference between the inverted modulus of subgrade and base layer and the laboratory test value when the FWD was loaded at different layers of the flexible pavement, but the difference in the inverted modulus under the different working conditions and using the traditional inversion method was not analyzed. Liao et al. [18] adopted the Beckman beam method to test the static deflection of semirigid pavement layer by layer and used the elastic layered system to invert the modulus of the cement-stabilized gravel base and asphalt surface. However, because the Beckman beam method is a static test method, the test error is relatively large.

In the inverted asphalt pavement, there is a graded gravel transition layer with relatively low strength between the cement-stabilized crushed stone base and the asphalt layer, which makes the pavement structure more complex and the inverted modulus more variable. In addition, because the asphalt surface is greatly influenced by the temperature and exhibits obvious viscoelastic properties, the accuracy of the modulus inversion results of the lower layers is significantly affected, which can be improved using the layer-by-layer inversion modulus method. In this paper, a layer-by-layer inversion modulus method was proposed. Further, based on the dynamic response test section of the asphalt pavement of Sichuan-Guangzhou Expressway, the inverted modulus of the three structures using the traditional inversion method and the layer-by-layer inversion method was compared.

2. Test Scheme and Inversion Method

2.1. Test Scheme. The Sichuan Sui-Guang Expressway adopts the S1 structure, four lanes in two directions; the total length of the test roadway is 646.8 m, including three types of pavement structures, as shown in Table 1. Among them, S1 (semirigid structure) is 99 m in length, S2 (inverted structure 1) is 301 m in length, S3 (inverted structure 2) is 246.8 m in length, and the total thickness is 89 cm. By referring to “Highway Subgrade and Pavement Field Test Regulations”

(JTGE60-2008), the resilient modulus of the subgrade and cushion layer was tested through the load-bearing board test (Figure 1), and the PRIMAX1500 FWD was used to test the dynamic deflection of each layer from the base layer to the top of the upper layer (Figure 2), in which the sensor was installed 0 cm, 20 cm, 30 cm, 40 cm, 50 cm, 60 cm, 90 cm, 120 cm, 150 cm, 180 cm, and 210 cm away from the loading center, respectively. In addition, the FWD test of the cement-stabilized crushed stone base layer is 30 days after its construction completed, and the subsequent test intervals of each layer are within 48 h.

2.2. Layer-by-Layer Inversion Modulus Method. The layer-by-layer inversion modulus method is to firstly load FWD to the top surface of the base course to test deflection value and to determine the inverted modulus of the cement-stabilized crushed stone layer, subgrade, and cushion layer. Then, while inverting the modulus of the transition layer, the material parameters (including the conditions of fixed modulus of part of the structural layer and limiting the initial value and maximum and minimum modulus of all structural layers) were substituted in the inversion; finally, the inverted modulus of the structural layer was comprehensively determined based on multiple inversion result. The modulus of the asphalt surface layer can also be determined following the procedure above. During the inversion, the deflection value of each structural layer was adopted, and the modulus of each structural layer needs to be determined through multiple inversions layer by layer. If it is necessary, field test methods such as load-bearing plates can be used to determine the modulus of part of layers. This method reduces the number of variables of the inverted structural layer, improving the inversion accuracy, and the layer-by-layer deflection test reduces the influence of the test error.

Based on the iterative method, to invert the pavement structure layer modulus is relatively mature [19], and Mao’s [20] study shows that the modulus of the linear and non-linear inversion of the graded pavement is relatively consistent, and the graded gravel layer can be considered a linear elastic material for inversion. Smith et al. [21] compare the existing inversion methods and believe that the dynamic inversion method is not perfect enough and the time and frequency dominated inversion methods have certain drawbacks. Therefore, this paper uses an ECERCALC5.0 program to invert the pavement structure layer modulus.

3. Modulus Inversion of Each Structure Layer of the Pavement

3.1. The Measurement of the Modulus of Graded Gravel and Subgrade Using the Load-Bearing Plate Method. The load-bearing plate method is mainly used to test the modulus of graded crushed rock and subgrade for comparison with the inverted modulus and is also used to determine the modulus of the graded crushed rock cushion layer indirectly. The test results of the resilient modulus of graded gravel and subgrade are shown in Table 2. The tested average modulus of

TABLE 1: The structure of the test section.

Pavement structure	S1 (semirigid structure)	S2 (inverted structure 1)	S3 (inverted structure 2)	
The asphalt mastic macadam SMA upper surface layer (cm)		4		
The SBS modified asphalt AC-20°C middle surface layer (cm)		6		
The lower surface layer	The type The thickness (cm)	Asphalt AC-20°C 8	The SBS modified asphalt AC-20°C 8	ATB-25 12
The graded crushed stone transition layer (cm)		—	12	
The cement-stabilized crushed stone base (cm)		28	20	
The cement-stabilized crushed stone subbase (cm)		28	24	20
The graded crushed stone cushion layer (cm)		15	15	15
The total pavement thickness (cm)		89	89	89



FIGURE 1: Field test of the bearing plate.



FIGURE 2: FWD field testing.

the cushion layer by the bearing plate method is 309 MPa, and the average subgrade modulus is 161 MPa.

3.2. Influence of Modulus of the Graded Gravel Cushion Layer on the Inverted Modulus of Subgrade and Cement-Stabilized Gravel. The inversion accuracy of the modulus of each structural layer using the iteration method tends to decrease

with the increase of the number of structural layers, and the optimal number is 3~4. For the subgrade and graded crushed stone cushion layer, they can be regarded as two layers for inversion when FWD is loaded on the top surface of the base course, and they must be treated as one layer when the top surface of other structural layers is loaded. But when they are regarded as two layers of inversion, and the maximum value of modulus of the graded crushed stone cushion layer is not limited, the inverted modulus value is 2271 MPa, which exceeds the upper limit of 700 MPa recommended by “Asphalt Pavement Design Specification JTG050-017.” Therefore, it is necessary to study the influence of the modulus of graded crushed stone cushion layer on the inversion results of subgrade modulus and cement-stabilized crushed stone modulus. The following conclusions can be drawn from Figure 3:

- (1) The inverted modulus of subgrade and cement-stabilized crushed stone both decrease with the increase of set modulus of the stone cushion layer from 100 MPa to 800 MPa, but the decreasing amplitude of the inverted modulus of subgrade, from large to small, is semirigid structure (38.44%), inverted structure 1 (23.43%), and inverted structure 2 (19.98%), while the decreasing amplitude of inverted modulus of cement-stabilized crushed, from small to large, is semirigid structure (8.11%), inverted structure 1 (20.69%), and inverted structure 2 (37.39%).
- (2) As the modulus of the graded crushed stone cushion layer increases, the modulus curve of the subgrade shows two different stages, and two inflection points appear when the cushion modulus is 200 MPa (semirigid structure) and 150 MPa (inverted structure). Except for the inverted structure 2, the modulus curve of cement-stabilized crushed stone decreases linearly with the increase of the modulus of the graded crushed stone cushion layer; the modulus curve of cement-stabilized crushed stone of the inverted structure 2 shows two different stages, and the inflection point appears when the cushion modulus is 300 MPa. Smaller modulus of the graded

TABLE 2: Test modulus of the subgrade and graded gravel.

Structural layer	Modulus (MPa)							Average value (MPa)	Standard deviation	Variation coefficient (%)
Subgrade	97	175	220	166	192	132	144	161	37.5	23.3
Cushion layer	400	217	301	385	266	284	—	309	64.6	20.9

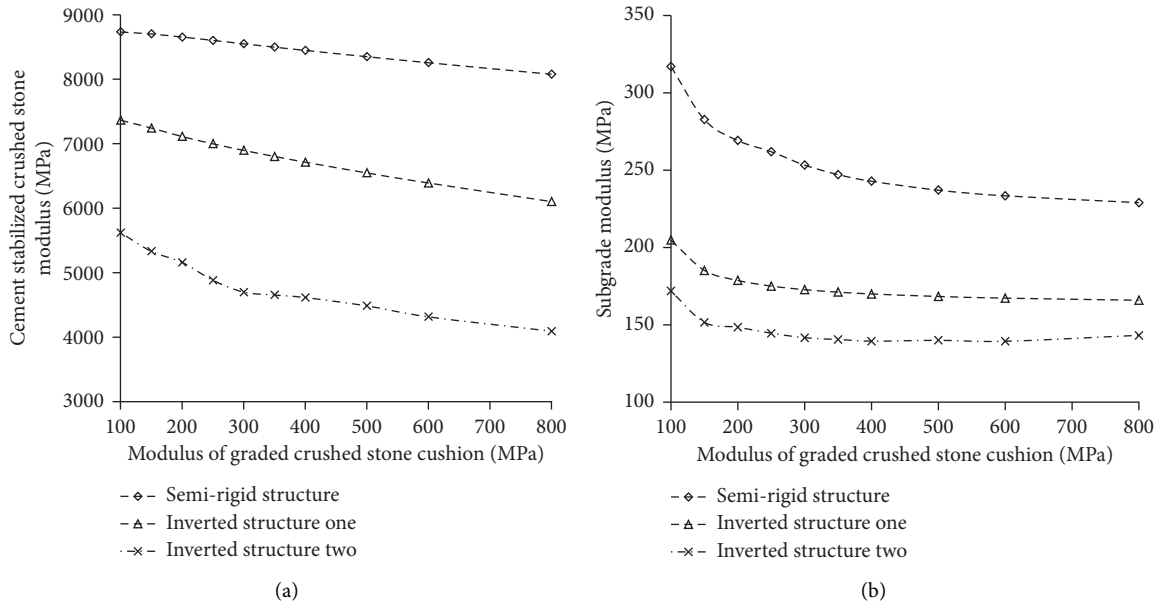


FIGURE 3: Influence of the variation of cushion modulus on modulus inversion of the structure layer.

crushed stone cushion layer has a greater impact on subgrade modulus and cement-stabilized crushed stone modulus, and the influence degree has a certain dependence on the pavement structure characteristics.

- (3) Although the tested resilient modulus of the structure layer using the bearing plate method is the static elastic modulus, and the inverted modulus using the deflection value tested by FWD is the dynamic value, they show a high correlation [22–24]; besides, the inverted modulus of graded crushed stone cushion layer is much greater than the measured value.

3.3. Modulus Inversion of Subgrade. Based on the test of the subgrade modulus using the bearing plate, the FWD load was applied to the top surface of each structural layer to test the dynamic deflection to inverse their modulus, as shown in Tables 3 and 4.

- (1) The inverted modulus of different pavement structures with different thicknesses of the cement-stabilized crushed stone layer is different; this is because when the FWD load is applied to the top surface of the base course, the inverted modulus of the thicker cement-stabilized crushed stone layer is relatively large. At the same time, in the pavement structure system, the subgrade is considered to extend infinitely in the depth direction, the equivalent modulus of the subgrade and the cushion layer is mainly dominated by the subgrade modulus, and the ratio of

the cushion modulus to the subgrade modulus is much smaller than the base modulus and cushion modulus. Moreover, by regarding the subgrade and cushion layer as two layers and one layer, the inverted modulus of the cement-stabilized gravel layer is 6881 MPa and 6330 MPa, respectively, indicating that combining them as one layer has little effect on the inversion value of the modulus of the cement-stabilized crushed stone layer.

- (2) When the FWD load is applied to the top surface of the underlying layer of three different structures, the difference in inverted equivalent modulus of the cushion top surface is the largest, in which the equivalent modulus of the cushion top surface of the semirigid structure is the largest, and that of the inverted structure 2 is the smallest. At the same time, when the FWD is loaded at different structural levels, the variation coefficient of the equivalent modulus of the top surface of the cushion layer, from larger to small, is semirigid structure (53.18%), inverted structure 1 (34.35%), and inverted structure 2 (27.28%). This is mainly because the performance of the asphalt mixture is relatively sensitive to temperature, showing obvious characteristics of viscoelastic and delayed elastic recovery [25, 26], and the deflection and the inverted modulus value are both affected by the test temperature. Besides, differences in the thickness of the underlying layer or asphalt type

TABLE 3: The inverted modulus of the structural layer (FWD on the top surface of the base course) (MPa).

Structure type	4-layer system	3-layer system	3-layer system	4-layer system
Semirigid structure	190	220	202	201
Inverted structure 1	166	167	172	172
Inverted structure 2	144	144	141	140
Note	Base course, subbase course, cushion layer, and subgrade	Cement-stabilized crushed stone layer, cushion layer, and subgrade	Cement-stabilized crushed stone layer, cushion layer with a modulus of 309 MPa, and subgrade	Base course, subbase course, cushion layer with the modulus of 309 MPa, and subgrade

TABLE 4: Inverted equivalent modulus of the top surface of the cushion layer.

Pavement structure	Layer subjected to FWD						Note
	Base course	Transition layer	Underlying layer	Middle surface layer	Upper surface layer	Average value	
Semirigid structure	243	—	502	189	191	281	
Inverted structure 1	206	127	314	165	204	203	Cement-stabilized crushed stone layer, asphalt surface layer, and subgrade were, respectively, combined with the cushion layer to perform inversion
Inverted structure 2	174	93	108	121	168	133	
Average value	207	110	308	159	188	194	

between different pavement structures induce the inversion error. At the same time, as the number of inversion variables increases, the inversion accuracy decreases, and a thicker asphalt layer can reduce its influence on the load transfer. Using the deflection of the top surface of the base course to inverse the modulus is beneficial for improving the inversion accuracy of the equivalent modulus of the top surface of the cushion layer. Therefore, the layer-by-layer inversion method is recommended to determine the modulus of each structural layer.

- (3) The subgrade of the field test section is constructed continuously, and the material difference is small. The subgrade modulus under each structural layer should be the same, and when the FWD load is applied to the top surface of the base course, the average value of the inverted subgrade modulus of three sections is 172 MPa, which is 1.07 times that of the test result using the bearing plate. Therefore, the modulus of subgrade and the graded crushed stone transition layer of this section are taken the test value of the bearing plate, and the equivalent modulus of the cushion top surface is calculated to be 204 MPa, which is basically the same as the inverted equivalent modulus of the top surface of cushion layer 207 MPa. It is furtherly proving the reasonability of combining the subgrade and cushion layer into one layer.

3.4. Determination of Inverted Modulus of the Graded Crushed Stone Transition Layer. The graded crushed stone is a nonlinear granular, and its modulus is greatly affected by the stiffness of the underlying layer, so the bearing plate method cannot truly reflect the modulus of graded crushed stone transition layer of the loaded asphalt pavement, and the variability of the modulus of the graded crushed stone is large [27, 28]. It can be seen from Figure 4 that as the modulus of the graded crushed stone transition layer increases, the equivalent modulus of the top surface of the cushion layer of inverted structure changes less, while the inverted modulus of the asphalt surface layer and cement-stabilized crushed stone gradually decrease using the traditional inversion method, and the decreased amplitude of modulus of the asphalt surface layer is less than that of the cement-stabilized crushed stone layer; their decreased amplitude of modulus shows flexion points at 200–300 MPa and 300–500 MPa, respectively.

According to Table 5, it can be known that when the FWD is loaded on the top surface of the graded crushed stone transition layer, the average value of the inverted modulus of the graded gravel transition layer in three test sections is 243 MPa, which is lower than the value tested by the bearing plate. Because the graded crushed stone is a kind of nonlinear and discrete material, its strength is highly dependent on stress; when the underlying layer is a semirigid material, the modulus of the graded crushed stone transition layer (the modulus of the graded crushed stone transition

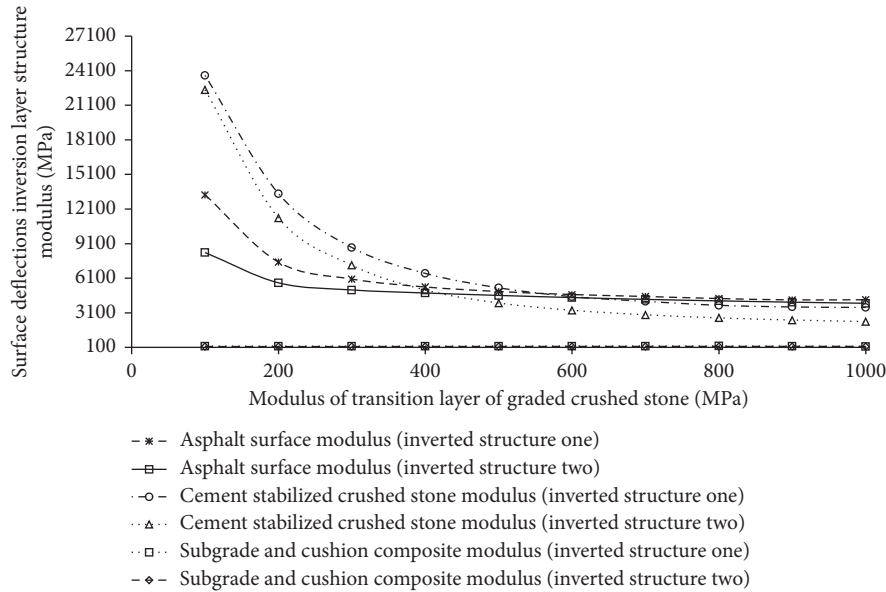


FIGURE 4: Influence of modulus of the graded crushed stone transition layer on modulus inversion of each structure layer.

TABLE 5: The inverted modulus of the graded crushed stone transition layer (MPa).

Pavement structure	Transition layer	Layer subjected to FWD			Note
		Underlying layer	Middle surface layer	Upper surface layer	
Inverted structure 1	265	150	103	163	Cement-stabilized crushed stone layer, asphalt surface layer, and subgrade were, respectively, combined with the cushion layer to perform inversion
Inverted structure 2	220	100	100	114	
Average value	243	125	102	139	

layer tested by the load-bearing board is often above 400 MPa) is greater than that when the underlying layer is subgrade. Before laying the lower asphalt layer, the inverted modulus of the graded crushed stone transition layer is greater than that based on the tested deflection by applying FWD on the top surface of the asphalt layer; this is mainly because the strength of the graded crushed stone transition layer depends on the stress. When the FWD is loaded on the top surface of the asphalt layer, the stress level of the graded crushed stone layer is lower, inducing the lower modulus. The inverted modulus of graded crushed rock by the traditional inversion method is often lower than the actual value. For the inverted asphalt pavement, the modulus of the graded crushed stone transition layer inverted by the traditional inversion method is often lower than the actual value, while the modulus tested by the bearing plate method is often higher than the actual value. Therefore, the dynamic deflection tested by applying the FWD on the top surface of the graded crushed stone transition layer is used to invert its modulus.

3.5. *Modulus Inversion of the Cement-Stabilized Crushed Stone Layer.* The accuracy of the inverted modulus of the inverted pavement using the EVERCALC software is lower than that of the flexible pavement. When the FWD is loaded on

the asphalt pavement, the accuracy of the inverted modulus of the cement-stabilized crushed stone is less than that when the FWD is directly loaded on the top surface of the base course. According to Table 6, the following can be known:

- (1) Under the condition of the same thickness of cement-stabilized crushed stone and pavement structure composition, with the increase of the thickness of the asphalt layer, the inverted modulus of cement-stabilized crushed stone gradually increases, and the inverted modulus of the base course based on the dynamic deflection of the pavement surface is the largest. Besides, the modulus of cement-stabilized crushed stone also has a certain relationship with its thickness.
- (2) The modulus of the graded crushed stone transition layer has a great influence on the modulus inversion of cement-stabilized crushed stone. When the modulus of the graded crushed stone transition layer is 400 MPa, the inverted modulus of the cement-stabilized crushed stone is 0.55~0.97 times that of 243 MPa. Moreover, the closer the loading position is to the graded crushed stone transition layer, the smaller the effect of the modulus of the graded crushed stone transition layer on the modulus of the

TABLE 6: The inverted modulus of cement-stabilized crushed stone (MPa).

Pavement structure	The modulus of the transition layer	Layer subjected to FWD				Upper surface layer
		Base course	Transition layer	Underlying layer	Middle surfacelayer	
Semirigid structure	—	8417	—	4779	6732	11468
Inverted structure 1	Inverted value	6330	7104	2846	8490	17715
	243 MPa	—	7188	1725	3113	10980
	400 MPa	—	6725	1600	2027	6518
Inverted structure 2	Inverted value	4762	5187	7299	8707	21773
	243 MPa	—	5076	2376	2690	9116
	400 MPa	—	4903	1744	1768	5070

cement-stabilized crushed stone layer is. At the same time, the greater the modulus of the graded crushed stone transition layer, the smaller the inverted modulus of cement-stabilized crushed stone.

- (3) The graded crushed stone is a kind of nonlinear and discrete material, and its modulus is greatly affected by external factors such as load and humidity. In order to accurately invert the modulus of cement-stabilized crushed stone, the FWD is recommended to load on the top surface of the base course to test deflection, so as to reduce the influence of other structural layers on the inversion results. According to different structures, different moduli of cement-stabilized crushed stone of the semirigid structure, the inverted structure 1, and the inverted structure 2 are selected as 8417 MPa, 6330 MPa, and 4762 MPa, respectively.

3.6. Modulus Inversion of the Asphalt Surface. Because the modulus of the asphalt surface is greatly affected by temperature, the inversion result needs to be corrected based on the reference temperature of 20°C. It can be known from Table 7 that the inverted modulus of asphalt surface is affected by asphalt mixture type, the thickness of asphalt surface, and the modulus of the graded crushed stone transition layer; the greater the modulus of the graded crushed stone transition layer, the lower the inverted modulus of the asphalt surface layer, but the dispersion of the inverted modulus will be greater. But, the influence of asphalt mixture type and the thickness of the asphalt surface layer is not obvious. On the whole, the thicker asphalt mixture has less influence on the modulus inversion of the asphalt surface, so the equivalent modulus of the asphalt mixture is selected based on the deflection of the pavement surface. Besides, under different inversion conditions, the inverted modulus of the asphalt surface is quite different, but its result using the traditional inversion method is closer to that using the layer-by-layer inversion method. Therefore, under different inversion criteria, the inverted modulus of the asphalt surface layer is more discrete, and it is necessary to test the deflection layer by layer to reduce the influence of the material and structural characteristics of each layer above on the inverted modulus of the structural layer.

4. The Determination of Modulus of the Structural Layer in the Test Section

As a kind of discrete material, the strength of the graded crushed stone is greatly affected by the load level and shows obvious nonlinearity, which makes its modulus value often underestimated during inversion, and the cement-stabilized crushed stone layer causes the most significant error during the modulus inversion of the inverted structure. At the same time, the modulus of subgrade and the graded crushed stone cushion layer is greatly affected by seasons and rainfall, so they are not fixed during the layer-by-layer inversion. The comparison between the inverted modulus using the layer-by-layer inversion method and the traditional inversion method is shown in Table 8.

- (1) The difference in the inverted equivalent modulus of the top surface of the cushion layer using these two methods is relatively small, and the result of the layer-by-layer inversion method is 1.01~1.23 times that of the traditional inversion method. This is corresponding to the conclusions through numerical analysis in the literature [29].
- (2) Because the graded crushed stone material has obvious nonlinearity, when it is in different layers, its modulus varies greatly, and it is related to the strength of the pavement structure and adjacent layers. Both inversion methods underestimate the modulus of the graded crushed rock transition layer, and the modulus of the graded crushed rock transition layer determined by the layer-by-layer inversion method is 1.4 to 2.2 times that of the traditional inversion method; besides, the thinner the cement-stabilized crushed stone layer, the greater the difference in the modulus determined by these two methods. This is because the modulus of graded crushed stone has obvious load dependence, and when the FWD is transferred to the graded crushed stone structure layer, it is already smaller than the value loaded on the top surface of this layer. Leading to a small inverted modulus, however, when the FWD is directly loaded on the top surface of the graded crushed stone structure layer, the load is greater than that on the pavement surface, and because the asphalt surface layer is not paved, the bearing plate area

TABLE 7: Inverted modulus of the asphalt surface (MPa).

Pavement structure	The modulus of the base course	The modulus of the transition layer	Layer subjected to FWD		
			Underlying layer	Middle surface layer	Upper surface layer
Semirigid structure	The determination of modulus inversion		5852	4634	12054
	Modulus of base course 8417 MPa		2043	3418	16626
Inverted structure 1	The determination of modulus inversion		10413	6884	11514
	The determination of modulus inversion	The modulus of the transition layer 243 MPa	7576	4444	8823
		The modulus of the transition layer 400 MPa	3598	3585	7045
	The determination of modulus inversion		10847	6535	9072
	Modulus of base course 6330 MPa	The modulus of the transition layer 243 MPa	5025	3077	12216
		The modulus of the transition layer 400 MPa	1494	1606	7454
Inverted structure 2	The determination of modulus inversion		6703	7349	9831
	The determination of modulus inversion	The modulus of the transition layer 243 MPa	4627	5927	7065
		The modulus of the transition layer 400 MPa	3477	4898	6359
	The determination of modulus inversion		6396	7006	7257
	Modulus of base course 4762 MPa	The modulus of the transition layer 243 MPa	3005	4144	9257
		The modulus of the transition layer 400 MPa	1651	2556	6073

TABLE 8: The comparison between the inverted modulus using the layer-by-layer inversion method and traditional inversion method (MPa).

Structure layer	Inversion calculated layer	Modulus using the layer-by-layer inversion method	Modulus using the traditional inversion method
Semirigid structure	Asphalt surface	16626	12054
	Cement-stabilized crushed stone layer	8417	11468
	Equivalent modulus of the top surface of the cushion layer	207	191
Inverted structure 1	Asphalt surface	12216	11514
	Graded crushed stone transition layer	243	163
	Cement-stabilized crushed stone layer	6330	17715
	Equivalent modulus of the top surface of the cushion layer	207	204
Inverted structure 2	Asphalt surface	9257	9831
	Graded crushed stone transition layer	243	114
	Cement-stabilized crushed stone layer	4762	21773
	Equivalent modulus of the top surface of the cushion layer	207	168

is small, the surrounding top surface is in an unconstrained state, and the 3d stress state cannot be formed inside the graded crushed stone, which makes the measured modulus is still smaller than the actual value but slightly larger than the inverted modulus using the traditional inversion method.

- (3) For the semirigid structure and the inverted structure, their moduli of the cement-stabilized crushed stone are both overestimated by the traditional inversion method; but for the inverted structure, the modulus of

cement-stabilized crushed stone determined by the layer-by-layer inversion method is 0.2~0.4 times that of the traditional inversion method, and for the semirigid asphalt pavement, the modulus of cement-stabilized gravel determined by the layer-by-layer inversion method is 0.74 times that of the traditional inversion method. The inverted modulus of cement-stabilized crushed stone has a certain correlation with its thickness and modulus of the adjacent layer. In the inverted asphalt pavement, the graded crushed stone

structure layer above the cement-stabilized crushed stone layer greatly weakens the bearing capacity of the cement-stabilized crushed stone layer, making the inverted modulus value much smaller than the material's actual value. Therefore, inverted asphalt pavement should adopt the layer-by-layer inversion modulus method to determine the modulus of each structural layer.

- (4) While using the layer-by-layer inversion method and traditional inversion method to determine the modulus of cement-stabilized crushed stone, FWD is, respectively, loaded on the top surface of the base course and the pavement surface, the shape, and amplitude of the load distribution on the top surface of the cement-stabilized crushed stone layer are quite different, in which, with the traditional inversion method, the load transferred to the top surface of the cement-stabilized layer is in the shape of a bell with high in the middle and low on both sides, and the spreading ability to the surroundings is worse than the uniform distribution. Besides, the longer the load transfer path, the more the upper layer of the cement-stabilized gravel layer, and the more complicated the material properties, the greater the degree of overestimation of the inverted modulus [29] Because the thickness of the asphalt layer on the top surface of the inverted structure 2 is large, and the thickness of the cement-stabilized crushed stone layer is small, the modulus of the cement-stabilized crushed stone inverted by the traditional inversion method will be higher than the layer-by-layer inversion method. At the same time, the traditional inversion method underestimates the modulus of the graded crushed stone transition layer, and under certain conditions of the pavement deflection, the inverted modulus of cement-stabilized crushed stone is overestimated, and the degree of overestimation is related to the degree of underestimation of the modulus of the graded gravel transition layer. Therefore, for the inverted asphalt pavement, the modulus value obtained by the traditional inversion method is much higher than that obtained by the layer-by-layer inversion method.

In summary, while using the deflection tested by FWD to invert the modulus of asphalt pavement, the layer-by-layer inversion method is recommended; if the conditions are limited, for the inverted asphalt pavement, at least the deflection of the pavement surface, the top surface of the graded crushed stone transition layer, and the top surface of the base course need to be tested.

5. Conclusions

The modulus of the structural layer is determined by the characteristics of structure and material. The modulus tested by the indoor experiment cannot represent the modulus of the structural field layer. In the inverted asphalt pavement, there is a graded gravel transition layer of the granular body

with relatively low strength and nonlinearity. For the modulus inversion of the inverted asphalt pavement, the point is the determination of the modulus of the graded crushed stone transition layer and the cement-stabilized crushed stone layer. While using the traditional inversion method, the structure and material properties of the upper layer will influence the inversion accuracy of the modulus of the underlying structure layer. The layer-by-layer inversion method is better than the traditional inversion method, especially for the inverted asphalt pavement structure.

According to the "Asphalt Pavement Design Specification JTGO50-017," during the design of pavement structure, structural adjustment coefficients are introduced in the determination of material parameters of base course; however, the modulus and adjustment coefficients in the mechanical empirical method are obtained based on statistical data analysis, and their adaptability is doubtful when the test condition and environment change. By contrast, the accuracy of determining the modulus of each structural layer through the layer-by-layer inversion method is better than that of the traditional inversion method, which can effectively determine the modulus of each layer and structural adjustment coefficients, providing a basis for pavement design and analysis. The disadvantage is that the layer-by-layer inversion modulus method cannot be directly used to determine the modulus of each layer of the existing road, which should be tracked and tested from the construction period. In the future, the application of the layer-by-layer inversion method should be verified through more on-site work points and pavement structure types.

Data Availability

The data used to support the findings of this study are available from the corresponding author upon request.

Conflicts of Interest

The authors declare that they have no conflicts of interest.

Acknowledgments

This study was supported by the Sichuan Transportation Science and Technology Project (Grant nos. 4-1 and 2015) and the Sichuan Province Science and Technology Planning Project (Application Fundamental Research) (Grant no. 2019YJ0667).

References

- [1] L. J. Zhou, "Study on attenuation law and backcalculation methods of semi-rigid pavement structure layer modulus," Master's Degree Thesis, Shandong University, Jinan, China, 2012.
- [2] H. M. Park and Y. R. Kim, "Prediction of remaining life of asphalt pavement with falling-weight deflectometer multi-load-level deflections," *Transportation Research Record: Journal of the Transportation Research Board*, vol. 1860, no. 1, pp. 48–56, 2003.
- [3] G. Wang, X. Qin, D. Han, and Z. Liu, "Study on seepage and deformation characteristics of coal microstructure by 3D

- reconstruction of CT images at high temperatures,” *International Journal of Mining Science and Technology*, vol. 31, no. 2, pp. 175–185, 2021.
- [4] L. Zhou, J. M. Lin, X. P. Lin, and Q. Wu, “Temperature adjustment factor for back-calculated modulus of asphalt pavement layer,” *Journal of Tongji University*, vol. 39, no. 11, pp. 1641–1645, 2011.
- [5] Y. Zhang, Y. Xie, Y. Zhang, J. Qiu, and S. Wu, “The adoption of deep neural network (DNN) to the prediction of soil liquefaction based on shear wave velocity,” *Bulletin of Engineering Geology and the Environment*, vol. 80, no. 6, pp. 1–8, 2021.
- [6] C. Xiao, Y. J. Qiu, J. Zhen, and L. Bao-Xian, “Study on measured dynamic response of asphalt pavement under FWD load,” *Journal of Highway and Transportation Research and Development*, vol. 31, no. 2, pp. 1–81, 2014.
- [7] H. Mun Park, Y. R. Kim, and S. Park, “Temperature correction of multiloading-level falling weight deflectometer deflections,” *Transportation Research Record: Journal of the Transportation Research Board*, vol. 1806, no. 1, pp. 3–8, 2002.
- [8] Y. L. Xu, B. M. Tang, G. D. Xie, and S. Chen, “Backcalculated modulus correction coefficient for asphalt concrete layer based on FWD,” *Journal of Chang’an University (Natural Science Edition)*, vol. 32, no. 3, pp. 24–29, 2012.
- [9] D. Y. Yin and P. E. D. M. Mrawira, “Comparison between laboratory investigation and non-destructive testing methods for mechanistic characterization of Asphalt pavement,” in *Proceedings of the Transportation Research Board 87th Annual Meeting*, pp. 2621–2634, TRB, Washington, DC, USA, January 2008.
- [10] Y. G. Zhang, J. Qiu, and Y. Zhang, “The adoption of ELM to the prediction of soil liquefaction based on CPT,” *Natural Hazards*, vol. 107, no. 20, pp. 1–11, 2021.
- [11] A. Sangghaleh, E. Pan, R. Green, R. Wang, X. Liu, and Y. Cai, “Backcalculation of pavement layer elastic modulus and thickness with measurement errors,” *International Journal of Pavement Engineering*, vol. 15, no. 6, pp. 521–531, 2014.
- [12] Y. G. Zhang, J. Tang, R. P. Liao et al., “Application of an enhanced Bp neural network model with water cycle algorithm on landslide prediction,” *Stochastic Environmental Research and Risk Assessment*, vol. 35, pp. 1–19, 2020.
- [13] Y. Mehta, R. Roque, “Evaluation of FWD data for determination of layer moduli of pavements,” *Macromolecular Bioscience*, vol. 14, no. 4, pp. 515–525, 2003.
- [14] C. Y. Zhuang, Y. L. Ye, and L. Wang, “Conversion coefficient for backcalculated modulus of unbound aggregate base asphalt pavement,” *Journal of Chongqing University*, vol. 37, no. 4, pp. 100–108, 2014.
- [15] R. N. Stubstad, “LTPP data analysis: feasibility of using FWD deflection data to characterize pavement construction quality,” Federal Highway Administration, McLean, VA, USA, FHWA/20-50/09, 2002.
- [16] W. Nassar, I. L. Al-Qadi, G. W. Flintsch, and A. Appea, “Evaluation of pavement layer response at the virginia smart road,” *Geo-Denver*, vol. 286, pp. 104–118, 2000.
- [17] P. Solanki, M. Zaman, K. K. Muraleetharan, and D. Timm, “Evaluation of resilient moduli of pavement layers at an instrumented section on I-35 in oklahoma,” *Road Materials and Pavement Design*, vol. 10, no. 1, pp. 167–188, 2009.
- [18] G. Y. Liao, C. Lu, and X. M. Huang, “Layered measure and analysis of mechanical responses within asphalt pavement,” *Journal of Southeast University (Natural Science Edition)*, vol. 40, no. 5, pp. 1061–1065, 2010.
- [19] C. Mark, “An updated empirical model for ground control in U.S. multiseam coal mines,” *International Journal of Mining Science and Technology*, vol. 31, no. 2, pp. 163–174, 2020.
- [20] J. Mao, “Analysis on structure characteristic of rubblization and asphalt overlay pavement based on falling weight deflectometer data backcalculation,” Master’s Degree Thesis, Southwest Jiao-Tong University, Chengdu, China, 2010.
- [21] K. D. Smith, J. E. Bruinsma, M. J. Wade, K. Chatti, J. M. Vandebossche, and H. T. Yu, “Using falling weight deflectometer data with mechanistic-empirical design and analysis,” vol. 1, Federal Highway Administration, Washington, DC, USA, 2017, FHWA-HRT-16-009.
- [22] J. P. Luan, “Research on field contrast test of the red sandstone subgrade resilient modulus,” *Foreign Highway*, vol. 28, no. 6, pp. 54–56, 2008.
- [23] Y. Zhang, J. Qiu, Y. G. Zhang, and Y. Xie, “The adoption of a support vector machine optimized by GWO to the prediction of soil liquefaction,” *Environmental Earth Sciences*, vol. 80, no. 9, 2021.
- [24] H. Rafezi and F. Hassani, “Drilling signals analysis for tricone bit condition monitoring,” *International Journal of Mining Science and Technology*, vol. 31, no. 2, pp. 187–195, 2021.
- [25] X. Li, N. X. Liang, and L. Chen, “Dynamic modulus and time-temperature equivalence equation of asphalt concrete,” *Journal of Chang’an University (Natural Science Edition)*, vol. 34, pp. 35–40, 2014.
- [26] Y. G. Zhang, J. Tang, Z. Y. He, J. Tan, and C. Li, “A novel displacement prediction method using gated recurrent unit model with time series analysis in the erdaohe landslide,” *Natural Hazards*, vol. 1, pp. 1–31, 2021.
- [27] Y. X. Sheng, P. An, and D. Wei, *The Construction Technology of Asphalt Pavement Reinforced Gravel Construction*, People’s Transportation Press, Beijing, China, 2015.
- [28] F. P. Li and E. H. Yan, *The Structural Design and Construction Application Guide of Asphalt Stabilized Gravel and Grade*, People’s Transportation Press, Beijing, China, 2009.
- [29] A. F. Jiang and Z. K. Yao, “Calculation of surface equivalent modulus of subgrade in the pavement structure,” *Journal of Tongji University*, vol. 29, no. 5, pp. 536–540, 2001.

Research Article

Calculation Model of Shear Capacity of Multiple Composite Core Column Joints Based on Softened Tension-Compression Bar Model

Xu Wentao ¹ and Yang Chengyu²

¹College of Architecture and Engineering, Xinjiang University, Urumqi 830047, China

²Chengdu Benchmark Fangzhong Architectural Design Co., Ltd., Chengdu, China

Correspondence should be addressed to Xu Wentao; cpsrgusu@163.com

Received 7 July 2021; Accepted 13 August 2021; Published 1 September 2021

Academic Editor: Zhiyong Chen

Copyright © 2021 Xu Wentao and Yang Chengyu. This is an open access article distributed under the Creative Commons Attribution License, which permits unrestricted use, distribution, and reproduction in any medium, provided the original work is properly cited.

This paper aims to study the seismic performance of multiple composite core column joints. The influence of the stress mechanism, axial compression ratio, and shear span ratio on the failure mode, hysteretic performance, and shear capacity of the multiple composite core column joints was studied through the low-reversed cyclic loading tests of three specially designed and manufactured multiple composite core column joints. The angle ratio method is used to calculate the effective area of the vertical tie bar, and based on the mechanism of the softening tension-compression bar, the formula for calculating the shear capacity of the joint with multiple composite core column is established. In addition, it is also verified by the test data in this paper. The experimental results show that when the axial compression ratio increases from 0.26 to 0.45, the number and width of cracks at the beam end decrease. When the shear span ratio increases from 1.67 to 2.22, the number and width of cracks at the joint beam end increase. The average value and standard deviation of the ratio between the measured value and the calculated value of the shear capacity are 0.97 and 0.16, indicating that the proposed calculation method has a high agreement with the actual value and strong engineering application.

1. Introduction

Beam-column joints play an important role in the transmission and distribution of internal forces and are also the key to the seismic performance of the structure in the frame structure. Most of the ordinary reinforced concrete beam-column joints show brittle failure, which is not conducive to the seismic resistance of the structure [1–3]. To explore a new type of reinforcement and improve the transmission and distribution of internal forces in the frame, much attention has been paid by researchers. In recent years, multiple composite reinforced core columns can effectively guarantee the realization of “strong column and weak beam” and have good shear bearing capacity and seismic performance under earthquake action, which has attracted increasing attention of researchers. As the core index of seismic shear capacity is particularly important, many researchers have done a series of studies on it [4–12].

You et al. [13] comprehensively analyzed the seismic tests of numerous international frame joints, found the important correlation between the stress state of longitudinal bars after yield and the number of longitudinal bars that affect the shear capacity of joints, and proposed the shear capacity formula of such failure-type joints. Xing et al. [14–16] proposed a modified calculation model for reinforced concrete joints with orthogonal beams on the basis of the model of softened tension-compression bars [17, 18]. Yang [19] studied the influence of axial compression ratio, stirrup spacing, stirrup ratio, and stirrup form on the seismic performance of multiple composite core columns and proposed the corresponding calculation formula of shear capacity and design suggestions. Wakabayashi et al. [20] and Omine et al. [21] found that the seismic performance of cored columns was significantly better than that of ordinary reinforced concrete columns in their studies under low-cyclic reciprocating loads. Kadoya et al. [22] found that the

initial stiffness and strength of columns with core columns are about 1.2 times that of ordinary reinforced concrete columns. At present, most of the joint researches at home and abroad are made of reinforced concrete beam-column joints in the form of ordinary reinforcement. Although the research on the seismic performance of composite core columns has made some progress, there are few reports on the seismic performance of composite core columns, especially the calculation of its shear capacity needs to be further studied.

Based on the above analysis, this paper carried out pseudostatic tests on the beam-column joints composed of multiple composite core columns, analyzed the effects of axial compression ratio and shear span ratio on the seismic performance of the joints, and proposed a formula for calculating the shear capacity of the multiple composite core column joints based on the mechanism of softening the tension and compression rods. It provides reference for the popularization and use of such nodes in engineering construction.

2. Materials and Methods

To avoid the contingency caused by single data, three reinforced concrete beam joints with multiple composite core columns were prepared for parallel tests. The beam section size of each node is 150 mm × 380 mm, the column section size is 400 mm × 400 mm, and the concrete protective layer thickness of the beam and column is 20 mm. The specimens BCJ-1, BCJ-2, and BCJ-3 were designed and manufactured with axial compression ratio and shear span ratio as variables. Specific joint dimensions and reinforcement can be found in Figures 1 and 2 and Table 1.

The measured compressive strength of concrete cube used in the test is 58.6 MPa, and the measured material properties of steel bars with different diameters are shown in Table 2.

The static loading method is used as shown in Figure 3 in the experiment of this paper. The loading process is mainly divided into the following two steps:

- (1) Vertical load was applied to the top of the node column by a hydraulic Jack.

The first application of axial pressure is 0.4 times to ensure that the device is not loosened, and then two further cycles of 0.4 times. Finally, the axial pressure applied at the top of the column is 1 time and remains constant.

- (2) Horizontal displacement load is applied to the joint column end through the actuator.

Before the formal loading, 5 kN force was used to push and pull the joint specimen three times for trial loading to ensure the normal working of each device, acquisition system, and fixed device. After the complete system is tested to work normally, the horizontal load is returned to 0. The step size of initial loading of horizontal displacement is 2 mm, 4 mm, 6 mm, 8 mm, and 10 mm in turn, and then the step size remains

10 mm. Each step size is repeated three times until the specimen is damaged or the horizontal load is less than 0.85 times the peak load, and the loading is finished. The vibration frequency of the load is the simulated seismic load, as shown in Figure 4.

3. Results and Discussion

3.1. Phenomena and Failure Modes. For multiple composite core column joints, the frame columns are always in the elastic stage, and the core areas of the columns and joints have no obvious damage under the reciprocating action of horizontal displacement loads. With the loading process, penetration cracks appear at the beam-column junction, and cross oblique cracks appear at the beam end away from the edge of the column. Concrete in this area gradually spall off with the subsequent loading, and obvious plastic failure occurs at the edge of the beam away from the column. The failure modes of each specimen are shown in Figures 5 to 7.

It can be found that the number and width of cracks at the beam end decrease as the axial compression ratio increases from 0.26 (node BCJ-1) to 0.45 (node BCJ-2) when the specimen is damaged. However, the horizontal displacement of failure is just the opposite. The horizontal displacement of BCJ-1 node is 70 mm, while that of BCJ-2 node is 50 mm. This is because the increase of axial compression ratio will cause the concrete at the core of the joint to be subjected to greater compression, so as to delay the generation of cracks at the beam and column ends at the core of the joint. It is shown that increasing the axial compression ratio can delay the development of the beam end cracks but reduce the ductility of the joint under seismic load. Similarly, when the shear-span ratio increases from 1.67 (node BCJ-1) to 2.22 (node BCJ-3), the number and width of fractures at the joints increase. This is because when the shear span ratio increases, the second-order effect of joints becomes more obvious, which intensifies the generation and development of beam-end cracks. For details, see the red mark in the revised manuscript. Increasing the shear-span ratio will accelerate the generation of fractures at the joints.

3.2. Hysteretic Behavior. The hysteretic curves of each specimen are shown in Figures 8 to 10. In the early stage of loading, the hysteretic loop area and residual deformation of each joint are small, and the stiffness degradation of the specimen is not obvious. The area and residual deformation of the hysteresis loop gradually increase with the increase of the load. When the horizontal displacement load reaches its peak, the stiffness of the joint degrades obviously. With the continuous loading, the hysteresis loop area of the curve increases, the maximum load at all levels begins to decrease, and the rising part of the curve tends to be gentle. The hysteresis curves of the three specimen nodes all show a spindle shape without obvious pinching, and the load strength and specimen stiffness do not significantly degrade when the load of the same level is loaded each time. The cumulative damage of the frame joints under cyclic loads at

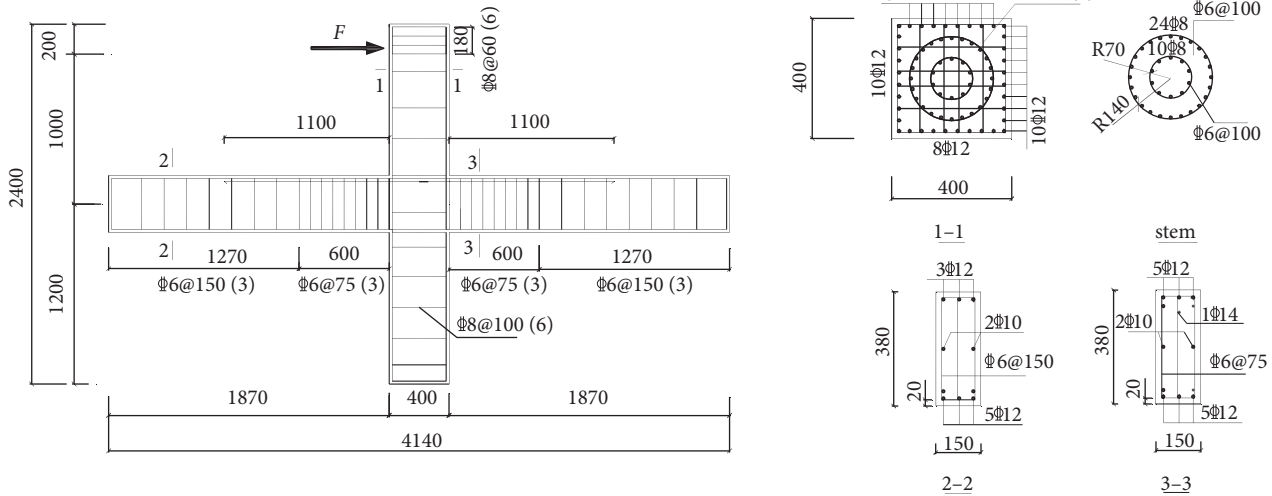


FIGURE 1: Detailed drawing of reinforcement for BCJ-1 (BCJ-2) joints.

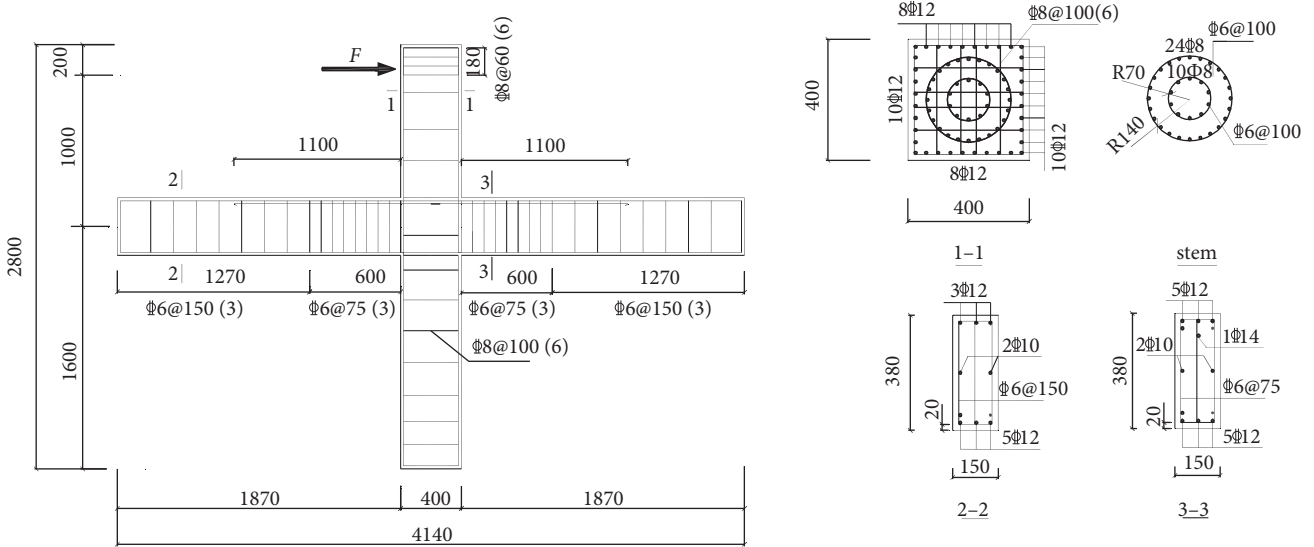


FIGURE 2: Detailed drawing of reinforcement for BCJ-3 joints.

all levels is small, and the residual deformation of the joints under cyclic loads at all levels is uniform after the peak load. However, the load-displacement hysteresis curves of the beam-column joints with common reinforcement form mostly present bow and inverse “S” shape [23–25], which proves that the multicomposite core column joints have better seismic performance than the beam-column joints with common reinforcement form.

Skeleton curve of the node refers to the line between the first loading curve of the node and the peak points of hysteretic loops in the hysteretic loop curve under the action of low-cycle reciprocating load. The skeleton curve drawn by the line of the peak points of each hysteretic loop under low-cycle reciprocating load is shown in Figure 11. The initial stiffness of the frame joints increases by about 21.6 kN/mm, and the peak load increases by about 103.5 kN, when the axial compression ratio increases from 0.26 to 0.45. As for the effect of the shear to span ratio, the

initial stiffness of the node decreases by about 1.3 kN/mm and the peak value by about 22.9 kN, when the shear to span ratio increases from 1.67 to 2.22. The results show that the increase of axial compression ratio can significantly increase the initial stiffness and peak load of the composite core column joints, while the shear span ratio is just the opposite.

3.3. Calculation of Horizontal Shear Stress on Nodes. The force analysis of nodes is shown in Figure 12.

The upper half of the node is taken as the isolation body, and the horizontal shear force of the node has the following equilibrium relationship:

$$V_{jh} = T_{b1} + C_{b2} - V_{c1}. \quad (1)$$

According to the geometric relationship, the vertical shear force of the node is

TABLE 1: The detailed parameters of the frame node in test.

Project		BCJ-1	BCJ-2	BCJ-3	
Rectangular frame column	Section (mm × mm)	400 × 400	400 × 400	400 × 400	
	Angle steel	4Φ12	4Φ12	4Φ12	
	Unilateral longitudinal bars	10Φ12+8Φ12	10Φ12+8Φ12	10Φ12+8Φ12	
	Stirrup	Φ8@100[6 limbs]	Φ8@100[6limbs]	Φ8@100[6limbs]	
Outer mandrel XZ-1	Section (mm × mm)	280×280(circle)	280×280(circle)	280×280(circle)	
	Longitudinal bars	24Φ8	24Φ8	24Φ8	
	Stirrup	Φ6@100	Φ6@100	Φ6@100	
	Section (mm × mm)	140 × 140 (circle)	140 × 140 (circle)	140 × 140 (circle)	
Mandrel	Inner mandrel XZ-2	Longitudinal bars	10Φ8	10Φ8	10Φ8
		Stirrup	Φ6@100	Φ6@100	Φ6@100
		Strength of concrete (MPa)	C45	C45	C45
		Axial pressure (kN)	1560	2750	1560
	Lower column height	2.4	2.4	3.2	
	Height of reverse bending point of lower column	1.2	1.2	1.6	
	Height of upper column	1.9	1.9	1.9	
	Height of upper column reverse bending point	1.0	1.0	1.0	
	Experimental axial compression ratio	0.26	0.45	0.26	
	Shear span ratio	1.67	1.67	2.22	
Beam	Section (mm × mm)	150 × 380	150 × 380	150 × 380	
	Concrete strength (MPa)	C45	C45	C45	
	Stirrup	Φ6@75/150(3)	Φ6@75/150(3)	Φ6@75/150(3)	
	Beam length (m)	3.75	3.75	3.75	
	Length of reverse bending point (m)	1.87	1.87	1.87	
	Midspan compression bars	3Φ12	3Φ12	3Φ12	
	Negative bending regions	5Φ12+1Φ14	5Φ12+1Φ14	5Φ12+1Φ14	
	Lower longitudinal bars	5Φ12	5Φ12	5Φ12	
	Longitudinal bars	2Φ10	2Φ10	2Φ10	

TABLE 2: Property of steel bars.

Diameter (mm)	Yield strength f_y (N/mm ²)	Ultimate strength f_u (N/mm ²)	Elastic modulus E_s (N/mm ²)
6	434.60	605.20	2.0×10^5
8	539.70	706.70	2.0×10^5
10	490.24	659.45	2.0×10^5
12	484.20	624.90	2.0×10^5
14	455.10	639.45	2.0×10^5

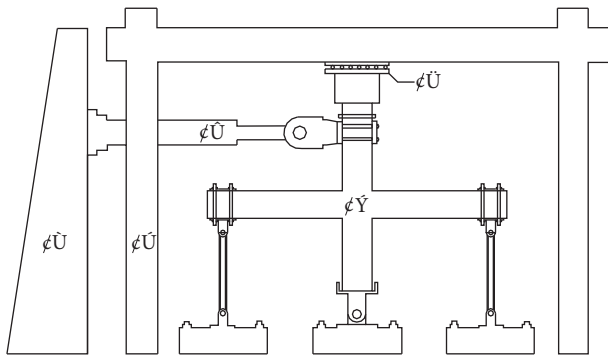


FIGURE 3: Schematic diagram of loading device. Note: ① reaction wall, ② gantry mounting, ③ MTS actuator, ④ horizontal rolling system, and ⑤ test specimen.

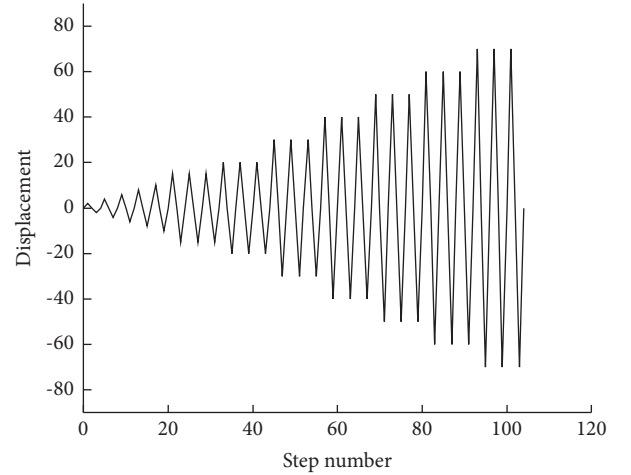


FIGURE 4: The vibration frequency of the load.

$$V_{jv} \approx \left(\frac{h'_b}{h'_c} \right) \times V_{jh}, \quad (2)$$

$$T_{b1} = \frac{M_{b2}}{h'_b}, \quad (3)$$

$$C_{b2} = \frac{M_{b1}}{h'_b}, \quad (4)$$

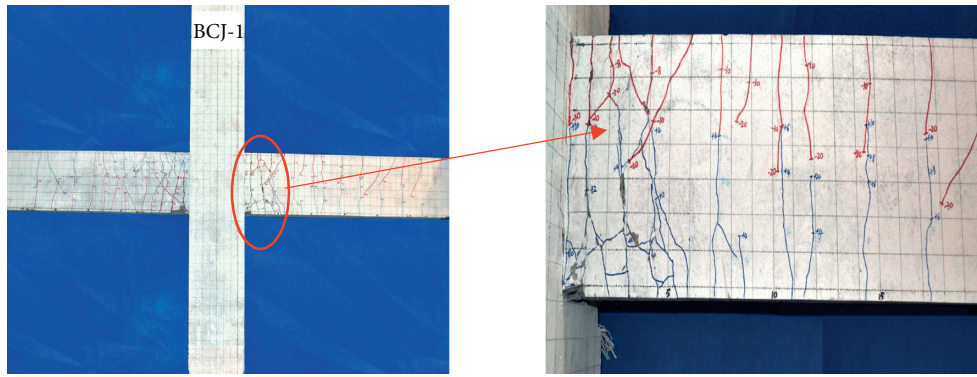


FIGURE 5: BCJ-1 node failure pattern diagram.

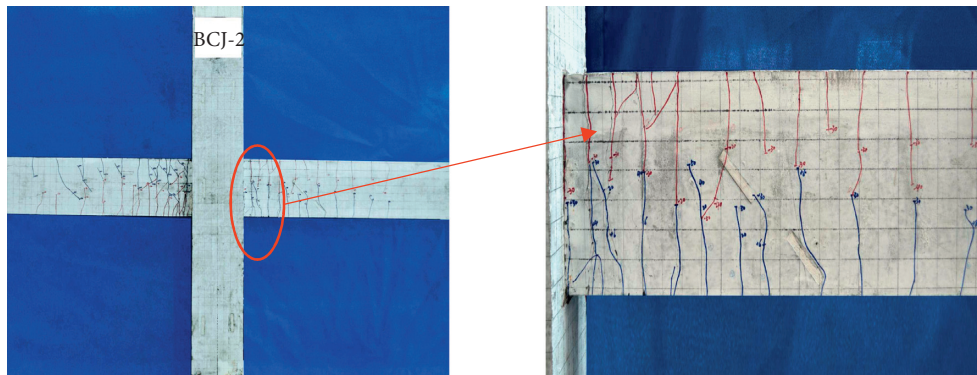


FIGURE 6: BCJ-2 node failure pattern diagram.

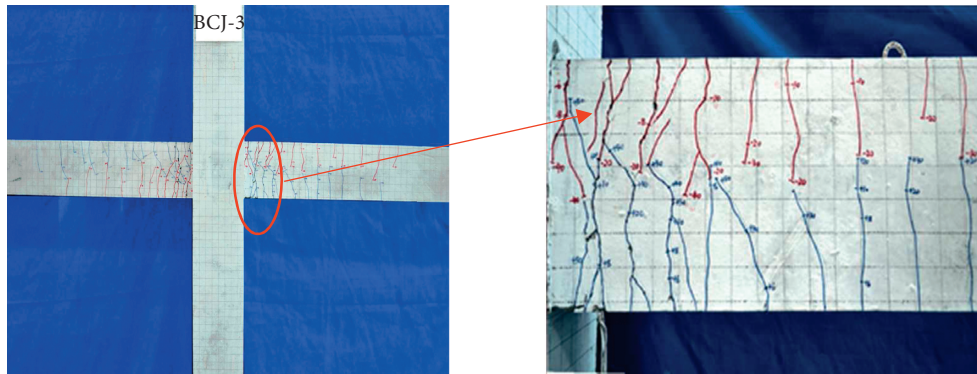


FIGURE 7: BCJ-3 node failure pattern diagram.

where V_{jh} is the horizontal shear force of the node, T_{b1} is the tensile force of the reinforcement of the beam on the right side of the node, and C_{b2} is the pressure of the beam on the left side.

The orientation of T_{b1} and C_{b2} is assumed to be consistent although not necessarily in the actual force, for simplicity of calculation. V_{c1} is the horizontal shear force at the column end at the node, which is equal to the load value of horizontal loading. M_{b1} and M_{b2} are the bending moments at the end of the beam; h'_b and h'_c are the internal moment arms of the beam and column, respectively, the approximate distance between the center lines of upper and

lower longitudinal bars of the beam is taken to calculation the h'_b .

According to equations (1), (3), and (4), we can get

$$V_{jh} = \frac{M_{b1} + M_{b2}}{h'_b} - V_{c1}. \quad (5)$$

Balanced by the bending moment of the node, the following equation can be obtained:

$$M_{c1} + M_{c2} = M_{b1} + M_{b2}. \quad (6)$$

Among them,

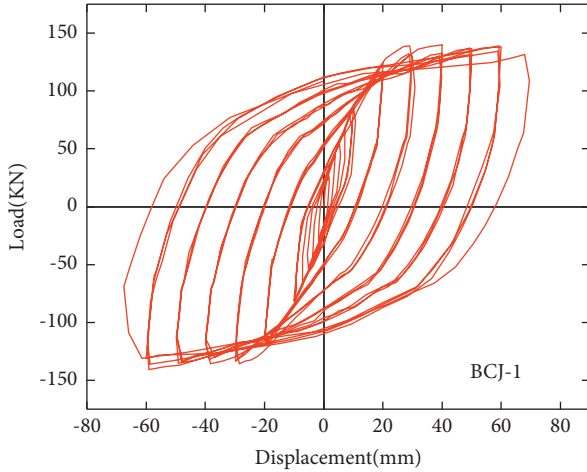


FIGURE 8: BCJ-1 load-displacement hysteresis curve.

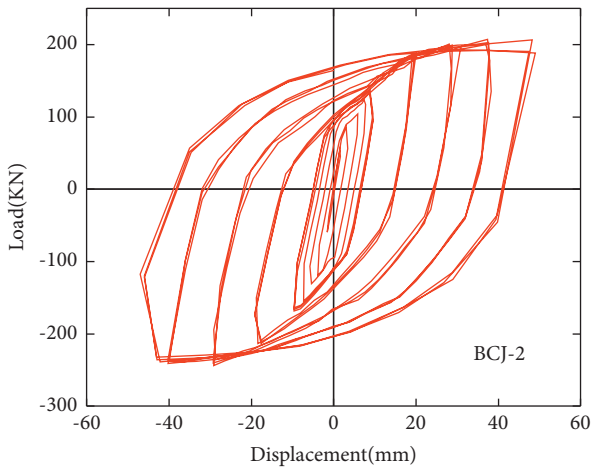


FIGURE 9: BCJ-2 load-displacement hysteresis curve.

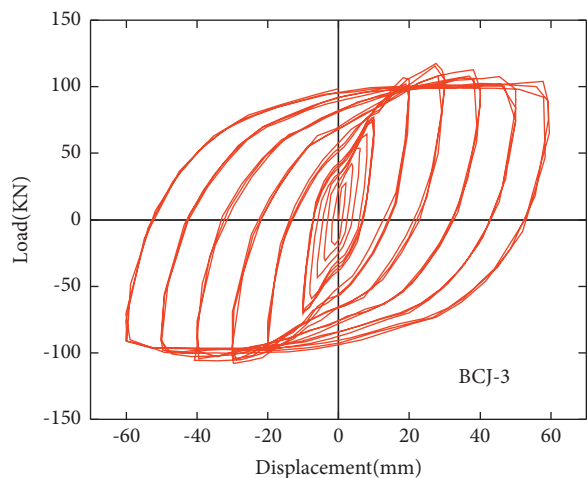


FIGURE 10: BCJ-3 load-displacement hysteresis curve.

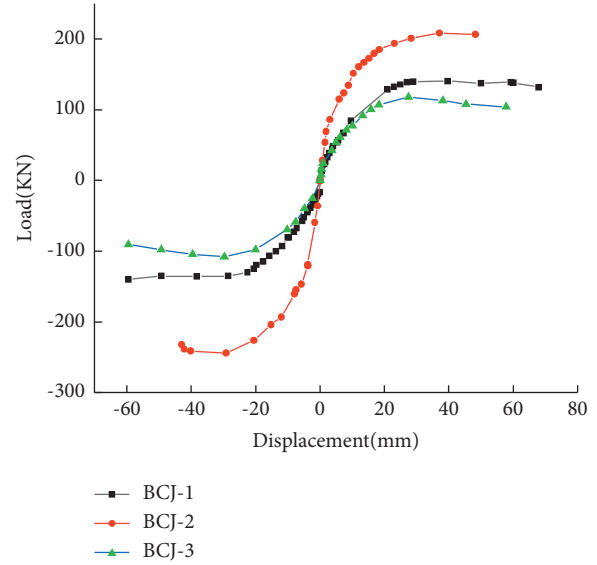


FIGURE 11: Comparison diagram of skeleton curve.

$$\begin{cases} M_{c1} = V_{c1}h_1, \\ M_{c2} = V_{c2}h_2, \end{cases} \quad (7)$$

$$V_{c1} = V_{c2}. \quad (8)$$

Equations (6) to (8) can be deduced as follows:

$$\begin{aligned} V_{c1} &= \frac{M_{b1} + M_{b2}}{h_1 + h_2} \\ &= \frac{M_{b1} + M_{b2}}{h - h_b}, \end{aligned} \quad (9)$$

where M_{c1} and M_{c2} are bending moments at the upper and lower column ends; h is the distance between the reverse bending points of the upper and lower columns; h_1 and h_2 are the distance between the reverse bending points of the upper and lower columns and the core area of the joint, respectively; and h_b is the height of the cross section of the beam.

By combining equations (9) and (5), we can get

$$V_{jh} = \frac{M_{b1} + M_{b2}}{h'_b} \left(1 - \frac{h'_b}{h - h_0} \right). \quad (10)$$

The shear forces on the three nodes in the horizontal direction are finally calculated, as shown in Table 3.

4. Calculation Formula of Shear Capacity Based on Softening Tension-Compression Bar Model

The complex mechanical behavior of the whole structure is abstracted into a relatively simple strut-and-tie model by taking the compression concrete as the compression struts; and the steel bar in the tension zone as the tie bar. The simplified softened strut-and-tie model is a model proposed by Professor Huang Shijian to calculate the shear capacity of beam-and-column joints on the basis of the softened strut-

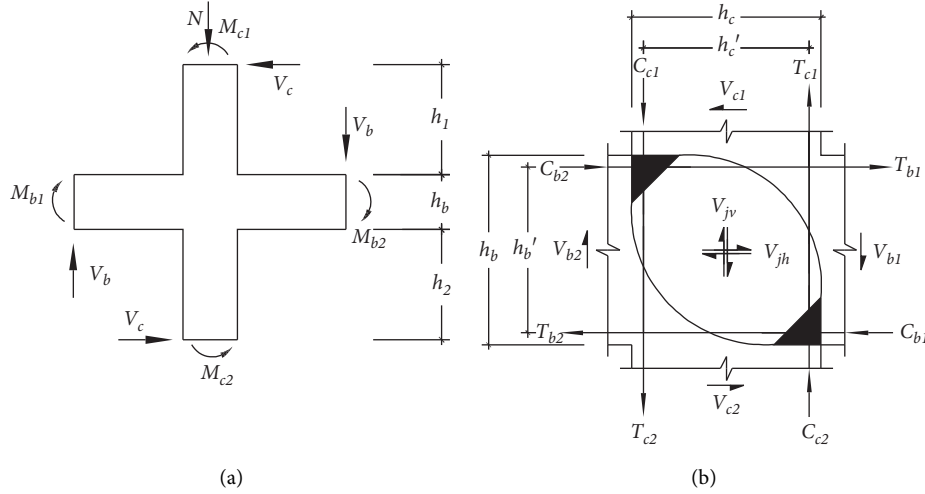


FIGURE 12: Schematic diagram of force of nodes: (a) diagram of external forces on node and (b) analysis of the internal forces on node.

and-tie model [26, 27]. The schematic diagram of the softened strut-and-tie model is shown in Figure 13. The model is composed of oblique, horizontal, and vertical parts. The oblique part is composed of a baroclinic bar, and the included angle between the baroclinic bar and the horizontal axis is θ ; the horizontal part is composed of a horizontal tie bar and two gentle compression struts, which are composed of stirrups at the nodes; the vertical part consists of a vertical tie bar and two steep compression struts, which are composed of the longitudinal bars of the columns [15]. The specific calculation method and calculation process are as follows:

The horizontal shear bearing capacity of this model, V_j is calculated as follows:

$$V_j = K\zeta f'_c A_{str} \cos \theta, \quad (11)$$

where θ is the included angle between the baroclinic bar and the horizontal direction, which can be determined by the following equation:

$$\theta = \tan^{-1} \left(\frac{h_b''}{h_c''} \right). \quad (12)$$

For the convenience of calculation, b and c in the equation are assumed to be the distances between the center lines of the outermost reinforcement of the beam and column, respectively, and the inclination direction and magnitude of the baroclinic bar in the joint area and the main compressive stress of the concrete in the core area are considered to be the same.

The area A_{str} of the baroclinic bar can be calculated as follows:

$$A_{str} = a_s \times b_s, \quad (13)$$

where a_s and b_s are the effective height and width of the baroclinic bar, respectively, determined by the following equation:

$$a_s = \sqrt{a_b^2 + a_c^2}, \quad (14)$$

$$b_s = \min \left\{ b_b + 2 \times \frac{a_c}{6}, b_c \right\}, \quad (15)$$

where a_b is the height of the compression zone of the beam cross section and a_c is the height of the compression zone of the column cross section, which can be determined by the following equation:

$$a_b = \frac{h_b}{5}, \quad (16)$$

$$a_c = \left(0.25 + 0.85 \frac{N}{A_g f'_c} \right) h_c, \quad (17)$$

where b_b is the beam cross-section width, b_c is the column cross-section width, h_b is the beam cross-section height, h_c is the column cross-section height, N is the axial pressure, determined according to the test, A_g is the column cross-section area, and f'_c is the compressive strength of the concrete cylinder. According to the conversion formula of "Standard for test methods of concrete physical and mechanical properties" (GB/T50081-2019) [28], the compressive strength of the concrete cube is converted into the compressive strength of the cylinder. K is the tension/compression bar coefficient. Professor Huang Shijian [26] suggested the following equation for calculation:

$$K = K_h + K_v - 1, \quad (18)$$

where K_h is the horizontal tie bar coefficient and K_v is the vertical tie bar coefficient. The values of the two are shown in the following equation:

TABLE 3: The shear on the three nodes in the horizontal direction.

Specimen	BCJ-1	BCJ-2	BCJ-3
$V_{jh} \text{KN}$	668.71	1161.32	708.58

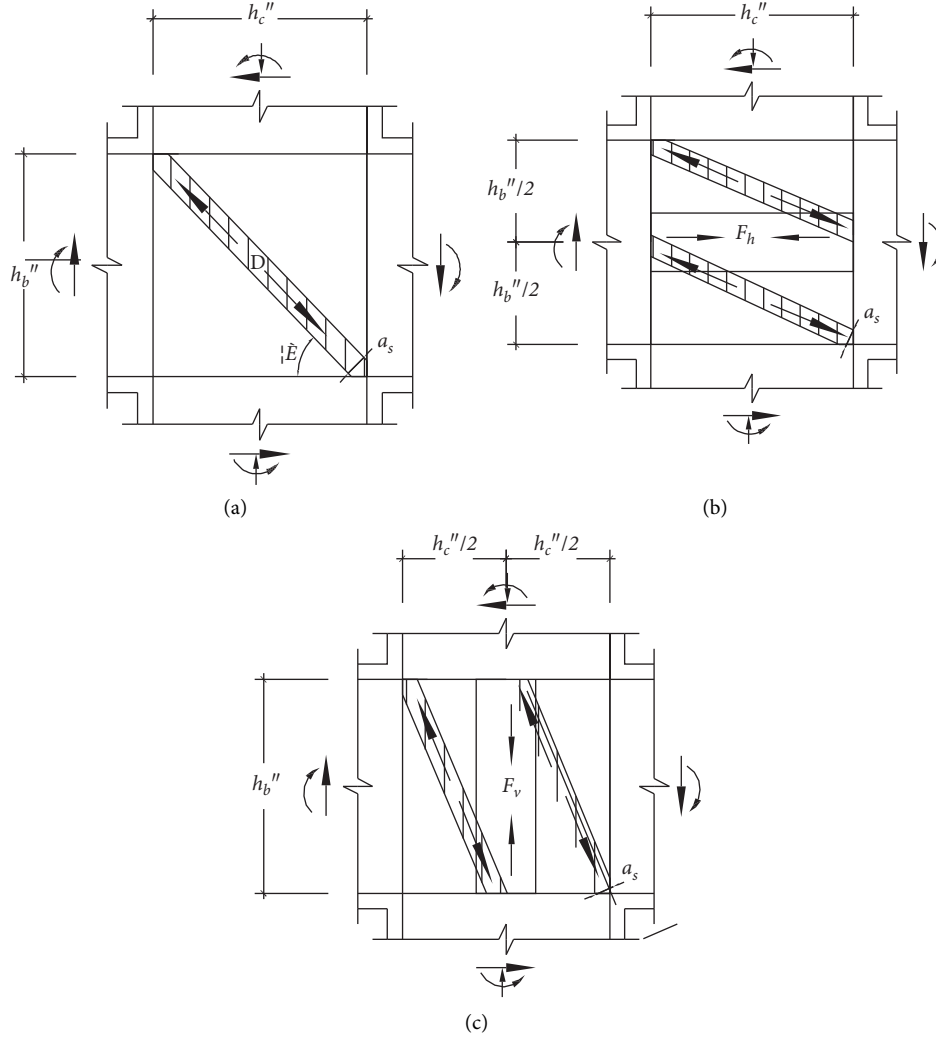


FIGURE 13: The strut-and-tie model of the node: (a) oblique part, (b) horizontal part, and (c) vertical part.

$$\begin{cases} K_h = 1 + \frac{(\overline{K}_h - 1)A_{th}f_{yh}}{\overline{F}_h} \leq \overline{K}_h, \\ K_v = 1 + \frac{(\overline{K}_v - 1)A_{tv}f_{yv}}{\overline{F}_v} \leq \overline{K}_v, \end{cases} \quad (19)$$

where $A_{th}f_{yh}$ is the product of the area of the horizontal tie bar and the yield strength of the corresponding steel bar and $A_{tv}f_{yv}$ is the product of the area of the vertical tie bar and the yield strength of the corresponding reinforcing bar. If the tie bar consists of different types of reinforcement, then $A_{th}f_{yh}$ and $A_{tv}f_{yv}$ shall be the sum of the products of different types.

\overline{K}_h is the balance coefficient of the horizontal tie bar and \overline{K}_v is the balance coefficient of the vertical tie bar, which can be calculated as follows:

$$\begin{cases} \overline{K}_h \approx \frac{1}{1 - 0.2(\gamma_h + \gamma_h^2)}, \\ \overline{K}_v \approx \frac{1}{1 - 0.2(\gamma_v + \gamma_v^2)}, \end{cases} \quad (20)$$

where γ_h is the ratio of the horizontal tie bar to the horizontal shear stress of the node and γ_v is the ratio of the vertical tie bar to the horizontal shear stress of the node, which can be calculated as follows:

$$\begin{cases} \gamma_h = \frac{2 \tan \theta - 1}{3}, \\ \gamma_v = \frac{2 \cot \theta - 1}{3}, \end{cases} \quad (21)$$

\bar{F}_h is the balance tension of the horizontal tie bar, and \bar{F}_v is the balance tension of the vertical tie bar. They can be calculated by the following equation:

$$\begin{cases} \bar{F}_h = \gamma_h \times (\bar{K}_h \zeta f'_c A_{str}) \times \cos \theta, \\ \bar{F}_v = \gamma_v \times (\bar{K}_v \zeta f'_c A_{str}) \times \sin \theta, \end{cases} \quad (22)$$

ζ is the softening coefficient of concrete under compression and can be calculated as follows:

$$\zeta \approx \frac{3.35}{\sqrt{f'}} \quad (23)$$

The main calculation steps of the modified strut-and-tie model are as follows :

- (1) Determine relevant parameters of nodes: b_b , b_c , h_b , h_c , h_b'' , h_c'' , A_{th} , A_{tv} , and f'_c .

Considering that all the stirrups at the joints do not yield when the joints fail, the joint area is simply divided by force. All the area of the stirrups at the middle half participates in the force, while only half of the area of the reinforcing bars at both sides participates in the force [14]. See Figure 14 for specific zones.

The vertical tie bar is composed of the longitudinal bar of the column, and the reinforcement partition of the longitudinal bar participating in the force is shown in Figure 15. It is composed of longitudinal bars of core column and longitudinal bars of rectangular column. According to the stress zone, the calculation method of A_{tv} is as follows:

$$\begin{aligned} A_{tv} &= A_{tvj} + A_{tvx}, \\ \cos \alpha &= \frac{h''/4}{R}, \end{aligned} \quad (24)$$

$$A_{tvx} = m \times \frac{\pi - 2\alpha}{\pi} \times A_{tvx1} + n \times A_{tvx2},$$

where A_{tv} is the effective area of the vertical tie bar, A_{tvj} is the effective area of the longitudinal bars of the rectangular column, A_{tvx} is the effective area of the longitudinal reinforcement of the core column, A_{tvx1} is the effective surface of the longitudinal reinforcement of the outer core column, and A_{tvx2} is the effective area of the longitudinal reinforcement of the inner core column.

- (2) Calculate the height a_b of the compression zone of the joint beam cross section (equation (16)).
- (3) Calculate the height of the compression zone of the joint column cross section a_c (equation (17)).

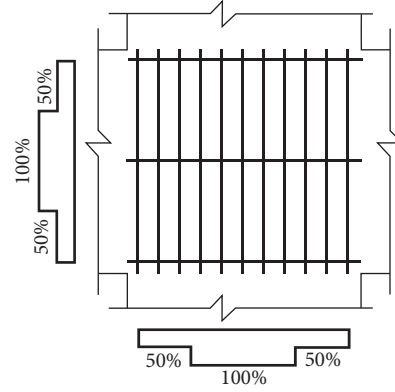


FIGURE 14: The area partition diagram of the node.

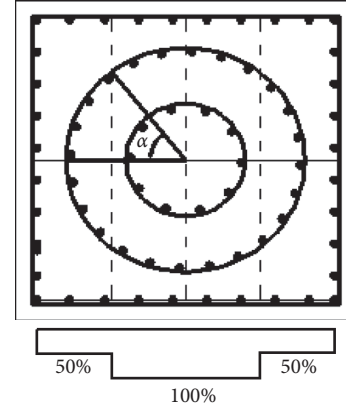


FIGURE 15: Diagram of column A_{tv} calculation method.

TABLE 4: The shear force calculation results of each joint are compared with the test results.

Node number	V_j	V_{jh}	V_j/V_{jh}	Average	Standard deviation
BCJ-1	707.25	668.71	1.058		
BCJ-2	975.61	1161.32	0.840	0.965	0.16
BCJ-3	707.25	708.58	0.998		

- (4) Calculate the effective height of the baroclinic bar in the joint area (equation (14)).
- (5) Calculate the effective width of the baroclinic bar in the joint area is calculated, b_s (equation (15)).
- (6) Calculate the softening coefficient ζ of concrete (equation (23)).
- (7) Calculate γ_h and γ_v (equation (21)).
- (8) Calculate \bar{K}_h and \bar{K}_v (equation (20)).
- (9) Calculate \bar{F}_h and \bar{F}_v (equation (22)).
- (10) Calculate K_h and K_v (equation (19)).
- (11) Calculate K (equation (18)).
- (12) Calculate V_j (equation (11)).

The comparison between the calculation results and the test results of the shear capacity of the three multiple composite core column joints (calculated according to the above steps) is shown in Table 4. The average value and standard deviation of the ratio between the calculated value and the measured value are 0.965 and 0.16 respectively. It can be seen that the calculated value of the shear capacity based on the softened tension-compression bar model is in good agreement with the experimental value. The results indicate that it is feasible to use the angle ratio to calculate the effective area of the longitudinal reinforcement of the core column.

5. Conclusion

- (1) According to the experimental study, the three specimens of multiple composite core column joints were all damaged by plastic hinge at the beam end, conforming to the seismic design of “strong column and weak beam” and had better seismic performance compared with ordinary beam-column joints.
- (2) The hysteresis curves of the joint specimens all show full spindle shape, and the hysteresis loops are relatively full. Increasing the axial compression ratio can significantly improve the initial stiffness and peak load of the joint, while increasing the shear span ratio will lead to a slight decrease in the initial stiffness and peak load.
- (3) When the modified softened tension-compression bar model is used to calculate the shear at the joints, a calculation method for the effective area of the vertical tension-compression bar suitable for multiple composite core columns is proposed. Compared with the test results, the model value is slightly lower than the test value, which indicates that the calculation results of this method are safer when designing the shear capacity of frame joints and can provide a theoretical basis for the structural design of practical engineering.

Data Availability

The data used to support the findings of this study are included within the article.

Conflicts of Interest

The authors declare that there are no conflicts of interest regarding the publication of this study.

Acknowledgments

This study was financially supported by the National Natural Science Foundation of China (no. 51868073), and its support is gratefully appreciated.

References

- [1] J. Tang, J. Feng, and T. Pang, “Experimental study on shear strength in core area of reinforced concrete frame beam-column joints,” *Journal of Nanjing Institute of Technology*, vol. 31, no. 4, pp. 61–75, 1985.
- [2] J. Fu, “Experimental study on seismic behavior of reinforced concrete frame joints considering axial compression ratio,” *Journal of Chongqing Jianzhu University*, vol. 22, no. Z1, pp. 60–66, 2000.
- [3] W. Wang, J. Xue, H. Zhang et al., “Seismic damage analysis of frame structure in 5.12 Wenchuan earthquake and its seismic implications,” *World Earthquake Engineering*, vol. 25, no. 4, pp. 131–135, 2009.
- [4] G. Wang, X. Qin, D. Han, and Z. Liu, “Study on seepage and deformation characteristics of coal microstructure by 3D reconstruction of CT images at high temperatures,” *International Journal of Mining Science and Technology*, vol. 31, no. 2, pp. 175–185, 2021.
- [5] Y. Zhang, Y. Xie, Y. Zhang, J. Qiu, and S. Wu, “The adoption of deep neural network (DNN) to the prediction of soil liquefaction based on shear wave velocity,” *Bulletin of Engineering Geology and the Environment*, vol. 80, no. 6, pp. 5053–5060, 2021.
- [6] S. Shao, C. Wu, H. Min et al., “A novel coating technology for fast sealing of air leakage in underground coal mines,” *International Journal of Mining Science and Technology*, vol. 31, no. 2, pp. 313–320, 2021.
- [7] Y.-G. Zhang, J. Qiu, Y. Zhang, and Y. Wei, “The adoption of ELM to the prediction of soil liquefaction based on CPT,” *Natural Hazards*, vol. 107, 2021.
- [8] H. Rafezi and F. Hassani, “Drilling signals analysis for tricone bit condition monitoring,” *International Journal of Mining Science and Technology*, vol. 31, no. 2, pp. 187–195, 2021.
- [9] Y. Zhang, J. Qiu, Y. Zhang, and Y. Xie, “The adoption of a support vector machine optimized by GWO to the prediction of soil liquefaction,” *Environmental Earth Sciences*, vol. 80, no. 9, 2021.
- [10] H. Zhao, T. Ren, and A. Remennikov, “A hybrid tubular standing support for underground mines: compressive behaviour,” *International Journal of Mining Science and Technology*, vol. 31, no. 2, pp. 215–224, 2021.
- [11] Y.-G. Zhang, J. Tang, Z.-Y. He, J. Tan, and C. Li, “A novel displacement prediction method using gated recurrent unit model with time series analysis in the Erdaohe landslide,” *Natural Hazards*, vol. 105, no. 1, pp. 783–813, 2020.
- [12] P. An, W. Xia, Y. Peng, and G. Xie, “Comparative filtration and dewatering behavior of vitrinite and inertinite of bituminous coal: experiment and simulation study,” *International Journal of Mining Science and Technology*, vol. 31, no. 2, pp. 233–240, 2021.
- [13] Y. You, J. Fu, S. Bai et al., “A new recognition of the calculation formula of shear capacity of seismic reinforced concrete frame joints,” *Journal of Chongqing Jianzhu University*, vol. 41, no. 1, pp. 18–29, 1997.
- [14] G. Xing, *Research on Failure Mechanism and Design Method of Interior Joint with Different Depth Beams in RC Frame Structure*, Chang’an University, Xi’an, China, 2010.
- [15] G. Xing, Z. He, D. Niu et al., “Analytical model for shear strength of reinforced concrete beam-column-slab exterior joints,” *Journal of Central South University*, vol. 45, no. 9, pp. 3277–3282, 2014.
- [16] G. Xing, L. I. U. Bo-quan, and N. Di-tao, “Shear strength of reinforced concrete frame joints using modified softened strut-and-tie model,” *Engineering Mechanics*, vol. 30, no. 8, pp. 60–66, 2013.
- [17] S. J. Hwang and H. J. Lee, “Analytical model for predicting shear strengths of interior reinforced concrete beam-column joints for seismic resistance,” *ACI Structural Journal*, vol. 97, no. 1, pp. 35–44, 2000.

- [18] S. J. Hwang and H. J. Lee, "Analytical model for predicting shear strengths of exterior reinforced concrete beam-column joints for seismic resistance," *ACI Structural Journal*, vol. 96, no. 5, pp. 846–857, 1999.
- [19] J. Yang, *Study on Seismic Performance of High-Strength Concrete Columns with Multiple Composite Central Reinforcement*, Chang'an University, Xi'an, China, 2019.
- [20] M. Wakabayashi, K. Minami, Y. Nishimura et al., *Anchorage of Bent Bar in Reinforced Concrete Exterior Joints*, Japan Concrete Institute, Tokyo, Japan, 1983.
- [21] H. Omine, I. Sadamura, H. Yashiro et al., *Study on the Strengthening of Reinforced concrete Columns by central Reinforcing Steel Element*, Architectural Institute of Japan, Tokyo, Japan, 1999.
- [22] H. Kadoya, J. Kawaguchi, and S. Morino, *Experimental Study On Strength And Stiffness of Bare Type CFT Column Base With Central Reinforcing Bars*, American Society of Civil Engineers, Reston, VA, USA, 2006.
- [23] Framework Node Thematic Research Group, "Experimental study on shear strength of core area of reinforced concrete frame beam-column joints under low cyclic load," *Journal of Building Structures*, vol. 4, no. 6, pp. 1–17, 1983.
- [24] B. Liu, S. Huang, A. Zhou et al., "Experimental study on seismic behavior of eccentric beam-column joints in reinforced concrete frames," *Journal of Building Structures*, vol. 20, no. 5, pp. 50–58, 1999.
- [25] Q. Zheng, E. Fang, C. Ke et al., "Experimental study on seismic behavior of reinforced concrete large eccentric beam-column joints," *Journal of Building Structures*, vol. 20, no. 6, pp. 2–10, 1999.
- [26] S.-J. Hwang and H.-J. Lee, "Strength prediction for discontinuity regions by softened strut-and-tie model," *Journal of Structural Engineering*, vol. 128, no. 12, pp. 1519–1526, 2002.
- [27] D. Gao, K. Shi, and S. Zhao, "Calculation method for shear capacity of steel fiber reinforced concrete beam-column joints based on softened strut-and-tie model," *Journal of Civil Engineering*, vol. 47, no. 9, pp. 101–109, 2014.
- [28] GB/T50081-2019, *Standard for Test Methods of Concrete Physical and Mechanical Properties*, National Standard of the People's Republic of China, China Building Industry Press, Beijing, China, 2019.

Research Article

Improvement of Automatic Calculation Method of CASE Bearing Capacity

Guosong Liu  and Junlin Wang 

Faculty of Water Science and Engineering, Zhengzhou University, Zhengzhou 450001, China

Correspondence should be addressed to Junlin Wang; junlinwang@zzu.edu.cn

Received 29 July 2021; Revised 15 August 2021; Accepted 17 August 2021; Published 29 August 2021

Academic Editor: Zhiyong Chen

Copyright © 2021 Guosong Liu and Junlin Wang. This is an open access article distributed under the Creative Commons Attribution License, which permits unrestricted use, distribution, and reproduction in any medium, provided the original work is properly cited.

Because of the reliance on the empirical parameter CASE damping coefficient J_c , the high-strain CASE method is not recommended. The automatic bearing capacity calculation method RAU can avoid this, but it cannot be applied to friction piles. Based on the analysis of the automatic calculation method of bearing capacity RAU, considering the influence of pile side soil resistance unloading, this paper improved the RAU method through the influence of pile side soil damping on the velocity of the pile mass point during the stress wave propagation process. In this paper, we compare the collected static load test results of test piles with the improved automatic method results. The unary linear regression analysis is carried out with the help of statistical tools. The unary linear regression of the improved automatic method bearing capacity results on the static load test bearing capacity results is established. The improved automatic method solves the problem that the RAU method is only applicable to end-bearing piles and can be applied to the quality analysis and bearing capacity calculation of the high-strain curve of the driven pile.

1. Introduction

The pile is a columnar member that penetrates the soil, which is the main foundation form at present. An important content of pile foundation inspection is the bearing capacity inspection. There are two main technical routes to determine the bearing capacity of pile foundations: the static load method and the high-strain measurement method [1, 2]. In the static load method, the static load is set on the top of the foundation pile, and the Q-s curve and the bearing capacity of the foundation pile are obtained according to the applied static load and the measured pile settlement. The high-strain measurement method applies an impact load to the pile head and measures the stress and velocity-time history curve of the pile head to solve the bearing capacity of the pile by the wave theory.

The static load method test results are relatively more accurate and reliable. However, due to the long experiment period and high cost, the static load method can only select a few piles, and it is not easy to carry out large-scale inspections. Therefore, it is necessary to use a simple and fast

high-strain dynamic test method as a supplement to the static load method.

The modern commonly used high-strain measurement method originated from the wave equation method proposed by Smith [3] in the 1960s. After years of theoretical development and experience accumulation, many theoretical routes have been innovated and improved [4–17], resulting in forming two common methods have been formed: the CASE method and the measured curve fitting method [1, 2]. The CASE method is a closed solution method of the high-strain variation test method and simplifies the pile-soil conditions. It is assumed that the stress-strain relationship between the pile soil is ideally rigid and plastic, and the dynamic resistance is all concentrated on the pile tip, thereby decoupling the wave equation. This closed solution method is simple and fast and can generally provide real-time results on site, which is beneficial for pile driving monitoring and estimation of pile bearing capacity on site. The fitting method can be applied to more pile-soil conditions [18–31] and can simulate hysteresis damping, radiation damping, soil plugging effects, and various pile-soil

nonlinear problems, but the analysis requires high-quality software and highly skilled personnel. Therefore, more time is required on the machine for analysis and generally can only be completed when the test is completed and returned to the room.

Due to its complexity, the fitting method cannot be used to determine whether there is any problem in the process of driving piles by monitoring the process of driving piles, and it is not easy to estimate the bearing capacity quickly at the project site. Therefore, the CASE method is difficult to be completely replaced by a fitting method. However, the key parameter of the CASE method CASE damping coefficient J_c depends on human given, so many scholars have studied this.

In the 1970s, Rausche et al. [5, 6] concluded that the J_c value was related to the type of soil at the bottom of the pile through a large number of static and dynamic comparisons. The finer the soil particles, the larger the J_c value. The suggested values of J_c for different pile bottom soils are given above [5]. Fellenius et al. [32, 33] concluded that the J_c value of the CASE method is related to the type of pile, the test site, and the pile driving resistance through a dynamic and static comparison of four prefabricated steel piles in moraine soil. Holm et al. [34] compared the static and dynamic prestressed square piles in loose sand and found that the average value of J_c should be twice as high as that recommended by the PDI company established by Goble et al. Thompson and Goble [35] further found that if the J_c value is selected according to the general recommendations, the dynamic resistance in the sand is likely to be significantly underestimated, and the bearing capacity is too high. Although Wong [36] agreed that the CASE damping coefficient mainly depends on the type of soil below the pile and found that the actual selection of the J_c value was different from the recommended value in the United States, therefore, he believed that more dynamic and static comparisons are needed to reasonably select the J_c value.

Chinese scholars have also studied this topic. Chen [37] pointed out that when there is a lack of regional experience, long piles, large-diameter cast-in-place piles, and so on, due to their own characteristics and possible construction problems, it may affect the corresponding J_c value and reduce the accuracy of the bearing capacity judgment. Zai [38] believed that the J_c value is related to the dissipation of stress wave energy during propagation. Generally speaking, the longer the pile length, the higher the pile internal resistance and the greater the J_c value. Liwen [39] found that if the actually exciting pile displacement does not reach the elastic limit, the J_c value is related to the pile displacement. Ju [40] believed that the J_c value is also related to the geometry and size of the pile. Wu [41] pointed out that the J_c value of piles in soft soils should usually be appropriately increased to eliminate part of the side resistance.

Gradually, more and more people doubt whether the CASE damping coefficient has a clear physical meaning. Zhang and Sun [42] pointed out that the impedance Z in the definition of J_c is related to the state of the pile, so J_c cannot be only related to the nature of the soil at the bottom of the pile. According to the derivation of the formula, Liwen [39]

found that J_c was essentially only the ratio of the dynamic resistance to the total resistance, so as long as there is nonnegligible lateral resistance, the J_c value cannot be completely determined by the soil properties. Li [43] further pointed out that the approximate assumption of CASE is the key to the large variation range of the CASE damping coefficient and the ambiguity of its physical meaning. Xie [44] also agreed that there are contradictions between the approximate assumptions of the CASE method and its derivation process. To and Smith [45] found that the CASE damping coefficient J_c cannot be backanalyzed as a simple constant, which means that J_c must contain dynamic effects. Tchepak [46] also believed that changes in the actual pile-soil and construction techniques can affect J_c . Paikowsky and Stenersen [47] conducted a statistical analysis of the dynamic and static comparisons of various types of driven piles collected in the PD/LT-2000 database and found that the J_c value varies greatly, and many data seriously exceed the normal range of values. Despite so many years of development, the selection of the J_c value still relies heavily on the experience of the inspector.

In order to avoid the error caused by selecting the J_c value based on experience, the American PDI (Pile Dynamics, Inc.) company has been trying to find an algorithm to eliminate the dynamic resistance of the soil automatically and directly obtain the static resistance called bearing capacity. Automatic calculation method [7] is referred to as automatic method. Goble et al. proposed an automatic method suitable for end-bearing piles, which is represented by the computer symbol RAU. On the basis of RAU, this paper revised the RAU method through the analysis of RAU and the derivation of its influence on pile side resistance, making it able to be applied to friction piles, and its effectiveness is verified by statistical methods.

2. The Basic Theory of Wave Equation

Considering the pile as a one-dimensional continuous elastic bar, its vibration equation is

$$\frac{\partial^2 u}{\partial t^2} - C^2 \frac{\partial^2 u}{\partial x^2} = 0, \quad (1)$$

where $u(x, t)$ is the displacement of pile mass; $C = \sqrt{E/\rho}$ is the velocity of the stress wave; E is the elastic modulus; ρ is the density of pile body. By solving the equation, the travelling wave theory shows that the propagation of the stress wave can be regarded as the superposition of the ascending wave and the descending wave in the pile shaft.

The CASE method makes three basic assumptions as follows:

- (1) The pile body impedance is constant; except for the constant section, the pile body material is uniform without obvious defects.
- (2) When the stress wave propagates along with the pile, there is no energy loss or waveform distortion caused by other factors except the influence of soil resistance.

- (3) Only the dynamic damping of the soil at the bottom of the pile is considered and the dynamic damping of the soil at the side of the pile is ignored, and the static resistance is always constant. The static resistance of the soil to the pile has nothing to do with the displacement between the pile and soil but is only related to the existence of the relative displacement between the pile and soil.

Based on these three basic assumptions, the CASE calculation expression of the ultimate bearing capacity was derived using the travelling wave theory and wave equations to derive:

$$R = R_t - J_t ZV(L, t) \\ = (1 - J_c) \frac{[F(t_1) + ZV(t_1)]}{2} + (1 + J_c) \\ \times \frac{[F(t_1 + 2L/C) - ZV(t_1 + 2L/C)]}{2}, \quad (2)$$

where R_t is the total resistance; $Z = \rho CA$ is pile impedance; t_1 is the first calculation time and is generally the peak time of the velocity curve; and J_c is the CASE damping coefficient, generally related to the type of pile subsoil, which can be selected within a scope according to the actual situation. Rausche et al.'s recommendations are shown in Table 1 [5].

The CASE method assumes that the dynamic resistance is concentrated at the bottom of the pile. If the dynamic resistance on the side of the pile is indeed negligible, and the dynamic resistance is always proportional to the speed of the pile interface, then the dynamic resistance will not exist when the speed of the bottom of the pile is zero, RAU can be obtained. Based on this, when the bottom velocity of the pile is zero, the total dynamic resistance of the whole pile will be the static resistance; as long as the static resistance of all sections of the pile body is at its maximum value, the limit of the whole pile can be directly obtained. The pile tip velocity is

$$V_b(t) = \frac{1}{2Z} \left[F(t_1) + ZV(t_1) - F\left(t_1 + \frac{2L}{C}\right) + ZV\left(t_1 + \frac{2L}{C}\right) \right]. \quad (3)$$

The ultimate bearing capacity is the ultimate bearing capacity of the pile when velocity in (3) is equal to zero, and the influence of J_c will disappear completely.

It is apparently only when the pile is completely moved, the soil resistance at the side of the pile has little effect, the resistance of the soil does not decrease significantly, and the unloading of the soil at the side of the pile is not obvious that this value is suitable. In fact, it is easy to prove that when it is an end-bearing pile, the soil resistance on the side of the pile is almost zero, so when the speed of the pile tip is zero, the displacement and the static resistance are maximum. Therefore, at this time, the exact solution of bearing capacity is the maximum ultimate bearing capacity stimulated. For friction piles, when the pile tip speed is zero, due to the wave effect, the pile body's speeds have been negative values, and the pile side soil has been unloaded. Unloading of the pile

body caused the side resistance to decrease or even negative resistance, thus, offset to 0. Only in the upper and lower wave superimposed area of the pile body, due to the late unloading, the speed is slow, and there is still a certain lateral resistance. That is to say, the pile side soil resistance assumed by the RAU method can only be maintained near the pile tip, and the residual total resistance of the upper soil layer can be ignored due to unloading. Therefore, the soil resistance obtained by the RAU method is almost only the static soil resistance near the pile end, so we can use the static soil resistance on the upper side of the pile to modify the RAU method.

3. The Influence of Pile Side Soil Resistance on the Movement Speed of Pile Mass

Considering the influence of the pile side soil resistance [7], only the uniform foundation is considered here for the convenience of calculation, and the multilayer foundation is regarded as the superposition of multiple uniform foundations. Assuming that the pile is completely moved, adequate displacement is generated everywhere in the pile body, and the static resistance can be fully exerted. Before the stress wave propagates to the pile tip, the damping effect of the soil around the pile can be divided into two parts: static resistance using the static and plastic model and dynamic resistance using Newtonian viscous body model; the resistance per unit length of the pile body is

$$R = R_s + \eta \cdot Z \cdot V, \quad (4)$$

where R_s is the static resistance; V is the mass velocity; η is the damping coefficient. If the pressure and compression deformation are positive and the pile constitutive relation satisfies Hooke's law, the governing equation can be obtained:

$$\begin{cases} V = -\dot{\varepsilon}, \\ F = AE\varepsilon, \\ \rho AV = -F' - R_s - \eta ZV, \end{cases} \quad (5)$$

where “ $\dot{}$ ” means taking the derivative of space; “ $\dot{}$ ” represents the derivative with respect to time, so the corresponding characteristic line and compatibility relation are

$$\begin{cases} dx = \pm Cdt, \\ dF = \mp ZdV - R_s dx - \eta ZV dx. \end{cases} \quad (6)$$

For discontinuous waves, it still has

$$\begin{cases} dx = \pm Cdt, \\ [F] = \pm Z[V]. \end{cases} \quad (7)$$

After combining (6) and (7), the following can be obtained:

$$ZdV = -ZdV - R_s dx - \eta ZV dx. \quad (8)$$

It can be transformed as

TABLE 1: Goble et al.'s recommendations for J_c selection.

Type of pile subsoil	Pure sand	Silty sand and sandy silt	Silt	Silty clay and clay silt	Ball clay
J_c scope	0.05~0.20	0.15~0.30	0.20~0.45	0.40~0.70	0.60~1.10

$$2 \frac{dV}{dx} + \eta V + \frac{R_s}{Z} = 0. \quad (9)$$

This is an ordinary differential equation of first order. If the initial particle vibration velocity of each ground layer is V_0 , then its solution is

$$V(x) = \left(V_0 + \frac{R_s}{\eta Z} \right) e^{-(\eta/2)x} - \frac{R_s}{\eta Z} \quad (10)$$

This is an exponential function. Equation (10) shows that when the pile is completely moved, during the propagation of the stress wave, the peak velocity of the particles decays approximately exponentially as the depth increases.

4. Automatic Method of Bearing Capacity considering Soil Resistance of Pile Side

When the wave propagates to the pile tip, if the influence of the attenuation of the pile body internal resistance and the change of the pile side dynamic resistance with time is not considered, for any point e of the pile body, E is the time when the pile top corresponds to point e along the characteristic line. After propagating to point e for the first time, according to the feature line and the compatibility relationship on the feature line, the following equation can be derived:

$$\begin{cases} F_1 + ZV_1 = F_e + ZV_e + R, \\ F_E - ZV_E = F_e - ZV_e + R, \end{cases} \quad (11)$$

where F_1, V_1 are in the initial downlink wave state; F_e, V_e is point e state; R is the soil limit resistance above point e . During stress wave propagation, the pile velocity can be easily obtained:

$$V(x) = V_e = \frac{1}{2Z} (F_1 + ZV_1 - F_E + ZV_E). \quad (12)$$

Then, the computable expression form is

$$V(x) = \frac{1}{2Z} \left[f(t_1) + ZV(t_1) - f\left(t_1 + \frac{2x}{C}\right) + ZV\left(t_1 + \frac{2x}{C}\right) \right]. \quad (13)$$

Based on (13) and (10) combined with the formation situation, the reflected take-off point of the interval ending at the pile bottom can be calculated. After data fitting or substitution calculation, each stratum's average unit pile side static resistance value R_{si} and dynamic damping coefficient η_i can be obtained. The lateral resistance of the superposition area of upstream and downstream waves under the pile body has been included in the RAU method, so it is not calculated here.

Thus, the total soil static resistance on the upper side of the pile can be obtained:

$$R_{ss} = \sum R_{si} \cdot L_i, \quad (14)$$

where L_i is the thickness of the i th layer of foundation soil. The total static resistance is

$$R_s = RAU + R_{ss}. \quad (15)$$

5. Comparison of Automatic Method Results and Static Load Results

Based on the above theoretical derivation, the author selected some of the piles from the dynamic test of the China Steel Metal Products Quality Supervision and Inspection Center and some documents [48] to be completely moved by the heavy hammer, in which the pile body was not unloaded prematurely, and the pile bottom reflection was obvious. The driven piles are automatically calculated by the improved method in this paper. Moreover, the static load test results were analyzed by SPSS with one-variable linear regression [49]. The result of the automatic method is used as the independent variable, and the result of the static load test is used as the dependent variable. Because of the high accuracy of the static load test, the analysis results can be judged whether the results of the automatic bearing capacity calculation method in this paper can be used to predict the actual ultimate bearing capacity of the pile. The scatter plot of the ultimate bearing capacity results is shown in Figure 1.

The ratio statistics for automatic versus static methods are shown in Table 2.

The regression analysis results are shown in Tables 3 and 4.

The studentized residual plot is shown in Figure 2.

The regression equation can be obtained as $\hat{y} = 1.113x - 222.745$. Among them, the regression coefficient $\beta_1 = 1.113$, the regression coefficient is close to 1, and the tested t value is 22.992, Sig. ≤ 0.001 , suggesting that the regression coefficient is highly significant, and the static load test results are consistent with the unitary linear regression of the results calculated by the automatic method. As can be seen from Figure 2, all points are in the range of $(-3, 3)$ and there are no outliers. This indicates that the static resistance calculated by the automatic method in this paper is in good agreement with the static resistance obtained by the static load test, and the improved automatic method can be used to predict the ultimate bearing capacity of the pile foundation.

Because the distribution of residuals in the residual graph is abnormal, the curve regression is used to analyze and confirm again. The quadratic curve was used for regression analysis and compared with linear regression. The results of quadratic regression analysis are shown in Tables 5 and 6, and the model fitting diagram is shown in Figure 3.

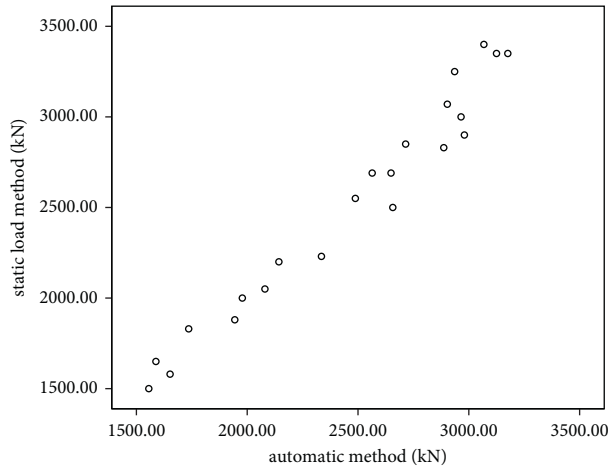


FIGURE 1: The bearing capacity relationship between automatic method and static load method.

TABLE 2: Ratio statistics.

Mean value	Median	Minimum	Maximum	Standard deviation	Coefficient of variation
0.984	0.980	0.902	1.063	0.047	0.040

TABLE 3: Anova.

Model	Sum of squares	df	Mean square	F	Sig.
Regression	7583612.335	1	7583612.335	528.623	<0.001
Residual	286919.483	20	14345.974		
Total	7870531.818	21			

TABLE 4: Coefficients.

Model	Unstandardized coefficients		Standardized coefficients	t	Sig.
	B	Std. error	Beta		
(Constant)	-222.745	121.821		-1.828	0.082
x	1.113	0.048	0.982	22.992	<0.001

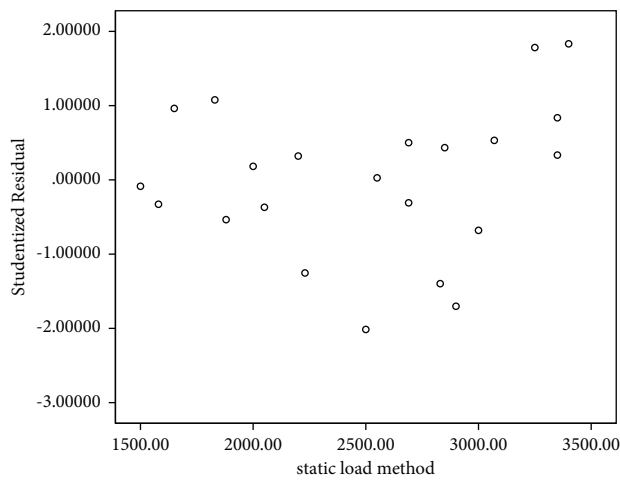


FIGURE 2: Studentized residual plot.

TABLE 5: Anova.

	Sum of squares	df	Mean square	F	Sig.
Regression	7616015.500	2	3808007.750	284.273	<0.001
Residual	254516.318	19	13395.596		
Total	7870531.818	21			

TABLE 6: Coefficients.

	Unstandardized coefficients		Standardized coefficients	t	Sig.
	B	Std. error	Beta		
x	0.276	0.540	0.244	0.512	0.615
x * * 2	<0.001	<0.001	0.741	1.555	0.136
Constant	715.047	614.351		1.164	0.259

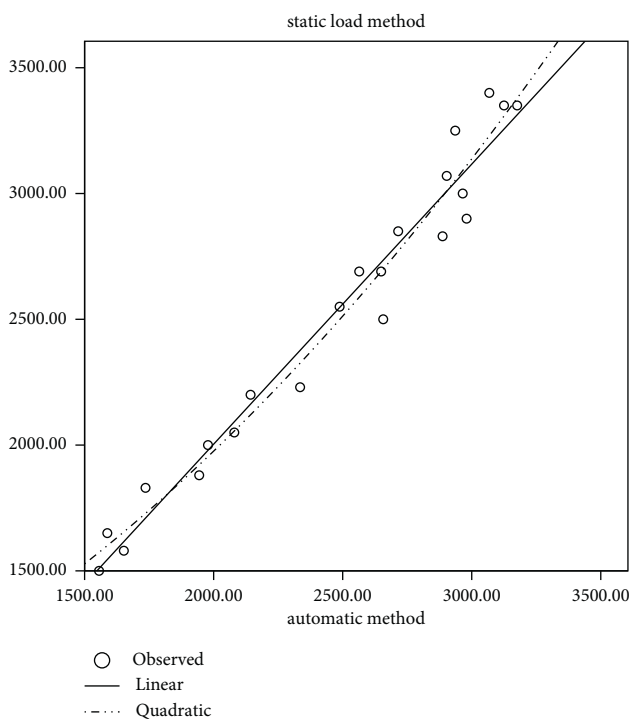


FIGURE 3: Model fitting diagram.

According to Table 3, the linear regression $SSE = 286919.483$, $SST = 7870531.818$. According to Table 5, the quadratic curve regression $SSE = 254516.318$, $SST = 7870531.818$. So, the coefficient of determination of the linear regression is less than that of the quadratic curve. It can be inferred that the fitting effect of the quadratic curve is better than that of linear regression. This means that with the increase of ultimate bearing capacity of the pile, the use of an improved automatic method will underestimate the bearing capacity. The reason for the analysis may be that the lateral friction resistance of the pile with high bearing capacity is relatively large in the pile as the data source in this paper. This indicates that when the lateral friction resistance of the pile is very large, the automatic method results in this paper will significantly underestimate the ultimate bearing capacity.

6. Conclusions

- (1) For the pile that is completely moved by the heavy weight and can produce sufficient penetration, the relationship between the velocity of the pile mass and the depth of the stress wave peak is an exponential function. Based on this relationship and the formula of the velocity of the pile mass, the ultimate static resistance of the soil around the pile can be obtained. Thus, the improved RAU automatic bearing capacity can be obtained.
- (2) In this paper, the results of the method in the improvement of the static load test results of regression effect are very good; this is because the regression coefficient is close to 1, and a good regression coefficient is 1, which means in this paper, the improved method of automatic static resistance is almost equal to the ultimate bearing capacity of the pile in this paper. The results of the improved method can be used automatically for driven pile bearing capacity estimation, the monitoring and controlling of the pile driving, and could be used to judge the quality of the high-strain dynamic test acquisition curve.
- (3) The improved automatic method is not suitable for piles with high bearing capacity, especially high side resistance.
- (4) In order to more accurately judge the effectiveness of the method for more pile types, it is better to conduct more data analysis.

Data Availability

The permeability and dissolution data used to support the findings of this study are included in the article. The foundation pile testing data used to support the findings of this study were supplied by Junlin Wang under license and so cannot be made freely available.

Conflicts of Interest

The authors declare that there are no conflicts of interest regarding the publication of this paper.

Acknowledgments

This research was funded by the National Natural Science Foundation of China, Grant no. 51978630.

References

- [1] MOHURD, JGJ106 - 2014, *Technical Code for Testing of Building Foundation Piles*, China Architecture & Building Press, Beijing, China, 2014.
- [2] ASTM, D4945-17, *Standard Test Method for High-Strain Dynamic Testing of Deep Foundations*, America, New York, NY, USA, 2012.
- [3] E. A. L. Smith, "Pile-driving analysis by the wave equation," *Journal of the Soil Mechanics and Foundations Division*, vol. 86, no. 4, pp. 35–61, 1960.
- [4] P. W. Forehand and J. L. Reese, "Prediction of pile capacity by the wave equation," *Journal of the Soil Mechanics and Foundations Division*, vol. 90, no. 2, pp. 1–25, 1964.
- [5] F. Rausche, G. G. Goble, and G. E. Likins, "Dynamic determination of pile capacity," *Journal of Geotechnical Engineering*, vol. 111, no. 3, pp. 367–383, 1985.
- [6] F. Rausche, F. Moses, and G. G. Goble, "Soil resistance predictions from pile dynamics," *Journal of the Soil Mechanics and Foundations Division*, SM9, vol. 98, no. 9, pp. 917–937, 1972.
- [7] X. Wang and S. Wu, *Dynamic Measurement Technology of Foundation Pile*, science press, Beijing, China, 2001.
- [8] X. Hu, S. Ma, and K. Wang, "Influence of positions of sensor on results measured on a high strain pile," *Journal of Vibration and Shock*, vol. 30, no. 4, pp. 259–264, 2011.
- [9] Y.-g. Zhang, J. Tang, Z.-y. He, J. Tan, and C. Li, "A novel displacement prediction method using gated recurrent unit model with time series analysis in the Erdaohe landslide," *Natural Hazards*, vol. 105, no. 1, pp. 783–813, 2020.
- [10] X. Ma, G. Zhu, L. Liu et al., "Response of saturated clay ground during pile driving," *Chinese Journal of Rock Mechanics and Engineering*, vol. 39, no. 1, pp. 205–216, 2020.
- [11] W. Jiang, G. Zhu, and J. Zhang, "A direct high-strain method for the bearing capacity of single piles," *Rock and Soil Mechanics*, vol. 41, no. 10, pp. 3500–3508, 2020.
- [12] Y. Zhang and L. Yang, "A novel dynamic predictive method of water inrush from coal floor based on gated recurrent unit model," *Natural Hazards*, vol. 105, no. 2, pp. 2027–2043, 2020.
- [13] X. Liu, S. Song, Y. Tan et al., "Similar simulation study on the deformation and failure of surrounding rock of a large section chamber group under dynamic loading," *International Journal of Mining Science and Technology*, vol. 31, no. 3, pp. 495–505, 2021.
- [14] Y. G. Zhang, Z. Zhang, and S. Xue, "Stability analysis of a typical landslide mass in the Three Gorges Reservoir under varying reservoir water levels," *Environmental Earth Sciences*, vol. 79, no. 1, pp. 1–14, 2020.
- [15] Y. G. Zhang, S. Y. Zhu, J. K. Tan, L. Li, and X. Yin, "The influence of water level fluctuation on the stability of landslide in the Three Gorges Reservoir," *Arabian Journal of Geosciences*, vol. 13, no. 17, 2020.
- [16] H. Jing, J. Wu, Q. Yin, and K. Wang, "Deformation and failure characteristics of anchorage structure of surrounding rock in deep roadway," *International Journal of Mining Science and Technology*, vol. 30, no. 5, pp. 593–604, 2020.
- [17] Y. G. Zhang, S. Y. Zhu, W. Q. Zhang, and H. Liu, "Analysis of deformation characteristics and stability mechanisms of typical landslide mass based on the field monitoring in the Three Gorges Reservoir, China," *Journal of Earth System Science*, vol. 128, no. 1, p. 1, 2019.
- [18] A. E. Holeyman, "Dynamic non-linear skin friction of piles," in *Proceedings of the international Symposium on Penetrability and Drivability of Piles*, vol. 1, pp. 173–176, San Francisco, CA, USA, August 1985.
- [19] M. F. Randolph, "Modeling of the soil plug response during pile driving," in *Proceedings of the 9th Southeast Asian Geotechnical Conference*, Bangkok, Thailand, December 1987.
- [20] S. L. Lee, Y. K. Chow, G. P. Karunaratne, and K. Y. Wong, "Rational wave equation model for pile-driving analysis," *Journal of Geotechnical Engineering*, vol. 114, no. 3, pp. 306–325, 1988.
- [21] R. Salgado, D. Loukidis, G. Abou-jaoude, and Y. Zhang, "The role of soil stiffness non-linearity in 1D pile driving simulations," *Géotechnique*, vol. 65, no. 3, pp. 169–187, 2015.
- [22] X. Hao, W. Du, Y. Zhao et al., "Dynamic tensile behaviour and crack propagation of coal under coupled static-dynamic loading," *International Journal of Mining Science and Technology*, vol. 30, no. 5, pp. 659–668, 2020.
- [23] Z. Zhang, M. Deng, J. Bai, S. Yan, and X. Yu, "Stability control of gob-side entry retained under the gob with close distance coal seams," *International Journal of Mining Science and Technology*, vol. 31, no. 2, pp. 321–332, 2020.
- [24] Y. Zhang, Y. Xie, Y. Zhang, J. Qiu, and S. Wu, "The adoption of deep neural network (DNN) to the prediction of soil liquefaction based on shear wave velocity," *Bulletin of Engineering Geology and the Environment*, vol. 80, no. 6, pp. 5053–5060, 2021.
- [25] Y. G. Zhang, J. B. Qiu, Y. Zhang, and Y. Y. Wei, "The adoption of ELM to the prediction of soil liquefaction based on CPT," *Natural Hazards*, vol. 107, no. 1, pp. 539–549, 2021.
- [26] Y. G. Zhang, X. Q. Chen, R. P. Liao et al., "Research on displacement prediction of step-type landslide under the influence of various environmental factors based on intelligent WCA-ELM in the Three Gorges Reservoir Area," *Natural Hazard*, vol. 107, no. 2, pp. 1709–1729, 2021.
- [27] R. Shakeri, A. Mesgouez, and G. Lefeuvre-Mesgouez, "Transient response of a concrete tunnel in an elastic rock with imperfect contact," *International Journal of Mining Science and Technology*, vol. 30, no. 5, pp. 605–612, 2020.
- [28] Y. Zhang, J. B. Qiu, Y. G. Zhang, and Y. L. Xie, "The adoption of a support vector machine optimized by GWO to the prediction of soil liquefaction," *Environmental Earth Sciences*, vol. 80, no. 9, 2021.
- [29] Y.-g. Zhang, J. Tang, R.-p. Liao et al., "Application of an enhanced BP neural network model with water cycle algorithm on landslide prediction," *Stochastic Environmental Research and Risk Assessment*, vol. 35, no. 6, pp. 1273–1291, 2021.

- [30] L.-K. Chen, R.-P. Yuan, X.-J. Ji et al., "Modular composite building in urgent emergency engineering projects: a case study of accelerated design and construction of Wuhan Thunder God Mountain/Leishenshan hospital to COVID-19 pandemic," *Automation in Construction*, vol. 124, Article ID 103555, 2021.
- [31] L.-K. Chen, P. Liu, L.-M. Zhu, J.-B. Ding, Y.-L. Feng, and F. Moreu, "A simplified iterative approach for testing the pulse derailment of light rail vehicles across a viaduct to near-fault earthquake scenarios," *Proceedings of the Institution of Mechanical Engineers - Part F: Journal of Rail and Rapid Transit*, Article ID 095440972098741, 2021.
- [32] B. H. Fellenius, "The analysis of results from routine pile load tests," *Ground Engineering*, vol. 13, no. 6, pp. 19–31, 1980.
- [33] B. H. Fellenius, A. J. O'Brien, R. E. Riker et al., "Dynamic monitoring and conventional pile testing procedure," *A Program Presented in Symposium Dynamic Measurement of Piles and Piers*, pp. 1–24, 1983.
- [34] G. Holm, M. Jansson, and B. Moller, "Dynamic and static load testing of friction piles in loose sand," in *Proceedings of the 2nd International Conference on the Application of Stress Wave Theory to Pile Foundation*, pp. 240–243, Stockholm, Sweden, May 1984.
- [35] C. D. Thompson and G. Goble, "High case damping constants in sand," in *Proceedings Of the 3rd International Conference On the Application Of Stress Wave Theory To Pile Foundation*, pp. 555–556, Ottawa, Canada, May 1988.
- [36] P. K. Wong, "The use of pile driving analyzer at a hospital complex in Malaysia," in *Proceedings of the 3rd International Conference on the Application of Stress Wave Theory to Pile Foundation*, pp. 762–770, Ottawa, Canada, May 1988.
- [37] F. Chen, "FEIPWAPC pile wave analysis program using characteristics," *Chinese Journal of Geotechnical Engineering*, vol. 12, no. 5, pp. 65–75, 1990.
- [38] J. Zai, "Pile dynamic testing experiences in Shanghai," in *Proceedings Of the 3rd International Conference On the Application Of Stress Wave Theory To Pile Foundation*, pp. 781–792, Ottawa, Canada, May 1988.
- [39] K. Liwen, "PDA-case dynamic pile test study," *Chinese Journal of Geotechnical Engineering*, vol. 13, no. 2, pp. 41–50, 1991.
- [40] Q. Ju, "Determination of bearing capacity of single pile by CASE method of high strain dynamic test pile," *Geotechnical Engineering*, vol. 5, no. 2, pp. 34–39, 1993.
- [41] Z. Wu, *Development and Application of PDA Power Test Pile Method in Guangdong*, *Pile Foundation Album*, pp. 540–542, Shanxi University Union Press, Taiyuan, China, 1992.
- [42] L. Zhang and J. Sun, "Dynamic measurement and CAPWAPC analysis of large diameter overlong pile in shanghai Area," in *Proceedings of the 1990 Proceedings Of the Workshop on PDA Development Applications*, pp. 280–296, Shanghai, China, 1990.
- [43] D. Li, "On the Application Limitations of High Strain Dynamic Test Pile Method," *Testing Technology Of Pile Foundation Engineering*, pp. 88–95, China Building Materials Industry Press, Beijing, China, 1993.
- [44] L. Xie, "An analysis on the nature of CASE method and on the cause of underestimated pile load capacity by this method," *Chinese Journal of Geotechnical Engineering*, vol. 21, no. 1, pp. 46–51, 1999.
- [45] P. To and I. M. Smith, "A note on finite element simulations of pile driving," *International Journal for Numerical and Analytical Methods in Geomechanics*, vol. 12, no. 2, pp. 213–219, 1988.
- [46] S. Tchepak, "Dynamic and sonic pile integrity testing-A contractor's experience," in *Proceedings of the 4th International Conference on the Application of Stress Wave Theory to Pile Foundation*, pp. 339–344, Hague, Netherlands, September 1992.
- [47] S. G. Paikowsky and K. L. Stenersen, "The performance of the dynamic methods, their controlling parameters and deep foundation specifications," in *Proceedings of the 6th International Conference on the Application of Stress Wave Theory to Pile Foundation*, pp. 281–304, Sao Paulo, Brazil, September 2000.
- [48] Committee of Soil Dynamics, *Application Case and Analysis of Soil Dynamic Engineering*, China Construction Industry Press, Beijing, China, 1998.
- [49] G. Molloy, *Regression Analysis and Linear Models*, Larsen and Keller, New York, NY, USA, 2018.